

ASTER-BASED LITHOLOGIC AND ALTERATION MAPPING IN KHETRI COPPER BELT, INDIA

A THESIS

*Submitted in partial fulfilment of the
requirements for the award of the degree*

of

DOCTOR OF PHILOSOPHY

in

EARTH SCIENCES

By

ASHISH MISRA



DEPARTMENT OF EARTH SCIENCES
INDIAN INSTITUTE OF TECHNOLOGY ROORKEE
ROORKEE-247 667 (INDIA).

MAY, 2008

**© INDIAN INSTITUTE OF TECHNOLOGY ROORKEE, ROORKEE, 2008
ALL RIGHTS RESERVED**

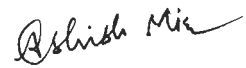


INDIAN INSTITUTE OF TECHNOLOGY ROORKEE ROORKEE

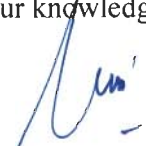
CANDIDATE'S DECLARATION


I hereby certify that the work which is being presented in the thesis entitled **ASTER-BASED LITHOLOGIC AND ALTERATION MAPPING IN KHETRI COPPER BELT, INDIA** in partial fulfilment of the requirements for the award of the degree of Doctor of Philosophy and submitted in the Department of Earth Sciences of the Indian Institute of Technology Roorkee, Roorkee is an authentic record of my own work carried out during a period from January 2003 to May 2008 under the supervision of Dr. Ravi P. Gupta, Professor, and Dr. Amit K. Sen, Associate Professor, Department of Earth Sciences, Indian Institute of Technology Roorkee, Roorkee.

The matter presented in this thesis has not been submitted by me for the award of any other degree of this or any other Institute.


(ASHISH MISRA)



This is to certify that the above statement made by the candidate is correct to the best of our knowledge.



(Ravi P. Gupta)
Supervisor


(Amit K. Sen)
Supervisor

Date: 23rd May, 2008

The PhD Viva-Voce Examination of **Mr. Ashish Misra**, Research Scholar, has been held on 20/10/2008.

 
Signature of Supervisors


Signature of External Examiner

To the Spirit of Human Knowledge

ॐ

आ नो भद्राः क्रतवो यन्तु विश्वतः ॥५॥
- ऋग्वेद

Let noble thoughts come to us from all sides.
- *Rigvéda*

Abstract

The thesis presents a detailed account of the analysis of an ASTER dataset of a mineralized region in northwest India, the Khetri Copper Belt. ASTER acquires data in the geologically important wavelength regions of the electromagnetic spectrum, namely the visible-near-infrared-through-shortwave-infrared (VNIR-SWIR; 0.5-2.5 μm), and the thermal-infrared (TIR; 8.0-11.5 μm) in 14 discrete strategically selected spectral bands. Most alteration minerals related to various kinds of mineralization have characteristic spectral signatures in the solar reflective VNIR-SWIR region. Important rock forming silicate minerals, like quartz and feldspar, have diagnostic spectral features in the TIR wavelength region. ASTER data of the study area in these two spectral regions have been digitally processed to map the lithologies and surface/alteration mineral assemblages, using existing and improved methods of image processing. The TIR data has been processed to map lithology and the VNIR-SWIR data has been used to map surface/alteration minerals.

KCB is a structurally complex and regionally metamorphosed NNE-SSW striking linear polymetallic-sulfide mineralized belt consisting primarily of early Proterozoic metasedimentary rock units, and late Proterozoic basic and acidic intrusives. The older psammitic Alwar Group (mainly pure and impure quartzites, and micaceous quartzites), and younger pelitic Ajabgarh Group (mainly phyllites, schists, impure marbles and calc-silicate units) comprise the main lithostratigraphic units of KCB; along with many small stocks, sills and dikes of granite, dolerite and amphibolite. The study area is marked by a prominent NNE-SSW striking cataclastic/shear zone along which numerous felsic (granitic and pegmatitic) intrusives are emplaced. Small, but significant sulfide mineralization, and associated rock alteration close to the surface in a few places and in vicinity of these intrusives are observed. Previous TM-based remote sensing studies in a part of the study area have indicated anomalous zones of OH^- alteration. This study has been designed to investigate the extent to which ASTER can improve

the existing understanding of the alteration patterns of the area and the associated lithologic units. Ground truth in the form of fieldwork, and laboratory analyses (thin-section petrography and trace-metal geochemistry) of selected field samples have been used to validate the results of ASTER data analysis.

Retrieval of reflectance and emissivity information from the at-sensor radiance data has involved an assessment of various radiometric, atmospheric and topographic correction methods and selecting the best technique for use in spectral processing. Best atmospheric correction for the 9-band VNIR-SWIR data has been achieved using a hybrid approach which is based on enhancement of MODTRAN-based atmospheric correction through Modified Flat-Field correction of the result. This has served as the basic data in spectral processing for surface/alteration mapping objective. The standard Level 2 surface emissivity product has been used in the detailed spectral processing for the lithologic mapping objective.

ASTER TIR at-sensor radiance and surface emissivity data have been used to produce the surface lithologic maps of the study area. Decorrelation stretch processing and lithologic indices calculated using the TIR radiance data for quartz-rich and mafic-rich rocks have provided best qualitative lithologic discrimination. Full spectral processing of the surface emissivity data has produced a lithologic map of the area with the major lithologic units classified into six classes: namely, 'mica schist', 'felsic granite', 'mafic diabase', 'pink quartzite', 'brown to dark brown sand', and 'brown to dark brown sandy loam', based on the matches of the image-derived end-member spectra with the reference spectral library spectra (Johns Hopkins University spectral library). Two approaches for quantitative silica abundance estimation have been investigated. Method 1 is based on the spectral modeling of the surface-emissivity spectra; whereas Method 2 is based on Metal Mining Agency of Japan's (MMAJ) original 'K-value' method. The two results have subsequently been compared in specific context of the study area. Results of the analysis indicate a general overall correspondence with the reported and mapped lithologic units of the study area.

The VNIR-SWIR reflectance data have been used to generate surface/alteration mineral distribution maps for the study area. A number of minerals have been mapped through different approaches, which involved use of band ratios, relative absorption band depth images (RBDs), Feature-oriented Principal Components Selection (FPCS) technique, spectral indices, and Boolean logical operator-based alteration group mapping. The full spectral processing of the reflectance data has helped in unique identification and mapping of a variety of surface/alteration mineral species based on spectral matches with a reference spectral library spectra (United States Geological Survey spectral library; speclib05).

Validation of the results of ASTER-based spectral lithologic and alteration mapping based on the ground-truth has revealed that despite its multispectral nature, ASTER data can provide valuable and reliable surface lithologic and mineral maps which can be directly used in prospecting for mineral deposits.

Acknowledgement

To the Almighty: For being my Ultimate Friend!

Like everyone else who passes through the thick and thins of PhD research, its challenges and vicissitudes, joys of discovery and triumph over seeming dead-ends; as I come to placing on record my gratefulness to the people whose variously tendered help and support has enabled me to see my work to fruition, I too am filled with a multitude of emotion! This acknowledgement is an expression of both reverence and fervency.

To begin, and indeed so, I offer my sincerest thanks to my PhD supervisors Dr. Ravi P. Gupta and Dr. Amit K. Sen. I thank Dr. Ravi P. Gupta for accepting me under his guidance and introducing me to the wonderful world of geological remote sensing. Even as I recognize that I have not truly been the kind of a student he wanted, his unfailing support towards whatever little I am worth has been instrumental in keeping my self-confidence healthy. I also wish to acknowledge him for his critical assessments, immaculate observation, open-hearted support and mentoring. On the other hand, Dr. Amit K. Sen has provided me the kind of emotional support I needed the most. His innate abilities of composure and forbearance are some of the real-life lessons I have gained immensely from. I wish to thank him for his caring support, for keeping me focused and steady, for his belief that my work is special and important, and thus, for keeping my own faith alive!

I would like to thank the Heads of the Department of Earth Sciences, IIT Roorkee, during the tenure of my research, namely: Dr. B. Parkash, Dr. V.N. Singh, and Dr. Ravi P. Gupta for their academic help and encouragement. I also wish to thank the Deans of Post Graduate Studies and Research, IIT Roorkee, namely: Dr. A.K. Awasthi, Dr. R.N. Goyal, and Dr. H.O. Gupta for their administrative and indirect, yet crucial, help all through this time.

Before I had decided to arrive at IIT Roorkee to continue my studies and take up PhD research, three persons kindled in me a love for the science and art of geology, namely: Dr. Salil Agarwal, Dr. M. K. Pandit, and Dr. R.S. Sharma, all at the Department of Geology, University of Rajasthan. I wish to thank them for showing their trust in my abilities and pushing me forward to explore the best and the unknown.

My special thanks are due for Dr. R.M. Manickawasagam, former Head of the Institute Instrumentation Centre, IIT Roorkee; Dr. R. Krishnamurthy, Associate Professor, Dept. of Earth Sciences, IIT Roorkee; Dr. R.S. Goel, former Deputy Director General, Geological Survey of India, Western Region, Jaipur; and Dr. Sunil Solanki, Senior Manager (Geology),

Hindustan Copper Limited, Khetri Nagar, Jhunjhunu, for sharing their valuable and useful field experience and knowledge on Khetri Copper Belt, and showing interest in my work.

My stay in IIT Roorkee might have become less meaningful and exciting but for the opportunity to serve as the Assistant Warden (residential), at Cautley Bhawan, IIT Roorkee for about 3 ½ years. Apart from the regular research-work, this additional role has been one of the most enriching, rewarding and satisfying experience of my stay at IIT Roorkee. The exceptional love and warmth of the Bhawan staffers has perennially bolstered my self-esteem and honed my personality as a complete and responsible person. There are too many of them to name, but they all command my heartfelt and warm gratitude. For providing me this opportunity I would like to thank the Deans of Students' Welfare, IIT Roorkee, Dr. Ranvir Singh and Dr. V.K. Gupta, and the Chief Wardens of Cautley Bhawan, Dr. N.K. Goel, and Dr. R.P. Saini. I wish to especially thank Dr. R.P. Saini for showing his continued and fatherly support and concern towards my research work.

During this research many people have knowingly and unknowingly, and directly and indirectly provided critical technical help. Among them, I wish to acknowledge Sh. Biswajayee Airaraj Patra, for his help with the ICP-MS analysis of field samples; Sh. Sanjay Gupta, for providing copies of important software; and Dr. Ravi Gupta, for his crucial help in MATLAB programming.

For being the most direct source of inspiration and support, I would like to thank my former lab seniors, namely: Dr. Ashis K. Saha, University of Delhi; Dr. Umesh K. Haritashya, University of Nebraska at Omaha, USA; and Dr. D.P. Kanungo, Central Building Research Institute, Roorkee.

Friends make life interesting and fun. They also serve as harmonizers and pillars of support. For friendly support, concern, inquisition, and inspiration I would like to thank my former colleagues: Dr. Harish Gupta, Dr. Vivesh Vir Kapur, Dr. Balaji Bhosle, Dr. Narendra Meena, Dr. Ranjan Deka, Dr. Bikash Sahoo and Dr. Uday Singh.

For a special band of friends – Vishnu, Deepmala, Vineeta, Gunjan, Mrunalini and Archana – who made every moment of my stay in Roorkee full of laughter and helped me to counter the inadvertent tensions of research through evening get-togethers and much relished 'ludo' sessions, there goes a very warm Thank You!

My former and current lab mates and department friends – Aniket Chakraborty, Vivek Bastariya Sharma, Lekh Raj, Ratan Samadder, Arundhati Biswas, Prabhu Prasad Das, Aparna Shukla, and Nisha Rani are acknowledged for their congeniality, friendliness and ready help. I wish to particularly thank Aparna for her most diligent and genuine interest and concern

towards my work. I don't think I would have been able to reach this end without her moral, emotional, physical and spiritual support. No word can fully express how fortunate I feel to have her with me.

My line of friends I am grateful towards is rather long, but I cannot let this become an excuse for not mentioning their names. The shaping of me as who I am, is to a large extent a reflection of how blessed I have been to discover some truly wonderful friendships. Pawan, Himanshu, Prashant, Rahul, Anurag, Alok, Apoorva, Nitin, Sandeep, Rajiv, and Tej Bahadur Bhaiya – these names have been my understanding of selfless love, support, and meaning of 'friendship'. I thank them all from the core of my heart!

I wish to thank François Blondeau, a very special friend, for his sincere worries, unflinching support and faith, encouragement, advice and motivation through countless long-distance and prolonged telephone calls, all the way from Paris.

This part comes at the closing of this space, but it is here that my heart becomes truly overwhelmed! No words can sufficiently describe how it feels to have such wonderfully exceptional family as mine. My two sisters, their husbands and in-laws, and my cute-sweet nephew Sanu have forever remained the people I can back on, anytime. I wish to thank them for all of their love, care, concern, persistence, faith and admiration.

Papa-Mummy, this acknowledgement is actually all of your own! It is to you that I owe the most and first. Thank you for your patience in allowing me to stay away from you. You know as well as I, that this overstretched period has been a real test not only for me, but for you too. No statement can be an extravagant emotional overture of how blessed I feel to have you as my parents. This work could have neither started, nor seen this light but for your blessings, love, emotional support and true concern.

Thank you, all!

May, 2008
Roorkee

Ashish Misra

Contents

	<u>Page No.</u>
Abstract	i
Acknowledgement	v
Contents	ix
List of Figures	xiii
List of Tables	xxiii
Chapter 1: Introduction	1
1.1 General Background	1
1.2 Indian scenario and motivation	3
1.3 Study area and adopted approach	3
1.4 Scope and objectives	5
1.5 Scientific Impact	6
1.6 Organization of the thesis	8
Chapter 2: Study Area – Regional and Local Geology	9
2.1 Khetri Copper Belt: An Overview	9
2.1.1 Review of the geological literature on KCB	10
2.1.2 Geology of the North Khetri Copper Belt (NKCB)	11
2.2 Study area: location, accessibility, physiography and geology	15
2.2.1 Location	15
2.2.2 Accessibility	15
2.2.3 Physiography, climate and vegetation	15
2.2.4 Geology	21
2.2.4.1 Structure	23
2.2.4.2 Lithology	23
2.3 Distribution of known mineralization	25
2.4 Surface indicators of mineralization: gossans and alterations	28
2.5 Ore localization and metalogenesis: focus on lithologic controls	30
Chapter 3: Data and Methodology	33
3.1 Introduction	33
3.2 Remote sensing image data	33
3.3 Ancillary data and creation of a GIS database	35
3.4 Field and laboratory data	37
3.5 Software tools	37
3.6 Methodology overview	38

Chapter 4: Field and Laboratory Studies – Petrography and Geochemistry	41
4.1 Statement of purpose	41
4.2 Area selection and definition of analytical objectives for field and laboratory studies	41
4.3 Field studies	45
4.3.1 Representative litho-units	45
4.3.2 Mineralized areas	45
4.4 Macroscopic and microscopic petrography	48
4.4.1 Sampling	48
4.4.2 Representative rocks	52
4.4.3 Altered rocks	56
4.5 Trace-metal geochemistry	61
4.5.1 Sample preparation: weathered and fresh samples	61
4.5.2 Instrumentation and calibration	63
4.5.3 Results	64
4.5.3.1 Representative litho-units	64
4.5.3.2 Regional anomaly, Kalota	65
4.5.3.3 Mineralized areas	67
 Chapter 5: Infrared Spectroscopy and Geologic Remote Sensing – Theory, Background and ASTER Application	 73
5.1 Introduction and scope	73
5.2 Electromagnetic radiation and geologic remote sensing	74
5.3 Infrared spectroscopy of minerals and rocks	76
5.3.1 Electronic processes	78
5.3.2 Vibrational processes	80
5.4 Literature review: Geologic remote sensing for lithologic/mineral mapping and mineral exploration	88
5.4.1 Developments in sensor and data processing technology	89
5.4.2 Multispectral remote sensing for mineral exploration: Legacy of Landsat	90
5.4.3 Hyperspectral remote sensing for mineral identification and mapping: AVIRIS and others	92
5.4.4 Application of ASTER data in lithologic/mineral mapping for resource exploration	93
 Chapter 6: Data Preprocessing – Atmospheric and Topographic Corrections	 95
6.1 Introduction and statement of purpose	95
6.2 Atmospheric Correction	96
6.2.1 Overview	96
6.2.2 ASTER L2 VNIR-SWIR surface reflectance data and its evaluation	101
6.2.3 Atmospheric correction of ASTER LIB data	103
6.2.3.1 Radiometric and geometric corrections	105
6.2.3.2 Atmospheric correction of ASTER VNIR-SWIR data	111

and reflectance retrieval	
6.2.3.2.1 Methods of relative atmospheric correction	111
6.2.3.2.2 Methods of absolute atmospheric correction	113
6.2.3.2.3 Discussion on atmospheric correction results	119
6.2.3.2.4 Hybrid FLAASH+MFF correction	120
6.2.3.3 Atmospheric correction of ASTER TIR data to retrieve surface radiances	121
6.2.3.3.1 Radiance recalibration	122
6.2.3.3.2 ISAC Correction	123
6.3 Topographic correction	125
6.3.1 A brief review of existing techniques	125
6.3.2 C-correction of ASTER VNIR-SWIR surface reflectance image data	127
6.4 ASTER TIR surface emissivity retrieval	133
6.4.1 Theoretical Background	133
6.4.2 Review of the existing techniques for separation of T and ϵ	134
6.4.3 Computation of the surface emissivity image of the study area	136
6.4.4 ASTER Level 2 standard surface emissivity product (AST_05): TES algorithm	137
6.4.5 Selection of the final surface emissivity data	138
Chapter 7: ASTER TIR Data Processing for Lithologic Mapping	141
7.1 Statement of Purpose and Introduction	141
7.2 Lithologic mapping using ASTER TIR data	141
7.2.1 ASTER TIR Decorrelation Stretch	143
7.2.2 Quartz, carbonate and mafic indices	147
7.2.3 Spectral processing of ASTER TIR surface emissivity data	151
7.2.3.1 MNF transformation	153
7.2.3.2 PPI and end-member selection	157
7.2.3.3 End-member identification using ENVI Spectral Analyst™	161
7.2.3.4 SAM classification	167
7.2.3.5 MTMF™ processing and classification	171
7.3 Silica weight percent estimation using ASTER TIR surface emissivity data	177
7.3.1 Theory and previous studies	178
7.3.2 Spectral modeling of TIR emissivity spectra	181
7.3.3 The K-value method	197
7.3.4 Comparison of silica weight percent mapping results	205
7.4 Note on the effects of spatial resolution, vegetation and surface coatings on ASTER-based lithologic mapping	205
Chapter 8: ASTER VNIR-SWIR Data Processing for Alteration Mapping	207
8.1 Statement of purpose	207
8.2 Spectral characteristics of target alteration minerals	208
8.3 ASTER VNIR-SWIR surface reflectance data processing	215
8.3.1 Band composites	216
8.3.2 Decorrelation stretch images	221

8.3.3 Band ratios, RBD images, and ratio composites	225
8.3.4 PCA and FPCS processing for alteration mineral mapping	237
8.3.5 ASTER SWIR spectral indices	245
8.3.6 Argillic and Phyllic alteration mapping using Boolean logical algorithms	249
8.4 ASTER VNIR-SWIR full spectral mapping of alteration minerals	255
8.4.1 Preparation of a vegetation mask	256
8.4.2 Determination of target spectra	258
8.4.3 End-member identification	259
8.4.4 SAM classification	283
8.4.5 MTMF™ processing	293
8.5 Spectral classification limitations and linear mixing	299
Chapter 9: Synthesis of Results and Interpretation	301
9.1 Statement of purpose and introduction	301
9.2 Validation of spectral mapping results	302
9.2.1 Spectral lithologic mapping	303
9.2.2 Spectral surface/alteration mineral mapping	310
9.3 Relating trace-metal anomalies with ASTER spectral maps	323
Chapter 10: Summary and Conclusions	329
References	351
Appendix A	369
Appendix B	373
Appendix C	377
Appendix D	381

List of Figures

<u>Figure No.</u>	<u>Caption</u>	<u>Page No.</u>
Figure-1.1:	Interdependencies of the chapters in the thesis.	7
Figure 2.1:	Location and generalized geological map of the Khetri Copper Belt (modified after Heron, 1923)	13
Figure-2.2:	Some important places in the study area. The background is a hill-shaded image of the study area, derived from a digital elevation model (DEM). Inset is a shaded relief map of the Indian subcontinent showing study area location.	17
Figure-2.3:	Compiled reference lithological map of the study area (after GSI, 1997 and Gupta, 1974).	19
Figure-3.1:	Overview of the research methodology adopted in the study.	40
Figure-4.1:	Landsat-5 TM 7/5 ratio; the regional alteration anomaly interpreted on the above image occurs as a semi-circular dark zone just north of Kalota, shown by a yellow ellipse.	43
Figure-4.2:	Field view of the interpreted regional anomaly; camera is facing due west. Note the tonal differences in soil color.	43
Figure-4.3:	Distribution of field samples analyzed petrographically and geochemically. The background is a perspective view of the study area (ASTER band 3 draped over DEM) facing due North. Sample locations are marked in red; prominent places within the study area have been demarcated, including the three main areas of mineralization.	53
Figure-4.4:	Hand specimen photographs and photomicrographs of the main rock types in the study area: a. Arkosic quartzite; b. Pure quartzite; c. Banded amphibole feldspathic quartzite; d. Orthoamphibolite; e. Calc-silicate (actinolite marble); f. Andalusite-biotite schist; and g. Granite. Photomicrographs have been taken with a 50x objective; the top/left photomicrograph is in plane polarized light and the one on the bottom/right is in crossed polars. Hand specimens have been cut across to reveal fresh surfaces and banding, if present.	54
Figure-4.5:	Hand-specimen photographs and photomicrographs of samples collected from mineralized and altered areas. The scheme of photomicrographs is the same as in Figure-4.4. Description about the samples has been given in the text.	58-59
Figure-4.6:	Procedure of sample preparation for trace-metal analysis through ICP-MS	62
Figure-4.7:	The PerkinElmer® Elan® 9000 ICP-Mass Spectrometer	63

Figure-4.8:	Trace-metal concentrations in the eight representative rock types of the area. For the rock types corresponding to the sample IDs given in the legend, see Table-4.2.	65
Figure-4.9:	a. Locations of the samples within the regional anomaly; Concentrations of 6 metallic elements in: b. relatively fresh cores of the samples, and c. weathered surfaces.	66
Figure-4.10:	Relative comparison of metal (Cu) enrichment in the fresh and weathered parts of the samples collected from the regional anomaly towards the north of Kalota; it can be observed that the regolith is generally enriched in Cu.	67
Figure-4.11:	Trace-metal values for: (a) fresh and (b) weathered parts of the samples collected adjacent to the Akwali underground mines. Except samples B/4 and B/5, which are andalusite-mica schist samples, remaining samples are all of orthoamphibolite.	68
Figure-4.12:	Arsenic content of the regolith and fresh parts of the analyzed Akwali samples.	69
Figure-4.13:	a. Sampling pattern; and b. Trace-metal distribution in the samples from Suredi ki Dhani area.	70
Figure-4.14:	a. Sampling pattern; and b. Trace-metal distribution in the samples from Tutiwali-Ladniwali gossanized zone.	71
Figure-4.15:	a. Sampling pattern; and b. Trace-metal distribution in the samples from Bilaiwali.	72
Figure-5.1:	Sources of EMR for remote sensing and atmospheric transmission (modified after Lillesand and Kiefer, 2000).	75
Figure-5.2:	Spectral signature diagram of a variety of geologic materials (from Hunt, 1977)	77
Figure-5.3:	Spectra of minerals with diagnostic features in the VNIR region of EM spectrum resulting due to electronic processes. Labeled arrows indicate specific absorption features due to conduction band (CB), crystal field (CF) or charge transfer (CT) effects. Spectra have been taken from USGS spectral library (speclib05; Clark et al., 2003).	80
Figure-5.4:	Examples of mineral spectra with features in SWIR region of the EM spectrum related to OH ⁻ and H ₂ O molecules, indicated by arrows. Spectra have been taken from USGS spectral library (speclib05; Clark et al., 2003).	82
Figure-5.5:	Examples of mineral spectra in the SWIR region exhibiting diagnostic absorption features (indicated by arrows) due to metal-O-H stretching (a) and (b), and CO ₃ ²⁻ (b). Spectra have been taken from USGS spectral library (speclib05; Clark et al., 2003).	85
Figure-5.6:	Diagram illustrating the location of features and the type of	85

vibrational process responsible for the spectral features for silicates in the TIR region (after Hunt, 1980).

- Figure-5.7: Examples of silicate mineral spectra with emissivity features in the TIR. Spectral features are related to Si-O stretching vibrations within the silicate crystal structure and shift to longer wavelengths with increasing isolation of the SiO₄ tetrahedra. For discussion, refer to the text. Spectra have been taken from Arizona State University (ASU) thermal emission spectral library. 87
- Figure-6.1: Solar irradiance on top of atmosphere and in Earth's surface: absorption by major atmospheric constituents results in selective transmittance of specific wavelengths, leaving only a part of the EM spectrum amenable to orbital remote sensing (after Chahine, 1983) 98
- Figure-6.2: ASTER data calibration and surface reflectance/emissivity retrieval; processing flow for atmospheric and topographic correction 104
- Figure-6.3: Result of crosstalk correction of ASTER SWIR bands: *a* shows the corrected SWIR bands 4-6-8 in RGB; the raw SWIR radiance-at-sensor continuum-removed spectrum of the sample pixel (marked by a yellow diamond symbol on the image) is shown in *b*, and the spectrum of the same pixel after crosstalk correction is shown in *c*. Notice the false absorption feature in band 8 of the uncorrected data, and its removal after correction. Difference between the two spectra is shown in *d*. ASTER SWIR band-centers have been marked in the plots. Radiance units are Wm⁻² sr⁻¹ and the wavelength is in micrometers 109
- Figure-6.4: Comparison of the spectra of the test pixel obtained after application of the various atmospheric correction procedures, viz. (a) Log Residuals, (b) Internal Average Relative Reflectance, (c) Flat Field, (d) Modified Flat Field, (e) Empirical Line, (f) FLAASH, (g) Top of Atmosphere apparent reflectance model, and (h) Dark Object Subtraction (Chavez) method. The JHU library spectrum of the material constituting the pixel, i.e. reddish-brown medium to fine sandy loam has been shown in (i). Wavelength unit is micrometers. 118
- Figure-6.5: Spectrum of the test pixel after the hybrid FLAASH+MFF correction. The JHU soil spectral library spectrum of the constituent soil type (reddish-brown medium to fine sandy loam) resampled to ASTER bandpasses has also been shown for comparison. Wavelength is in micrometers. 121
- Figure-6.6: Comparison of results obtained for the radiometric-atmospheric corrections of ASTER TIR radiance data of the study area. Radiance units are in Wm⁻² sr⁻¹ and the wavelength is in micrometers. 125

Figure-6.7:	Derivation of input parameters for the C-correction of the ASTER hybrid FLAASH+MFF-corrected reflectance data of the study area: a. ASTER stereo-DEM (ASTI4DEM); b. Slope image derived from the DEM; c. Aspect image derived from the DEM; and d. Cosine of the Local Illumination Image (IL) computed through slope, aspect images and solar zenith and azimuth data input in eq. 7.	129
Figure-6.8:	Hierarchical preprocessing of the ASTER VNIR-SWIR data used in the present study (bands 3-2-1 in R-G-B): A. Original LIB radiance-at-sensor data; B. Image after hybrid atmospheric correction; C. topographically normalized final reflectance image.	131
Figure-6.9:	Comparison of surface emissivity estimation results: a. Reference-channel-derived image-; b. Emissivity Normalization-derived image-; c. Alpha Residuals-derived image-; d. L2 TES standard emissivity product (ASL_05) based image-spectra for the dominant rock type (pure/pink quartzite) from a common pixel; and e. Reference spectrum (JHU spectral library) for the same rock type.	139
Figure-7.1:	Emissivity spectra of (a) dunite, (b) gabbro, (c) diorite, (d) granite, (e) pink quartzite, (f) dolomitic marble. Hemispherical reflectance spectra from JHU spectral library has been converted to emissivity using Kirchhoff's law. The corresponding spectra resampled to ASTER TIR bandpasses have been shown in dashed lines, and the positions of the bands have been marked on the top. Wavelength is in μm .	142
Figure-7.2:	ASTER LIB TIR recalibrated radiance-at-sensor image: a) 14-12-10 in RGB, and b) DCS of the same. Notice the dramatic improvement in hue and contrast differences after DCS processing, allowing better visual discrimination of the surfaces.	145
Figure-7.3:	Quartz, carbonate and mafic indices have been shown as a-c as single indices; and as R-G-B composites as d-f, for recalibrated radiance-at-sensor data, ISAC-corrected surface radiance data, and L2 surface radiance data, respectively. Note the differences in distribution of greens, and topographic effects on the three RGB composites.	149
Figure-7.4:	Spectral processing workflow.	152
Figure-7.5:	a-e) MNF bands 1-5, and f) the eigenvalues plot.	155
Figure-7.6:	MNF bands composites: a) 1-2-5 in RGB, and b) 1-4-5 in RGB. Notice the unique distribution of the blue pixels corresponding to the amphibole-bearing rocks, and the reds, pinks and oranges pertaining to the siliceous rocks as marked on the geologic map (Figure-2.3, Chapter 2)	155
Figure-7.7:	Results of the PPI TM calculated using the 5 MNF bands of the ASTER surface emissivity dataset: a) PPI TM plot, and b) color representation of the distribution of pure/extreme pixels in the	159

- image. Hotter colors represent higher DN values, or pixels which have been identified as extreme in greater number of PPI™ iterations, identified by the accompanying legend.
- Figure 7.8: a) The PPI™-derived pure pixel n-dimensional scatter-plot seen using n-Dimensional Visualizer™, and b) the average spectra of clusters lying on the extreme ends of the axes, identified as the image end-members. 159
- Figure-7.9: a. Best Spectral Analyst™ matches to the six unknown image end-members; b. The same spectra resampled to the ASTER TIR bandpasses. Notice the loss of some important spectral features between 9.3 μm and 10 μm due to coarse spectral resolution of ASTER TIR data. 165
- Figure-7.10: Spectral lithologic map generated using SAM on ASTER TIR surface emissivity data and the six spectral image end-members determined using PPI™. 169
- Figure-7.11: a-f Matched Filter processed images for the six image end-members; g-l their respective infeasibility images. 173
- Figure-7.12: Classified output of MTMF™ processing of ASTER L2 surface emissivity data. The background is ASTER band 1 image, with spatial resolution of 15 m. Notice the limitations posed by coarse 90 m spatial resolution and effects of vegetation on spectral classes, especially the class 'Mica Schist'. Excellent discrimination has been achieved between the two surface lithologic categories of mafic and felsic rocks, shown respectively in green and blue/yellow colors. Quartz-rich surfaces with some micaceous/clay content have been mapped as class 'Felsic Granite' 175
- Figure-7.13: Results of spectral modeling of the full resolution JHU lab spectrum of quartz monzonite contained within wavelength range 8-12 μm. Gaussian 3-term and 4-term fit results have been shown in a and b; c and d show the Fourier 1st Order and 2nd Order fit results; and e-g show the results of Polynomial 2nd Order, 3rd Order and 4th Order fits, respectively. The R² values have also been shown with each graph, respectively. 187
- Figure-7.14: Results of spectral modeling of the JHU lab spectrum of quartz monzonite resampled to the system response function of ASTER TIR sensor. Gaussian 3-term and 4-term fit results have been shown in a and b; c and d show the Polynomial 2nd Order and 3rd Order fit results; and e shows the Fourier 1st Order fit result. The R² values have also been shown with each graph, respectively. 189
- Figure-7.15: Linear regression between Polynomial curve-fit modeled emissivity minima and corresponding SiO₂ weight percentages of the JHU spectral library minerals: a. using all 34 spectra; b. excluding spectra of dunite and picrite. 191
- Figure-7.16: Linear regression between Gaussian 3-term curve-fit modeled 192

	emissivity minima and corresponding SiO ₂ weight percentages of the JHU spectral library minerals: a. using all 34 spectra; b. excluding spectra of picrite and rhyolite.	
Figure-7.17:	Linear regression between Polynomial 2 nd order curve-fit modeled emissivity minima and corresponding SiO ₂ weight percentages of the JHU spectral library minerals: a. using all 34 spectra; b. excluding spectra of picrite and rhyolite.	193
Figure-7.18:	Linear regression between Fourier 1 st order curve-fit modeled emissivity minima, and corresponding SiO ₂ weight percentages of the JHU spectral library minerals.	194
Figure-7.19:	SiO ₂ weight percent map of the study area generated using spectral modeling of the TIR surface emissivity spectra. The emissivity minimum in the reststrahlen band has been modeled using a Polynomial 2 nd Order function. The original 90 m resolution image has been resized to 15 m resolution for a smoothed visualization.	199
Figure-7.20:	SiO ₂ weight percent map of the study area obtained using the method proposed by MMAJ (2000). The original 90 m resolution image has been resized to 15 m resolution for a smoothed visualization. Notice the overall correspondence of the silica distribution with the spectral lithological maps obtained through analysis of the ASTER LIB and L2 emissivity data, shown in Figures-7.3, 7.11 and 7.12.	201
Figure-7.21:	Histogram for the silica weight percent map derived through spectral modeling of the ASTER surface emissivity data by Polynomial 2 nd Order curve-fitting and application of the empirically derived linear regression fit relation.	203
Figure-7.22:	Histogram for the silica weight percent map derived using the MMAJ's K-value relationship between ASTER emissivity and silica weight percent for the study area.	203
Figure-8.1:	a. USGS library spectra of some key alteration minerals; b. the same spectra convolved to the ASTER VNIR-SWIR bandpasses.	211
Figure-8.2:	a. Continua-removed USGS library spectra of some key alteration minerals; b. the same spectra are shown convolved to the bandpasses of the 9 VNIR-SWIR bands of ASTER.	213
Figure-8.3:	RGB FCCs with maximum spectral information: a. SWIR FCC 4-6-8; b. VNIR-SWIR FCC 6-3-1.	219
Figure-8.4:	Decorrelation stretch color composite of SWIR band 4-6-8 highlighting spectral information for specific mineralogy classes.	223
Figure-8.5:	Relative Band Depth (RBD) ratio schematic (modified after Crowley et al., 1989).	227
Figure-8.6:	Some band-ratio results for the study area: a. ferric iron 2/1; b.	229, 231

ferrous iron $(5/3)+(1/2)$; c. amphibole, $6/8$; d. epidote, chlorite, amphibole, $(6+9)/(7+8)$; e. Mg-OH $(6+9)/(8+8)$; f. carbonate, chlorite, epidote $(7+9)/8$. The color ramp shows the relative concentrations of the individual surface constituents mapped on ratios.

(contd...) g. sericite/muscovite/illite, $(5+7)/6$; h. alunite/kaolinite/pyrophyllite, $(4+6)/5$; the color ramp shows the relative concentrations of the surface constituents mapped on the individual ratios.

- Color ratio composite (CRC) of band ratios for phengitic/sericitic, and kaolinitic alteration in the study area; it can be seen that these minerals, which are typical of phyllic and argillic alteration, are concentrated broadly along the main NE-SW trending cataclastic/shear zone, and appear in light yellow-white colors. The same colors can also be seen for Chandmari (north), about 6km due east of Khetri, and about 3km southeast of Babai, and indicate alteration related to possible mineralization in these pockets.
- CRC of band ratios highlighting, in respective colors, the concentrations of clay minerals (red), amphiboles (green), and lateritic regolith (blue). The pink colors, as with the CRC in fig. 8.7, have been mapped primarily along the main cataclastic/shear zone. Amphibole-rich rocks/surfaces appear in bright green, while the lateritic surfaces in blue-cyan colors. However, there is an ambiguity in mapping of the lateritic surfaces with vegetation. Also, the general concentration of the clay minerals in the soils of the eastern plains has been brought out on this CRC. Notice also the yellow-red pocket towards the north in what is now the abandoned open-cast Chandmari mine and adjacent overburden dumps of mainly altered andalusite schist and phyllite, with banded amphibole quartzites.
- Color composite of PC7-PC6-PC4 in RGB; see the text for description.
- Mineral abundance images: a. alunite; b. illite; c. kaolinite; d. kaolinite+smectite; obtained from FPCS processing of 4-band spectral subsets of ASTER VNIR-SWIR surface reflectance image data. Vertical striping due to filter-scratch defect in SWIR focal array makes information from the western part of the study area redundant and useless.
- ASTER SWIR spectral indices for the study area calculated using the transform coefficients in Table-8.6 for: a. alunite; b. kaolinite; c. calcite; and d. montmorillonite.
- Boolean Logical Statements to map (A) argillic, and (B) phyllic alteration.
- Maps of argillic (A, red) and phyllic (B, yellow) alteration in the study area generated using Boolean Logical Statements shown in

figure 8.12. The base image is ASTER band 1.

Figure-8.14:	Vegetation mask created by thresholding an NDVI image of the study area.	257
Figure-8.15:	Image subsets used in image-derived end-member spectral library creation; ASTER bands 6-3-1 have been shown in RGB.	261
Figure-8.16:	PPI TM -derived image end-member spectra using vegetation-masked VNIR-SWIR reflectance image data, referred to as Case 1.	263
Figure-8.17:	PPI TM -derived image end-member spectra using vegetation-masked SWIR reflectance image data, referred to as Case 2.	263
Figure-8.18:	a-h, PPI TM -derived image end-member spectra respectively for the 8 windows of VNIR-SWIR reflectance data, referred to as Case 3.	265-267
Figure-8.19:	a-h, PPI TM -derived image end-member spectra respectively for the 8 windows of SWIR reflectance data, referred to as Case 4.	269-271
Figure-8.20:	SAM-classified alteration/surface mineral map of the study area for Case 1.	285
Figure-8.21:	SAM-classified alteration/surface mineral map of the study area for Case 2.	287
Figure-8.22:	SAM-classified alteration/surface mineral map of the study area for Case 3.	289
Figure-8.23:	SAM-classified alteration/surface mineral map of the study area for Case 4.	291
Figure-8.24:	MTMF TM -classified alteration/surface mineral map of the study area for Case 1; prominent banding due to SWIR filter-scratch problem can be noticed in the western part of the image. Background is ASTER band 1 image. Notice also that the class 'calcite/anorthite' also covers the pixels representing built structures (towns; e.g. Khetri and Babai). Differences between MTMF TM classification and SAM classification occur primarily because the MTMF TM -classified image represents 'stacked' classes, such that the top-most class is visible while other classes representing the same area (same pixels) are invisible due to overlap.	295
Figure-8.25:	MTMF TM -classified alteration/surface mineral map of the study area for Case 2; banding due to SWIR filter-scratch problem is more pronounced on this map, as only SWIR bands have been used to produce the classification. Background is ASTER band 1 image (grey shades). Differences between MTMF TM classification and SAM classification occur primarily because the MTMF TM -classified image represents 'stacked' classes, such that the top-most class is visible while other classes representing the	297

same area (same pixels) are invisible due to overlap.

- Figure-9.1: Synthesis of data processing outputs for validation of spectral lithologic mapping: a) Compiled lithologic map of the study area; b) DCS of radiance-at-sensor data (13-12-10 in RGB); c) Spectral index composite (quartz-carbonate-mafic in RGB); d) Weight percent SiO₂ map computed using the K-value technique and ASTER TIR L2 surface emissivity data; e) Spectral lithologic map derived from MTMF™ processing of ASTER TIR L2 surface emissivity data. 305
- Figure-9.2: Lithologic disposition of field samples used for validation of the spectral classification results of ASTER VNIR-SWIR surface reflectance data. 315
- Figure-9.3: Continuum-removed pixel surface reflectance spectra of field samples used in validation of the spectral mineral mapping. The broad vertical lines indicate the positions of the main absorption features. 317
- Figure-9.4: Copper trace-metal content map for the samples analyzed from the study area. Three sites with samples containing significantly high copper content have been shown in zoomed windows along with their corresponding SAM-classified mineral/alteration map windows for Case 3. 325

List of Tables

<u>Table No.</u>	<u>Caption</u>	<u>Page No.</u>
Table-2.1:	Stratigraphic succession of KCB rock units.	22
Table-2.2:	Important rock units exposed in the study area (after Gupta, 1974).	24
Table-3.1:	Salient characteristics of remote sensing sensors used in this study	34
Table-3.2:	Scene acquisition details for the remote sensing image data used in this research	34
Table-3.3:	General description of the various kinds of ASTER data products used for analysis in this study (for detailed description of the sensor and the data, see the official ASTER websites: <i>asterweb.jpl.nasa.gov</i> and <i>www.ersdac.or.jp/eng/index.E.html</i>)	35
Table-3.4:	Specifications of the ancillary data used in the study.	36
Table-4.1:	Field characteristics of the main litho-units in the study area.	49-51
Table-4.2:	Thin-section microscopy of the samples for the representative rock types in the study area.	55
Table-5.1:	Some important hyperspectral sensors for geologic remote sensing.	90
Table-5.2:	Some pertinent examples of Landsat-based remote sensing studies for mineral exploration.	91
Table-5.3:	Examples of ASTER data application in lithologic and alteration mapping.	94
Table-6.1:	Maximum radiance values for all ASTER bands and all gain states. Values corresponding to the ASTER data used in this study have been shown in bold italics.	107
Table-6.2:	Calculated Unit Conversion Coefficients for each ASTER band. Values corresponding to the ASTER data used in this study have been shown in bold italics.	107
Table-6.3:	ENVI FLAASH input parameters for the ASTER scene used in the present study.	116
Table-6.4:	Acquisition parameters for the ASTER LIB dataset used in the present study.	117
Table-6.5:	Solar exo-atmospheric irradiance values for the nine reflective	117

	bands of ASTER (VNIR+SWIR) (Thome et al., 2001)	
Table-6.6:	Haze value computation for ASTER VNIR+SWIR bands using the image-based DOS technique (COST method; Chavez, 1996) under moderate scattering atmospheric conditions (Chavez, 1989)	117
Table-6.7	ASTER TIR radiance recalibration coefficients and estimated changes in radiances and temperatures computed using original and recalibrated radiances for some standard temperatures.	123
Table-6.8:	C-correction parameters for the solar reflective ASTER VNIR-SWIR bands	129
Table-7.1:	Top three Spectral Analyst™ matches to the six end-member spectra using reference spectral library containing JHU mineral, rock and soil spectra.	163
Table-7.2:	Top three Spectral Analyst™ matches to the same six end-member spectra using reference spectral library containing JHU rock and soil spectra alone.	163
Table-7.3:	MTMF™ scores and thresholds used for classification of the six image end-members	172
Table-7.4:	Results from fitting the ASTER spectral library igneous rock spectra with 3- and 4-term Gaussian function. N = number of samples; R^2 = Correlation coefficient. For Case 9, the value of N less than 35 indicates that the Gaussian model failed to adequately fit certain spectra (the fit values were obtained excluding those spectra). Wavelength range shown is from the centroid value of the first channel to the centroid value of the last channel (after Hook et al., 2005).	180
Table-7.5:	Results of the spectral modeling of JHU igneous rock spectra. Except for polynomial 2 nd order curve fitting, all other values are for JHU spectra resampled to the ASTER TIR system response function.	184-185
Table-7.6:	Summary of linear regression results for various curve-fitting models investigated to estimate the emissivity minima. N=no. of rock spectra used; m and c are the slope and intercept of the linear model ($y=mx+c$); R^2 =regression coefficient; ND=Not Determined.	194
Table-8.1:	Spectral characteristics of the reflectance spectra of some target alteration minerals in the wavelength range 0.4-2.5 μm . HS/LS => high/low sulfidation	209
Table-8.2:	Useful band ratios and RBDs for alteration mapping using ASTER VNIR-SWIR data.	226
Table-8.3:	Some useful color ratio composites for alteration mapping using ASTER VNIR-SWIR surface reflectance image data.	227

Table-8.4:	Eigenvector matrix of PCT of 9-band ASTER VNIR-SWIR dataset	239
Table-8.5:	Eigenvector matrices for the four target alteration minerals for the study area. For all target minerals, the abundances are displayed in PC4 image	239
Table-8.6:	Transform coefficients for ASTER SWIR bands used in calculation of spectral indices. (from Yamaguchi and Naito, 2003; Table 3)	246
Table-8.7:	End-member spectral identification using ENVI's Spectral Analyst™ for Case 1: Vegetation-masked full image, ASTER VNIR+SWIR 9-band reflectance data	273
Table-8.8:	End-member spectral identification using ENVI's Spectral Analyst™ for Case 2: Vegetation-masked full image, ASTER SWIR 6-band reflectance data	273
Table-8.9:	End-member spectral identification using ENVI's Spectral Analyst™ for Case 3: Image-subsets for 8 different mineralized areas, ASTER VNIR+SWIR 9-band reflectance data	274-278
Table-8.10:	End-member spectral identification using ENVI's Spectral Analyst™ for Case 4: Image-subsets for 8 different mineralized areas, ASTER SWIR 6-band reflectance data	279-282
Table-8.11:	Case 1: MTMF™ thresholds for end-member spectral class abundance images.	293
Table-8.12:	Case 2: MTMF™ thresholds for end-member spectral class abundance images.	293
Table-9.1:	Validation of spectral lithologic mapping using ASTER TIR data (ND=Not Determined)	307
Table-9.2:	Validation of ASTER VNIR-SWIR spectral mineral mapping results.	312,313
Table-9.3:	Trace-metal values of some field samples (for the complete list, see Appendix A).	324

1.1 General background

In today's rapidly industrializing world, stress on known deposits of economic minerals has led to an invigorated hunt for new deposits. The task is made difficult due to the lack, or the inadequacy, and/or the inaccuracy of geologic information for large areas of the world. In particular context of mineral exploration, one of the basic requirements is the availability of accurate lithological, structural and alteration maps. Conventionally, this task has been performed by field-intensive and time-consuming surveys, which have obvious limitations in terms of wholesome coverage and economics of the job. This has necessitated the development of advanced mineral exploration techniques utilizing geophysical and remote sensing methods.

Developments in technologies that aid in faster and dependable assessment of mineral potential of geologically favorable regions are highly desirable. Remote sensing and Geographic Information Sciences (GIS) are two such inter-related tools in realization of this need. Since the launch of first Landsat satellite in 1972, rapid developments in sensor technology, imaging and non-imaging spectroscopy, methods of information extraction through digital image processing, and integrated analysis of a variety of geospatial data focusing on mineral exploration through GIS, have virtually revolutionized the mineral exploration scenario in the world.

Until the turn of this century, Landsat data continued to be the mainstay of most geologic applications of the remote sensing technology, since they provide global, cost-effective and widely understood data. Hyperspectral remote sensing, though having superior capability, continues to be of limited geographic extent and is cost-intensive. Limited success has been achieved in its operationalization from spaceborne platform, and is still under development.

After the launch of the first EOS satellite, called Terra, carrying onboard the Advanced Spaceborne Thermal Emission and reflection Radiometer (ASTER) sensor in addition to four other remote sensing systems in December 1999, a quantum leap has been achieved in the capability of remote sensing towards mapping of lithology and alteration minerals relevant for mineral exploration. In addition to enhanced coverage of the spectral regions with useful alteration mineralogical information, the uniqueness of ASTER is its complementary multispectral coverage of additional windows in the thermal infrared region of the electromagnetic spectrum. This augments lithological mapping objectives in addition to alteration mapping. This capability is currently not available from any other operating spaceborne remote sensing system. Therefore, ASTER data provides in one package, the potential to map the regional lithology, and the accompanying alteration minerals, which can significantly aid in scaling down the time and monetary aspects of mineral exploration activities worldwide. The work presented in this thesis reports in detail, the procedures and results of an assessment of the potential, advantages and limitations of ASTER data towards identification and mapping of lithology and alteration in a well-documented mineralized region, the Khetri Copper Belt, in northwest India.

Geological materials (rocks and minerals) are characterized by their unique and distinctive spectral response in specific wavelength regions of the spectrum. The most important of these are in the Visible through Near InfraRed to ShortWave InfraRed (VNIR-SWIR, 0.4-2.5 μm) and Thermal InfraRed (TIR, 8.0-12.0 μm) range. Mineral deposits of economic value are usually associated with alteration of the rock in which they are hosted. These alterations serve as guides for their exploration. Based on their chemical composition and crystal structure, these minerals exhibit typical responses to incident electromagnetic radiation (EMR), which are shown in the form of spectral curves for either reflected or emitted radiation. The most important region of the EMR where the diagnostic spectral features for most alteration minerals occur is the VNIR-SWIR (Hunt 1980; Clark et al. 2003; Chapter 5,

this thesis). However, the spectral features for the silicates (particularly quartz and feldspars), which are the most important and abundant rock-forming minerals, occur in TIR region of the EMR, and are typically associated with the emitted radiation (Salisbury and D’Aria 1992; Hook et al. 1999; Chapter 5, this thesis).

1.2 Indian scenario and motivation

Although remote sensing based mineral exploration has become a norm in most parts of the world, only very limited studies of this nature have been undertaken in India. And even among these, attention has been focused primarily on structural interpretation and use of limited spectral resolution Landsat TM data for regional anomaly detection. There are no reported studies on use of high spectral/spatial resolution ASTER in mineral exploration activity from India in standard scientific publications. Although excellent geologic database exists for the Indian region, studies focused particularly on alteration mapping have not been reported. Alteration mapping on a regional basis can significantly aid in the overall understanding of the mineral potential of the areas that have so far remained under-explored. Since such an exercise cannot be adequately and reliably conducted purely through field surveys, the capabilities of high spectral resolution remote sensing can be utilized to fill the gap. To fulfill this objective and to establish a framework within which similar studies can be conducted for other parts of the country, an exhaustive analysis of ASTER data for a mineralized region in Khetri Copper Belt has been conducted as reported in this thesis.

1.3 Study area and adopted approach

The Khetri Copper Belt (KCB) forms the northern entity of the Aravalli mountain range in Rajasthan, northwest India, and extends for about 80 km from Singhana in the NE to Raghunathgarh in the SW. The NW–SE striking transverse Kantli Fault divides the belt into

two parts - viz., North KCB (NKCB) and South KCB (SKCB) (Das Gupta 1968; Gupta 1974). KCB is a well studied, thoroughly documented, regionally metamorphosed mineralized belt, and is among the main indigenous sources of base metals (Cu, Co, Pb, Zn and related metals) in the country. The lithostratigraphic categories in KCB consist primarily of early Proterozoic metasedimentary rock units, and late Proterozoic basic and acidic intrusives. The older psammitic Alwar formation (mainly pure and impure quartzites, and micaceous quartzites), and younger pelitic Ajabgarh formation (mainly phyllites, schists, impure marbles and calc-silicate units) comprise the main lithostratigraphic units of KCB, along with many small stocks, sills and dikes of granite, dolerite and amphibolite. The study area is marked by a prominent NNE-SSW striking cataclastic/shear zone long which numerous felsic (granitic and pegmatitic) intrusives are emplaced. Small, but significant sulfide mineralization close to the surface in a few places and in vicinity of these intrusives is observed. Primary rock alteration in the form of sericitization, chloritization and carbonatization is widespread all along the shear zone. Secondary alteration due to weathering is common and is manifested as chloritization, kaolinization, scapolitization, and as small gossans and limonitic/jarositic surfaces in sulfide-bearing areas. Base metal deposits in KCB are considered to be conformable, sediment hosted and stratabound (Deb et al., 1989) and are genetically different from those of southern Rajasthan (Goyal, 2001). However, some recent reports favor an epigenetic mode of mineralization with convincing arguments in favor of a new mineral deposit class, called the iron-oxide-copper-gold (IOCG) type, KCB (e.g., Knight et al., 2002). A more detailed account of the study area and its geology has been provided in Chapter 2.

1.4 Scope and objectives

The research is aimed at investigating the capabilities of ASTER multispectral spaceborne sensor to map lithology and alteration in a base metal mineralized region, with a case study in a part of the Khetri Copper Belt in the Proterozoic Delhi Fold Belt of northwest India.

This approach followed here has allowed for an evaluation of the potential of ASTER remote sensing image data as a supporting and indirect evidential tool for known mineral anomalies in a well studied mineralized region. Results of remote sensing based alteration and lithologic mapping for the study area can, therefore, be directly compared with the field observations and geologic maps, and thus the study can serve as a test case to explore the potential of the technology for other areas. Briefly, the study has been designed to fulfill the following research objectives:

- To evaluate the use of high resolution multispectral spaceborne ASTER remote sensing data towards its potential to map unique minerals and rocks, in comparison with the TM data; and towards this end
- To evaluate the various techniques of atmospheric and topographic corrections to retrieve the physical values of surface reflectance and emissivity, respectively for the data in VNIR-SWIR and TIR wavelength regions
- To generate a spectral lithologic map of the study area using thermal multispectral data and to evaluate the methods of quantitative silica abundance estimation
- To produce spectral surface/alteration mineral maps of the study area using data in the VNIR-SWIR range
- To validate the results of remote sensing image analyses through published geological, and methodically collected field and laboratory data; and
- To investigate the possible relationships between mapped alteration and trace-metal concentrations in selected parts of the study area

1.5 Scientific Impact

The goal of this research is to show the extent to which ASTER remote sensing data can be used to distinctly map and identify individual minerals that constitute the surfaces of the exposed rocks and regolith. Surface material maps can be separated based upon whether they represent alteration minerals or surface rock units (lithology). For the present study, the investigations have provided a better understanding of the distribution of specific minerals which can be linked to existing and potential mineralized areas, and can thus serve as an exploration aid.

In nutshell, the main scientific contributions of this research are outlined as follows:

1. First ever detailed report of ASTER data analysis from an Indian region for mineral exploration
2. Successful implementation of a novel technique to retrieve surface reflectances from at-sensor radiance data using a combination of radiative transfer-based absolute and relative approaches of atmospheric correction
3. Extension of the existing techniques of quantitative silica abundance estimation techniques based on Gaussian fit modeling to incorporate computationally more efficient modeling techniques based on Polynomial spectral curve-fitting
4. Creation of a first-ever spectral lithologic map of the study area based on multispectral surface emissivity data
5. Creation of a first-ever spectral alteration map of the study area using multispectral solar reflective data
6. First direct comparison of remote sensing data based spectral maps with trace-metal concentrations of rock units from the study area, and thus
7. Establishing ASTER data as a potential tool for mineral exploration in the Indian terrain

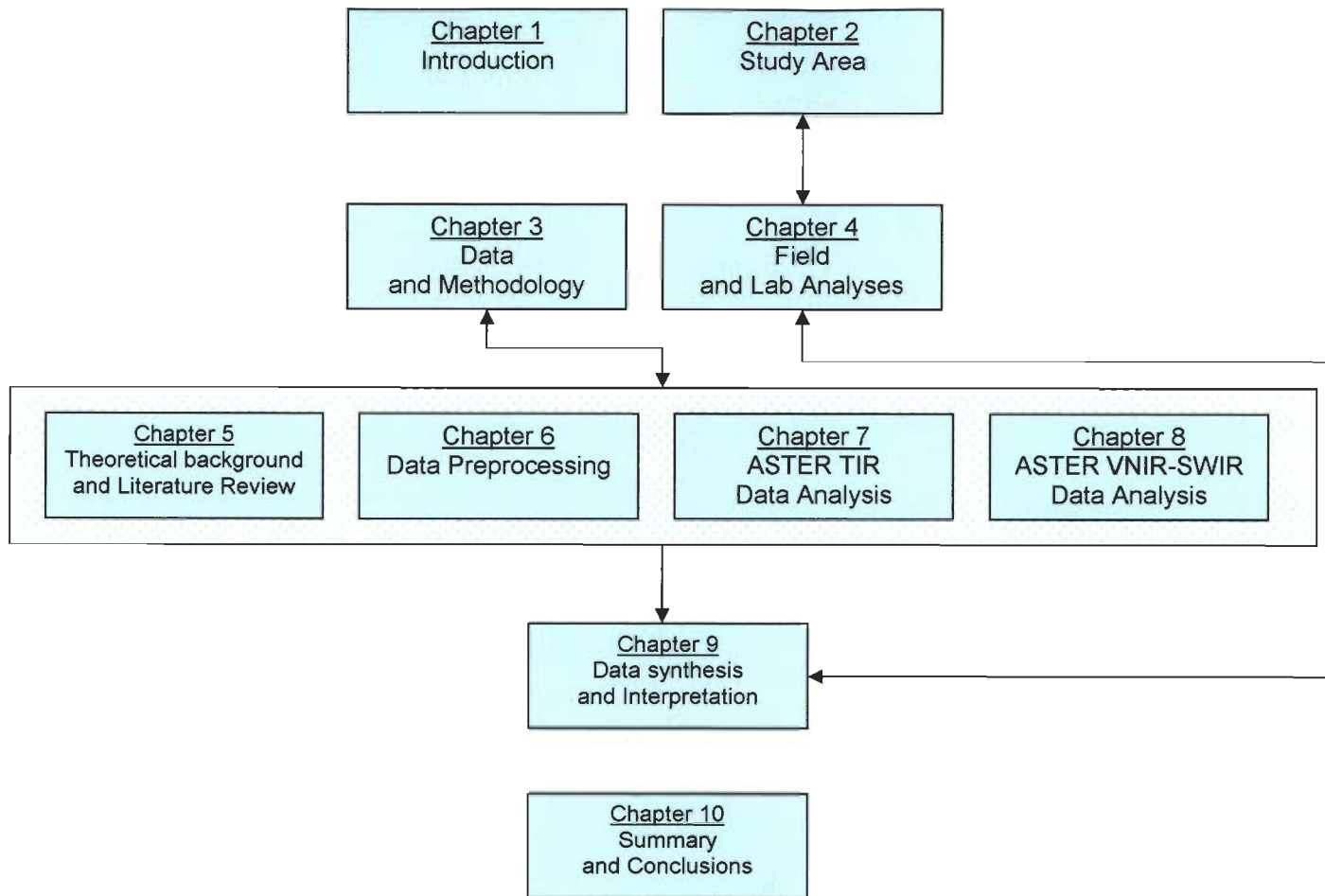


Figure-1.1 Interdependencies of the chapters in the thesis.

1.6 Organization of the thesis

This research has investigated the potential and capability of ASTER data in lithologic and alteration mapping with a case study in the Khetri Copper Belt, in northwest India. Exhaustive analysis of ASTER data has involved investigation of data preprocessing and processing methods currently in vogue. The VNIR-SWIR and TIR data have been treated separately owing to the basic nature of the data, i.e. while VNIR-SWIR data represent the reflected solar radiation, the TIR data are essentially the emitted part of the recorded solar radiation. A ground truth database has been created to validate and interpret the findings of ASTER data analysis. The thesis has been organized in 10 chapters and 4 appendices on the basis of the treatment of the following components:

1. Background literature review pertaining to the geology of the study area (Chapter 2)
2. Discussion of the methodology and data employed (Chapter 3)
3. Ground truth database development, in terms of field visits and laboratory investigations (petrographic and geochemical) of selected field samples (Chapter 4)
4. Review of the theory of geologic remote sensing and state-of-the-art of remote sensing applications in lithologic and alteration mapping with focus on the use of ASTER data (Chapter 5)
5. Preprocessing of ASTER data for removal of radiometric, atmospheric and topographic effects and retrieval of the basic surface physical data (reflectance and emissivity) using existing and novel approaches (Chapter 6)
6. Analysis of ASTER TIR data for lithologic mapping and SiO₂ abundance estimation using existing and novel techniques (Chapter 7)
7. Analysis of ASTER VNIR-SWIR reflectance data for surface/alteration mineral mapping (Chapter 8)
8. Synthesis of ASTER data analysis results with ground truth and validation of the results (Chapter 9)
9. Summary and conclusions (Chapter 10)

The chapter interdependencies have been shown in Figure-1.1.

Study Area – Regional and Local Geology

2.1 Khetri Copper Belt: an overview

The Khetri Copper Belt (KCB) is one of the main copper producing mineral regions in India. KCB forms the northern entity of the Aravalli mountain range in Rajasthan, northwest India, and extends for about 80 km from Singhana in the NE to Raghunathgarh in the SW. The NW–SE striking transverse Kantli Fault divides the belt into two parts - *viz.*, North KCB (NKCB) and South KCB (SKCB) (fig. 1). Kantli River flows from NE to SW along this fault. The belt itself separates the Great Indian Thar desert in the west, from the fertile alluvial plains of Ganga and Yamuna in the east. The study area is located immediately north of the Kantli Fault.

Structurally, KCB is a part of the North Delhi Fold Belt (NDFB) and is characterized by a complex multiphase structural history of magmatism, metamorphism and copper-iron mineralization. Heron (1923) proposed that the KCB is covered by rocks of the Delhi Supergroup, which is further divided into (1) an older Alwar Group dominated by psammitic rocks, and (2) a younger Ajabgarh Group dominated by pelitic rocks (fig. 2.1). This stratigraphic scheme for KCB has been adopted by most subsequent workers in the area (*e.g.*, Das Gupta, 1968; Gupta, 1974); however, recent studies by Chakrabarti and Gupta (1992) indicate a pre-Delhi status for the rocks of the KCB.

Metallurgical history in KCB dates back to 3rd Century B.C. Carbon isotope dating of mining and metallurgical relicts (wood supports and slag heaps) in the area indicates that the copper mining and metallurgy in the region dates back to the Harappan age. Brooke (1864) gave the first recorded account of the deposits in KCB, detailing the process of working and smelting at Singhana and Madhan-Kudan mines in the area in his time. There is little doubt, however, that during Mughal period the area witnessed a great deal of activity.

Much of the ancient as well as current mining activity recorded from the region is concentrated in the NKCB. Some of the important copper mines of the area are Madhan-Kudan and Kolihan (both underground), and Chandmari (open-pit, abandoned). There is a minor, but important prospect in Akwali, which lies towards the southern end of NKCB. Recent mine development activity in the belt is concentrated in the northern-most part of NKCB beyond Singhana at Banwas.

2.1.1 Review of the geological literature on KCB

The KCB is marked by a large number of scattered heaps of slag close to old workings and associated man-made structures. The early history of the region is not fully known, but references to a flourishing copper trade during the Harappan age have been found in ancient Sanskrit literature. After independence, exploration activity by private and public sector undertakings have resulted in accumulation of a large database with corresponding literature in published and unpublished form. About 150 exploration reports and 115 scientific publications (with a few in international journals) are devoted to the geology, ore deposits, and exploration of the Khetri Copper Belt. Mineral Exploration Corporation Limited (MECL) has synthesized this wealth of literature in a 'Compendium on Khetri Copper Belt' (Narsimhan, 1989).

In 1945, a company under the name of Jaipur Mineral Corporation ventured to prospect the Madan hill, but after not-so-encouraging results of drilling, abandoned the site in 1947. Systematic exploration activity was initiated in 1954 by the Geological Survey of India (GSI) (Roy, 1962), including geophysical and geochemical and biogeochemical surveys (Dunn, 1965, Paul, 1968). Biogeochemical studies have not been successful in the region (Balasundaram, 1972). Heron (1923, 1925, 1935), Das Gupta (1968) and Gupta (1974) mapped the area at various levels of detail. Muktinath et al. (1969) and Rao (1971) gave a brief account of gossans, sampled from a few localities in the belt. Deb (1948) described the ore minerals from the region in detail for the first time.

Various public and private enterprises, viz., GSI, Indian Bureau of Mines (IBM), Hindustan Copper Limited (HCL), and the Pyrite and Phosphorite Chemicals Limited (PPCL), have carried out extensive drilling and exploratory mining in the area over the last four decades to test surface anomalies and find the grade and extent of sulfide deposits. Most of the studies in the area have been concentrated on the two main producing mines – Madhan-Kudan and Kolihan (Rao and Rao, 1966, 1968a,b; Mukherjee, 1966, 1967a,b, 1968; Chandra Chowdhury et al., 1971). Wall-rock alterations in the region have been discussed by Das Gupta (1962a,b,c; 1964a), Das Gupta et al. (1963, 1965, 1971) and Sikka et al. (1966a,b). Genetic aspects of the ores of Madhan-Kudan and Kolihan in particular and KCB in general have been discussed by Varma and Krishnanunni (1963), Das Gupta (1963, 1964b) and Mukherjee (1969). Roy Chowdhury and Das Gupta (1965) and Roy Chowdhury and Venkatesh (1971) have discussed the regional controls of ore localization in the belt. Vardhan and Narasimhan (1971) have discussed the economic potential of the belt. Excluding the three main mines (Madhan-Kudan, Kolihan, and Chandmari having around 85 million tonnes of ore at 1% Cu, production + reserve), ore reserves of about 58 million tones at 1.4% Cu have been estimated by GSI and Mineral Exploration Corporation Limited (MECL) in 15 prospects in KCB, of which Banwas, Chandmari Intervening and Chandmari South are located close to the existing mines..

2.1.2 Geology of the North Khetri Copper Belt (NKCB)

The NKCB consists of two great plains (Shekhawati Plains) separated by NE-SW trending hill ranges, intricately dissected by ravines where the argillaceous units lie exposed. The hilly area generally rises southward towards Kantli River.

NKCB is characterized by an unconformable basement-cover relationship between the high grade paragneiss-quartzite-calc-silicate rock sequence and copper hosted metasedimentary sequence. The metasedimentary rocks (feldspathic quartzite with magnetite, banded amphibole-quartzite, garnetiferous chlorite schists, mica schists, and quartzite) of the NKCB display a

NNE–SSW to NE–SW trend and are folded into a number of regional anticlines and synclines, with culminations and depressions (Das Gupta, 1968; Gupta, 1974; Naha et al., 1988). The intrusive rocks in the NKCB are largely represented by mafic and granitoid rocks. Besides, minor amounts of felsic volcanics have also been reported (Golani et al., 1992; Gupta et al., 1998). The geological setting of copper hosted thick pile of folded metasedimentary sequence is interpreted as an intracontinental tensional basin deposit (footnote, GSI, 1997).

Two main deformation stages affected the Proterozoic sequence, probably at the end of Proterozoic-I (as indicated by 1700 Ma syn-second deformation Gothro Granite) (footnote, GSI, 1997). The earlier deformation produced folds with axes subparallel to stretching lineation plunging towards NW-SE to NNW-SSE direction. The associated gently dipping tangential shear zones indicate an overall shear in the NW to NNW direction, which, however, did not induce appreciable tectonic stacking of lithologic successions. The later stage of deformation produced folds (macroscopic sinistral fold near Khetri-Rajota) and crenulation cleavage generally striking NNE-SSW. The axis of later folds plunges gently towards South (as towards North of Kalota) with occasional plunge reversal. Large dextral shear zones, such as the NE-SW Singhana-Jaspura shear zone and the Babai-Taonda shear zone (running diagonally across the study area) are responsible for the arcuate shape of the Proterozoic sequence. Prograde metamorphism associated with earlier deformation is characterized by a pressure decrease and is followed by a temperature increase, linked to granitic emplacement during later deformation. Late tectonic stages are characterized by brittle deformation and the development of regional NE-SW striking fault zones as well as localized NW-SE trending transverse faults (footnote, GSI, 1997). Within the Proterozoic sequence, stratabound copper deposits with a cumulative strike length of 16 km, show broad stratigraphic control by Fe-Mg rich and carbonate bearing metasediments (garnetiferous chlorite schist and amphibole-bearing quartzite), which correspond to the transition zone between near shore detrital facies (represented by lower quartzite) and deeper argillaceous marine sediments (at the top).

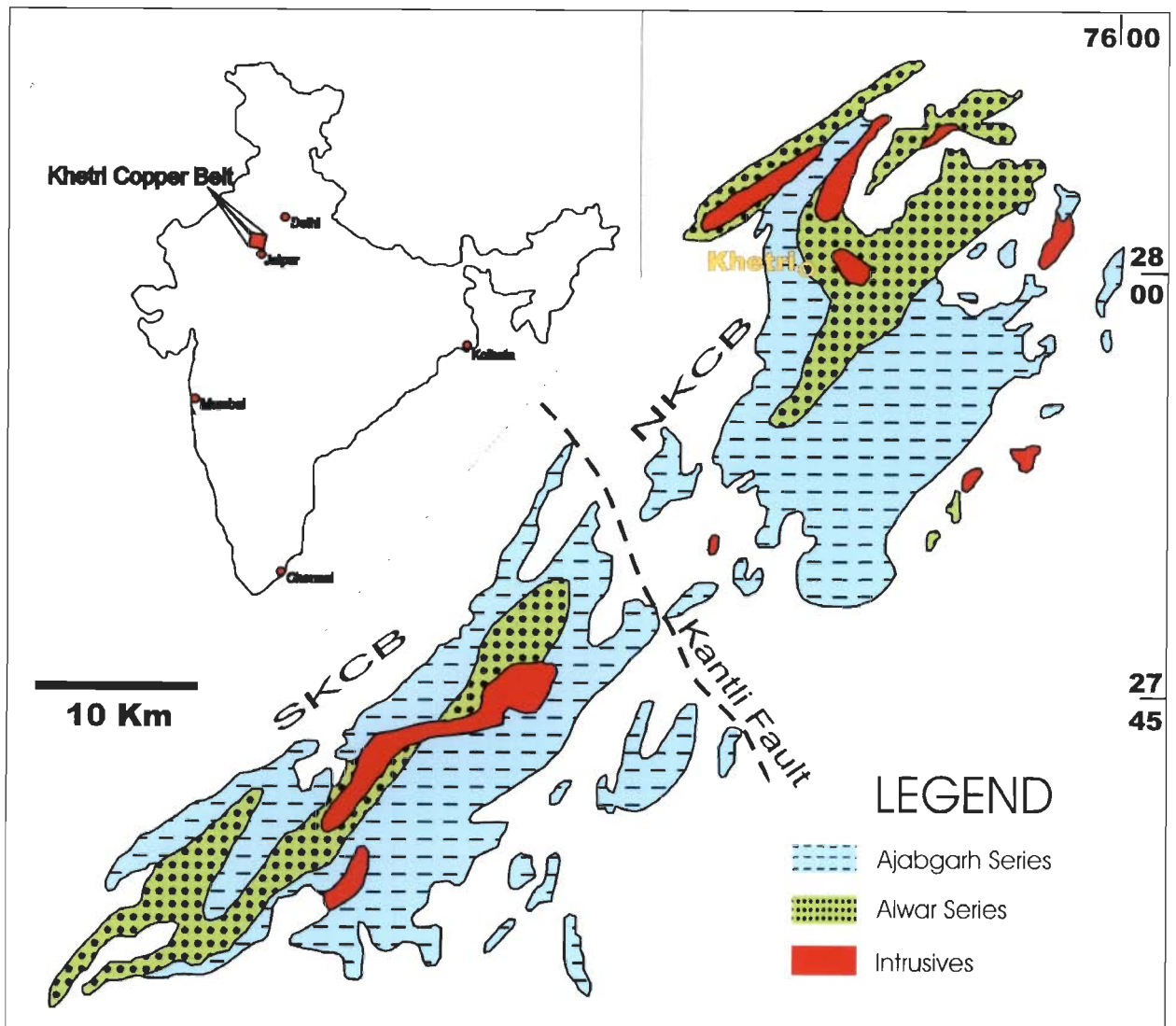


Figure-2.1 Location and generalized geological map of the Khetri Copper Belt (modified after Heron, 1923)

2.2 Study area: location, accessibility, physiography and geology

2.2.1 Location

The study area lies in the southern part of the NKCB. It falls within the Survey of India toposheets 45M/9 and 45M/13, in the Jhunjhunu district of Rajasthan state. The geographic extent of the study area lies from 75° 43' 14" E to 75° 50' 45" E longitudes and 27° 53' 5" N to 27° 59' 47" N latitudes. Khetri, which is the most populous town in the area, lies to its north. The Chandmari and Akwali prospects form the northern and southern bounds of the study area, respectively (fig. 2.2).

2.2.2 Accessibility

The area is well connected to the major urban centers, like Delhi and Jaipur by all season metalled roads, and railways. Most large villages in the study area, like Babai and Papurna, lay enroute the Jaipur-Khetri state highway (fig. 2.2). Nearest railway station is at Chirawa, about 30 km from Khetri.

2.2.3 Physiography, climate and vegetation

Regionally, the area consists of slightly undulating terrain in the east and moderately high hilly ranges to the west of the state highway up to Papurna, where it transects the ranges; thereafter it again forms the general divide. Beyond the hills of the west lies the great Indian Thar Desert. Nearly NS trending hills of Madhogarh lie to the south-west of the area.

The most prominent topographic features of the study area are manifested by the quartzite ridges. A prominent ridge about 3.5 km north of Papurna, having nearly uniform relief for a length of about 3 km, is one of the most interesting landforms in the area. It is capped by pure quartzites and attains a maximum relief of about 800 m above average sea level. The hills, in general, are moderately dipping on the western and steeply dipping and scree covered on

their eastern flanks; and represent the limbs of a regional fold called the Babai anticline. The area is lithologically diverse, and different litho-units have undergone different amounts of weathering. The quartzites are the most resistant of the rocks followed by the amphibolites and the calc-silicates and calcareous rocks. The meta-pelites, feldspathic quartzites and felsic intrusives (granites, granodiorites and pegmatites) have yielded to the agents of weathering in most part. The main reason for this differential weathering is that the feldspar of the rocks is more susceptible to weathering in the hot and dry climate of the region than the carbonates.

There is no perennial drainage in the study area, though rivulets and *nālās* of varying magnitude dissect the hill flanks and are fairly dense and normally follow the structural trends in the rock units. The Kantli River and the underlying fault lie to the south of the study area. In general, the drainages are radial to dendritic in pattern. Most of the westerly flowing drains disappear in the desert of the Thar, while some form feeders to the Kantli River flowing westwards. Barring a few and sporadic natural springs, most groundwater is deep and the yield is low. The agriculture is seasonal and highly monsoon dependent.

Climatologically the area represents a typical tropical semi-arid to arid climate. The mercury fluctuates between the far ends of the thermometer for summer and winter seasons, with temperature crossing the 45° Celsius mark in peak summers, and going below 4° Celsius in the winters. Rainfall is moderate to scanty, with an average precipitation of 25 to 30 cm annually.

The vegetation in the area is quite sparse and scanty. Xerophytes dominate the natural vegetation, which is also controlled by the bedrock regolith. The quartzites, carbonates and the intrusives (both felsic and mafic) in most part are barren and devoid of vegetation, while the schists and phyllites along with alluvium provide the best ground for vegetation in the area. Among the trees, *Boswellia serrata*, *Euphorbia rinulia*, *Anogeissies latifolia*, *Anogeissus pendula* and *Acacia senegal* predominate. *Euphorbia royallina* and *Cactus* bushes along with spear grass are commonly observed (Gupta, 1974).

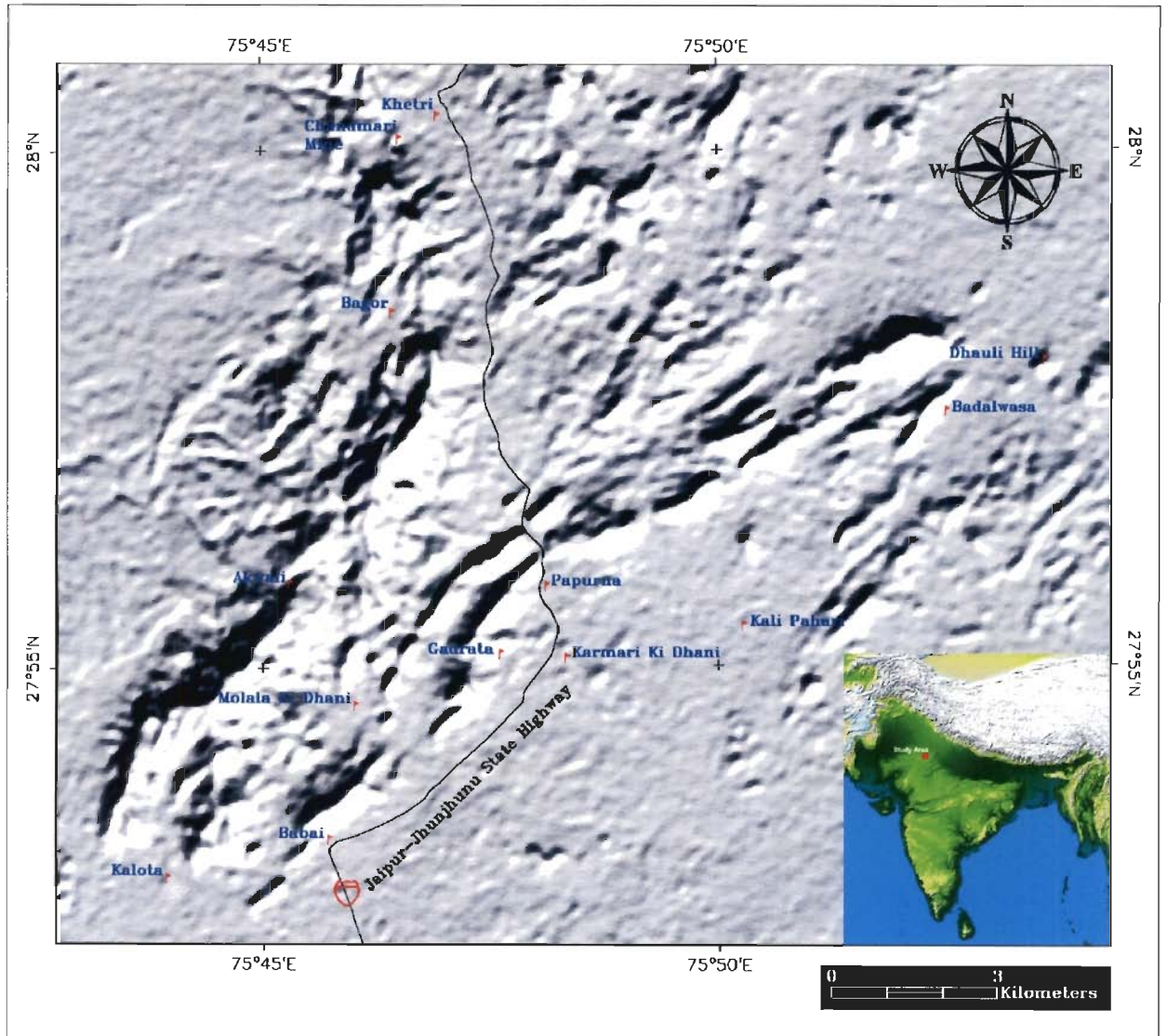


Figure-2.2 Some important places in the study area. The background is a hill-shade image of the study area, derived from a digital elevation model (DEM). Inset is a shaded relief map of the Indian subcontinent showing study area location.

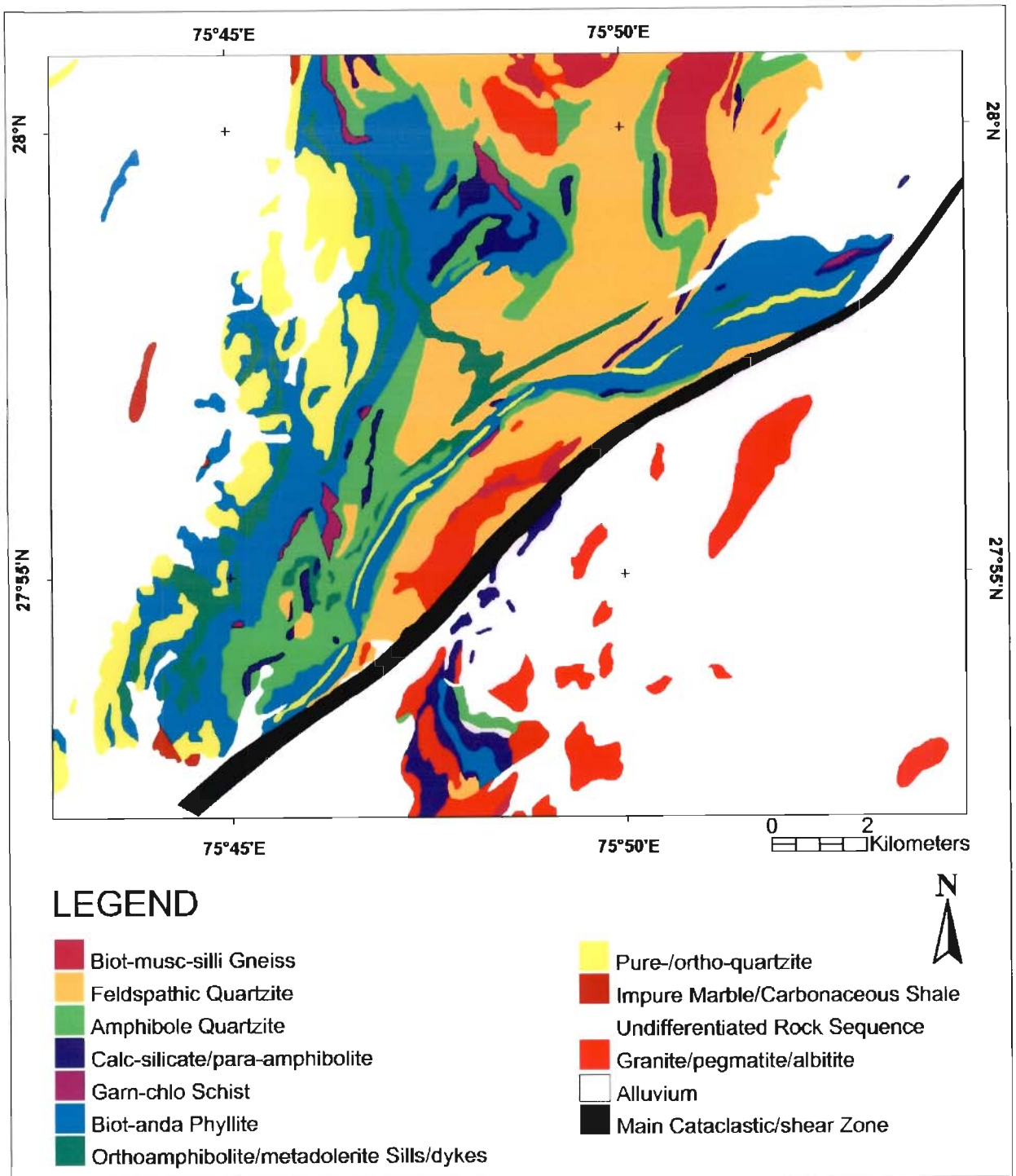


Figure-2.3 Compiled reference lithologic map of the study area (after GSI, 1997 and Gupta, 1974).

2.2.4 Geology

The Babai-Khetri area represents a regionally metamorphosed terrain with low to medium grade metasedimentary rocks, such as various kinds of quartzites (banded feldspathic quartzites, micaceous quartzites, amphibole bearing banded quartzites, arkosic and banded arkosic quartzites, and pure quartzites) and metapelites (schists and phyllites), and has witnessed a history of polyphase intrusions of intracratonic felsics and mafics (granites, granodiorites and pegmatites, and amphibolites, respectively). These rocks comprise the two major stratigraphic divisions of the Delhi Supergroup - viz., the Alwar Group (largely psammatic) and the Ajabgarh Group (largely pelitic) (Heron, 1923). All subsequent workers (Das Gupta, 1968; Roy Chowdhury and Das Gupta, 1965; Chandra Chowdhury et al., 1971; Gupta, 1974) have followed Heron in this correlation, though they have differed in concluding the order of superposition of various litho-units. The eastern part of the area largely comprises of impure carbonate rocks and para-amphibolites. The stratigraphical sequence of various litho-units of the KCB by different workers has been summarized in Table-2.1.

Table-2.1 Stratigraphic succession of KCB rock units.

Source →	Heron (1923)	Das Gupta (1968)	Gupta (1974)	
Delhi Supergroup	{	Intrusives	Soil dune sand, alluvium Chert-ankerite veins, quartz veins Younger amphibolite dykes (originally dolerite rocks) Sulfide mineralization and Fe-Mg metasomatism and other types of alteration leading to the formation of anthophyllite, cummingtonite, chlorite, biotite, etc., part of albitization Granites, granite gneisses, aplite, pegmatites, quartz veins, feldspathisation producing extensive albite and locally microcline	Soils, wind-borne sands and alluvium. Supergene alterations Sulfide mineralization and associated hypogene alterations Granites-granodiorites-pegmatites
		Ajabgarh Group (mainly pelitic)	Older amphibolites, epidiorites (originally dioritic rocks) Unit 8: Carbon phyllites, phyllites, mica-schists, sillimanite schists, etc. (local) Unit 7: Quartzites, quartz schists with phyllites, mica schists, marbles, carbin phyllites, etc. Unit 6: Phyllites, mica schists, etc. (local) Unit 5: Marbles, dolomites, amphibolites, calc-gneisses, amphibole quartzites, quartzites, scapolite gneisses, mica schists and phyllites Unit 4: Phyllites, andalusite-bearing phyllites and schists, biotite schists, sericite schists, garnet schists, chlorite schists, schists with staurolite, kyanite, sillimanite, scapolite and amphibole-biotite schists, carbon phyllites, quartzites, etc.	Orthoamphibolites Unit F: Meta-pelites (same as in Unit D) Unit E: Orthoquartzites, quartzites with phyllitic bands Unit D: Meta-pelites. Quartz-mica schists and phyllites, andalusite, garnet and staurolite bearing. Graphite phyllites. Locally graphite tremolite marbles.
		Alwar Group (mainly psammitic)	~~~~~Gradational contact~~~~~	~~~~~Gradational contact~~~~~
			Unit 3: Amphibole quartzites, amphibole gneisses, marbles, dolomites, amphibolites, etc. Unit 2: Quartzites with local arkose, biotite quartzites, orthoquartzites, protoquartzites etc., bands of phyllites, mica schists, hematite and/or magnetite quartzites, etc. Unit 1: Mica schists, phyllites, feldspathic schists, biotite gneisses, garnet-mica-schists, etc. <i>Base not exposed</i>	Unit C: Banded amphibole quartzites, amphibole marbles, para-amphibolites, less commonly quartz-mica schists. Locally banded iron-ores. Unit B: Banded quartzites, dominantly arkosic, less commonly amphibole and mica-bearing. Unit A: Mica-schists with quartzitic bands and micaceous quartzites. <i>Base not exposed</i>

2.2.4.1 Structure

Structurally, the area is quite complex, and the region reveals a history of tectonic deformation with at least three generations of folding and faulting on micro-, meso- and macro levels. The following discussion is based on the field investigations by Das Gupta (1968), Gupta (1974) and fieldwork by the author.

In the area around Babai, the rocks are folded into a longitudinal anticline trending NNE-SSW. The nose of this fold is exposed west of Babai, plunging south. The fold becomes overturned towards east when traced north-eastwards along the strike, near Bamno ki Dhani. On the east, the Babai anticline is flanked by a tightly appressed longitudinal syncline (the Papurna-Taonda syncline) extending up to Taonda in the northeast. The rocks lying towards the east of Babai are separated from the main fold by a major thrust, called the Babai-Taonda thrust. The thrust zone is marked by slickensides and shearing-brecciation. Widespread alterations in the form of silicification, muscovitization-sericitization, limonitization, and sometimes carbonatization and chloritization are observed all along the thrust-zone. At places, *e.g.*, near Saintali ki Dhani and Karmari ki Dhani, rich sulfide mineralization is present. Also, along the thrust, bodies of granite-granodiorites have been emplaced.

A large number of faults (longitudinal and transverse) and thrusts following the contacts or cutting across the various litho-units are present in the area. Invariably they are marked by shear zones and often by alterations and mineralization (*e.g.*, the Tutiwali-Ladniwali mineralized zone). A major transverse fault runs across western hilly part of the study area and passes from the south of Akwali and Gadrata.

2.2.4.2 Lithology

The area has been mapped by various workers on different scales (Heron, 1923; Das Gupta, 1968; Gupta, 1974). Gupta (1974) mapped the area on a scale of 4" = 1 mile (1:15840), identified two major categories of rocks in the field, and classified them according to the

scheme shown in Table-2.2. Taking the map prepared by him as reference, most rock types have been located in the field and field samples have been analyzed in the laboratory (see Chapter 4 for details). However, the rocks classified as para-amphibolites have not been studied by the author in the field, since the fieldwork has been concentrated mainly in the area west of the Babai, and most of the para-amphibolites mapped by Gupta (1974) occur towards the east of Babai. Similarly, ferruginous quartzite and conglomeratic quartzite outcrops are spatially small and have been ignored at the scale and requirements of the present study.

Table-2.2 Important rock units exposed in the study area (after Gupta, 1974).

Quartzites

1. Banded arkosic quartzites
2. Banded amphibole quartzites
3. Micaceous quartzites
4. Pure/peak quartzites

Metapelites

1. Graphite phyllites
2. Quartz-mica-chlorite schists and phyllites
3. Garnetiferous quartz-mica schists and phyllites
4. Andalusite phyllites
5. Staurolite-andalusite phyllites

Para-amphibolites

1. Actinolite-tremolite amphibolites
2. Garnet-actinolite amphibolites
3. Hornblende amphibolites
4. Garnet-hornblende amphibolites
5. Diopside-hornblende amphibolites
6. Cummingtonite-grunerite amphibolites

Marbles

1. Actinolite-tremolite marbles
2. Diopside-hornblende marbles
3. Graphite-tremolite marbles

Intrusives

- Orthoamphibolites
- Granite-granodiorites
- Pegmatites
- Aplites

2.3 Distribution of known mineralization

The various zones of copper and iron mineralization are grouped as 1) major zones, and 2) minor occurrences. It has been observed that the iron mineralization zones are concentrated towards the east and the copper mineralization zones to the west of the study area. In the following paragraphs, some of the important zones have been discussed briefly:

1. Major zones: Three major zones of sulfide mineralization and one zone of iron mineralization have been observed in the study area. These are – (i) Akwali zone, (ii) Tutiwali-Ladniwali zone and (iii) Saintali ki Dhani – Karmari ki Dhani zone for copper; and (iv) Dhauli Hill zone for iron. All of the above zones have been visited by the author and systematic rock samples have been collected for various laboratory analyses, as discussed in Chapter 4.

The *Akwali zone* extends from Akwali group of workings in the northeast to Bhootwali-Paniwali workings in the southwest for a distance of nearly 3.5 km. The mineralized host rocks are graphite phyllites and andalusite phyllites, which have been intruded by orthoamphibolites. Several xenolithic lenticular bodies of the gossanized phyllites are observed in the amphibolites. The phyllites are overlain by orthoquartzites. Alterations such as kaolinitization, silicification, and limonitization are commonly noted along the transverse faults in the orthoquartzites. The graphite phyllites are highly sheared and fractured and constitute a prominent shear zone, especially at and close to their contact with the orthoamphibolites. Limonitic coatings over phyllites in such cases are commonly observed, though there is no prominent continuous gossan in this zone.

The *Tutiwali-Ladniwali zone* is the largest continuous gossan zone in the area. It is commonly 5-10 m wide on surface and runs for a continuous strike length of about 3 km starting from Silatighati in the south through the old pits of Tutiwali and terminating about 1.2 km north of Ladniwali old pit. The gossan and the mineralization are located

close to the axial zone of Babai anticline. It has followed a shear-brecciated zone along a strike fault parallel to the axial-plane of the fold. Various types of arkosic and banded amphibole quartzites constitute the host rocks. In the vicinity of the mineralized zone, the host rocks exhibit pronounced wall-rock alterations in the form of extensive chloritization-limonitization of amphiboles and widespread introduction of chlorite, limonite, quartz, and rarely carbonates along the fractures and shear planes. Often the rocks are altered to quartz+limonite±chlorite±feldspars (or clays) assemblage, especially in the amphibole quartzite sequence.

The *Saintali ki Dhani – Karmari ki Dhani zone* extends for a strike length of 2.3 km from Saintali ki Dhani in the northeast to Karmari ki Dhani in the southwest. A large excavation close to the Babai-Khetri road running for about 100 m in NE-SW direction and a sheared gossan zone extending all along Saintali ki Dhani to Karmari ki Dhani are pertinent indicators of sulfide mineralization in this area. The zone is marked by intense shearing-brecciation and alterations in the form of muscovitization-sericitization, silicification, calcification, chloritization, limonitization, kaolinitization, and very common malachite stains, specks and encrustations. The main Babai-Taonda cataclastic shear (thrust) zone passes through this area. The granites have been emplaced along the thrust zone. The mineralizing solutions, which appear to favor the zones of cataclasis and brecciation along the shear zone have altered all kinds of rocks, viz., micaceous quartzites, para-amphibolites and granites as all of them exhibit hypogene alterations (such as development of muscovite, sericite, chlorite, carbonate, quartz) to varying degrees. Electromagnetic (Paul, 1968) and geochemical (Balasundaram, 1972) surveys have revealed anomalous centers in this zone; however the drilling by GSI could not intersect any prospective horizon.

2. Minor occurrences: A number of minor occurrences of copper and iron have been reported from the study area. Most of the minor occurrences are located towards the

west of the Babai-Khetri road, and the iron occurrences are concentrated in the northeastern part of the study area. Of the minor occurrences for copper, the notable ones are:

- a. The *Gatardi old workings* immediately north of Kalota (dark coloured small mounds about 15 m high) composed of graphite phyllites. The rocks are highly altered with well developed limonitic gossan and malachite staining.
- b. The *Kemli old pit and workings*, which lie towards NE of the Gatardi old workings in graphite phyllites. Massive quartzites underlie the graphite phyllites and are exposed due to ancient mining. Limonite gossan and malachite staining provide an indirect evidence of sulfide mineralization in this zone.
- c. The *Bilaiwali old working*, which lies on a small hillock towards the west of Babai, at a distance of about 0.5 km. It is confined to micaceous feldspathic quartzites which are sheared and brecciated and show limonitization and silicification.
- d. The old workings near *Suredi ki Dhani*, about 1.5 km NE of Babai on an angular hillock about 10 m high. The various rock types are micaceous quartzites with thin phyllite bands, mica phyllites and schists, banded actinolite marbles and para-amphibolites. These rocks have been intruded and cut-across by pegmatites. The sulfide mineralization has taken place in micaceous feldspathic quartzites containing thin bands of mica phyllites. Several secondary minerals such as large amounts of carbonates, muscovite-sericite, quartz, chlorite, talc, clay minerals and limonite with malachite stains are noted on the surface.
- e. A few gossan zones 3-4 km *east of Babai* in mica phyllites and schists, para-amphibolites, quartzites, and micaceous quartzites. These have subsequently been intruded by granites. Gossan consists of malachite stains, porous limonitic

coatings, and a few gangue minerals such as quartz, carbonates, chlorite etc. A large part is concealed under transported sand cover.

- f. Limonitic gossan zones associated with sheared graphite phyllites in the valley *west of Gadrata* hill are observed. The gossans constitute angular fragments of graphite phyllites in a variegated matrix of limonite along with quartz, calcite, albite, muscovite, chlorite, talc, and clays.
- g. The *Dhulang Hill old workings* are located about 5 km northeast of Papurna. A few abandoned old workings, gossans, and associated alterations indicate sulfide mineralization in this region. The rocks are micaceous quartzites containing thin bands of phyllites. The contacts of phyllites with quartzites are sheared, which are the preferred mineralization loci. An alteration halo extending for about 20 m, and characterized by a high amount of muscovite-sericite and quartz, with minor carbonates and chlorite is observed.

Of the above minor occurrences reported from the area described above, the author has located and sampled the sites a-d.

2.4 Surface indicators of mineralization: gossans and alterations

As the present study involves use of remote sensing data which records information from the top few micrometers of the surface, it is important to have a good understanding of the surface indicators of ore deposits. Two main categories of surface manifestations of deep seated mineralization are observed in the study area, as described briefly in the following paragraphs:

1. *Variegated limonitic gossan zones with malachite and azurite staining*: A brief account of gossans in KCB has been given by Rao (1971) and Muktinath et al. (1969). Gupta (1974) has provided an exhaustive account of the gossan zones and their characteristics from the study area. In the present area, the gossan zones occur in a wide variety of forms and associations. They often form bands and lenticular elongated irregular bodies

swelling occasionally to thickness of up to 10 meters. Gossans occur on varying topographical levels ranging from top and flanks of hills and mounds to floor of the valleys, sometimes covered with wind-borne sand. The gossans occur in graphite-phyllites, andalusite-garnet-quartz-mica phyllites, quartzites, banded amphibole and arkosic quartzites, para-amphibolites, graphite phyllites interbedded with graphite-actinolite marbles, banded amphibole-diopside marbles, and granites and pegmatites. Sometimes sheared fragments of host rocks occur in gossan samples. The gossans are both *in situ* and transported. The gossans, in general, contain limonite (hematite-goethite-lepidocrocite), specks of malachite, and azurite, many hypogene gangue minerals such as quartz, muscovite, sericite, chlorite, carbonates, and rarely cuprite and erythrite. The gossanized rocks can be grouped under the following five categories: (i) limonite-quartz rock; (ii) limonite-quartz-carbonate rock; (iii) limonite-chlorite rock; (iv) limonite-chlorite-quartz-carbonate rock; and (v) limonite-quartz-chlorite-graphite rock. Biotite and scapolite have also been observed in some samples (Gupta, 1974).

2. *Alteration – hypogene and supergene*: In the present area, a wide variety of lithologies serve as host rocks for mineralization, such as graphite phyllites, quartz-biotite phyllites, garnetiferous-andalusite phyllites (Akwali), graphite-quartz-biotite phyllites interbedded with graphite-actinolite marble, quartzites and banded amphibole-arkosic quartzites (Tutiwali), micaceous quartzites interbedded with quartz-mica phyllites (Suredi-ki-Dhani), quartz-mica phyllites (northwest of Kalota), banded amphibole-diopside marbles (Karmari-ki-Dhani), granites-pegmatites and para-amphibolites and micaceous quartzites (Saintali ki Dhani – Karmari ki Dhani zone). The rocks in the vicinity of these mineralizations are altered as a result of hydrothermal activity. These wall-rock alterations are of different degrees and of varying intensities, leading to mineral assemblages of both phyllic and argillic varieties of hypogene origin. Alteration in the form of chloritization and silicification is more widespread. Subsequent to, and

accompanying, chloritization is biotitization as seen in the Akwali zone. Other associated wall-rock alterations are carbonitization, muscovitization, sericitization, scapolitization and amphibolization. The amphibolization (anthophyllite-cummingtonite-grunerite) is common in the northern half of the study area (Das Gupta, 1964a). In the last stage of hypogene alterations (epithermal), extensive silicification, chloritization and sericitization took place (Gupta, 1974). Surficial alteration in the form of secondary silicification, calcification, kaolinization and gossanization took place during oxidation, weathering and supergene activity. Extensive limonitization is reported along the shear planes. These supergene alterations have superimposed over the hypogene alterations and have affected the primary host rocks as well.

2.5 Ore localization and metallogenesis: focus on lithologic controls

Since the aim of the present study is to evaluate the potential of ASTER multispectral remote sensing data in lithologic and alteration mapping, it will be useful to summarize the foregoing discussion about the study area with a special focus on alteration mineral occurrence in the region and their lithological and structural associations as an indirect aid to decipher the controls of ore localization.

The geologic controls of ore localization and the metallogenic processes in the KCB are still a matter of controversy. Following detailed geological and structural mapping of the major part of KCB, earlier workers suggested that the copper mineralization in Khetri is essentially epigenetic hydrothermal and derived from the granitic intrusions in the belt (Roy Chowdhury and Das Gupta, 1965). Mineralizing solutions responsible for large-scale iron-magnesium metasomatism in the metasedimentary country rocks were thought to be guided by faults and shear zones during deformation of the belt. Later, a partly syngenetic origin of the sulfides was favored for stratabound copper deposits of the KCB (Das Gupta, 1974; Deb et al., 1989), as well as for the pyrite-pyrrhotite deposits in Saladipura, SKCB (Ray, 1974). The proposed

metallogenic process for both types of deposits (Sarkar and Das Gupta, 1980; Sarkar et al., 1980) involves sedimentary-diagenetic ore deposition in shallow marine sediments, subsequently affected by metamorphism and deformation, within rift-related basins of Early- to Middle-Proterozoic age (Sinha-Roy, 1988; Deb and Sarkar, 1990). The recent re-interpretation of particular metamorphosed facies in the Khetri Copper Belt as former volcanogenic rocks has led some workers to suggest a primary volcanosedimentary or volcanic-exhalative origin, rather than a syndiagenetic origin for Khetri Copper Deposits (Basu, 1986; Das Gupta, 1992; Golani et al., 1992). As evident from the distribution and proximity of known mineralizations to the structural features, the sulfide and iron oxide mineralization in the region shows strong affinity to structural discontinuities and shearing, while some lithologic control on ore localization has also been observed. A detailed account on the controls of ore localization in the study area has been given by Roy Chowdhury and Das Gupta (1965), Roy Chowdhury and Venkatesh (1971), and Gupta (1974).

While mapping of structural features using remote sensing is a widely practiced method, the application of the technology in detection and mapping of the lithologic and surface mineralogic features has been at the core of the present investigation. Spectral analysis of ASTER multispectral remote sensing data and the validation of spectral mapping results discussed in the successive chapters has been based primarily on the 'ground-truth' discussed in the preceding paragraphs.

3.1 Introduction

The data used in this research has been categorized into two groups – remote sensing image data and ancillary data, consisting of geologic and topographic maps of the study area. In addition to these, a separate database comprising of field observations (field photographs and GPS-controlled field location data) and data generated in laboratory (petrographic and geochemical data) has also been created (discussed in Chapter 4). In the following sections, the salient features of various kinds of data used in this study have been described.

3.2 Remote sensing image data

Remote sensing image data of the study area comprises of:

1. ASTER Level-1B (L1B) 14-band at-sensor radiance data, which is the primary image data
2. ASTER on-demand higher level standard science products (Level-2 or L2 data) for VNIR-SWIR surface radiance and surface reflectance (AST_09 and AST_07, respectively), and TIR surface radiance and surface emissivity data (AST_09T and AST_05, respectively)
3. Landsat-5 TM data for a 512×512 pixel subset of the study area, used in preliminary analysis (as discussed in Chapter 4), and
4. An IRS 1D PAN image of a part of the study area (for resolution enhancement)

The remote sensing image data have been selected for dates with minimum vegetation cover, since vegetation greatly affects the quality of radiation reflected/emitted by materials of geologic interest (rocks and soils) and obscures their spectral signatures. Table-3.1 provides the salient characteristics of the sensor systems used in this study; details of data acquisition (date and time) have been provided in Table-3.2. Landsat TM thermal band has not been used. Descriptions of the various kinds of ASTER data types with nomenclature used by the Land Processes Distributed Active Archive Center (LP-DAAC) of NASA have been provided in Table-3.3. It is to be noted that this nomenclature is different from that used by the Earth Resources Data Analysis Center (ERSDAC) of Japan, which also distributes the ASTER data.

Table-3.1 Salient characteristics of remote sensing sensors used in this study.

Sensor/ sensor subsystem	Band Number	Spectral Range (μm)	Spatial Resolution (m)	Quantization Levels (bits)
ASTER VNIR	1	0.52-0.60	15	8
	2	0.63-0.69		
	3N [#]	0.78-0.86		
	3B [*]	0.78-0.86		
ASTER SWIR	4	1.60-1.70	30	8
	5	2.145-2.185		
	6	2.185-2.225		
	7	2.235-2.285		
	8	2.295-2.365		
	9	2.360-2.430		
ASTER TIR	10	8.125-8.475	90	12
	11	8.475-8.825		
	12	8.925-9.275		
	13	10.25-10.95		
	14	10.95-11.65		
Landsat-5 TM	1	0.45-0.52	30	8
	2	0.52-0.60		
	3	0.63-0.69		
	4	0.76-0.90		
	5	1.55-1.75		
	7	2.08-2.35		
	6	10.4-12.5	120	8
IRS 1D PAN	PAN	0.5-0.75	5.8	8

nadir-looking band; * back-looking band, for stereo view and DEM generation

Table-3.2 Scene acquisition details for the remote sensing image data used in this research.

Remote Sensing Image Data	Date and Time of Scene Acquisition
ASTER L1B	October 5, 2002; 05:43:51 UTC (Z)
Landsat-5 TM (path 147, row 41)	January 25, 1995; 05:30:00 UTC (Z)
IRS 1D PAN (path 95, row, 52)	January 30, 2000; 06:00:00.390 UTC (Z)

Table-3.3 General description of the various kinds of ASTER data products used for analysis in this study (for detailed description of the sensor and the data, see the official ASTER websites: asterweb.jpl.nasa.gov and www.ersdac.or.jp/eng/index.E.html).

Aster Product Name	Level	Description
AST_L1B: ASTER L1B Registered Radiance at the Sensor	L1B	This product is generated from L1A data (generated from L0 data by applying parallax correction and geometric correction and segmented into scenes) by applying radiometric correction and resampling using a specific map projection method.
AST_05: ASTER On-Demand L2 Surface Emissivity	L2	This product is generated from L1B TIR data by applying the temperature and emissivity separation (TES) algorithm of Gillespie et al. (1998).
AST_07VD: ASTER On-Demand L2 Surface Reflectance VNIR	L2	This product is generated by atmospheric correction of L1B data with atmospheric parameter inputs from other satellite systems onboard Terra
AST_07SD: ASTER On-Demand L2 Surface Reflectance SWIR	L2	This product is generated by atmospheric correction of L1B data with atmospheric parameter inputs from other satellite systems onboard Terra
AST_09VD: ASTER On-Demand L2 Surface Radiance VNIR	L2	This product is generated from L1B data by applying atmospheric correction to the VNIR and SWIR bands.
AST_09SD: ASTER On-Demand L2 Surface Radiance SWIR	L2	This product is generated from L1B data by applying atmospheric correction to the VNIR and SWIR bands.
AST_09T: ASTER On-Demand L2 Surface Radiance TIR	L2	This product is generated from L1B data by applying atmospheric correction to the TIR bands.
AST14DEM: ASTER On-Demand L3 DEM	L3	This DEM produced by stereo correlation of nadir and aft Band 3 data

3.3 Ancillary data and creation of a GIS database

Ancillary data in the form of topographic maps and geologic maps of the study area in analog (hardcopy or paper) format have been processed to create a geocoded coregistered digital database using standard GIS tools. In addition to this, a Digital Elevation Model (AST14DEM) created from ASTER L1A stereo image pair (bands 3N and 3B) of the study area has been obtained from the LP-DAAC's EOS Data Gateway (EDG). This DEM has been used for remote sensing image data preprocessing (topographic corrections) and creation of Digital Terrain Models (DTMs) for display and analysis purposes. The specifications of the various ancillary data sources in this category have been summarized in Table-3.4.

Table-3.4 Specifications of the ancillary data used in the study.

Data	Scale	Year of Production
Survey of India Topographic Maps coded 45M/9 & 45M/13	1:50000	1989 (surveyed 1985-87)
Geologic Maps:		
1. Heron, 1953	1:250000	1953
2. Das Gupta, 1968	1:100000	1968
3. Gupta, 1974	1:6000	1974
4. GSI, 1997	1:50000	1997

The standard GIS processing involves conversion of analog data into digital format either as raster images or vector shapes, followed by georeferencing the data layers based upon a user-defined geographic reference system, and co-registration of different layers so that they can be overlain within a common geospatial frame. In this study, the topographic maps have been scanned; georeferenced using Geographic Latitude/Longitude coordinate system with WGS84 datum and ellipsoid, mosaicked, and reprojected in UTM projection system with WGS84 datum and ellipsoid to create a topographic base map of the study area. All other data have been co-registered to this base map.

A DEM has been created from the topographic map by vectorizing the contours (at 20m elevation levels) through conventional onscreen digitization, rasterization and interpolation through non-linear triangulation (Triangular Irregular Network (TIN) modeling). This DEM has been used along with ASTER stereo DEM for topographic correction of remote sensing image data as described in detail Chapter 6.

One of the basic requirements of this research is the availability of a geologic map to be used for ground-truthing of the results of remote sensing spectral analyses. Geologic maps from the various sources shown in Table-3.4 have been scanned, and subsequently co-registered to the base map mosaic and with each other. Lithologic boundaries of these maps have been vectorized as segments, followed by topology creation and construction of vector polygons. Through labeling of the vector polygons, analog geologic maps have been converted into georeferenced vector digital lithologic maps. Relevant lithologic information common to all

such maps has been compiled to create the final reference lithologic map of the study area, as shown in Chapter 2 (fig. 2.3). This map has been used for validation and final interpretations (Chapter 9) of ASTER-based spectral lithologic and alteration mapping, as described in Chapters 7 and 8, respectively.

3.4 Field and laboratory data

Field visits during two field seasons (January-February 2004 and 2005) have been made to collect field data and samples for subsequent laboratory investigations. The details of the sampling and analysis techniques, and obtained results have been provided in Chapter 4. Briefly, the field data collection has involved collection of GPS-controlled location data, identification and sampling of known/reported mineralizations, field photography of prominent field features, information collection on geomorphology and geobotany, as well as identification of type areas of major lithologic categories, and their sampling. The rock and soil samples collected during the fieldwork have been subsequently analyzed through petrographic microscopy and ICP-MS trace-metal geochemistry.

3.5 Software tools

A variety of GIS and image processing software tools have been used to process the remote sensing and ancillary geodata. All computing has been carried out in Microsoft Windows environment. Basic image analysis and GIS thematic data layer preparation has been carried out using ERDAS Imagine (versions 8.6 and 8.7), and ILWIS (version 3.2) software. Atmospheric correction of ASTER LIB image data and subsequent spectral analysis has been carried out using ITTVIS ENVI (version 4.2). Topographic correction has involved use of ERDAS Imagine Spatial Modeler and Spectral Analysis Workstation modules, in addition to statistical data analysis in Microsoft Excel and Golden Grapher (version 5.0). Spectral

modeling of ASTER TIR surface emissivity data (AST_05) has been carried out using the Curve-fitting Toolbox and dedicated programming in MATLAB environment. Standard digital image processing and vector graphics software have been used for creation and editing of the manuscript and figures shown in this thesis.

3.6 Methodology overview

To meet the research objectives, the following methodology has been adopted:

1. A comprehensive and exhaustive literature review pertaining both to the methods of lithologic and alteration mapping using multispectral remote sensing image data, as well as to the particular capabilities of ASTER data in such applications.
2. Collection and conversion of all available analog map data into digital format, followed by geocorrection and spatial co-registration
3. Co-registration of the remote sensing image data with the ancillary map data and orthorectification using a digital elevation model (ASTER stereo DEM)
4. Creation of a vector database of the topographic and geologic map data
5. Precise atmospheric and topographic correction of the remote sensing image data to obtain surface reflectance image of the study area
6. Evaluation of the available Temperature and Emissivity Separation (TES) methods to obtain a surface emissivity image from ASTER TIR L1B radiance-at-sensor data and comparison with the standard ASTER TIR emissivity product
7. Generation of a silica weight percent map for the study area using existing as well as novel approaches
8. Spectral processing of the VNIR-SWIR surface reflectance data to determine alteration and bedrock mineralogy of the exposed surfaces

9. Collection of field samples, their laboratory petrography and trace-metal geochemistry to understand the nature of rock alteration and for verification of remote sensing analyses
10. Data synthesis, establishing an alteration model for the study area, and confirming using field and laboratory petrographic data

The broad conceptual framework and methodology adopted in this research has been shown in Figure-3.1.

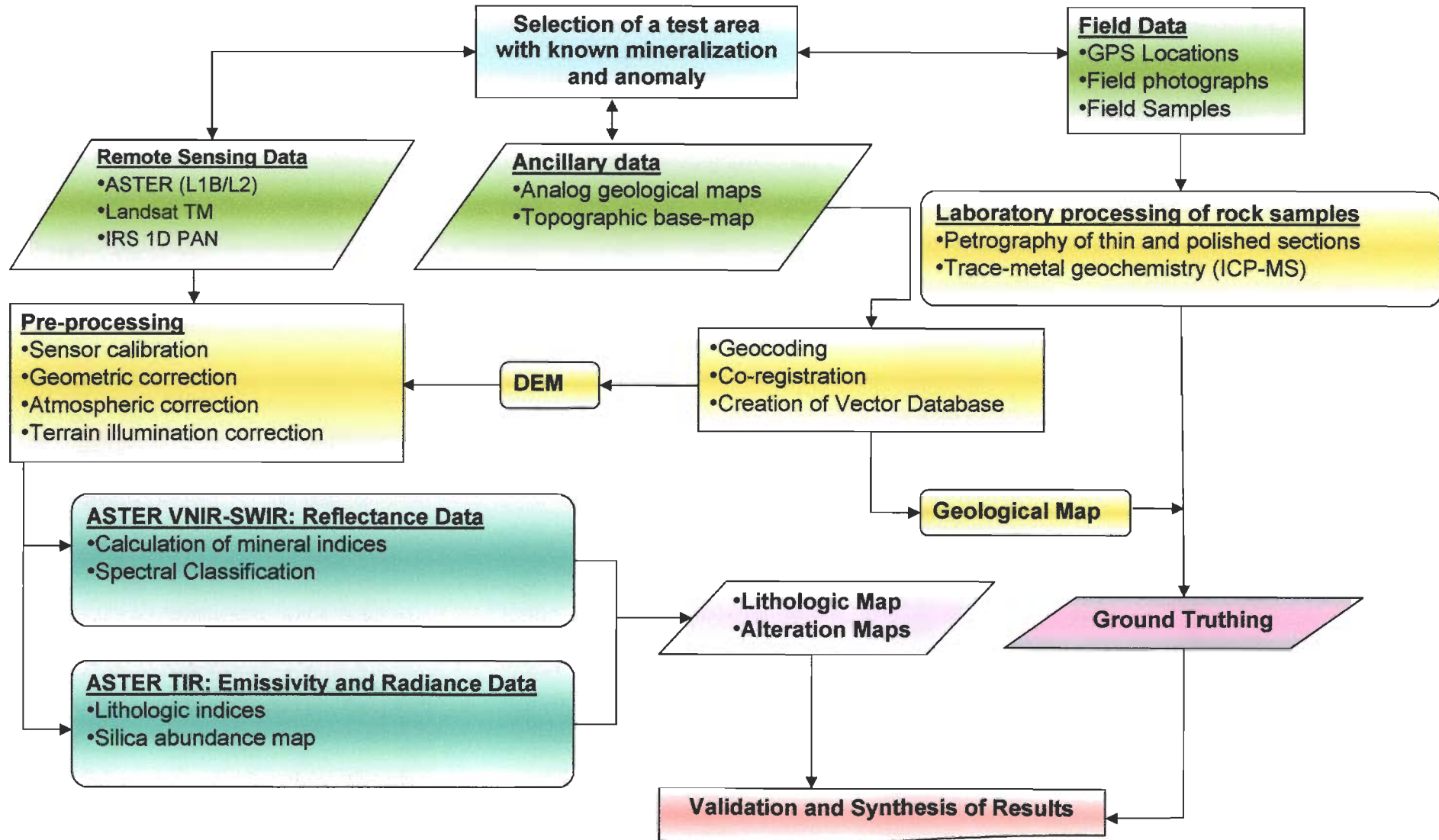


Figure-3.1 Overview of the research methodology adopted in the study.

Field and Laboratory Studies: Petrography and Geochemistry

4.1 Statement of purpose

The primary objective of field and laboratory studies has been to substantiate and verify the findings of spectral mineral/lithologic mapping using ASTER data, since the combined response of surface materials within a pixel controls the spectral response recorded by the remote sensor. The analyses have involved field data collection (field photographs, GPS locations of type-rock areas and mineralized areas, and their field sampling); petrography of rock thin-sections to understand the bulk mineral constitution, and alteration (if any); and trace-metal geochemistry of rock samples to study the metal anomalies associated with alteration and (consequently) spectral signatures defining potentially mineralized areas.

4.2 Area selection and definition of analytical objectives for field and lab studies

Previous studies based on Landsat TM data of the study area have indicated the presence of a regional anomalous zone of OH alteration towards the north of Kalota, as observed on the processed TM images (TM7/TM5 ratio image, fig. 16.62 in Gupta, 2003; see fig. 4.1). The primary basis of the selection of the study area was to study the exact nature of this anomaly. On the basis of tonal variations in regolith observed in the field (fig. 4.2) and petrographic analysis of field samples collected from the area (described later), which indicate the existence of some clay minerals and chlorite in the amphibolites, banded amphibole quartzites and metapelites constituting the anomalous zone, it has been interpreted that the feature is mainly due to the widespread secondary (supergene) alteration and weathering of rolled amphibolite rock fragments, with some contribution from the vegetation cover.

The individual analytical objectives identified for the field and laboratory studies have been briefly introduced in the following paragraphs. The details of the results obtained from the studies have been explained in subsequent sections.

Field studies: Field studies have been carried out to establish the ground-truth through collection of field data related with geomorphology, geological setting and botanical characteristics (vegetation cover) of the rock units in the study area. The fieldwork has been carried out during two field seasons (January-February, years 2004 and 2005), and has been guided by the interrelationship of the nature of geologic information recorded by remote sensing (ASTER images) and its real-world occurrence. In most part, the fieldwork has been carried out in the southwestern hilly part of the study area where good outcrops of all major rock units are available, and within the interpreted regional OH⁻ anomaly zone.

Petrography: Thin-sections of rock samples collected from the type-rock areas, known mineralized areas, and from the interpreted regional OH⁻ alteration anomaly (fig. 4.1) have been examined under the microscope to determine the mineral constitution of the rocks and to ascertain the nature of their alteration (whether primary or secondary). Emphasis has been laid upon identification of the primary and alteration mineralogy. Effects of secondary weathering and the role of rock texture have been studied in greater detail as they have direct impact on the reflected electromagnetic radiation reaching the remote sensor.

Trace-metal geochemistry: Trace-metal concentrations of six metallic elements, viz. – copper, cobalt, molybdenum, lead, zinc and arsenic for selected rock samples from type-rock areas (representative litho-units), known mineralized areas, and the regional OH⁻ anomaly zone have been determined using an Inductively Coupled Plasma – Mass Spectrometer (ICP-MS). In order to see the effects of weathering and metal leaching by atmospheric precipitable water, the weathered surface chips (approximately 0.5 cm thick), and the relatively fresh parts of some samples have been analyzed separately.

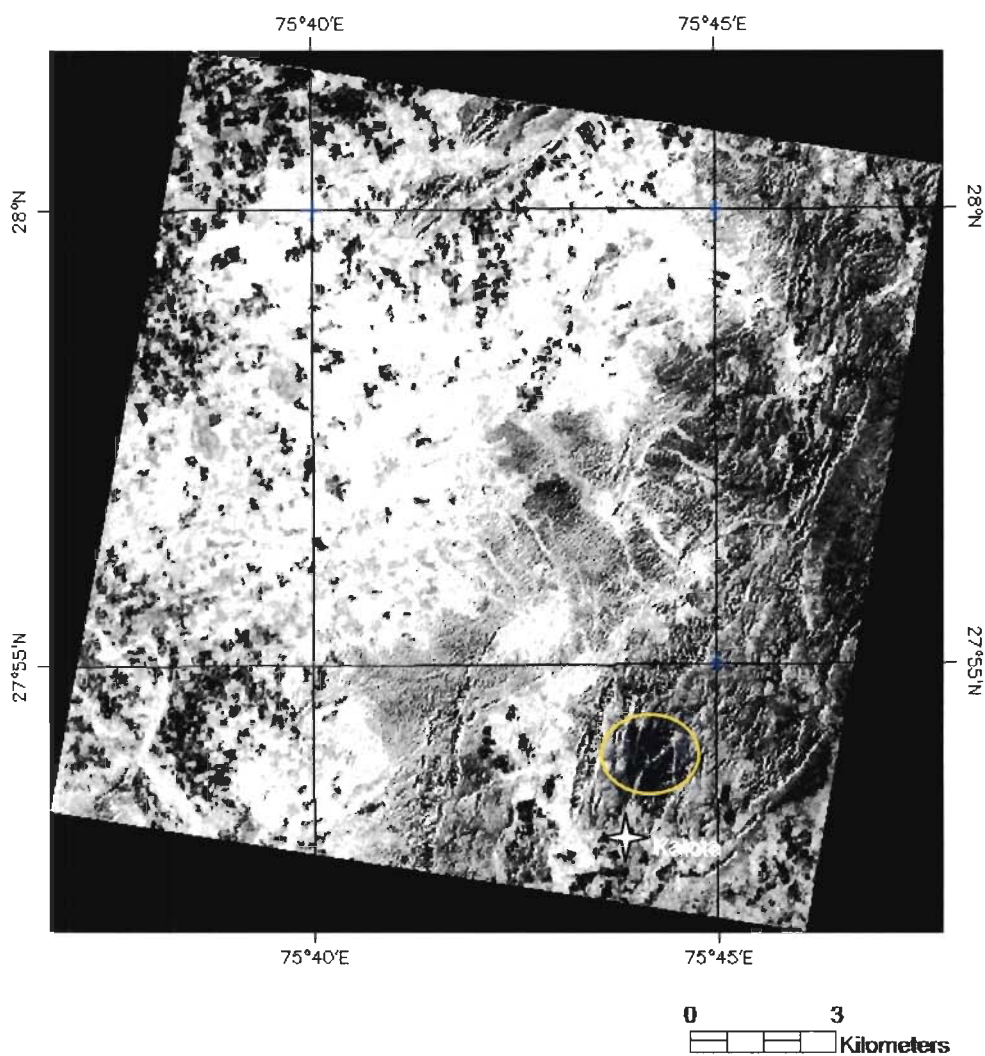


Figure-4.1 Landsat-5 TM 7/5 ratio; the regional alteration anomaly interpreted on the above image occurs as a semi-circular dark zone just north of Kalota, shown by a yellow ellipse.



Figure-4.2 Field view of the interpreted regional anomaly; camera is facing due west. Note the tonal differences in soil color

4.3 Field studies

4.3.1 Representative litho-units

Using the lithologic map of the area compiled after Gupta (1974) and GSI (1997) as base map, areas with uniform lithologic settings (type-rock locations), and with known mineralization have been identified in the field and their GPS locations have been recorded. GPS data have been subsequently digitally transferred to the master database for direct verification and validation of spectral mapping results. Table-4.1 summarizes the prominent field characteristics of the main lithostratigraphic units, with focus on their expressions on remote sensing images (particularly the ASTER image) of the area.

4.3.2 Mineralized areas

There is widespread base metal (mainly copper) and iron mineralization reported from the study area (Gupta, 1974; Narsimhan, 1989). The more important of these mineralized sites have been identified in the field and systematic sampling has been carried out. Broadly, there are two categories of mineralizations – major and minor. Chandmari and Akwali are the major copper deposits, whereas Dhauli Hill is the main iron ore deposit in the study area. A brief introduction of these mineralized zones has been given in section 2.3, Chapter 2. The field characteristics of these sites have been described as follows:

Chandmari – Mineralization is limited mainly to the banded amphibole quartzites in contact with the garnetiferous chlorite schist and andalusite-quartz-mica schist at the base of the Khetri Fort. The abandoned Chandmari open-pit mine is approximately 200 m deep and runs in an arcuate shape. Large heaps of highly limonitized overburden of mainly andalusite-mica schist lay adjacent to the mine. The area is faulted and distinct gossan capping can be observed beside the mine site.

Akwali – Here the mineralization is hosted by andalusite and graphite phyllites/schists. The adit of the Akwali old working has been bored through an overlying outcropping sill of orthoamphibolite. Exploratory mining through an incline cut through the underlying biotite-andalusite schist has been carried out by the Geological Survey of India (GSI) which has intersected rich mineralized zones. Although there are no conspicuous visible signs of alteration in the outcropping orthoamphibolite, the valleys intercepting the mineralized site carry convincing evidences of mineralization in the form of cobbles of pyrite-chalcopyrite bearing graphite phyllites/schists. A traverse to the old working passes through rich gossanized zones within highly limonitized schist and banded amphibole quartzites.

Dhauri hill – The iron ore deposits of Taonda, lying towards the north-eastern part of the study area, are scattered and in general are of insignificant economic value. However, the lone magnetite-specularite deposits of Dhauri hill, located about 800 m SE of Taonda village, are economically viable and are under exploitation by private miners using crude shallow open-cut methods. Gupta (1974) has carried out detailed structural and lithologic study of the area and reported that this deposit occurs in banded calc-silicates (amphibole-diopside marbles), cut across by granitic rock bodies and is feldspathized on the western flank of the hill. Thick calcite veins with over 3 cm large well-developed calcite rhombs have been observed by the present worker during the walk up to the hill-top. The iron-ore body occurs as banded ferruginous quartzites in a concordant relationship with the enclosing calc-silicates. Co-folding of the relatively more brittle ore body with the enclosing calcareous and calc-silicate rocks has resulted in its shearing, faulting and fracturing. Chertification, feldspathization and scapolitization are the main manifestations of rock alteration in the area.

Suredi ki Dhani (Surhari) – Along the gravel road to Molala ki Dhani from Babai, within the broad main shear zone, two small mounds lying close to Suredi ki Dhani bear rich marks of subsurface copper mineralization. Gossanized surface rock, malachite stains, and carbonaceous sooty black surface indicating archaic slag heaps bear testimony to shallow copper

mineralization in the area. The micaceous feldspathic quartzite rock body is highly altered, sheared and intruded by pegmatite veins. Carbonate and plagioclase veins over 3-4 cm thick cut across the feldspathic quartzite host rock particularly near the pegmatites. The mounds are aligned in an 'L' form, and extend for about 100 m on both arms. Vegetation is absent on the rocky surfaces, although the flanks are covered with cacti and desert grass. Small blocks of arable land lie in the valley region between the two mounds.

Bandha ki Dhani – In the foothill region of the Bagor ridge, at the base of the Bagor Fort two mounds are seen with rich malachite stains and slag dumps indicating old mining and smelting activity. These are believed to be an extension of the extensive Tutiwali-Ladniwali-Bhootwali gossanized zone with documented copper and iron mineralization (Gupta, 1974). The banded amphibole quartzite rock body is gossanized with ferruginous rock surfaces, and is in traceable contact with garnetiferous chlorite schist and calc-silicates. By the shape and size of the old-mining pits it appears that the mineralization, though rich, is shallow and limited. Vegetation is moderate with mainly *Acacia nilotica* (Keekar) as the dominant vegetation type.

Karmari ki Dhani – The Karmari old working pit lies just beside the main Babai-Khetri state highway and is at road-level. The pit is ~10 m deep and ~50 m across, with slag dumps in the vicinity. Mineralization appears to be confined to the feldspathic quartzites that form the country rock. Just beside the pit is a mound of leucocratic granite. The granite is moderately altered (weathering of feldspars to clay), and relatively fine grained, indicating its near-surface emplacement. The site marks one vertex of the Karmadi ki Dhani - Silati ki Dhani mineralized shear zone.

Bilaiwali (Babai) – It is a small linear micaceous feldspathic quartzite hillock, about 500 m southwest of Babai, trending NNE-SSW, and extending for about 150 m. This outcrop is bounded by transverse faults, and makes up a part of the eastern limb of the main Babai anticline. It falls within the main cataclastic/shear zone, and is highly altered. Thick feldspar and remobilized quartz veins fill the fractured rock mass. Evidences of shearing in the form of

fault breccia and shatter effects are seen on the ridge. The accompanying mineralization is evidenced by sporadic malachitized surfaces. The southern tip of the hillock retains the marks of abandoned old working, in the form of pits and slag dumps. Alteration is widespread and diverse. Kaolinization, chloritization and silicification are the main forms of alteration in this part. Vegetation is scanty to nil on the ridge-top, while some thorny bushes cover the slopes.

4.4 Macroscopic and microscopic petrography

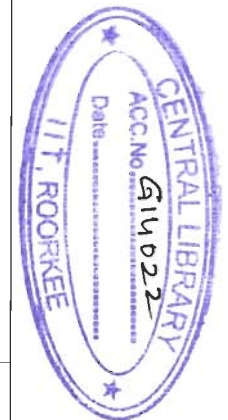
4.4.1 Sampling

During field work spread over two field seasons, 276 surface rock/soil samples (altered as well as fresh, wherever possible) have been collected for subsequent laboratory analyses to develop a ground-truth database. Figure-4.3 shows the sample locations displayed on a perspective view of the study area (ASTER band 3 draped over AST14DEM). The sampling has been conducted such that a part of it covered the representative rocks of the region, while the other part covered the reported mineralized sites with anticipated alteration features. In general, the samples have been collected from the surfaces of morning Sun-facing slopes having minimal vegetation interference. Most of the sampling has been restricted to the region west of the main state highway having good rock exposures. Wherever possible the sampling has been carried out in a regular fashion with normal sample spacing of about 30-50 m to match the nominal spatial resolution (30 m) of the remote sensing data (ASTER SWIR and Landsat TM). The samples have been used to understand the nature of alteration in the respective mineralized sites, and the alteration mineralogy of the region as a whole.

Table-4.1 Field characteristics of the main litho-units in the study area.

Lithostratigraphic unit (Gupta, 1974)	Relief and geomorphology	Vegetation cover	Alteration	Implications for remote sensing
<i>Unit A:</i> Mica-schists with quartzitic bands and micaceous quartzites	Low to moderate relief; good outcrops observed along the Khetri-Babai road, especially around Papurna; low drainage density; form NNE aligned topographic ridges towards the western limb of the Babai anticline	Scanty vegetation cover	Lying within the Babai-Taonda shear zone, this unit has been highly intruded by felsic igneous rocks (granites, aplites and pegmatites); strongly altered by primary hydrothermal and secondary weathering processes, especially in the form of kaolinization of feldspars	The unit appears in lighter tones on the RS image; as against mafic phyllites/mica-schists of Unit D, the mica-schists are distinct due to their light colored minerals; proximity to the main shear/cataclastic zone (Babai-Taonda shear zone) and high degree of surface weathering promises good alteration detection using ASTER data
<i>Unit B:</i> Banded quartzites, dominantly arkosic, less commonly amphibole and mica-bearing	Low relief; form valleys and slopes; highly dissected by drainage; best exposures are found towards the west of Bandha ki Dhani.	Scanty vegetation cover	Alteration limited to weathering of feldspars and chloritization of amphiboles rendering the rocks of this unit friable to touch and easily denudable	This unit appears in light tones on the RS images; weathering products of feldspars and amphiboles (clay minerals and chlorite) have well defined absorption features in the SWIR range enabling their effective detection, identification and mapping using ASTER data
<i>Unit C:</i> Banded amphibole quartzites, amphibole marbles, para-amphibolites, less commonly quartz-mica schists. Locally banded iron-ores	Variable relief; while amphibole bearing pelitic rocks form valleys and low relief slopes, the resistant Fe-carbonate-bearing calc-silicates form mounds with distinct rustic surfaces; variable drainage density	Moderate vegetation cover over banded amphibole quartzites, and scanty cover over calc-silicates	Alteration appears to be controlled primarily by surface weathering processes; in most part, chloritization of amphiboles in most rock types within this unit is the dominant alteration; surface iron staining (and malachite staining in a few places) is also noted; dolomitization of calc-	The high iron content of the rocks of this unit has a bearing on their remote detection using the RS data in the VNIR range; in addition, calcite/dolomite/chlorite all have well defined absorption features in the SWIR region of EMR; however, limited spectral resolution of ASTER is likely to affect very clear

		(amphibole marbles); cacti growth is distinct over calc-silicate mounds	silicates is evident in field; para-amphibolites towards the east of Babai exhibit stronger alteration	distinction among chlorite and calcite/dolomite since their absorption features coincide
<i>Unit D: Meta-pelites. Quartz-mica schists and phyllites, andalusite, garnet and staurolite bearing. Graphite phyllites. Locally graphite tremolite marbles</i>	In general these rocks occupy low relief areas; highly dissected by drainage controlled by structural elements; good outcrops of these rocks are observed in the western part of the study area; rocks, in general, have high mafic content making them appear dark in the field	Good vegetation cover, in general	Alteration appears to be primarily due to the agents of physico-chemical weathering; iron leaching from the amphiboles leaves the surface stained by limonite; amphiboles have altered to chlorite/biotite; carbonaceous matter of the graphite phyllites and tremolite marbles makes them stand out due to their sooty black surfaces, which are sometimes also malachite stained	As with Unit C, the rocks of Unit D appear in darker tones on the RS data. Their Fe content (limonitic surfaces) and weathered surfaces rich in chlorite and Fe-oxide make them well-identifiable using ASTER data, for reasons mentioned above
<i>Unit E: Massive quartzites, quartzites with phyllitic bands</i>	High relief; the rocks of this unit form the highest ridges and peaks that stand out topographically; very light colored rocks; minimal drainage; highly resistant to weathering	Scanty to nil vegetation cover	Almost completely unaltered; limonitic and pitted surfaces observed in the rocks of this unit towards the western limb of the Babai anticline; surfaces have distinct desert varnish layer owing to the arid climate and high relief	Except for the limonite and desert varnish, which have characteristic absorption features in the VNIR-SWIR region, these rocks lack any detectable alteration mineralogy using ASTER data. Their high relief and quartz abundances (almost purely quartzitic) make them good choices to test the applicability of the TIR data in silica abundance estimation and lithologic mapping
Unit F: Meta-pelites (same as in Unit D)	Most geomorphic characteristics are similar to the rocks of unit D, except that these are relatively	Moderate vegetation cover	Same as in unit D	Same as in unit D



	less weathered, though a clear distinction is difficult in the field, except for their superposition to massive quartzites			
Intrusives: orthomphibolite	Mostly high to moderate relief; negligible drainage; dark grey-green appearance in the field; in places slight weathering has resulted in limonitic staining of these rocks	Scanty vegetation cover	Mostly the orthoamphibolites are unaltered; weathering has resulted in chloritization of hornblende; no distinct primary alteration is visible in hand specimens; surfaces are limonitized in a few locations	These rocks stand out clearly on the RS images due to their scanty vegetation, dark tones, discordant intrusive nature and high contrast with the background in most places. Chlorite and limonite of these rocks is amenable to detection by ASTER VNIR-SWIR data. Mafic mineralogy can be well mapped using the TIR data
Intrusives: granite/granodiorite/ aplite/pegmatite/albite	Low relief; highly weathered; occupy the eastern half of the study area in particular; the soil and regolith obtained from these rocks is rich in Fe-minerals, clay minerals and mica, and occupies large tracts in the eastern and southeastern part of the study area	Moderate to good vegetation cover	Both primary and secondary modes of alteration is observed; alteration dominant along the main cataclastic zone, with brecciation common; development of clay minerals, scapolite, and limonite are the main evidences of alteration in these rocks; albitization is widespread	In general these rocks are leuco- to mesocratic, which leads to their brighter appearance on RS images. Clay minerals and scapolite have well defined absorption features in SWIR region, whereas limonite can be well detected using VNIR data. Albite has diagnostic absorption features in SWIR region, while feldspars in general can be identified using the data in the TIR range.

4.4.2 Representative rocks types

The region is represented by mainly five categories of rock types – quartzites (orthoquartzites, amphibole-bearing quartzites, micaceous, feldspathic or arkosic quartzites), meta-pelites (phyllites, schists), calc-silicates/carbonates (mafic-rich marbles), mafic metamorphics (para-amphibolites), mafic intrusives (orthoamphibolites), and felsic intrusives (granite, granodiorite, pegmatite, aplite and albitite). There are numerous variants of these rock types as the rocks of one category usually grade into the other over short distances. Seven samples from relatively large and uniform rock outcrops of the main litho-units, without any known close or inferred mineralization have been used to understand and describe the representative lithology of the area. The petrographic characteristics of these samples have been summarized in Table-4.2 and their hand-specimen photographs have been shown in Figure-4.4a-g.

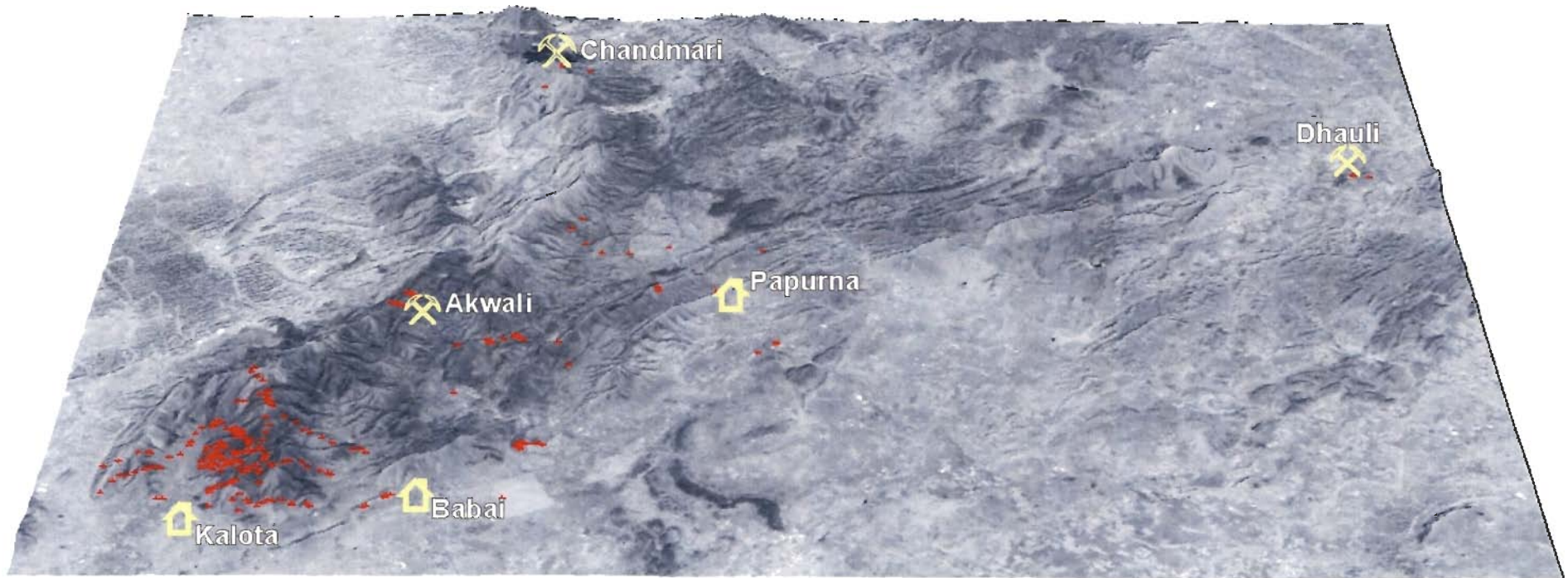


Figure-4.3 Distribution of field samples analyzed petrographically and geochemically. The background is a perspective view of the study area (ASTER band 3 draped over AST14DEM) facing due North. Sample locations are marked in red; prominent places within the study area have been demarcated, including the three main areas of mineralization.

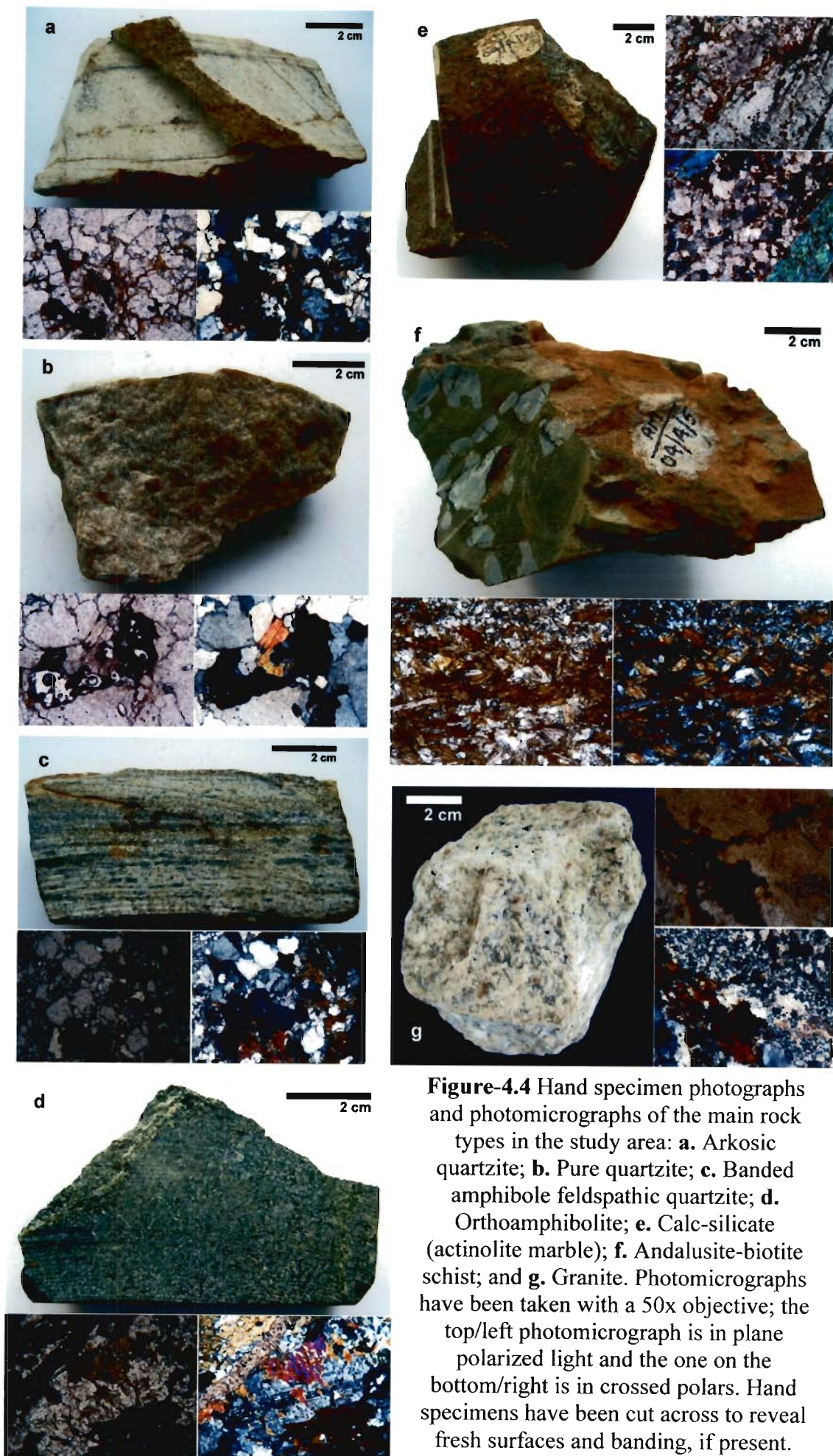


Figure-4.4 Hand specimen photographs and photomicrographs of the main rock types in the study area: **a.** Arkosic quartzite; **b.** Pure quartzite; **c.** Banded amphibole feldspathic quartzite; **d.** Orthoamphibolite; **e.** Calc-silicate (actinolite marble); **f.** Andalusite-biotite schist; and **g.** Granite. Photomicrographs have been taken with a 50x objective; the top/left photomicrograph is in plane polarized light and the one on the bottom/right is in crossed polars. Hand specimens have been cut across to reveal fresh surfaces and banding, if present.

Table-4.2 Thin-section microscopy of the samples for the representative rock types in the study area

S.No.	Rock Type	Sample ID	Location	Major Minerals	Minor Minerals	Remarks
1	Arkosic Quartzite	A1	N 27 54 37.4 E 75 45 52.2	Quartz	Plagioclase and some opaques	Iron oxide veins have been observed along the fractures and quartz grain boundaries; quartz grains are angular and tightly packed. Feldspar has weathered to give a cloudy appearance. The texture is coarse, and the grain sizes are variable.
2	Orthoquartzite	A3	N 27 59 35.9 E 75 46 28.6	Quartz	Stray grains of hornblende (and actinolite) in cavities, and iron oxides along a linear fracture	Tightly packed anhedral quartz grains. Some iron oxide staining along a fracture observed.
3	Banded Amphibole Quartzite	A6	N 27 53 33.8 E 75 44 59.5	Quartz	Hornblende, plagioclase feldspar and opaques	The hornblende occurs in thin bands, and has been altered to iron bearing minerals and opaques. Quartz is anhedral, and the texture varies across the bands, from large grains to small grains.
4	Granite	GRANIT	N 27 55 11.4 E 75 48 18.7	Quartz, K-feldspar	Some muscovite, plagioclase, and iron-oxide	Uneven anhedral quartz and visibly altered orthoclase; a few veinlets of secondary iron oxide. Some sericite has developed along the periphery of feldspar and quartz grains
5	Andalusite Schist	A5	N 27 59 42.7 E 75 46 43.1	Andalusite, chlorite	Some quartz and opaques (magnetite?)	The chlorite grains are uniformly distributed and heterodirectionally oriented in a groundmass of quartz. A large grain of andalusite (chiastolite) is also visible.
6	Calc-silicate (amphibole marble)	A2	N 27 55 00.8 E 75 46 46.6	Calcite, actinolite	Quartz, opaques (magnetite?)	The calcite is anhedral with a shattered appearance and the actinolite varies from columnar to acicular form. Both minerals have been altered and are embedded in a brownish fine grained matrix of Fe-bearing calcic mineral. The opaques have developed more around the tremolite-actinolite grains.
7	Amphibolite	AM1	N 27 55 14.5 E 75 45 51.5	Hornblende, K-feldspar	Actinolite, biotite and opaques, and iron stains	Slightly weathered. Hornblende is the main amphibole mineral, with some actinolite. In a few places the hornblende is seen to alter to biotite. Plagioclase appears cloudy.

4.4.3 Altered rocks

About 70 samples from the sites with known/ interpreted mineralization (and interpreted alteration) have been analyzed with the main objective of determining the alteration mineral assemblages present in the area. In general, the alteration minerals have been grouped as those of purely supergene / low temperature-pressure / weathering-related origin, and those related to hypogene / high temperature-pressure / hydrothermal activity-related origin. It has been found that while the dominant alteration mechanism in the region is chemical weathering, evidences of destroyed imprints of hydrothermal alteration are also preserved in some samples. Since the environment of mineralization in the region varies widely, as well as the type of mineralized host rock, the petrographic analyses of samples from individual sites have been discussed separately in the following paragraphs:

Akwali – In this area, systematic sampling has been carried out along two lines close to the adit of the old working. Samples along one line have been used for detailed petrographic analysis. Out of the seven samples used, five samples belong to the overlying orthoamphibolite sill, and the remaining two samples to the andalusite-biotite schist that forms the valley rock. The feldspar of the amphibolite has weathered to clay, while evidences of relict hydrothermal biotitization of hornblende have been observed (fig. 4.5a). Large grains of opaques (magnetite) have also been observed in orthoamphibolite.

Suredi ki Dhani (Surhari) – Along four lines, fifteen samples have been collected from this site. Thin-sections of these samples display a diverse alteration pattern. The micaceous feldspathic quartzite host rock has been altered variously due to shearing and emplacement of pegmatite. Alteration is both primary and secondary. Common alteration minerals in the area include sericite, calcite, chlorite, kaolinite, graphite, and Fe-bearing secondary minerals (fig. 4.5b-h).

Tutiwali-Ladniwali – As discussed in previous sections, this zone is one of the largest continuous gossan zones in the study area. Of the ten samples collected from this zone, three samples intercept iron-ore old-workings. Limonitization of the banded amphibole feldspathic

quartzite is the main form of alteration in this area. In addition to this, the thin-sections studied reveal presence of chlorite, biotite and opaques as well (fig. 4.5i-j).

Bilawali (Babai) – Out of the seven samples collected from this site, thin-sections of five samples have been studied under microscope. Lying within the main shear zone, the alteration of the parent micaceous feldspathic quartzite is diverse. The main alteration minerals include sericite, chlorite, secondary quartz, clay minerals (possibly kaolinite and montmorillonite), malachite, hornblende and biotite (fig. 4.5k-n).

Regional alteration zone North of Kalota – On a Landsat TM 7/5 ratio image, OH⁻-rich regions are represented by darker tones due to OH⁻ and H₂O absorption in TM band 7. A preliminary analysis of the Landsat 5 TM data (acquired in January, 1995) of the study area exhibited a large circular region to the North of Kalota village (fig. 4.1), which had been interpreted to be an alteration zone related to some hydrothermal activity in the area. To support and validate this interpretation, a large number of field samples have been collected in a grid fashion (see fig. 4.3). Petrographic analyses of 28 samples along a 3 km long profile traverse (at 50 m average spacing) passing through the interpreted regional OH⁻ alteration anomaly have been carried out. Weathering has been found to be the primary source of alteration, though the samples from the eastern part of the sampled area have shown some evidences of relict hydrothermal activity (chloritization, biotitization and kaolinization). The samples cover a wide range of rock types. In hand specimens and in thin-sections, limonitization, chloritization, sericitization and biotitization have been observed as the main forms of alteration (fig. 4.5o-q). Some samples, especially of altered orthoamphibolite and banded amphibole feldspathic quartzite also contain considerable amount of opaques (possibly magnetite).

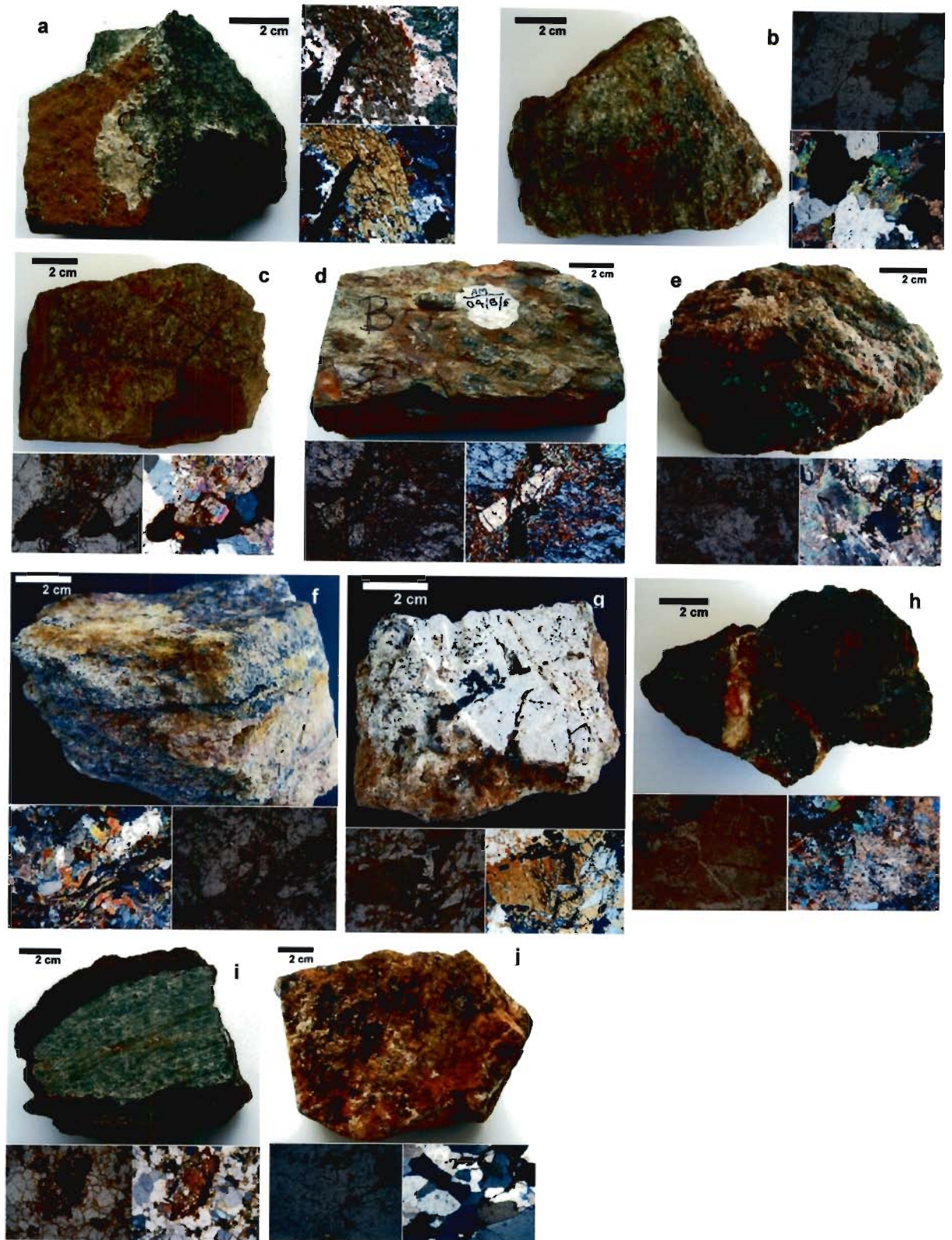


Figure-4.5 Hand-specimen photographs and photomicrographs of samples collected from mineralized and altered areas. The scheme of photomicrographs is the same as in Figure-4.5. Description about the samples has been given in the text.

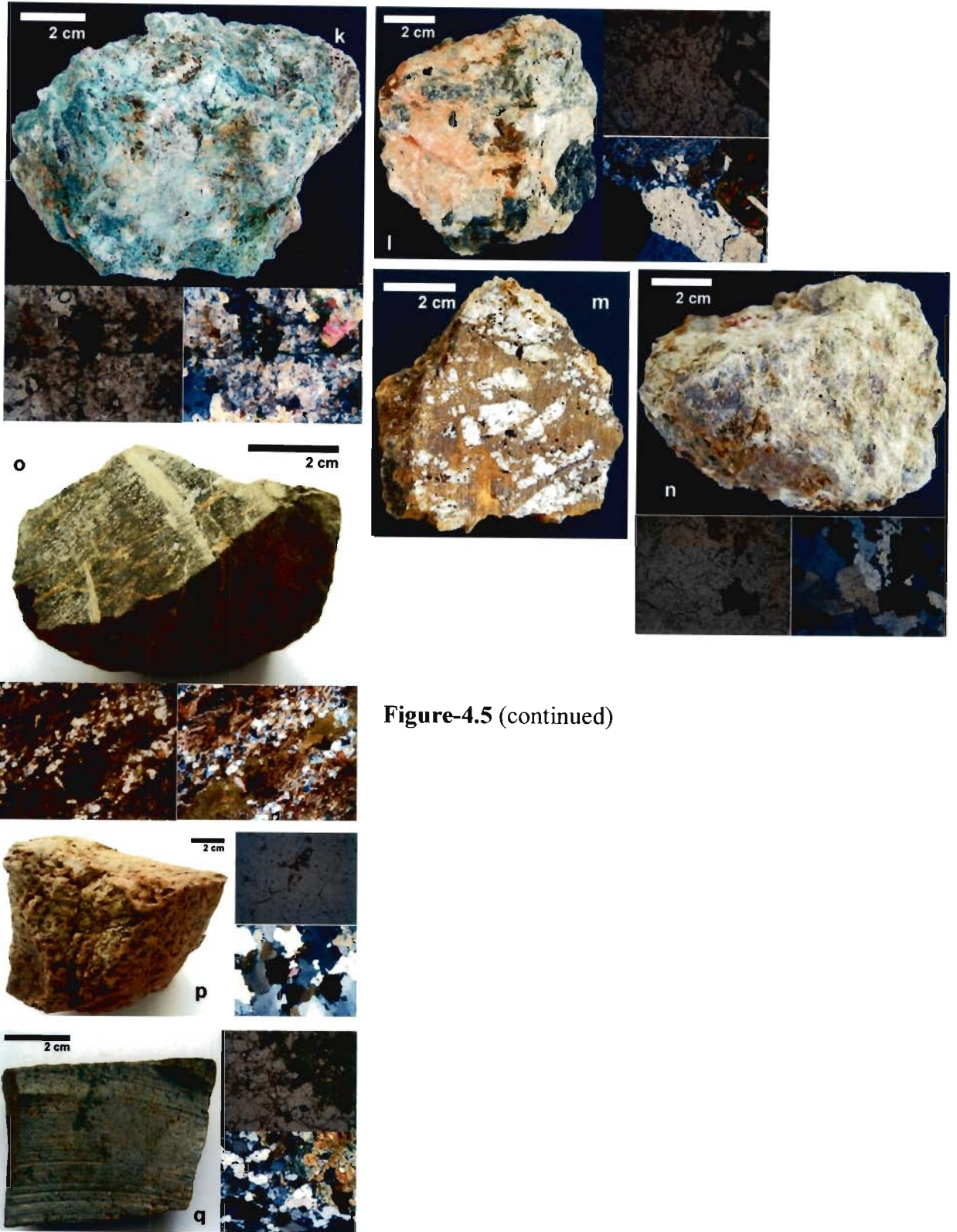


Figure-4.5 (continued)

4.5 Trace-metal geochemistry

To understand the relationship of alteration with the distribution and dispersion of metal content of the rocks, and to ascertain the effect of metal content of regolith on the remote sensing signatures, over 70 rock and soil samples have been analyzed for their trace-metal content, which includes six metallic elements *viz.* – Cu, Co, Mo, Zn, Pb and As.

4.5.1 Sample preparation: weathered and fresh samples

Since optical remote sensing is limited by its limited depth penetration, which is usually up to only few microns, for acceptable ground-truth support, it is essential that only information about the surface environment be collected and compared with the remote sensing results. For this reason, the fresh and the weathered (regolith) parts (wherever feasible) have been analyzed separately. This approach has helped in understanding the metal dispersion controls of weathering on metal concentrations.

Figure-4.6 summarizes the main steps involved in the preparation of rock samples for trace-metal geochemistry. There are mainly three stages in sample preparation for chemical digestion. The first two stages are essentially dry, whereas the last stage involves wet geochemistry. The first stage involves separation of the weathered and the fresh part, which is achieved by ‘chipping off’ the outer 5 mm skin of the sample, and using the chips and the inner core separately. In the second stage, the two sub-samples are crushed using a jaw crusher and then coned and quartered. A portion of each is oven-dried overnight to expel all adsorbed water. The dried samples are then pulverized in a ball mill, sieved, and then again pulverized using a pulverizer and sieved again to obtain < 200 micron particle size. In the third and wet stage, the weathered samples are first treated with concentrated H₂O₂ solution to release the carbonaceous content as CO₂, and then oven-dried. In the next step, 0.05g each of samples is weighed into previously acid-cleaned and dried Teflon beakers. The samples are now ready for digestion.

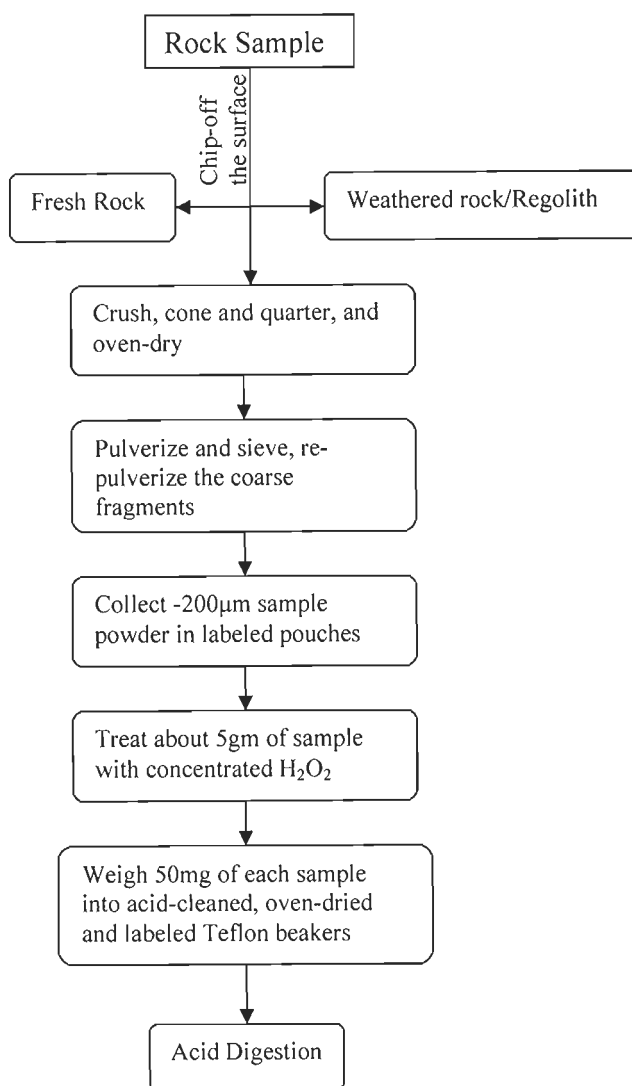


Figure-4.6 Procedure of sample preparation for trace-metal analysis through ICP-MS.

The acid digestion of samples has been carried out according to following standard procedure:

- A. Adding HF+HNO₃ in the ratio of 3:1 (for 50 mg sample, 10 ml HF and 3 ml HNO₃) to the sample in Teflon beakers and leaving overnight at room temperature with lid closed
- B. Heating the beakers on a hotplate for 12 hours with lid tightly closed
- C. Cooling the beakers at room temperature and observing for any remaining solid particles; if yes, drying the sample on a hotplate and repeating step A; else proceeding to step D
- D. Drying the sample completely on a hotplate, and adding 2 ml of 6N HCl
- E. Drying the sample, and adding 1 ml of 10% HNO₃
- F. Adding triple-distilled (TD) or Micropore™ filtered water to make it 100 ml by volume
- G. Filtering using vacuum suction apparatus and micropore filter paper and collecting in labeled containers

4.5.2 Instrumentation and calibration

The trace-metal concentrations have been analyzed with a PerkinElmer® Sciex™ make Elan® 9000 ICP-Mass Spectrometer (for instrument details see *las.perkinelmer.com*, fig 4.7) housed at the Institute Instrumentation Center of IIT Roorkee, India.

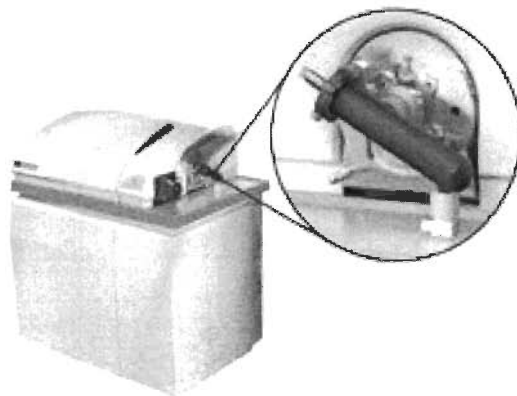


Figure-4.7 The PerkinElmer® Elan® 9000 ICP-Mass Spectrometer

Instrument calibration is an important and essential pre-requisite. This is usually achieved by running the instrument with internal standard materials of known elemental concentrations. In case of geological materials, the standard materials are powders of rock samples from type regions and with standardized documentation readily available to anyone. Rock standards are supplied by many organizations in the world. For the present study, three United States Geological Survey (USGS) standards have been used for this purpose:

1. BCR2 – Basalt from Columbia river
2. QLO – Quartz latite from Lake County, Oregon
3. SDC1 – Mica schist from Washington D.C.

In addition to above, multi-element standards at 10 ppb and 100 ppb levels have also been used for instrument calibration. The results are usually obtained in the units of parts per billion (ppb), which are recalculated for the sample weight used, and converted into the units of $\mu\text{g/g}$ or parts per million (ppm).

4.5.3 Results

The results of trace-metal geochemistry have been summarized in Appendix A. In the following sections, the main findings of the geochemical analysis have been discussed in some detail. The three sections separately cover the results for the representative rocks, the samples from the interpreted regional anomaly, and the mineralized rocks, respectively.

4.5.3.1 Representative litho-units

The primary objective behind determining the trace-metal content of the representative litho-units has been to find out the 'background value', *i.e.* the metal values that are normally present in the non-mineralized rocks of the area. Metal 'anomalies' can, therefore, be located for areas and regions where there is a significant deviation from these background values. It has been observed that the greatest variation in trace-metal content of the regolith in this area occurs in arsenic, followed by cobalt, copper, lead-zinc, and molybdenum (fig. 4.8). Arsenic values range from less than 1 ppm in orthoamphibolite to over 250 ppm in meta-pelites, Apart from the calc-silicates, which are mostly deficient in Cu, the other rock types of the area have Cu values within the range of 50-100 ppm. It has also been observed that in addition to Cu, the rocks in the region have anomalous Zn values, particularly in the amphibole-bearing rocks, such as ortho- and para-amphibolites and banded amphibole-arkosic quartzites. The proximity of the andalusite-mica schist sample (A5) used for the analysis to the Chandmari opencast mine can explain its anomalous metal concentrations, especially As. Trace-metal values for both granite and pegmatite are relatively similar, indicating that these come from a common source.

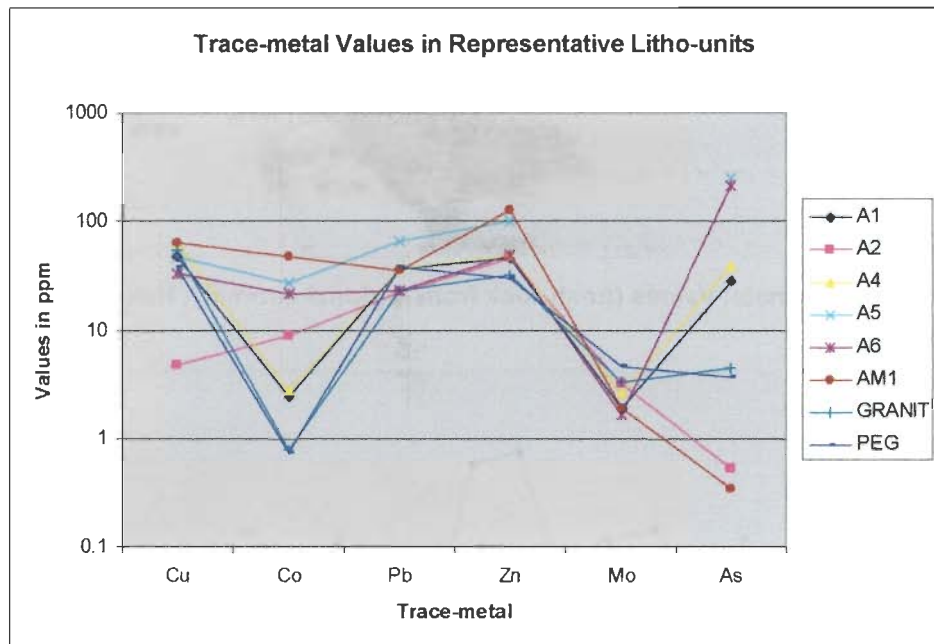


Figure-4.8 Trace-metal concentrations in the eight representative rock types of the area. For the rock types corresponding to the sample IDs given in the legend, see Table-4.2.

4.5.3.2 Regional anomaly, Kalota

The semi-circular regional anomaly towards the north of Kalota interpreted from a Landsat-5 TM 7/5 ratio image is about 3 km in diameter and is confined primarily within the anticlinal core (fig. 4.9a). Samples from a line across this region have yielded anomalously high Cu and As values, particularly from altered/weathered metapelites. Two phyllitic schist samples - B3/19 and B3/20 – have yielded Cu values significantly above the background. The arsenic content of these samples is also anomalously high. This can be explained from the fact that the samples have been taken from a highly weathered, limonitized outcrop, in contact with a weathered orthoamphibolite rock body. The weathered surfaces are, in general and regardless of the rock type, relatively enriched in Cu content than the fresh parts (fig. 4.10). For example, in the seventeen samples, all, except three, samples have Cu values at least two times as high as in the fresh part. This can be explained on the basis of various factors, such as chemical reactivity, atomic mass and ionic radii, which play important role in the relative accumulation / removal of a metal under the effects of chemical weathering in the presence of atmospheric precipitable water at different pH levels.

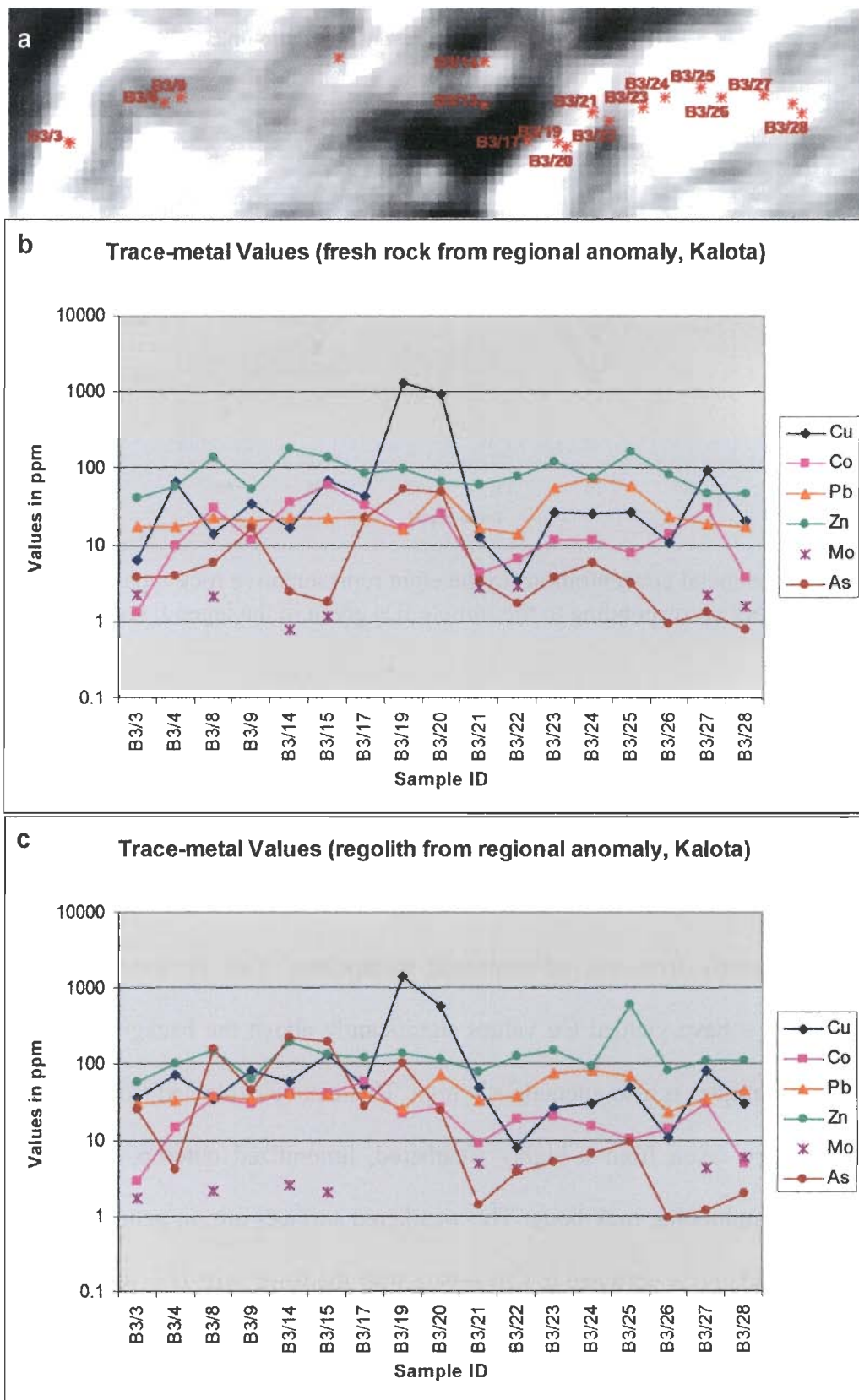


Figure-4.9 a. Locations of the samples within the regional anomaly; Concentrations of 6 metallic elements in: **b.** relatively fresh cores of the samples, and **c.** weathered surfaces.

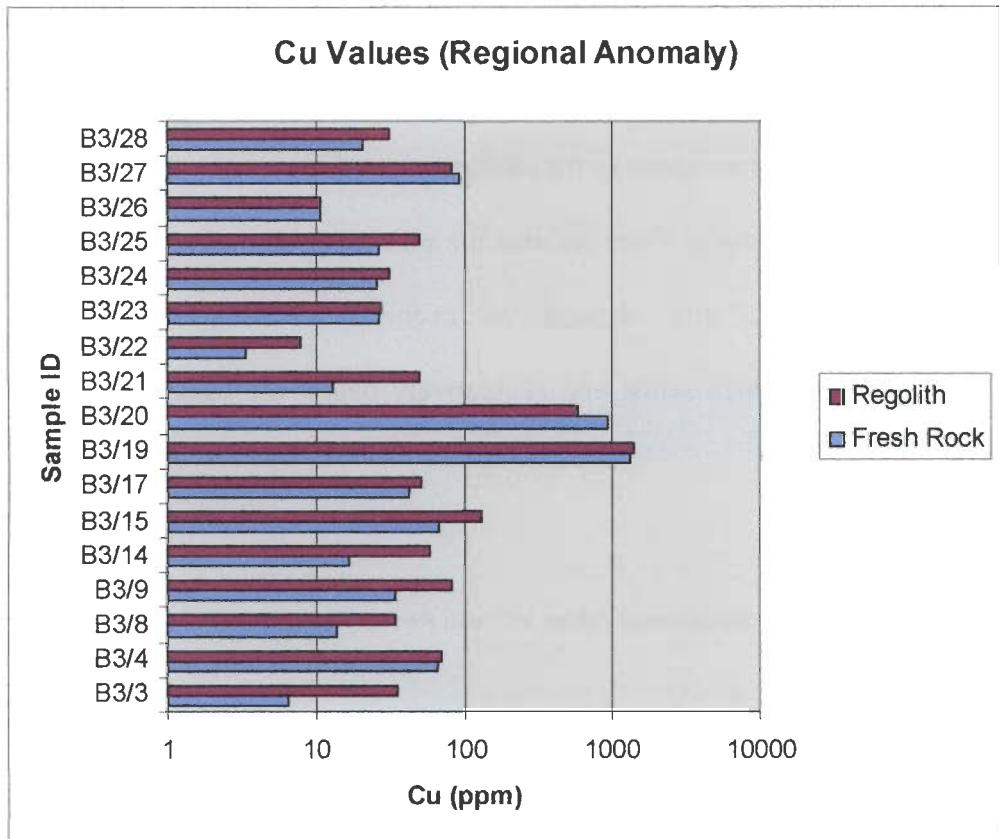


Figure-4.10 Relative comparison of metal (Cu) enrichment in the fresh and weathered parts of the samples collected from the regional anomaly towards the north of Kalota; it can be observed that the regolith is generally enriched in Cu.

4.5.3.3 Mineralized areas

Of the sampled known mineralized areas, four sites have been chosen for more detailed analysis. These are – Akwali, Suredi ki Dhani, Tutiwali-Ladniwali, and Bilaiwali (Babai). Sampling in these sites has been carried out in a profile mode, so that variation in trace-metal concentration both laterally and across rock types can be assessed and understood. In the following sections, the trace-metal analysis results for these sites have been discussed in some detail.

Akwali – The samples of this area represent two rock types, the orthoamphibolite and the andalusite-mica schist. The most peculiar observation from the trace-metal geochemical results for the seven samples from Akwali area has been the anomalous concentration of arsenic in the weathered surfaces. Arsenic content of the regolith from the area is roughly 100-200 times higher than the fresh rock. Although this observation holds true for most of the amphibolite

samples from all areas, in Akwali the trend is not restricted just to the amphibolites. Even though the sampling has been carried out adjacent to the existing exploratory incline of GSI, the Cu values of the samples are close to the background values in most part. Interestingly, Zn values in the amphibolite samples from the area are much above the background, going up to 150 ppm. The remaining metallic elements are evenly distributed. Cu is relatively more enriched in the andalusite-mica schist and is relatively below the background values in the amphibolites.

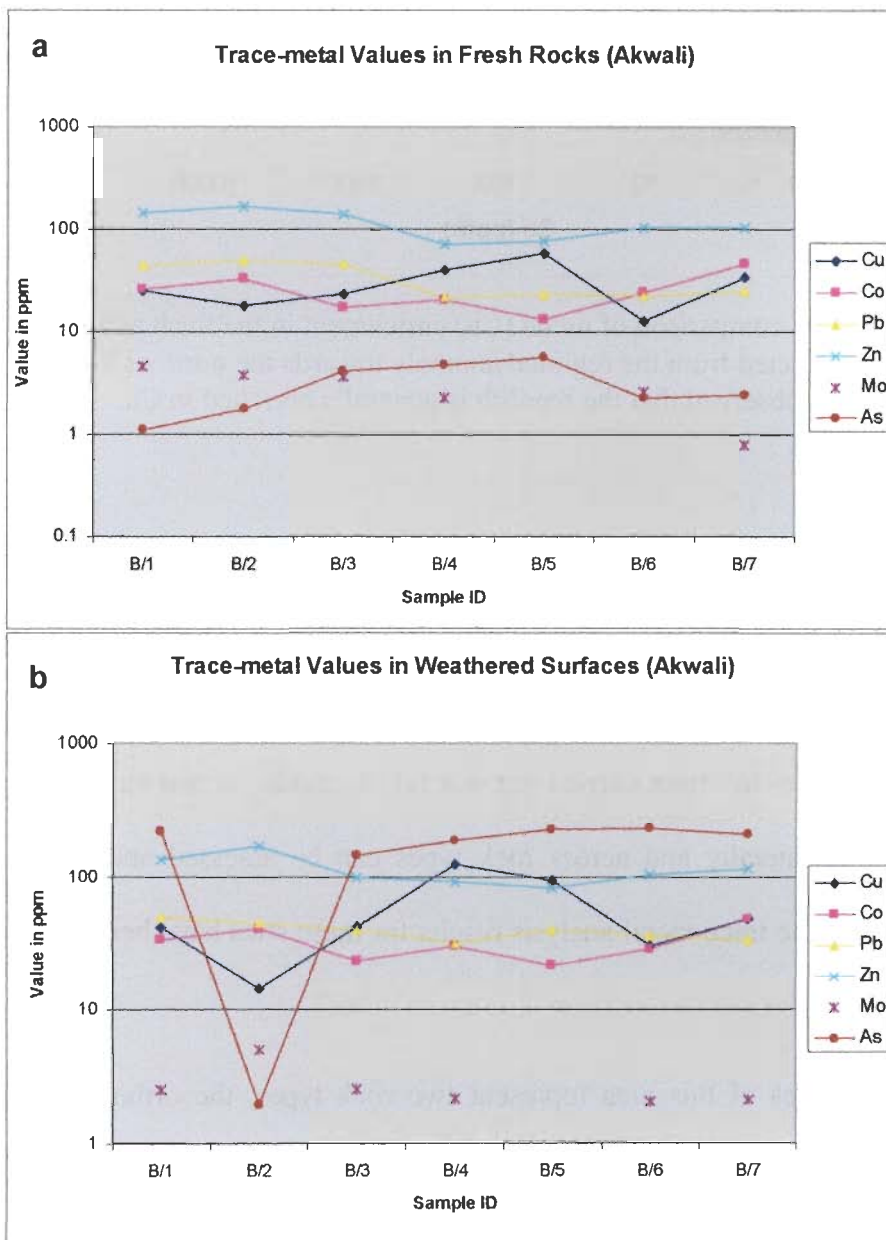


Figure-4.11 Trace-metal values for: (a) fresh; and (b) weathered parts of the samples collected adjacent to the Akwali underground mines. Except samples B/4 and B/5, which are andalusite-mica schist samples, remaining samples are all of orthoamphibolite.

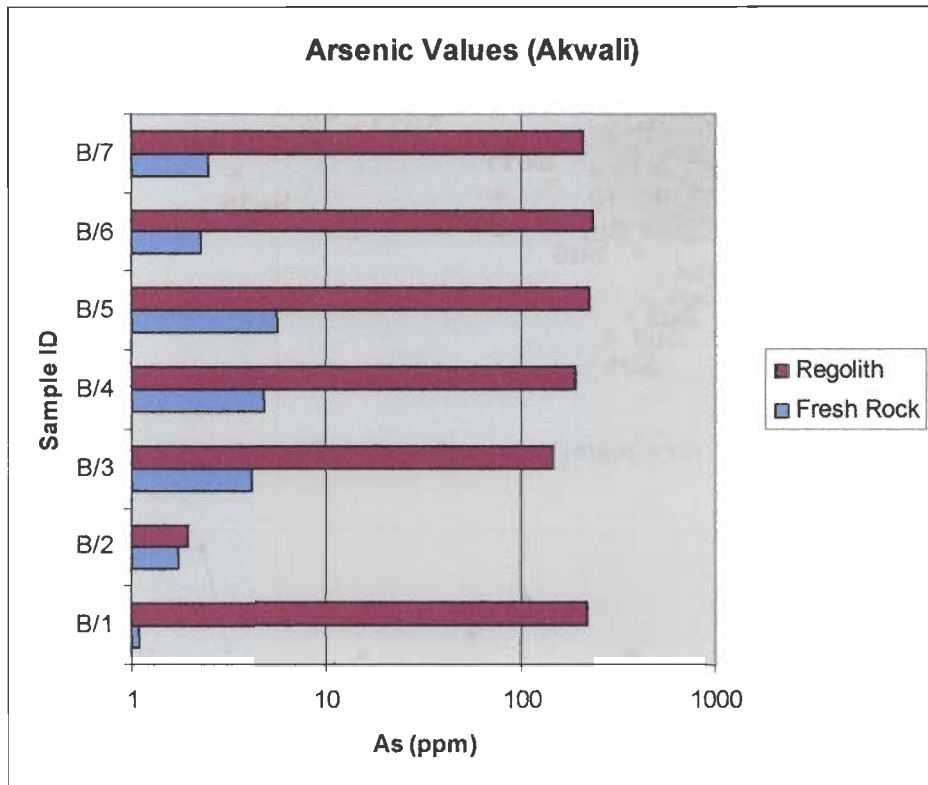


Figure-4.12 Arsenic content of the regolith and fresh parts of the analyzed Akwali samples.

Suredi ki Dhani – The sampling pattern for the 15 samples from Suredi ki Dhani is shown in Figure-4.13a. Whole-rock samples have been used for analysis, since the samples are highly altered. It has been observed that the nature of mineralization in the area is dominantly of copper with some cobalt mineralization. The concentrations of both of these metals in the samples of the area are significantly above the background values for unaltered quartzite rocks. A general correspondence among concentrations of Cu, Co and As has been observed for the samples from this area in terms of the trends for these metals in the samples regardless of the nature of alteration.

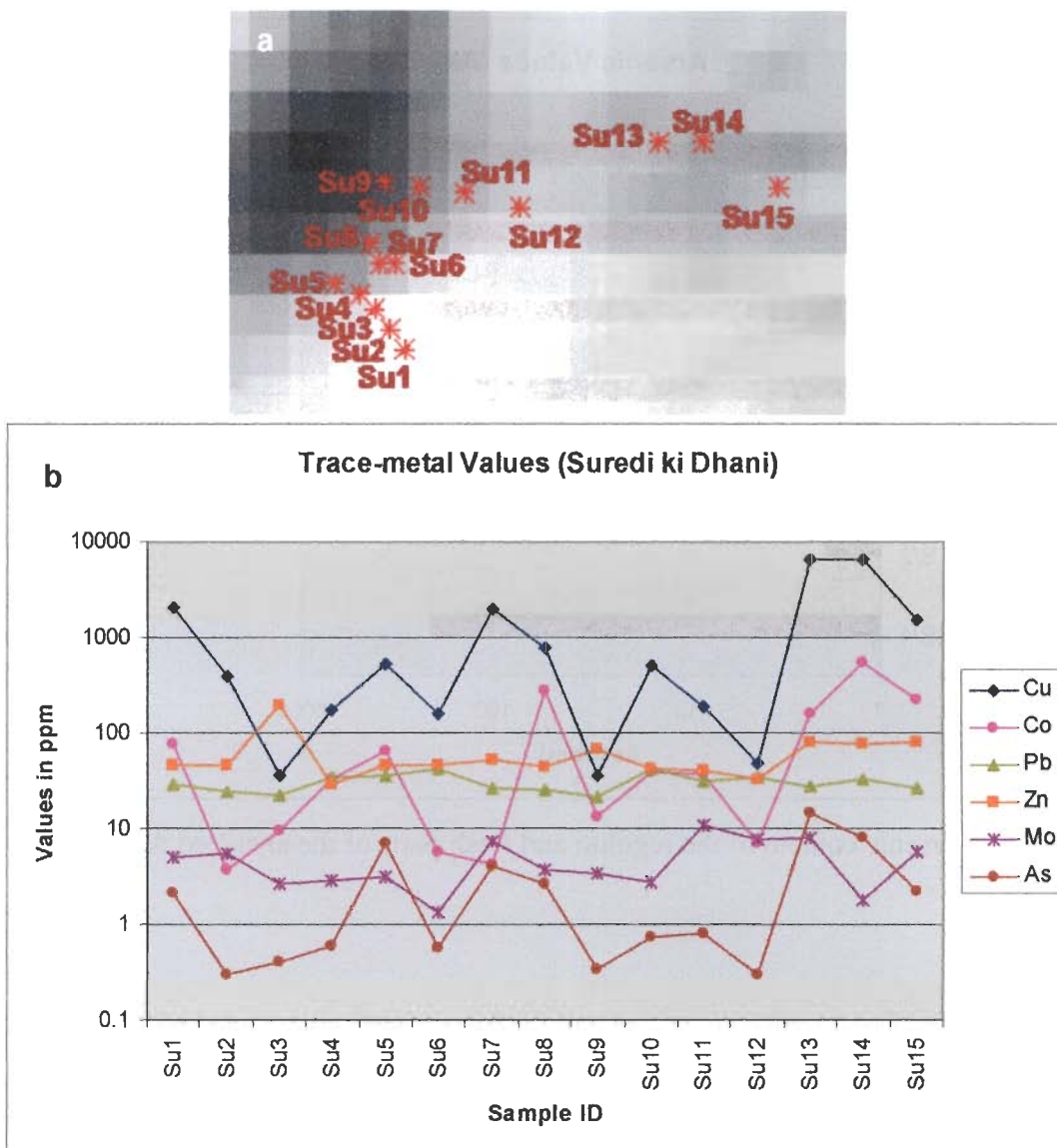


Figure-4.13 a. Sampling pattern; and **b.** Trace-metal distribution in the samples from Suredi ki Dhani area.

Tutiwali-Ladniwali – The sampling pattern for this area is shown in Figure-4.14a. The samples consist of two rock types – banded amphibole feldspathic quartzite and calc-silicate. Except one sample collected from the main gossan zone, which has Cu value higher than the background, the remaining samples do not exhibit any significant metal anomaly.

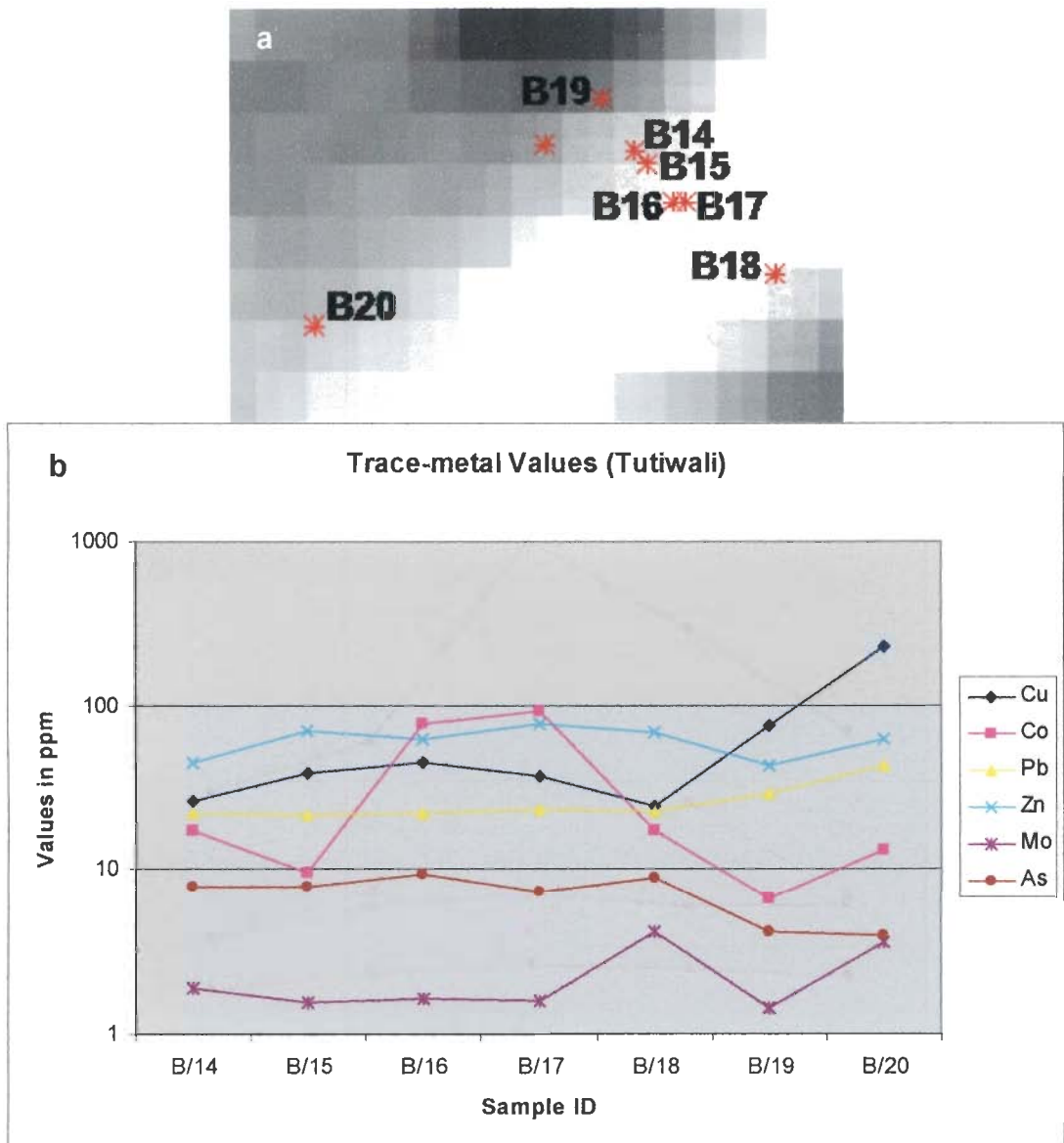


Figure-4.14 a. Sampling pattern; and **b.** Trace-metal distribution in the samples from Tutiwali-Ladniwali gossanized zone.

Bilaiwali (Babai) – The samples from this site exhibit the most pronounced alteration observed in the study area (fig. 4.5). As expected, the highly malachite-stained surfaces have significant Cu concentrations; particularly in one sample (T3) in which the Cu values are as high as 69000 ppm or roughly 7% (see Fig. 4.5k and 4.15b). The samples also appear to be relatively enriched in Pb and Zn.

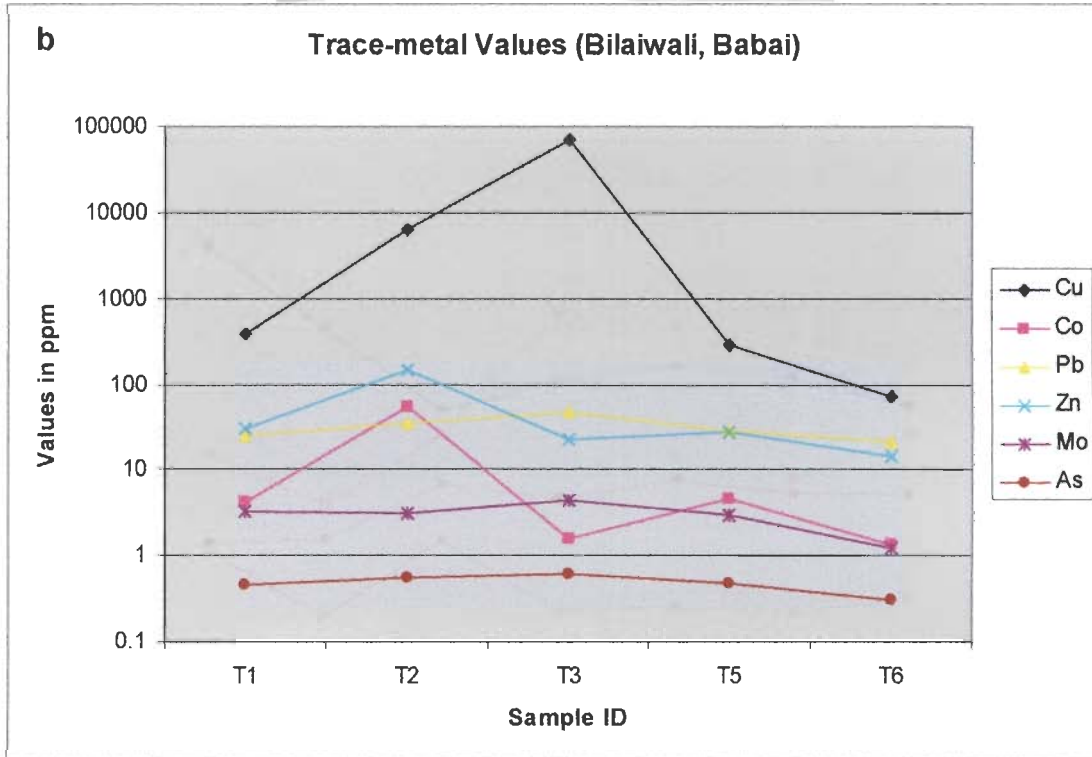
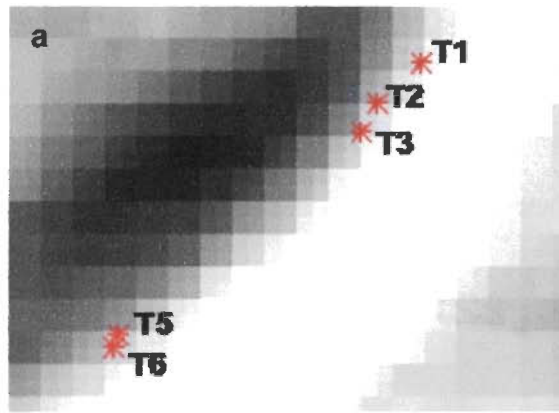


Figure-4.15 a. Sampling pattern; and b. Trace-metal distribution in the samples from Bilaiwali.

Infrared Spectroscopy and Geologic Remote Sensing – Theory, Background and ASTER Application

5.1 Introduction and scope

To understand the nature of geologic surfaces through spectral measurements the most important and fundamental requirement is the knowledge of the processes that influence the electromagnetic radiation upon its interaction with the geologic materials. This governs the application of remote sensing in geologic studies directed towards spectral lithologic/mineral identification and mapping in a given area of interest. As the present study is focused on the use of ASTER data towards this end, it is imperative to evaluate the capabilities of the sensor in light of the existing understanding of the underlying spectroscopic principles.

The region of the electromagnetic spectrum of greatest importance for geologic and mineral exploration applications is the infrared (1.0 μm to about 100 μm). Therefore, in this chapter the current state of knowledge about infrared spectroscopy as applied in geologic remote sensing has been reviewed. The study area is a well-documented base metal (copper, zinc, lead, and associated metals) sulfide deposit with distinct alteration mineralogy, as discussed in detail in Chapters 2 and 4. This has guided an extensive literature review of the application of remote sensing in mineral exploration activity around the world, with a special focus on two aspects relevant to the present study: 1) exploration of economic mineral deposits using remote sensing, and 2) particular application and advantage of ASTER data in such studies. The review presents the salient aspects of geologic remote sensing with a focus on mapping of lithologic and mineral units related with mineralization. The success of the technique, as will be seen, lies in the explicit success of a remote sensor in credible lithologic

and mineral mapping as this alone provides the most direct information regarding the mineral potential of an area.

5.2 Electromagnetic radiation and geologic remote sensing

In remote sensing, Electromagnetic Radiation (EMR) is the main communication link between the sensor and the object (Hunt, 1980). EMR displays properties of both particles and waves (Harris and Bertolucci, 1989). It is represented as photons with discrete energy levels, propagating away from the source at the velocity of light, characterized by mutually perpendicular oscillating electric and magnetic fields, themselves perpendicular to the direction of wave propagation. A detailed discussion of the physics of EMR can be found in any standard remote sensing text (e.g., Siegel and Gillespie, 1980; Lillesand and Kiefer, 2000; Gupta, 2003; Jensen, 2006).

The primary source of EMR for passive terrestrial remote sensing is the Sun, which is a blackbody (an ideal thermal radiator) at a temperature of about 6000°K. The Earth radiates EMR as a graybody at a temperature of about 300°K. The spectral distribution of radiation emitted by a blackbody is related to its temperature by the Planck's Law:

$$w_{bb(T,\lambda)} = (c_1 / \lambda^5) \times \left[\frac{1}{\left(\frac{c_2}{\lambda T} - 1 \right)} \right] \quad (1)$$

where $w_{bb(T,\lambda)}$ is radiance as a function of temperature and wavelength in $\text{W}/\text{cm}^2/\mu\text{m}$; λ is the wavelength in μm ; c_1 is the first radiation constant ($2\pi hc^2$); c_2 is the second radiation constant (ch/k); k is Boltzmann constant ($1.38 \times 10^{-23} \text{ W/s/}^\circ\text{K}$); h is Planck's constant; c is the velocity of light; and T is the absolute temperature, in $^\circ\text{K}$ (Kahle, 1980). The spectral distribution of radiation for Sun and Earth are shown in Figure-5.1a.

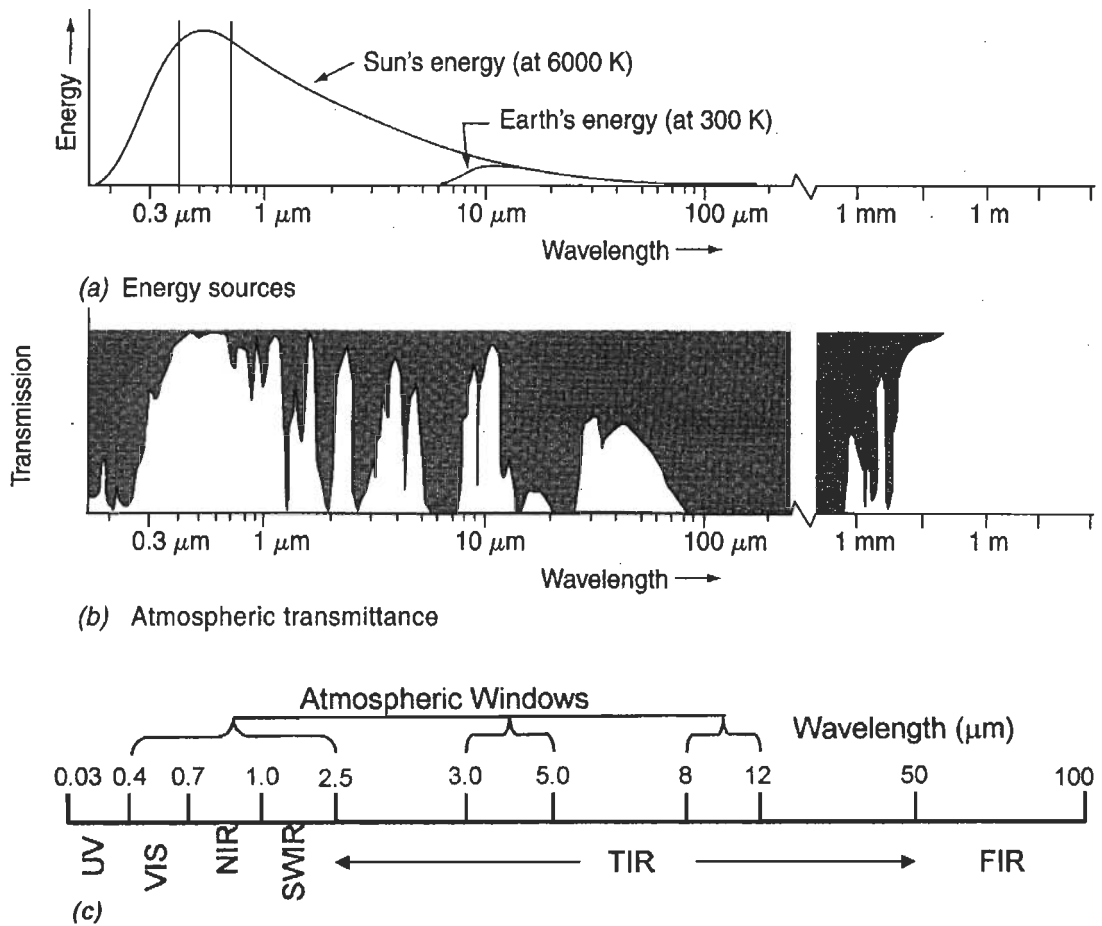


Figure-5.1 Sources of EMR for remote sensing and atmospheric transmission (modified after Lillesand and Kiefer, 2000).

The wavelength regions that are most useful in remote sensing of the Earth's surface are restricted due to the composition of Earth's atmosphere (Elachi, and van Zyl, 2006; Schott, 1997) which allows only selective parts of the EMR to reach Earth's surface and travel back to the remote sensor (see fig. 5.1b). A more detailed discussion on the atmosphere, and its influence on remote sensing image data (in context of atmospheric correction of ASTER data), has been presented in Chapter 6. The visible part of the EM spectrum is contained within a very narrow part (0.4-0.7 μm). The region of the EM spectrum between 0.7 μm to about 100 μm is called the infrared region. In Figure-5.1b we observe that the most important 'atmospheric windows' (Lillesand and Kiefer, 2000; fig. 5.1c) for reflected solar EMR exist in the visible

through near infrared (VNIR) to shortwave infrared (SWIR) (0.4-2.5 μm), whereas Earth's emitted radiation is at its maximum in the thermal infrared region (7.0-15.0 μm) of the EM spectrum. These atmospheric windows are the most commonly used wavelength ranges for terrestrial remote sensing, as each represents unique physical phenomena. An atmospheric window in the wavelength region 3.0-5.0 μm also exists, but is hard to utilize since solar reflected and thermal emitted radiation together contribute to the signal reaching the remote sensor in this range. This makes the interpretation of the spectral data difficult, and therefore this wavelength range is less commonly used.

5.3 Infrared spectroscopy of minerals and rocks

Infrared spectroscopy is the study of how the electromagnetic radiation in the infrared region interacts with matter. Primary rock forming minerals as well as many secondary weathering and alteration minerals exhibit wavelength-dependent (spectral) absorption features throughout the visible and infrared regions of the EM spectrum. These features result from the selective absorption of photons with discrete energy levels and depend on the elemental composition, crystal structure, and chemical bonding characteristics of a mineral, and are therefore diagnostic of mineralogy (Hunt, 1980; Clark, 1999). The spectrum of a mineral is governed by a total effect of the following factors (Gupta, 2003):

- Spectra of dominant anions
- Spectra of dominant cations
- Spectra of ions occurring as trace constituents
- Crystal field effect

The main diagnostic features in a spectrum are the absorption bands. There are two main categories of processes that cause absorption of radiation at visible and infrared wavelengths: 1) electronic processes, which occur at higher energies (or higher frequencies, or shorter wavelengths), and 2) vibrational processes, which occur at lower energies (or lower

frequencies, or longer wavelengths). Absorption of radiation occurs only when the energy of the incident radiation is equivalent to the energy required to activate the process (Harris and Bertolucci, 1989). A diagrammatic representation for some common minerals in terms of the dominant processes causing absorption has been shown in Figure-5.2. In the following sections the physical bases of these processes have been described in some detail.

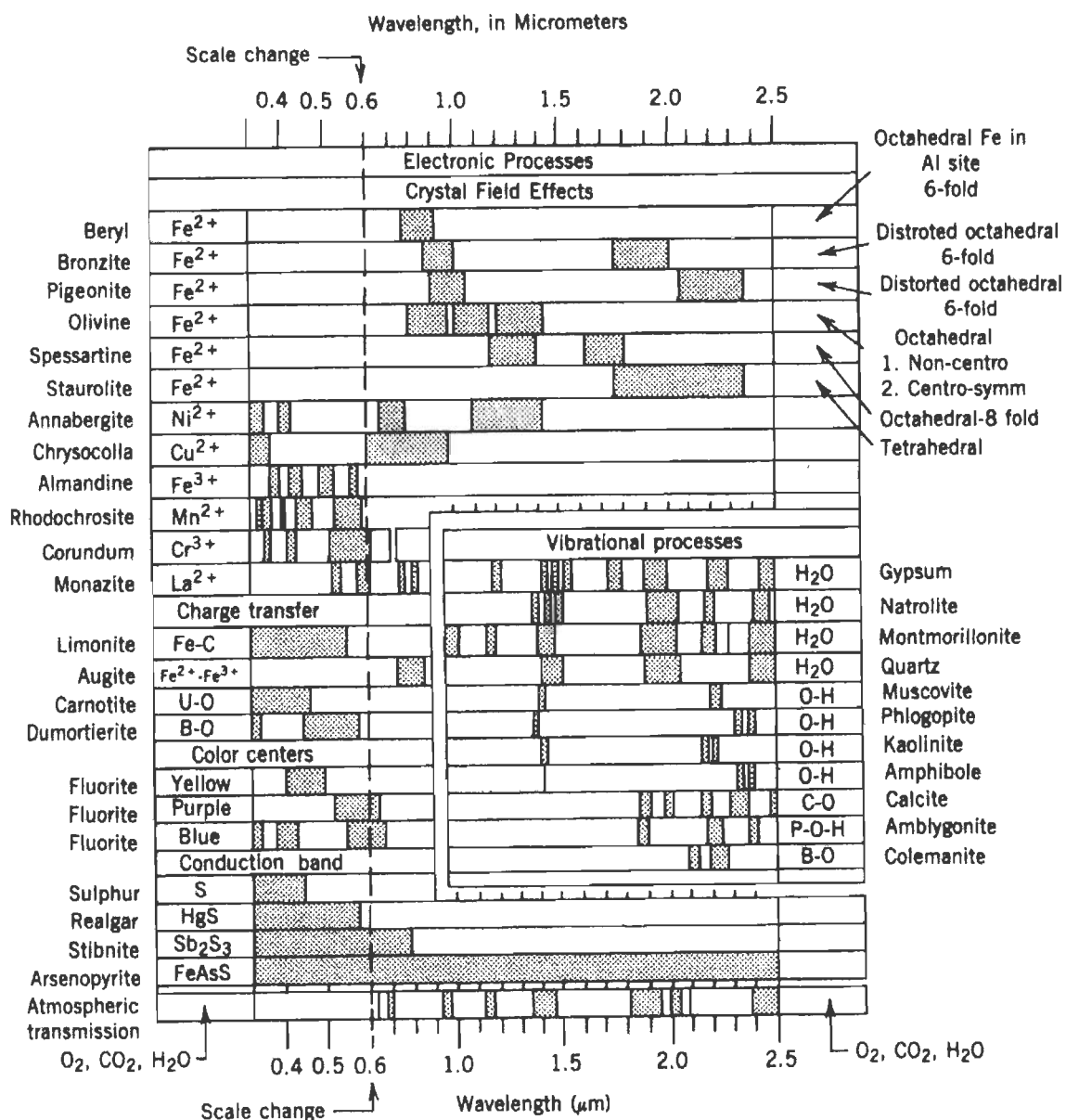


Figure-5.2 Spectral signature diagram of a variety of geologic materials (from Hunt, 1977).

5.3.1 Electronic processes

Electronic processes are related to changes in the distribution of electrons within and between atomic orbitals in a crystal field (Burns, 1993). If the energy change associated with the redistribution of electrons is equal to the energy of incident EM radiation, then absorption at that discrete energy occurs. The specific causes of these processes can be categorized into four groups – crystal field effects, color centers, conduction bands, and charge transfer between atoms (Hunt, 1977; Hunt, 1980; Burns, 1993; Clark, 1999). Most of the features observed in the VNIR spectral region are due to the presence of transition metals, which are defined as those elements that have unfilled or partially filled *d* or *f* orbitals. For a thorough review of electron orbitals and crystal field theory, see Burns (1993). Of the transition metals, iron is most abundant in Earth's crust. Figure-5.3 shows stacked spectra of some minerals with diagnostic spectral features in the VNIR region. The subtle spectral differences are due to changes in elemental composition, valence state, cation coordination number, crystal symmetry or chemical bonding characteristics (Hunt, 1977; Burns, 1993).

Crystal field effects are due to photon interaction with the outer, unfilled *d* and *f* orbitals in transition metals, usually iron (Burns, 1993). The *d* orbitals of an isolated Fe^{3+} ion, for example, have equivalent energy levels. However, when Fe^{3+} ions are located in a crystal field, the energy levels are split, allowing electrons to transfer from lower to higher levels upon absorption of photons with the corresponding energy. The degree of separation between orbital energy levels is primarily a function of the cation valence, coordination environment, and site symmetry (Burns, 1993).

Spectral features due to color centers result from lattice defects caused by vacancies or impurities in a crystal structure. The absorption of energy due to color centers usually occurs in the ultraviolet (UV) and visible region. For example, the yellow color of many diamonds is due to the presence of N_2 in the crystal structure (Burns, 1993; Clark, 1999; Nassau, 2000).

Charge transfer absorptions are caused by the transfer of electrons between ions. Inter-element electron transitions can be divided into two types, 1) metal-to-metal, or 2) oxygen-to-metal transitions (Burns, 1993). Metal-metal charge transfer can occur between the same metal in different valence states (*e.g.*, Fe^{2+} and Fe^{3+}), or between different metals (Fe^{3+} and Ti^{3+}). For example, $\text{Fe}^{2+} \rightarrow \text{Fe}^{3+}$ electronic transition is responsible for the broad 0.8 μm feature in the Fe-rich clinopyroxene, hedenbergite (fig. 5.3). Oxygen-metal charge transfers generally occur at higher energies (shorter wavelengths) of the UV region, but absorption band edges can influence the visible spectrum as well, *e.g.* absorption band edge leading to red color due to Fe^{3+} and O^{2-} electronic transitions of hematite (Burns, 1993).

Conduction bands can occur in minerals where electrons occupy two distinct energy levels, 1) the conduction band (high energy), where electrons are free to move about the crystal lattice, and 2) the valence band (low energy), where electrons are bound to the atomic nucleus (Clark, 1999). The difference between the two energy levels is called the band gap, and in semi-conductors the band gap corresponds to photon energies in the VNIR region. Elemental sulfur and the sulfide mineral cinnabar, for example, exhibit strong absorption of UV and short-wavelength visible radiation resulting in their characteristic yellow and red colors, respectively (fig. 5.3) (Clark, 1999).

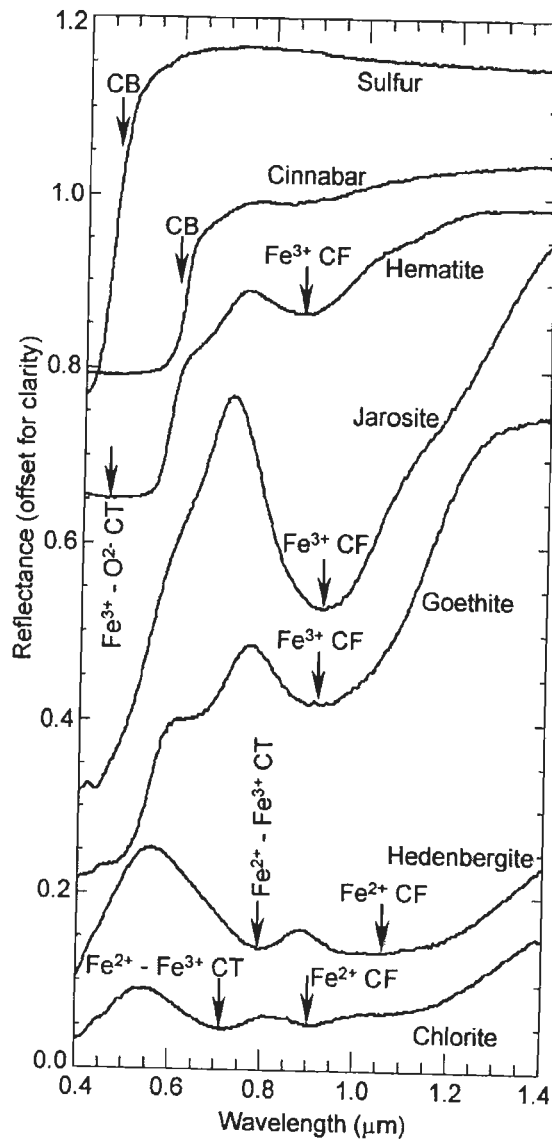


Figure-5.3 Spectra of minerals with diagnostic features in the VNIR region of EM spectrum resulting due to electronic processes. Labeled arrows indicate specific absorption features due to conduction band (CB), crystal field (CF) or charge transfer (CT) effects. Spectra have been taken from USGS spectral library (speclib05; Clark et al., 2003).

5.3.2 Vibrational processes

Vibrational processes are related to atomic vibrations that cause a change in the charge distribution of a molecule. Since molecules in most minerals are ionic structures and consist of charged particles, the vibration of these particles can result in an oscillating electric dipole (Burns, 1993; Harris and Bertolucci, 1989; Gaffey et al., 1993). If the frequency of the electric field component of the EMR matches the frequency of the oscillating dipole, then absorption of

that discrete frequency occurs. A molecule with n atoms has $3n$ fundamental modes of vibration (Gaffey et al., 1993). These vibration modes can be divided in two groups, 1) internal modes where bond lengths and bond angles oscillate, and 2) external modes where molecule rotates about one of the three mutually perpendicular axes or moves as a rigid unit along one of these axes (Gaffey et al., 1993). For a molecule with $3n$ fundamental modes, there are 6 external modes that represent translational and rotational motion; therefore there are $3n-6$ internal vibrational modes ($3n-5$ for a linear diatomic molecule). In solid minerals, external modes can occur, but the frequency of these modes corresponds to wavelengths that are no longer than can be observed through the Earth's atmosphere, so internal stretching and bending modes for most rock-forming minerals dominate the TIR spectrum between $8\ \mu\text{m}$ and $12\ \mu\text{m}$ (Clark, 1999). Absorption of radiation can also occur at integral multiples of a fundamental vibrational frequency, known as overtones, or at additive sums of fundamental vibrational frequencies, known as combination tones (Hunt, 1980; Gaffey et al., 1993; Clark, 1999).

In the SWIR region, absorptions due to overtones and combination tones occur, and minerals that contain water, hydroxyl, carbonate and sulfate molecules show diagnostic spectral features (Gaffey et al., 1993). Molecular water may be present in a variety of sites within a crystal structure, physically adsorbed onto mineral grains, or in fluid inclusions. Hydrated sulfates like gypsum, opal, zeolites, and montmorillonite clays are examples of minerals with molecular water. The internal fundamental vibration modes of liquid water occur at $2.903\ \mu\text{m}$, $3.106\ \mu\text{m}$, and $6.08\ \mu\text{m}$ (Hunt, 1977; Clark et al., 1990a), which are difficult to observe remotely due to the presence of water in atmosphere. Overtones and combinations of these fundamental vibration frequencies occur at $1.88\ \mu\text{m}$, $1.45\ \mu\text{m}$, $1.38\ \mu\text{m}$, $1.14\ \mu\text{m}$, and $0.98\ \mu\text{m}$, and can be observed in the SWIR region and used to identify certain minerals in the laboratory (Hunt, 1977). Figure-5.4 shows a plot of some important minerals with diagnostic features related to the presence of water: illite, montmorillonite, muscovite and gypsum.

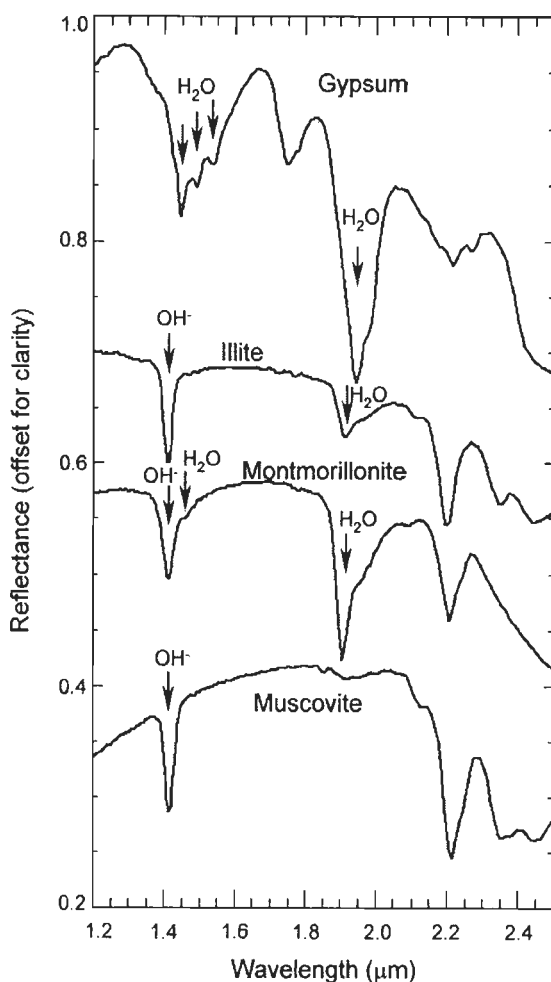


Figure-5.4 Examples of mineral spectra with features in SWIR region of the EM spectrum related to OH⁻ and H₂O molecules, indicated by arrows. Spectra have been taken from USGS spectral library (speclib05; Clark et al., 2003).

Minerals with hydroxyl ions bound to metal cations also exhibit absorption features in the SWIR region. This constitutes a large group of minerals including alunite, jarosite, goethite, as well as all phyllosilicate minerals. Hydroxyl has a fundamental stretching mode that produces an absorption feature around 2.75 μm, just outside the SWIR region (Hunt, 1977). The first overtone of this fundamental mode occurs at 1.4 μm and is characteristic of minerals with OH⁻ anions, but nothing at 1.9 μm is indicative of a mineral with OH⁻ anions, and no molecular water (Clark et al., 1990a) (*e.g.*, muscovite in fig. 5.4). In laboratory measurements, this can be used to differentiate between muscovite/illite and muscovite or sericite, but in remote sensing measurements, atmospheric water causes strong absorption features around 1.4 μm and 1.9 μm, making this distinction difficult.

Hydroxyl anions are also bound to various metal cations within crystals. The different cations that bond with OH^- result in fundamental metal-OH stretching and bending modes that vary with cation composition (typically Al, Mg, or Fe), and display overtones and combinations in the SWIR region that can be diagnostic (Hunt, 1977; Clark et al., 1990a). For example, hydrous clay minerals that have cations such as Al, Mg or Fe bonded to OH^- molecules show spectral absorption features between 2.2 μm and 2.4 μm due to O-H stretching plus metal-O-H bending combination modes (Clark, 1999); Figure-5.5a shows the spectral curves of hydrous silicate minerals in the SWIR region, for example.

Carbonate minerals, such as calcite and dolomite also exhibit diagnostic absorption features in the SWIR due to combinations and overtones of fundamental vibrations that occur at longer wavelengths (Gaffey, 1987; Hunt, 1977; Clark et al., 1990a). The strongest absorptions in the SWIR occur at 2.541 μm and 2.340 μm for calcite, but shift to 2.516 μm and 2.319 μm for dolomite due to Mg substitution for Ca. Weaker absorptions occur around 2.1 μm , 2.0 μm , and 1.9 μm (Hunt, 1977; Clark et al., 1990a), but are often not observed in remote sensing due to atmospheric interference and mixing with other minerals. Sulfate minerals that are hydrated will have absorption features in the SWIR due to the presence of either structural H_2O or OH^- molecules, but non-hydrous sulfate minerals will not have absorption features in this region (Ross, 1974; Gaffey et al., 1993; Crowley, 1991). Figure-5.5b shows SWIR spectral features of some important carbonate and sulfate minerals expected in the geological setup of the present study area: pyrophyllite, alunite, jarosite, calcite and dolomite.

Vegetation spectra in the SWIR are characterized by major water absorption features at 1.45 μm , 1.94 μm , and 2.47 μm , with secondary features at 0.96 μm , 1.12 μm , 1.54 μm , and 1.67 μm (Ustin et al., 1999). Also organic compounds such as protein, cellulose, lignin and starch have fundamental vibration modes in the 5.0 μm to 8.0 μm region and display combinations and overtones in the SWIR (Ustin et al., 1999).

The fundamental vibration modes for silicate minerals cause strong absorption features in the 8.0-12.0 μm region, which is known as the Si-O stretching region (Salisbury, 1993), and forms part of the larger TIR atmospheric window as well as the region of highest emitted radiation of the Earth (see fig. 5.1), making it ideal for terrestrial geologic remote sensing applications (Kahle et al., 1993; Hook et al., 1999). The spectral features in this region appear as reflectance maxima (emissivity minima, as per Kirchhoff's law (Nicodemus, 1965)) because the intensity of absorption features at these wavelengths is high enough to induce a 'mirror-like opacity' resulting in high reflectance values (Salisbury, 1993). These reflectance peaks are also called reststrahlen bands, meaning 'residual ray' (Elachi and van Zyl, 2006). The emissivity maxima in silicates that are associated with the Christiansen frequency occur near 8.0 μm , just before the onset of the intense absorption due to Si-O vibration. At longer wavelengths, stretching and bending modes lead to additional spectral features. These have been summarized in Figure-5.6. There is a complex relationship between the fundamental vibrational absorption bands, the absorption coefficient and the refractive index of the mineral, which is reviewed in further detail by Schanda (1986), and Elachi and van Zyl (2006).

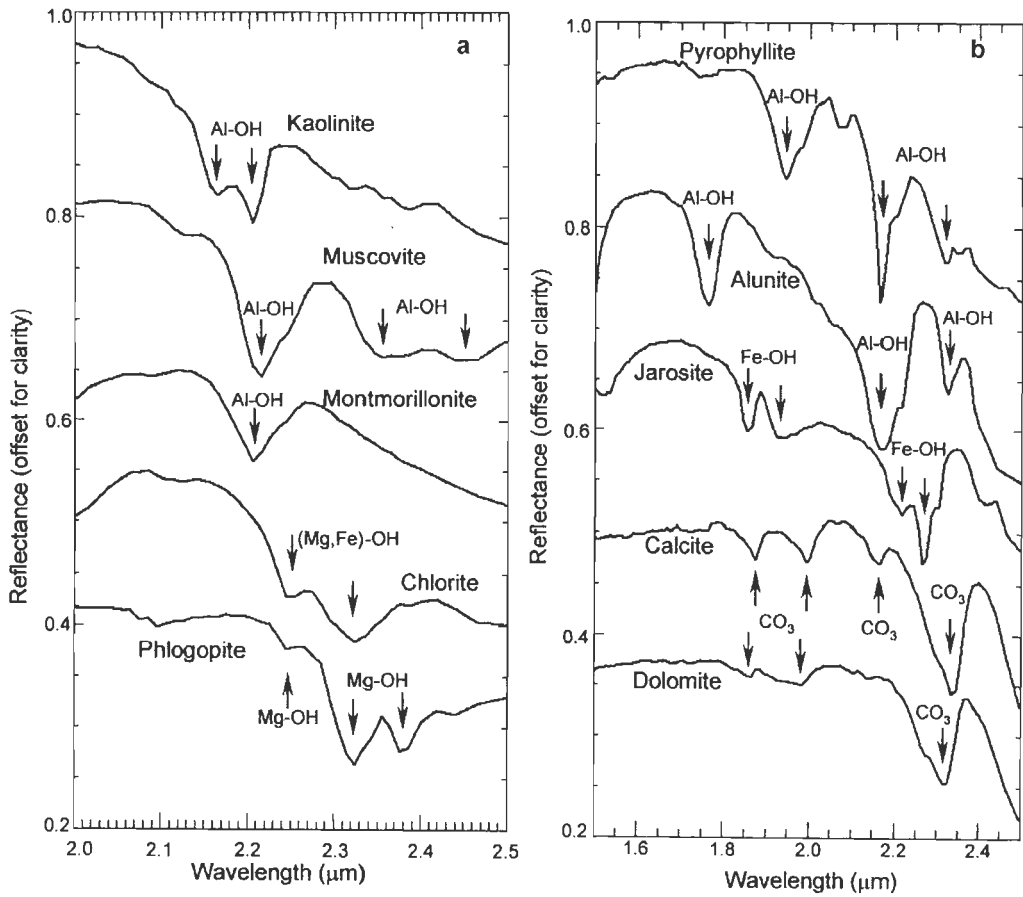


Figure-5.5 Examples of mineral spectra in the SWIR region exhibiting diagnostic absorption features (indicated by arrows) due to metal-O-H stretching (a) and (b), and CO_3^{2-} (b). Spectra have been taken from USGS spectral library (speclib05; Clark et al., 2003).

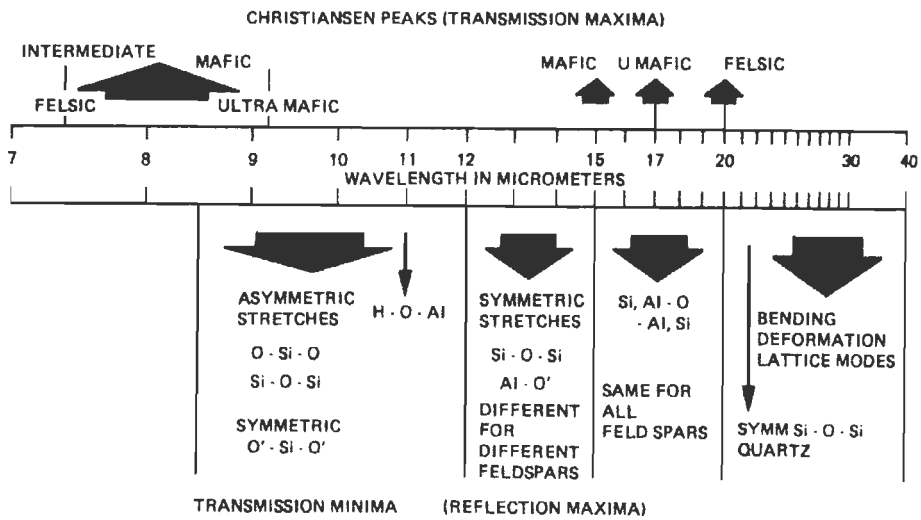


Figure-5.6 Diagram illustrating the location of features and the type of vibrational process responsible for the spectral features for silicates in the TIR region (after Hunt, 1980).

A very useful characteristic of the silicate rock spectra in the TIR region is that there is a systematic shift in the emissivity minima for different rock types, and is linked with their total silica content (Hunt, 1980; Kahle et al., 1993; Salisbury and D'Aria, 1992; Sabine et al., 1994). The locations of the Christensen peak and the minimum band migrate fairly systematically to longer wavelengths as the material changes from felsic to mafic (Elachi and van Zyl, 2006) with the increasing isolation (decreasing polymerization) of SiO_4 tetrahedral molecules in the crystal structure (Farmer, 1974; Hook et al., 1999). The SiO_4 tetrahedron consists of one silicon atom bonded to 4 surrounding oxygen atoms in a tetrahedral arrangement and is the fundamental building block of all silicate minerals and hence most rock types. These SiO_4 tetrahedra may be isolated from each other (nesosilicates), or may be linked, by shared oxygen atoms, into chains (inosilicates), 2-dimensional sheets (phyllosilicates), or 3-dimensional framework structures (tectosilicates) (Klein and Hurlburt, 1985). A strong double emissivity minimum occurs in quartz between 8.2 μm and 9.2 μm , with a characteristic peak at 8.626 μm (see fig. 5.7). In general, tectosilicates such as quartz and feldspars have emissivity minima around 9.0 μm ; phyllosilicates such as muscovite and clay minerals have emissivity minima around 9.5 μm ; inosilicates such as hornblende have emissivity minima at around 10.0 μm ; and nesosilicates such as fayalite have emissivity minima at around 11.0 μm (fig. 5.7). This systematic behavior has been exploited for quantitative silica abundance estimation using ASTER TIR surface emissivity data as discussed in detail in Chapter 7.

Carbonates and sulfate minerals also have diagnostic spectral emissivity features in the TIR region (Hook et al., 1999). Fundamental modes for the CO_3^{2-} ion occur at 7.07 μm , 9.41 μm , 11.36 μm , and 14.71 μm (Hunt, 1977; White, 1974). The 9.41 μm fundamental mode is due to totally symmetric C-O stretching and is not active in the infrared, as it does not produce an oscillating electric dipole (Hunt, 1977). Only the 11.36 μm band is present in the TIR atmospheric window region, but measurable variations in the wavelength position of this band result from the cation substitution in carbonate minerals and are diagnostic of mineralogy

(White, 1974; Lane and Christensen, 1997). Fundamental modes for SO_4^{2-} ion occur at 9.05 μm , 10.17 μm , 16.37 μm and 22.22 μm , and cation substitution in sulfate minerals can cause the location of resultant absorption bands to vary between 8.1 μm and 10.4 μm (Ross, 1974). The strongest emissivity feature for alunite around 9.0 μm is due to S-O stretching in the SO_4^{2-} molecule (Ross, 1974). Alunite also displays secondary spectral emissivity features at 8.58 μm and 9.75 μm . The TIR spectra of some vegetation types display weak emissivity features due to organic compounds like cellulose and lignin, but have very high emissivity values and low spectral contrast (difference between maximum and minimum emissivity) (Salisbury and D'Aria, 1992). Combined with canopy scattering, which further reduces spectral contrast, vegetation in general behaves like a blackbody emitter (Salisbury and D'Aria, 1992).

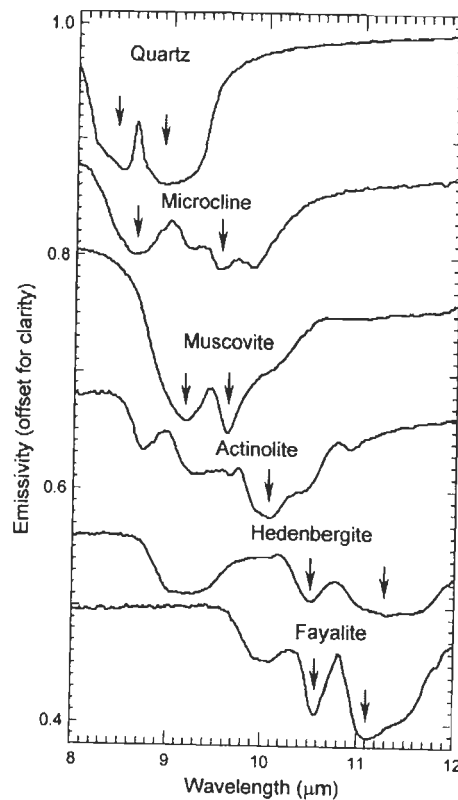


Figure-5.7 Examples of silicate mineral spectra with emissivity features in the TIR. Spectral features are related to Si-O stretching vibrations within the silicate crystal structure and shift to longer wavelengths with increasing isolation of the SiO_4 tetrahedra. For discussion, refer to the text. Spectra are from Arizona State University (ASU) thermal emission spectral library.

5.4 Literature review: Geologic remote sensing for lithologic/mineral mapping and mineral exploration

In order to see how geologic remote sensing for mineral exploration has developed and improved since the successful launch of the first Landsat satellite in 1972, a comprehensive review of the relevant literature has been made. It may be mentioned that while active ('all season') remote sensing has proven its merit in geologic applications in general and mineral exploration (structural mapping) in particular, it has been kept out of the purview of this review, since the focus of the present study is on surface compositional mapping, and not on structural mapping. The available scientific literature on remote sensing applications in mineral exploration and geology can be grouped into the following four categories:

1. Development of instrumentation (sensor) technology and methods of data processing
2. Multispectral remote sensing in mineral exploration, and geologic mapping
3. Hyperspectral remote sensing for surface mineral mapping
4. Application of ASTER data in lithologic/mineral mapping for resource exploration

A wealth of scientific literature is available on the applications of remote sensing technology in geology, with special focus on mineral exploration activities. Most mineral deposit models include some common elements that are relevant for remote sensing: tectonic setting, lithological association, alteration, and structural control (Sabine, 1999). Most of the studies using remote sensing as a tool for mineral exploration have utilised the unique spectral signatures of specific alteration minerals that serve as guide minerals in exploration. Many mineral deposits have typical and unique alteration mineral assemblages, and most of the alteration minerals have diagnostic spectral signatures, as discussed in preceding sections. The utility of a remote sensor in mineral exploration activity weighs largely on its coverage of the spectral regions where these spectral features lie.

5.4.1 Developments in sensor and data processing technology

Operational use of orbital remote sensing in geology began after the launch of first Landsat satellite named ERTS-1 in 1972. Beginning with just 4 spectral channels and coarse spatial resolution, the developments in sensor technology have been phenomenal and rapid in terms of both spectral and spatial resolutions of the sensors and data quality (radiometric parameters). Today there is a wide selection available among remote sensing systems dedicated to geological applications from aerial and space platforms. Available remote sensing systems have been broadly categorized into two categories – multispectral and hyperspectral, depending upon the number and width of spectral channels in which they record data. For example, sensors such as Landsat MSS, TM and ETM+, SPOT MX, IRS LISS sensors, and JERS OPS are all multispectral sensors useful in geologic applications. On the other hand there is a wide range of airborne hyperspectral sensors with hundreds of narrow and contiguous spectral channels (see Table-5.1). Spaceborne hyperspectral remote sensing is still in early stages of development, though some success has been achieved with the launch of Hyperion sensor onboard the EO-1 platform in November 2000. However, poor data quality (low signal to noise ratio) has hampered widescale use of its data.

Parallel advancements in data processing technology during the last 30 years of remote sensing research have been made and a framework for image analysis, processing routines, field calibration and validation of datasets, and nominal wavelength ranges for surface mineral detection have been established (*e.g.*, Abrams et al., 1977; Kahle and Rowan, 1980; Goetz et al. 1983; Marsh and McKeon 1983; Kahle and Goetz, 1983; Gillespie et al., 1986; Taranik, 1988; Clark et al., 1993; Kahle et al., 1993; Hook et al., 1999; Sabine, 1999; Kruse, 1999; Hook et al., 2001; Cudahy et al., 2000; Rowan and Mars, 2003; Hubbard et al., 2003; among many others).

Table-5.1 Some important hyperspectral sensors for geologic remote sensing.

Name	No. of Channels	Spectral range (μm)	Bandwidth (nm)	IFOV (mrad) or Spatial Resolution (m)
AHS	48	0.43-12.7	20-1500	2.5 mrad
AMSS	46	0.5-12.0	20-590	2.1-3.0 mrad
AVIRIS	224	0.4-2.45	9.4	4-20 m
CASI	288	0.43-0.87	2-12	0.5-10 m
DAIS 7915	79	0.5-12.3	15-2000	1.1-3.3 mrad
GERIS	63	0.4-2.5	16-120	2.5-5 mrad
HYDICE	206	0.4-2.5	7.6-14.9	0.8-4 m
ISM	128	0.8-3.2	12.5-25	3.3-11.7 mrad
MAIS	71	0.44-11.8	20-800	3-4.5 mrad
MIVIS	20	0.4-0.8	8-500	4-15 m
	8	1.2-1.5		
	64	2.0-2.5		
	10	8.2-12.7		
SFSI	122	1.2-2.4	10	0.5-10 m
HyMAP	100	0.4-2.5	10-20	2-10 m
SEBASS	128	3.0-5.0	35-65	2 m
	128	7.5-13.5		
MASTER	25	0.4-2.4	40-700	5-50 m
	15	3.1-5.2		
	10	7.8-12.9		
HyperspecTIR	227	0.45-2.45	5-12	0.5-10 m
Hyperion	220	0.4-2.5	10	30 m

5.4.2 Multispectral remote sensing for mineral exploration: Legacy of Landsat

Initial success in operational use of remote sensing for lithologic/mapping was achieved using data from the Landsat MSS and TM (and ETM+) sensors (*e.g.*, Abrams et al., 1983; Podwysocki et al., 1983; Hutsinpillar and Taranik, 1988), and these sensors continue to be the most widely used multispectral remote sensors for geologic applications.

Goetz et al. (1983) and Sabins (1999) have provided a general overview of the use and potential of multispectral passive remote sensing in mineral exploration activity, with emphasis on the application of Landsat TM data. Most studies that have utilized the Landsat data have focused primarily in discriminating lithologies (*e.g.*, Crósta and Moore, 1989; Qari, 1989; Kenea, 1997; van der Meer et al., 1997; Mickus and Johnson, 2001), and identifying hydrothermally altered areas as a tool to aid in field exploration of ore deposits (see Table-5.2 for some indicative examples based on the use of Landsat data for mineral exploration).

Table-5.2 Some pertinent examples of Landsat-based remote sensing studies for mineral exploration.

Area and objective	Data used	Data processing	Results	Reference
South-central Nevada, USA; discrimination of hydrothermally altered rocks	Landsat MSS	Band ratioing, contrast stretching and color compositing for visual discrimination	Except in case of shale and siltstone, good discrimination achieved between hydrothermally altered and unaltered rocks	Rowan, Goetz and Ashley (1977)
Southern Arizona, USA; separation of lithologies, discrimination of hydrothermal alteration and structural mapping	Landsat MSS and aircraft scanner data simulating Landsat 4 TM	Band ratios, principal component and canonical transformations	Iron-oxide-rich areas well distinguished, TM simulator data found to be more useful for alteration mapping	Abrams, Brown, Lepley and Sadowski (1983)
Central East Greenland; iron oxide staining for exploration of stockwork molybdenum and other base metals	Landsat MSS	Spectral ratioing and factor analysis to generate color composites for digital classification of limonitic rust zones	About 88 significant rust zones identified in Tertiary igneous province and Precambrian metamorphic province	Conradsen and Harpøth (1984)
Aquaba-Levant structure in Wadi Araba-Jordan Graben; hydrothermal alteration mapping	Landsat TM	Ratioing, principal component analysis and IHS decorrelation	Enhanced spectral discrimination of phyllosilicates and iron oxides through decorrelation processing	Kaufmann (1988)
Hamerslay Province, Western Australia; discrimination and identification of ferric oxides	Landsat TM	Principal component analysis of band ratios	Discrimination between hematite and goethite-rich areas achieved	Fraser (1991)
Central Mexico; comparison of techniques for spectral enhancement of hydrothermally altered rocks in a vegetated area	Landsat TM	Object oriented principal component analysis (OOPCA, also called feature oriented principal component selection, or FPCS or Crosta technique), spectral decorrelation, and IHS transform	Best discrimination of hydrothermally altered volcanics from the unaltered achieved through statistical decorrelation techniques.	Ruiz-Armenta and Prol-Ledesma (1998)
Guanajuato district, Mexico; Spectral enhancement of selected pixels to identify hydrothermally altered rocks	Landsat TM	Band subtraction and principal component analysis	Hydrothermally altered rocks discriminated in heavily vegetated terrain and new zones of argillic alteration identified	Torres-Vera and Prol-Ledesma (2003)
Southern Iranian volcanic sedimentary belt; porphyry copper alteration mapping	Landsat ETM+	Crósta technique	Iron-oxide and hydroxyl-bearing minerals mapped	Ranjbar, Honarmand and Moezifar (2004)

5.4.3 Hyperspectral remote sensing for mineral identification and mapping:

AVIRIS and others

Airborne imaging spectrometers (or hyperspectral sensors) operating in the VNIR-SWIR region such as AVIRIS (Airborne Visible Infrared Imaging Spectroradiometer; Table-5.1; Vane et al., 1993; Green et al., 1998) and those operating in the TIR region such as SEBASS (Spatially Enhanced Broadband Array Spectrograph System; Table-5.1; Hackwell et al., 1996) have enabled precise mineralogical identification and mapping owing to high spectral resolution comparable with that of laboratory spectroscopy, and superior data calibration such that a direct comparison between remote spectral measurements and laboratory spectra of minerals became possible. Some of the more popular geologic hyperspectral remote sensing systems are given in Table-5.1. Among these, AVIRIS is the benchmark hyperspectral sensing system operating in the VNIR-SWIR region. The application of AVIRIS in mineral exploration activity has been in determining the point, local and regional distribution of a class of minerals with strong molecular absorption features associated with hydrothermal alteration, and numerous studies have amply demonstrated the use of its data towards this end (Carrere and Abrams, 1988; Hook and Rast, 1990; Swayze et al., 1992; Sommer et al., 1993; Boardman and Huntington, 1996; Farrand, 1997; Beratan et al., 1997; Crósta et al., 1998; Rowan et al., 2000; Berger et al., 2003). AVIRIS spectra have been used to map ammonium minerals (Baugh et al., 1998), alkaline and carbonatite rock types (Rowan et al., 1995; Bowers and Rowan, 1996), carbonate, clay, and iron oxide mineral units and subunits found in sedimentary rocks (Boardman and Goetz, 1991; Clark et al., 1992) and evaporate minerals (Crowley, 1993).

Hyperspectral remote sensing in the TIR region is a relatively new field. The main applications of TIR hyperspectral sensing is in mapping the main rock-forming silicate minerals that have their diagnostic features in the TIR region. Studies based on SEBASS and MASTER data (Vaughan et al., 2003, 2005) have demonstrated the potential of hyperspectral TIR sensing in mineral mapping.

5.4.4 Application of ASTER data in lithologic/mineral mapping for resource exploration

From the foregoing sections, it is evident that the best results of remote sensing for mineral exploration can be obtained from spectral data that covers spectral regions of geologic interest, in large number of closely spaced bands. This typically corresponds to the hyperspectral remote sensing. Operational orbital hyperspectral remote sensing is still in its nascent stage. Existing airborne hyperspectral remote sensing has limitations of geographic coverage, cost, and data processing expertise which hinders the popular use of hyperspectral remote sensing for mineral exploration. A major development in bridging this gap was achieved with the launch of ASTER in December 1999, as it provides high quality, global data with unique spectral coverage in VNIR-SWIR and TIR atmospheric windows (Yamaguchi et al. 1998). Although multispectral by all definitions, ASTER data has provided a first superior alternative to the Landsat TM data widely used and understood by most geologic remote sensing specialists. In addition to its finer spectral coverage (5 bands) of the range covered by the single 'TM band 7' (2.08-2.35 μ m) where absorption features of key alteration minerals lie, ASTER also provides best spectral coverage (5 bands) of the TIR atmospheric window relevant to lithologic mapping applications from a spaceborne platform. Hence, ASTER offers a unique advantage of complementary geologic information (alteration minerals and lithology). ASTER multispectral data not only offer global coverage at affordable cost, but also flexibility in data processing as it can be handled and processed using existing image processing technology designed to handle multispectral as well as standard hyperspectral data. Therefore, in more than one sense, ASTER data bridges the gaps between existing multispectral and hyperspectral sensors, and can be called a hybrid system. Since launch, numerous studies have amply demonstrated the utility of ASTER data in geology, particularly in lithologic mapping and hydrothermal alteration mineral detection and mapping. Some of the most demonstrative of these have been summarized and tabulated in Table-5.3.

Table-5.3 Examples of ASTER data application in lithologic and alteration mapping

Study area and data	Rocks/minerals mapped	Reference
Mountain Pass, California, USA; L1B VNIR-SWIR calibrated to surface reflectance and L2 (AST_05) TIR surface emissivity	Calcitic rocks distinguished from dolomitic rocks; Fe-muscovite distinguished from Al-muscovite; quartzose and carbonate rocks mapped using TIR data	Rowan and Mars (2003)
Cuprite, Nevada, USA; L1B VNIR-SWIR calibrated to surface reflectance	Hydrothermal alteration minerals – opal, alunite, kaolinite, muscovite and calcite	Rowan et al. (2003)
Patagonia, Argentina; L1B VNIR-SWIR	Hydrothermal alteration minerals – alunite, illite, kaolinite and smectite	Crósta et al. (2003)
Central Andes; L1B VNIR-SWIR calibrated to surface reflectance	Ferric-iron mineral suites (using VNIR data) and clay-sulfate mineral discrimination (using SWIR data)	Hubbard et al. (2003)
Beishan Mountains, China, and Mt. Fitton, Australia; L1B TIR	Mafic-rich, quartz-rich and carbonate-rich rocks	Ninomiya et al. (2005)
Hiller Mts., Nevada, USA and Tres Virgenes-La Reforma, Baja California Sur, Mexico; L2 (AST_05) TIR surface emissivity	Quantitative estimation of SiO ₂ weight percent	Hook et al. (2005)
Mordor, NT, Australia; L1B VNIR-SWIR and calibrated TIR surface emissivity	4 felsic and 4 mafic lithologic classes mapped using VNIR-SWIR data, and 2 classes of mafic-ultramafic rocks and 4 classes of quartzose-intermediate rocks mapped using TIR surface emissivity data	Rowan et al. (2005)
Central Brazil; L1B SWIR calibrated to surface reflectance	Hydrothermal hydroxyl-bearing alteration minerals in a densely vegetated terrain	Galvão et al. (2005)
Zagros magmatic arc, Iran; L1B VNIR-SWIR calibrated to surface reflectance	Discrimination between phyllically and argillically altered rocks	Mars and Rowan (2006)
Infiernillo porphyry deposit, Argentina; L1B normalized to relative reflectance	Hydrothermal alteration zone mapping – minerals characterizing silicic, potassic, and phyllic zones mapped	Tomasso and Rubinstein (2006)
Reko Diq, Pakistan; L1B VNIR-SWIR calibrated to surface reflectance and L2 (AST_05) TIR surface emissivity	Hydrothermal alteration mapping – silicic (quartz-bearing), phyllic (muscovite), argillic (alunite) and propylitic (chlorite)	Rowan et al. (2006)
Cerro La Mina, Patagonia, Argentina; L1B SWIR calibrated to surface reflectance	Identification and mapping of advanced argillic, argillic and silicic hydrothermal alteration zones	Ducart et al. (2006)
Chadormalu paleocrater, Bafq region, Central Iran; L1B VNIR-SWIR-TIR	Sodic, potassic and silicic-phyllic alteration minerals distinguished	Moghtaderi et al. (2007)
Chocolate Mts., California, USA; L1B VNIR-SWIR-TIR	Gold-related lithologic and alteration minerals mapped. Alunite, kaolinite, muscovite and montmorillonite distinguished and mapped.	Zhang et al. (2007)

Data Preprocessing – Atmospheric and Topographic Corrections

6.1 Introduction and statement of purpose

One of the primary challenges in the use of passive orbital (spaceborne) remote sensing for terrestrial applications is the accurate removal of atmospheric and topographic effects on the signal reaching the remote sensor, so that the surface physical parameters such as ‘surface reflectance’ in the solar reflective region and ‘surface emissivity’ in the thermal emissive region can be retrieved. On its two-way journey through the atmosphere, the solar EMR reaching the sensor is affected by atmospheric scattering and absorption, which severely impact the physical interpretability of the remote sensing image data. Likewise, topographic heterogeneity leads to directional effects on the reflected and emitted radiation, as well as introduction of terrain adjacency effects (diffuse irradiance) on the signal reaching the remote sensor, thereby impacting the true nature of the target radiance. It is vital to remove these atmospheric and topographic effects from the image data prior to further image processing, such that a physically meaningful interpretation about the targets of interest can be made. In remote sensing parlance, this process is usually referred to as ‘atmospheric correction’ and ‘topographic correction’, respectively, and comes under the pre-processing stage of image analysis.

This chapter deals with the atmospheric and topographic correction of the multispectral ASTER dataset used in this study. Existing techniques of atmospheric and topographic correction have been explored and applied to these data and a comparative evaluation has been made to produce the final surface reflectance and surface emissivity image data, to be used in further detailed image analysis for lithologic and alteration mapping as reported in detail in Chapters 7 and 8, respectively.

6.2 Atmospheric Correction

6.2.1 Overview

The data recorded by a remote sensor is a combination of signals representing the reflected + emitted + transmitted radiation from material or target of interest as well as undesired instrument noise, and atmospheric scattering and absorption effects, along with the effects of illumination geometry and topographic variations on the Earth's surface. One of the most important steps before remote sensing data could be used for further processing and interpretation is the removal of these undesired and interfering signals, to get a true idea of the material of interest and its spectral characteristics, which is the basis on which all of the processing results depend.

Some of the important reasons in support of radiometric and atmospheric correction of high spatial resolution remotely sensed data, such as that of ASTER, in geological studies are (Lu et al., 2002):

1. within-scene comparison of spectrally similar materials and hence in spectral classification
2. quantitative analysis of remotely sensed data with comparison and use with laboratory derived reflectances for known materials
3. accurate material mapping using band-arithmetic

The measured radiance-at-sensor is controlled by the transmission of solar EMR through the atmosphere, and is mathematically expressed as (simplified from Chandrasekhar, 1950):

$$L_{sen,\lambda} = E_{o,\lambda} / \pi \{ L_{a,\lambda} + \tau_d \rho_\lambda \tau_u / (1 - E_\downarrow) \} \quad (1)$$

Where:

$L_{sen,\lambda}$ = total radiance arriving at the sensor at wavelength (or band) λ ($\text{Wm}^{-2} \text{sr}^{-1}$)
 $E_{o,\lambda}$ = top of the atmosphere solar irradiance (Wm^{-2})

$L_{a,\lambda}$ = radiance (ratio of reflected to incident irradiance) of the atmosphere (path radiance, dimensionless)

τ_d = downward transmittance (ratio of transmitted to incident irradiance) of the atmosphere (dimensionless)

ρ_λ = spectral reflectance of the surface (dimensionless)

τ_u = upward transmittance of the atmosphere (dimensionless)

E_\downarrow = downwelling irradiance of the atmosphere (sky irradiance, dimensionless)

The actual reflectance from an object depends on various parameters, such as the solar elevation, surface slope and its orientation, surface anisotropy, and atmospheric constituents (governed by the latitude and longitude, and elevation of the area). Atmospheric conditions can vary significantly both spatially and temporally, as a result of molecular scattering and absorption in the atmosphere. There are two main effects of atmosphere, *i.e.* scattering and absorption. These effects depend on the wavelength coverage of a given sensor system. The main effects of the atmospheric scattering on remotely sensed data are upwelling atmospheric radiance or path radiance (Slater, 1980) with is additive in nature, and atmospheric absorption with multiplicative characteristics. Generally, in visible to infrared bands (as in ASTER VNIR and SWIR) the main atmospheric effects are air molecule and aerosol particle scattering (respectively following Rayleigh and Mie scattering patterns), which are additive and create image haze. Air molecules are stable, but the character of aerosol particles is often variable and their influence is difficult to estimate. In the visible bands, the multiplicative component of atmospheric absorption caused by water vapor or other gases is very weak and can be safely ignored. Therefore, the impact on short wavelengths is mainly from the additive atmospheric scattering. However, in the NIR and SWIR wavelengths, the influence of atmospheric scattering is negligible and the main atmospheric effect is due to atmospheric absorption caused by water vapor, carbon dioxide, ozone, methane and other gases (see fig. 6.1). Normally, the contents of carbon dioxide, carbon oxide and methane are stable, but water vapor is variable. A good atmospheric correction model should have the capability to simulate the above phenomena and to correct for the influences of scattering and absorption (Lu et al., 2002).

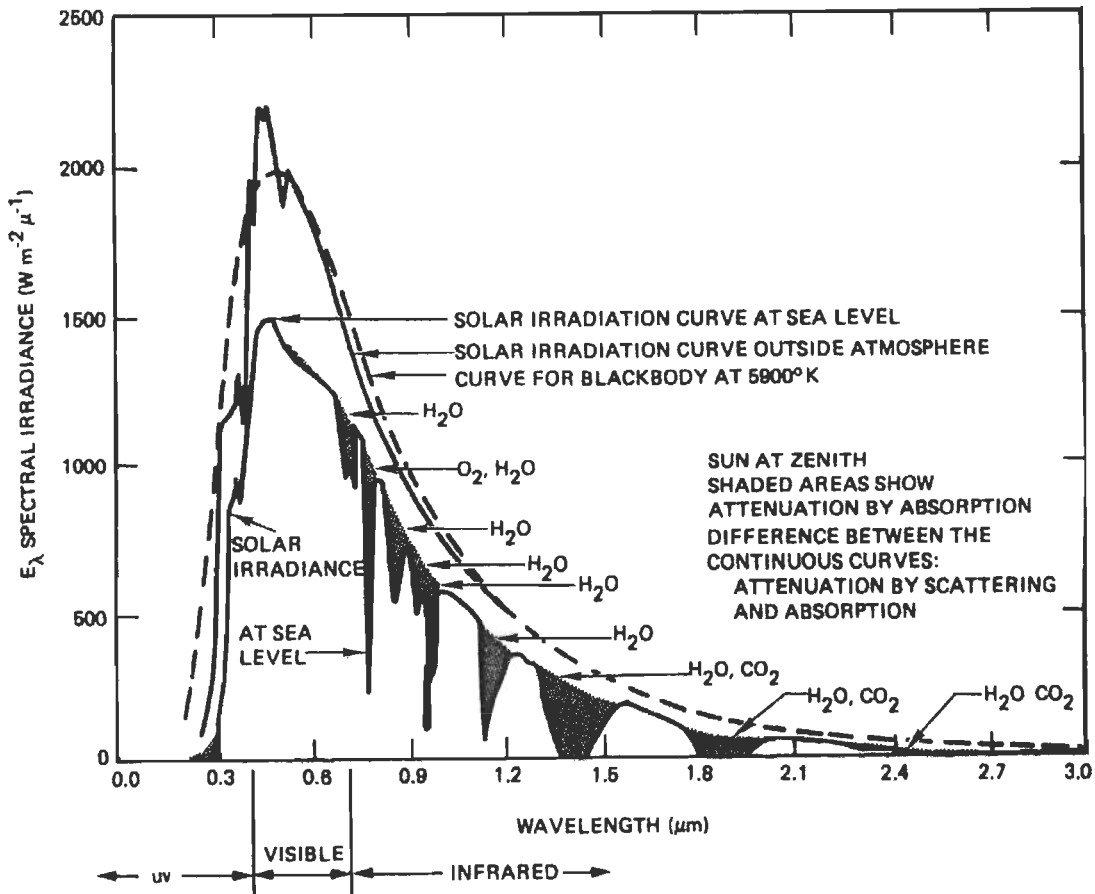


Figure-6.1 Solar irradiance on top of atmosphere and on Earth's surface; absorption by major atmospheric constituents results in selective transmittance of specific wavelengths, leaving only a part of the EM spectrum amenable to orbital remote sensing (after Chahine, 1983).

The basic model to obtain true surface reflectance from radiance-at-sensor may be expressed as a rearrangement of equation 1, as follows:

$$\rho_{\lambda} = \frac{K\pi \left(\frac{(L_{sen,\lambda} - L_{a,\lambda})}{\tau_u} \right)}{E_{o,\lambda} \cos \theta_z \tau_d + E_{\downarrow}} \quad (2)$$

Where:

K = correction factor for the annual variations in Earth-Sun distance computed from Julian day,

$L_{sen,\lambda}$ = radiance-at-sensor in band λ ,

$L_{a,\lambda}$ = the atmospheric upwelling radiance scattered at the sensor for the same band (path radiance)

τ_u, τ_d = path atmospheric transmittances of the upwelling (ground surface-sensor path) and downwelling (sun-ground surface path) flows, respectively,

$E_{o,\lambda}$ = solar irradiance at the top of the atmosphere for band λ ,

θ_z = solar zenith angle, and

E_{\downarrow} = diffuse irradiance at the surface.

Here, it is useful to differentiate between the ‘true’ surface reflectance and the ‘apparent’ or ‘scaled’ surface reflectance. While true surface reflectance incorporates spatial heterogeneities mostly owing to topographic variations in a scene (controlled by the variables in the denominator in the above equation), the apparent surface reflectance is primarily an estimate of the surface reflectance based on the atmospheric variables alone.

Two groups of calibration methods have been identified (Thome et al. 1997):

1. Absolute radiometric-atmospheric correction, and
2. Relative calibration methods

The absolute correction methods convert remotely sensed digital numbers into units of surface reflectance or radiance by removing the effects of atmospheric attenuation, illumination heterogeneity due to topographic variations and solar conditions. Common models for absolute atmospheric correction include the radiative transfer theory based algorithms/computer codes such as 6S (Second Simulation of the Satellite Signal in the Solar Spectrum) (Tanre et al., 1990; Vermote et al., 1994), MODTRAN (Moderate Resolution Atmospheric Radiance and Transmittance) model, and its predecessor LOWTRAN (Berk et al., 1989; Matthew et al., 2000), and image-based DOS (dark-object subtraction) model (Chavez, 1988, 1989, 1996; Kaufman et al., 1997).

The second class of calibration methods focuses on relative atmospheric correction. These methods remove or normalize the variation within a scene and normalize the intensities between images of same study area collected on different dates. The methods for relative correction include histogram adjustment, dark-pixel subtraction, and multi-date normalization using a regression model approach.

According to the model characteristics and complexity, three groups of models have been identified as following (Lu et al., 2002):

1. *Physics-based calibration models*: The physics-based radiative transfer models require many simulation submodels and use a variety of parameters. Such models can produce high surface reflectance accuracy. These models include the 6S (Vermote et al., 1997) and MODTRAN (Berk et al., 1989) radiative transfer models. These are often very complex and require many input parameters from the *in situ* field atmospheric information acquired at the time of remote sensing data acquisition.
2. *Image-based calibration models*: These include the apparent reflectance model of Markham and Barker (1986), and the image-based DOS model (Chavez, 1988, 1989, 1996; Kaufman and Sendra, 1988; Kaufman et al., 1997), which assume that the atmospheric impact is uniform on the whole image and that spectrally dark objects exist in the scene. Such dark objects are required to have zero reflectance, particularly in the infrared region; and mostly deep-water bodies, dark shadows or dense vegetation are used as such dark objects. The image-based DOS and the improved image-based DOS methods developed by Chavez (1988 and 1996, respectively) take into account the additive path radiance and the multiplicative atmospheric transmittance factors (which are ignored in the apparent reflectance model). Such models do not require any *in situ* atmospheric information. Inputs required to implement these models are based on image measurements and the information from remote sensing data header file, which records the important information pertaining to image acquisition such as – image date, Sun elevation and azimuth angles, and band specific gains and biases. Where an image header is not available, the image acquisition date can be used to derive needed parameters.
3. *Relative calibration models*: The third group of models is useful for relative calibration when no information on the scene acquisition and atmospheric conditions is known, as

is often the case with historic data, and include models based on: ‘invariant-objects’ (Hall et al., 1991), ‘histogram matching’ (Richter, 1996), ‘dark pixel subtraction’ (e.g. Kaufman and Sendra, 1988; Liang et al., 1997; Teillet and Fedosejevs, 1995) or regression equations. These models use scene statistics (whole or selected part) to generate relative reflectance from radiance-at-sensor or raw DN data.

A number of computer programs have been written to simulate the radiative transfer model. These include the ATREM program (short for ATmosphere REMoval), developed by CSES, University of Colorado which is based on the 6S radiative transfer model. The ACORN (short for Atmospheric CORrection Now; ImSpec LLC) and FLAASH (Fast Line-of-sight Atmospheric Analysis of Spectral Hypercubes) developed by Spectral Sciences Inc. in collaboration with ITTVIS, Inc., are both based on the MODTRAN radiative transfer model. Similarly, most of the popular commercial off-the-shelf (COTS) image processing software, like ERDAS Imagine and ENVI provide in-built procedures to calibrate remote sensing images to apparent reflectance and/or relative reflectance. These software packages use image-statistics based methods, like *Flat Field* (Roberts et al., 1986; Carrere and Abrams, 1988), *Modified Flat Field* (Green, 1990), *Internal Average Relative Reflectance* (Kruse, 1987), *Empirical Line* (Conel et al., 1987), and *Log Residuals* (Green and Craig, 1985).

6.2.2 ASTER L2 VNIR-SWIR surface reflectance data and its evaluation

Level2 (L2) standard atmospherically corrected surface reflectance data (AST_07) for the study area produced ‘on-demand’ was procured from the EOS Data Gateway (EDG) and evaluated.

The on-demand L2 surface reflectance data are generated using the 9 VNIR-SWIR bands (between 0.52 μm and 2.40 μm) from an ASTER Level-1B image. According to LP-DAAC (Land Processes Distributed Active Archival Center), USGS, the atmospheric correction involves deriving a relationship between the surface radiance/reflectance and the top-of-atmosphere (ToA) radiance from information on the scattering and absorbing

characteristics of the atmosphere. Once this relationship is established, it is used to convert the original radiance values to atmospherically corrected surface radiance and reflectance values.

The atmospheric correction algorithm for VNIR is based on a Look-Up Table (LUT) approach that uses results from a Gauss-Seidel iteration of the Radiative Transfer Code (RTC) (ASTER Algorithm Theoretical Basis Document (ATBD); Thome et al., 1999). This methodology is based on the reflectance-based, vicarious calibration approach of the Remote Sensing Group (RSG) at the University of Arizona, USA. The algorithm is based on the relationship between the angular distribution of radiance, scattering and absorption in the atmosphere, and the surface properties. The RTC used to generate the LUT for the atmospheric correction is based on the following parameters: solar zenith angle, satellite view angle, relative azimuth angle between the satellite and sun, molecular scattering optical depth, aerosol scattering optical depth, aerosol scatter albedo, aerosol size distribution parameter, and surface reflectance. The initial versions of the algorithm relied on external climatological sources for information on atmospheric absorption and scattering parameters. For later versions, this information is being obtained from other Terra sensors like the Multi-angle Imaging Spectroradiometer (MISR) and the Moderate-Resolution Imaging Spectroradiometer (MODIS). A digital elevation model provides the slope and elevation information for accurate modeling of surface reflectance. There are three groups of ancillary data inputs used in the atmospheric correction of ASTER radiance and reflectance:

- *Ozone data input:* The NCEP/TOVS (National Centers for Environmental Prediction/TIROS (Television & Infrared Observation Satellite) Operational Vertical Sounder) data are acquired from a NOAA satellite, and provides the ancillary column ozone data twice daily. Naval Research Laboratory's (NRL) Ozone Climatology data set is the alternative data source for column ozone.
- *Aerosol data input:* NRL's Aerosol Climatology ancillary data.

- *Temperature, atmospheric pressure, and moisture profile data inputs:* The source of these data is the NCEP-GDAS (Global Data Assimilation System) available at every 6 hours temporal frequency. The alternative is the NRL Climatology data set. These data sets are based on modeling, simulation, and prediction, and therefore, they are static, monthly, averaged data sets.

Neglect of the SWIR crosstalk phenomenon (Appendix D) and inefficient compensation for atmospheric water absorption due to absence of onboard additional atmospheric bands in ASTER has resulted in (generally) anomalously low values in bands 5 and 7 and high values in band 9 in these data, making them unsuitable for spectral processing, since the primary mineral absorption features are lost due to these discrepancies. Such discrepancies have been noticed by other workers also (*e.g.*, Mars and Rowan, 2006). For this reason, the primary L1B data has been put to rigorous radiometric, atmospheric and topographic corrections using existing methods and used instead.

6.2.3 Atmospheric correction of ASTER L1B data

In the following sections, the radiometric preprocessing and atmospheric correction of ASTER L1B data as implemented in the present study are discussed. Due to the differences in their basic nature, data in the VNIR-SWIR region (9 bands) and the TIR region (5 bands) have been processed separately. An overview of the preprocessing scheme adopted in this study has been shown in Figure-6.2.

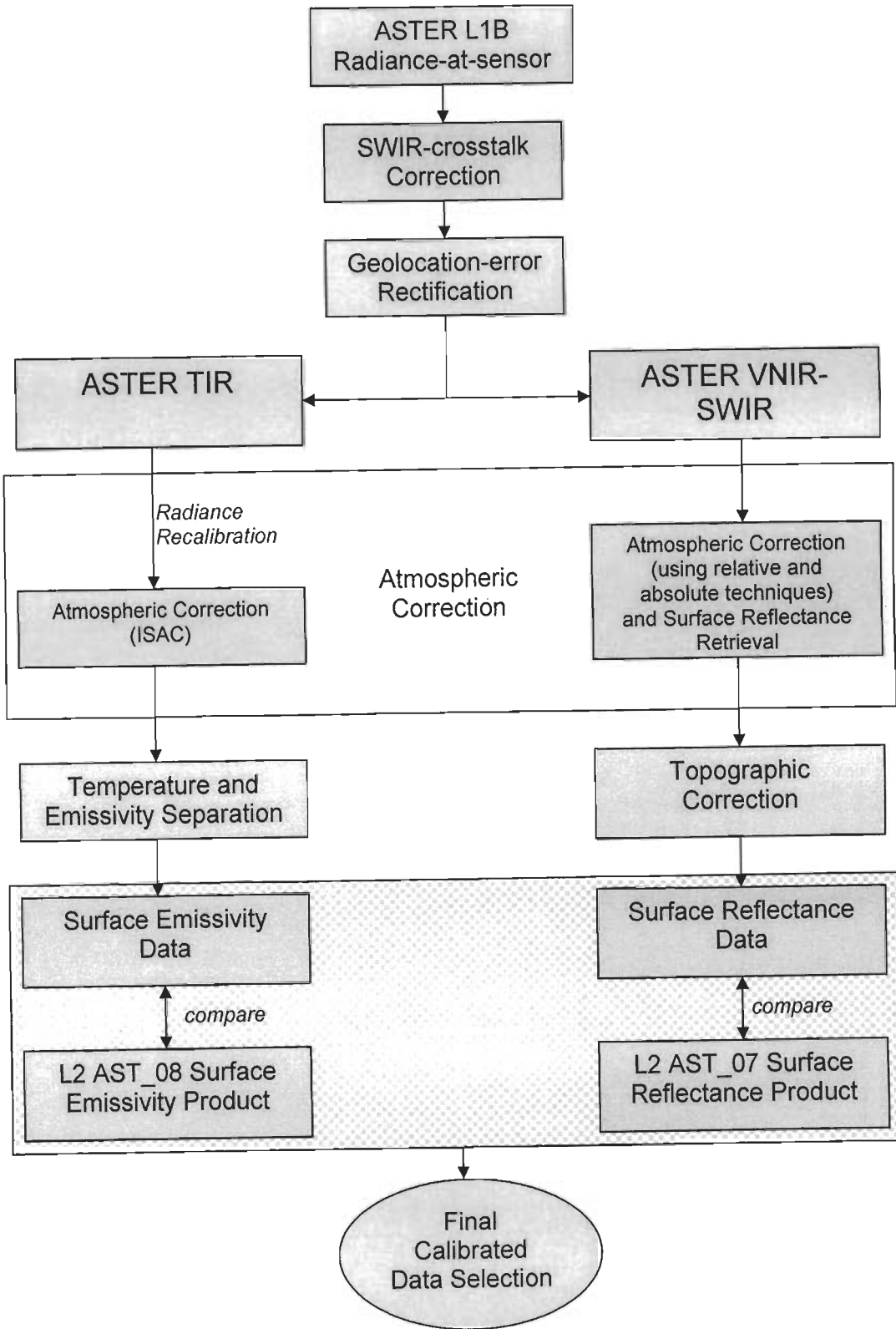


Figure-6.2 ASTER data calibration and surface reflectance/emissivity retrieval; processing flow for atmospheric and topographic correction

6.2.3.1 Radiometric and geometric corrections

The image data is usually provided in the form of raw digital numbers (DNs). The procedure used to convert the DN to physical units of radiance is called ‘sensor calibration’ (Mather, 2004). Sensor calibration is a vital step, since surface reflectance estimation heavily relies on the accuracy of the radiance values (as surface reflectance is a ratio between the incident radiation, or irradiance, and the surface radiance/emittance of the target). The various stages of radiometric preprocessing are described in the following paragraphs. After its launch, errors in radiometric accuracies of SWIR bands and geolocation have been discovered in ASTER data. The data used in the present study were obtained prior to these discoveries, and hence these errors are present in the data. To avoid error propagation which is inadvertent in subsequent processing and image analysis, it is vital to account for these errors. Description and correction of these errors have been provided in this section, prior to exhaustive implementation of various atmospheric correction techniques as described in subsequent sections.

Sensor Calibration: To convert the L1A data to scaled DN, the ASTER Level-1A DN are converted on a detector-by-detector basis using the Slope/Inclination (A), Gain (G) and Offset (D) values from the Radiometric Conversion Coefficients (RCC) table that is appended with the Level-1A dataset in the HDF file. The RCC information determines how the Level-1A DN are converted into Level-1B calibrated DN. Information from both the on-board and vicarious calibration sources is used in the generation of RCC table. Using the following equations, L1A data (for respective subsystems) are converted to at-sensor radiance:

$$L_{VNIR,SWIR} = AV/G + D \text{ (for VNIR-SWIR data), and}$$

$$L_{TIR} = AV + CV^2 + D \text{ (for TIR data)}$$

Where:

L = scaled radiance ($W/m^2/sr/\mu m$); A = Linear coefficient; C = non-linear coefficient; G = gain; D = offset; V = Signal (DN value).

Both intra-telescope and inter-telescope registration correction for all the bands are accomplished relative to the reference band for each sub-system (bands 2, 6, and 11). The

Level-1B dataset is produced by applying the radiometric calibration and geometric correction coefficients to Level-1A data. The Level-1B radiance dataset offers the same number of bands at the same resolution as the Level-1A. The original radiances and supplied DN values as L1B data are related to each other according to the following scaling procedure (Abrams et al., 2003; ASTER User's Handbook):

- (i) a DN value of zero is allocated to dummy pixels
- (ii) a DN value of 1 is allocated to zero radiance
- (iii) a DN value of 254 is allocated to the maximum radiance for VNIR and SWIR bands
- (iv) a DN value of 4094 is allocated to the maximum radiance for TIR bands
- (v) a DN value of 255 is allocated to saturated pixels for VNIR and SWIR bands
- (vi) a DN value of 4095 is allocated to saturated pixels for TIR bands

To convert from DN to radiance-at-sensor, the unit conversion coefficients (UCCs, defined as radiance per 1 DN) are used. Radiance (spectral radiance; $\text{Wm}^{-2}\text{sr}^{-1}\mu\text{m}^{-1}$) is obtained from image DN values, based on band number and gain state (specified in image header file) as follows:

$$\text{Radiance} = (\text{DN value} - 1) \times \text{UCC}$$

The maximum radiances depend on both the spectral bands and the gain settings and are shown in Table 6.1, and the UCCs for each band are given in Table 6.2 (Abrams et al., 2003).

Table-6.1 Maximum radiance values for all ASTER bands and all gain states. Values corresponding to the ASTER data used in this study have been shown in bold italics.

Band No.	Maximum radiance (W/(m ² *sr*μm))			
	High Gain	Normal Gain	Low Gain 1	Low Gain 2
1	170.8	427	569	N/A
2	179.0	358	477	
3N	106.8	218	290	
3B	106.8	218	290	
4	27.5	55.0	73.3	73.3
5	8.8	17.6	23.4	103.5
6	7.9	15.8	21.0	98.7
7	7.55	15.1	20.1	83.8
8	5.27	10.55	14.06	62.0
9	4.02	8.04	10.72	67.0
10	N/A	28.17	N/A	N/A
11		27.75		
12		26.97		
13		23.30		
14		21.38		

Table-6.2 Calculated Unit Conversion Coefficients for each ASTER band. Values corresponding to the ASTER data used in this study have been shown in bold italics.

Band No.	Coefficient (W/(m ² *sr*μm)/DN)			
	High Gain	Normal Gain	Low Gain 1	Low Gain 2
1	0.676	1.688	2.25	N/A
2	0.708	1.415	1.89	
3N	0.423	0.862	1.15	
3B	0.423	0.862	1.15	
4	0.1087	0.2174	0.290	0.290
5	0.0348	0.0696	0.0925	0.409
6	0.0313	0.0625	0.0830	0.390
7	0.0299	0.0597	0.0795	0.332
8	0.0209	0.0417	0.0556	0.245
9	0.0159	0.0318	0.0424	0.265
10	N/A	6.822 x 10⁻³	N/A	N/A
11		6.780 x 10⁻³		
12		6.590 x 10⁻³		
13		5.693 x 10⁻³		
14		5.225 x 10⁻³		

ASTER SWIR Crosstalk and Correction: ASTER SWIR crosstalk defect – which is essentially a leakage of incident signal mainly from band 4 to nearby SWIR bands – and its correction has been discussed by Iwasaki et al. (2001) and Iwasaki and Tonooka (2005); and have been summarized in Appendix D. The LIB data used in this study has been corrected for this defect using a software tool obtained from ERSDAC, Japan.

The crosstalk-corrected SWIR image (bands 4-6-8 in R-G-B) is shown in Figure-6.3a. Spectrum of a sample pixel prior to SWIR crosstalk correction is shown in Figure-6.3b, and the corresponding spectrum of the same pixel after crosstalk correction is shown in Figure-6.3c. A difference spectrum for crosstalk uncorrected and crosstalk corrected sample pixel spectra is shown in Figure-6.3d. It can be seen that the crosstalk-corrected sample pixel spectrum has reduced values, with greatest reduction in bands 5, 7 and 9, of the order of $0.2 \text{ W/m}^2/\text{sr}/\mu\text{m}$.

Geolocation error and correction: Geolocation discrepancies of the order of 200-300m have been detected in the original geocoded ASTER LIB data. Such discrepancies are greatest in data covering areas near the poles and in topographically heterogeneous terrain, hampering direct comparisons between topographic maps and GPS-controlled field locations. Details of this phenomenon have been provided in Appendix D.

The geolocation error for the ASTER image data used in this research has been corrected using the online software tool available at the official ASTER website of JPL, NASA (asterweb.jpl.nasa.gov) prior to rigorous atmospheric correction described in subsequent sections. The geo-correction results have been subsequently checked using GPS data for select field locations, and the geolocation accuracy has been found to be well within 30 m, which is the basic spatial unit (pixel size) of both TM and ASTER SWIR sensors.

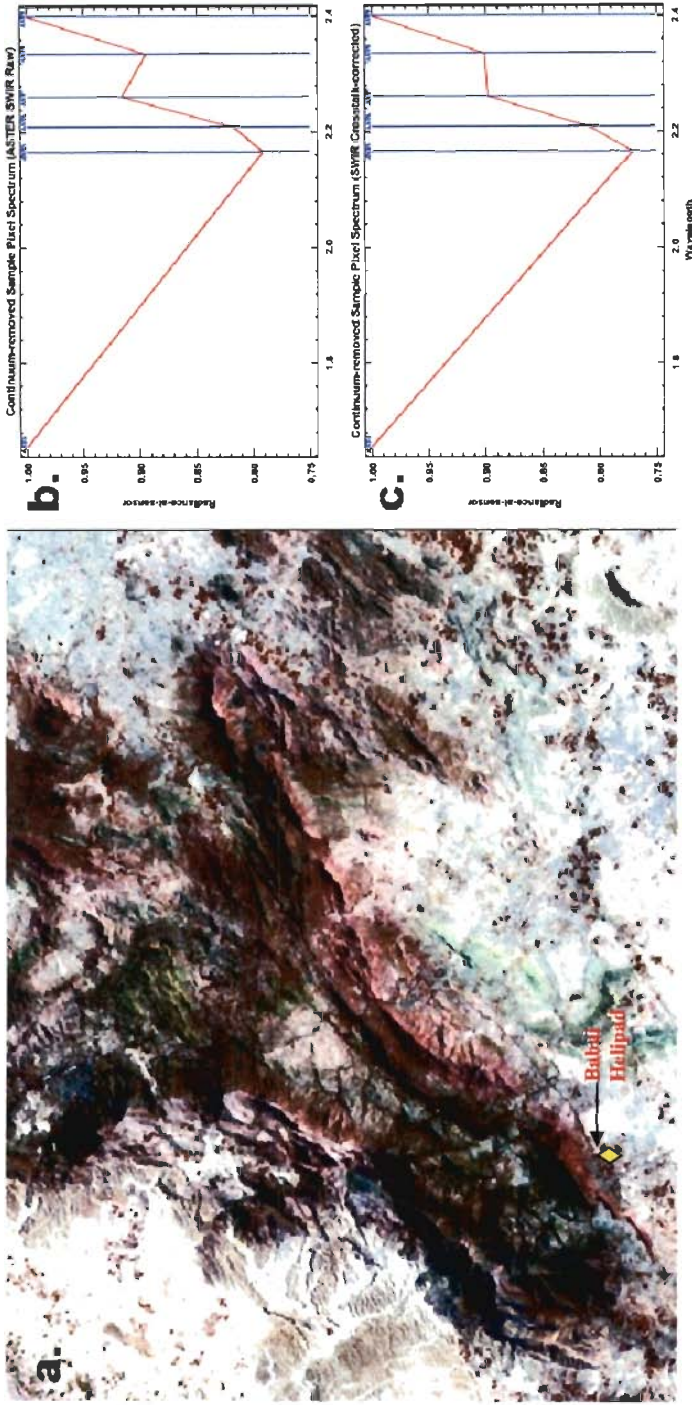


Figure-6.3 Results of crosstalk correction of ASTER SWIR bands; (a) shows the corrected SWIR bands 4-6-8 in RGB; the raw SWIR radiance-at-sensor continuum-removed spectrum of the sample pixel (marked by a yellow diamond symbol on the image) is shown in (b), and the spectrum of the same pixel after crosstalk correction is shown in (c). Notice the false absorption feature in band 8 of the uncorrected data, and its removal after correction. Difference between the two spectra is shown in d. ASTER SWIR band-centers have been marked in the plots. Radiance units are $Wm^{-2} sr^{-1}$ and the wavelength is in micrometers

6.2.3.2 Atmospheric correction of ASTER VNIR-SWIR data and reflectance retrieval

In the following sections, the atmospheric correction and data calibration of SWIR-crosstalk- and geolocation-corrected ASTER VNIR-SWIR data using various available atmospheric correction techniques to obtain the final 9-band surface reflectance image data have been described. Both relative and absolute atmospheric correction methods have been tested and discussed. The results of different methods of atmospheric correction have been inter-compared using reflectance spectrum of a common pixel in all the outputs, referred to as the test pixel spectrum. The pixel represents a flat homogeneous ground surface of an abandoned helipad, with composition similar to reddish-brown medium to fine sandy loam, and lies immediately east of the Babai village in the southern part of the study area (for location refer to fig. 6.3a). ENVI and ERDAS software packages have been used conjunctively for atmospheric correction of the image data.

6.2.3.2.1 Methods of relative atmospheric correction

1. *Relative reflectance using Log Residuals*: Log Residuals calibration (Green and Craig, 1985) removes solar irradiance, atmospheric transmittance, instrument gain, topographic effects, and albedo effects from radiance data. This transform creates a pseudo reflectance image that is useful for analyzing mineral-related absorption features. The logarithmic residuals of a dataset are defined as the input spectrum divided by the spectral geometric mean, divided by the spatial geometric mean. The geometric mean is used because the transmittance and other effects are considered multiplicative; it is calculated using logarithms of the data values, hence the name 'Log Residuals'. The 'spectral mean' is the mean of all bands for each pixel and partially removes topographic effects. The 'spatial mean' is the mean of all pixels for each band

and accounts for the solar irradiance, atmospheric transmittance, and instrument gain.

Figure-6.4a shows the Log Residuals-corrected spectrum of the test pixel.

2. *Relative reflectance using IARR method:* The Internal Average Relative Reflectance (IARR) calibration (Kruse, 1987) normalizes the data to a scene average spectrum. This is particularly effective for reducing hyperspectral data to relative reflectance in an area where no ground measurements exist and little is known about the scene. It works best for arid areas with no vegetation, and hence is suitable for the data used in this study. An average spectrum is calculated from the entire scene and is used as the reference spectrum, which is then divided into the spectrum for each pixel of the image. Figure-6.4b shows the IARR-corrected relative reflectance spectrum of the test pixel.
3. *Relative reflectance using the Flat Field and the Modified Flat Field techniques:* The Flat Field technique ((Roberts et al., 1986; Carrere and Abrams, 1988) is used to normalize the data to the spectrum of a known spectrally neutral ‘flat field’ in the scene. The flat field selected is usually a spectrally uniform and bland site within the scene (Clark et al., 2002). The Modified Flat Field (MFF) method (Green, 1990), as implemented in ERDAS Imagine software, requires that the analyst knows the material of the flat field and has a laboratory spectrum of that material. In MFF, each input pixel spectrum is divided by the flat field and then multiplied by the spectrum. For the study area, 44 pixels from Babai helipad (see fig. 6.4) representing spectrally and spatially homogeneous reddish-brown loamy sand surface were used as a flat field. Library spectrum of this material available in the ASTER spectral library was used with the MFF procedure to calibrate the data to relative reflectance. The results of the FF and MFF calibration for the test pixel have been shown in Figure-6.4c and d.
4. *Relative reflectance using Empirical Line method:* The Empirical Line technique is a simple slope/intercept calculation (Conel et al., 1987). This method forces the image spectra to match the selected field/laboratory spectra. A linear regression is used for

each band to equate DN/radiance and reflectance. This is equivalent to removing the solar irradiance and the atmospheric path radiance. The following equation shows how the empirical line gain and offset values are calculated (in ENVI):

$$\text{Reflectance (field spectrum)} = \text{gain} \times \text{radiance (input data)} + \text{offset}$$

When the analyst has a pair or more of the spectral ground control points and their corresponding laboratory/field spectra, a linear fit is calculated, defined by its slope and intercept for each image band. In practice, it is necessary to select both high and low albedo areas from the image (Roberts et al., 1985). Each (empirically derived) line is then used to generate a look-up table (LUT) to adjust the input DNs to relative reflectance values defined by the spectral ground control areas. The bright and dark objects used for Empirical Line calibration of the ASTER image data used in this study were the Babai helipad in the southern part of the image, and a small dam in the northern-central part of the image. The corresponding laboratory spectra used for the materials of these areas were brown fine loamy sand, and distilled water, both taken from the Johns Hopkins University (JHU) spectral library. The result of EL calibration is shown using the spectrum of the test pixel in Figure-6.4e.

6.2.3.2.2 Methods of absolute atmospheric correction

1. *Surface reflectance retrieval using FLAASH*: FLAASH (Fast Line-of-Sight Atmospheric Analysis of Spectral Hypercubes) is a MODTRAN4-based atmospheric correction software package developed by the Air Force Phillips Laboratory, Hanscom AFB and Spectral Sciences, Inc. (Adler-Golden et al., 1999). It provides accurate, physics-based derivation of apparent surface reflectance through derivation of atmospheric properties such as surface albedo, surface altitude, water vapor column, aerosol and cloud optical depths, and surface and atmospheric temperatures from high spectral resolution data. FLAASH operates in the 0.4–2.5 μm spectral range. In

FLAASH, first the MODTRAN simulations of spectral radiance are performed for various atmospheric, water vapor, and viewing conditions (solar angles) over a range of surface reflectances to establish look-up tables (LUTs) for the atmospheric parameters of column water vapor, aerosol type, and visibility for subsequent use. Typically, the 1.13 μm water band is used to estimate water vapor, and a ratio of in-band and out-of-band radiance values allows estimation of absorption band depths for a range of water vapor column densities. FLAASH also derives pressure altitudes by applying the same method to the 0.762 μm oxygen-absorption band. The radiance spectra are extracted from the input data and compared against the MODTRAN LUTs on a pixel-by-pixel basis to determine scaled surface reflectance. FLAASH offers an additional option of correcting for EMR scattered from adjacent pixels. Spatially averaged reflectance is used to account for the radiance contributions originating from parts of the surface not in the direct line of sight of the sensor (adjacency effect; Adler-Golden et al., 1999; Mathew et al., 2003). FLAASH provides additional flexibility when compared to the other atmospheric correction programs used typically with hyperspectral data, such as ACORN (Atmospheric CORrection Now) and ATREM (Atmosphere REMoval) in that it allows custom radiative transfer calculations for a wider range of conditions including off-nadir viewing and all MODTRAN standard aerosol models (Kruse, 2004). The FLAASH input parameters for the ASTER VNIR-SWIR image data of the study area have been summarized in Table-6.3 and the test pixel spectrum is shown in Figure-6.4f.

2. *Top-of-Atmosphere (apparent) reflectance*: Estimation of apparent reflectance from digital satellite data for most satellite sensors involves conversion of raw binary data (digital numbers, or DNs) to radiance-at-sensor using the gain and offset values, and subsequent computation of the reflectance using the following basic model (Markham and Barker, 1986, 1987) which is a simplification of the primary model shown in

equation 2, and is commonly referred to as the Top-of Atmosphere (ToA) or planetary reflectance model:

$$\rho_{\lambda} = \frac{\pi L_{\lambda} d^2}{E_{sun\lambda} \cos \theta_z} \quad (3)$$

Where:

L_{λ} = radiance-at-sensor, d = Earth-Sun distance measured in AU, $E_{sun\lambda}$ = band specific exo-atmospheric solar irradiance, and θ_z = solar zenith angle (90° -solar elevation angle) in radians.

The factors of atmospheric transmittance (τ_u , τ_d ; upward and downward), path radiance (L_a), and diffuse sky irradiance (E_{\downarrow}) have been ignored in this model, while approximation for K has been made as d^2 . For the dataset used, the parameters of the apparent reflectance model (top-of-atmosphere reflectance) are provided in Table-6.4, and the band-specific exo-atmospheric solar irradiances for ASTER obtained from World Radiation Center (WRC, Switzerland) are given in Table-6.5. Test pixel spectrum after correction using this technique is shown in Figure-6.4g.

3. *Image-based DOS*: Chavez (1988) suggested a method to correct for the additive ‘haze’ (path radiance) effect of the atmosphere for the Landsat TM data. This method is good for correcting shorter wavelength bands than the longer wavelengths since atmospheric scattering is dominant at shorter wavelengths. Chavez (1989) suggested further improvements in the original technique by specifying the model atmospheric conditions to compute the ‘haze’ value. Chavez (1996) developed the method further by incorporating the multiplicative parameters (atmospheric transmittance) also in the correction procedure and named the technique as COST.

Using a moderate atmospheric scattering model (λ^{-1} ; Chavez, 1989), and assuming at least a minimum 1% reflectance pixel exists in the scene, the haze values have been determined for the 9 solar reflective VNIR-SWIR bands of ASTER data based on the basic radiance to reflectance relation given in equation 2, as summarized in Table-6.6.

The gains and offsets used in estimating the final haze parameters have been obtained from the image metadata and the value of τ_d (downward atmospheric transmittance; eq. 2) has been estimated as an approximation of $\cos\theta_z$ (with a value of 0.8122 for the ASTER scene used in this study, where θ_z is the solar zenith angle (=35.690479 degrees); Chavez, 1996). Since ASTER bands are all nadir looking (except band 3b, which has not been used in this study), the value of τ_u (upward atmospheric transmittance; eq. 2) has been estimated as 1.0 ($\tau_u = e^{-\delta \sec(\theta_v)}$); where δ is the atmospheric optical depth, calculated *in situ*, and θ_v is the satellite viewing angle, which is 0 in case of nadir looking sensors). Details of the technique can be found in Chavez (1989) and Chavez (1996). The test pixel spectrum obtained after atmospheric correction using the image-based DOS technique has been shown in Figure-6.4h.

Table-6.3 ENVI FLAASH input parameters for the ASTER scene used in the present study.

Parameter		Value
General	Scene Center	27.833723 75.750792
	Sensor and Sensor Type	ASTER; Multispectral
	Sensor Altitude (km)	705
	Ground Elevation (km)	0.5 (default 0.0)
	Pixel size (m)	15
	Flight date and time	Oct. 5, 2002; 05:43:51 UTC (Z)
Atmospheric Model		Tropical
Aerosol Model		Rural
Water Retrieval		No
Water Column Multiplier		1.000
Aerosol Retrieval		2 Band (K-T)
Initial Visibility (km)		25
Kaufman-Tanre (K-T) Aerosol Retrieval	K-T Upper Channel	Band5 (2.167 μm)
	K-T Lower Channel	Band2 (0.661 μm)
	Max. Upper Channel Reflectance	0.10
	Reflectance Ratio	0.45
Advanced Settings	Aerosol Scale Height (km)	2.00
	CO ₂ Mixing Ratio (ppm)	390.00
	Adjacency Correction (yes/no)	Yes
	MODTRAN Resolution (cm ⁻¹)	15
	MODTRAN Multiscatter Model	Scaled DISORT
	Number of DISORT Streams	8
	Scale Factor for Radiance Image	10.0
Output Reflectance Scale Factor	10000	

Table-6.4 Acquisition parameters for the ASTER LIB dataset used in the present study.

Parameter	Value
Solar direction (azimuth and elevation), deg	153.210649, 54.309521
Solar zenith angle (90° - solar elevation angle), deg	35.690479
Date and time of scene acquisition	Oct. 5, 2002; 05:43:51 UTC (Z)
Julian day for the acquisition date and time	2452552.738785
Earth-sun distance (d), AU	1.0000594926008028

Table-6.5 Solar exo-atmospheric irradiance values for the nine reflective bands of ASTER (VNIR+SWIR) (Thome et al., 2001):

ASTER band (band center in μm)	$E_{sun\lambda}$ ($\text{W}/\text{m}^2/\text{sr}/\mu\text{m}$)
AST_1 (0.556)	1847.00
AST_2 (0.661)	1553.00
AST_3 (0.807)	1118.00
AST_4 (1.656)	232.50
AST_5 (2.167)	80.32
AST_6 (2.209)	74.92
AST_7 (2.262)	69.20
AST_8 (2.336)	59.82
AST_9 (2.400)	57.32

Table-6.6 Haze value computation for ASTER VNIR+SWIR bands using the image-based DOS technique (COST method; Chavez, 1996) under moderate scattering atmospheric conditions (Chavez, 1989)

ASTER Band Number	Minimum Scaled Digital Number (DN_{min})	Minimum Band-specific Radiance-at-sensor (L_{min})	Band-specific Solar Irradiance ($E_{sun\lambda}$)	Radiance for a 1% reflecting surface ($L_{\rho=1\%}$) $= \frac{\rho E_{sun\lambda} \cos\theta_z \tau_d \tau_u}{\pi d^2}$	Haze value for each band (L_{haze}) $= L_{min} - L_{\rho=1\%}$
AST_1	53	35.152	1847	3.878358569	31.27364
AST_2	36	24.78	1553	3.261012917	21.51899
AST_3	31	25.86	1118	2.34759333	23.51241
AST_4	36	7.609	232.5	0.488207021	7.120793
AST_5	37	2.5056	80.32	0.168657152	2.336943
AST_6	35	2.125	74.92	0.157318151	1.967682
AST_7	35	2.0298	69.2	0.145307208	1.884493
AST_8	30	1.2093	59.82	0.125610942	1.083689
AST_9	35	1.0812	57.32	0.120361404	0.960839

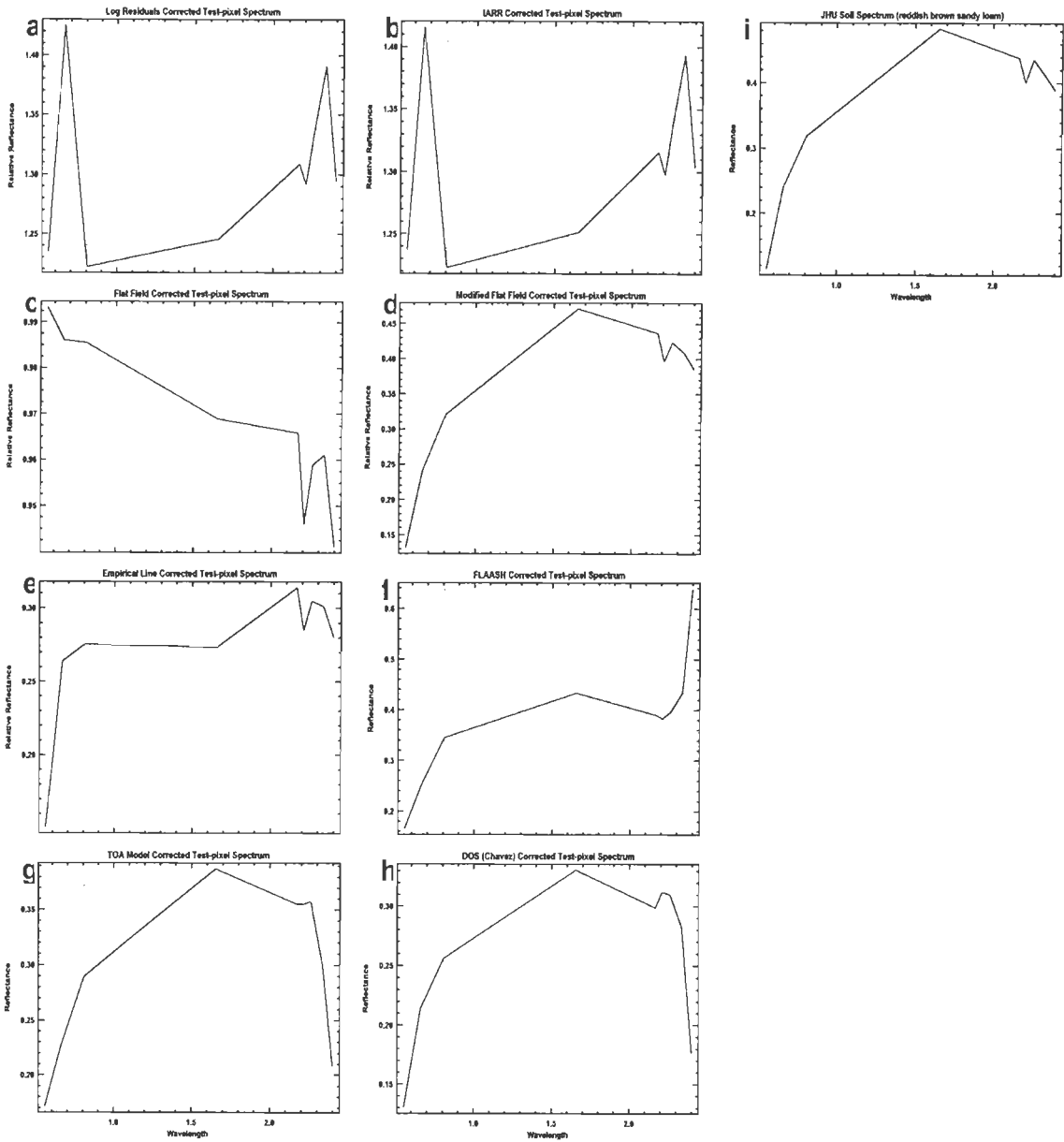


Figure-6.4 Comparison of the spectra of the test pixel obtained after application of the various atmospheric correction procedures, (a) Log Residuals, (b) Internal Average Relative Reflectance, (c) Flat Field, (d) Modified Flat Field, (e) Empirical Line, (f) FLAASH, (g) Top of Atmosphere apparent reflectance model, and (h) Dark Object Subtraction (Chavez) method. The JHU library spectrum of the material constituting the pixel, *i.e.* reddish-brown medium to fine sandy loam has been shown in (i). Wavelength unit is micrometers.

6.2.3.2.3 Discussion on atmospheric correction results

Figure-6.4 shows the results of the various radiometric-atmospheric correction methods tested above in comparison with the JHU laboratory spectrum of the main constituent of the field material of the test pixel, *i.e.* reddish-brown fine sandy loam. Following observations have been made on the basis of a comparative inspection of the spectral plots in terms of the curve shape and absorption feature band position, as shown in Figure-6.4:

1. The Log Residuals- and IARR-corrected reflectance spectra show a very high degree of match, primarily because the basic correction mechanism is similar in the two cases. There is a gross mismatch between the expected sample pixel spectrum and the spectrum for the same sample pixel using relative correction methods like IARR, FF, and Log Residuals, in terms of curve shape, absorption band position and absolute reflectance values. Due to these reasons, the results of these techniques were summarily discarded.
2. The MFF-corrected test-pixel spectrum shows excellent match with the lab spectrum. This is primarily because the same area was used in the correction procedure. An evaluation of spectra from other known materials in the study area revealed the consistency of the method, since the absorption features expected in those pixels were found to be well represented.
3. The Empirical Line calibration yielded acceptable results with the main absorption feature at band 6 well preserved. However, unexpectedly low reflectance in band 4 was observed in the test spectrum. Because of this reason, this result was also deemed unfit.
4. The ToA (apparent reflectance) model yielded rather 'flat' results, and the expected absorption feature at band 6 is not seen prominently in the test-pixel spectrum. Moreover, the spectral variability anticipated between pixels with very different surface composition was found to be very weak. Therefore this result was also discarded.

5. The COST or image-based DOS technique was found to suffer from grave inaccuracies in the SWIR bands. It can be mentioned that in the original method, Chavez (1996) had used only the VIS-NIR bands (Landsat TM1-TM4). In this study too, the reflectance values of the test-spectrum for the three ASTER VIS-NIR bands were relatively accurate and close to the absolute reflectance values. However, since the expected absorption feature at band 6 is lost in this technique, the result was considered unfit for further use.
6. The output of the FLAASH corrected sample pixel spectrum has a close match with the lab spectrum, except for band 8 and 9. The absorption feature at band 6 is rather subdued and, there is an anomalously high reflectance in band 9, similar to that observed in the L2 AST_07 product.

From the above observations, it can be inferred that the best correction for atmospheric effects is possible when some information about the field area is available. Best calibration is achieved when *in situ* field spectral measurements are made, or at least some knowledge of the field material from a location identifiable on the remote sensing image is available and a laboratory spectrum of that material exists.

6.2.3.2.4 Hybrid FLAASH+MFF correction

In view of the above, and the fact that the FLAASH-corrected data represent the best correction in absence of any field information, the FLAASH-corrected data was further refined by applying MFF-correction to them. This has been named as the 'Hybrid FLAASH+MFF correction', and the result of this correction (fig. 6.5) has been selected for further processing. Thus, the best atmospheric correction has been obtained using the hybrid method, where first an absolute atmospheric correction was applied to the radiance-at-sensor data, with a subsequent MFF correction to remove the effects of overcorrection for path radiance at shorter wavelengths and atmospheric absorption near band 9.

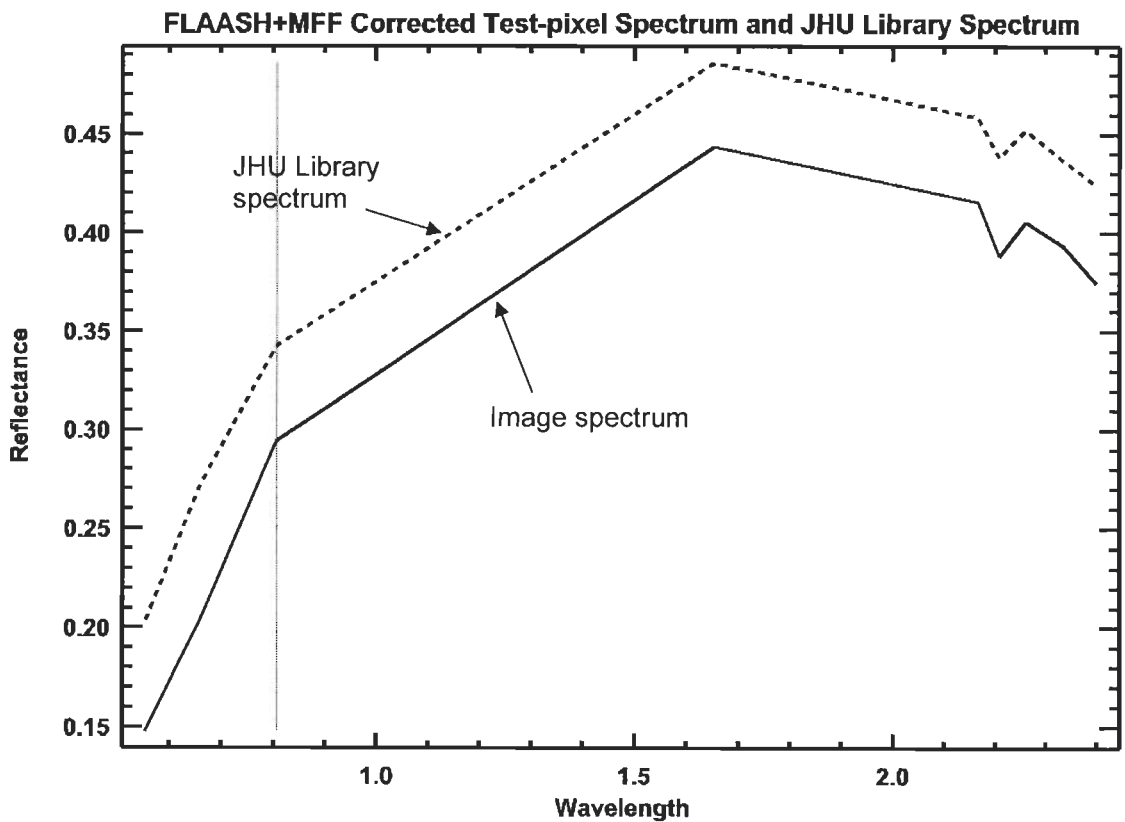


Figure-6.5 Spectrum of the test pixel after the Hybrid FLAASH+MFF correction. The JHU soil spectral library spectrum of the constituent soil type (reddish-brown medium to fine sandy loam) resampled to ASTER bandpasses has also been shown for comparison. Wavelength is in micrometers.

6.2.3.3 Atmospheric correction of ASTER TIR data to retrieve surface radiances

Like data in VNIR-SWIR range, image data in TIR spectral window is also affected by the atmospheric interference. The effect in this case is primarily due to multiplicative absorption, and the contribution due to atmospheric scattering is rather negligible. Atmospheric water is the main constituent which attenuates the radiances sensed remotely in the TIR region. The purpose of atmospheric correction of ASTER TIR at-sensor radiance data is to account for these influences and to retrieve surface radiances which are to be used to estimate the surface emissivities through one of the procedures discussed in later sections. The surface emissivity data thus obtained forms the mainstay of all further processing to map the lithologic units in the study area, as discussed in Chapter 7.

In the following sections, the data preprocessing steps followed to atmospherically correct the radiance-at-sensor data using the In-Scene Atmospheric Compensation (ISAC) procedure have been described after radiometric recalibration of the at-sensor radiances as discussed below.

6.2.3.3.1 Radiance recalibration

Radiometric Calibration Coefficient (RCC) versions 1.x and 2.x used for ASTER TIR products processed before 8 February 2006 included an error caused from delay in RCC updating. This error has been reduced for RCC version 2.09 or later, applied to products observed after October 2002, but is large in earlier RCC versions, particularly versions 2.05 and 2.06 applied to products observed from February 2001 to October 2002, although the error depends on a scene observation date (Tonooka et al., 2003; Sakuma et al., 2005).

Since the ASTER scene used in the present study was acquired on October 5, 2002, (and processed according to RCC version 2.06), in order to preserve radiometric accuracy and precision, coefficients obtained from ERSDAC, Japan (<http://deco.cis.ibaraki.ac.jp/RECAL/>) were used with the original radiances to recalibrate the data, according the following relationship:

$$\textit{New Radiance} = A \times \textit{Original Radiance} + B$$

The values of the coefficients A and B in the above relationship have been reproduced in Table-6.7.

Table-6.7 ASTER TIR radiance recalibration coefficients and estimated changes in radiances and temperatures computed using original and recalibrated radiances for some standard temperatures.

ASTER Band Number	A	B	Estimated Changes (Upper: Radiance, Lower: Temperature)			
			@270K	@300K	@320K	@340K
10	1.022966	-0.1132	-0.000 -0.00K	+0.102 +0.56K	+0.196 +0.85K	+0.313 +1.11K
11	1.045742	-0.2380	+0.000 +0.00K	+0.203 +1.13K	+0.387 +1.72K	+0.613 +2.26K
12	1.078325	-0.4292	+0.000 +0.00K	+0.343 +1.96K	+0.647 +3.01K	+1.014 +3.96K
13	1.044944	-0.2640	+0.000 +0.00K	+0.175 +1.18K	+0.320 +1.84K	+0.489 +2.46K
14	1.057163	-0.3339	+0.000 +0.00K	+0.204 +1.51K	+0.371 +2.37K	+0.562 +3.17K

6.2.3.3.2 ISAC Correction

The atmospheric correction of the ASTER TIR recalibrated at-sensor radiance data has been performed using an algorithm similar to the In-Scene Atmospheric Compensation (ISAC) algorithm (Johnson and Young, 1998; Hernandez-Baquero, 2000), as implemented in the ENVI software package, described briefly as follows.

The algorithm assumes that the atmosphere is uniform over the data scene and that a near-blackbody surface exists within the scene. The location of the blackbody surface is not required for this correction. A single layer approximation of the atmosphere is used. Existence of nil reflected downwelling radiance is also assumed. The algorithm first determines the wavelength that most often exhibits the maximum brightness temperature. This wavelength is then used as the reference wavelength. Only spectra that have their brightest temperature at this wavelength are used to calculate the atmospheric compensation. At this point, for each wavelength, the reference blackbody radiance values are plotted against the measured radiances. A line is fitted to the highest points in these plotted data and the fit is weighted to assign more weight to regions with denser sampling. The compensation for this band is then applied as the slope and offset derived from the linear regression of these data with their computed blackbody radiances at the reference wavelength.

Upwelling atmospheric radiance and atmospheric transmission are approximated using the following method. First, the surface temperature of every pixel is estimated from the data and used to approximate the brightness temperature using the Planck function and assuming an emissivity of 1.0. Next, a line is fitted using one of two methods – Top-of-Bins or Normalized Regression to a scatter plot of radiance vs. brightness temperature. Top-of-Bins method fits a line to the top of the scatter plot of radiance vs. brightness temperature. The top of the scatter plot corresponds to those pixels whose emissivity is closest to 1.0. This Top-of-Bins fit is achieved by doing a standard least squares regression on the top 5% of the data in the scatter plot. On the other hand, the Normalized Regression method first fits a line to the scatter plot of radiance vs. brightness temperature by doing a standard least squares regression. The residuals of this fit are then compared to a normal probability plot. Another regression is done on the residuals in the normal plot. Points that are 3 times the Noise Equivalent Sensor Response (NESR) away from the regression line are deemed outliers and are removed. A final regression is done on the scatter plot using this reduced set of pixels. The atmospheric upwelling and transmission are then derived from the slope and offset of this line (ENVI User's Guide, 2005).

Figure-6.6 shows the initial at-sensor radiance, the recalibrated radiance and the surface radiance spectra of a pixel obtained after the atmospheric correction using the above-mentioned procedure. The fitting method used for the estimation of the upwelling atmospheric radiance and atmospheric transmission is the Normalized Regression method, with a corresponding NESR value of 0.25. The estimated curves for upwelling atmospheric radiances and atmospheric transmission for the five ASTER TIR channels are shown in Figure-6.9a-b, respectively.

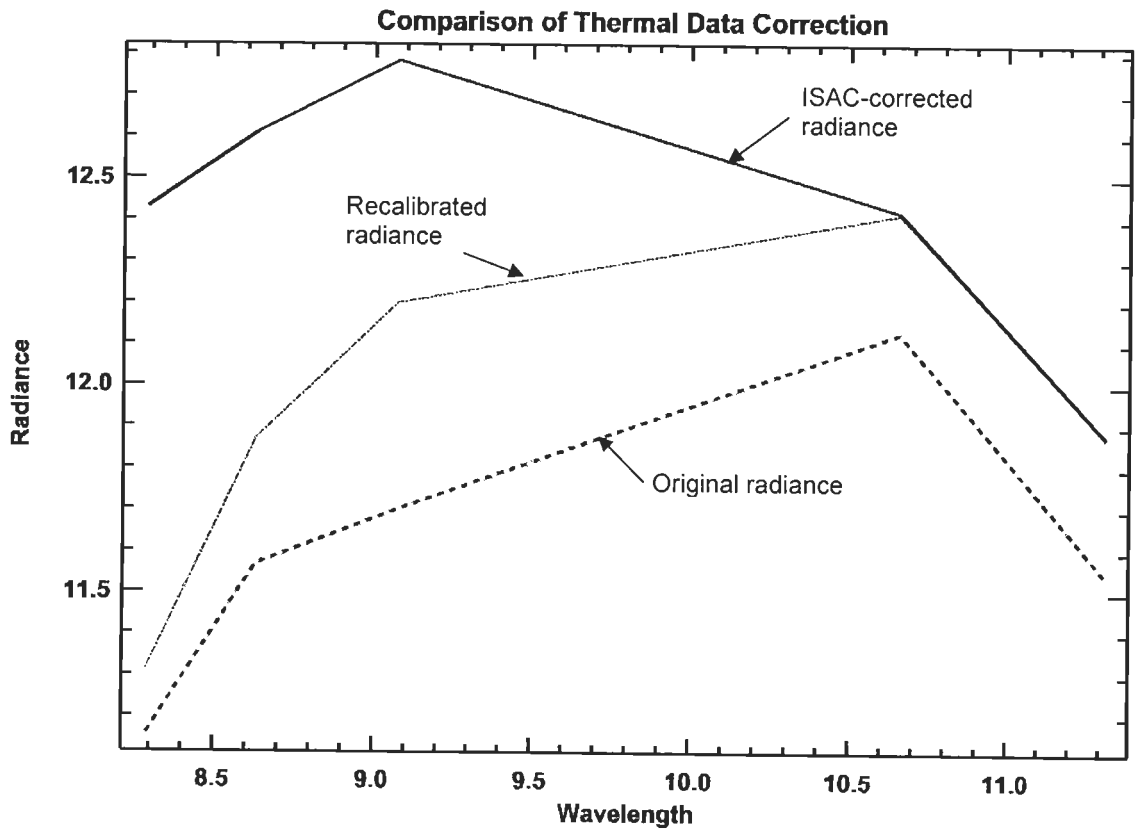


Figure-6.6 Comparison of results obtained for the radiometric-atmospheric corrections of ASTER TIR radiance data of the study area. Radiance units are in $\text{Wm}^{-2} \text{sr}^{-1}$ and the wavelength is in micrometers.

6.3 Topographic correction

6.3.1 A brief review of existing techniques

The irradiation on a slope varies strongly with slope azimuth relative to the Sun, and the reflectance of the slope varies with the angles of incidence and exitance relative to the slope normal. Topographic correction involves standardizing imagery for these two effects (Shepherd and Dymond, 2003). Various methods of topographic correction or topographic normalization have been developed over the last two decades. Apart from the band-ratioing methods, these are categorized under those dealing with Lambertian surfaces (surfaces exhibiting pure diffuse reflection) and those with non-Lambertian surfaces (surfaces with non-uniform diffuse reflection) (Riano et al., 2003).

Cosine method: For horizontal to near-horizontal surfaces a Lambertian model can be assumed and the most widely used topographic normalization method for such surfaces is the ‘cosine method’ of Teillet et al. (1982), expressed as:

$$\rho_H = \rho_T \left(\frac{\cos \theta_z}{IL} \right) \quad (6)$$

Where:

ρ_H and ρ_T are respectively the reflectances for topographically horizontal and undulating surfaces; θ_z is the solar zenith angle; and IL is the local illumination angle computed using the following equation:

$$IL = \cos \theta_p \cos \theta_z + \sin \theta_p \sin \theta_z \cos(\varphi_a - \varphi_o) \quad (7)$$

Where:

θ_p is the slope angle; θ_z is the solar zenith angle; φ_a is the solar azimuth angle; and φ_o is the aspect angle. The slope angle, the aspect angle are the derivatives of the Digital Elevation Model (DEM). To compute the aspect and slope, a DEM of the same spatial size and resolution as the image to be topographically corrected is used.

Civco method: As the cosine model overcorrects the image in areas of low illumination, Civco (1989) suggested an alternate model, which is written as:

$$\rho_H = \rho_T + \left[\rho_T \left(\frac{IL_m - IL}{IL_m} \right) \right] \quad (8)$$

Where:

IL_m is the average illumination value of the study area.

C method: The bidirectional reflectance distribution function (BRDF) describes how reflectance varies according to the changes in the angles of incidence and illumination (Sandmeier and Itten, 1997), and is applied to ascertain the reflectance variation for undulating surfaces with variation in illumination geometry. Various methods of topographic correction for non-Lambertian surfaces (topographically rugged terrain) have been proposed. C-correction method has been found to be the most useful of these methods (Gupta et al., 2007). It is a statistically based method and an improvement upon the existing statistical-empirical method of Teillet (1982). Mathematically, this method is expressed in the following form:

$$\rho_H = \rho_T \left(\frac{\cos \theta_z + c_k}{IL + c_k} \right) \quad (9)$$

Where, c_k is the ratio between the intercept and slope of the regression line between IL and ρ_T in band k: $\rho_T = m_k IL + b_k$; such that, $c_k = b_k / m_k$.

6.3.2 C-correction of ASTER VNIR-SWIR surface reflectance image data

The 9-band VNIR-SWIR surface reflectance dataset was corrected for the influences of topographic heterogeneities by applying C-correction to them. The c-factor values were obtained through the following procedure. ASTER stereo DEM (AST14DEM; fig. 6.7a) was used for the computation of DEM derivatives, such as slope and aspect (fig. 6.7b-c). These were combined using equation 7 to compute a local illumination angle image ($\cos IL$; fig. 6.7d) of the study area. The cosine of the local illumination angle image data was regressed against the input surface reflectance data and a simple linear fit was calculated for the plot, for every band. The slope (m) and intercept (b) of the linear fit were used to determine the c-factor (defined as b/m ; Table-6.8). The topographically normalized surface reflectance image was then calculated using equation 9. Figure-6.8 shows the results of hierarchical processing for atmospheric and topographic correction of the ASTER VNIR-SWIR image data.

Table-6.8 C-correction parameters for the solar reflective ASTER VNIR-SWIR bands

ASTER Band	b	m	$c = b/m$
AST_1	0.098371	0.050668	1.941494147
AST_2	0.100966	0.075211	1.342440391
AST_3	0.151379	0.107363	1.409963808
AST_4	0.199021	0.138965	1.432168109
AST_5	0.179831	0.113777	1.58056143
AST_6	0.174731	0.124506	1.403401316
AST_7	0.175251	0.114804	1.52652626
AST_8	0.134875	0.100594	1.340786612
AST_9	0.108046	0.065128	1.658995101

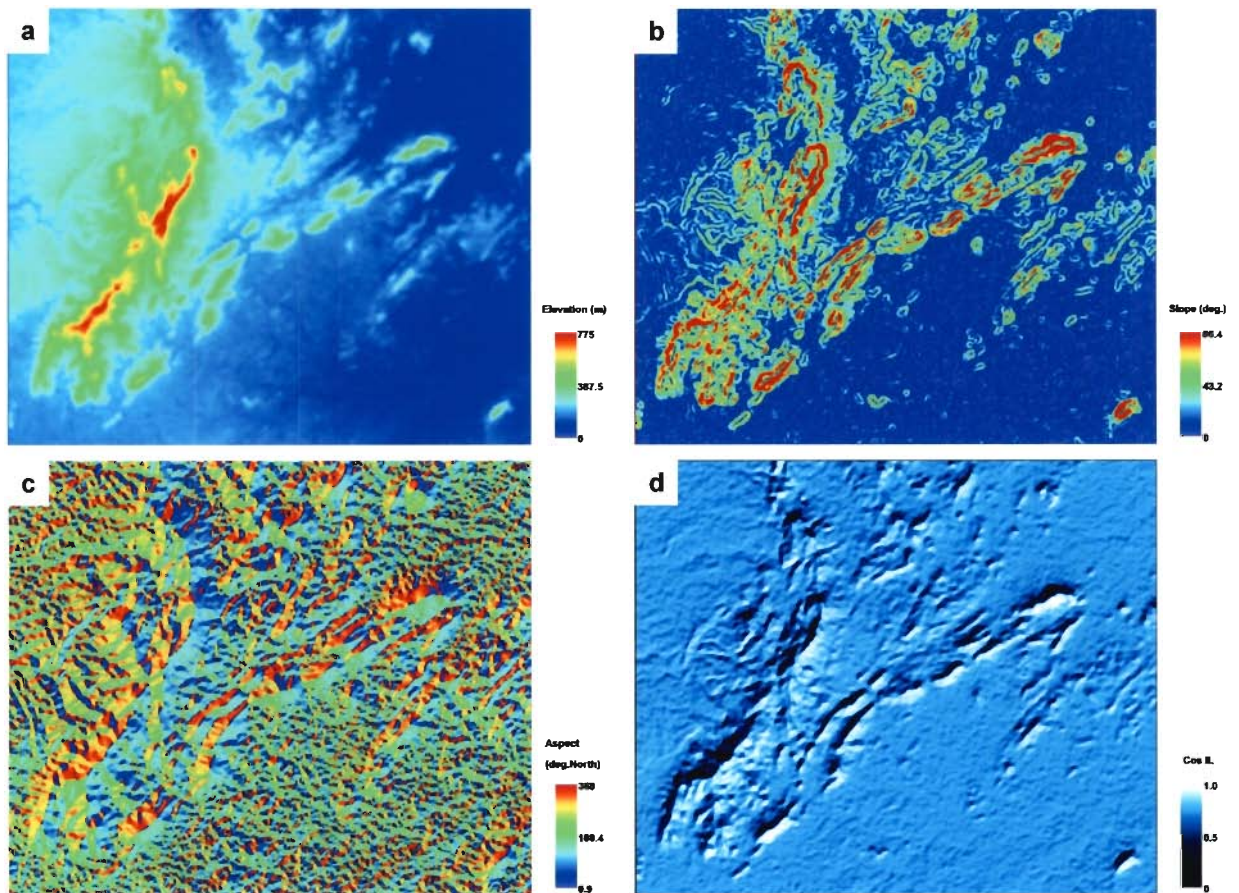


Figure-6.7 Derivation of input parameters for the C-correction of the ASTER hybrid FLAASH+MFF-corrected reflectance data of the study area: a. ASTER stereo-DEM (AST14DEM); b. Slope image derived from the DEM; c. Aspect image derived from the DEM; and d. Cosine of the Local Illumination Image (IL) computed through slope, aspect images and solar zenith and azimuth data input in eq. 7.

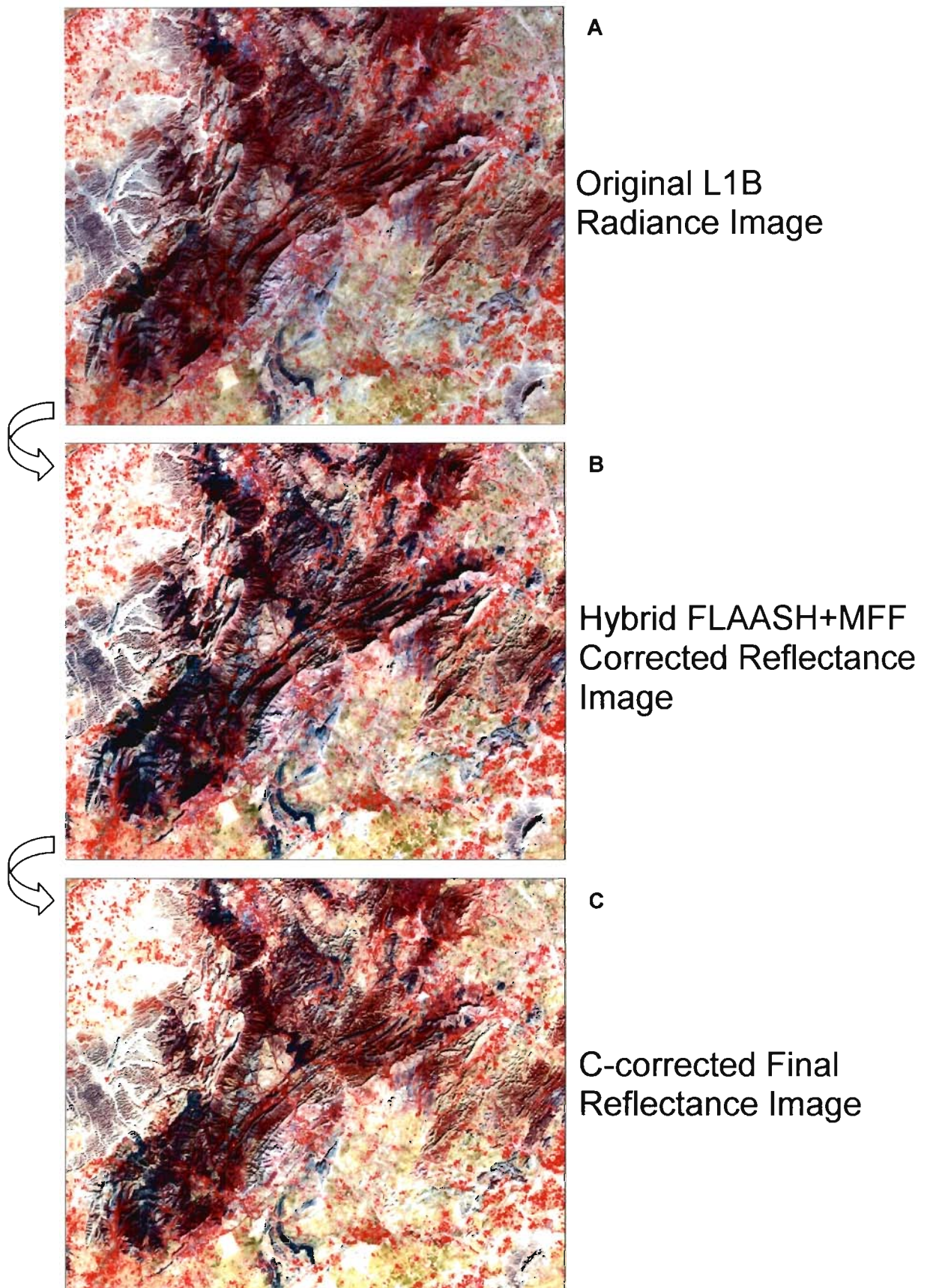


Figure-6.8 Hierarchical preprocessing of the ASTER VNIR-SWIR data used in the present study (bands 3-2-1 in R-G-B): A. Original L1B radiance-at-sensor data; B. Image after hybrid atmospheric correction; C. topographically normalized final reflectance image.

6.4 ASTER TIR surface emissivity retrieval

6.4.1 Theoretical Background

ASTER's five TIR channels permit the separation of measured radiances into a single surface kinetic temperature and an emissivity pseudo-spectrum, without having to make such broad assumptions about the surface emissivity as required when using one- or two-channel broad-band thermal scanners, such as Landsat TM/ETM+ and Advanced Very High Resolution Radiometer (AVHRR). Broad-band scanners are of greatest use over oceans, for which emissivities are well known. ASTER's capability is of greatest use over the land surface, for which emissivities are not known in advance.

TIR radiation (8-14 μm) is emitted from a surface in proportion to its kinetic temperature (T) and emissivity (ϵ). Emissivity is an intrinsic property of the surface and is independent of irradiance. Temperature is not an intrinsic property of the surface; it varies with the irradiance history and meteorological conditions. The radiance from a perfect emitter (*i.e.*, a blackbody for which $\epsilon = 1.00$) is exponentially related to temperature, as described by Planck's Law:

$$B_{\lambda} = \frac{c_1}{\pi\lambda^5} \left(\frac{1}{e^{\frac{c_2}{\lambda T}} - 1} \right) \quad (10)$$

Where:

B = blackbody radiance ($\text{Wm}^{-2}\text{sr}^{-1}\mu\text{m}^{-1}$); λ = wavelength (μm); $c_1 = 2\pi hc_2$ ($3.74 \times 10^{-16} \text{ Wm}^2$; 1st radiation constant); T = temperature (K); $h = 6.63 \times 10^{-34} \text{ Js}^2$ (Planck's constant) $c = 2.99 \times 10^8 \text{ ms}^{-1}$ (speed of light); $c_2 = hc/k$ ($1.44 \times 10^4 \mu\text{mK}$; 2nd radiation constant); $k = 1.38 \times 10^{-23} \text{ Wsk}^{-1}$ (Boltzmann's constant).

The radiance R from a real surface, however, is less by the factor ϵ : $R_{\lambda} = \epsilon_{\lambda} B_{\lambda}$. ASTER integrates radiance emitted from a number of surface elements. This radiance is attenuated during passage through the atmosphere, which also emits TIR radiation. Some of this radiance

is emitted directly into the scanner (path radiance); some strikes the ground and is then reflected into the scanner. For most terrestrial surfaces the reflectivity ρ and ε are complements: $\rho_\lambda = 1 - \varepsilon_\lambda$ (Kirchhoff's Law). For most terrestrial surfaces, the value of emissivity is in the range $\sim 0.7 < \varepsilon < 1.0$ (Prabhakara and Dalu, 1976), although surfaces with $\varepsilon < 0.85$ are restricted to deserts.

It is necessary to compensate for atmospheric effects, including E_\downarrow (eq. 2), if T and ε_λ are to be recovered accurately. Incident radiance from adjacent scene elements (pixels) varies with terrain roughness (Li et al., 1998) but is typically less than E_\downarrow and is usually ignored. The basic problem in estimating T and ε from remotely sensed data is that the data are under-deterministic: there are more unknowns than measurements (because there is an emissivity value for each image band, plus the kinetic temperature and atmospheric parameters). Historically, the chief reason for TIR measurements has been to estimate surface kinetic temperatures. This task is made easier if the emissivities are known *a priori* because the remote-sensing problem can then be made deterministic. Suitable targets thus include the oceans, for which emissivities have been measured independently and are essentially the same everywhere (e.g., Masuda et al., 1988).

6.4.2 Review of the existing techniques for separation of T and ε

Historically the main reason for TIR measurements has been to estimate temperatures. This task is deterministic for important scenes for which emissivity is not in question. Inversion of the TIR equations for T and ε has been attempted using various deterministic and non-deterministic approaches. The former are restricted to areas for which one or more of the unknowns are known, such as for the oceans, snowfields and glaciers, and closed-canopy forests and include the 'split-window' techniques. Most ocean-temperature studies have utilized data from AVHRR, which has two channels, at 10.3-11.3 μm and 11.5-12.5 μm , thereby 'splitting' the TIR spectral window. Joint analysis of the two 'split-window' channels

can compensate for atmospheric effects while solving for T (e.g., Barton, 1985; McMillan and Crosby, 1984; Prabhakara et al., 1974). Split-window algorithms rely on empirical regression relating surface radiance measurements to water temperatures.

Several authors have examined extending the split-window technique to land surfaces (e.g., Price, 1984; Becker, 1987; Vidal, 1991). They all conclude, however, that large errors arise there due to unknown emissivity differences. Over land, the unknown emissivities are a greater source of inaccuracy than atmospheric effects. Inaccuracy of only 0.01 in ϵ causes errors in T sometimes exceeding those due to atmospheric correction (Wan and Dozier, 1989). In general, land emissivities cannot be estimated this closely, and must be measured if accurate kinetic temperatures are to be recovered. As a result, the usefulness of split-window methods for land is limited and the non-deterministic nature of TIR remote sensing needs be addressed head-on. Many geologic studies, however, have utilized enhancements such as decorrelation stretching that do not recover T and ϵ (Kahle et al., 1980; Abrams et al., 1991). A spectral-unmixing approach has been used to separate a non-linear measure of T from ϵ (Gillespie, 1992), but the separation is imperfect. Kealy and Hook (1993) have reviewed some of the techniques of temperature-emissivity separation. The inversion techniques for the problem of land-surfaces are grouped under those, which (Gillespie et al., 1999; ASTER TES ATBD) –

- a) Determine spectral shape but not T
- b) Require multiple observations under different conditions
- c) Assume a value for one of the unknowns
- d) Assume a spectral shape
- e) Assume a relationship between spectral contrast and ϵ

All of the above approaches require independent atmospheric correction. The temperature-independent spectral indices (TISI) of Becker and Li (1990), thermal log residuals and alpha residuals (Hook et al., 1992); and spectral emissivity ratios (Watson, 1992a; Watson et al., 1990) recover spectral shape. The day-night two-channel method (Watson, 1992b) solves

the problem of indeterminacy in principle. In practice, however, this approach magnifies measurement 'noise' greatly and requires 'pixel-perfect' registration between the two images. Other techniques have been based on an assumed value for a 'model' emissivity at one wavelength (Reference Channel method; Lyon, 1965), or an assumed maximum emissivity (ϵ_{\max}) value at an unspecified wavelength (Normalized Emissivity Method, or NEM) (Gillespie, 1985; Realmuto, 1990). One of the methods required only that the emissivity be the same at two wavelengths (Barducci and Pippi, 1996). However, this assumption is commonly violated for ASTER, with only five channels. The 'alpha-derived emissivity' (ADE) method utilizes an empirical relationship between the standard deviation and mean emissivity to restore amplitude to the alpha-residual spectrum, thereby recovering T also (Hook et al., 1992; Kealy and Gabell, 1990; Kealy and Hook, 1993). As the ADE method relies on Wien's approximation for inversion, slope errors are introduced into the ϵ spectrum. The Mean-MMD method (Matsunaga, 1994) avoids Wien's approximation and uses a modified ADE empirical relationship based on the minimum-maximum emissivity difference (MMD).

6.4.3 Computation of the surface emissivity image of the study area

Attempts have been made to estimate surface emissivities using the atmospherically corrected ASTER LIB radiance data for the study area. Three of the techniques described in the previous section – the Reference Channel (Kahle, et al., 1980), the Normalized Emissivity Method (Realmuto, 1990) and the Alpha Residuals (Kealy and Gabell, 1990; Kealy and Hook, 1993) – are available in ENVI, and have been tested on the ASTER TIR radiance image data. The input requirements and resulting surface emissivities for individual methods have been discussed briefly as follows.

The Reference Channel emissivity technique assumes that all the pixels in one channel (band) of the thermal infrared data have a constant emissivity. Using this constant emissivity, a temperature image is calculated and these temperatures are used to calculate the emissivity

values in all the other bands using the Planck function. In the present study, a constant emissivity value of 0.96 has been used for band 1.

The Emissivity Normalization (NEM) technique calculates the temperature for every pixel and band in the data using a fixed emissivity value. The highest temperature for each pixel is used to calculate the emissivity values using the Planck function. For the ASTER data of the study area, NEM-derived emissivities have been computed using a fixed emissivity value of 0.96.

Alpha Residuals technique produces alpha residual spectra that approximate the shape of emissivity spectra. Wien's approximation of the Planck's Function is used so the equation can be linearized with logarithms. The temperature and emissivity terms are separated and means are used to subtract the temperature term out (ENVI User's Guide, 2005). The alpha residual spectra are a function of emissivity only and have a similar shape as emissivity spectra but have a zero mean. Therefore emissivity spectra have to be scaled for direct comparison with alpha residual spectra. Emissivity spectra can be calculated from alpha residual spectra using empirical data as described in the Kealy and Hook (1993).

6.4.4 ASTER Level 2 standard surface emissivity product (AST_05): TES algorithm

A standard L2 surface emissivity dataset (AST_05) of the study area generated using the Temperature and Emissivity Separation (TES) algorithm (Gillespie et al., 1998, 1999; ASTER TES ATBD) with the 5-band L1B TIR radiance data have been acquired from the EOS Data Gateway (EDG), and evaluated in this study. A brief description of the TES algorithm has been given below.

The TES algorithm hybridizes two established algorithms by first estimating the temperature and band emissivities using the Normalized Emissivity Method, and then

normalizing the emissivities by their average value. Next, an empirical relationship adapted from the Alpha Residual method is used to predict the minimum emissivity from the spectral contrast (min-max difference or MMD) of the normalized values, permitting recovery of the emissivity spectrum with improved accuracy. TES uses an iterative approach to remove reflected sky irradiance. Input to TES consists of land-leaving radiances (compensated for atmospheric absorption and path radiance) and downwelling sky irradiance. Based on numerical simulation, TES can recover temperatures within about ± 1.5 K, and emissivities within about ± 0.015 (Gillespie et al., 1999). Limitations arise from the empirical relationship between emissivity values and spectral contrast, compensation for reflected sky irradiance, and ASTER's precision, calibration, and atmospheric correction (Gillespie et al., 1998).

6.4.5 Selection of the final surface emissivity data

The Reference Channel method-, the Emissivity Normalization method-, the Alpha Residuals method-derived surface emissivity images and the standard L2 AST_05 surface emissivity image procured from EDG have been compared with each other and with a reference library spectrum. JHU spectral library spectrum of a peak quartzite has been used to check the quality and accuracy of each result. Figure-6.9a-d shows the emissivity spectra of a common quartzite pixel in all different image datasets, and the corresponding JHU library spectrum for pink quartzite has been shown in Figure-6.10e. From the figure it is evident that while all methods preserve the spectral shape, and are similar, the differences exist in terms of spectral slope, and the depth of the main Si-O absorption feature centered near band 12. Alpha Residuals-derived data was rejected since the absolute emissivity values had no direct physical use in quantitative terms. The AST_05 standard surface emissivity product exhibits closest match in terms of shape and absolute values to the library spectrum, and hence it has been used for further processing as described in detail in Chapter 7.

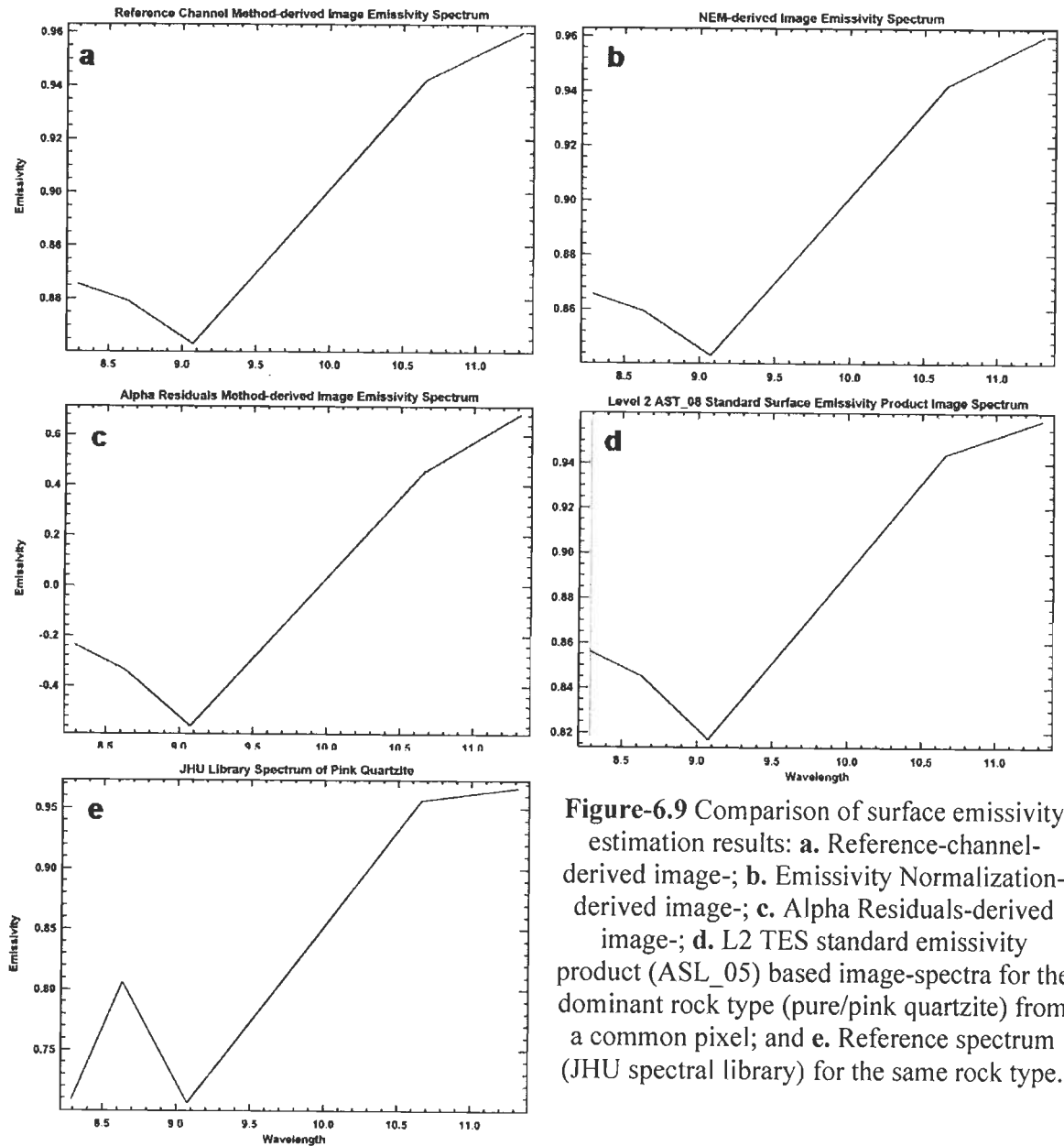


Figure-6.9 Comparison of surface emissivity estimation results: **a.** Reference-channel-derived image-; **b.** Emissivity Normalization-derived image-; **c.** Alpha Residuals-derived image-; **d.** L2 TES standard emissivity product (ASL_05) based image-spectra for the dominant rock type (pure/pink quartzite) from a common pixel; and **e.** Reference spectrum (JHU spectral library) for the same rock type.

ASTER TIR Data Processing for Lithologic Mapping

7.1 Statement of purpose and introduction

In this chapter the potential of ASTER TIR data in qualitative and quantitative lithologic mapping has been explored. The presence of diagnostic spectral features (reststrahlen band or minima in emissivity curves) of rock forming silicates, sulfates and carbonates in the thermal infrared range (7-15 μm) allows their detection, identification and mapping using remote sensing techniques. Also, the property of a systematic shift in the spectral signatures of silicate minerals, based on their crystal structure has been used to estimate their absolute quantitative distribution using thermal infrared remote sensing. As mineralization in the area is closely associated with major structures as well as host lithology (Chapter 2), the success of lithologic mapping has an important bearing on its utility in identification of favorable sites for mineral exploration activity in the area.

7.2 Lithologic mapping using ASTER TIR data

Most of the important rock-forming silicate minerals have their diagnostic spectral features in the TIR region (7.0-14.0 μm) (Lyon, 1965; Hunt and Salisbury, 1974, 1975, 1976; Salisbury and D'Aria, 1992). The variation in silicate mineralogy from felsic to mafic is represented as a shift of the main spectral feature (Si-O stretching region or reststrahlen band, Hook et al., 1999) towards longer wavelengths (see fig. 7.1). This characteristic has been utilized in mapping silicate mineralogy using multi/hyperspectral TIR data. Another spectral feature in silicate mineral spectra between 8.5 and 12.0 μm occurs due to the H-O-Al bond at 11.0 μm , and is characteristic of clay minerals.

The test area represents metamorphosed rocks with almost pure silicates (quartzites) on one end, and impure carbonates (actinolite-diopside marbles and other calc-silicates) and mafic rocks (amphibolites) on the other. The intrusives in the area range from leuco- to mesocratic granites and granodiorites, to melanocratic amphibolites. The rocks are variously weathered. Scanty to nil vegetation cover for most rocky surfaces and a semi-arid climate and makes the study area favorable for remote lithologic mapping. ASTER TIR L1B radiance-at-sensor and L2 processed surface radiance/emissivity data of the study area have been variously digitally processed to generate lithologic maps, as discussed in the following sections. The scheme of processing has been designed to hierarchically grow from simple to advanced methods of data processing, to exhaustively evaluate their relative merits with the ASTER data.

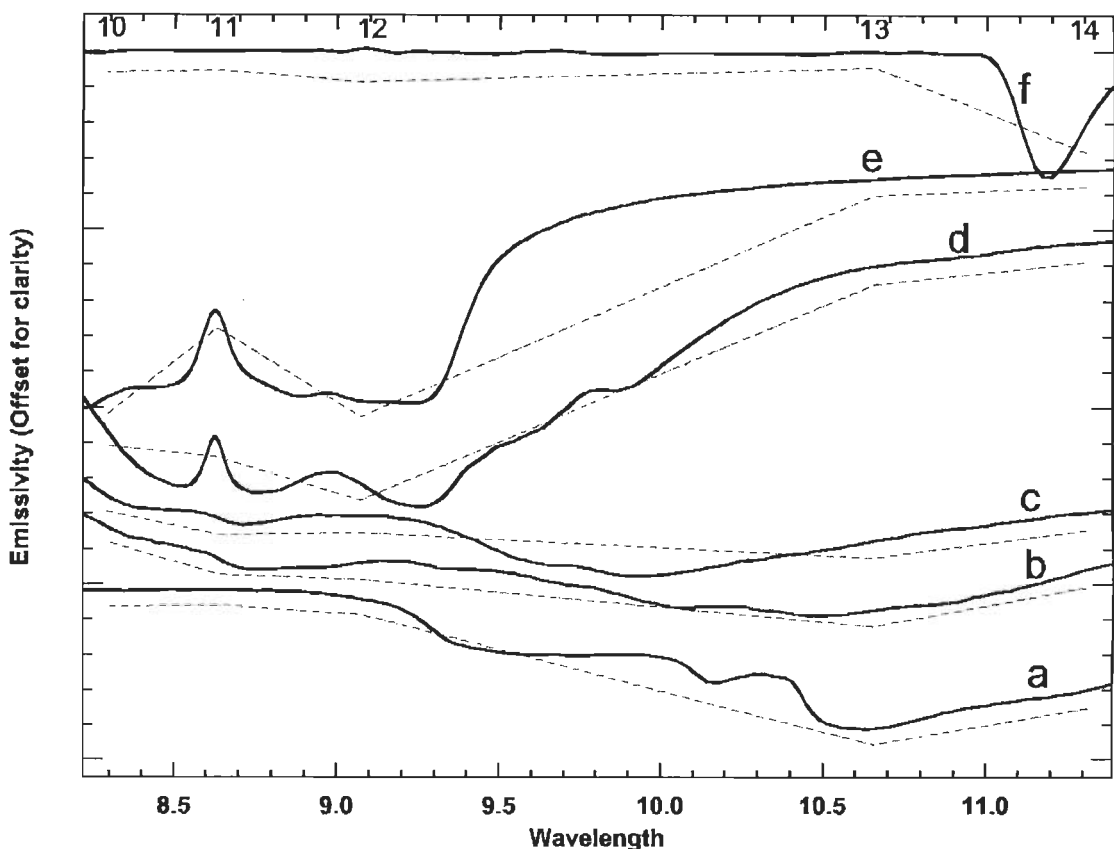


Figure-7.1 Emissivity spectra of (a) dunite, (b) gabbro, (c) diorite, (d) granite, (e) pink quartzite, (f) dolomitic marble. Biconical reflectance spectra from JHU spectral library have been converted to emissivity using Kirchhoff's law. The corresponding spectra resampled to ASTER TIR bandpasses have been shown in dashed lines, and the positions of the bands have been marked on the top. Wavelength is in μm .

7.2.1 ASTER TIR Decorrelation Stretch

Unlike image data in the VNIR range, the bands in multi-channel thermal images are, in general, highly correlated. The thermal infrared surface radiance is a function of both the surface temperature and surface emissivity. In general, surface temperature variations across the scene are limited to < 30% (Gillespie et al., 1986) and emissivity variations among geologic materials are minimal (ranging from 0.7 to 0.9). This means that the variation in the radiance values for the same pixel in different bands is relatively small, which results in low contrast and hue-saturation differences. To overcome this, a process called Decorrelation Stretch (DCS) is usually applied (Gillespie et al., 1986; Gillespie, 1992). DCS suppresses surface temperature effects which dominate the radiant spectral flux measured in all bands, and at the same time enhances the subtle spectral features arising from emissivity variations. In DCS, data from three or more bands are transformed to principal components and then stretched to equalize the variance along three statistically independent axes. The stretched data are then transformed back into the approximate original RGB coordinate system for display as a color composite image. Resulting images represent variations in spectral reflectance (for VNIR-SWIR data), or emissivity (for TIR data), by hue and overall albedo, or surface temperature, by intensity (Sabine, 1999). DCS has been widely used with data from TIR instruments, especially Thermal Infrared Multispectral Scanner (TIMS) (*e.g.*, Kahle, 1987; Kahle et al., 1988; Sabine et al., 1994; Hook et al., 1998; Ramsey et al., 1999; Vaughan et al., 2005). The ‘standard’ DCS channels are selected such that wavelength channels centered about 10.5 μm (TIMS band 5), 9.2 μm (TIMS band 3), and 8.3 μm (TIMS band 1) are assigned to red, green and blue colors, respectively.

DCS has been applied to the five recalibrated radiance-at-sensor TIR channels of the ASTER L1B data of the study area, using three at a time and assigning them to the RGB color scheme. As with the TIMS data reported in literature, the best results of DCS have been obtained for RGB composites 13-12-11 (band centered about 10.657 μm in red, 9.075 μm in

green, and 8.634 μm in blue) and 14-12-10 (band centered about 11.318 μm in red, 9.075 μm in green, and 8.291 μm in blue). An RGB composite of TIR bands 14-12-10 has been shown in Figure-7.2a, whereas Figure-7.2b shows the DCS equivalent of the same.

On the DCS image, the more siliceous surfaces appear in reds and pinks, such as the peak quartzites and the alluvium. This is due to the fact that band 12 lies close to the main Reststrahlen feature (emissivity minimum) for silica (centered about 9.0 μm ; fig. 7.1), while bands 14 and 10 form the edges. For example, the orthoquartzite (peak/pure quartzite) ridges of the Alwar Group occurring dominantly along the western limb of the Babai anticline, and the aolian sands of the Thar Desert lying towards the west of the study area, are all shown in prominent red/pink hues. Mafic rocks and clay-rich surfaces appear in blue-violet and magenta-purple hues, respectively. This is because clay has a low emissivity for band 14 (11.32 μm), and relatively high emissivity values in bands 12 (9.08 μm) and 10 (8.29 μm). Areas in shades of green are most likely to be mixtures of arable soil/regolith rich in iron, and vegetation (mostly cropland). Mineralogically, the green+red areas on the DCS 14-12-10 image are most likely to represent the mineral albite, which has an emissivity minimum around 8.43 μm , shoulder of the minimum at about 9.0 μm , and general emissivity high beyond 10.0 μm . The intermediate hues represent mixtures of these surfaces. The inherent horizontal banding in the TIR data can be seen more pronouncedly in the DCS images. The spatial resolution (90 m) of ASTER TIR poses a great limitation in absolute interpretation of the lithology, as discussed in detail later. Nevertheless good qualitative lithological discrimination has been achieved through DCS processing.

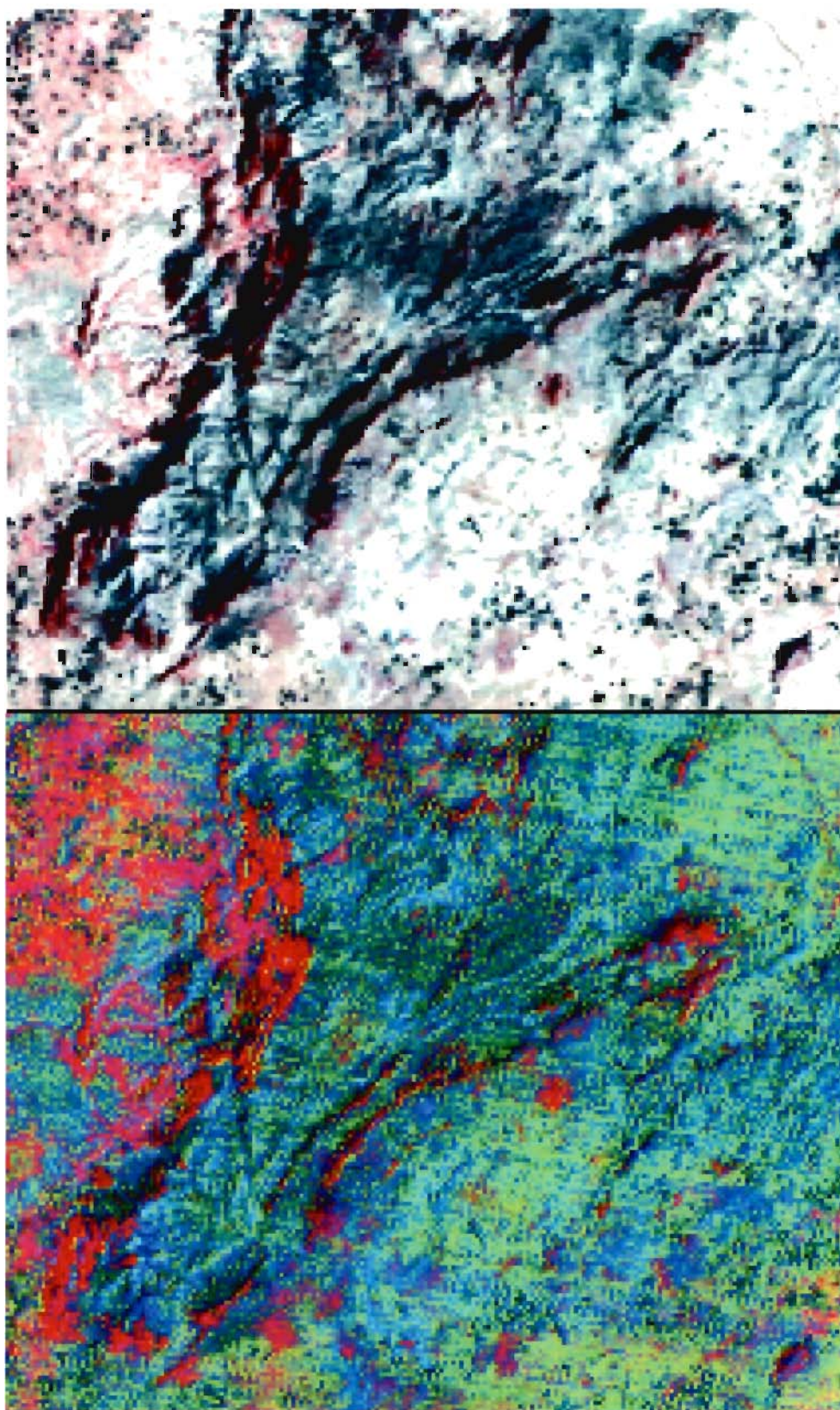


Figure-7.2 ASTER L1B TIR recalibrated radiance-at-sensor image: **a)** 14-12-10 in RGB, and **b)** DCS of the same. Notice the dramatic improvement in hue and contrast differences after DCS processing, allowing better visual discrimination of the surfaces.

7.2.2 Quartz, carbonate and mafic indices

Ninomiya et al. (2005) proposed three lithologic indices for ASTER TIR raw radiance-at-sensor data – quartz index, carbonate index, and mafic index – and advocated that even atmospherically uncorrected radiance data can yield valuable information about these lithologic groups. In this study, the L1B atmospherically uncorrected recalibrated radiance-at-sensor, ISAC-corrected surface radiance, and L2 surface radiance data over the study area have been used in calculation of the three indices, as reproduced below (Ninomiya et al., 2005):-

1. Quartz index: $QI = \frac{(AST_B11)^2}{AST_B10 \times AST_B12}$
2. Carbonate index: $CI = \frac{AST_B13}{AST_B14}$
3. Mafic index: $MI = \frac{AST_B12 \times (AST_B14)^3}{(AST_B13)^4}$

In above equations, AST_Bn (where, $10 \leq n \leq 14$) stands for the ASTER band n . The results of the computation of these indices have been shown in Figure-7.3. It can be readily observed that while there is a general correspondence between the quartz and mafic indices for the three datasets, there are considerable discrepancies in the index for carbonate rich rocks, which appears to over-map such areas. This can be explained if we look at the emissivity spectrum of mafic carbonate rocks (dolomitic marble; fig. 7.1f). The spectrum is representative of calcite and dolomite, the two principal carbonate minerals. The emissivity low for carbonates lies close to the emissivity low for the ultramafic rocks (e.g., dunite). For coarse spectral resolution data as in ASTER TIR, the emissivity minima for carbonates and mafic/ultramafic rocks almost coincide. In addition to this, in the study area, the carbonate rocks are rarely pure; they are mafic-rich and are interbedded with para-amphibolites. In general, the mafic index has been found to work consistently well for all the three datasets. However, the atmospherically corrected L1B radiance data have yielded unusually low quartz distribution relative to that obtained using radiance-at-sensor and surface radiance data, which could be due to inaccurate atmospheric correction for band 11.

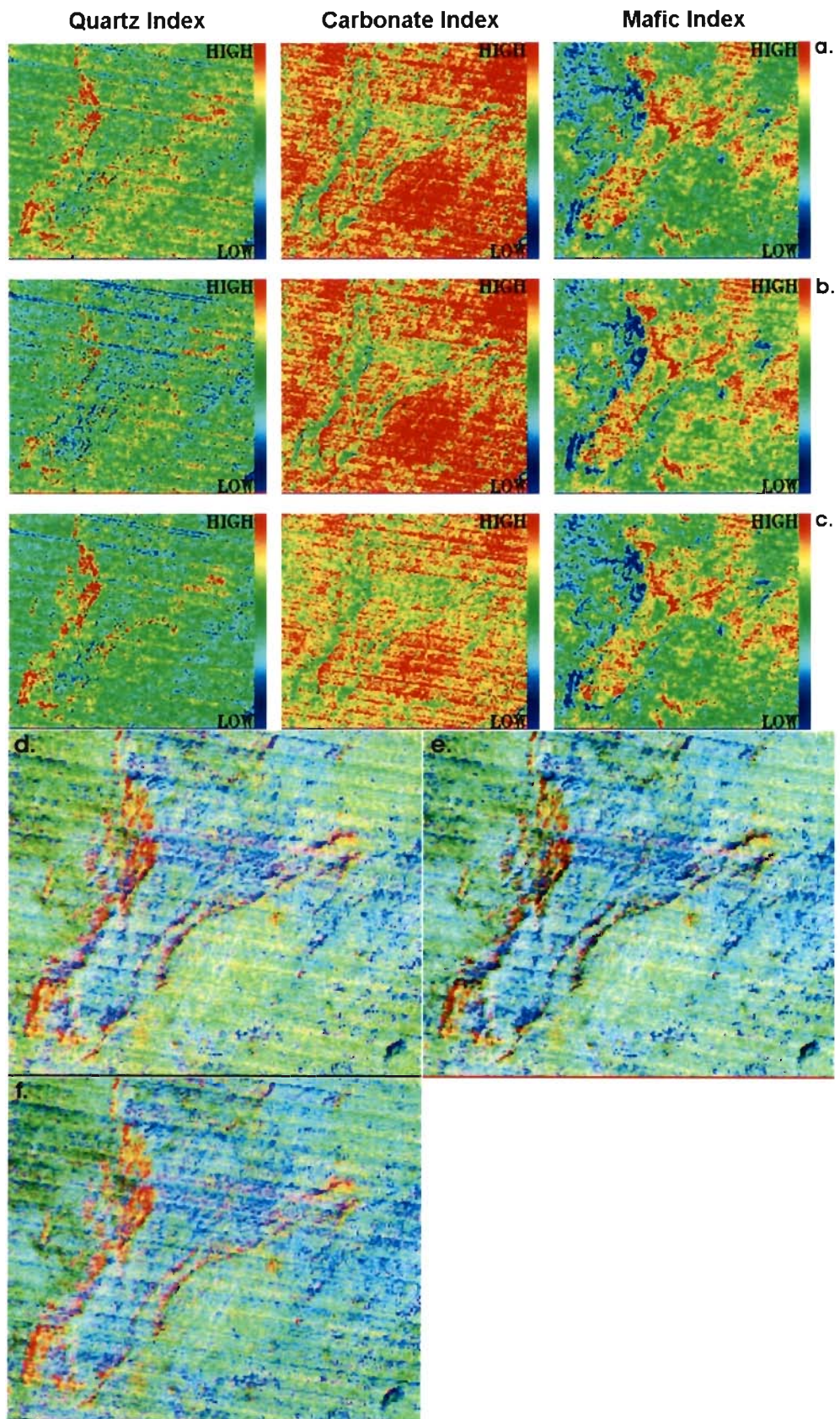


Figure-7.3 Quartz, carbonate and mafic indices have been shown as a-c as single indices; and as R-G-B composites as d-f, for recalibrated radiance-at-sensor data, ISAC-corrected surface radiance data, and L2 surface radiance data, respectively. Note the differences in distribution of greens, and topographic effects on the three RGB composites.

7.2.3 Spectral processing of ASTER TIR surface emissivity data

The 5-band standard ASTER L2 surface emissivity data (AST_05) obtained from LP-DAAC's EOS Data Gateway (EDG) produced after applying the Temperature and Emissivity (ϵ) Separation (TES) algorithm (Gillespie et al., 1998) to the L1B radiance-at-sensor data, has been spectrally processed using a hierarchical method proposed by Kruse and Boardman (2000) and Kruse et al. (2003) as integrated within the ENVI software (ENVI User's Guide, 2005). The sequential steps involved in the spectral processing have been shown in Figure-7.4. There are primarily two major steps involved in the spectral processing – selection of the spectral end-members (minerals/rocks), and the suitable classification algorithm for spectral mapping.

In view of the absence of any field spectral data, the mineral/rock end-members have been derived from the image itself, using an automated technique called Pixel Purity Index (PPI™), described in later section. While the technique is useful in the absence of any field spectral data, it also minimizes the differences that might exist in a controlled laboratory spectral measurement; and the pixel averaged field spectrum of the same material, and the results are, in general, more representative of the variability inherent within the remotely observed scene.

Two classification algorithms have been used for spectral classification of the end-members: 1) the Spectral Angle Mapper (SAM), and 2) the Mixture Tuned Matched Filtering (MTMF™). The salient features of these algorithms have been provided in relevant sections in the following paragraphs. The results of the classification have been discussed (partly in this chapter, and in greater details in Chapter 9) by comparing them with the geological map of the area, and the ground-truth (Chapter 4).

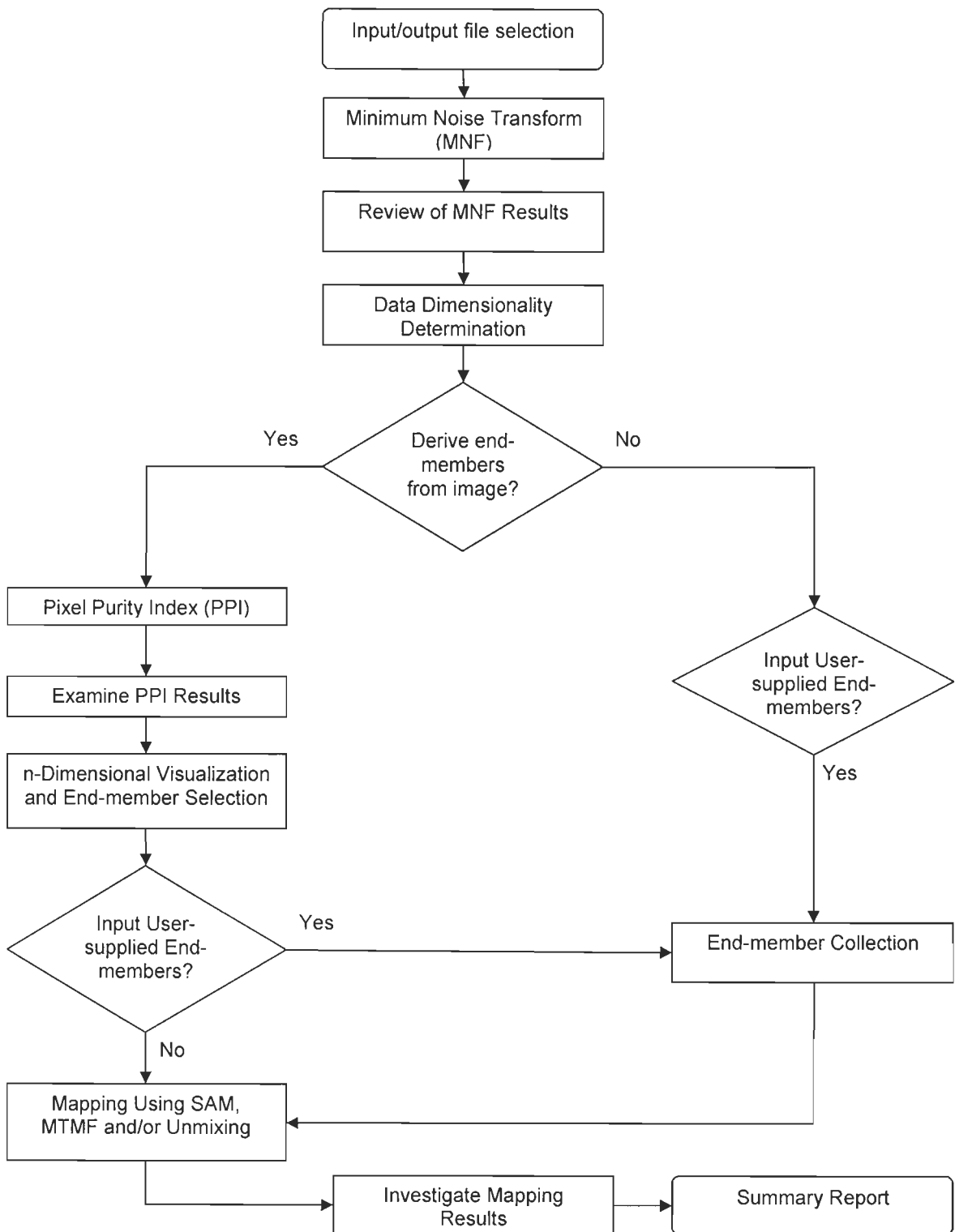


Figure-7.4 Spectral processing workflow.

7.2.3.1 MNF transformation

The Minimum Noise Fraction (MNF) transform is commonly used with hyperspectral or imaging spectrometer data to determine the inherent dimensionality of image data, to segregate noise in the data, and to reduce the computational requirements for subsequent processing (Boardman and Kruse, 1994). The MNF transformation algorithm implemented in ENVI has modified from Green et al. (1988) and comprises of two cascaded Principal Components Transformations (PCTs). The first PCT, based on an estimated noise covariance matrix, decorrelates and rescales the noise in the data. This step results in transformed data in which the noise has unit variance and no band-to-band correlations. The second step is a standard PCT of the noise-whitened data. For the purposes of further spectral processing, the inherent dimensionality of the data is determined by examination of the final eigenvalues and the associated images. The data space can be divided into two parts: one part associated with large eigenvalues and coherent eigenimages, and a complementary part with near-unity eigenvalues and noise-dominated images. By using only the coherent portions, the noise is separated from the data, thus improving spectral processing results (ENVI User's Guide, 2005).

The five MNF bands obtained after application of the MNF transformation to the five-band surface emissivity dataset have been shown in Figure-7.5a-e, and the eigenvalues plot of these bands has been shown in Figure-7.5f. It can be seen from the figure that mutually exclusive lithologic information is contained in MNF bands 1, 4 and 5, whereas MNF bands 2 and 3 suffer from the effects of scan-banding. Figure-7.6a and b show MNF bands 1-2-5 and 1-4-5 as RGB composites. It can be seen that there is an interesting correspondence between the MNF band composite 1-2-5 and the DCS images shown in Figure-7.2. Mafic rocks have been distinctly mapped in MNF band 5 (blue hues), whereas MNF band 1 generally maps the siliceous rocks (orange and red hues, quartzites and aolian sands).

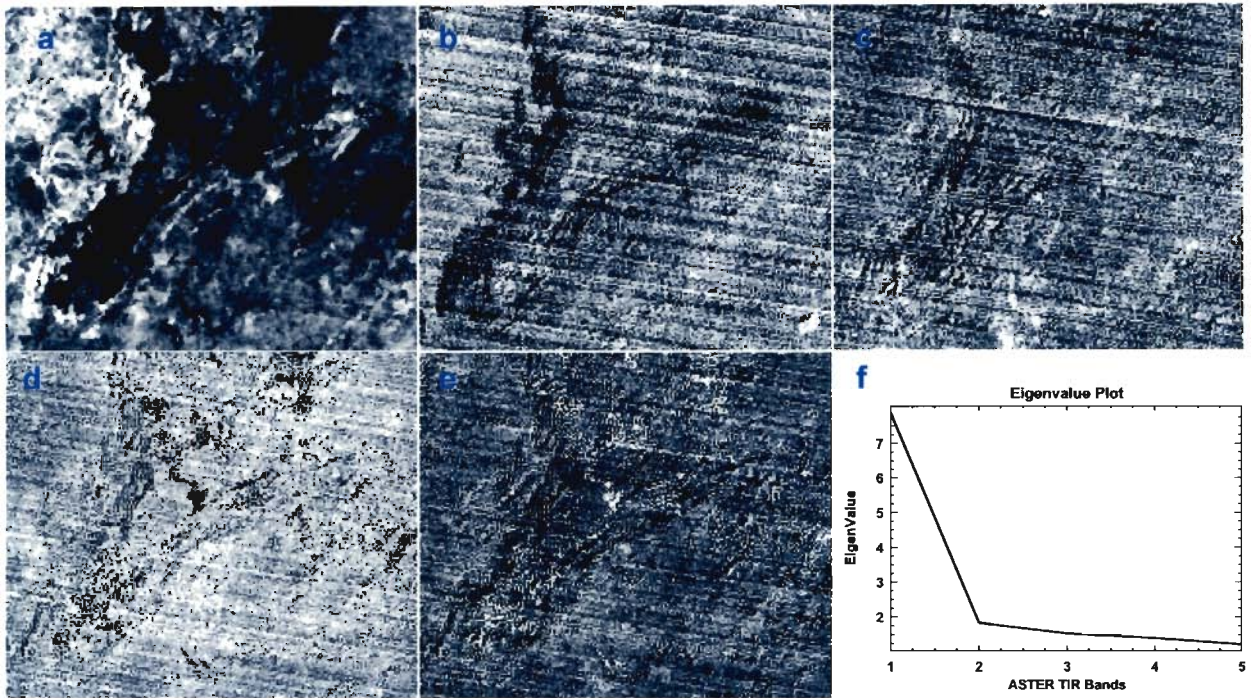


Figure-7.5 a-e) MNF bands 1-5, and f) the eigenvalues plot.

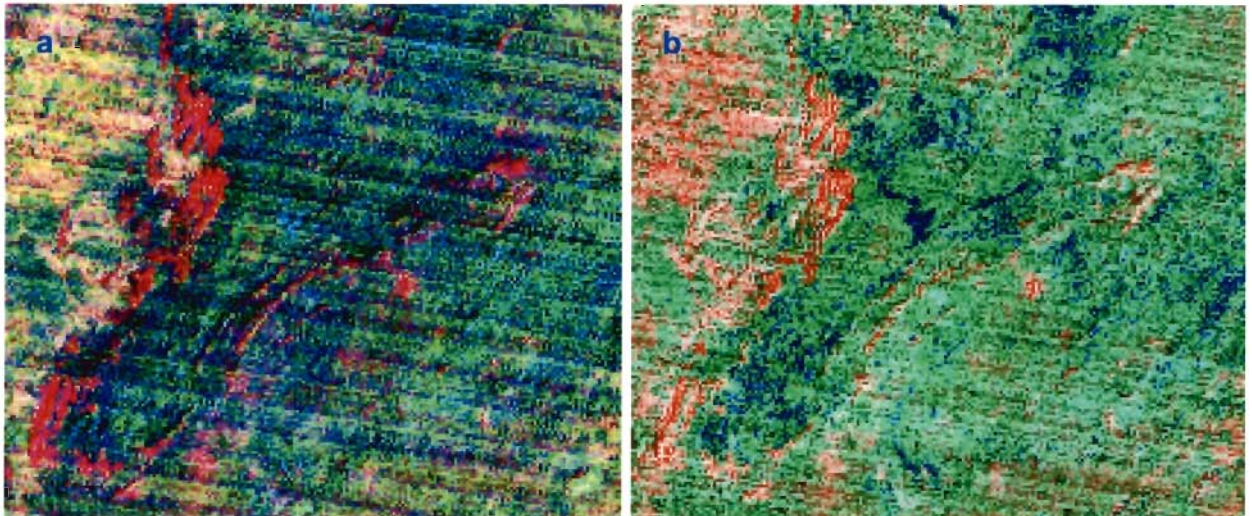


Figure-7.6 MNF bands composites: a) 1-2-5 in RGB, and b) 1-4-5 in RGB. Notice the unique distribution of the blue pixels corresponding to the amphibole-bearing rocks, and the reds, pinks and oranges pertaining to the siliceous rocks as marked on the reference geologic map (Figure-2.3, Chapter 2)

7.2.3.2 PPI and end-member selection

Pixel Purity Index (PPI™) is a commonly used technique to find the most spectrally pure (extreme) pixels in multispectral and hyperspectral images (ENVI User's Guide, 2005). The spectrally purest pixels typically correspond to mixing end-members. The PPI™ is computed by repeatedly projecting n -dimensional scatter-plots onto a random unit vector. The extreme pixels in each projection, *i.e.* the pixels that fall onto the ends of the unit vector, are recorded and the total number of times each pixel is marked as extreme is noted. A PPI™ image is created in which the DN of each pixel corresponds to the number of times that pixel was recorded as extreme.

PPI™ has been calculated for the five MNF bands having dimensionality above a threshold of 0.15. Using a PPI™ threshold of 2.500, 5000 PPI iterations yielded 15,756 pure pixels. The plateau shape of the PPI™ curve indicates minimal variation in the number of extreme pixels determined with successive PPI™ iterations, and therefore the values can be safely regarded as representative of the end-member distribution in the image. The PPI™ plot and image have been shown in Figure-7.7a-b, respectively.

In ENVI, the end-member selection is usually done by examining the n -dimensional scatter-plot using the n -Dimensional Visualizer™ tool, which interactively displays the pure-pixel data cloud in n -dimensions with flexible user control, and allows selection of groups of data clusters which correspond to the potential end-members. Preliminary examination of the 10,000 pure pixels in the n -Dimensional Visualizer™ showed that the default end-members identified were sufficiently distinct (see fig. 7.8a) and could be used *per se*. In the present case, the number of possible image end-members is 6 (the number of image end-members is limited to $n+1$, where n is the number of bands used in the PPI™ iteration, for the present case n represents the 5 MNF bands). The spectra of the six image end-members have been shown in Figure-7.8b.

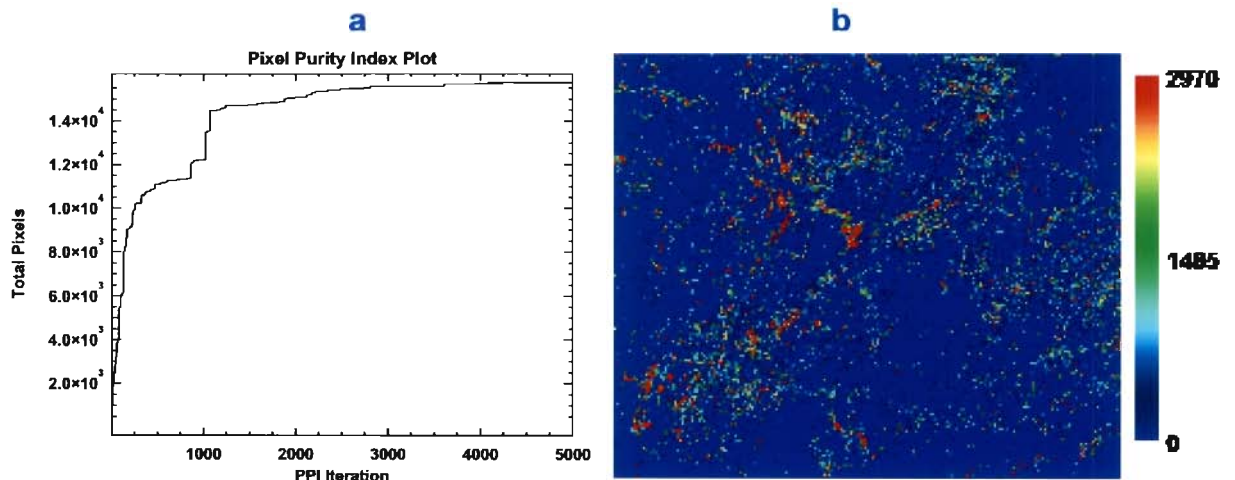


Figure-7.7 Results of the PPI™ calculated using the 5 MNF bands of the ASTER surface emissivity dataset: a) PPI™ plot, and b) color representation of the distribution of pure/extreme pixels in the image. Hotter colors represent higher DN values, or pixels which have been identified as extreme in greater number of PPI™ iterations, identified by the accompanying legend.

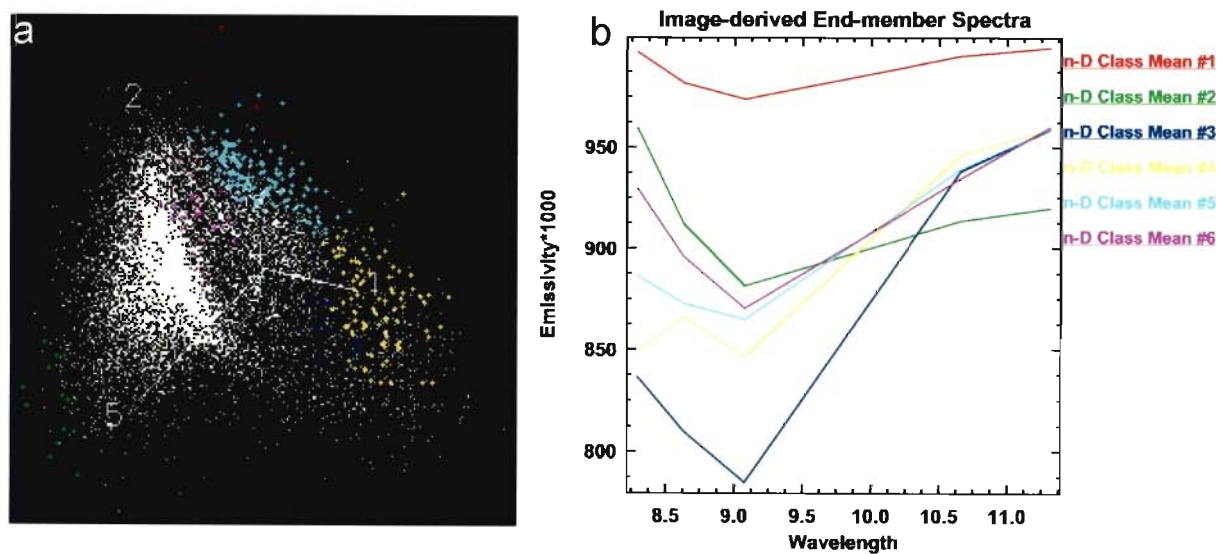


Figure 7.8 a) The PPI™-derived pure pixel n-dimensional scatter-plot seen using n-Dimensional Visualizer™, and b) the average spectra of clusters lying on the extreme ends of the axes, identified as the image end-members.

7.2.3.3 End-member identification using ENVI Spectral Analyst™

In order to identify the unique spectra of the image end-members representing specific rock types, ENVI's Spectral Analyst™ module along with a reference spectral library has been employed. The Spectral Analyst™ uses ENVI techniques, such as binary encoding (Mazer et al., 1988), Spectral Angle Mapper (SAM) (Kruse et al., 1993), and Spectral Feature Fitting (SFF™) (Clark et al., 1990b, 1992; Crowley and Clark, 1992) to rank the match of an unknown spectrum to the materials in a spectral library (ENVI User's Guide, 2005).

Two reference spectral libraries have been compiled after converting the hemispherical reflectance spectra from the JHU spectral library to emissivity spectra using the Kirchhoff's law (Nicodemus, 1965) and contain emissivity spectra of well characterized 324 minerals, 25 soil types, 34 coarse-grained igneous rocks and 25 coarse-grained metamorphic rocks. The JHU spectral library mineral spectra, however, are measured as bidirectional (biconical) reflectances, which cannot be used for quantitative estimation of emissivities through the application of Kirchhoff's Law, as only hemispherical reflectances can be used in this way. They can, nevertheless, be used with full confidence 'qualitatively' (*i.e.*, in terms of the curve-shape, and not the absolute values) for most remote sensing applications where spectral 'curves' are required to identify the unknown materials, as in the present case. Appendix B provides the details about the spectral measurement procedure and salient features of the individual categories of spectra contained in the JHU spectral library. The spectra have subsequently been resampled to the bandpasses of the ASTER TIR channels. SAM and SFF have been given equal weights (0.5 each) in determining the overall best fit score.

It has been observed, however, that this automated technique is only moderately successful due to the following reasons:

1. The materials (mineral/rock/soil) with best spectral match scores do not necessarily represent the actual surface materials, as their mapped abundances are significantly higher than what can be expected. This owes to the fact that the diversity of surface

materials is in reality wider than the number of end-members determinable (in this case, 6) through PPITM approach, which is restricted to $n+1$. This shortcoming can be overcome if the end-member spectra are supplied externally, such as through field measurements. Alternatively, by using smaller subsets of the image individually with PPITM, an end-member spectral library can be created with a greater diversity and range of end-member spectra. As for the former, no field spectra for the study area have been collected, and due to coarse spatial resolution and smaller size of the study area the latter method was not considered suitable for the ASTER emissivity dataset; although this technique has been used for the higher spatial resolution VNIR-SWIR data (discussed in detail in Chapter 8).

2. Owing to the differences in the individual match scores between the two matching techniques used (SAM and SFFTM), instead of a single best match a range of materials could be predicted with relatively equal or marginally different, overall scores. Similarly, by using different library spectra, different materials receive the top scores (see Tables 7.1 and 7.2 for a comparison among the top three best matches obtained using one of the two reference spectral libraries, and the inherent ambiguities). It has been found that more than one reference spectra representing mineralogically widely different rocks/soils receive the same overall score due to the unequal scores for the two individual techniques. It has been observed that where the unknown spectrum has well defined diagnostic 'absorption' features, SFFTM yields results with a better match, and for spectra without any diagnostic feature, SAM match results appear to be superior. As no single technique could be considered sufficiently accurate, it becomes necessary that the decision about the candidacy of a particular reference spectrum for its match to the unknown end-member spectrum be made with great caution. Therefore, the closest matches have been examined interactively individually with the unknown spectrum in both normal and continuum (Clark and Roush, 1984; Clark, 1999) removed mode, with

a background support of the field knowledge, to assign the reference material spectrum to the unknown spectrum.

Table-7.1 Top three Spectral Analyst™ matches to the six end-member spectra using reference spectral library containing JHU mineral, rock and soil spectra.

Serial number	Unknown image end-member spectrum ID	Top three reference spectral library materials with the best overall scores	Overall score	SAM score	SFF score
1	n-D class mean # 1	Alunite Nepheline Augite	0.995 0.994 0.993	0.992 0.993 0.992	0.998 0.994 0.994
2	n-D class mean # 2	Nepheline Saponite Augite	0.982 0.981 0.980	0.980 0.980 0.970	0.985 0.982 0.990
3	n-D class mean # 3	Granite Alunite Tremolite Schist	0.971 0.960 0.957	0.971 0.928 0.959	0.971 0.992 0.955
4	n-D class mean # 4	Quartz Quartz Chloritic Gneiss	0.995 0.992 0.990	0.989 0.982 0.981	1.000 1.000 1.000
5	n-D class mean # 5	Alunite Tremolite Schist Alunite	0.974 0.974 0.972	0.970 0.949 0.961	0.979 0.998 0.983
6	n-D class mean # 6	Jadeite Jadeite Augite	0.984 0.976 0.973	0.988 0.986 0.953	0.979 0.966 0.992

Table-7.2 Top three Spectral Analyst™ matches to the same six end-member spectra using reference spectral library containing JHU rock and soil spectra alone.

Serial number	Unknown image end-member spectrum ID	Top three reference spectral library materials with the best overall scores	Overall score	SAM score	SFF score
1	n-D class mean # 1	Augite-hypersthene andesite Mafic basalt/diabase Syenite gneiss	0.982 0.978 0.972	0.988 0.992 0.987	0.976 0.963 0.958
2	n-D class mean # 2	Augite-hypersthene andesite Mafic basalt/diabase Granodiorite	0.967 0.951 0.941	0.982 0.983 0.974	0.951 0.919 0.909
3	n-D class mean # 3	Felsic granite Tremolite schist Intermediate monzonite	0.971 0.957 0.956	0.971 0.959 0.975	0.971 0.955 0.937
4	n-D class mean # 4	Chloritic gneiss Brown loamy fine sand Reddish brown fine sandy loam	0.990 0.989 0.989	0.981 0.979 0.978	1.000 1.000 1.000
5	n-D class mean # 5	Tremolite schist Intermediate monzonite Quartz monzonite	0.974 0.965 0.961	0.949 0.971 0.958	0.998 0.959 0.963
6	n-D class mean # 6	Augite-hypersthene andesite Granodiorite Mafic basalt/diabase	0.964 0.958 0.950	0.975 0.986 0.954	0.953 0.931 0.946

Keeping these observations in mind, the best matches to the unknown image-derived end-member spectra obtained through Spectral Analyst™ in combination with geologic background knowledge of the study area (Chapter 2 and Chapter 4) have been shown in Figure-7.9a. Figure-7.9b shows the same spectra convolved to ASTER TIR bandpasses. It can be readily observed, that low spectral resolution of ASTER TIR and inadequate coverage of the main spectral feature (between 9.3 μm and 10 μm) limits the use of ASTER data in finer mineralogic identification.

Note: The names of the spectral matches ('felsic' granite and 'mafic' diabase), shown in the figures and used subsequently, are the ones present in the reference spectral library (JHU spectral library). The same nomenclature has been retained so that the specificity of the sample used in building the spectral library is retained and the corresponding mineralogic characteristics of the samples can be identified and referenced by anyone. The nomenclature does not relate with the actual nature of the rock types (since granite is essentially felsic, and diabase is essentially mafic!).

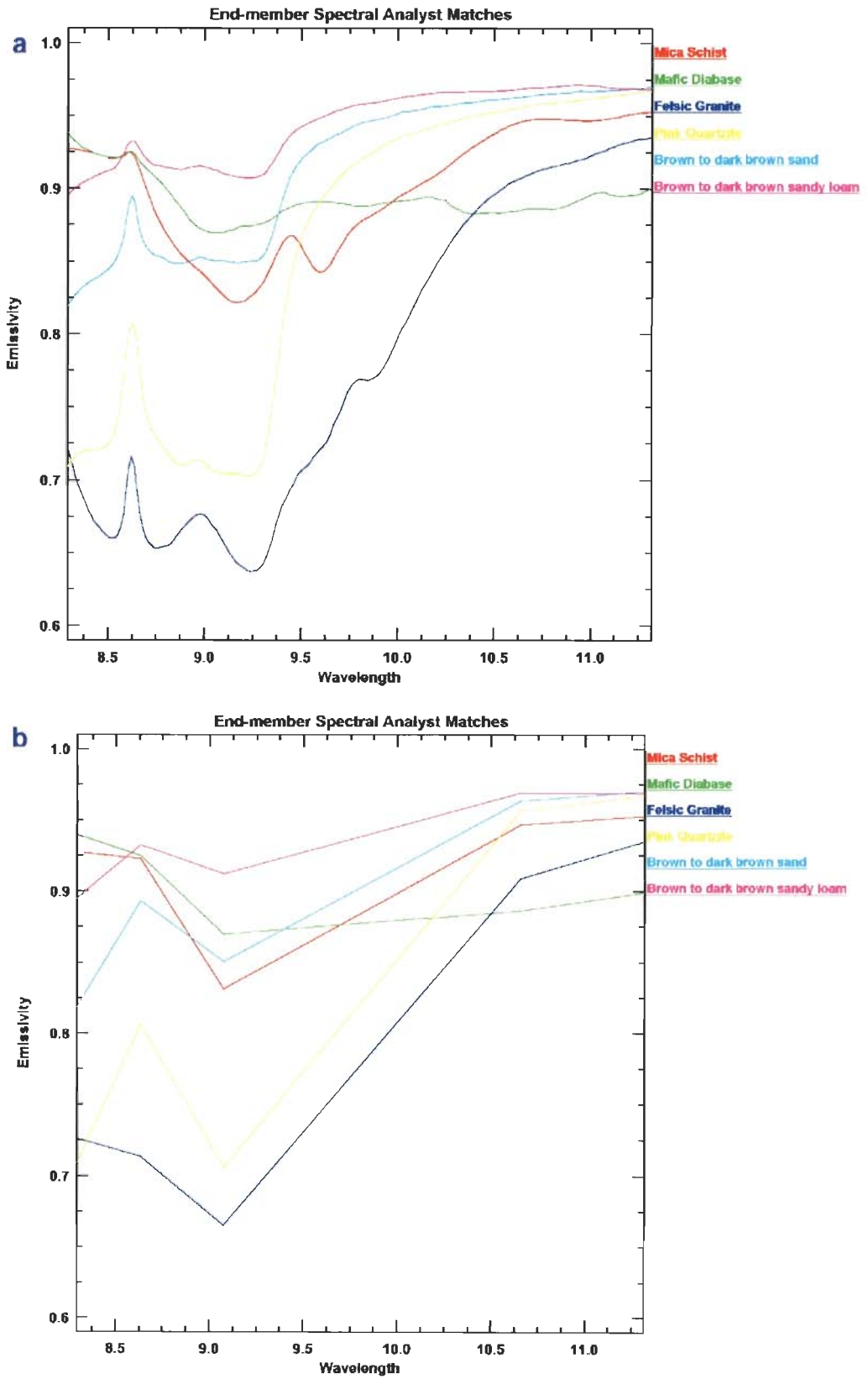


Figure-7.9 a. Best Spectral Analyst™ matches to the six unknown image end-members; b. The same spectra resampled to the ASTER TIR bandpasses. Notice the loss of some important spectral features between 9.3 μm and 10 μm due to coarse spectral resolution of ASTER TIR data. Wavelength is in micrometers.

7.2.3.3 SAM classification

The Spectral Angle Mapper (SAM) is a physically-based classification algorithm that uses an n -dimensional angle to match pixels to reference spectra (Kruse et al., 1993). The algorithm determines the spectral similarity between two spectra by calculating the angle between the spectra, treating them as vectors in a space with dimensionality equal to the number of bands. This technique, when used with calibrated reflectance data, is relatively insensitive to illumination and albedo effects. SAM compares the angle between the end-member spectrum vector and each pixel vector in n -dimensional space. Smaller angles represent closer matches to the reference spectrum. Pixels further away than the specified maximum angle threshold in radians are not classified.

Using a threshold of 0.05 radians with the PPI derived image end-member spectra, a SAM classified lithologic map has been generated as shown in Figure-7.10. In this image, the surfaces classified as 'mica schist' collectively represent the metapelites (schists and phyllites). The surfaces classified as 'mafic diabase' are primarily amphibolite rocks and other such rocks rich in amphibole minerals. Surfaces classified as 'felsic granite' are basically quartz-rich rocks and soils with some feldspar and muscovite. Pure quartzites are clearly classified as 'pink quartzite'. The aolian sands of the western part of the study area have been clearly classified as brown to dark brown sand, whereas the cultivated regions in the eastern part and the weathered metapelites, carbonates and arkosic quartzites in the central part of the study area have been classified as brown to dark brown sandy loam. The SAM classification is limited by the number of spectral end-members used to train the classifier. As more spectral end-members are used to classify the image, the spectral diversity of the diverse surface materials can be more fully realized.

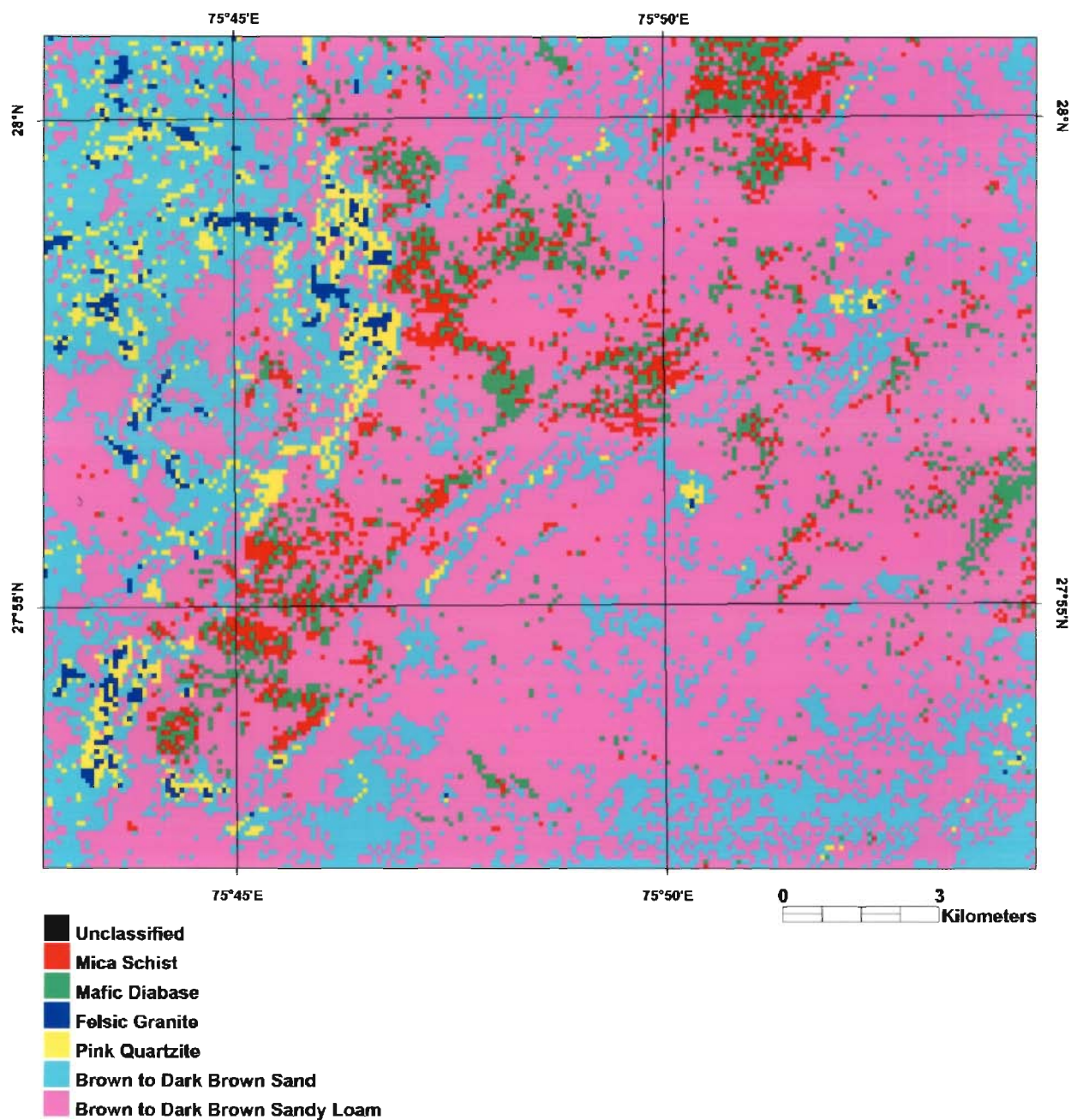


Figure-7.10 Spectral lithologic map generated using SAM on ASTER TIR surface emissivity data and the six spectral image end-members determined using PPI™.

7.2.3.4 MTMF™ processing and classification

Matched Filtering or Orthogonal Subspace Projection technique (Harsanyi and Chang, 1994; Boardman et al. 1995) is commonly used to find the abundances of user-defined end-members using a partial unmixing approach. In this method not all of the end-members in the image need to be known. This technique maximizes the response of the known end-member and suppresses the response of the composite unknown background, thus matching the known signature. It provides a rapid means of detecting specific materials based on matches to library or image end-member spectra. This technique may find some false positives for rare materials.

A modified version of this technique, called the Mixture-Tuned Matched Filtering (MTMF™) has been implemented in ENVI. MTMF™ performs matched filtering that also adds an output ‘infeasibility’ image to the results. The infeasibility image is used to reduce the number of false positives that are sometimes found when using matched filtering. Pixels with a high infeasibility are likely to be matched-filter false positives. Correctly mapped pixels will have a matched-filter score above the background distribution around zero and a low infeasibility value. The infeasibility values are in noise sigma units which vary in DN scale with matched-filter scores. The results of MTMF™ processing appear as a series of gray-scale images (two for each selected end-member). The matched filtering floating point results provide a means of estimating the relative degree of match to the reference spectrum and the approximate sub-pixel abundance. Pixels with a high matched-filter result and high infeasibility are ‘false positive’ pixels and do not match the target (ENVI User’s Guide, 2005).

For the study area, the MTMF™ processing of the ASTER surface emissivity data has been used to produce six abundance (MTMF™ score) images and their respective six infeasibility score images, as shown in Figure-7.11a-l. These images have been interactively stretched using linear stretch for better visual discrimination. Table-7.3 shows the MTMF™ score ranges and the thresholds used in individual cases to produce the final classification output.

Table-7.3 MTMF™ scores and thresholds used for classification of the six image end-members.

MTMF End-member	Score Range	Threshold
MTMF End-member1	-0.989424 to 1.031486	0.095
MTMF End-member2	-0.919444 to 1.217289	0.150
MTMF End-member3	-0.913721 to 1.288750	0.450
MTMF End-member4	-0.931269 to 1.459700	0.500
MTMF End-member5	-1.447824 to 1.821196	0.250
MTMF End-member6	-2.047239 to 1.789476	0.250

Since the MTMF™ results are separate grayscale images in the form of match results for individual end-member spectrum, in order to show the results collectively, the thresholded MTMF™ results were first density-slice color-coded, saved as class images, and converted to vector polygons. The vector files were then saved as regions of interest (ROIs) and displayed over a higher resolution ASTER band 1 image to produce the final MTMF™-classified image output, as shown in Figure-7.12.

Since the MTMF™ results for the last two end-members (brown to dark brown sand, and brown to dark brown sandy loam overlap the pixels thresholded for the other classes, and also because their general distribution is wide and non-lithology-specific, they have not been shown on the final MTMF™ class image.

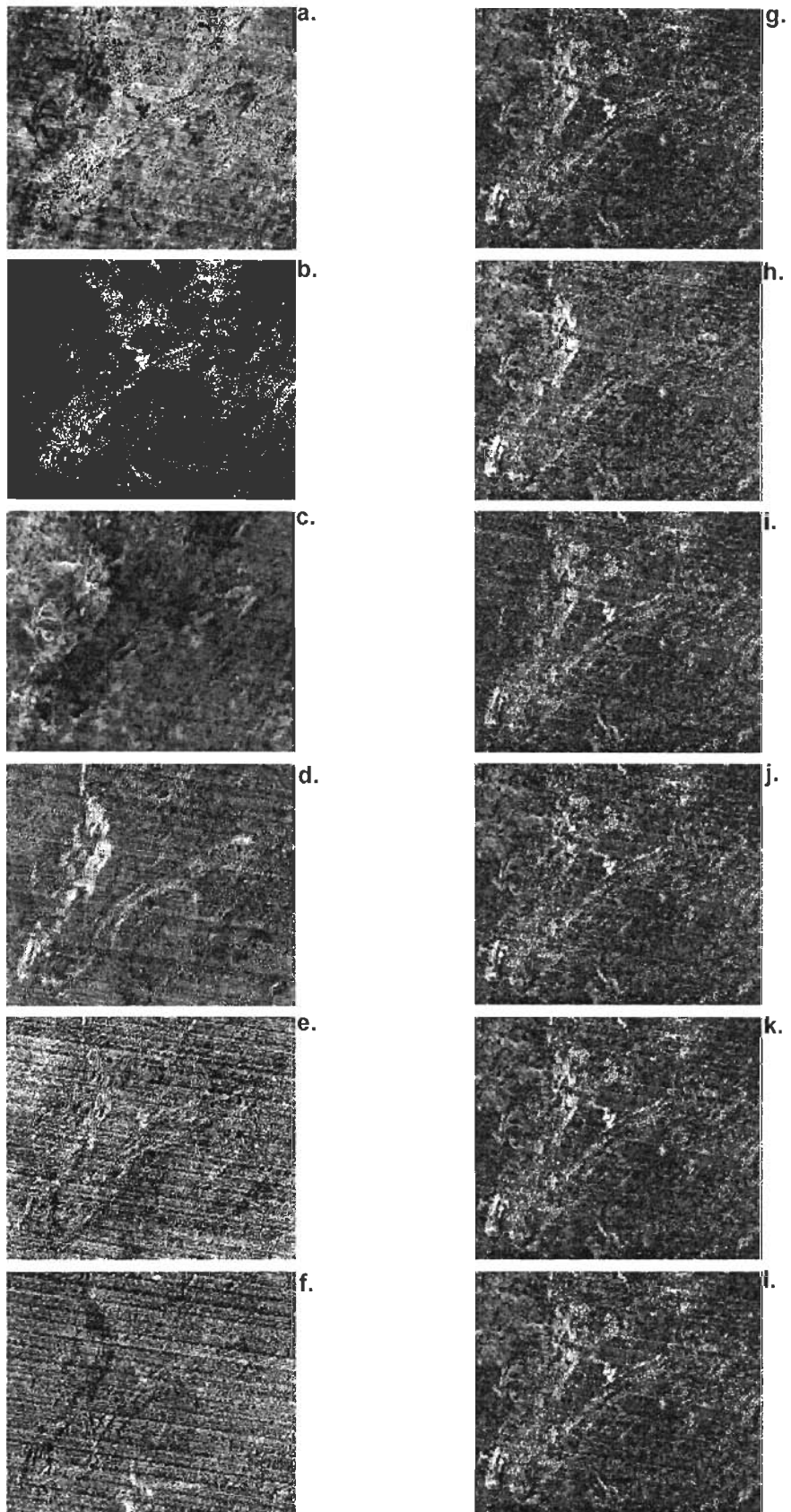


Figure-7.11 a-f Matched Filter processed images for the six image end-members; g-l their respective infeasibility images.

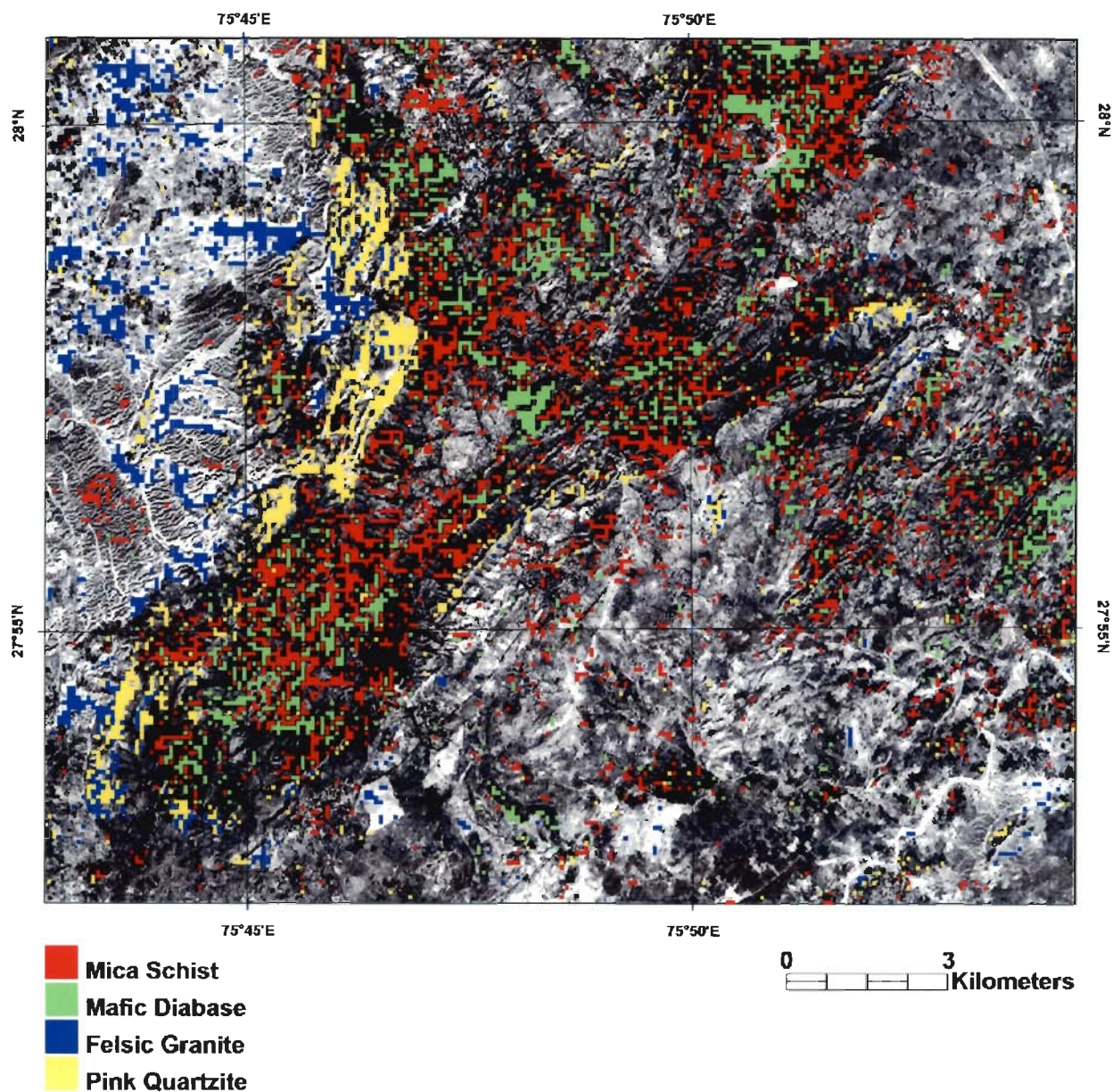


Figure-7.12 Classified output of MTMFTM processing of ASTER L2 surface emissivity data.

The background is ASTER band 1 image, with spatial resolution of 15 m. Notice the limitations posed by coarse 90 m spatial resolution and effects of vegetation on spectral classes, especially the class 'Mica Schist'. Excellent discrimination has been achieved between the two surface lithologic categories of mafic and felsic rocks, shown respectively in green and blue/yellow colors. Quartz-rich surfaces with some micaceous/clay content have been mapped as class 'Felsic Granite'.

7.3 Silica weight percent estimation using ASTER TIR surface emissivity data

In the preceding sections, methods of qualitative estimation of surface lithology using ASTER TIR radiance/emissivity data have been described. Studies utilizing thermal infrared data have demonstrated that it is possible to distinguish between rock types based on differences in silicate mineralogy (Kahle and Rowan, 1980; Lahren et al., 1988; Abrams et al., 1991; Watson et al., 1996; Cudahy et al., 1999; Hook et al., 1994; Bandfield, 2002). Quantitative estimation of mineralogic or chemical abundances using TIR data is a relatively new and under-explored field. More recent studies have used the shift in the emissivity minimum to estimate the weight percent silica of igneous rocks (Gillespie et al., 1986; Sabine et al., 1994; Hook et al., 2005). Variations in silicate mineralogy are particularly useful in geological mapping because they are an important criterion in classifying and interpreting igneous rocks as well as sedimentary and metamorphic rocks derived from them.

In the following sections, two independent methods of silica weight percent mapping using ASTER TIR surface emissivity data have been described. Method 1 is a novel and rather broad-based approach that utilizes the spectral modeling of the surface-emissivity spectra with a reference curve derived from spectral library data to empirically determine the coefficients of a linear fit and applying the relationship to unknown emissivity data to map the silica weight percentages. A variety of curve-fitting models have been tested to determine the best spectral model to estimate the emissivity minimum for individual pixel spectrum and using this information to empirically estimate the silica weight percentages for an unknown pixel. Method 2 is based on Metal Mining Agency of Japan's (MMAJ) original 'K-value' method, which is an empirically derived linear relationship between ASTER TIR surface emissivity and SiO₂ concentrations of 194 fresh/weathered rock/mineral samples, determined chemically (MMAJ, 2001). The two results have subsequently been compared in specific context of the study area.

7.3.1 Theory and previous studies

Reststrahlen band: The reflectance and emissivity spectra of minerals/rocks exhibit diagnostic features at various wavelengths caused by the interaction of EM energy with the atoms and molecules that make up the minerals and rocks and provide a means for their remote discrimination and identification. The various atomic/molecular processes involved have been described in Chapter 5. In case of infrared wavelengths, the interaction generally leads to the promotion of molecules from vibrational ground state to excited state. Different Si-O bonded structures vary in their interaction with EM energy in thermal infrared wavelengths. Collectively, the Si-O spectral features in the thermal infrared are referred to as the 'Reststrahlen Band'. The emissivity minimum for this band occurs at shorter wavelengths (8.5 μm) for tectosilicates (*e.g.*, quartz and feldspars), and progressively longer wavelengths for phyllosilicate, inosilicate, sorosilicate, and nesosilicate structures (Hunt, 1980). Because framework/tectosilicates dominate the felsic igneous rocks and chain silicates dominate the mafic igneous rocks, the minimum for the reststrahlen band shifts to shorter wavelengths as SiO_2 content increases (fig. 7.1).

Development of the method: In order to take advantage of the systematicity of shift in the reststrahlen minimum in igneous rock composition, it is necessary to establish a technique for the determination of the minimum as well as the most suitable chemical parameter. Gillespie et al. (1986) determined the minimum using a Gaussian function. Sabine et al. (1994) expanded on Gillespie's work by evaluating the relationship between the Gaussian minimum and a variety of chemical and modal parameters. Sabine et al. (1994) found that highest correlation existed between the SiO_2 content and the Gaussian minimum. The Gaussian minima for the samples used by Sabine et al. (1994) were determined from emissivity spectra derived from Thermal Infrared Multispectral Scanner (TIMS) data over Desolation Wilderness, northern Sierra Nevada, California, where the main rock units comprise granitoids with SiO_2 weight percentages ranging from 50% to 70%. The TIMS instrument is a multispectral scanner that

acquires data in 6 wavelength channels in the thermal infrared (7.0-13.0 μm), and is a forerunner to the ASTER instrument. In order to determine the weight percent SiO_2 , Sabine et al. (1994) regressed the emissivity minima from the TIMS emissivity spectra against the weight percent SiO_2 obtained from field samples. Sabine et al. (1994) determined a linear relationship between the minimum wavelengths, which was obtained by fitting a 3-term Gaussian function (Berk et al., 1998) to TIMS data, and the weight percent SiO_2 , which was obtained by chemical analysis of samples from locations in the TIMS imagery. They also showed the fit values for the spectra of the field samples. Since the input data used by them were area and sensor specific, the inherent artifacts made the findings of only limited applicability and use. Hook et al. (2005) further generalized the approach by applying the method to the spectra of 35 igneous rock samples from ASTER spectral library instead of spectra from any specific sensor. The SiO_2 weight percent of these samples lie in the range of 43% to 76%. Hook et al. (2005) used the following Gaussian functions to determine the emissivity minima of the library spectra:

$$f(x) = A_0 e^{\frac{-z^2}{2}} \quad (3\text{-term Gaussian}) \quad (1)$$

$$f(x) = A_0 e^{\frac{-z^2}{2}} + A_3 \quad (4\text{-term Gaussian}) \quad (2)$$

Where:

$$z = \frac{x - A_1}{A_2}, \text{ and } x = \text{wavelength } (\mu\text{m})$$

A_0 through A_3 are the fit values for the Gaussian function $f(x)$. The 4 terms of the Gaussian function correspond to the amplitude, position of the minimum value, area enclosed by the function and offset, respectively.

In their study, Hook et al. (2005) calculated the Gaussian-fit values for the full resolution laboratory spectra and the laboratory spectra convolved to the 5 TIR bandpasses of ASTER, and 10 TIR bandpasses of the MODIS and ASTER Simulator (MASTER) instrument.

In all they used 9 different band-combinations to calculate the 3- and 4-term Gaussian fit values to determine the effects of band selection and resolution on emissivity minimum of the 35 igneous rock spectra, and thus obtained about 630 different fit values (2 fits each for 35 spectra and 9 channel combinations; in one case 32 spectra were used). The position coefficient of the fit (term A_1) from each sample in each dataset was plotted against its corresponding laboratory weight percent SiO_2 value and a least squares fit performed on each dataset. Table-7.4 gives the least-squares fit correlation coefficients (R^2) obtained by them for the 9 cases investigated.

Table-7.4 Results from fitting the ASTER spectral library igneous rock spectra with 3- and 4-term Gaussian function. N = number of samples; R^2 = Correlation coefficient. For Case 9, the value of N less than 35 indicates that the Gaussian model failed to adequately fit certain spectra (the fit values were obtained excluding those spectra). Wavelength range shown is from the centroid value of the first channel to the centroid value of the last channel (after Hook et al., 2005).

Case	Sample Set	3-term Gaussian		4-term Gaussian	
		N	R^2	N	R^2
1	7-14 μm (full resolution)	35	0.6617	35	0.7082
2	8-12 μm (full resolution)	35	0.7925	35	0.8034
3	MASTER 1-10 channels (7.737-12.888 μm)	35	0.8216	35	0.8307
4	MASTER 1-9 channels (7.737-12.131 μm)	35	0.7705	35	0.7867
5	MASTER 2-10 channels (8.153-12.888 μm)	35	0.4719	35	0.105
6	MASTER 2-9 channels (8.153-12.131 μm)	35	0.71	35	0.7755
7	MASTER 3-8 channels (8.604-11.289 μm)	35	0.4846	35	0.2565
8	ASTER (8.287-11.289 μm)	35	0.5832	35	0.662
9	ASTER (8.287-11.289 μm) excluding ultramafics	32	0.7581	32	0.7615

In general, they concluded that the Gaussian model fits the spectra best when the full resolution spectra in the wavelength range 8.0-12.0 μm are used. This is due to the fact that the main reststrahlen feature for the emissivity spectra lies within this range. They also describe the influence of atmosphere and the importance and influence of its correction on the spectra in the ability of the Gaussian model to correctly locate the emissivity minima (Hook et al., 2005).

7.3.2 Spectral modeling of TIR emissivity spectra

Approach and objective: This section describes an approach for determining the measure of the shift in the emissivity minima by modeling the emissivity spectra. The basic premise of the method has been described by Gillespie et al. (1986), Sabine et al. (1994) and most recently by Hook et al. (2005), as discussed previously. The present work builds upon the findings of Hook et al. (2005) and explores the universality of the approach, with special reference to the ASTER surface emissivity data of the study area.

The two important objectives with regard to the analysis undertaken in this study are:

1. To test the curve-fitting options other than the Gaussian model to obtain the emissivity minima values, in order to appraise the generality of the method, and
2. To see whether the approach is capable of yielding reliable results with ASTER data, as in the present case, since these are globally available and the ability to map weight percent silica from these data is highly desirable.

Data and tools: Spectral modeling has been carried out using the full resolution and resampled JHU igneous rock spectral library (34 spectra, for 22 different rock types), which had been computed from the original biconical reflectance spectra using Kirchhoff's Law. JHU biconical reflectances are available in the wavelength range of 0.4-14.0 μm (details of the JHU spectral library have been provided in Appendix B), since the wavelength region of interest (reststrahlen band) lies within 8.0-12.0 μm wavelength region, the spectra within this region alone has been used in modeling. The chemical descriptions of the samples used in JHU spectral library are publicly available, and hence serve as standard data for comparative studies.

JHU spectra convolved to the system response function of ASTER TIR sensor (obtained from the official ASTER website: asterweb.jpl.nasa.gov) have been modeled separately to see the effects of spectral sampling and general applicability of the procedure. The curve fitting functions explored include various forms of the Fourier, Gaussian, and Polynomial functions.

The initial processing has involved the creation of the database in ASCII file format for input to MATLAB. Segmentation of the database and initial data preparation was carried out using Microsoft Excel and Golden Grapher software. All subsequent processing, viz. spectral modeling has been carried out using MATLAB 7.0.1 software. Object-oriented programs have been written in MATLAB to compute the coefficients for the curve-fitting functions that are not available in MATLAB's CurveFit Toolbox as built-in.

Method and curve-fitting results: To test the reproducibility of the results and to validate the procedure suggested by Hook et al. (2005), JHU laboratory spectrum of quartz-monzonite has been used in the present study. Initially the curve-fitting had been carried out using the full resolution spectra within the wavelength region of 8.0-12.0 μm ; subsequently the spectrum of the same rock resampled to the system response functions of ASTER has been used with various curve-fitting functions. The results of the two exercises have been summarized in Figures 7.13a-g and 7.14a-e, respectively. Since the resampled spectral data had only five data values (corresponding to the five TIR bands), they could not be used with Polynomial 5th Order upwards and Fourier 2nd Order upwards curve-fitting functions. The JHU igneous spectral library rock types and their respective SiO₂ weight percentages have been shown in Table-7.5 along with the results of spectral modeling.

In Table-7.5, it can be readily seen that the modeled minima for Gaussian 3-term fitting and Polynomial 2nd Order fitting are almost exactly alike. This is due to the fact that the Gaussian model used in the fitting essentially calculates the coefficients by a transformation of the original equation so as to mimic a Polynomial 2nd Order function. The steps involved in calculation of the coefficients for the Gaussian 3-term fit function and the minima for the Polynomial 2nd Order fit have been described as follows:

Original form of the Gaussian 3-term function:

$$y = A_0 \cdot e^{-\frac{(x-A_1)^2}{2A_2^2}} \quad \dots(3)$$

Taking log on the two sides transforms the equation, thus:

$$\ln(y) = -\frac{1}{2A_2^2}x^2 + \frac{2A_1}{2A_2^2}x + \left(\ln(A_0) - \frac{A_1^2}{2A_2^2} \right) \approx ax^2 + bx + c \quad \dots(4)$$

The fit is actually done on equation 4, and the resultant coefficients are given as:

$$\begin{aligned} A_2 &= \sqrt{-\frac{1}{2a}} \\ A_1 &= \frac{2A_2^2 b}{2} \\ A_0 &= e^{\frac{c + \frac{A_1^2}{2A_2^2}}{2A_2^2}} \end{aligned} \quad \dots(5)$$

In case of the Polynomial 2nd Order curve fitting, the minimum of the fit (restricted to the wavelength range used) was derived using differential calculus, and the minimum for the fit is defined by the following equation:

$$x = -\frac{b}{2a}, \quad \dots(6)$$

Where b and a are the coefficients of the general form of the quadratic polynomial function given in equation 4. The Fourier 1st Order fit results were obtained using the 'fourier1' function available within MATLAB. For all analyzed fits, the fitting has been done using default values for fit parameters. A bisquare robust least-squares fitting mode and the Levenberg-Marquardt algorithm have been used in all cases. A startpoint of 0.01 for coefficient 'a1' of Gaussian 4-term fit has been used for the model lab spectrum. Full details of all fit results have been provided in Appendix C.

Results of the linear regression between the model minima derived through spectral modeling and SiO₂ content for the JHU spectra have been shown in Figures 7.15a-b, 7.16a-b, 7.17a-b and 7.18, respectively for the Polynomial 2nd Order fit for the full resolution test spectrum, and Gaussian 3-term, Polynomial 2nd Order and Fourier 1st Order fits for the resampled test spectrum. The linear regression fit coefficients for all cases have been summarized in Table-7.6.

Table-7.5 Results of the spectral modeling of JHU igneous rock spectra. Except for polynomial 2nd order curve fitting, all other values are for JHU spectra resampled to the ASTER TIR system response function.

S.No.	Rock Type	SiO ₂ Weight Percent	Gaussian 3-term	Fourier 1 st Order		Polynomial 2 nd Order			
			Modeled Minimum	Modeled Minimum	R ²	Resampled		Full Resolution (8-12 μm)	
						Modeled Minimum	R ²	Modeled Minimum	R ²
1	Augite-hypersthene	57.38	9.7113	7.932677	0.899879	9.712094	0.827423	9.703439	0.778378
2	Basaltic	53.3	9.9593	7.870974	0.914204	9.95954	0.949052	10.077037	0.814541
3	Anorthosite	53.41	9.9995	8.302489	0.782632	9.999143	0.765224	10.024408	0.841555
4	Aplite	75.8	8.1811	8.875575	0.988352	8.171279	0.937164	9.042101	0.739768
5	Basalt	50.54	10.379	8.193396	0.926784	10.375444	0.983383	10.64934	0.945863
6	Basalt	51.02	10.0895	7.33349	0.925425	10.091764	0.94879	10.12105	0.972581
7	Basalt	49.95	9.8118	8.290603	0.963387	9.812513	0.683494	9.752319	0.572048
8	Basalt	51.03	9.9219	8.250981	0.96707	9.925908	0.880904	9.947912	0.891777
9	Basalt	49.52	9.9856	8.311675	0.767236	9.988501	0.895064	10.006812	0.919883
10	Basalt	55.02	10.1316	7.141411	0.934455	10.133948	0.952191	10.18192	0.96178
11	Diabase	52.41	10.0074	8.456895	0.798672	10.011077	0.822244	10.034209	0.806517
12	Diabase	52.54	10.1297	7.052555	0.9053	10.131971	0.929241	10.166706	0.896783
13	Diorite	49.81	10.0329	8.11099	0.997387	10.032479	0.739976	9.983522	0.858998
14	Dunite	39.57	11.8532	8.225024	0.771672	11.971959	0.853452	16.097171	0.863052
15	Gabbro	44.2	10.1756	8.211361	0.946145	10.176262	0.845621	10.319962	0.89223

Table-7.5 continued...

16	Alkalic	73.44	8.5928	8.985647	0.977288	8.546343	0.906318	9.050734	0.728271
17	Granite	75.5	8.6269	8.994109	0.989545	8.54589	0.899462	9.039901	0.72508
18	Granite	69.1	8.3826	8.934305	0.993387	8.338296	0.919314	9.086725	0.737534
19	Granite	75.1	8.8057	9.056656	0.976274	8.761645	0.887281	9.196617	0.755927
20	Granodiorite	64.2	8.911	9.073971	0.989911	8.899423	0.944078	9.279372	0.744551
21	Granodiorite	56	9.6383	7.585602	0.99504	9.636568	0.972609	9.680088	0.894708
22	Ijolite	43.08	10.1208	8.360315	0.572427	10.12724	0.76787	10.061699	0.81989
23	Lamprophyre	45.94	10.1048	7.247546	0.955275	10.105619	0.990094	10.077844	0.972725
24	Monzonite	61.42	8.5857	8.948333	0.993159	8.588749	0.956623	9.22609	0.748891
25	Norite	48.42	10.0469	8.108363	0.999287	10.046304	0.741574	10.003722	0.861543
26	Norite	48.23	10.1359	7.134107	0.92996	10.139104	0.941712	10.091813	0.96376
27	Rhyolitic	75.78	9.5907	7.892435	0.963143	9.576584	0.683917	9.528899	0.720539
28	Picrite	51	11.1912	8.44952	0.452305	11.179184	0.940212	13.701049	0.907919
29	Picrite	68.9	10.9629	8.441101	0.416096	10.953725	0.949133	13.164358	0.914105
30	Quartz	73.9	8.5413	8.95095	0.999727	8.532455	0.939305	9.199014	0.716457
31	Rhyolite	70.87	9.4151	7.486278	0.947461	9.404847	0.763727	9.382595	0.638193
32	Alkalic	55.28	9.644	7.47352	0.887042	9.644118	0.886152	9.72953	0.802611
33	Nepheline	59.85	9.1906	9.198468	0.923946	9.19135	0.885268	9.6019	0.706755
34	Tonalite	63.08	8.6667	8.952438	0.946638	8.680592	0.932455	9.091145	0.705506

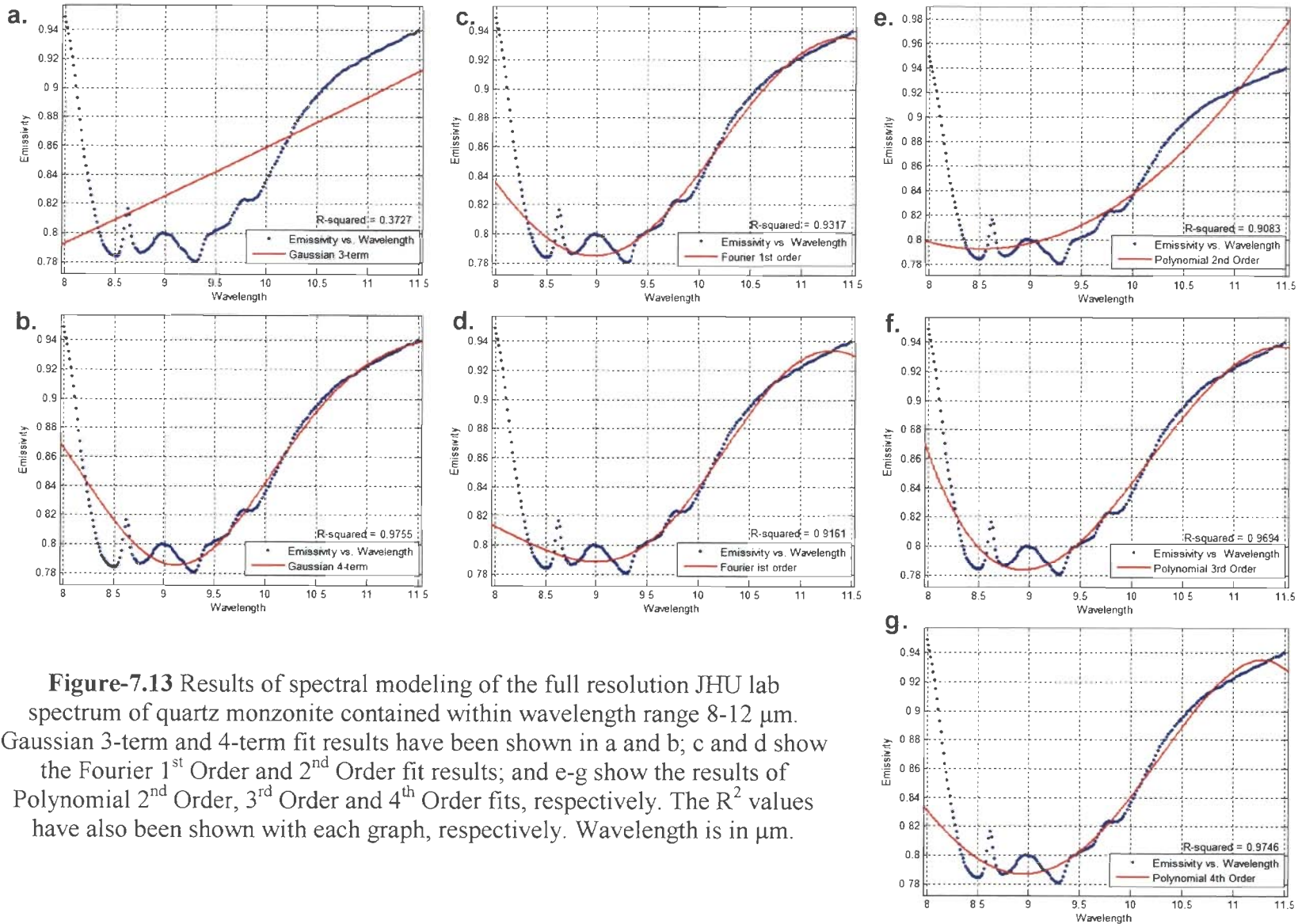


Figure-7.13 Results of spectral modeling of the full resolution JHU lab spectrum of quartz monzonite contained within wavelength range 8-12 μm . Gaussian 3-term and 4-term fit results have been shown in a and b; c and d show the Fourier 1st Order and 2nd Order fit results; and e-g show the results of Polynomial 2nd Order, 3rd Order and 4th Order fits, respectively. The R^2 values have also been shown with each graph, respectively. Wavelength is in μm .

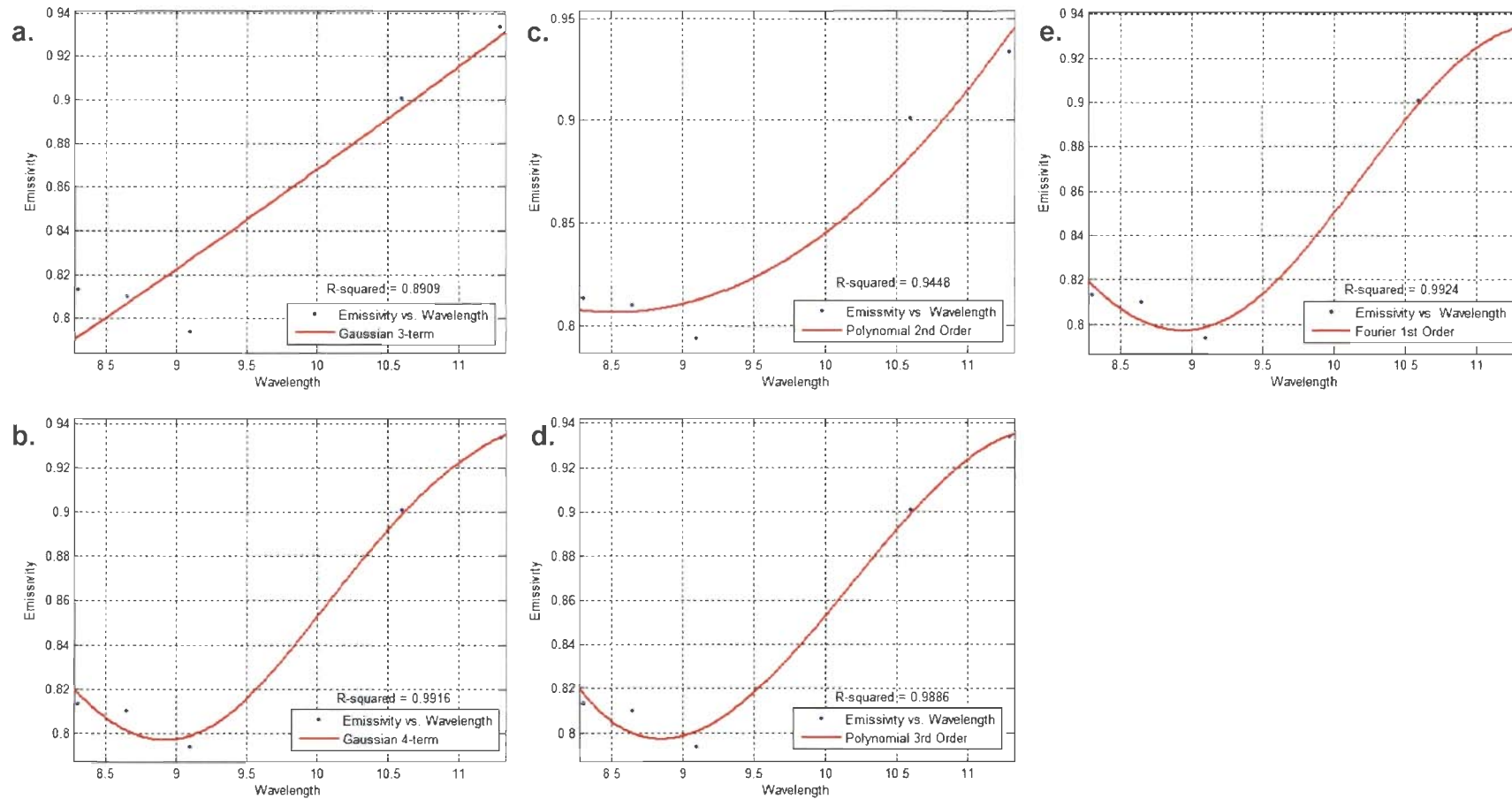


Figure-7.14 Results of spectral modeling of the JHU lab spectrum of quartz monzonite resampled to the system response function of ASTER TIR sensor. Gaussian 3-term and 4-term fit results have been shown in a and b; c and d show the Polynomial 2nd Order and 3rd Order fit results; and e shows the Fourier 1st Order fit result. The R^2 values have also been shown with each graph, respectively. Wavelength is in μm .

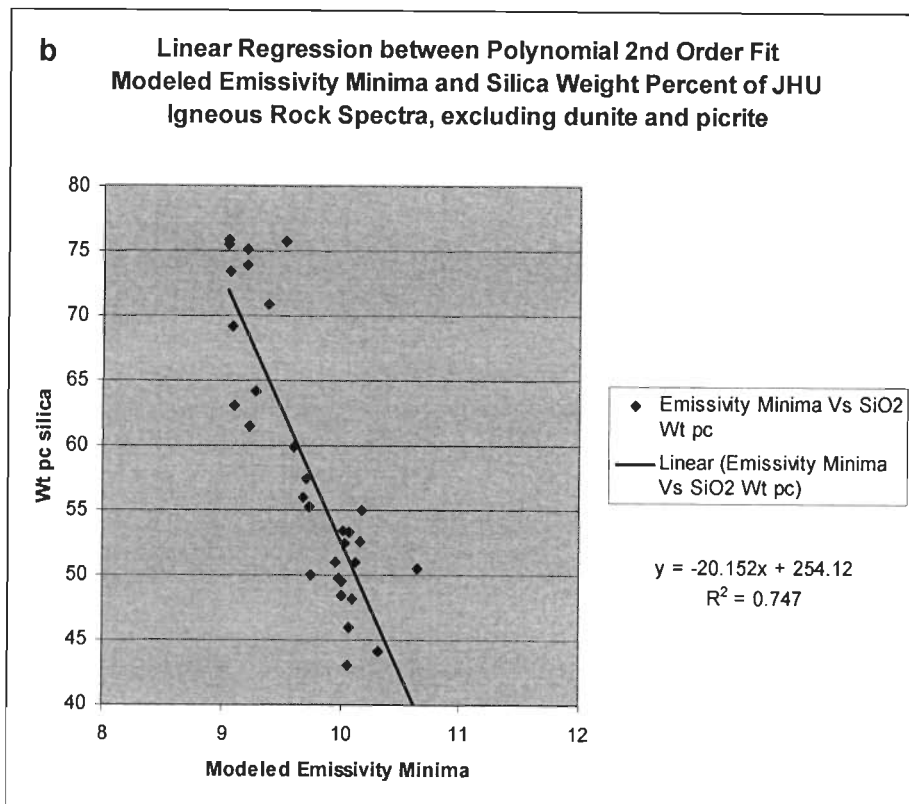
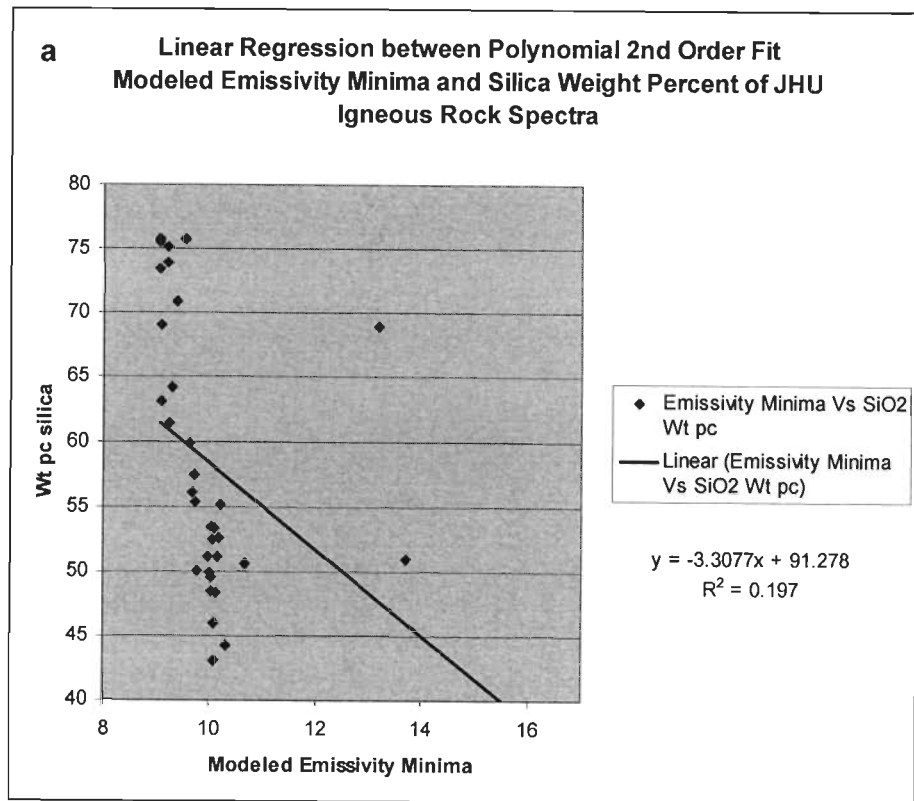


Figure-7.15 Linear regression between Polynomial curve-fit modeled emissivity minima and corresponding SiO₂ weight percentages of the JHU spectral library minerals: **a.** using all 34 spectra; **b.** excluding spectra of dunite and picrite.

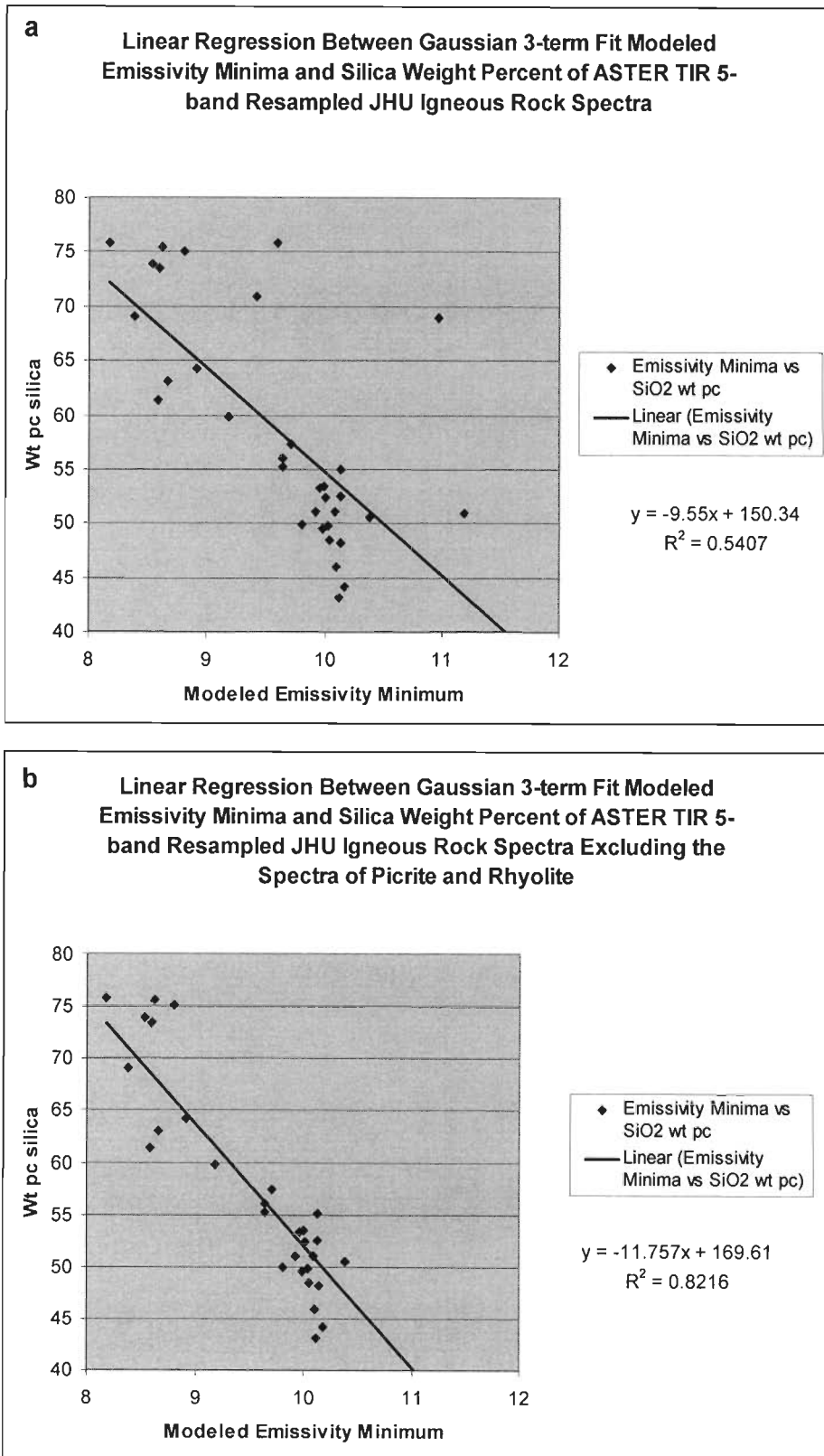


Figure-7.16 Linear regression between Gaussian 3-term curve-fit modeled emissivity minima and corresponding SiO₂ weight percentages of the JHU spectral library minerals: **a.** using all 34 spectra; **b.** excluding spectra of picrite and rhyolite.

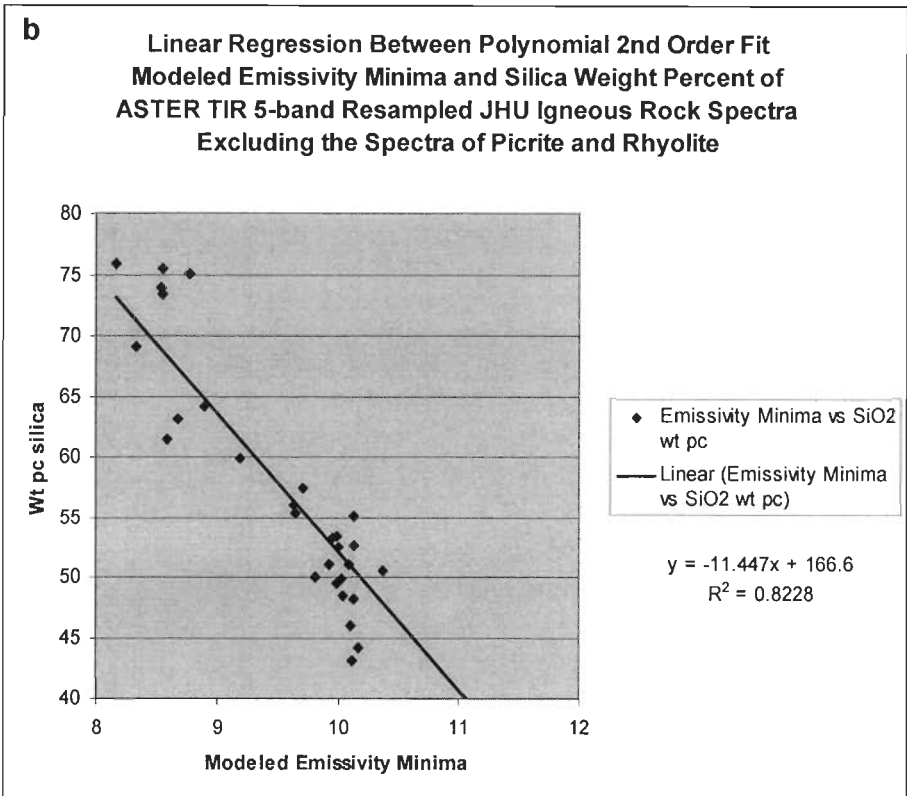
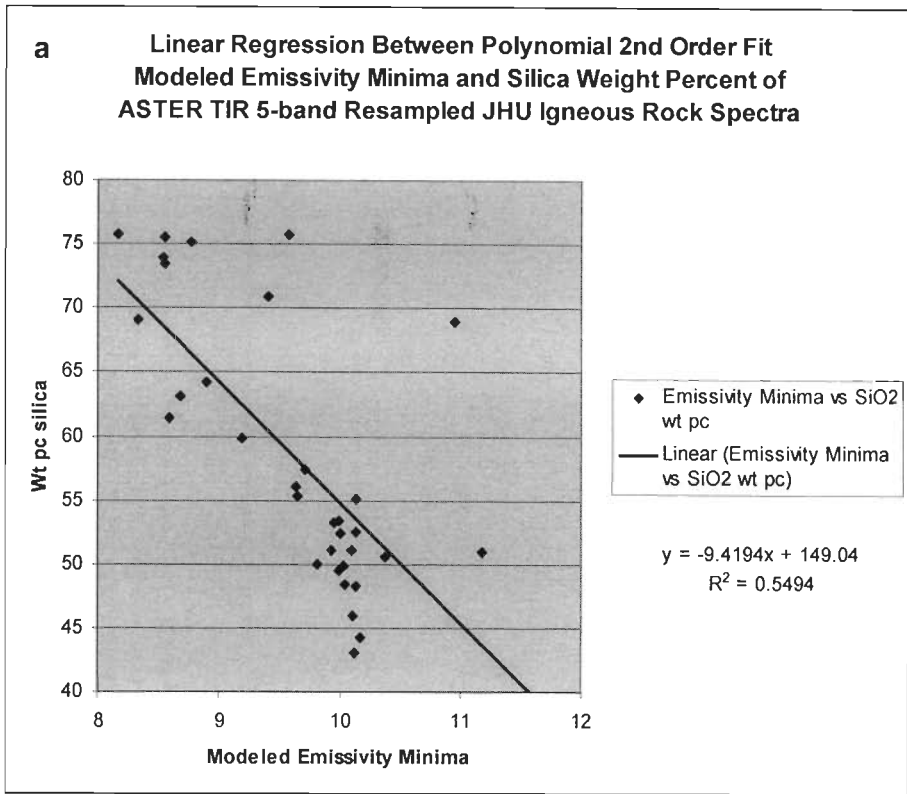


Figure-7.17 Linear regression between Polynomial 2nd order curve-fit modeled emissivity minima and corresponding SiO₂ weight percentages of the JHU spectral library minerals: **a.** using all 34 spectra; **b.** excluding spectra of picrite and rhyolite.

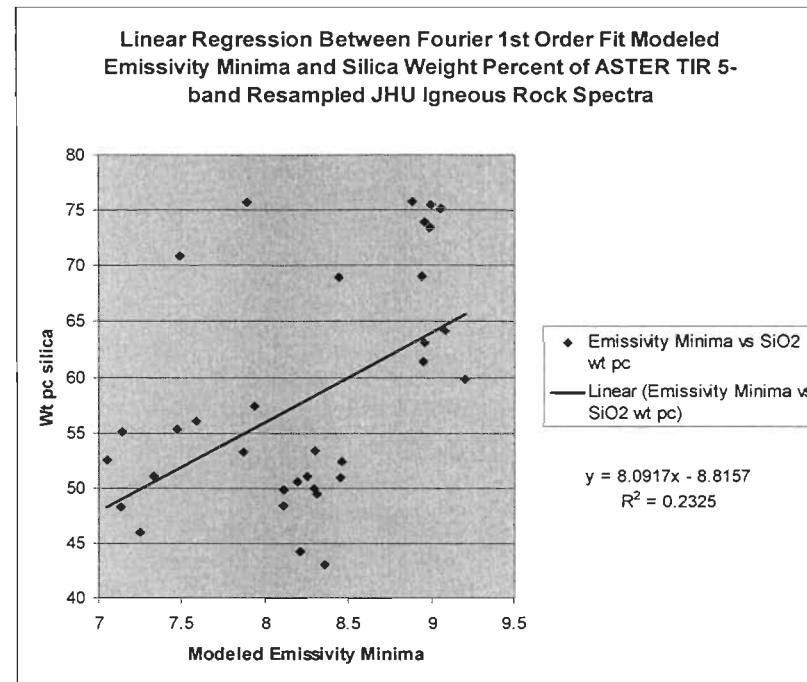


Figure-7.18 Linear regression between Fourier 1st order curve-fit modeled emissivity minima, and corresponding SiO₂ weight percentages of the JHU spectral library minerals.

Table-7.6 Summary of linear regression results for various curve-fitting models investigated to estimate the emissivity minima. N=no. of rock spectra used; m and c are the slope and intercept of the linear model ($y=mx+c$); R^2 =regression coefficient; *ND*=Not Determined

JHU Igneous Rock Spectra	Curve-fitting Model											
	Polynomial 2 nd Order				Gaussian 3-term				Fourier 1 st Order			
	N	m	c	R ²	N	m	c	R ²	N	m	c	R ²
8-12 μm full resolution	34	-3.3077	91.278	0.197	ND				ND			
	32	-20.152	254.12	0.747								
Resampled to ASTER TIR Bandpasses	34	-9.4194	149.04	0.5494	34	-9.55	150.34	0.5407	34	8.0917	-8.8157	0.2325
	30	-11.447	166.6	0.8228	32	-11.757	169.61	0.8276				

Discussion and selection of the fit model: From the full resolution test emissivity spectrum of quartz monzonite shown in Figure-7.13, and the various curve-fitting options investigated, it can be readily observed that while Gaussian 3-term function fails to adequately fit the spectrum ($R^2 = 0.3727$), Gaussian 4-term function yields very good fit ($R^2 = 0.9755$). However, equivalent quality fits have been obtained using the two Fourier ($R^2 = 0.9317$ and 0.9161) and the three successively higher order Polynomial fits ($R^2 = 0.9083$, 0.9694 and 0.9746 , respectively). In case of the sample spectrum resampled to the 5 TIR bandpasses of ASTER, the results reveal interesting insights. The Gaussian 3-term function here gives a good fit ($R^2 = 0.8909$), while an almost perfect fit is attained using Gaussian 4-term function ($R^2 = 0.9916$). The two Polynomial functions (2nd and 3rd order) also provide very good fits ($R^2 = 0.9448$ and 0.9886) respectively). The best fit, however, has been achieved using a Fourier 1st Order function ($R^2 = 0.9924$). This general improvement can be attributed primarily to low spectral sampling and omission of subtle spectral features in the resampled spectrum.

For most practical applications, a fit with R^2 value of 0.9 and above can be considered good. Since above results imply that more than one kind of fit can be used to model the spectrum, a more exhaustive analysis of the variations in the spectral shape becomes necessary to check the stability of the method. Table-7.5 lists the curve-fitting fit values (R^2) for the ASTER TIR resampled emissivity spectra of other rock types in the JHU spectral library as well as the Polynomial 2nd Order model fit for the full resolution spectra. For the various samples, it can be seen that while Fourier 1st Order function in general gives superior fit values, it fails in more than one cases (R^2 (Ijolite) = 0.5724; and R^2 (Pictite) = 0.4503 and 0.4160). Polynomial 2nd Order function provides more consistent results. Gaussian 3-term function gives similar results as obtained for the Polynomial 2nd Order function (for reasons described in previous section).

Linear regression of the various curve-fitting functions explored in this study against the SiO₂ values of the samples in JHU igneous rock spectral library have been summarized in Table-7.6. The main conclusions from the linear regression analysis are outlined as follows:

1. For the full resolution spectra, the linear fit is unacceptable when all samples are used ($R^2 = 0.197$), but improves significantly on omission of two ultramafic samples (dunite and picrite) ($R^2 = 0.747$) (fig. 7.15)
2. For the resampled library spectra, the linear fit for emissivity minima derived using Gaussian 3-term curve-fitting (fig. 7.16) improves significantly (R^2 changes from 0.5407 to 0.8216) on exclusion of 4 samples (2 each of picrite and rhyolite). Similar effects are observed for the linear fit for emissivity minima derived using Polynomial 2nd Order curve-fitting (fig. 7.17), with R^2 improving from 0.5494 to 0.8228 on exclusion of the 4 samples (2 each; picrite and rhyolite).
3. The Fourier function is summarily rejected, since the slope of the linear fit is positive (fig. 7.18), which is against the basic premise of the method that the emissivity minimum progressively shifts to longer wavelengths as the silica content decreases.

From the computing efficiency point of view, a Polynomial function is better than all other functions investigated. The polynomial fit results improve as the order of the function increases, but at the same time the efficiency of the model deteriorates. Polynomial 2nd Order function is the closest to the Gaussian 3-term function explored in previous studies. Also it is stable as well as efficient. For these reasons, it has been selected for use with the 5-band surface emissivity dataset of the study area to calculate the model emissivity minima.

Result: Using these values and applying the linear fit equation ($y = -11.447x + 166.6$) derived from the JHU spectral library data, a silica weight percent image of the study area has been generated, as shown in Figure-7.19. Pixels with negative and unreasonably high SiO₂ values

(above 100% SiO₂; confined to shadowed areas) have been assigned a value of 0 to maintain the color coherence of display. A histogram of the data values within 49-100% for the silica weight percent map generated has been shown in Figure-7.21. Three pixels had negative SiO₂ values, while 32 pixels had values above 97% SiO₂. Over 99.9% of the data has been found to contain SiO₂ values within the range of 49-97% SiO₂ (see fig. 7.21). About 50% of the area has been determined by this technique to contain SiO₂ weight percent of 60.274%; 98.5% data is represented by just three data values (55.017%, 60.274% and 65.530%), which are interpreted to represent the mafic rock bodies (calc-silicates, ortho/para-amphibolites), aolian sands and metapelites, and quartzites, respectively.

It has been concluded that the method is successful so long as the shape of the spectral emissivity curve can be reasonably modeled by the curve-fitting function used. Also, since the empirical relationship used in estimating silica weight percentages for unknown surfaces has been derived from igneous rock spectra, which may not be sufficiently representative of the lithologic diversity contained in a terrain such as the area under investigation, discrepancies due to inaccurate spectral modeling and unrepresentative regression coefficients cannot be ruled out.

7.3.2 The K-value method

A silica content image of the study area has been generated using the MMAJ's original 'K-value' method (MMAJ, 2001; Miyatake, 2002) and applying it on the ASTER L2 surface emissivity data. The K-value has been derived using an empirical approach based on laboratory data of 194 samples including both fresh and weathered rocks and minerals. The following simple linear relationship has been observed between the K-value and the actual SiO₂ weight percent (Miyatake, 2002):

$$SiO_2 (wt\%) = 57.11 + 286.88K \quad (7)$$

The K-value in the above expression is defined as:

$$K = -\log \left\{ \frac{\left(\frac{E_{10} + E_{11} + E_{12}}{3} \right)}{E_{13}} \right\} \quad (8)$$

where E_n is the emissivity for ASTER band n ($10 \leq n \leq 14$).

Using equations 7 and 8 with the ASTER L2 surface emissivity dataset of the study area, a silica weight percent image has been obtained, as shown in Figure-7.20. In this map, red and yellow hues typically correspond to siliceous regions, whereas blues and violets correspond to more mafic surface lithologies. While there is evidently an overestimation of the silica weight percentages for a few pixels confined to areas with deep hill shadows, over 99.91% of the data is represented by SiO_2 weight percent range of 52.2% to 100% and 98.75% of the data is represented by SiO_2 weight percent range of 52.2% to 90% (see data histogram in fig. 7.22). Also, the overestimation, in most part is conveniently within 5%. For minimum values (52.2% SiO_2), the error is well within 1%, since amphibolites, which are the rocks with minimum SiO_2 content in the area, normally contain SiO_2 within 52-56% range.

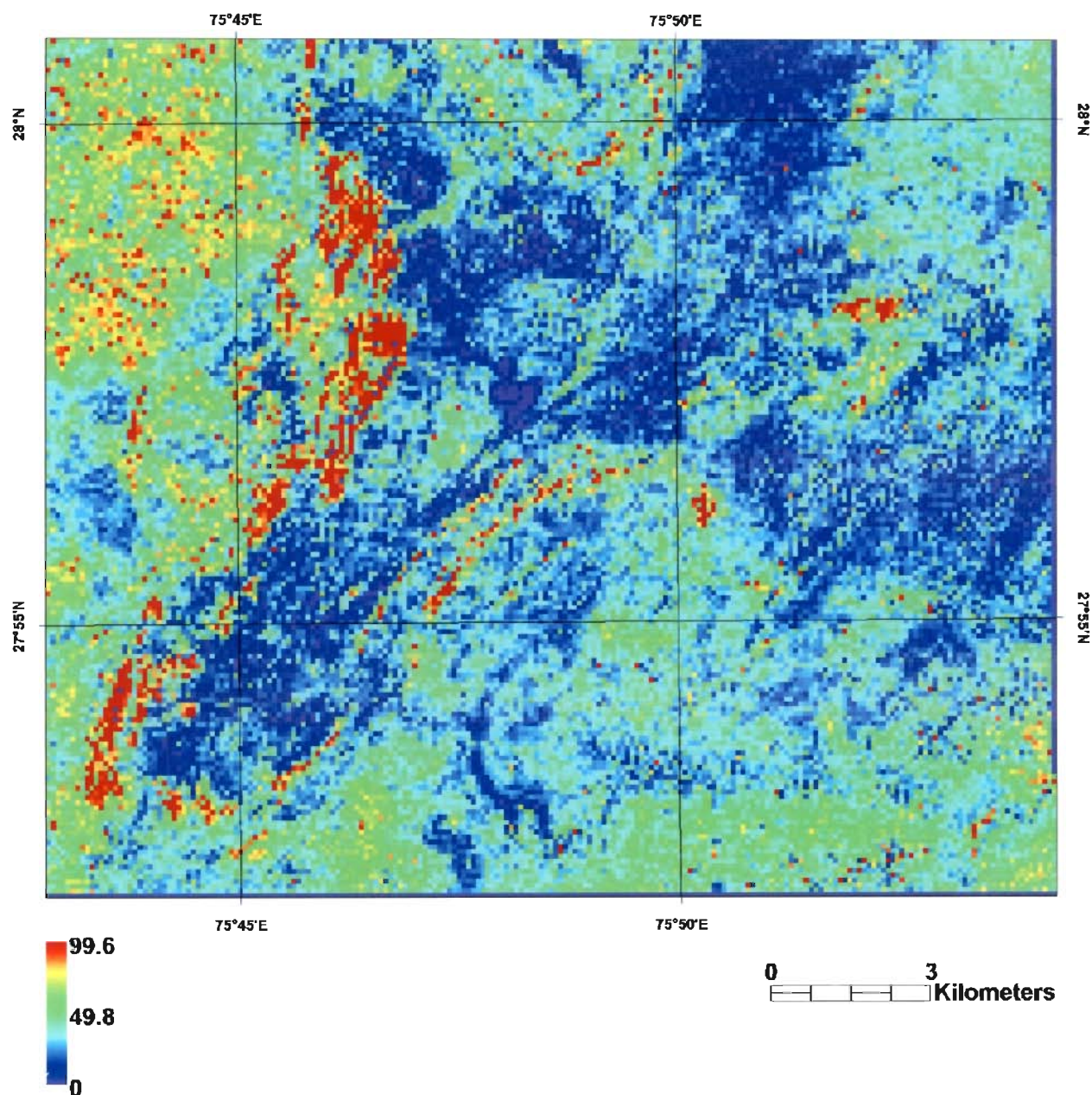


Figure-7.19 SiO₂ weight percent map of the study area generated using spectral modeling of the TIR surface emissivity spectra. The emissivity minimum in the reststrahlen band has been modeled using a Polynomial 2nd Order function. The original 90 m resolution image has been resized to 15 m resolution for a smoothed visualization.

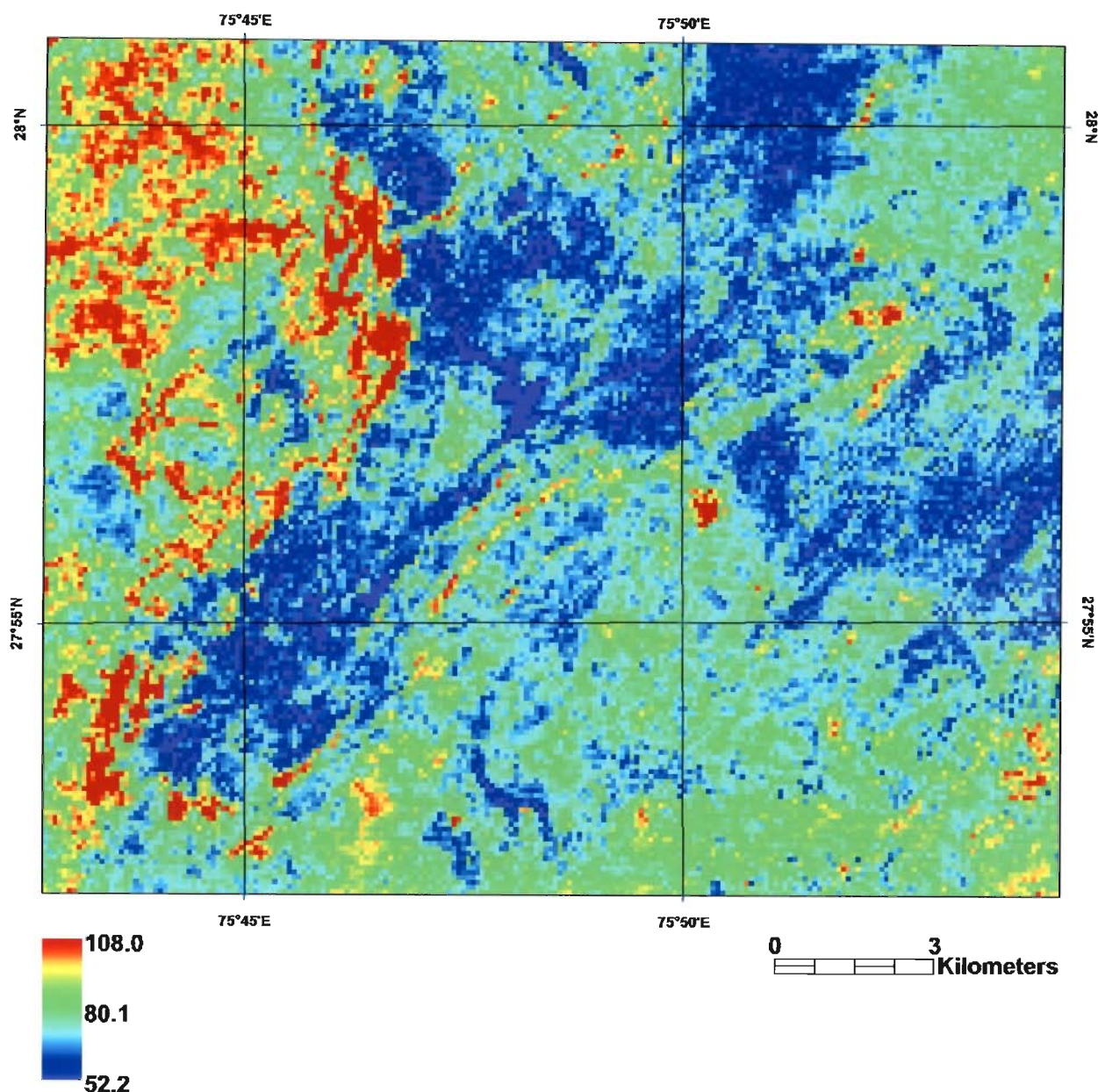


Figure-7.20 SiO₂ weight percent map of the study area obtained using the method proposed by MMAJ (2001). The original 90 m resolution image has been resized to 15 m resolution for a smoothed visualization. Notice the overall correspondence of the silica distribution with the spectral lithological maps obtained through analysis of the ASTER L1B and L2 emissivity data, shown in Figures-7.3, 7.11 and 7.12.

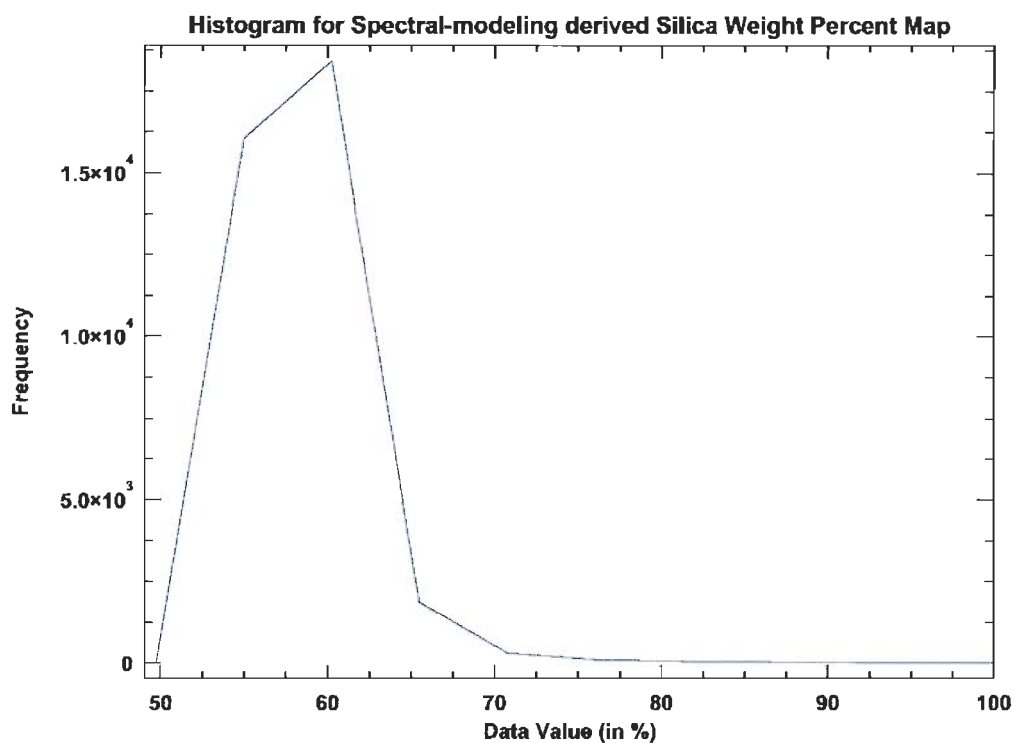


Figure-7.21 Histogram for the silica weight percent map derived through spectral modeling of the ASTER surface emissivity data by Polynomial 2nd Order curve-fitting and application of the empirically derived linear regression fit relation.

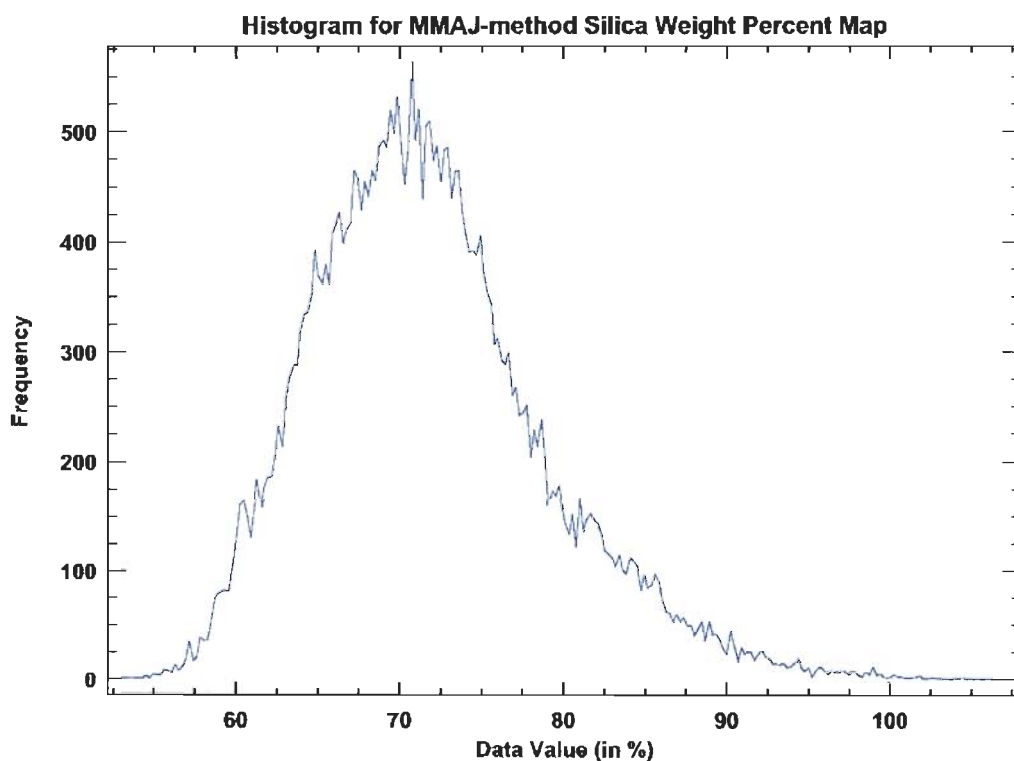


Figure-7.22 Histogram for the silica weight percent map derived using the MMAJ's K-value relationship between ASTER emissivity and silica weight percent for the study area.

7.3.4 Comparison of silica weight percent mapping results

As far as the qualitative distribution of SiO_2 is concerned, there is an overall agreement in the maps generated using the two techniques, with high silica areas shown in hotter colors (hues of red) and low silica areas in colder colors (hues of blue), respectively on the two image maps. It can be readily noticed that the silica content map derived using MMAJ's K-value technique is relatively smoother and more realistic, since the variation of the SiO_2 values in nature is rather gradational than abrupt (see the histograms in Figures 7.21 and 7.22, for the two methods). However, the success of the method based on spectral modeling of the emissivity spectra cannot be undermined. As noted by Hook et al. (2005), the method can be fine tuned to give better results if some laboratory data for the study area are available. It may also be noted for the present study, however, that the data redundancy and discrepancies in the absolute values of SiO_2 for the area could only be inferred from the available geologic information, since laboratory estimates of the actual SiO_2 content for the rocks were not available.

7.4 Note on the effects of spatial resolution, vegetation and surface coatings on ASTER-based lithologic mapping

The mixing of the mineralogic end-members in TIR is linear (Ramsay and Christensen, 1998) and has been utilized to determine the mineralogy of rocks in laboratory (*e.g.*, Hamilton et al., 1997; Ruff, 1998; Feely and Christensen, 1999; Hamilton and Christensen, 2000; Wyatt et al., 2001; Michalski et al., 2004). A number of recent studies using multispectral and hyperspectral data in the TIR range with spatial resolution varying from about 2 m (SEBASS; Vaughan et al., 2005) to about 6 m (MASTER; Hook et al., 2005) and 20 m (TIMS; Michalski et al., 2004) have demonstrated the effect of spatial resolution in addition to spectral resolution on lithologic mapping. Coarse spatial resolution of operational remote sensing data in TIR, such as that of ASTER, makes compositional mapping rather difficult and uncertain due to undesired spectral mixing.

The greatest limitation is posed by the effects of vegetation on spectral emissivity of natural surfaces, more so for the rocks, which even otherwise have low spectral emissivity contrasts. It is known that in TIR the vegetation approximates a black body with a very high emissivity that is invariant with wavelength (Salisbury and D'Aria, 1992). As a result, mixture with vegetation reduces the overall contrast of the mineralogic spectral features within a mixed pixel. The presence of vegetation may non-uniformly shallow spectra and may result in overestimated clay abundance in partially vegetated pixels (Michalski et al., 2004). The same factor is responsible for underestimation of quartz and feldspars, especially quartz – and thereby the SiO₂ weight percentages – for mixed pixels.

Similarly, thin desert varnish (mixed layer clay minerals with subordinate iron and manganese oxides; Potter and Rossman, 1977) coatings on rock surfaces, especially the orthoamphibolites in context of the present study, in an arid environment reduces the reflectance and spectral contrast with features unique to the rock (Rivard et al., 1993).

ASTER VNIR-SWIR Data Processing for Alteration Mapping

8.1 Statement of purpose

Knowledge accumulated from detailed studies of some ‘type’ ore deposits from across the globe has shown beyond doubts that the majority of ore deposits are closely related to their structural setting, host and source rocks, and the types of alteration (hydrothermal or supergene). Many of these factors can be evaluated with large swath remote sensing. The discussion of regional structural and lithological characteristics in Chapter 2 and ground-truth based on field and laboratory data in Chapter 4 suggest a close genetic relationship between the stratigraphy, structure and igneous events in Khetri Copper Belt and accompanying base metal mineralization. Structural complexity and semi-arid climate of the area present a great opportunity for remote investigation of the elements of mineralization outlined above.

One of the main goals of this research is to investigate the utility and capability of spaceborne remote sensing (ASTER data) to characterize the spectral features of alteration zones and host rocks. Structural elements have not been investigated in the present study as such studies have already been undertaken with proven success. Regional lithologic mapping has been successfully accomplished using the ASTER TIR data, as described in detail in Chapter 7. The main emphasis of this chapter is on investigating ASTER’s unique spectral coverage in the solar reflective SWIR region, where the characteristic spectral features of most alteration minerals occur, in conjunction with the three solar reflective VNIR channels, for mapping of characteristic alteration minerals and assemblages. The work presented here is the outcome of an attempt to exhaustively evaluate the processing techniques – both simple and advanced – to differentiate, identify and map the alteration mineralogy in the study area.

8.2 Spectral characteristics of target alteration minerals

In this section the spectral characteristics of the alteration minerals commonly reported from the study area have been reviewed to aid in the extraction of the spectral information contained in ASTER VNIR-SWIR surface reflectance data, as discussed in the following sections.

Based upon the ground-truth information collected from literature (Chapter 2), and fieldwork and laboratory analyses of rock samples (Chapter 4), a list of alteration minerals associated with mineralization and/or weathering of exposed rock surfaces in the study area has been compiled. Many of these minerals are characteristic of hydrothermal systems associated with igneous events, especially those of epithermal precious metal deposits and porphyry base metal deposits typical of the island arc environments. Others are related to physical and chemical processes of sub-aerial weathering. It must be remembered, however, that the discrimination of the type of alteration, and its relationship with, and utility for, mineralization is purely upon the interpretation of the expert geologist, since remote sensing simply provides the ‘evidence of occurrence’ of a specific mineral in the area of interest.

Table-8.1 provides an overview of the main spectral features (absorption bands) of these alteration minerals within the wavelength range 0.4-2.5 μm , since ASTER VNIR-SWIR bands cover this region. Figure-8.1 shows the laboratory spectral curves of these minerals, and the same spectra resampled to the 9 VNIR-SWIR bandpasses of ASTER. Figure-8.2 shows the continuum-removed spectra of these minerals in full resolution and resampled modes, respectively. The electronic processes, such as crystal field and charge transfer effects in the VNIR (for Fe^{2+} and Fe^{3+} ions) and molecular vibrational processes at frequencies corresponding to the SWIR wavelengths are the chief causes of these spectral features. The details of these processes have been discussed previously in Chapter 5.

Table-8.1 Spectral characteristics of the reflectance spectra of some target alteration minerals in the wavelength range 0.4-2.5 μm . HS/LS => high/low sulfidation

Alteration mineral (or mineral group)	Principal alteration category	Diagnostic absorption bands (μm)
Sericite (muscovite)	Sericitic or Phyllic (with associated quartz) (LS)	2.205 (strong)
Clay minerals (Kaolinite, montmorillonite/smectite, illite)	Argillic and advanced argillic (HS/LS)	For kaolinite: 2.165 and 2.21 doublet (strong, main) For smectite/montmorillonite: 2.215 (main) For Illite: 2.205 and 2.345
Alunite	Advanced argillic (alunitic) (LS)	1.764; 2.165 (main) ; 2.325
Biotite	Potassic (with associated K-feldspar or adularia)	1.20 (broad); 2.335 and 2.400 doublet (weak)
Calcite/dolomite	Carbonatization	For calcite: Two weak bands centered at 1.875 and 2.000; 2.335 (strong); 2.528 (strong) For dolomite: Two weak bands centered at 1.855 and 1.985; 2.315 (strong); 2.496 (strong)
Chlorite group	Propylitic (with some epidote and actinolite)	0.706 (broad, weak); 1.985 (broad, strong); 2.255 and 2.325 doublet (main)
Scapolite (meionite – marialite series)	Scapolitization	2.225 and 2.325 (weak)
Albite	Albitic	2.195 (main, weak)
Limonite group (goethite, hematite, jarosite)	Weathering	For goethite: 0.485 (narrow, strong); 0.970 (broad, strong); 2.400 (weak) For hematite: 0.539 (strong); 0.871 (strong) For jarosite: 0.4338 (narrow, weak); 0.930 (broad); 2.215 and 2.265 doublet (narrow, main)

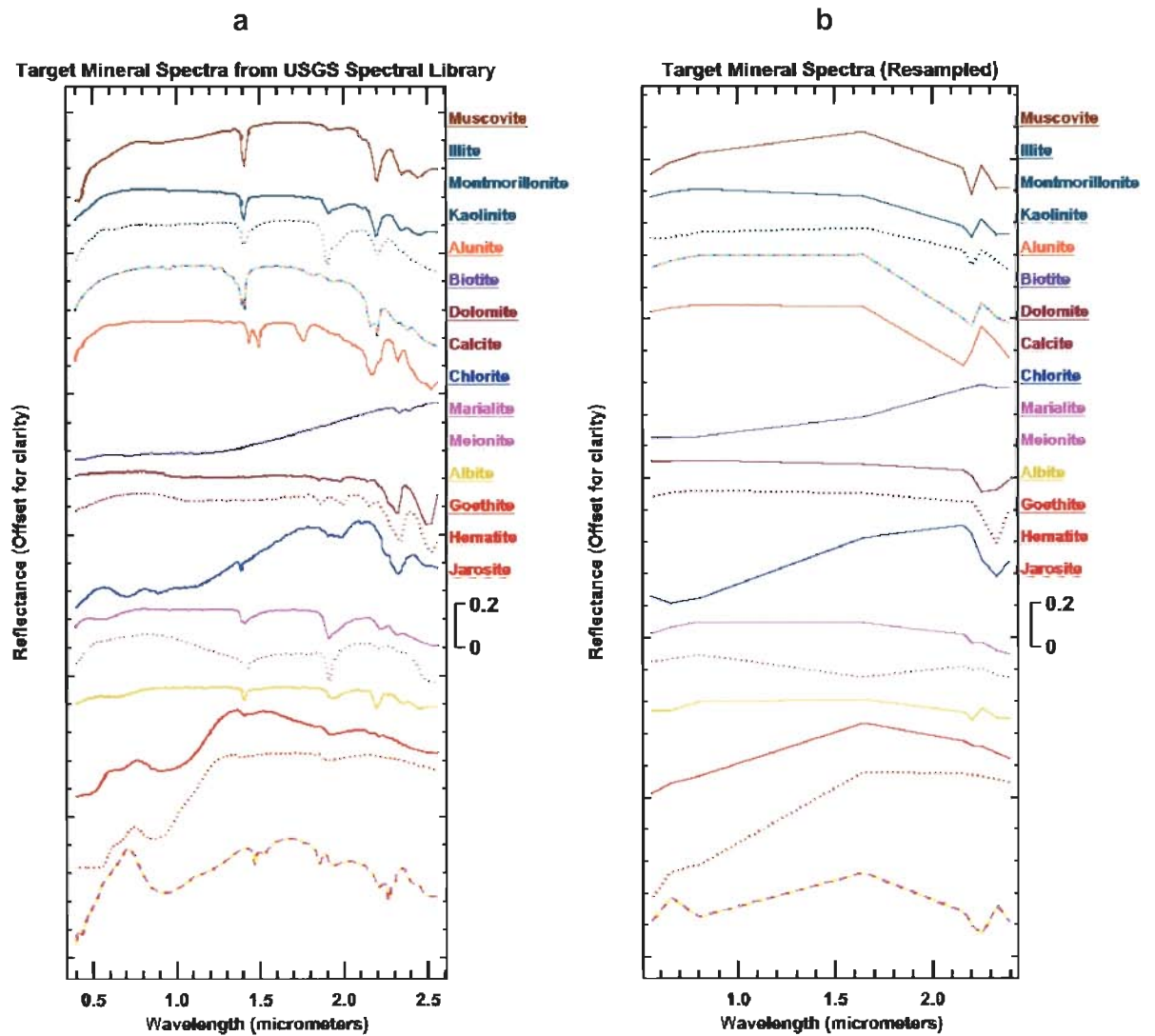


Figure-8.1 a. USGS library spectra of some key alteration minerals; b. the same spectra convolved to the ASTER VNIR-SWIR bandpasses.

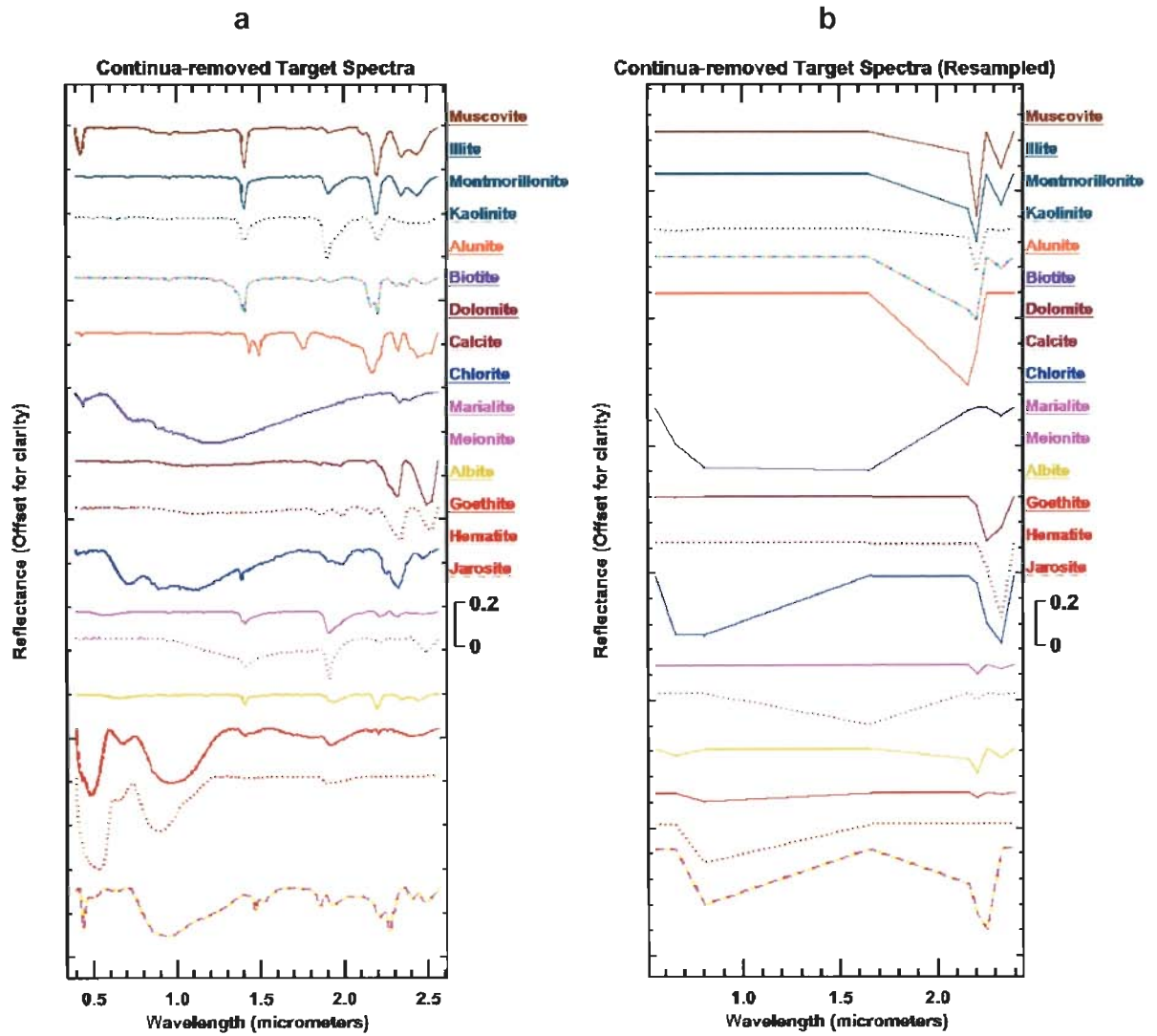


Figure-8.2 a. Continua-removed USGS library spectra of some key alteration minerals; **b.** the same spectra are shown convolved to the bandpasses of the 9 VNIR-SWIR bands of ASTER.

Discussion: From Figures-8.1 and 8.2 it can be readily observed that though valuable spectral information existing in the full resolution laboratory spectra is lost upon resampling to lower spectral resolution ASTER VNIR-SWIR bandpasses, important absorption features (spectral signatures) remain well-preserved even in the resampled spectra. Spectral band positions and relative depths are represented better in continua-removed spectra than that in the normal spectra. Also, it can be noticed that for minerals with similar spectral signatures (*e.g.*, illite and muscovite) in SWIR there is a greater possibility (almost inevitability) of ambiguous identification when the resampled spectral data is used. Differences between such spectra exist in the VNIR region (below 0.56 μm), but unfortunately there is no band in ASTER dataset in that wavelength region. Therefore, ambiguity in the identification of certain such minerals is quite likely when data from SWIR region alone is used. Withal, ASTER's special capabilities for unique alteration mineral identification owing to strategic placing of its SWIR channels have much to gain from, as is shown in the following sections.

8.3 ASTER VNIR-SWIR surface reflectance data processing

The atmospherically and topographically corrected 9-band VNIR-SWIR surface reflectance data have been variously digitally processed to highlight the zones of alteration, and to identify unique mineral constitution of the surfaces in the study area. The processing flow has been designed such that it hierarchically grows from a simple level of processing involving image enhancement and color display of 3-band composites, to image transformation (DCS, PCA and DPCS), band ratioing and spectral indices, logical operator-based band modeling, and finally to advanced spectral processing and image classification methods. These techniques and the results derived hence have been described in the following sections.

8.3.1 Band composites

Instruments that measure radiance in the VNIR-SWIR wavelength region offer the ability to begin image analysis by displaying images in color by assigning individual bands to the red, green and blue color in creating 3-band color composite images. This allows rapid basic preliminary image interpretation before having to analyze the full spectral dimensionality of the dataset.

The number of possible distinct 3-band RGB combinations of the 9 VNIR-SWIR bands is 84 (${}^nC_r = n!/(r!(n-r)!)$; $n=9$, $r=3$). Although the information from spectral curves of the materials can be used to select the appropriate band combinations, for an area without any firsthand information the wide range of spectral diversity restricts this approach. To overcome this difficulty, a statistical band selection technique called the Optimum Index Factor (OIF; Chavez et al., 1982) method has been used. The OIF ranks all possible RGB color combinations of multispectral remote sensing data on the basis of the total variance within the bands and the between-band correlations (Chavez et al., 1982; Chavez and Bowell, 1984). Higher OIF values indicate superior spectral contrast in the band-composite used. Mathematically, the OIF is expressed as follows:

$$OIF = \frac{\sigma_K + \sigma_L + \sigma_M}{|r_{KL}| + |r_{KM}| + |r_{LM}|} \quad \dots(1)$$

Where: $\sigma_{K/L/M}$ are the standard deviations for the three bands K, L, and M; and $|r_{KL/KM/LM}|$ are the absolute values of the correlation coefficients between bands K & L, K & M and L & M, respectively.

Applying OIF technique to the 20 distinct combinations of the 6-band SWIR, and 84 distinct band combinations of the 9-band VNIR-SWIR combined surface reflectance datasets, the best OIF values in RGB scheme were found to correspond to 4-6-8 (for SWIR data alone) and 6-3-1 (for VNIR-SWIR combined data) composites. Figure-8.3a-b shows these two band

composites. The images have been linearly stretched to bring about the full color contrast. Strong absorption of Fe-O bearing surfaces in band 1, strong reflectance of green and healthy vegetation in band 3, overall high rock reflectance in band 4, strong absorption by hydroxyl-bearing minerals/rocks and vegetation in band 6, and by carbonates/chlorite in band 8 form the spectral bases behind the distinct litho/mineralogic information content of these band-composites.

In SWIR band-composite 4-6-8 (fig. 8.3a), red-pink hues indicate regions with prominent OH⁻ absorption (*e.g.*, micaceous and clayey rocks), while green shades indicate areas dominated by Mg-OH bearing rocks (carbonates and chlorite). The overall dark tones represent phyllite and schist bearing regions having low albedo and absorption for both OH⁻ and chlorite. The peak quartzites and alluvium with high albedo and absence of these constituents appear in bright shades. Vegetation appears in dark colors due to general OH⁻ absorption.

Band composite 6-3-1 helps distinguish areas with vegetation from regions having OH⁻ and Fe-O absorption. Also, the superior spatial resolution of the VNIR bands (15 m) aids in highlighting the structural complexity of the area. On this image (fig. 8.3b), the iron-bearing surfaces have been prominently displayed in deep shades of red, OH-bearing surfaces have been displayed in blue shades and the healthy chlorophyll-dominant vegetation in bright green colors. The intermediate colors represent mixtures of these categories. Bright colors represent sandy soils, desert sands and quartzites, whereas metapelites again appear in dark tones. The main shear zone on this image appears in light blue-cyan colors whereas the amphibolites (chloritic surfaces) and carbonates appear in bright magenta shades. Many smaller bodies of these rocks are shown more clearly than on the 4-6-8 composite, primarily due to better spatial resolution.

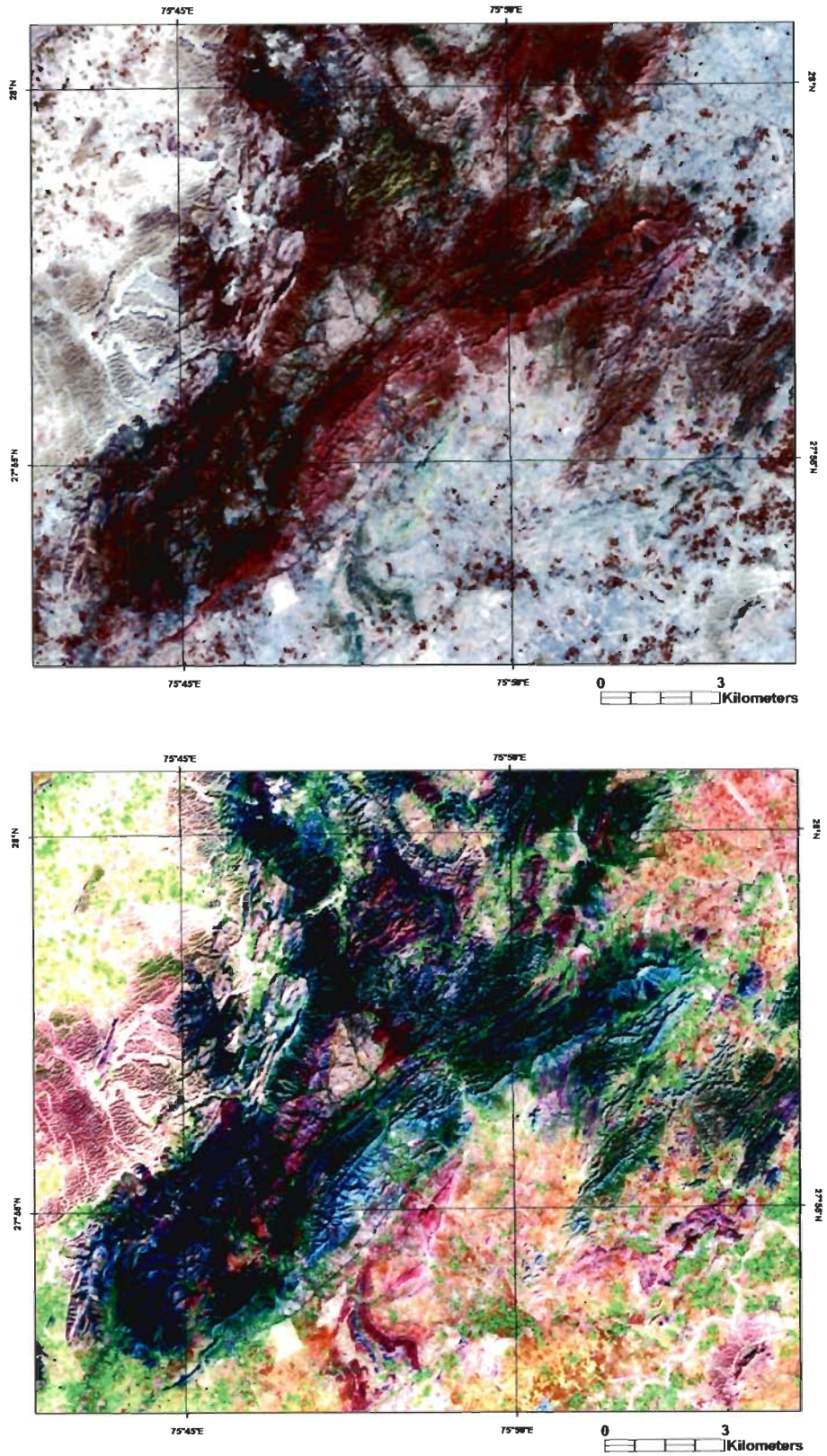


Figure-8.3 RGB FCCs with maximum spectral information: a. SWIR FCC 4-6-8; b. VNIR-SWIR FCC 6-3-1.

8.3.2 Decorrelation stretch images

As with the image data in TIR (Chapter 7), the SWIR data also suffer from high band-to-band correlation resulting in low spectral contrast between bands. To overcome this problem, the decorrelation stretch (DCS) procedure (described in Chapter 7) has also been applied to select RGB combinations of the 6 SWIR bands to highlight zones of alteration representing specific spectral absorption features. Two DCS band composites, *viz.* 4-6-8 and 5-7-9, have been found to display the most useful and explicit spectral information.

Figure-8.4 shows the DCS composite 4-6-8. The scan-blurring defects in ASTER SWIR due to filter scratch (for details see Appendix D; Iwasaki and Oyama, 2005) appear rather exaggerated on the DCS image, as indicated by white arrows. The DCS images exhibit the real value of ASTER SWIR data and the power of DCS technique, as with just a simple image enhancement important spectral information has been highlighted. Subtle color contrasts on simple band composites appear prominently on DCS images (for example compare the normal FCC 4-6-8 in fig. 8.3a with DCS 4-6-8 in fig. 8.4). On DCS 4-6-8, further distinction between surfaces with similar spectral signatures can be made. Carbonate rocks appear in lighter green to yellow hues since they lack the subtle Fe-O absorption feature in band 4, whereas amphibolites with chlorite-rich surfaces appear in relatively darker green shades. The main Babai-Taonda shear zone stands out prominently in bright red-pink colors. Dark blue colors on DCS image primarily exhibit shadows due to low sun angle and rugged topography, and for flat areas and well-lit slopes, it represents Fe-O-rich surfaces.

8.3.3 Band ratios, RBD images, and ratio composites

A division of numerical values in one band by those in another, pixel by pixel is called a band ratio. It is the oldest and the most widely used technique in discriminating surface cover types in a multi-band image dataset by suppressing the proportionally constant radiance values in the bands and enhancing the differences. Rowan et al. (1974) were the first to show with Landsat-1 MSS data of Silver Bell porphyry copper deposit area that a composite of ratios MSS1/MSS2, MSS2/MSS3 and MSS3/MSS4 in BGR provides a powerful means for discriminating hydrothermally altered areas from regional rock and soil units. The above approach has been adapted for various subsequent types of passive remote sensing data in solar reflective region, including ASTER.

Relative absorption Band Depth (RBD) images are a modification of the normal band ratios, as a three-point ratio formulation (fig. 8.5). RBD images are determined for individual absorption features by calculating ratios where the numerator is the sum of the neighboring bands of the central band (denominator) where the absorption feature occurs. The underlying concept for RBD is the removal of the continuum to improve the intensity of the absorption feature (Crowley et al., 1989). However, spectrally uncalibrated data can lead to results that are difficult to interpret (Crippen, 1988). Also, the terrain illumination differences due to topography can produce color variations in unadjusted ratio images for spectrally identical surface materials (Crippen, 1988; Crippen et al., 1988).

A number of band ratios and RBD indices have been proposed for ASTER (*e.g.*, Rowan and Mars, 2003). There are virtually limitless permutations and combinations in which the 9 VNIR-SWIR bands of ASTER can be ratioed and used together as color ratio composites (CRCs), which suit specific requirements. Specifically for alteration mineral mapping, a list of some of the most useful band ratios and RBD's has been compiled, as shown in Table-8.2. Table-8.3 lists some of the CRCs that display specific geologic information better.

Table-8.2 Useful band ratios and RBDs for alteration mapping using ASTER VNIR-SWIR data.

Alteration feature	Band ratio or RBD	Comments
Ferric iron, Fe ³⁺	$\frac{AST_2}{AST_1}$	Highlights general iron absorption in band 1
Ferrous iron, Fe ²⁺	$\frac{AST_5}{AST_3} + \frac{AST_1}{AST_2}$	
Laterite	$\frac{AST_4}{AST_5}$	High reflectance of Fe, Al-O in band 4
Gossan	$\frac{AST_4}{AST_2}$	Fe-O species-independent ratio
Ferrous silicates (biotite, chlorite, amphiboles)	$\frac{AST_5}{AST_4}$	Fe-O Cu, Au alteration
Ferric oxides (limonitic surfaces)	$\frac{AST_4}{AST_3}$	Can be ambiguous
Carbonate/chlorite/epidote	RBD8 = $\frac{AST_7 + AST_9}{AST_8}$	
Epidote/chlorite/amphibole	$\frac{AST_6 + AST_9}{AST_7 + AST_8}$	Useful to delineate endoskarn alteration
Amphibole/Mg-OH	$\frac{AST_6 + AST_9}{AST_8 + AST_8}$	Can confuse Mg-OH with carbonate
Amphibole	$\frac{AST_6}{AST_8}$	
Dolomite	RBD7 = $\frac{AST_6 + AST_8}{AST_7}$	Useful to distinguish dolomite from calcite
Sericite/muscovite/illite/smectite	RBD6 = $\frac{AST_5 + AST_7}{AST_6}$	Useful to delineate phyllic alteration
Alunite/kaolinite/pyrophyllite	RBD5 = $\frac{AST_4 + AST_6}{AST_5}$	Useful for argillic alteration mapping
Phengite (high SiO ₂ muscovite)	$\frac{AST_5}{AST_6}$	Phyllic alteration
Muscovite	$\frac{AST_7}{AST_6}$	Phyllic alteration
Kaolinite	$\frac{AST_7}{AST_5}$	Argillic alteration in granitic terrain
Clay minerals	$\frac{AST_5 \times AST_7}{(AST_6)^2}$	General formulation for OH-absorption by clays
Hydroxyl alteration	$\frac{AST_4}{AST_5}$	Approximation of TM5/TM7
Host Rock	$\frac{AST_5}{AST_6}$	

Table-8.3 Some useful color ratio composites for alteration mapping using ASTER VNIR-SWIR surface reflectance image data.

Feature	Display color		
	Red	Green	Blue
Al-OH minerals/ advanced argillic alteration	AST_{-5}/AST_{-6}	AST_{-7}/AST_{-6}	AST_{-7}/AST_{-5}
Clay, amphibole, laterite	$(AST_{-5} \times AST_{-7}) / (AST_{-6})^2$	AST_{-6}/AST_{-8}	AST_{-4}/AST_{-5}
Gossan, alteration, host rock	AST_{-4}/AST_{-2}	AST_{-4}/AST_{-5}	AST_{-5}/AST_{-6}
General lithologic discrimination	AST_{-4}/AST_{-7}	AST_{-4}/AST_{-1}	$\frac{AST_{-2}}{AST_{-3}} + \frac{AST_{-4}}{AST_{-3}}$
General discrimination	AST_{-4}/AST_{-7}	AST_{-4}/AST_{-3}	AST_{-2}/AST_{-1}

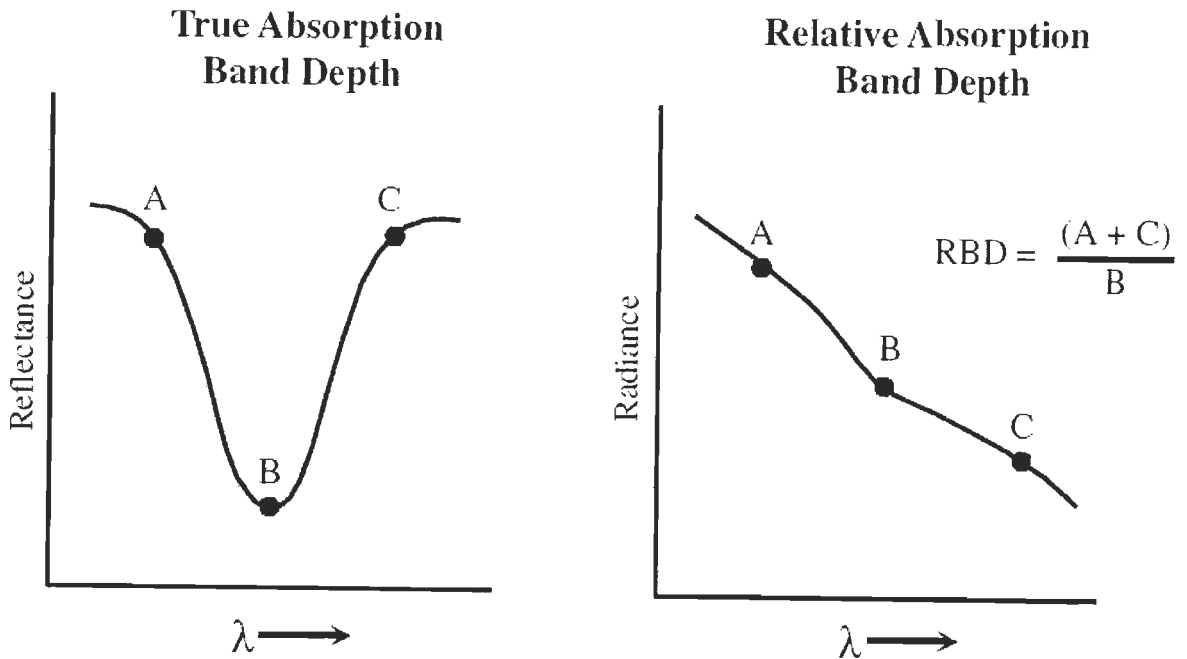


Figure-8.5 Relative Band Depth (RBD) ratio schematic (modified after Crowley et al., 1989).

Band ratios and RBDs with the most useful information content regarding the alteration in the study area have been shown in Figure-8.6. Color ratio composites with best alteration discrimination have been shown in Figure-8.7. Descriptions have been provided in the captions.

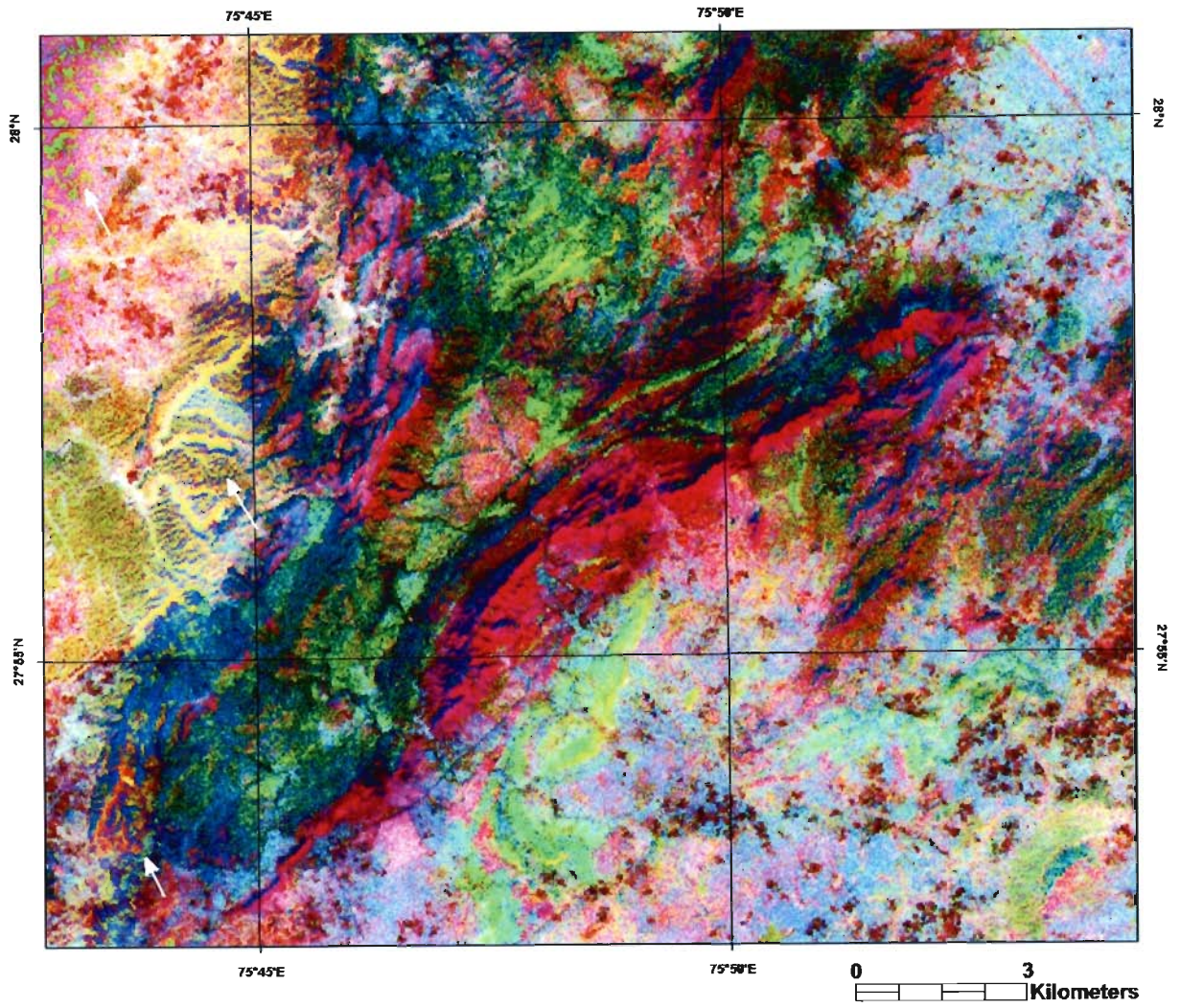


Figure-8.4 Decorrelation stretch color composite of SWIR band 4-6-8 highlighting spectral information for specific mineralogy classes.

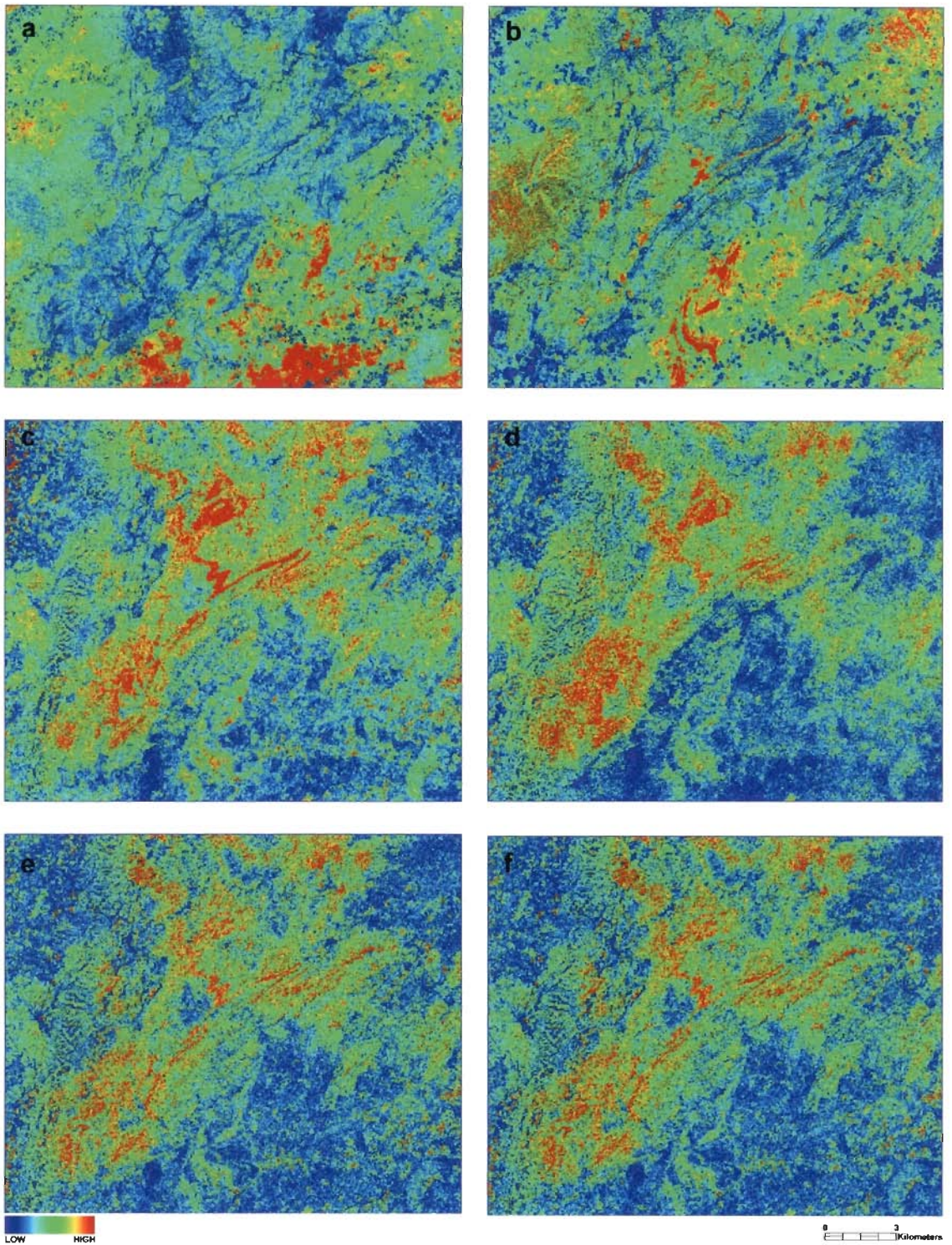


Figure-8.6 Some band-ratio results for the study area: a. ferric iron $2/1$; b. ferrous iron $(5/3)+(1/2)$; c. amphibole, $6/8$; d. epidote, chlorite, amphibole, $(6+9)/(7+8)$; e. Mg-OH $(6+9)/(8+8)$; f. carbonate, chlorite, epidote $(7+9)/8$. The color ramp shows the relative concentrations of the individual surface constituents mapped on ratios.

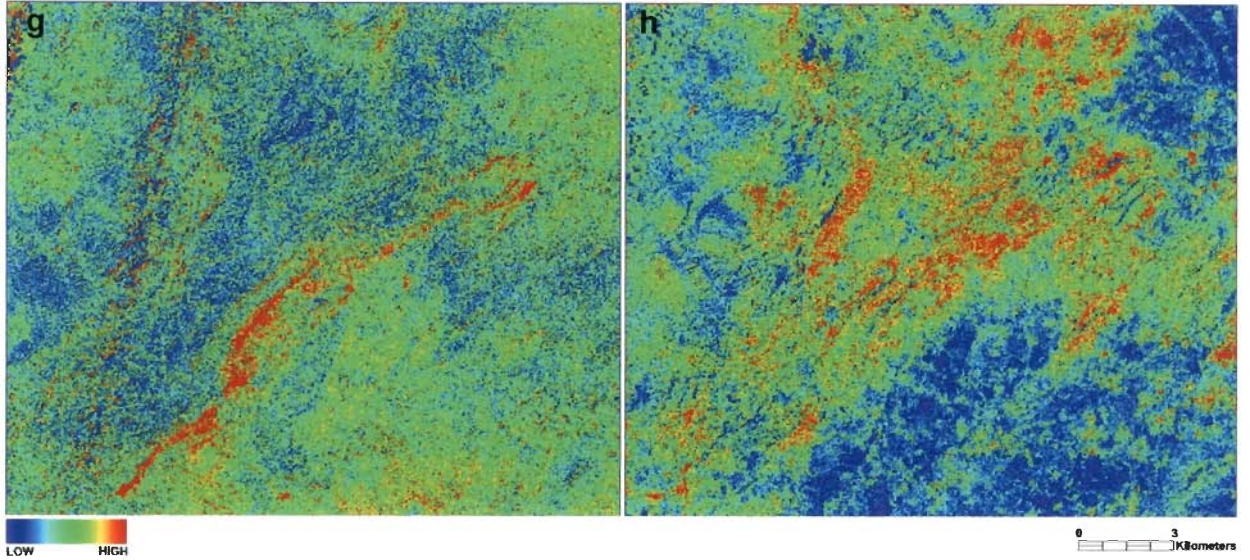


Figure-8.6 (contd...) g. sericite/muscovite/illite, $(5+7)/6$; h. alunite/kaolinite/pyrophyllite, $(4+6)/5$; the color ramp shows the relative concentrations of the surface constituents mapped on the individual ratios.

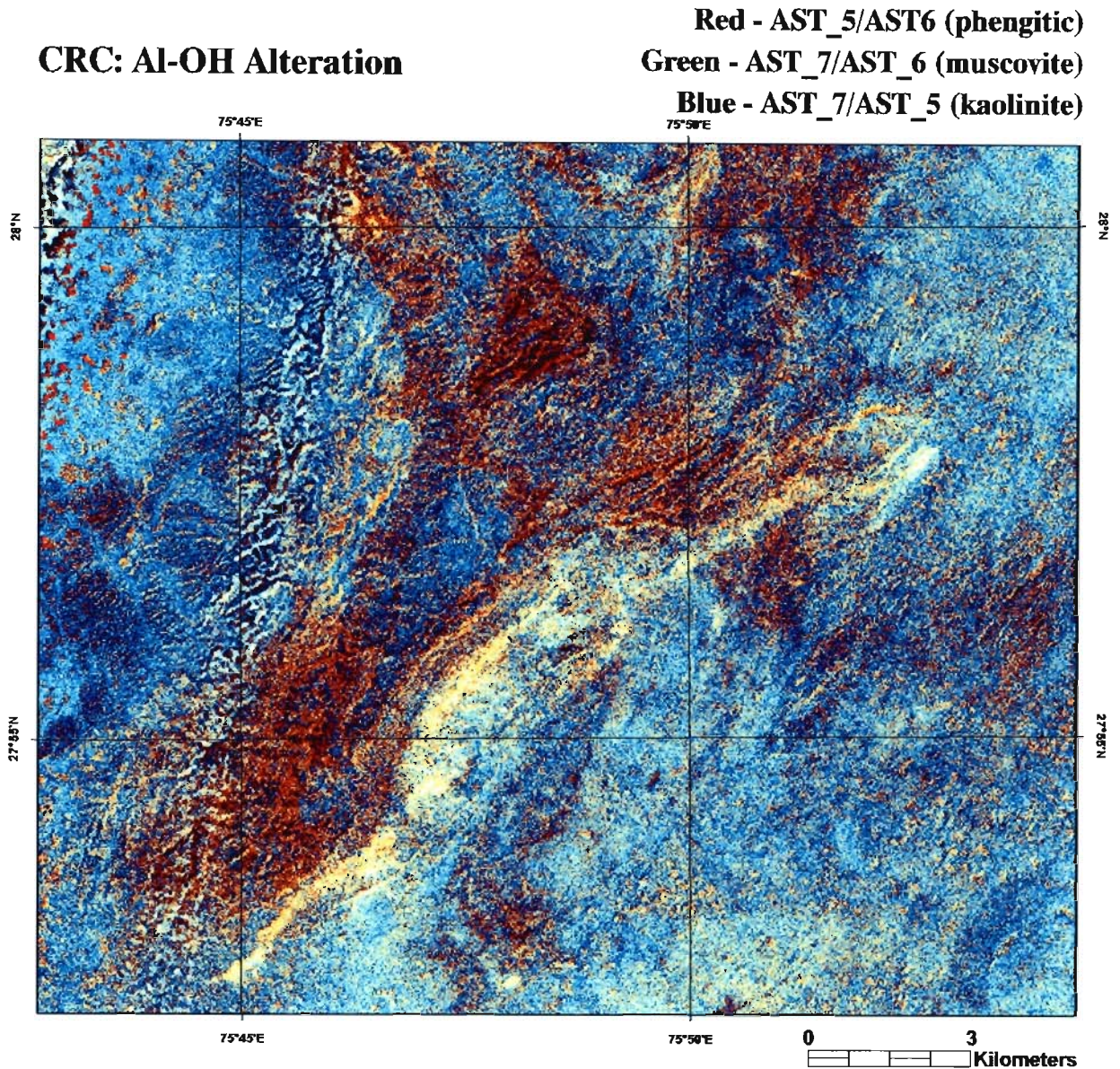


Figure-8.7 Color ratio composite (CRC) of band ratios for phengitic/sericitic, and kaolinitic alteration in the study area; it can be seen that these minerals, which are typical of phyllic and argillic alteration, are concentrated broadly along the main NE-SW trending cataclastic/shear zone, and appear in light yellow-white colors. The same colors can also be seen for Chandmari (north), about 6km due east of Khetri, and about 3km southeast of Babai, and indicate alteration related to possible mineralization in these pockets.

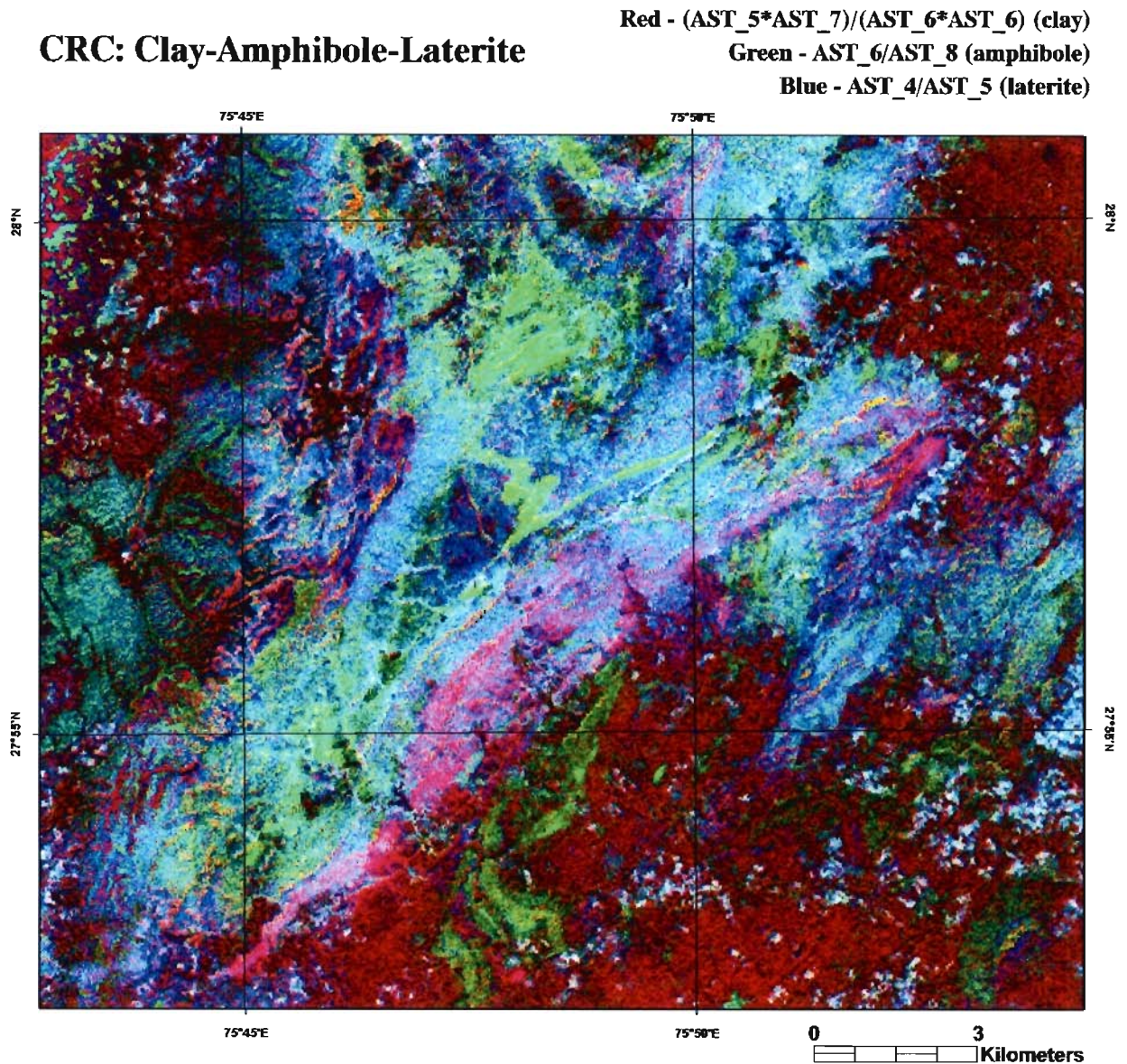


Figure-8.8 CRC of band ratios highlighting, in respective colors, the concentrations of clay minerals (red), amphiboles (green), and lateritic regolith (blue). The pink colors, as with the CRC in fig. 8.7, have been mapped primarily along the main cataclastic/shear zone. Amphibole-rich rocks/surfaces appear in bright green, while the lateritic surfaces in blue-cyan colors. However, there is an ambiguity in mapping of the lateritic surfaces with vegetation. Also, the general concentration of the clay minerals in the soils of the eastern plains has been brought out on this CRC. Notice also the yellow-red pocket towards the north in what is now the abandoned open-cast Chandmari mine and adjacent overburden dumps of mainly altered andalusite schist and phyllite, with banded amphibole quartzites.

8.3.4 PCA and FPCS processing for alteration mineral mapping

Most of the variation of radiant spectral flux measured by a sensor depends on topographic shading and albedo effects at the surface. Principal Components Analysis (PCA) is a powerful statistical technique that can be used to suppress irradiance effects that dominate all bands, therefore enhancing spectral reflectance features of geologic materials (Crósta et al., 2003). Feature Oriented Principal Component Selection (FPCS, Crósta and Moore, 1989) is a modification of PCA. In FPCS the PC Transformation (PCT) is performed for a select combination of bands in a multispectral dataset such that a relationship between the spectral responses of the target materials and the numeric values extracted from the eigenvector matrix used to calculate the PCs is established. Loughlin (1991) modified the FPCS technique for specific use with Landsat TM data, and proposed specific combinations of TM bands which ensured that certain materials (*e.g.*, vegetation) were not mapped and that the target materials were mapped on individual PCs. This approach has been applied successfully for mineral exploration in favorable sites using Landsat TM data (*e.g.*, Bastianelli et al., 1993; Davidson et al., 1993; Ruiz-Armenta and Prol-Ledesma, 1998; Carranza and Hale, 2002).

Crósta et al. (2003) suggested 4-band subsets for the nine ASTER VNIR-SWIR bands for use with the FPCS technique to uniquely map abundances of alunite (ASTER bands 1-3-5-7), illite (ASTER bands 1-3-5-6), kaolinite+smectite (ASTER bands 1-4-6-9) and kaolinite (ASTER bands 1-4-6-7) minerals. The spectral subsets were selected according to the position of characteristic spectral features of these alteration minerals. The method comprised of applying PCT to these band combinations separately, and examining the eigenvector matrices. The principal component band having highest numeric values for input bands containing the diagnostic spectral feature for the target material, but with opposite signs (+/-) is inferred to represent the abundance of that material.

In the present study, PCT has been performed on the combined ASTER VNIR-SWIR surface reflectance dataset. Examination of the eigenvector matrix for all 9 bands shown in Table-8.4 suggests that the PCs 7, 6 and 4 carry maximum information related to alteration minerals. An RGB color composite of PC7-PC6-PC4 is shown in Figure-8.9. On this color composite the carbonate/chlorite-clay-Fe-O-rich surfaces are displayed in shades of red and orange, since PC7 has maximum loadings from bands 5, 9 and 2 (and negative loadings from bands 8 and 6), in that order. PC6 displays amphibole-mineral rich surfaces in green, since it has maximum positive contribution from bands 5 and 6, and negative contribution from bands 9 and 8, in that order. PC4 shows the hard rocky surfaces with overall high reflectances in band 4, as it receives highest loadings from band 4 and low contributions from all remaining bands.

FPCS analysis has also been carried out for the four target minerals using ASTER band selections proposed by Crósta et al. (2003). The respective eigenvector matrices for the target alteration minerals have been shown in Table-8.5. In each case, the target mineral is mapped prominently on the PC4, as indicated by highest eigenvector loadings for the bands containing the characteristic spectral features with opposite signs (+/-) for the respective minerals. For example, the main absorption feature of alunite occurs at band 5, with high reflectances in adjacent bands 4 and 7. In FPCS processing of bands 1, 3, 5 and 7 targeting this mineral, examination of the eigenvector matrix shows maximum numeric difference for bands 5 and 7 in PC4. The results of the FPCS analysis have been shown as abundance images for individual minerals in Figure-8.10a-d. The main contrasting eigenvector loadings have been shown in bold letters. For minerals with similar spectral signatures (such as illite and muscovite), the abundance images show concentrations of the ambiguous minerals together. However, the main advantage of this technique is that with a relatively simple and robust processing, important spectral classes can be easily mapped.

Table-8.4 Eigenvector matrix of PCT of 9-band ASTER VNIR-SWIR dataset

Eigenvector	Band 1	Band 2	Band 3	Band 4	Band 5	Band 6	Band 7	Band 8	Band 9
PC 1	0.135407	0.234077	0.215003	0.355756	0.380139	0.383106	0.394079	0.405155	0.378628
PC 2	0.311811	0.347419	0.78755	0.114793	-0.15878	-0.1508	-0.16989	-0.19817	-0.18049
PC 3	0.458286	0.704428	-0.48208	-0.21998	-0.07781	-0.04208	-0.05604	0.017884	0.040927
PC 4	0.15742	-0.04399	-0.31186	0.834302	0.002415	0.07717	-0.1635	-0.33419	-0.18864
PC 5	0.344642	-0.28783	0.045433	-0.1427	-0.03978	0.293718	-0.4127	-0.29854	0.654714
PC 6	0.289582	-0.14072	0.014737	-0.30338	0.554224	0.356795	0.17675	-0.35706	-0.45923
PC 7	-0.4016	0.298572	0.009721	0.01117	0.461948	-0.37478	0.06757	-0.52103	0.34564
PC 8	-0.49516	0.339219	0.036487	-0.03671	0.07581	0.542826	-0.55409	0.079575	-0.15266
PC 9	-0.20131	0.139623	0.012959	-0.04399	-0.54437	0.417224	0.522317	-0.43607	0.06702

Table-8.5 Eigenvector matrices for the four target alteration minerals for the study area. For all target minerals, the abundances are displayed in PC4 image

<i>FPCS: ALUNITE</i>				
Eigenvector	ASTER Band 1	ASTER Band 3	ASTER Band 5	ASTER Band 7
PC1	0.482047	0.473477	0.521456	0.521089
PC2	0.345923	0.670186	-0.462078	-0.466553
PC3	-0.804964	0.571543	0.113576	0.111677
PC4	0.000139	0.003011	-0.708285	0.705920
<i>FPCS: ILLITE</i>				
Eigenvector	ASTER Band 1	ASTER Band 3	ASTER Band 5	ASTER Band 6
PC1	0.482959	0.472707	0.520558	0.521841
PC2	0.299682	0.701692	-0.460366	-0.453743
PC3	-0.822470	0.533000	0.156730	0.122028
PC4	-0.022030	0.009367	-0.701796	0.711975
<i>FPCS: KAOLINITE-SMECTITE</i>				
Eigenvector	ASTER Band 1	ASTER Band 4	ASTER Band 6	ASTER Band 9
PC1	0.456898	0.512167	0.515042	0.513479
PC2	0.888465	-0.223367	-0.288726	-0.278162
PC3	0.040718	-0.811611	0.242758	0.529810
PC4	-0.014703	0.170527	-0.769700	0.615034
<i>FPCS: KAOLINITE</i>				
Eigenvector	ASTER Band 1	ASTER Band 4	ASTER Band 6	ASTER Band 7
PC1	0.455275	0.513282	0.515450	0.513398
PC2	0.888505	-0.212208	-0.273055	-0.301608
PC3	0.055578	-0.828892	0.329355	0.448747
PC4	0.013960	0.066690	-0.742480	0.666394

PCA: 9-band ASTER VNIR-SWIR Dataset

**Red - PC7
Green: PC6
Blue - PC4**

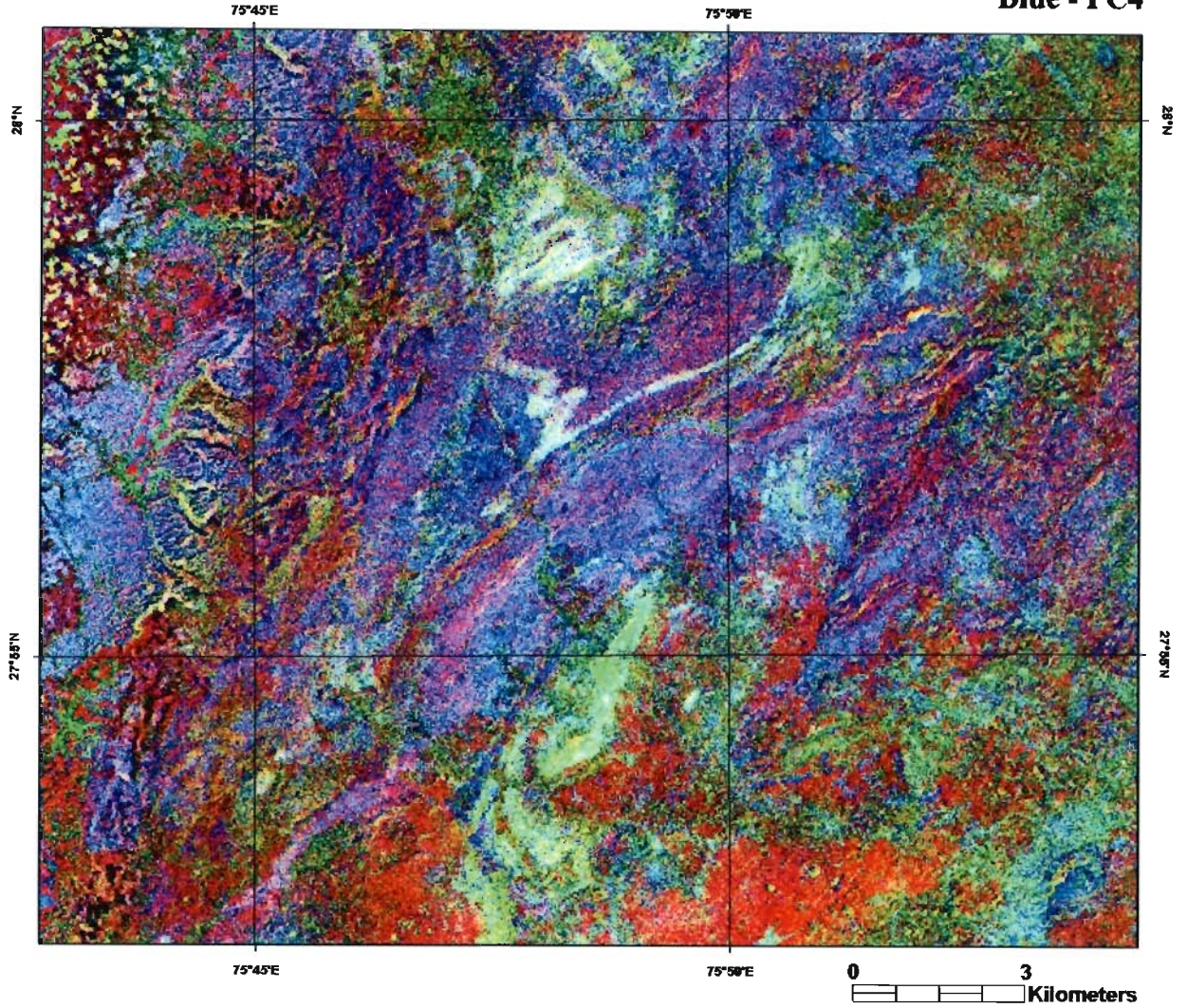


Figure-8.9 Color composite of PC7-PC6-PC4 in RGB; see the text for description.

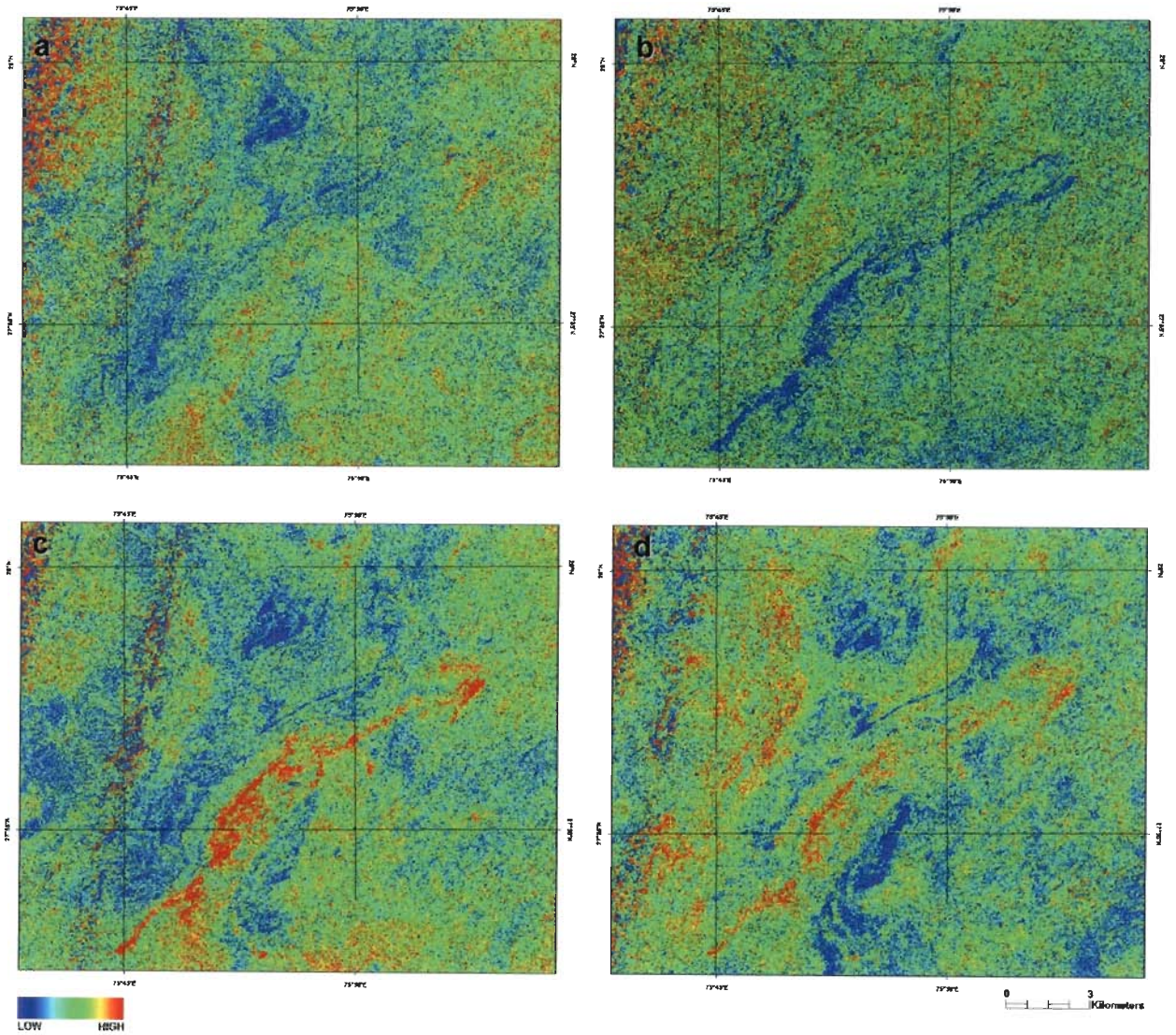


Figure-8.10 Mineral abundance images: a. alunit; b. illite; c. kaolinite; d. kaolinite+smectite; obtained from FPCS processing of 4-band spectral subsets of ASTER VNIR-SWIR surface reflectance image data. Vertical striping due to filter-scratch defect in SWIR focal array makes information from the western part of the study area redundant and useless.

8.3.5 ASTER SWIR spectral indices

A spectral index (Kauth and Thomas, 1976) is one of the approaches to quantify multispectral sensor response patterns (Yamaguchi and Naito, 2003). A spectral index is similar to PCA in that both are orthogonal transformations of multispectral data. A fundamental difference between these two is that the spectral indices define the transform axes to represent the spectral patterns of interest, while PCA determines the transform axes mathematically to maximize the variance of multispectral data (Yamaguchi and Naito, 2003). While better visual discrimination of surface materials can be achieved using careful color combination of specific PCs, as seen in the previous section, the physical meanings of colors in a PC composite are not clear in many cases, since PCA result is scene dependent and the transform coefficients change from scene to scene (Yamaguchi and Naito, 2003). In contrast, the spectral indices use pre-determined transform coefficients (Crist and Cicone, 1984), which enables a more certain interpretation of their physical meanings. The original spectral indices proposed for the four Landsat MSS bands (Kauth and Thomas, 1976) were called ‘Brightness’, ‘Greenness’, ‘Yellowness’, and ‘Nonsuch’. Over the years it has better come to be known as the Tasseled Cap Transformation (TCT) for assessing vegetation vigor (Crist and Cicone, 1984). Jackson (1983) showed that these indices were special cases of a class of spectral indices, formed by linear combinations of n spectral bands, in an n -dimensional space. In general the m -th spectral index in n -space ($m \leq n$) of an i -th pixel (${}_m Y^i$) can be represented by the following formula:

$${}_m Y^i = {}_m A_1 X_{1i} + {}_m A_2 X_{2i} + \dots + {}_m A_n X_{ni} \quad \dots(2)$$

Where: n is the total number of spectral bands, ${}_m A_n$ is the transform coefficient of n -th band data for the m -th spectral index, and X_{ni} is the n -th band data of the i -th pixel.

Yamaguchi and Naito (2003) proposed four spectral indices for the discrimination and mapping of four common alteration minerals using ASTER SWIR data. As the main spectral features of the target alteration minerals are concentrated in SWIR bands 5 to 9, these five

bands have been used by Yamaguchi and Naito (2003) to define the spectral indices for alunite, montmorillonite, kaolinite and calcite minerals, and an index for brightness. Using simulated ASTER data generated through spectral, spatial and radiometric convolution of an AVIRIS scene of Cuprite, Nevada, USA, they determined the transform coefficients of the first axis, brightness index through PCA. The second and higher order indices were calculated by them using the Gram-Schmidt Orthogonalization method (Jackson, 1983) with reflectance spectra of the four target minerals to obtain the transform coefficients for their respective spectral indices. The details of the technique can be found in Yamaguchi and Naito (2003). The spectral indices can be generated by simply multiplying the coefficients with the surface reflectance data for respective bands and summing them, according to equation 2. However, it is utmost important that the data calibration to surface reflectance is accurate. Two sets of transform coefficients were proposed by Yamaguchi and Naito (2003), one with second and higher order transform axes perpendicular to the brightness axis and not orthogonal to each other, and another with the transform axes orthogonal to each other too. By comparing the spectral indices for kaolinite generated using the two sets of transform coefficients with published maps they concluded that the second set was better since it generated exclusive mineralogical information. The transform coefficients recommended by Yamaguchi and Naito (2003) for the four alteration minerals have been reproduced in Table-8.6 and the resultant spectral indices for the study area have been shown in Figure-8.11a-d.

Table-8.6 Transform coefficients for ASTER SWIR bands used in calculation of spectral indices. (from Yamaguchi and Naito, 2003; Table 3)

Spectral Index	Band 5	Band 6	Band 7	Band 8	Band 9
<i>Alunite</i>	-0.694	-0.219	0.562	0.389	-0.048
<i>Kaolinite</i>	0.528	-0.795	0.212	0.174	-0.119
<i>Calcite</i>	-0.087	-0.212	0.322	-0.659	0.640
<i>Montmorillonite</i>	0.138	0.284	-0.134	0.499	-0.796

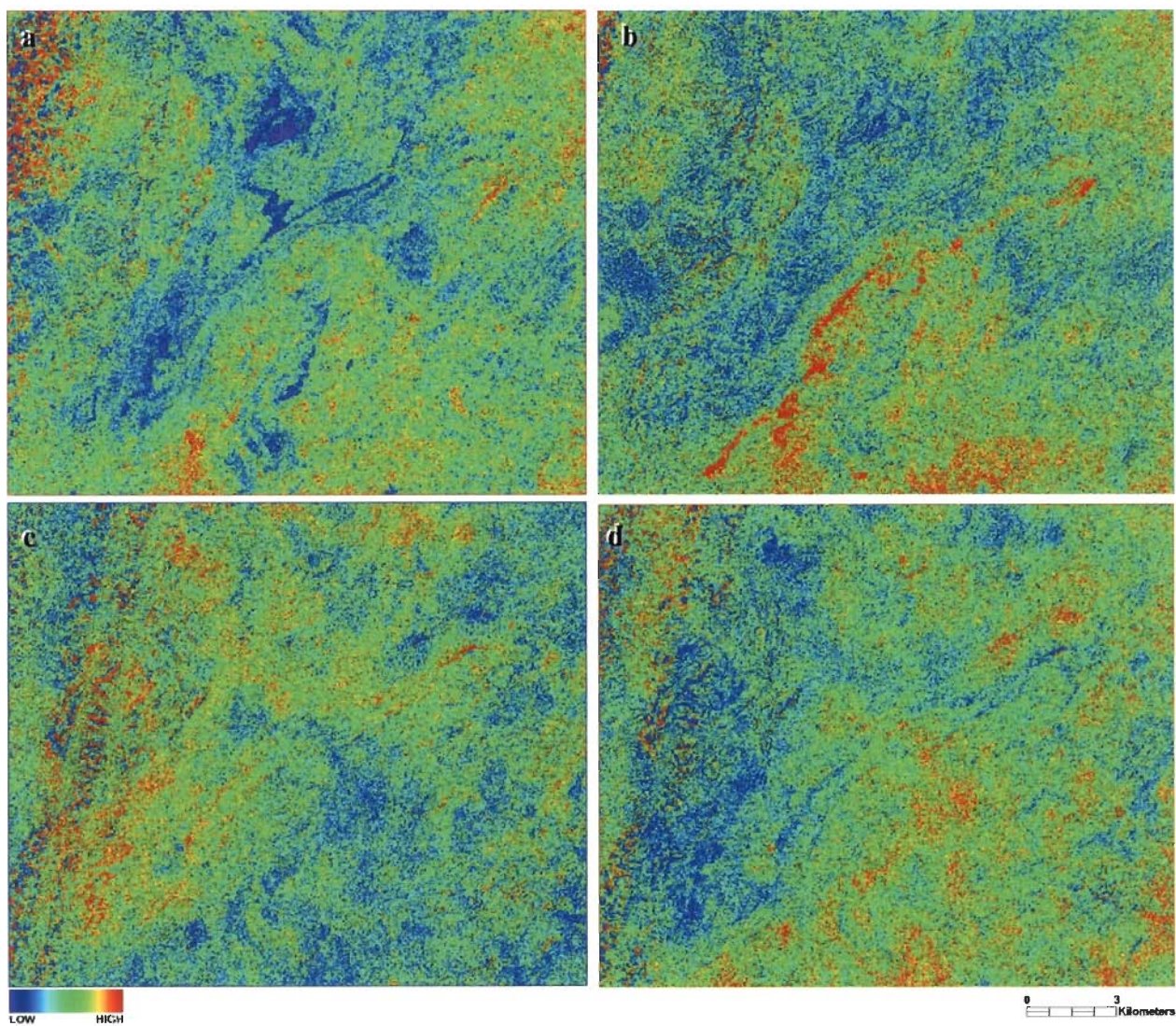


Figure-8.11 ASTER SWIR spectral indices for the study area calculated using the transform coefficients in Table-8.6 for: a. alunite; b. kaolinite; c. calcite; and d. montmorillonite.

8.3.6 Argillic and Phyllic alteration mapping using Boolean logical algorithms

Hydrothermal alteration of rocks is commonly manifested as alteration zones with a central core of quartz and potassium bearing zone (silicic and potassic; with mainly K-feldspar and biotite as main constituents), and progressively outward zones of hydrous minerals with characteristic spectral features in the SWIR region. Immediately next to the potassic zone is a broad phyllic zone (commonly limonitic due to oxidation of pyrite; characterized by illite/muscovite/sericite), farther next is an argillic zone (with kaolinite and alunite as index minerals), followed by an outermost propylitic zone (with chiefly chlorite, epidote and carbonate minerals) (Lowell and Guilbert, 1970). The constitution of the propylitic zone is affected heavily by the country rock composition; it is highly variable and hence difficult to characterize. On the other hand, the silicic and potassic zones are best mapped using data in the TIR range, and in most cases these zones are not well exposed.

With these considerations, Mars and Rowan (2006) proposed two identical Boolean logic algorithms selectively combining the ASTER band ratios for specific mineral groups to exclusively map rocks with argillic and phyllic alteration, and successfully applied them to a study area in the Zagros magmatic arc in Iran. In principle, their method involves the following steps:

- Masking vegetation using VNIR band ratio 3/2
- Masking dark pixels (shadow regions) using a threshold for band 4
- Mapping the 2.165 μm feature for argillic and 2.200 μm feature for phyllic alteration minerals
- Establishing a threshold to distinguish between argillic and phyllic alteration

Mars and Rowan (2006) implemented their algorithm using logical operators in Interactive Data Language (IDL) environment of the ENVI software package. When all constraints of the algorithms are met, a pixel is respectively classified as argillically or as

phylically altered. The resultant classified image is a byte image having values of 0 and 1, respectively for false and true results.

Widespread occurrence of plutonic intrusion and complex structural setup of the region offering weak zones for hydrothermal solutions to interact with country rock presents an opportunity to test the approach suggested by Mars and Rowan (2006) to map argillic and phyllic alteration zones in the study area. The range and threshold values for the band ratios used in their algorithm were determined by Mars and Rowan (2006) using four ASTER scenes of the study area in Iran, a calibration site in Cuprite, Nevada, USA, and laboratory spectra. However, the ranges and thresholds for the band ratios of the ASTER surface reflectance dataset of the present study area were determined empirically, and were found to deviate from those proposed by Mars and Rowan (2006), due to differences in the nature of surface lithology in the two cases. Implementation of the algorithm suggested by Mars and Rowan (2006) has been done using the Spatial Modeler module of ERDAS Imagine image processing suite. The method involved computation of spectral thresholds based on standard deviation and mean from the band ratios:

- $3/2$ – to mask vegetation
- $4/5$ – to map 2.165 μm absorption feature associated with argillic alteration
- $4/6$ – to map 2.200 μm absorption feature associated with phyllic alteration
- $5/6$ – ratio to delineate argillic and phyllic alteration
- $7/6$ – to map 2.200 μm absorption feature associated with argillic/phylic alteration

The thresholds were determined using an empirical relationship $[(\text{Mean})+1.5 \times (\text{Standard Deviation})]$ and adjustment through visual inspection of spatial distribution coherence of mapped pixels using various threshold values. The Boolean logical statements combining the various steps of the algorithms for argillic and phyllic alteration mapping respectively, have been summarized in Figure-8.12A-B. The resulting maps depicting the distribution of argillic and phyllic alteration in the study area have been shown in Figure-8.13A-B.

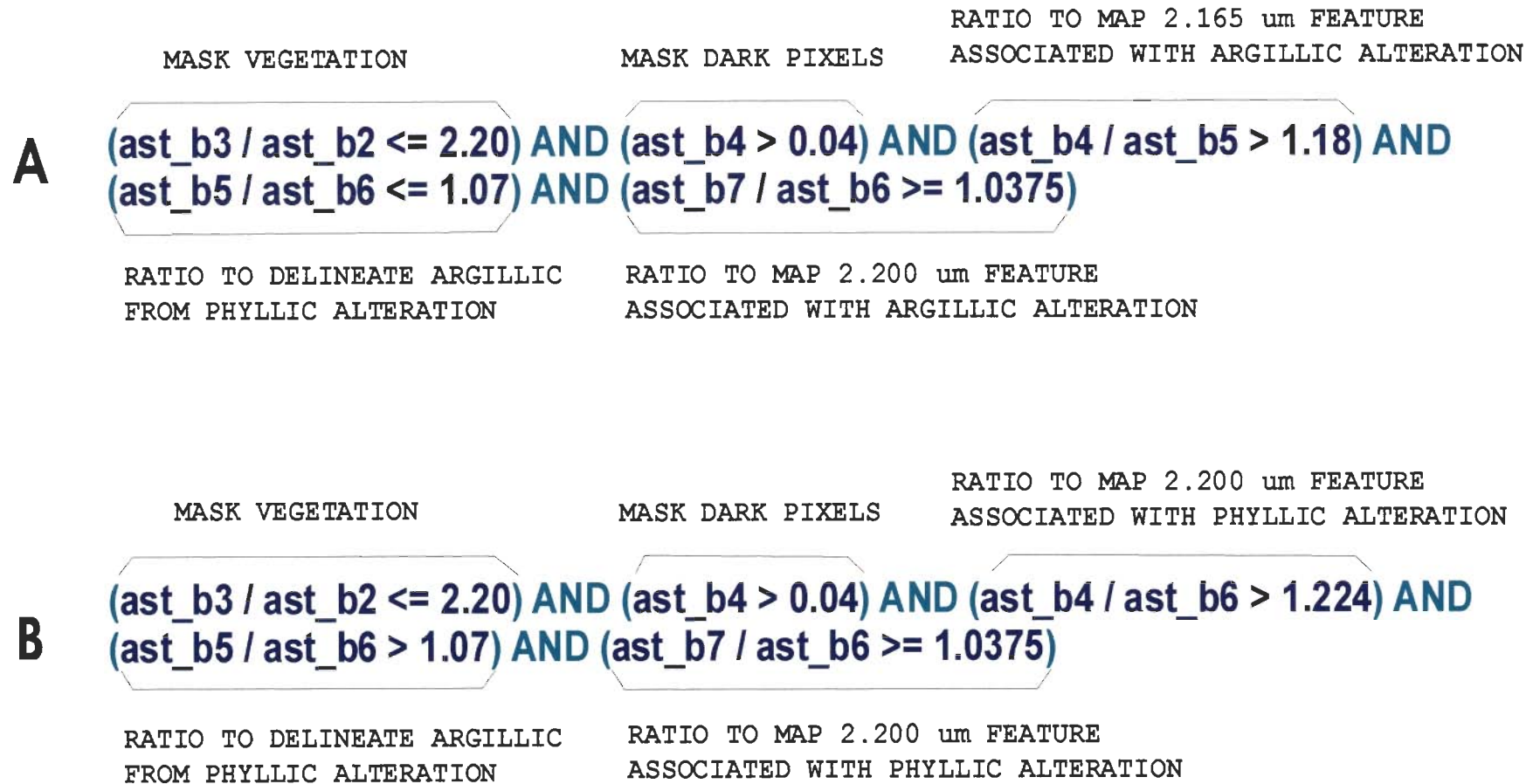


Figure-8.12 Boolean Logical Statements to map (A) argillic, and (B) phyllic alteration.

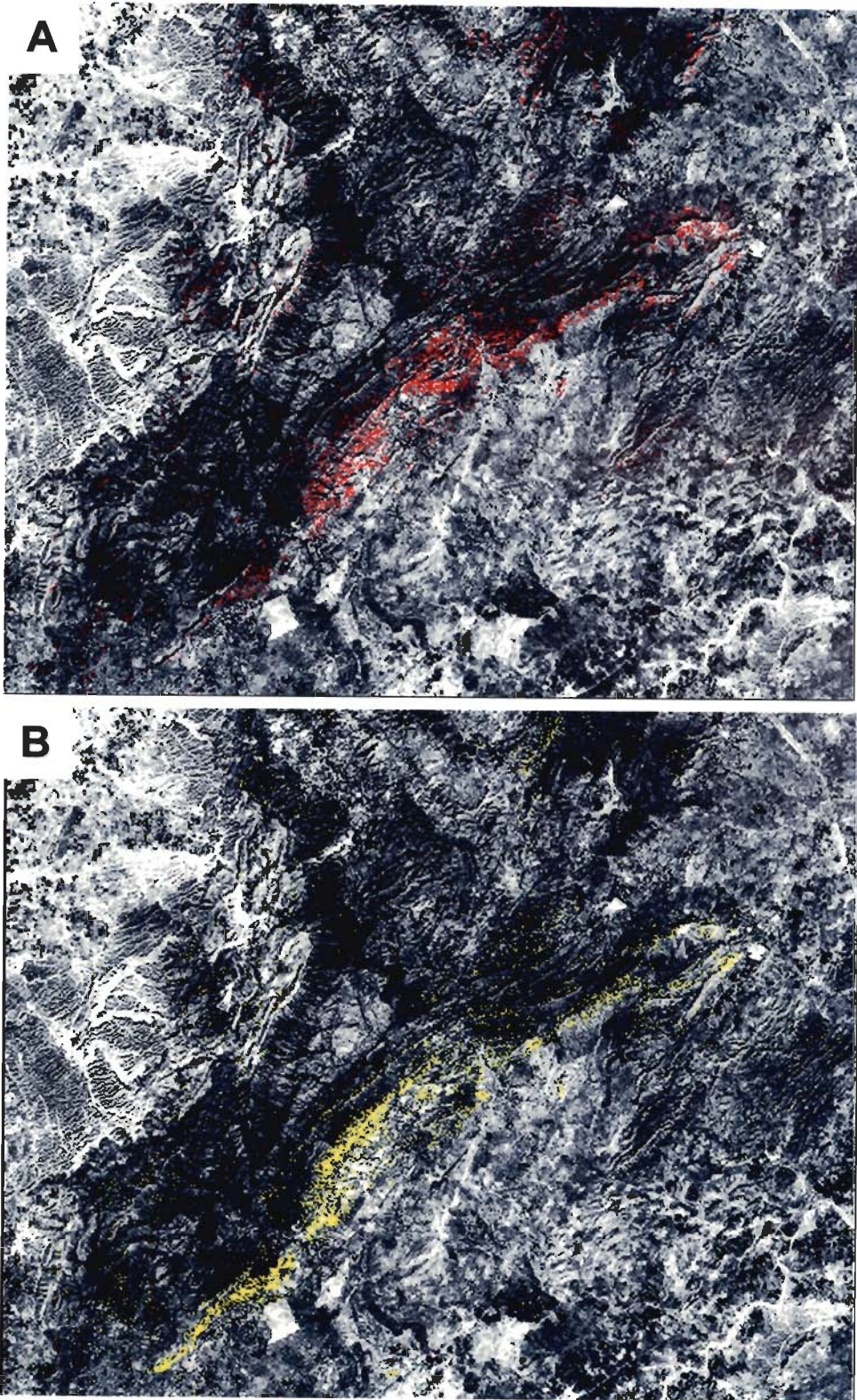


Figure-8.13 Maps of argillic (A, red) and phyllic (B, yellow) alteration in the study area generated using Boolean Logical Statements shown in Figure-8.12. The background image is ASTER band 1.

8.4 ASTER VNIR-SWIR full spectral mapping of alteration minerals

The alteration mapping methods discussed in preceding sections relied upon an understanding of the spectral signatures of the target alteration minerals outlined in the beginning of this chapter. Although such methods are strongly linked to composition, they are by and large focused only on specific wavelength regions and therefore neglect contributions from the rest of the spectrum. Feature mapping is particularly problematic for many materials (such as rocks) whose spectra do not contain well-defined absorptions. Instead of diagnostic features, these spectra are characterized by their continuum shapes and/or very broad absorptions (Mustard and Sunshine, 1999). Minerals with similar diagnostic spectral features are susceptible to ambiguous mapping using the techniques mentioned above. However, differences in the spectral shape (band depth and slope variations) exist for minerals with common diagnostic spectral features, which can be effectively utilized to differentiate among them.

A number of alternative and complementary approaches have been developed to address the above-mentioned issues, and have been grouped as either ‘spectral similarity’ mapping techniques, or ‘spectral detection’ mapping techniques. Under a spectral similarity search, a scene is examined to determine which pixels are most ‘similar’ to target spectra. The second category of mapping methods uses the full spectral response with spectral detectors or ‘matched filters’ to detect a spectrum of interest by highlighting pixels with similar spectral properties while simultaneously repressing all other background spectral signatures. As already described in Chapter 7, the former include the Spectral Angle Mapper (SAM) algorithm (Kruse et al., 1993) and Binary Encoding (Mazer et al., 1988), while the latter includes the Matched Filter algorithm (Harsanyi and Chang, 1994) and its adaptation - Mixture Tuned Matched Filter (MTMF™), as implemented in the ENVI software package. In the following paragraphs, two of these mapping techniques (SAM and MTMF™) have been applied to the ASTER VNIR-SWIR surface reflectance data of the study area to map the distribution of the target alteration

minerals. The basic data preparation has involved creation of a vegetation mask to exclude the vegetation dominated pixels from the analysis, determination of the target mineral spectra as image end-members through PPI™ method (described in Chapter 7), and spectral end-member identification using ENVI's Spectral Analyst™ module. These steps have been discussed in some detail in the following sections.

8.4.1 Preparation of a vegetation mask

The two primary reasons for excluding the vegetation-dominant pixels from the spectral analysis are:

1. Healthy vegetation almost completely obscures the spectral response of the underlying ground in the solar reflective region. This is particularly so for the chlorophyll-rich healthy vegetation, as it significantly decreases band 2 (or 0.661 μm) reflectance. But even sparse and dried vegetation significantly alters the native spectral response of the geological materials, as some organic-compound (typically cellulose) absorption features centered near 2.10 and 2.30 μm are near the wavelengths of some of the main Al-OH and Fe, Mg-OH absorption features.
2. Since vegetation is a material of non-interest geologically, inclusion of vegetation in the analysis can lead to loss of a possible geological end-member determinable through PPI (since the number of determinable end-members through PPI is constrained by $n+1$, where n is the number of spectral bands used).

With these considerations in view, a vegetation mask has been prepared to exclude the highly vegetated pixels from the analysis, while simultaneously prevent loss of a spectral end-member of geological significance. This has been achieved through generation of a Normalized Difference Vegetation Index (NDVI) image using ASTER bands 2 and 3 with the standard

NDVI equation $[(AST_3 - AST_2) \div (AST_3 + AST_2)]$. The range of the resulting NDVI image (0.021161 to 0.790892) has been interactively examined with different threshold values, and a value of 0.345 has been chosen as the best threshold to represent the vegetation-dominated pixels. The resultant vegetation mask has been shown in Figure-8.14.

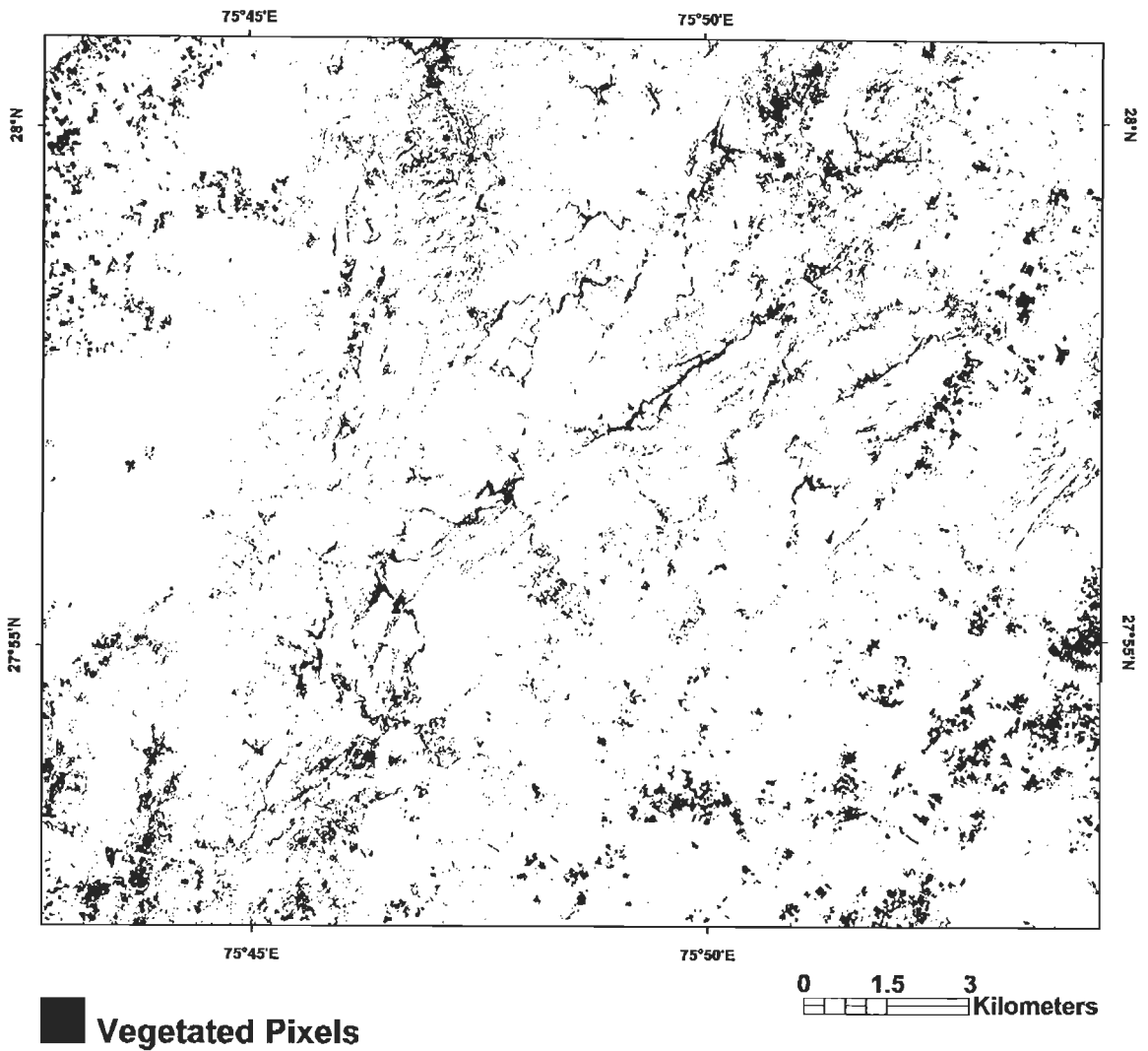


Figure-8.14 Vegetation mask created by thresholding an NDVI image of the study area.

8.4.2 Determination of target spectra

One of the most critical steps in the full spectral processing of the remote sensing image data is the determination of the 'target' spectra to adequately and distinctly map the materials of interest. Since in most cases the full spectral diversity of the materials present in a scene cannot be exhaustively determined through field or laboratory spectral measurements and there is always a risk of inaccurate atmospheric correction leading to a mismatch in field/laboratory spectral measurements and the actual image spectra, it has been considered better to derive the end-member class-spectra directly from the image data. The choice of the technique to achieve this objective is highly subjective, and varies depending on the ultimate objective of the study. The objective of this study is to map the main alteration minerals present in the study area, and to check if their distribution has any link with base metal mineralization.

The determination of the image end-members (target spectra) in this study has been achieved through the PPI™ approach. Emphasis has been laid upon the end-members having greater variations in the SWIR region, as this is the main wavelength region where the diagnostic features of the important target alteration minerals occur. Since the maximum possible end-members determinable through PPI™ in the present case is 10 (using all of the 9 VNIR+SWIR bands) and no field or laboratory spectral measurements have been made, the only possibility of expanding the end-member classes is by using smaller windows of the full image data and determining end-members separately for each one of them. A compiled end-member spectral library can thus be generated with a more complete representation of the spectral diversity which can (probably) lead to a wider spectral classification. However, this entails a risk too. Too many spectral classes render the final classified image difficult to interpret. A careful selection and 'grouping' of the similar spectral end-members obtained using individual windows guided by the analytical objectives can narrow-down the range and enhance the final interpretability.

With these points in view, the image end-members have been determined through PPI for the following four cases:

Case 1: For VNIR+SWIR combined data (9 bands) using the full scene

Case 2: For SWIR data alone (6 bands)

Case 3: For VNIR+SWIR combined data individually for 8 spatial windows (see fig. 8.15)

Case 4: For SWIR data alone individually for 8 spatial windows

The 8 image windows have been selected on the basis of *a priori* known mineralizations present in the area. The end-members determined for the 8 windows in the latter two cases have been subsequently combined to produce two separate end-member spectral libraries for use with the supervised mapping/classification algorithms discussed later. The end-member spectra for the four cases mentioned above have been shown in Figures 8.16, 8.17, 8.18a-h and 8.19a-h, respectively.

8.4.3 End-member identification

Efforts have been made with varying degrees of success to identify the 151 different image-derived end-member spectra using ENVI's Spectral Analyst™ module, as previously described in Chapter 7. In this case, the reference spectral library used is the United States Geological Survey (USGS) spectral library (speclib05; Clark et al., 2003). This library contains 481 spectra of well-characterized specimens of mineral, vegetation, snow, water and manmade materials within the solar reflective wavelength region (0.4 μm to 2.5 μm). The results of the exercise have been summarized in Tables 8.7, 8.8, 8.9 and 8.10, respectively for the four cases listed above. As with the TIR emissivity spectra in Chapter 7, the best spectral matches have been determined using a combination of SAM/SFF fit-method score (fit correlation coefficients) and examination of individual end-member spectrum in normal and continuum-removed mode along with that of the reference spectrum.

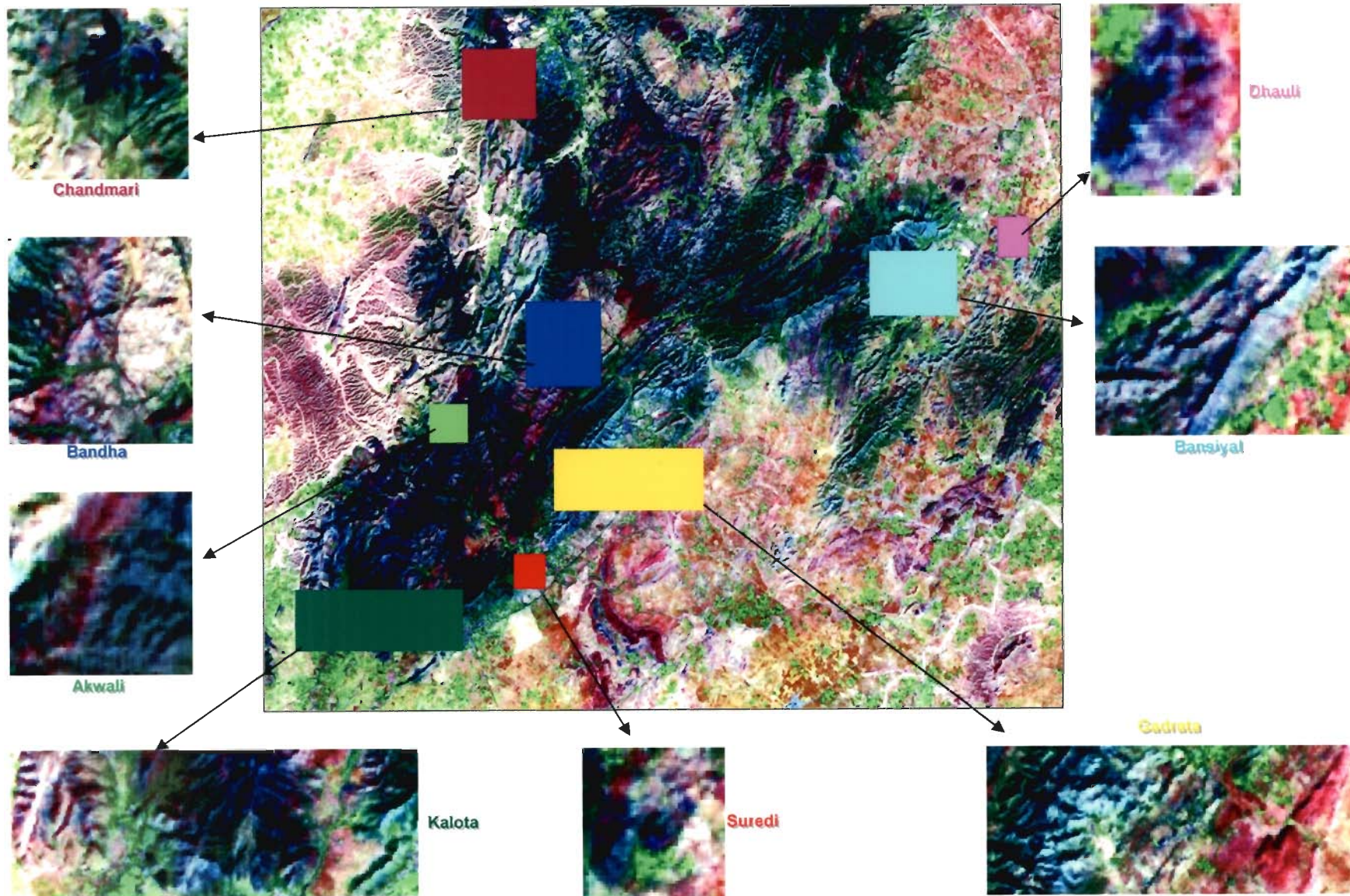


Figure-8.15 Image subsets used in image-derived end-member spectral library creation; ASTER bands 6-3-1 have been shown in RGB.

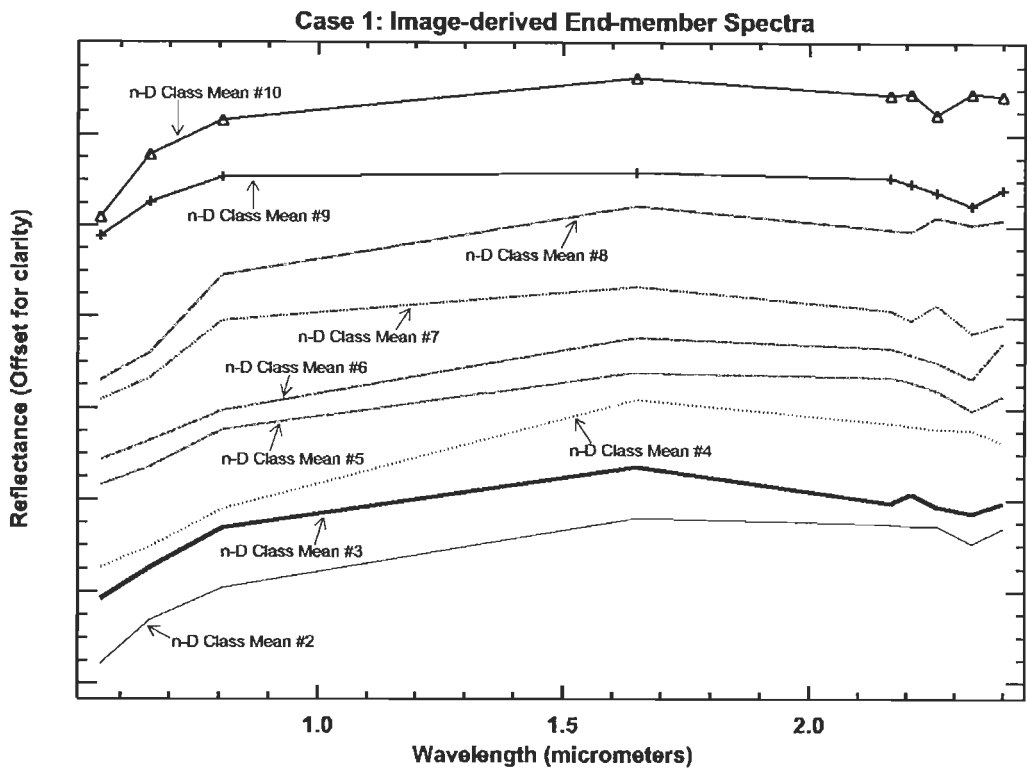


Figure-8.16 PPI™-derived image end-member spectra using vegetation-masked VNIR-SWIR reflectance image data, referred to as Case 1.

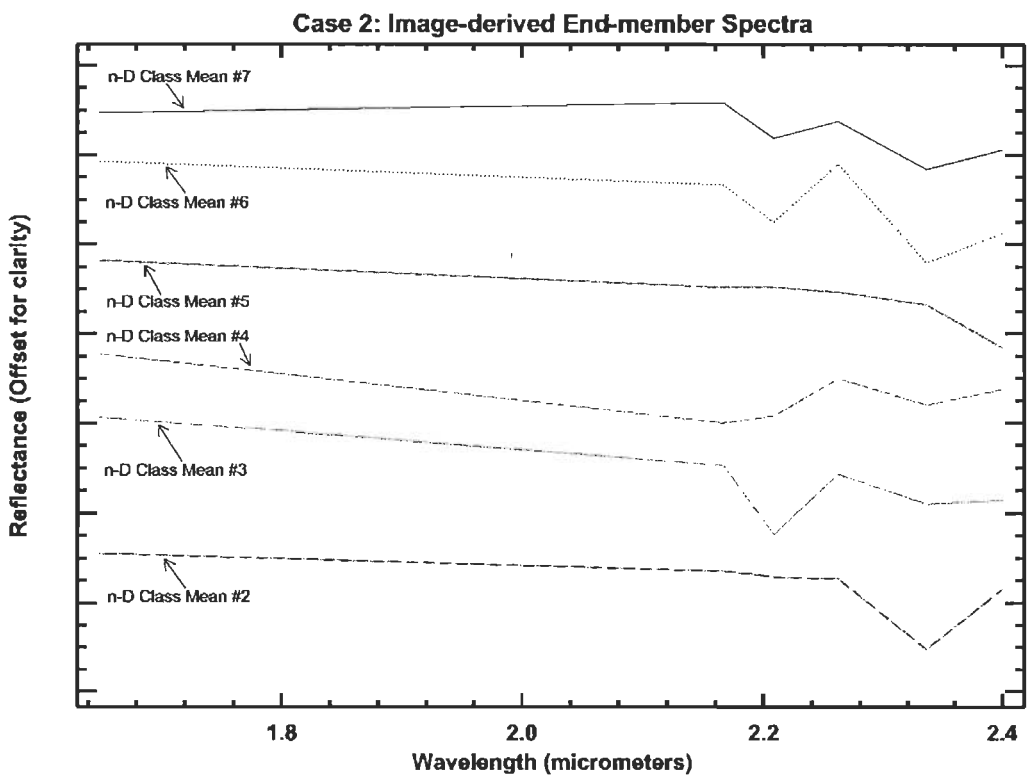


Figure-8.17 PPI™-derived image end-member spectra using vegetation-masked SWIR reflectance image data, referred to as Case 2.

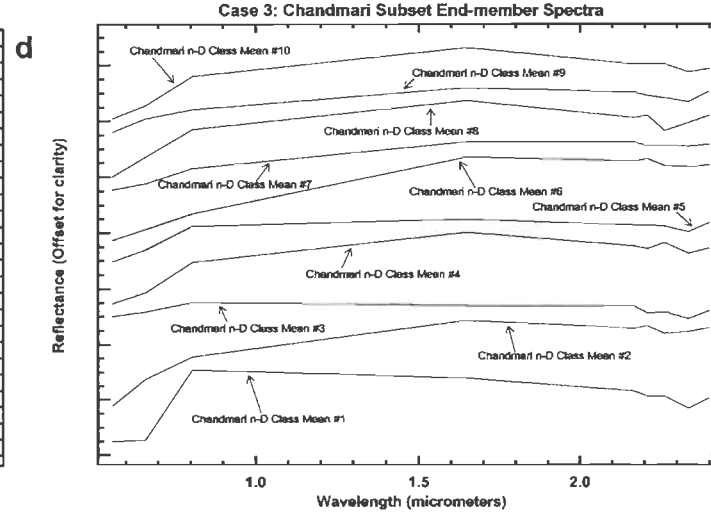
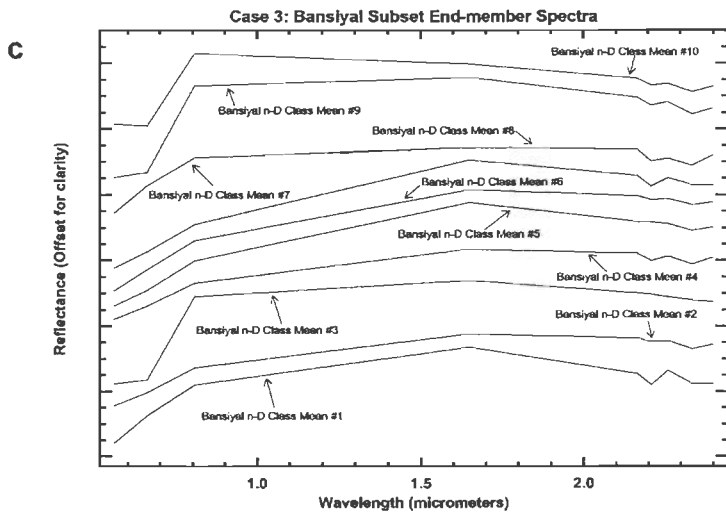
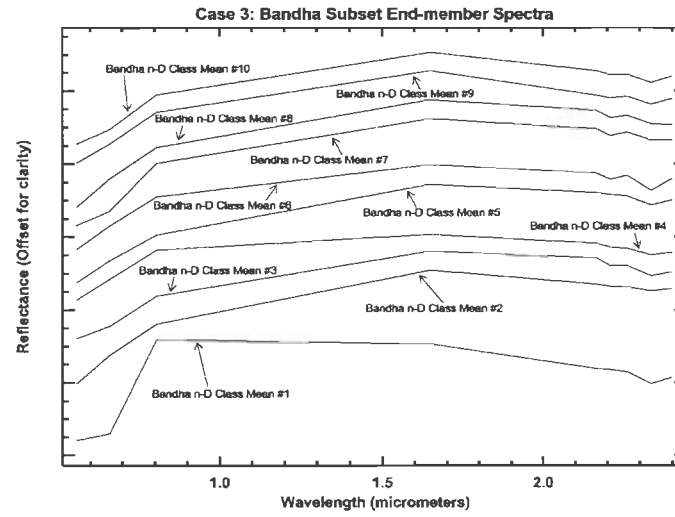
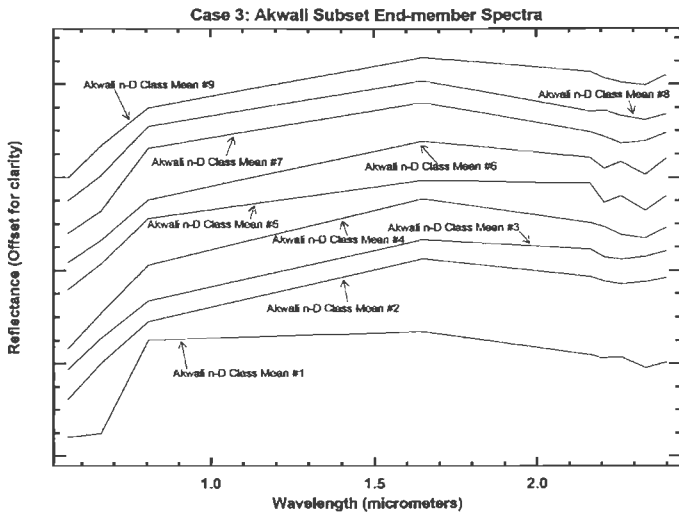


Figure-8.18 a-h, PPITM-derived image end-member spectra respectively for the 8 windows of VNIR-SWIR reflectance data, referred to as Case 3.

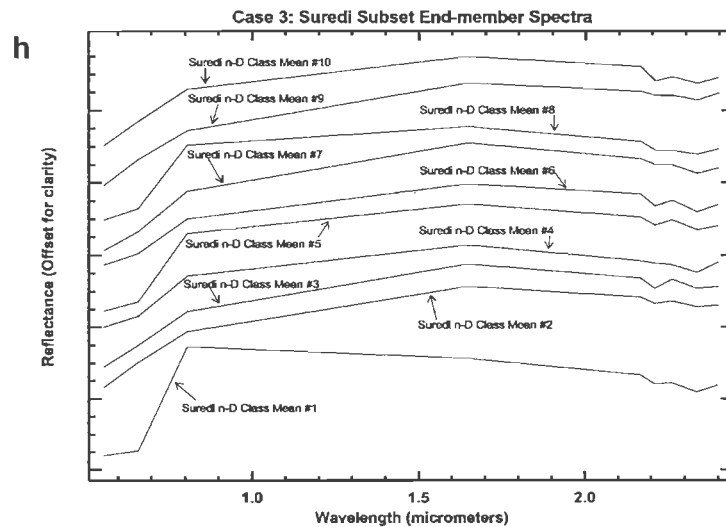
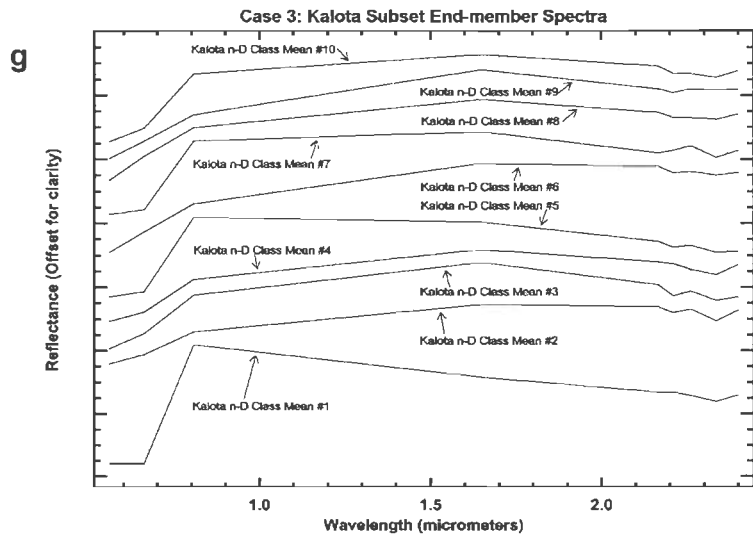
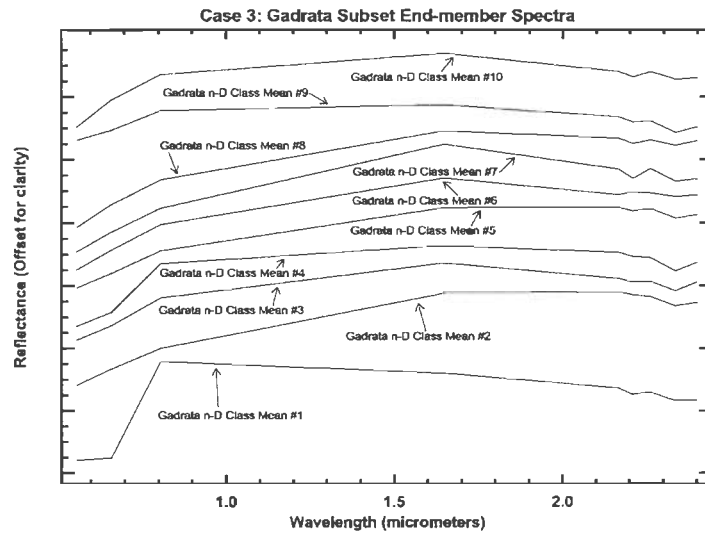
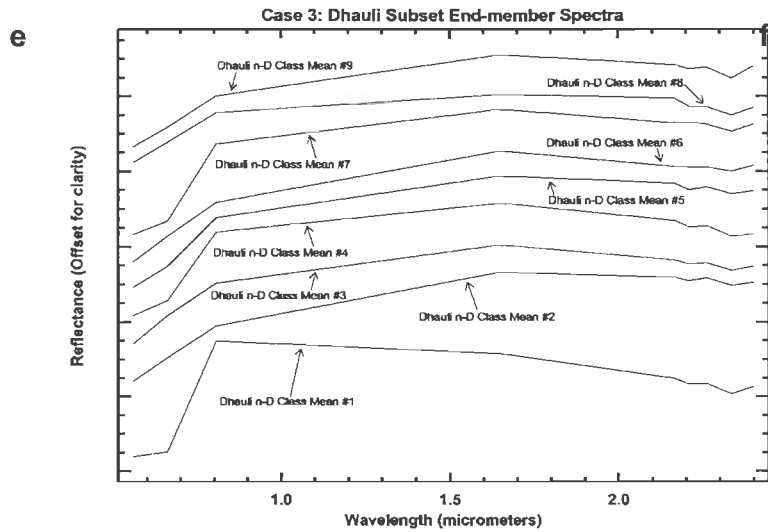


Figure-8.18 Continued.

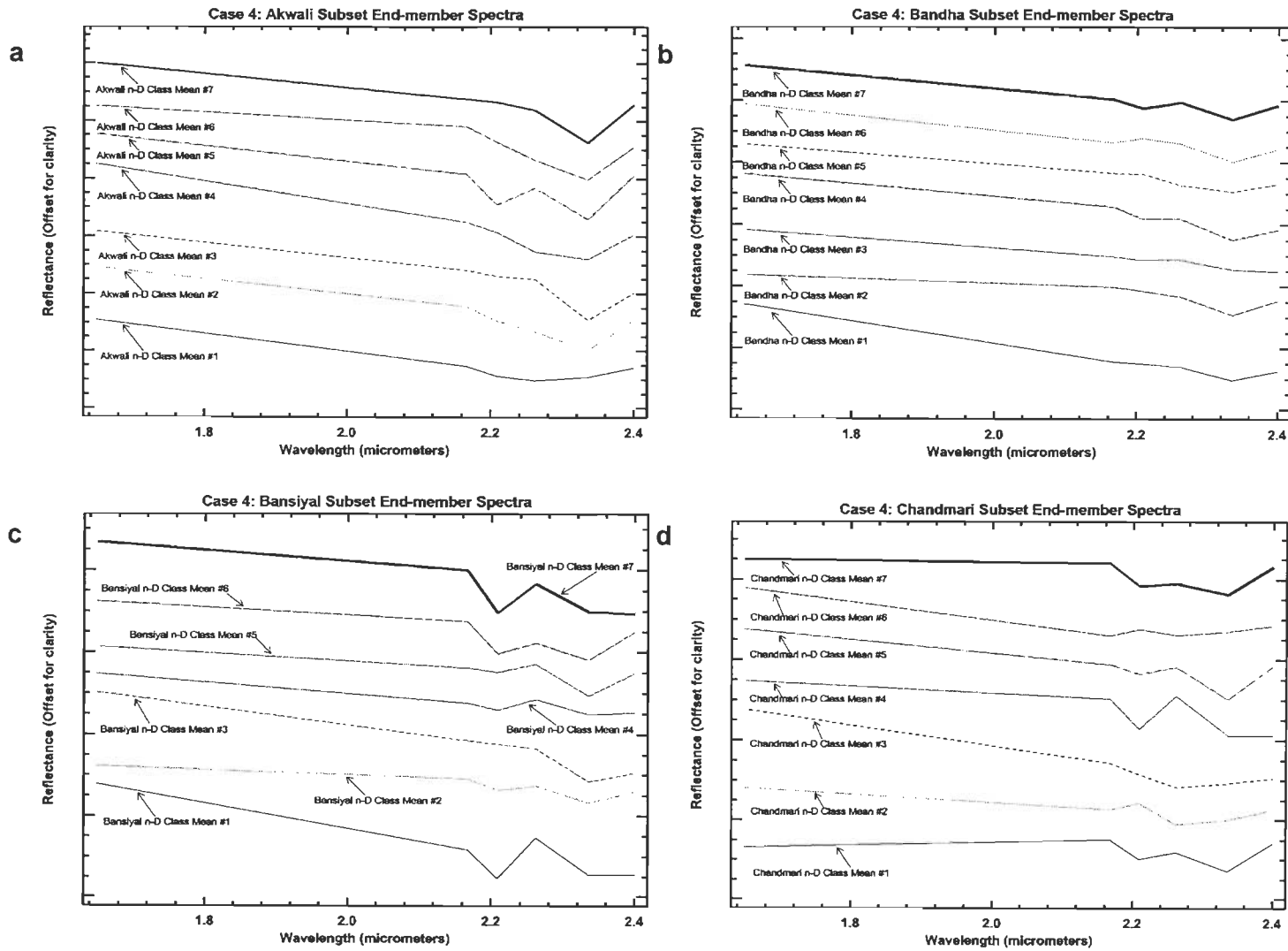


Figure-8.19 a-h, PPI™-derived image end-member spectra respectively for the 8 windows of SWIR reflectance data, referred to as Case 4.

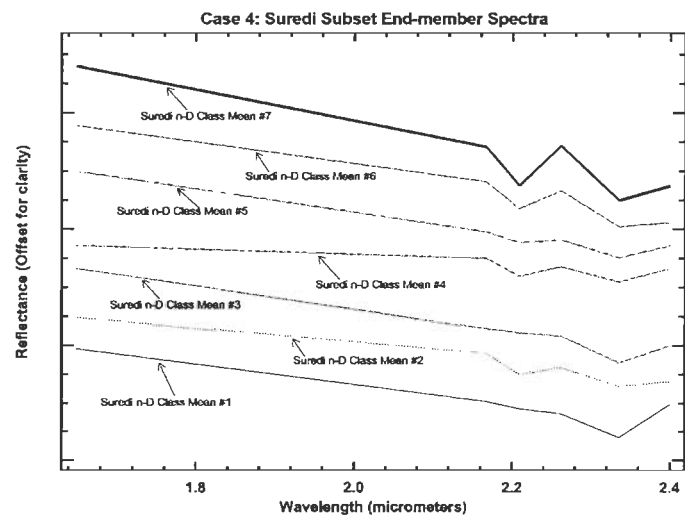
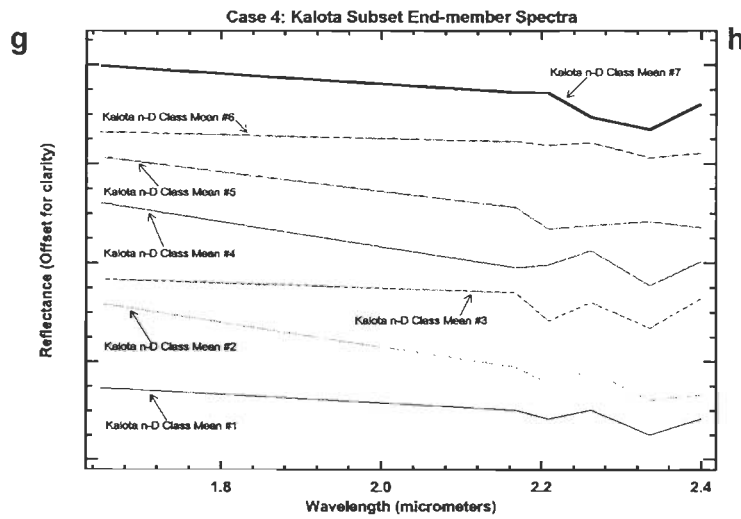
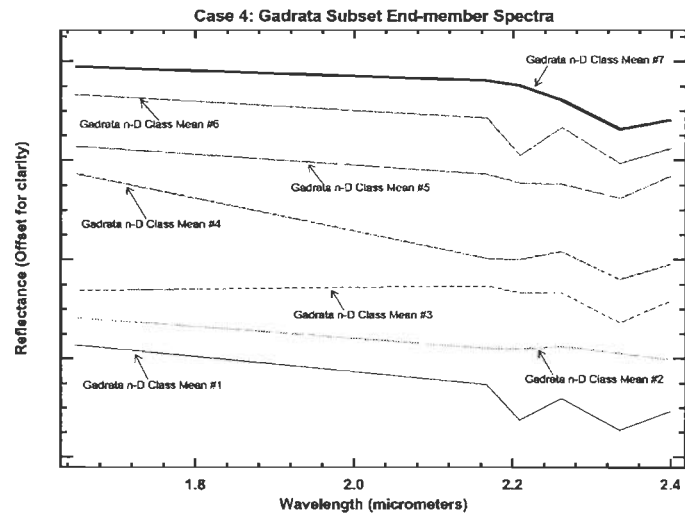
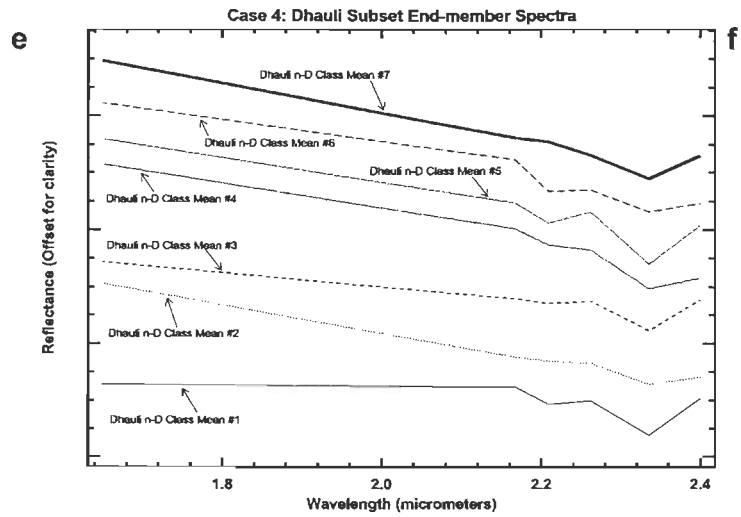


Figure-8.19 Continued.

Table-8.7 End-member spectral identification using ENVI's Spectral Analyst™ for Case 1:
Vegetation-masked full image, ASTER VNIR+SWIR 9-band reflectance data

S. No.	PPI-derived Unknown Image End-member ID	Top matches based on SAM+SFF scores (fit values in parentheses)	Top matches based on SFF scores (fit values in parentheses)	Remarks and best match based on visual inspection
1	n-D Class Mean #1	A flat spectrum with values close to 0; most likely it represents the 'shaded' pixels.		
2	n-D Class Mean #2	Tremolite (0.925) Phlogopite (0.909) Richterite (0.881)	Ferrihydrite (0.991) Hectorite (0.991) Tremolite (0.991)	Ferrihydrite or tremolite, and celsian (0.972, SFF)
3	n-D Class Mean #3	Adularia (0.811) Hematite (0.810) Phlogopite (0.802)	Adularia (0.906) Chromite (0.850)	Most likely surfaces with composition similar to adularia
4	n-D Class Mean #4	Rutile (0.938) Cuprite (0.923)	Nontronite (0.985) Quartz (0.961) Microcline (0.962)	The spectrum has non-distinct matches; distribution of this class in the image shows it as shaded pixels
5	n-D Class Mean #5	Corrensite (0.863) Richterite (0.840) Chlorite (0.832)	Labradorite (0.911) Richterite (0.872) Epidote (0.835)	Best visual match with corrensite, and may actually represent weathered amphibolites
6	n-D Class Mean #6	Epidote (0.755) Phlogopite (0.748)	Sphalerite (0.901) Grossular (0.843)	Most likely a combination of phlogopite and grossular
7	n-D Class Mean #7	Desert Varnish (0.845) Illite (0.735) Mizzonite (0.717)	Desert Varnish (0.926) Albite (0.639) Illite (0.626)	Best visual match with illite, though absorption in band 2 is perhaps due to some vegetation mixing
8	n-D Class Mean #8	Mizzonite (0.815) Lazurite (0.795) Illite (0.702)	Mizzonite (0.835) Quartz (0.775)	Most likely either mizzonite, or illite with some vegetation mixing
9	n-D Class Mean #9	Rhodonite (0.925) Anorthite (0.875)	Sphalerite (0.982) Rhodonite (0.962) Anorthite (0.925) Calcite (0.908)	Best visual match is with anorthite spectrum; however, it can also represent carbonate minerals.
10	n-D Class Mean #10	Andradite (0.887) Jarosite (0.852) Hematite (0.843)	Talc (0.951) Tremolite (0.930) Nitrite (0.913) Grossular (0.886)	The match is ambiguous, and the likely candidates for this spectrum can be the Fe ³⁺ bearing minerals.

Table-8.8 End-member spectral identification using ENVI's Spectral Analyst™ for Case 2:
Vegetation-masked full image, ASTER SWIR 6-band reflectance data

S. No.	PPI-derived Unknown Image End-member ID	Top matches based on SAM+SFF scores (fit values in parentheses)	Top matches based on SFF scores (fit values in parentheses)	Remarks and best match based on visual inspection
1	n-D Class Mean #1	A flat spectrum with values close to 0; most likely it represents the 'shaded' pixels.		
2	n-D Class Mean #2	Richterite (0.970) Tremolite (0.970) Celsian (0.951)	Riebeckite (0.995) Hornblende (0.987) Tremolite (0.987) Phlogopite (0.987)	Best visual matches is with tremolite, and the spectrum is most likely to represent calc-silicates or para-amphibolites
3	n-D Class Mean #3	Illite (0.975) Spodumene (0.969) Oligoclase (0.966)	Palygorskite (0.997) Muscovite (0.996) Spodumene (0.993) Montmorillonite (0.984)	On visual inspection, this spectrum is most likely to represent muscovite/sericite, illite, montmorillonite-bearing surfaces
4	n-D Class Mean #4	Topaz (0.973)	Topaz (0.986) Paragonite (0.983) Sillimanite (0.970)	Best spectral match on visual inspection is with topaz
5	n-D Class Mean #5 Table 8.8 continued...	Nepheline (0.993) Rutile (0.989) Hematite (0.989) Topaz (0.989)	Phalite, bytownite, mordenite, sepionite, clinoptilolite, butterite, hypersthene, and psilomelane (1.000) Chlorapatite, heulandite,	This spectrum has non-unique matches. However, based on field information and inspection of the class-distribution, this image end-member is most likely to

			stilbite, saponite, goethite (0.999)	represent iron rich surfaces depleted in silica, and/or zeolites in relatively higher concentrations.
6	n-D Class Mean #6	Desert Varnish (0.937) Grossular (0.889) Cookeite (0.878)	Desert Varnish (0.918) Mizzonite (0.853) Grossular (0.837) Cookeite (0.814)	Best visual spectral match is with desert varnish and cookeite, and it is most likely to represent weathered mafic surfaces.
7	n-D Class Mean #7	Grossular (0.979) Oligoclase (0.952) Dipyre (0.931) Illite (0.931)	Mizzonite (0.995) Grossular (0.977) Margarite (0.946) Tourmaline (0.939)	The best visual matches for this spectrum are with scapolite minerals (mizzonite, dipyre andmargarite), as well as with illite and oligoclase.

Table-8.9 End-member spectral identification using ENVI's Spectral Analyst™ for Case 3: Image-subsets for 8 different mineralized areas, ASTER VNIR+SWIR 9-band reflectance data

S. No.	PPI-derived Unknown Image End-member ID	Top matches based on SAM+SFF scores (fit values in parentheses)	Top matches based on SFF scores (fit values in parentheses)	Remarks and best match based on visual inspection
1	Akwali n-D Class Mean #1	Lazurite (0.814) Uvarovite (0.759) Celestite (0.738)	Celestite (0.838) Uvarovite(0.792) Microcline (0.754)	The steep slope between bands 3 and 2 is suggestive of the spectrum being that of vegetation than these minerals
2	Akwali n-D Class Mean #2	Hematite (0.933) Sphene (0.920) Andalusite (0.915)	Brucite and gibbsite (0.954) Pectolite (0.943) Hematite (0.940)	Most likely andalusite/hematite or brucite
3	Akwali n-D Class Mean #3	Sphene (0.949) Hematite (0.949) Andalusite (0.926)	Hematite (0.975) Brucite (0.965) Sphene (0.960) Rhodonite (0.947)	It has closest matches with hematite spectrum
4	Akwali n-D Class Mean #4	Hematite (0.903) Sphene (0.871) Andalusite (0.867) Phlogopite (0.822) Corrensite (0.815)	Sphalerite (0.925) Zincite (0.922) Grossular (0.911) Brucite (0.909)	Andalusite with some zinc-rich minerals
5	Akwali n-D Class Mean #5	Pyrope (0.852) Andalusite (0.850) Pyrrhotite (0.841) Hematite (0.804)	Vesuvian (0.853) Pyrrhotite (0.854) Tourmaline (0.834) Margarite (0.831)	Iron rich surfaces of mainly andalusite-bearing rocks with associated chlorite; pixels occupy shaded areas (low reflectance in band 4)
6	Akwali n-D Class Mean #6	Andalusite (0.844) Pyrope (0.841) Pyrrhotite (0.833) Desert Varnish(0.820)	Pyrrhotite (0.836) Vesuvian (0.830) Tourmaline (0.815) Margarite (0.813)	Same as above, but the pixels are in sun-lit slopes
7	Akwali n-D Class Mean #7	Kerogen(0.883) Covellite (0.806) Augite (0.780) Corrensite (0.741)	Kerogen (0.885) Augite (0.800) Covellite (0.752) Albite (0.733)	Vegetation-rich pixels with spectral matches to corrensite
8	Akwali n-D Class Mean #8	Kerogen (0.886) Covellite (0.859) Mizzonite (0.826) Hematite (0.825) Corrensite (0.823)	Kerogen (0.891) Augite (0.889) Sphalerite (0.867) Adularia (0.858)	Quartzose rocks bearing corrensite/scapolite + alunite (band 5 absorption)
9	Akwali n-D Class Mean #9	Hematite (0.928) Andalusite (0.901) Sphene (0.886) Pyrrhotite (0.869)	Sphalerite (0.944) Zincite (0.938) Grossular (0.933) Hematite (0.930)	Iron-rich surfaces
10	Bandha n-D Class Mean #1	Lazurite (0.740) Uvarovite (0.742)	Celestite (0.772) Uvarovite (0.692)	Vegetation (steep slope between band 2 and band 3)

Table-8.9 continued...

11	Bandha n-D Class Mean #2	Andalusite (0.946) Hematite (0.940) Pyrope (0.936) Sphene (0.931)	Sphalerite (0.979) Pyrrhotite (0.970) Grossular (0.967)	Illite+hematite-rich quartzose rock
12	Bandha n-D Class Mean #3	Desert Varnish (0.859) Corrensite (0.837) Kerogen (0.803) Prochlorite and nontronite (0.785)	Desert Varnish (0.829) Corrensite (0.799) Quartz (0.782) Mizzonite (0.772)	Desert Varnish on mafic surfaces with composition of corrensite/scapolite; and chlorite
13	Bandha n-D Class Mean #4	Pyrrhotite (0.925) Richterite (0.897) Tremolite and pyrope (0.896) Phlogopite (0.893)	Pyrrhotite (0.978) Grossular (0.953) Dipyre (0.944)	Pyrrhotite-bearing amphibole quartzite rocks (strong band 8 absorption with a secondary band 6 absorption)
14	Bandha n-D Class Mean #5	Tremolite (0.908) Phlogopite (0.906 & 0.891) Andalusite (0.888) Corrensite (0.887)	Hectorite, ferrihydrite, lizardite (0.990) Tremolite, saucanite (0.989) Meionite (0.980) Phlogopite (0.977)	Ferrihydrite-rich surfaces possibly containing phlogopite and tremolite, with some scapolite and corrensite (strong and singular band 8 absorption with a steeper slope between band 6 and band 7)
15	Bandha n-D Class Mean #6	Dipyre (0.869) Pyrrhotite (0.868) Tremolite (0.855) Phlogopite (0.848)	Dipyre (0.957) Grossular (0.936) Celsian (0.916) Meionite (0.905)	Scapolite-rich surfaces
16	Bandha n-D Class Mean #7	Lazurite (0.867) Mizzonite (0.859) Rutile (0.854)	Mizzonite (0.923) Celestite (0.911) Mizzonite (0.902) Quartz (0.898)	Scapolite-rich quartzose surfaces with higher vegetation cover (steep slope between band 2 and band 3)
17	Bandha n-D Class Mean #8	Pyrope (0.941) Andalusite (0.927) Illite (0.908) Hematite (0.901)	Witherite (0.995) Oligoclase (0.991) Illite (0.977) Pyrope, tourmaline (0.974)	Illite-rich surfaces with associated quartz and feldspar
18	Bandha n-D Class Mean #9	Pyrope (0.853) Andalusite (0.850) Pyrrhotite (0.847) Hematite (0.843) Illite (0.838)	Sphalerite (0.894) Pigeonite (0.889) Cookeite (0.884) Desert Varnish (0.869)	Desert Varnish on quartzose surfaces with high iron content, and some vegetation
19	Bandha n-D Class Mean #10	Desert Varnish (0.837) Corrensite (0.824) Kerogen (0.817) Mizzonite (0.787)	Desert Varnish (0.825) Corrensite (0.807) Kerogen (0.779) Quartz (0.767)	Same as above, but with higher density of vegetation
20	Bansiyal n-D Class Mean #1	Kaolinite-smectite (0.853) Montmorillonite (0.842) Muscovite (0.833)	Muscovite (0.975) Illite (0.965) Microcline (0.940) Muscovite (0.931, 0.908) Albite (0.895)	Clay minerals with composition dominantly that of kaolinite-smectite with muscovite and illite
21	Bansiyal n-D Class Mean #2	Desert Varnish (0.898) Corrensite (0.868) Richterite (0.840)	Desert Varnish (0.901) Richterite (0.894) Corrensite (0.863) Labradorite (0.855)	Desert Varnish/corrensite on amphibole-rich surfaces (mafic rocks)
22	Bansiyal n-D Class Mean #3	Lazurite (0.902) Rutile (0.828)	Rutile (0.891) Lazurite (0.865) Hydroxyl apatite (0.851)	Vegetation
23	Bansiyal n-D Class Mean #4	Desert Varnish (0.869) Pyrope (0.859) Andalusite (0.848) Illite (0.836)	Margarite (0.882) Mizzonite (0.862) Desert Varnish (0.861)	Andalusite-rich rocks with illite/scapolite
24	Bansiyal n-D Class Mean #5	Desert Varnish (0.902) Corrensite (0.877) Rutile, kerogen (0.855) Nontronite (0.840)	Corrensite (0.898) Desert Varnish (0.895) Richterite (0.889)	Desert Varnish/corrensite on amphibole rich surfaces (mafic rocks)
25	Bansiyal n-D Class Mean #6	Sphene (0.911) Desert Varnish (0.910) Andalusite, pyrope	Grossular (0.997) Mizzonite (0.983) Pyrrhotite (0.968)	Andalusite-rich surfaces with scapolite

Table-8.9 continued...

		(0.907)	Dipyre (0.963)	
26	Bansiyal n-D Class Mean #7	Illite (0.906) Goethite (0.877) Desert Varnish (0.866)	Illite (0.979) Quartz (0.919) Albite (0.919)	Illite+albite-rich surfaces in shaded areas; may also represent gossans
27	Bansiyal n-D Class Mean #8	Pyrrhotite (0.879) Andalusite (0.872) Pyrope (0.860)	Vesuvian (0.900) Pyrrhotite (0.897) Andalusite (0.870)	Andalusite+garnet-bearing rocks; possibly mineralized
28	Bansiyal n-D Class Mean #9	Lazurite (0.762) Celestite (0.738)	Celestite (0.854) Uvarovite (0.731)	Vegetation
29	Bansiyal n-D Class Mean #10	Uvarovite (0.842) Celestite (0.838)	Celestite (0.908) Uvarovite (0.796)	Vegetation
30	Chandmari n-D Class Mean #1	Celestite (0.633) Uvarovite (0.597) Lazurite (0.549)	Celestite (0.698) Uvarovite (0.514)	Vegetation
31	Chandmari n-D Class Mean #2	Hematite (0.920) Andalusite (0.896) Sphene (0.893)	Andradite (0.932) Dolomite (0.930) Clinocllore (0.911)	Garnetiferous andalusite schist rich in iron oxide/sulfate and chlorite
32	Chandmari n-D Class Mean #3	Tourmaline (0.854) Grossular (0.843) Pyrrhotite (0.838)	Pyrrhotite (0.896) Sphalerite (0.820) Vesuvian (0.815)	Same as above
33	Chandmari n-D Class Mean #4	Desert Varnish (0.834) Mizzonite (0.772) Kerogen (0.750) Illite (0.739)	Desert Varnish (0.825) Mizzonite (0.695) Quartz (0.670)	Illite+scapolite-rich surfaces
34	Chandmari n-D Class Mean #5	Kerogen, pyrrhotite (0.791) Epidote (0.789) Richterite (0.779) Hematite, rhodonite (0.775)	Sphalerite (0.807) Adularia, chromite (0.782) Labradorite (0.776)	Amphibole-bearing rocks rich in chlorite/epidote
35	Chandmari n-D Class Mean #6	Andradite (0.913) Zincite (0.893) Desert Varnish (0.884) Nontronite (0.872)	Dolomite (0.930) Clinocllore (0.927) Lizardite (0.921)	Garnetiferous rocks rich in corrensite
36	Chandmari n-D Class Mean #7	Cuprite (0.839) Rutile (0.836) Desert Varnish (0.816)	Quartz (0.869) Nontronite (0.832) Mizzonite (0.821)	Illite+scapolite-rich surfaces; inspection of these pixels in the image shows that these surfaces are actually shaded
37	Chandmari n-D Class Mean #8	Hematite (0.810) Andradite (0.771) Sphene (0.761)	Gibbsite (0.805) Andradite (0.789) Dolomite (0.775)	Strong band 7 absorption and a weak band 5 absorption indicate the pixels to represent jarosite- and alunite-rich surfaces
38	Chandmari n-D Class Mean #9	Hematite (0.822) Pyrrhotite (0.814) Andalusite (0.794)	Sphalerite (0.966) Grossular (0.890) Chromite (0.800)	Andalusite-bearing rocks rich in chlorite/epidote/phlogopite and iron-oxide (strong band 8 absorption and low overall reflectance)
39	Chandmari n-D Class Mean #10	Mizzonite (0.843) Lazurite (0.830) Kerogen (0.821)	Desert Varnish (0.830) Celestite (0.814) Uvarovite (0.808)	Strong band 8 absorption, absorption in band 2, and a weak feature around band 5 indicate that the spectrum is representative of chlorite/epidote/calcite-rich surfaces with some alunite. The steep slope between band 3 and 2, and high band 4 reflectance indicate that the material is probably a quartzose rock with some vegetation cover
40	Dhauli n-D Class Mean #1	Uvarovite (0.745) Celestite (0.741)	Celestite (0.898) Uvarovite (0.795)	Vegetation
41	Dhauli n-D Class Mean #2	Sphene (0.924) Pyrope, andalusite (0.923) Hematite (0.907)	Grossular (0.993) Pyrrhotite (0.989) Mizzonite (0.967) Dipyre (0.960)	Andalusite+hematite with scapolite

Table-8.9 continued...

42	Dhauri n-D Class Mean #3	Pyrrhotite (0.934) Pyrope (0.928) Andalusite (0.916) Tremolite (0.910) Hematite (0.905)	Grossular (0.984) Pyrrhotite (0.974) Mizzonite (0.970) Dipyre(0.965)	Andalusite and hematite with scapolite, illite and some tremolite
43	Dhauri n-D Class Mean #4	Lazurite (0.876) Mizzonite (0.828) Celestite (0.813)	Celestite (0.924) Uvarovite (0.862)	Vegetation
44	Dhauri n-D Class Mean #5	Mizzonite (0.876) Lazurite (0.867) Kerogen (0.841)	Mizzonite (0.919) Quartz (0.913)	Scapolite (mizzonite)
45	Dhauri n-D Class Mean #6	Hematite (0.891) Andalusite (0.887) Sphene (0.879)	Pigeonite (0.962) Chromite (0.954) Sphalerite (0.918)	Hematite with calcite and scapolite; and some alunite (?) (weak band 5 absorption)
46	Dhauri n-D Class Mean #7	Lazurite (0.858) Cuprite (0.809) Rutile (0.803)	Celestite (0.870) Uvarovite (0.866)	Vegetation dominant pixels of possibly calcite + alunite composition
47	Dhauri n-D Class Mean #8	Pyrrhotite (0.911) Andalusite (0.868) Pyrope (0.863)	Pyrrhotite (0.956) Sphalerite (0.917) Grossular (0.910)	Scapolite + Illite
48	Dhauri n-D Class Mean #9	Pyrrhotite (0.881) Pyrope (0.860) Andalusite (0.857)	Pyrrhotite (0.911) Sphalerite (0.890) Grossular (0.881)	Scapolite + Illite + Hematite
49	Gadrata n-D Class Mean #1	Lazurite (0.796) Rutile (0.723) Uvarovite (0.717)	Hydroxyl apatite (0.828) Rutile (0.826) Microcline (0.800)	Vegetation (steep slope between band 3 and 2)
50	Gadrata n-D Class Mean #2	Corrensite (0.904) Desert Varnish (0.899) Sphene (0.898)	Celsian (0.995) Meionite (0.994) Hectorite, lizardite, ferrihydrite, tremolite (0.977)	Tremolite + Calcite + Desert Varnish (prominent band 8 absorption for calcite with overall spectral curve shape similar to tremolite)
51	Gadrata n-D Class Mean #3	Desert Varnish (0.849) Corrensite (0.819) Richterite (0.812)	Desert Varnish (0.859) Sphalerite (0.815) Labradorite (0.813) Mizzonite (0.809)	Corrensite + Chlorite/epidote + Illite
52	Gadrata n-D Class Mean #4	Mizzonite (0.795) Lazurite (0.768) Corrensite (0.763)	Celestite (0.748) Uvarovite (0.706)	Vegetation
53	Gadrata n-D Class Mean #5	Desert Varnish (0.902) Corrensite (0.888) Sphene (0.887)	Grossular (0.943) Dipyre (0.941) Mizzonite (0.934) Mizzonite, Celsian (0.927)	Andalusite + illite + scapolite/chlorite + tremolite
54	Gadrata n-D Class Mean #6	Andalusite (0.904) Hematite (0.901) Pyrope (0.900)	Saponite (0.956) Pyrophyllite (0.942, 0.938) Topaz (0.938, 0.935)	Topaz/andalusite + amphibole (richterite) + montmorillonite (saponite)
55	Gadrata n-D Class Mean #7	Pyrope (0.872) Andalusite (0.841) Illite (0.839)	Muscovite (0.933, 0.932, 0.927) Illite (0.915) Muscovite (0.912)	Muscovite + illite + montmorillonite + kaolinite-smectite
56	Gadrata n-D Class Mean #8	Pyrope (0.936) Andalusite (0.935) Sphene (0.909) Hematite (0.907)	Vesuvian (0.977) Tourmaline (0.969) Pyrrhotite (0.958)	Andalusite + illite
57	Gadrata n-D Class Mean #9	Celsian (0.914) Dipyre (0.912) Grossular (0.909) Meionite (0.906)	Dipyre (0.927) Grossular, Mizzonite (0.917) Celsian (0.910)	Celsian + garnet (grossular)/scapolite (dipyre)
58	Gadrata n-D Class Mean #10	Pyrope (0.891) Montmorillonite (0.881) Kaolinite-smectite (0.876)	Muscovite (0.961, 0.954) Illite (0.953) Muscovite (0.952)	Muscovite + illite + kaolinite-smectite + albite + tourmaline
59	Kalota n-D Class Mean #1	Uvarovite (0.726) Lazurite (0.707)	Uvarovite (0.760) Celestite (0.733)	Vegetation
60	Kalota n-D Class Mean #2	Desert Varnish (0.844) Corrensite (0.794)	Desert Varnish (0.820) Richterite (0.779)	Amphibole (richterite) + Corrensite + Chlorite + Illite

Table-8.9 continued...

		Richterite (0.790)	Labradorite (0.720) Corrensite (0.708)	
61	Kalota n-D Class Mean #3	Mizzonite (0.815) Illite (0.806) Quartz (0.791)	Desert Varnish (0.809) Illite (0.775) Roscoelite (0.792) Quartz (0.758)	Illite-bearing quartzose rock
62	Kalota n-D Class Mean #4	Corrensite (0.832) Kerogen (0.812) Chlorite (0.722)	Corrensite (0.823) Kerogen (0.753) Labradorite (0.663)	Corrensite + Chlorite + Quartz/illite (most likely Quartz, chlorite-schist)
63	Kalota n-D Class Mean #5	Lazurite (0.799) Uvarovite (0.773)	Celestite (0.845) Hydroxyl apatite, microcline (0.828) Rutile (0.821)	Vegetation
64	Kalota n-D Class Mean #6	Andalusite (0.945) Sphene (0.928) Pyrope (0.920) Hematite (0.913)	Andalusite (0.979) Vesuvianite (0.959) Tourmaline (0.951)	Andalusite + Illite
65	Kalota n-D Class Mean #7	Lazurite (0.705) Mizzonite (0.690) Uvarovite (0.686)	Uvarovite (0.690)	Vegetation
66	Kalota n-D Class Mean #8	Hematite (0.925) Andalusite (0.908) Sphene (0.882)	Brucite (0.957) Hematite (0.938) Andalusite (0.905)	Iron-oxide-rich quartzose rock
67	Kalota n-D Class Mean #9	Augite (0.878) Andalusite (0.874) Hematite (0.865) Pyrope (0.862)	Pectolite, augite (0.923) Sodium bicarbonate (0.918) Gypsum (0.914)	Kaolinite-smectite, illite-rich quartzose rock
68	Kalota n-D Class Mean #10	Quartz (0.786) Mizzonite (0.784) Lazurite (0.776)	Quartz (0.823) Celestite (0.804) Uvarovite (0.764)	Quartz + Vegetation
69	Suredi n-D Class Mean #1	Celestite (0.744) Uvarovite (0.692)	Celestite (0.937) Uvarovite (0.726)	Vegetation
70	Suredi n-D Class Mean #2	Pyrope (0.955) Andalusite (0.942) Hematite (0.920) Illite (0.917)	Tourmaline (0.992) Pyrope (0.981) Illite, oligoclase (0.975)	Illite, kaolinite-smectite and iron-oxide-rich andalusite- bearing rock/soil
71	Suredi n-D Class Mean #3	Pyrope (0.913) Illite (0.902) Andalusite (0.886)	Brookite (0.944) Marialite, montmorillonite (0.943) Muscovite, cordierite, illite (0.942)	Illite/muscovite, kaolinite- smectite, albite, tourmaline, andalusite-bearing quartzose rock/soil
72	Suredi n-D Class Mean #4	Kerogen (0.789) Corrensite (0.757) Desert Varnish (0.729)	Kerogen (0.706) Corrensite (0.689) Desert Varnish (0.641) Quartz (0.636)	Altered amphibole-rich rock/soil with corrensite + chlorite (prochlorite) + illite
73	Suredi n-D Class Mean #5	Lazurite (0.852) Mizzonite (0.809) Rutile (0.797)	Celestite (0.893) Microcline (0.831) Uvarovite (0.830)	Vegetation-rich quartz/illite- bearing areas
74	Suredi n-D Class Mean #6	Desert Varnish (0.790) Illite (0.740) Mizzonite (0.739) Corrensite (0.721)	Desert Varnish (0.747) Quartz (0.666) Roscoelite (0.663)	Illite, corrensite-bearing quartzose rock/soil
75	Suredi n-D Class Mean #7	Corrensite (0.874) Kerogen (0.867) Desert Varnish (0.855) Mizzonite (0.849)	Corrensite, desert varnish (0.879) Richterite (0.845) Labradorite (0.841)	Corrensite + Illite + Chlorite
76	Suredi n-D Class Mean #8	Quartz (0.817) Mizzonite (0.804) Lazurite (0.791)	Quartz (0.867) Celestite (0.854) Uvarovite (0.804)	Vegetation
77	Suredi n-D Class Mean #9	Andalusite (0.918) Hematite (0.910) Sphene (0.906)	Sphalerite (0.965) Pyrrhotite (0.955) Grossular (0.946)	Corrensite, chlorite-rich andalusite-bearing rock/soil
78	Suredi n-D Class Mean #10	Andalusite (0.927) Pyrope (0.914) Pyrrhotite (0.872) Hematite (0.865) Illite (0.854)	Andalusite (0.957) Vesuvianite (0.932) Pyrope (0.923) Tourmaline (0.922) Illite (0.895)	Illite/muscovite, kaolinite- smectite, albite, tourmaline, andalusite-bearing quartzose rock/soil

Table-8.10 End-member spectral identification using ENVI's Spectral Analyst™ for Case 4: Image-subsets for 8 different mineralized areas, ASTER SWIR 6-band reflectance data

S. No.	PPI-derived Unknown Image End-member ID	Top matches based on SAM+SFF scores (fit values in parentheses)	Top matches based on SFF scores (fit values in parentheses)	Remarks and best match based on visual inspection
1	Akwali n-D Class Mean #1	Monticellite (0.906) Arsenopyrite (0.897) Carbon black (0.894)	Mascagnite (0.936) Axinite (0.934) Monticellite (0.930)	Sulfur bearing iron mineral; most likely pyrite; also good visual matches with hematite
2	Akwali n-D Class Mean #2	Grossular (0.866) Clinochlore (0.855) Chromite (0.844)	Grossular (0.955) Sphalerite (0.953) Clinochlore (0.872)	Best visual matches with rhodonite, prochlorite and corrensite; likely to represent chlorite and garnet
3	Akwali n-D Class Mean #3	Hectorite (0.912) Chrysotile (0.897) Meionite (0.888) Celsian, calcite (0.886)	Ferrihydrite, hectorite, lizardite (0.981) Tremolite (0.980) Meionite (0.978)	Best visual matches with celsian and richterite
4	Akwali n-D Class Mean #4	Carbon black (0.886) Chromite (0.884) Dolomite (0.881) Clinochlore (0.850)	Brucite (0.906) Sphalerite (0.903) Hematite, zincite (0.899) Grossular (0.886)	Best visual matches with almandine garnet; likely to represent iron-oxide soils containing garnet
5	Akwali n-D Class Mean #5	Chromite (0.828) Mizzonite (0.824) Grossular, cookeite (0.807)	Pyrrhotite, vesuvianite (0.836) Tourmaline, sphalerite (0.814) Andalusite (0.792)	Best visual matches with cookeite (chlorite), tourmaline and grossular
6	Akwali n-D Class Mean #6	Anorthite (0.903) Dolomite (0.888) Calcite (0.875)	Grossular (0.947) Sphalerite (0.923) Clinochlore (0.909)	Strong band 8 absorption and best visual inspection indicates that this is likely to represent chlorite or corrensite
7	Akwali n-D Class Mean #7	Anorthite (0.873) Chrysotile, strontianite (0.871) Calcite (0.869)	Sphalerite (0.883) Rhodonite (0.875) Calcite (0.860)	Same as above
8	Bandha n-D Class Mean #1	Chromite (0.852) Cookeite (0.843) Pectolite (0.835) Illite (0.828)	Ammonium chlorite (0.911) Axinite (0.906) Mascagnite (0.898)	Best visual match with cookeite (chlorite) and uvarovite (garnet)
9	Bandha n-D Class Mean #2	Chrysotile (0.953) Calcite (0.938) Anorthite (0.935)	Phlogopite (0.972) Rhodochrosite (0.971) Calcite (0.960)	Best visual matches with hornblende and prochlorite
10	Bandha n-D Class Mean #3	Arsenopyrite (0.952) Pyrite (0.950) Cordierite (0.941)	Cookeite (0.982) Mizzonite (0.978) Grossular (0.977)	Visually, the spectrum resembles with that of grossular, most spectra of topaz and oligoclase, best; scapolite minerals also exhibit resemblance to this spectrum
11	Bandha n-D Class Mean #4	Mizzonite (0.837) Grossular (0.820)	Grossular (0.930) Pyrrhotite (0.920) Dipyre (0.917)	Grossular and scapolite (mizzonite and dipyre)
12	Bandha n-D Class Mean #5	Dolomite (0.900) Anorthite (0.896) Clinochlore (0.891) Calcite (0.877)	Lizardite (0.964) Clinochlore (0.954) Epidote, dolomite (0.936)	Best visual matches with rhodonite and corrensite
13	Bandha n-D Class Mean #6	Vermiculite (0.863) Anorthite (0.816) Calcite (0.815)	Vermiculite (0.917) Richterite (0.850)	Best visual matches with cookeite, lepidocrosite and rhodonite
14	Bandha n-D Class Mean #7	Chromite (0.842) Mizzonite (0.829) Cookeite (0.828) Illite (0.827)	Cookeite (0.848) Pyrrhotite (0.845)	Grossular garnet + Cookeite (chlorite)
15	Bansiyal n-D Class Mean #1	Illite (0.873) Montmorillonite (0.835)	Illite (0.867) Muscovite (0.864)	Albite + Muscovite/illite + Microcline + Kaolinite-

Table-8.10 continued...

		Cookeite (0.828) Kaolinite (0.818)	Microcline (0.0.859)	smectite
16	Bansiya n-D Class Mean #2	Grossular (0.944) Mizzonite (0.921) Oligoclase (0.909)	Grossular (0.979) Mizzonite (0.960) Dipyre (0.931)	Grossular + Meionite (scapolite) + oligoclase
17	Bansiya n-D Class Mean #3	Hectorite (0.883) Calcite (0.868) Anorthite (0.857)	Sauconite (0.989) Ferrihydrite, lizardite (0.986) Tremolite (0.985)	Best visual matches with celsian, tremolite, richterite, and meionite; a stronger band 8 absorption indicates the presence of chlorite/epidote/phlogopite
18	Bansiya n-D Class Mean #4	Arsenopyrite (0.922) Syngenite (0.920) Sillimanite, topaz (0.918)	Lepidolite (0.944) Cookeite, illite (0.941) Muscovite (0.936)	Albite + scapolite + topaz
19	Bansiya n-D Class Mean #5	Grossular (0.877) Chrysotile (0.863) Celsian (0.861)	Dipyre (0.887) Grossular (0.870) Celsian (0.867)	Grossular + dipyre
20	Bansiya n-D Class Mean #6	Oligoclase, tourmaline, mizzonite (0.848) Grossular (0.841) Cordierite (0.835)	Vesuvianite (0.917) Andalusite (0.897) Pyrrhotite (0.892) Tourmaline (0.887)	Best visual matches with illite + desert varnish + tourmaline
21	Bansiya n-D Class Mean #7	Cordierite (0.953) Marialite (0.925) Muscovite, oligoclase (0.912)	Hydrogrossular (0.992) Muscovite (0.989) Cordierite (0.981)	Cordierite + albite + muscovite/illite + montmorillonite + scapolite
22	Chandmari n-D Class Mean #1	Pyrrhotite (0.890) Grossular (0.824) Tourmaline (0.823)	Pyrrhotite (0.957) Sphalerite (0.797) Grossular (0.775)	Best visual match with desert varnish; absorptions in band 6 and 8 indicate that this spectrum represents a mixture of illite- and chlorite-like surfaces
23	Chandmari n-D Class Mean #2	Dolomite (0.918) Galena (0.907) Anorthite (0.896)	Andradite (0.913) Dolomite (0.912) Clintonite (0.911) Clinocllore (0.899)	Best visual match with fassaite; absorption bands are centered near band 5 and 7, this indicates that the spectrum actually represents a mixture of possibly alunite and jarosite
24	Chandmari n-D Class Mean #3	Carbon black (0.889) Opal (0.867) Bassanite (0.853)	Gibbsite (0.946) Brucite (0.926) Hematite (0.921)	Jarosite (band 7 absorption)
25	Chandmari n-D Class Mean #4	Cordierite (0.913) Muscovite (0.905) Oligoclase (0.902)	Oligoclase (0.915) Muscovite (0.913) Brookite, montmorillonite (0.896)	Oligoclase + Cordierite + Montmorillonite + Scapolite + Muscovite/illite
26	Chandmari n-D Class Mean #5	Chromite (0.814) Mizzonite (0.801) Grossular (0.786)	Pyrrhotite (0.801) Sphalerite (0.780) Grossular (0.773)	Grossular (garnet) + Dipyre (scapolite) + Cookeite (chlorite)
27	Chandmari n-D Class Mean #6	Pyrite (0.843) Montecellite (0.834) Galena (0.828)	Ulexite (0.919) Axinite (0.913) Mascagnite, opal (0.903)	Band 5 absorption and general curve shape strongly indicate the material to be of buddingtonitic composition
28	Chandmari n-D Class Mean #7	Tourmaline (0.802) Grossular (0.800) Dolomite (0.795)	Sphalerite (0.859) Grossular (0.854) Pyrrhotite (0.837) Andalusite (0.809)	Illite + Chlorite + Andalusite
29	Dhauli n-D Class Mean #1	Grossular (0.912) Celsian (0.896) Meionite (0.896)	Pyrrhotite (0.904) Dipyre (0.894) Andalusite (0.883)	Dipyre
30	Dhauli n-D Class Mean #2	Chromite (0.886) Pyrite (0.885) Illite (0.879)	Cookeite (0.933) Chromite (0.927) Pigeonite (0.922)	Cookeite (chlorite) + Meionite (scapolite)
31	Dhauli n-D Class Mean #3	Chromite (0.854) Cookeite (0.833)	Chromite (0.845) Sphalerite (0.834)	Cookeite + dipyre

Table 8.10 continued...

		Anorthite (0.828) Mizzonite, calcite (0.825)	Pyrrhotite (0.825) Cookeite (0.808)	
32	Dhaulti n-D Class Mean #4	Vermiculite (0.855) Mizzonite (0.848)	Dipyre (0.977) Celsian (0.961) Meionite (0.954)	Scapolite
33	Dhaulti n-D Class Mean #5	Mizzonite (0.846) Grossular (0.835) Celsian (0.797)	Grossular (0.912) Dipyre (0.907) Pyrrhotite (0.869)	Scapolite + amphibole (riebeckite)
34	Dhaulti n-D Class Mean #6	Vesuvianite (0.861) Mizzonite (0.840) Opal (0.839)	Andalusite (0.942) Vesuvianite (0.940) Tourmaline (0.921)	Quartz + illite or scapolite + andalusite
35	Dhaulti n-D Class Mean #7	Chromite (0.863) Grossular (0.821) Clinocllore (0.815)	Chromite (0.907) Sphalerite (0.881) Grossular (0.848)	Best visual match with rhodonite; but the likely mineral is perhaps prochlorite
36	Gadrata n-D Class Mean #1	Mizzonite (0.879) Oligoclase (0.854) Cordierite (0.852)	Witherite (0.952) Tourmaline (0.948) Cinnabar (0.935)	Oligoclase + Scapolite + Cordierite + Illite
37	Gadrata n-D Class Mean #2	Galena (0.967) Arsenopyrite (0.962)	Natrolite (0.985) Kainite (0.984) Colemanite (0.982)	Quartz/topaz + Illite + Andalusite
38	Gadrata n-D Class Mean #3	Meionite (0.972) Celsian (0.962) Dipyre (0.937)	Celsian (0.986) Meionite (0.981) Dipyre (0.972)	Riebeckite (amphibole) + Dipyre (scapolite)
39	Gadrata n-D Class Mean #4	Cookeite (0.843) Vermiculite (0.819) Illite (0.819)	Ammonium chlorite (0.852) Axinite (0.851) Mascagnite (0.841)	Excellent matches with a variety of likely minerals: cookeite, topaz, desert varnish, sillimanite, beryl, rectorite; broad absorption across bands 5 and 6, and band 8 separated by a reflectance peak at band 7
40	Gadrata n-D Class Mean #5	Chromite (0.887) Anorthite (0.878) Dolomite (0.877) Cookeite (0.876)	Sphalerite (0.923) Chromite (0.923) Grossular (0.894)	Andalusite + chlorite/grossular
41	Gadrata n-D Class Mean #6	Oligoclase (0.955) Marialite (0.929) Cordierite (0.925)	Witherite (0.999) Oligoclase (0.973) Tourmaline (0.949) Illite (0.948)	Oligoclase + Scapolite + Tourmaline + Illite + Cordierite
42	Gadrata n-D Class Mean #7	Chrysotile (0.979) Anorthite (0.967) Calcite (0.955)	Chrysotile (0.997) Rhodochrosite (0.995) Calcite (0.995)	Because of a distinct band 8 absorption, a variety of minerals are likely candidates for this spectrum: Ferroan Chamosite (chlorite) + Hornblende + Celsian + Labradorite + Phlogopite + Calcite
43	Kalota n-D Class Mean #1	Grossular (0.944) Oligoclase (0.927) Cookeite (0.926)	Grossular (0.962) Mizzonite (0.952) Dipyre (0.944)	Grossular + Dipyre + Oligoclase + Cookeite
44	Kalota n-D Class Mean #2	Cookeite (0.862) Illite (0.846) Hydrogrossular (0.824)	Cookeite (0.877) Mizzonite (0.874) Oligoclase (0.866)	Scapolite + Chlorite + Cordierite + Muscovite
45	Kalota n-D Class Mean #3	Mizonite (0.889) Grossular (0.878) Tourmaline (0.864) Oligoclase (0.862)	Vesuvianite (0.932) Pyrrhotite (0.912) Tourmaline (0.907) Mizzonite (0.894)	Desert Varnish + Grossular + Oligoclase + Tourmaline + Illite + Cordierite
46	Kalota n-D Class Mean #4	Cookeite (0.798) Vermiculite (0.772) Illite (0.750)	Cookeite (0.779) Topaz (0.727) Ammonium chlorite (0.708)	Cookeite + Topaz + Sillimanite + Rectorite
47	Kalota n-D Class Mean #5	Opal (0.923) Montmorillonite (0.884) Bassanite (0.884)	Sanidine (0.954) Hematite (0.944) Chalcedony (0.941)	Quartz/chalcedony
48	Kalota n-D Class	Grossular (0.967)	Dipyre (0.987)	Grossular + oligoclase +

Table-8.10 continued...

	Mean #6	Oligoclase (0.959) Meionite (0.955) Celsian (0.949)	Grossular (0.985) Celsian (0.977)	labradorite + albite + celsian + quartz
49	Kalota n-D Class Mean #7	Anorthite (0.915) Dolomite (0.896) Chrysotile (0.887) Calcite (0.885)	Lizardite (0.973) Clinocllore (0.919) Anorthite (0.909) Epidote (0.908) Phlogopite (0.907)	Chlorite/epidote
50	Suredi n-D Class Mean #1	Chromite (0.859) Grossular (0.778) Clinocllore (0.769) Carbon black (0.760) Dolomite (0.758) Cookeite (0.757)	Chromite (0.869) Sphalerite (0.830) Pigeonite (0.786)	Chlorite + Phlogopite + Celsian
51	Suredi n-D Class Mean #2	Oligoclase, Cordierite (0.941) Marialite (0.933) Mizzonite (0.921)	Tourmaline (0.993) Pyrope (0.985) Illite (0.978) Oligoclase (0.976)	Oligoclase + Grossular + Illite + Scapolite + Albite
52	Suredi n-D Class Mean #3	Chromite (0.886) Chrysotile (0.876) Anorthite (0.874)	Vermiculite (0.914) Mizzonite (0.905) Dipyre (0.904)	Meionite + Grossular + Cookeite + Celsian
53	Suredi n-D Class Mean #4	Oligoclase (0.957) Grossular (0.945) Marialite (0.928) Albite (0.917)	Tourmaline (0.979) Mizzonite (0.962) Pyrrhotite (0.962)	Oligoclase + Grossular + Andalusite + Illite
54	Suredi n-D Class Mean #5	Chromite (0.889) Pyrite (0.885) Carbon black (0.881) Cookeite, ilite (0.871)	Pigeonite (0.925) Chromite (0.917) Ammonium chlorite (0.911)	Cookeite + Grossular + Albite + Oligoclase
55	Suredi n-D Class Mean #6	Mizzonite (0.887) Cordierite (0.878) Illite (0.873) Oligoclase (0.866) Muscovite (0.855)	Witherite (0.975) Ologoclase (0.955) Tourmaline (0.943) Mizzonite (0.937)	Tourmaline + Oligoclase + Cordierite + Marialite (scapolite) + Muscovite/illite + Montmorillonite + Grossular
56	Suredi n-D Class Mean #7	Illite (0.854) Cookeite (0.836) Hydrogrossular (0.812) Muscovite (0.812)	Muscovite (0.863) Oligoclase (0.852) Illite (0.837)	Muscovite + Montmorillonite + Cordierite + Albite + Grossular

8.4.4 SAM classification

Using a threshold angle of 0.05 radians and the end-members derived from the image through PPI for the four cases described above, Spectral Angle Mapper (SAM) classification has been performed on the ASTER reflectance image dataset. For Cases 1 and 2, since the number of end-members was limited, no grouping was necessary. However, as there was a rather large number of spectral classes for Cases 3 and 4 which could potentially render the classes too fine to differentiate in a single classified map, it was deemed necessary to reduce the actual number of truly distinct end-member spectral classes by grouping similar classes of the 8 different subsets. Thus, based upon the end-member spectral identification using the Spectral Analyst™, the number of distinct spectral classes for Case 3 was reduced from 78 to 28, and for Case 4 it was reduced from 56 to 32. The SAM classification results for the four cases obtained thus have been shown in Figures 8.20, 8.21, 8.22 and 8.23, respectively for the four cases identified and described earlier. It can be readily observed that due to filter-scratch in SWIR focal array the upper left part of the classified images in Figures 8.21 and 8.23 are difficult to interpret meaningfully.

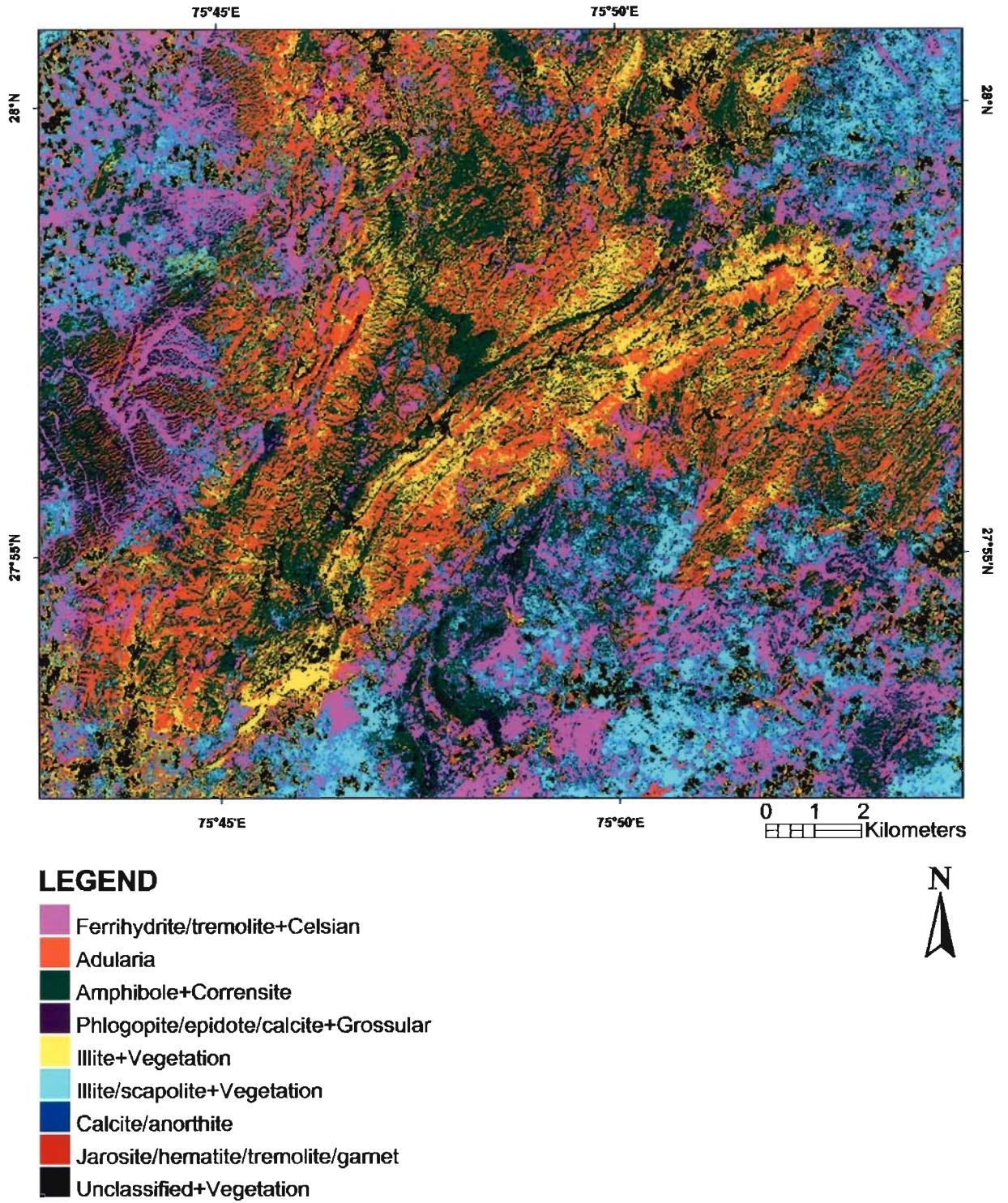
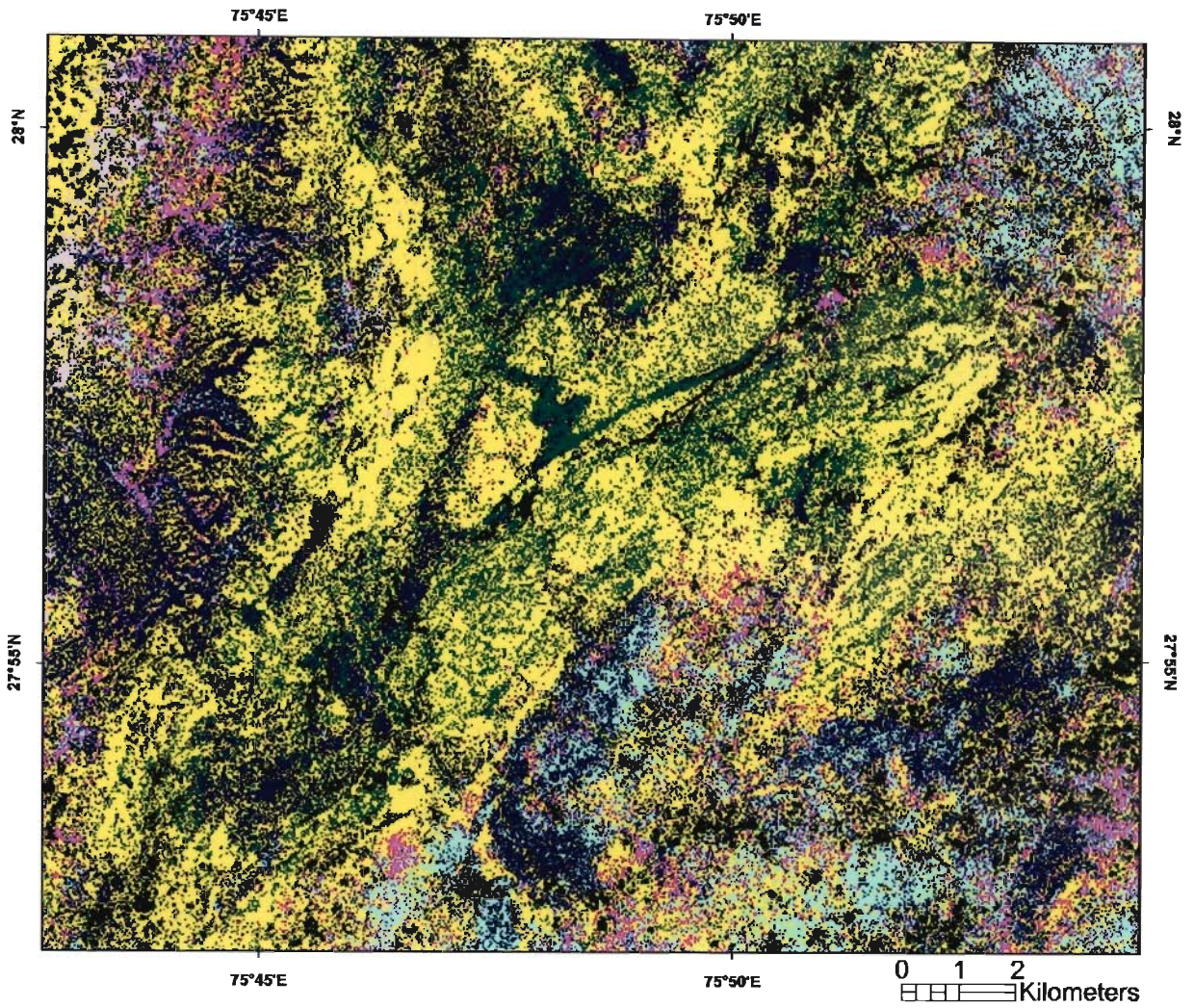


Figure-8.20 SAM-classified alteration/surface mineral map of the study area for Case 1.



LEGEND








-  Hornblende/tremolite+Phlogopite
-  Muscovite/illite+Montmorillonite+Oligoclase
-  Topaz/sillimanite
-  Iron-oxide+Topaz
-  Desert Varnish+Chlorite
-  Scapolite+illite+Oligoclase
-  Unclassified+Vegetation



Figure-8.21 SAM-classified alteration/surface mineral map of the study area for Case 2.

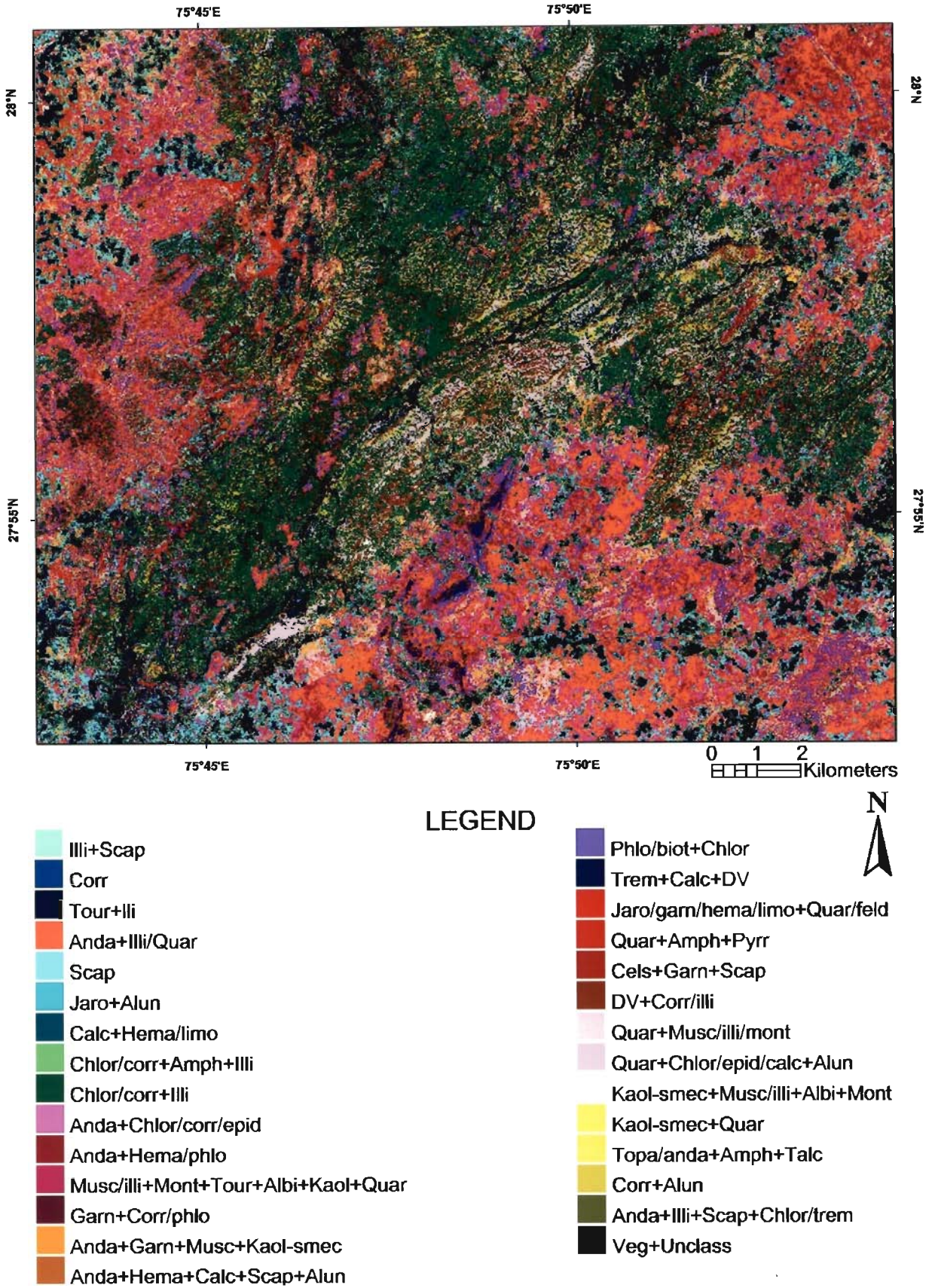


Figure-8.22 SAM-classified alteration/surface mineral map of the study area for Case 3.

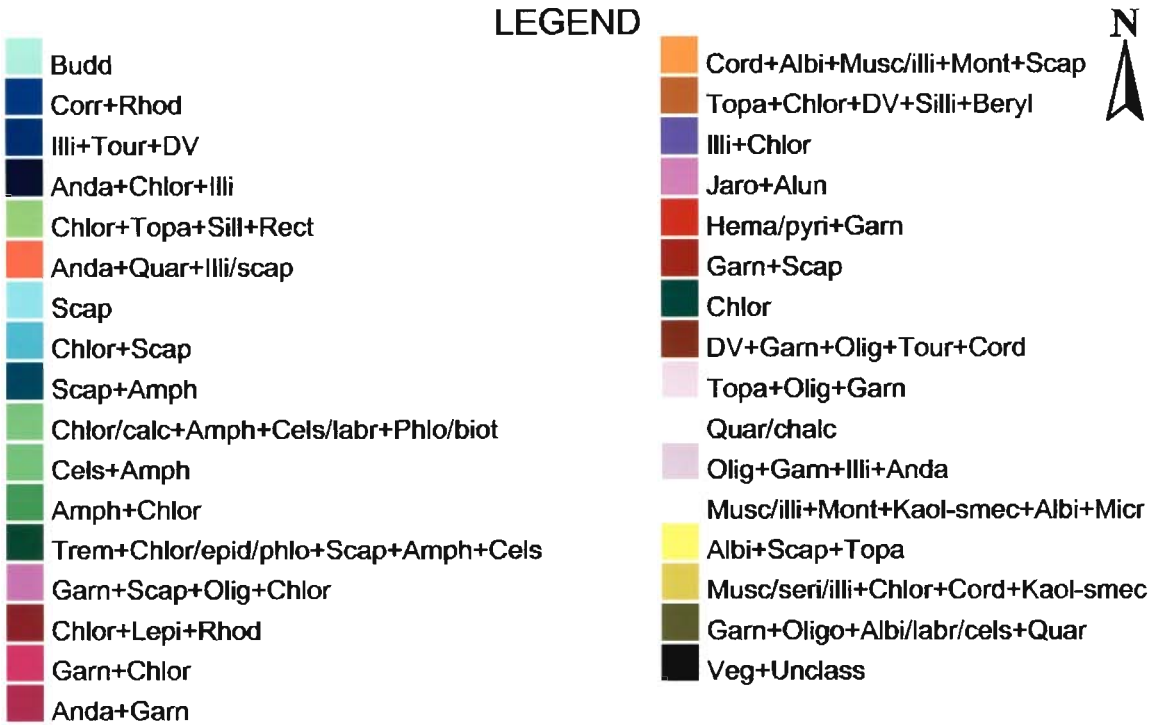
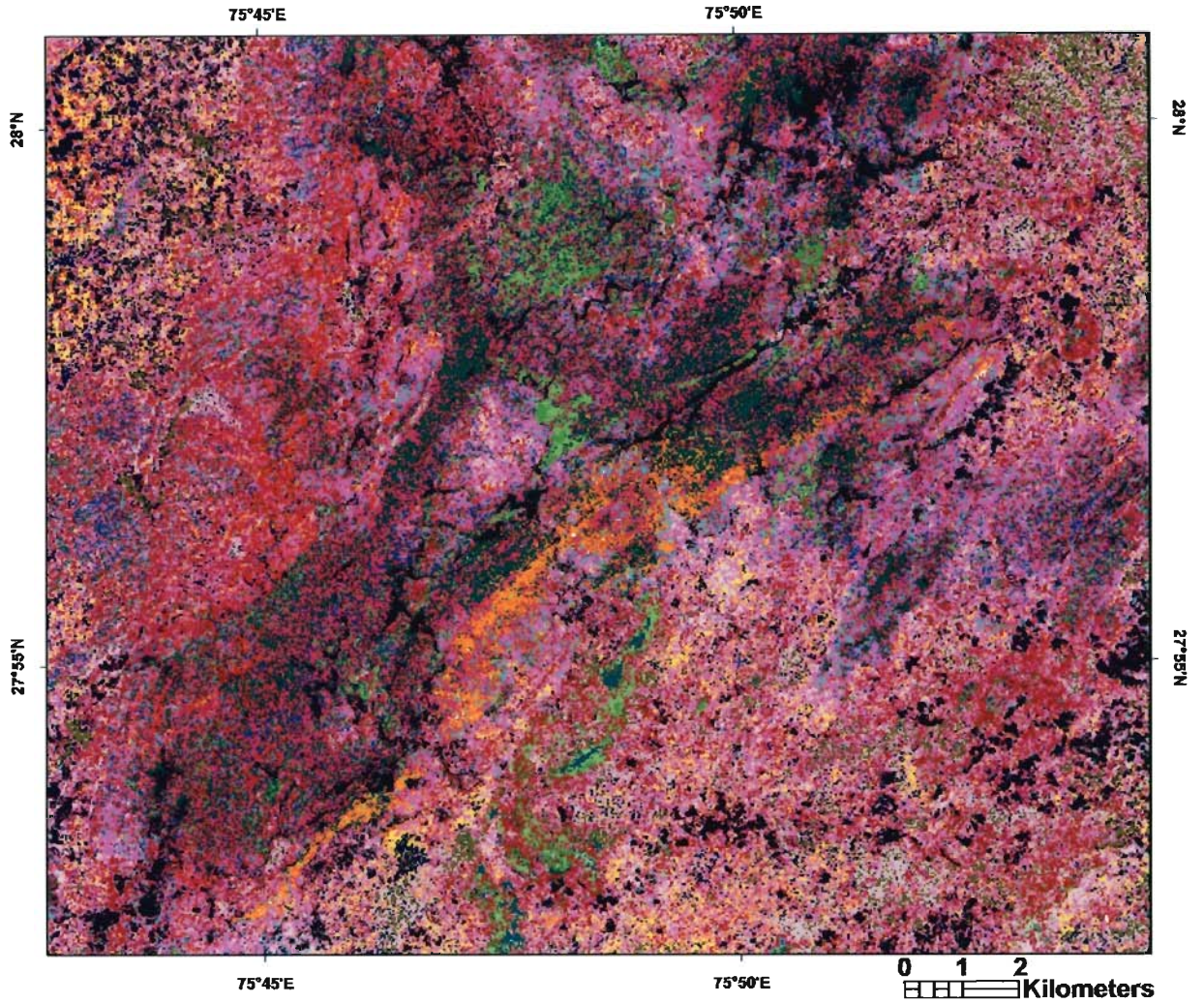


Figure-8.23 SAM-classified alteration/surface mineral map of the study area for Case 4.

8.4.5 MTMF™ processing

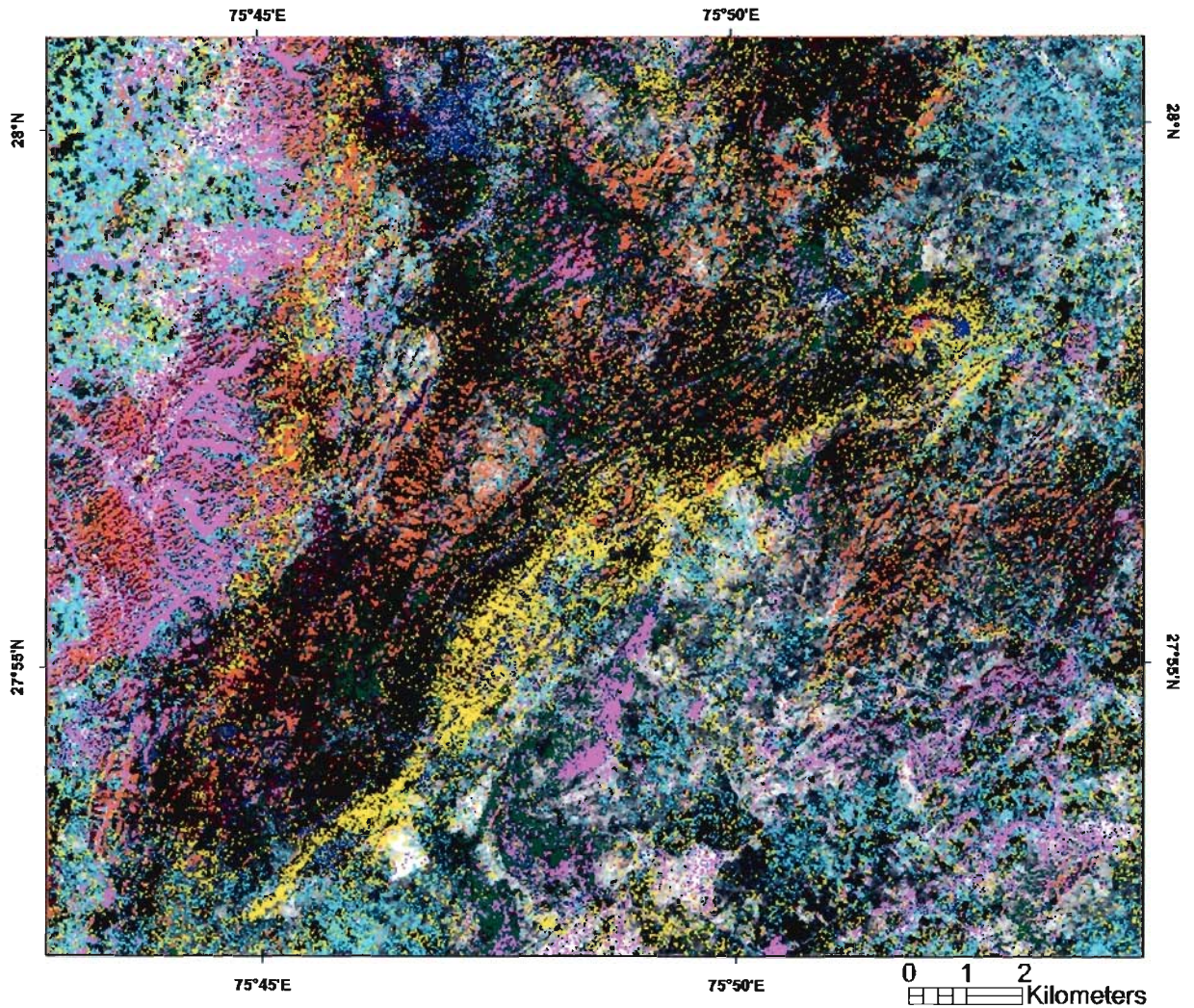
For Cases 1 and 2, Mixture Tuned Matched Filtering (MTMF™) processed images were produced for the respective end-member spectral classes. Although Cases 3 and 4 were also used for MTMF™ processing, the unmanageably large number of end-member spectral classes in these cases made the final combination difficult due to overlaps among different classes. The individual MTMF™ class-abundance images were interactively thresholded according to the procedure described in Chapter 7, to combine the different end-member spectral classes into single MTMF™ classified images, respectively for the two cases. The threshold value selection is rather subjective and can lead to slight variations in the final mineral map product. Threshold values can be chosen either liberally such that many pixels are classified together that are not truly the same, *i.e.* inclusion of false-positives; or conservatively, which results in missing of some pixels belonging to the true class. Some background knowledge of the field area and basic understanding of common geologic models are helpful, but not necessary. The threshold values used for Case 1 and Case 2 have been chosen conservatively, as summarized in Tables 8.11 and 8.12, and the resultant MTMF™ classified images are shown in Figures 8.24 and 8.25, respectively.

Table-8.11 Case 1: MTMF™ thresholds for end-member spectral class abundance images.

End-member	MTMF Range	Threshold Value
n-D Class Mean #2	-1.074001 to 1.449376	0.30
n-D Class Mean #3	-0.961481 to 1.131103	0.35
n-D Class Mean #4	-0.885976 to 0.882990	0.25
n-D Class Mean #5	-1.042887 to 1.232520	0.30
n-D Class Mean #6	-0.720868 to 0.774446	0.25
n-D Class Mean #7	-1.245776 to 0.935601	0.25
n-D Class Mean #8	-0.842181 to 0.705004	0.20
n-D Class Mean #9	-0.387703 to 0.615354	0.18
n-D Class Mean #10	-0.577745 to 1.035738	0.25

Table-8.12 Case 2: MTMF™ thresholds for end-member spectral class abundance images.

End-member	MTMF Range	Threshold Value
n-D Class Mean #2	-1.077680 to 1.230945	0.30
n-D Class Mean #3	-1.332536 to 1.242485	0.35
n-D Class Mean #4	-1.405884 to 1.266271	0.30
n-D Class Mean #5	-1.215086 to 1.040985	0.25
n-D Class Mean #6	-1.560063 to 1.092695	0.35
n-D Class Mean #7	-1.546180 to 1.369403	0.30

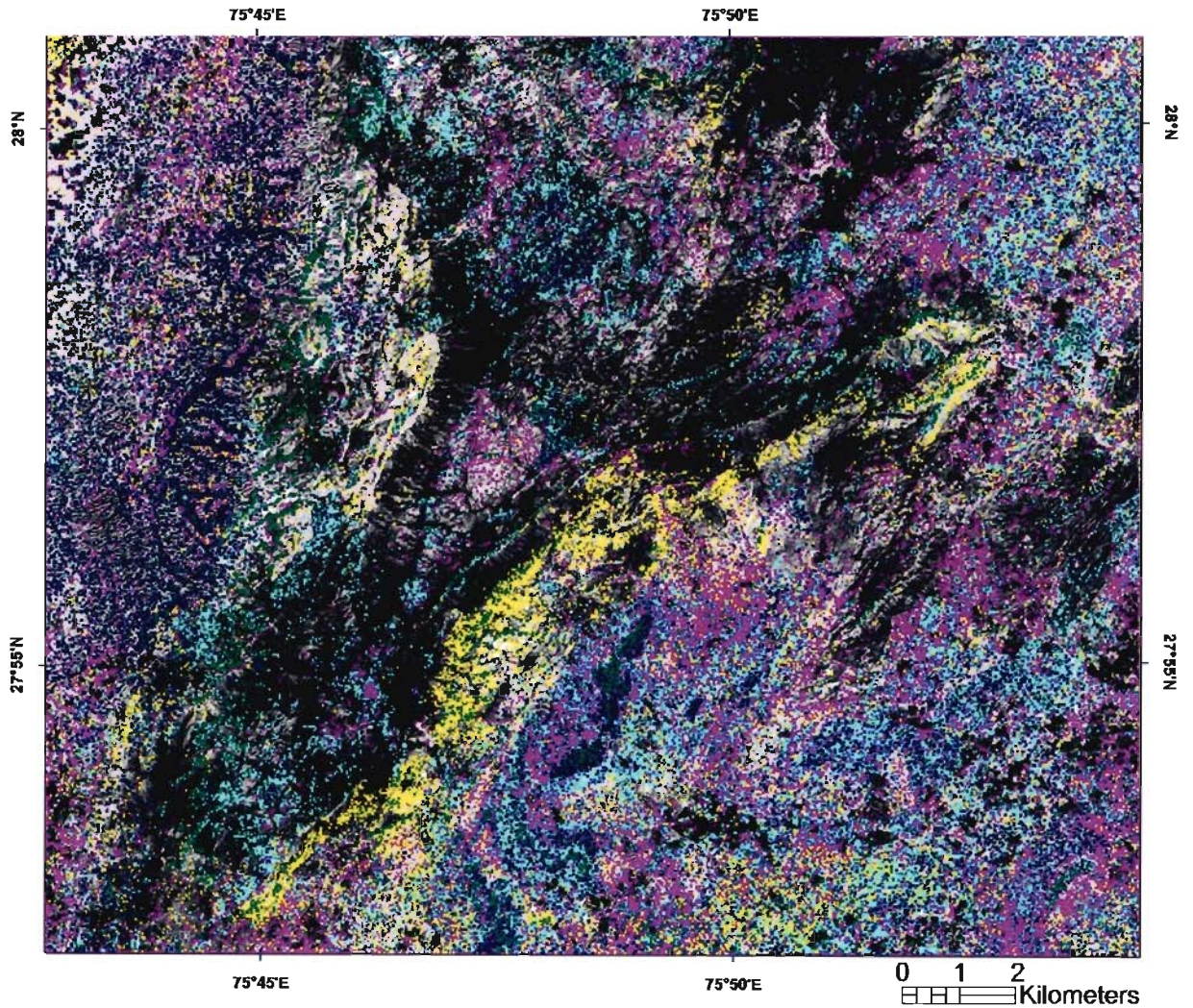


LEGEND

- Ferrihydrite/tremolite+Celsian
- Adularia
- Amphibole+Corrensite
- Phlogopite/epidote/calcite+Grossular
- Illite+Vegetation
- Illite/scapolite+Vegetation
- Calcite/anorthite
- Jarosite/hematite/tremolite/garnet
- Unclassified+Vegetation



Figure-8.24 MTMFTM-classified alteration/surface mineral map of the study area for Case 1; prominent banding due to SWIR filter-scratch problem can be noticed in the western part of the image. Background is ASTER band 1 image. Notice also that the class 'calcite/anorthite' also covers the pixels representing built structures (towns; e.g. Khetri and Babai). Differences between MTMFTM classification and SAM classification occur primarily because the MTMFTM-classified image represents 'stacked' classes, such that the top-most class is visible while other classes representing the same area (same pixels) are invisible due to overlap.



LEGEND

- Hornblende/tremolite+Phlogopite
- Muscovite/Illite+Montmorillonite+Oligoclase
- Topaz/sillimanite
- Iron-oxide+Topaz
- Desert Varnish+Chlorite
- Scapolite+Illite+Oligoclase



Figure-8.25 MTMF™-classified alteration/surface mineral map of the study area for Case 2; banding due to SWIR filter-scratch problem is more pronounced on this map, as only SWIR bands have been used to produce the classification. Background is ASTER band 1 image (grey shades). Differences between MTMF™ classification and SAM classification occur primarily because the MTMF™-classified image represents ‘stacked’ classes, such that the top-most class is visible while other classes representing the same area (same pixels) are invisible due to overlap.

8.5 Spectral classification limitations and linear mixing

Natural geologic surfaces are often covered with non-geologic materials (e.g. vegetation) or composed of mixtures of minerals with varying grain sizes or degrees of compaction/solidification. These factors greatly influence remote spectral measurements and limit the number of pixels that can be classified and mapped. This leads to a potential bias in mineral mapping. Mixing can exist at various scales and also affects the measured infrared spectral properties of an area. When minerals in a field of view are physically separated such that there is no scattering between components, the spectral signature of the area represents the sum of the fractions of each component and is thus a *linear mixture*. *Intimate mixing* occurs at smaller scales when different minerals are in close contact on a single scattering surface. The presence of rock coatings (such as desert varnish) causes another type of mixing that varies depending on the thickness of the coating and the wavelength of the scattered radiation. And at the smallest scales, molecular mixing occurs when a liquid, such as water is adsorbed onto a mineral surface or vegetation (Clark, 1999). Sub-pixel abundances of different surface cover types can all influence the nature of the spectral signature for a particular pixel. Subtle deviations from the 'type' signature can result in 'misclassification' of the pixel.

For broadband multispectral data such as that of ASTER, only spectral shapes and feature locations can be used for mineral identification. The Spectral Analyst™ analysis of the end-member spectra indicated the existence of a rather complex variety of minerals, since subtle spectral variations in image end-member spectra though principally related to the actual mineral chemistry are affected also by the differences in solar illumination geometry and topographic variations (despite earnest efforts to subjugate these effects). Therefore, spectra for the same material from sun-lit and shadowed parts have been determined as different end-members through PPI™, which highlights the pitfalls of a fully automatic processing. Also, the reference spectral libraries contain more than one spectrum for a single material, at different

levels of either purity or grain-size. While determining the spectral matches of the unknown end-members to these spectral library spectra, there is a fair chance that unrepresentative material with better overall curve-fit scores might appear as a match. Visual inspection and assigning is a more reliable way to determine the likely matches; but again, more than one reference spectra can appear to resemble the unknown spectrum and can hence introduce subjectivity in the spectral identification. Some background knowledge of the field study area can greatly check the levels of such subjectivity, as has been practiced in this study. Since the target alteration minerals expected in the study area were known beforehand, and the geologic ground-truth was available, a greater objectivity became possible in determining the spectral classes for the study area.

A mind-boggling variety of supervised classification techniques exist which can be used to classify the image to produce mineral maps. Two of these methods used in this study (SAM and MTMF™) are most widely used; typically with hyperspectral data for spectral analysis. While excellent overall agreement has been observed between the spectral classification results of two techniques, there also exist major disagreements. This can be explained as follows. The MTMF™ classification shown in Figures 8.24 and 8.25 represent ‘stacked classes’, *i.e.* the class pixels are not mutually exclusive. The same pixel has been found to match with more than one end-member spectral class. Manual thresholding has not completely eliminated the chance of overlap, and while combining the different thresholded density slices into a single classified output, due to pixel opacity the underlying classes become ‘invisible’. Perhaps a better way to represent the MTMF™-classes is a simple combination of three class-abundance images in RGB scheme, but in this way a single classification product cannot be generated! As discussed in detail in Chapter 9, comparison of the SAM classification results with the geologic ground-truth and published maps is in good agreement and thus these results represent the true spectral classes for the study area.

Synthesis of Results and Interpretation

9.1 Statement of purpose and introduction

In order to assess the usefulness and credibility of the results of spectral lithologic and alteration mapping described in Chapters 7 and 8, respectively, it is necessary to analyze them in light of existing field and laboratory evidences as described in Chapter 4. The field relationships, major and minor mineralogy, petrographic texture, surface coatings, and trace-metal content of the rock samples collected from the study area collectively constitute the bases on which the spectral signatures are defined. All spectral analysis techniques are based on the fundamental spectroscopic principles outlined in Chapter 5, and the extent to which laboratory spectra of minerals and rocks can be simulated through remotely sensed data is controlled largely by the degree of accurate retrieval of surface properties of reflectance and emissivity, as described in Chapter 6. Thus, a successful implementation of remote sensing analysis results for lithologic and mineral mapping is influenced at all stages of image analysis, starting right from data selection, which in the present case is that of ASTER.

This chapter, therefore, attempts to synthesize the results of image analysis contained in previous chapters and interprets them in a geologically meaningful way. In nutshell, the main focus of this chapter is to describe the results of ASTER-based spectral lithologic and surface/alteration mineral mapping through a comparative analysis of well-described geology, field locations and laboratory data and their representation on the respective spectral maps. Eight windows of the study area (fig. 8.15, Chapter 8), for areas with known mineralization and analyzed field samples have been used to serve this objective. Description is based on field evidence, hand specimen analysis and thin-section petrography. Limitations arising due to spatial and spectral resolution inadequacies, atmospheric and topographic correction

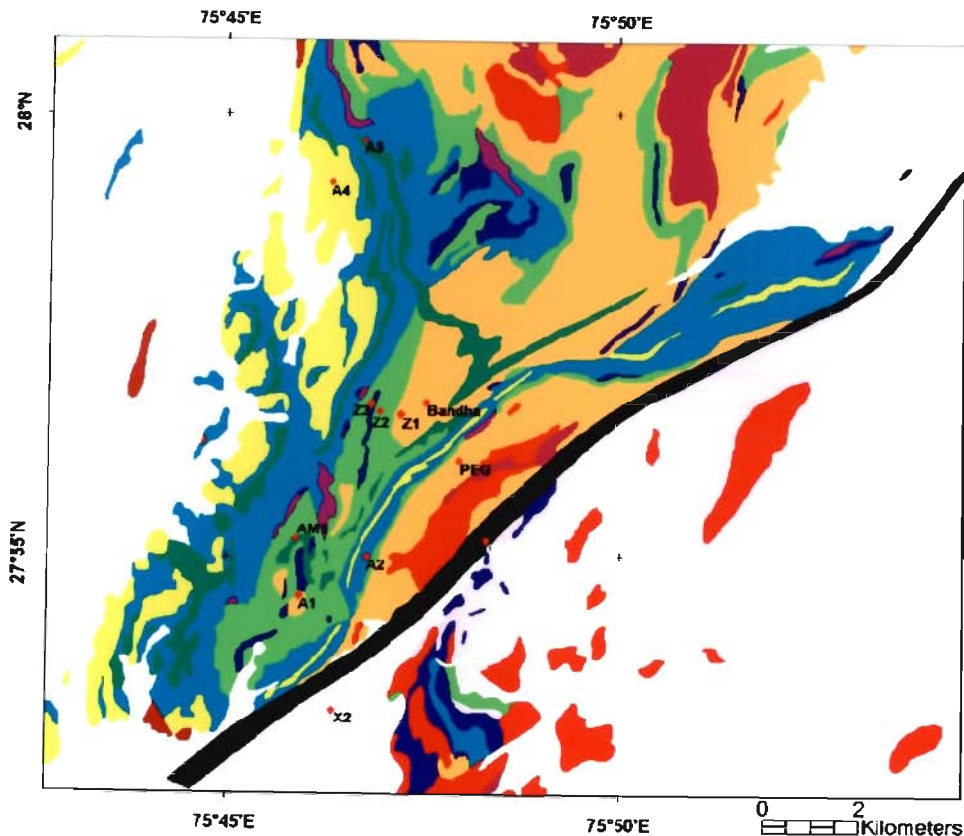
inaccuracies, and spectral mixing have been discussed at appropriate places. Associations of rock alteration with trace-metal anomalies have also been described.

9.2 Validation of spectral mapping results

As described in the following sections, the validation of spectral lithologic mapping (qualitative and quantitative; based on ASTER TIR radiance and emissivity data analysis; Chapter 7), and spectral surface/alteration mineral mapping (based on spectral analysis of ASTER VNIR-SWIR reflectance data, Chapter 8) has been done by simultaneously examining the compiled lithologic map, thin-section photomicrographs of field samples and spectral classification results. Of the eight image windows used for validation (fig. 8.15, Chapter 8) – *viz.*, Akwali, Chandmari, Dhauli, Suredi, Bandha, Bansiyal, Gadrata, and Kalota – first four represent areas with known mineralization and have been used to validate the results of (alteration/surface) mineral mapping, since site-specific field samples from these areas have been analyzed petrographically and geochemically. Image windows for Bandha, Gadrata and Bansiyal have been used for validation of ASTER TIR-based lithologic mapping since these areas contain a wider variety of rock types and associated alteration mineral assemblages, and are thus potential zones of mineralization, as observed on various spectral mineral maps. The window representing Kalota region has been used to see if spatially small trace-metal anomalies present in the regolith of the area and the associated alteration are also represented on ASTER spectral maps.

9.2.1 Spectral lithologic mapping

Figure-9.1 shows the compiled lithologic map of the study area, a DCS image (bands 13-12-10 in R-G-B), the weight percent SiO₂ map generated using the K-value technique, and spectral lithologic maps obtained using spectral indices of ASTER surface radiance data and the MTMF™ classification of L2 ASTER TIR surface emissivity data (for details see Chapter 7). Field locations of the type rock areas have been marked on the compiled lithologic map. Table-9.1 lists the field samples, their geographic latitude-longitude, major and minor mineralogy, SiO₂ weight percent values (pixel averaged) obtained through the spectral modeling and K-value methods, and spectral classes for the corresponding pixels determined using Spectral Analyst™ SAM/SFF fit-scores, as previously described in Chapter 7.



LEGEND

- | | |
|------------------------------------------------------------------------------------|-----------------------------------------------------------------------|
| ■ Biot-musc-silli Gne ss | ■ Pure-/ortho-quartzite |
| ■ Feldspathic Quartzite | ■ Impure Marble/Carbonaceous Shale |
| ■ Amphibole Quartzite | ■ Undifferentiated Rock Sequence |
| ■ Calc-silicate/para-amphibolite | ■ Granite/pegmatite/albitite |
| ■ Garn-chlo Schist | ■ Alluvium |
| ■ Biot-anda Phyllite | ■ Main Cataclastic/shear Zone |
| ■ Orthoamphibolite/metadolerite Sills/dykes | |

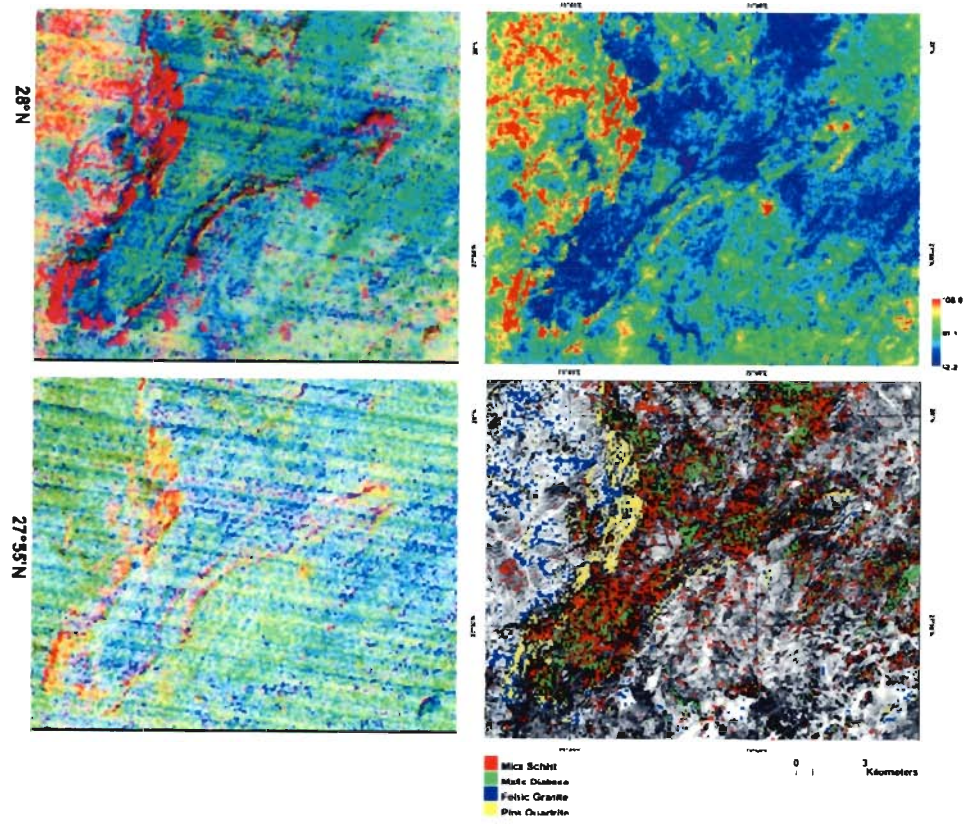


Figure-9.1 Synthesis of data processing outputs for validation of spectral lithologic mapping: **a)** Compiled lithologic map of the study area; **b)** DCS of radiance-at-sensor data (13-12-10 in RGB); **c)** Spectral index composite (quartz-carbonate-mafic in RGB); **d)** Weight percent SiO₂ map computed using the K-value technique and ASTER TIR L2 surface emissivity data; **e)** Spectral lithologic map derived from MTMF™ processing of ASTER TIR L2 surface emissivity data.

Table-9.1 Validation of spectral lithologic mapping using ASTER TIR data (ND=Not Determined)

Sample ID	Location (latitude/longitude)	Thin section mineralogy (ground-truth)		Spectral Analyst™- derived Pixel Composition (JHU spectral library as reference)	Weight per cent SiO ₂ (pixel averaged)		Remarks
		Major	Minor		K-value method	Spectral modeling- based	
A1	N 27° 54' 37.4" E 75° 45' 52.2"	Quartz	Plagioclase and some opaques	Brown to dark brown sandy loam	68.59	60.72	Differences in the composition derived through ASTER TIR surface radiance/emissivity data analysis and ground-truth are attributed mainly to the large pixel size (90m) of ASTER TIR, leading to spectral mixing, and GPS location and co- registration errors. Mismatches in SiO ₂ weight percent values obtained through the K-value technique and spectral modeling are within an overall range of 3-12%; also, values obtained through K- value technique are more representative.
A2	N 27° 55' 00.8" E 75° 46' 46.6"	Calcite, actinolite	Quartz, opaques (magnetite?)	Brown to dark brown sandy loam	65.36	58.72	
A4	N 27° 59' 13.6" E 75° 46' 20.4"	Quartz	Stray grains of hornblende in cavities, and iron staining along fractures and grain boundaries	Pink Quartzite	92.73	81.72	
A5	N 27° 59' 42.7" E 75° 46' 43.1"	Andalusite, chlorite	Quartz and opaques (magnetite?)	Mica Schist	65.54	59.49	
AM1	N 27° 55' 14.5" E 75° 45' 51.5"	Hornblende, K-feldspar	Biotite and opaques	Mafic diabase	59.55	56.22	
BANDHA	N 27° 56' 44.5" E 75° 47' 32.6"	Quartz, feldspar	Some opaques	Brown to dark brown sand	77.18	66.04	
GRANIT	N 27° 55' 11.4" E 75° 48' 18.7"	Quartz, K- feldspar (orthoclase/m icrocline)	Some muscovite, plagioclase, and iron-staining along grain- boundaries	Brown to dark brown sandy loam	70.59	61.73	
PEG	N 27° 56' 5.40" E 75° 47' 57.8"	ND (Pegmatite)		Brown to dark brown sandy loam	75.92	65.98	
Z1	N 27° 56' 38.3" E 75° 47' 12.4"	ND (Amphibolite dyke cutting across arkosic quartzites)		Mafic diabase	60.67	57.55	
Z2	N 27° 56' 38.0" E 75° 46' 58.5"	ND (Banded amphibole quartzite, type location)		Brown to dark brown sandy loam	69.82	59.45	
Z3	N 27° 56' 44.1" E 75° 46' 49.6"	ND (Calc-silicate outcrops)		Mafic diabase	60.38	55.90	

Since field samples represent point locations whereas a pixel spectrum in ASTER TIR data is a sum-total of the materials contained within an area of $90 \times 90 \text{m}^2$, and also since the spatial variation in lithology within the study area is high, it is not possible to exactly compare the results of spectral processing with field/lab data. However, in spite of these limitations, lithologic units identified using ASTER TIR data exhibit an overall correspondence to the geologic ground truth (lithologic map and petrography).

On different spectral lithologic maps (fig. 9.1b,c,e), best discrimination among the lithologic units has been achieved among the mafic and felsic rock units. For example, the pixel corresponding to field sample A4, which is shown as pure/ortho-quartzite on the lithologic map and composed almost wholly of quartz as seen under the microscope, is shown in distinct red color on the DCS image (fig. 9.1b) exhibiting strong absorption due to Si-O bending and stretching vibration modes in bands 12 ($9.075 \mu\text{m}$) and 10 ($8.291 \mu\text{m}$) centered at the main reststrahlen band (for details see Chapter 5); the same pixel has high values for the quartz index and is shown in bright red color on the spectral index composite (fig. 9.1c); SiO_2 weight percent values estimated through the K-value and spectral modeling approach both indicate significantly high SiO_2 content for this pixel ($\sim 93 \text{ wt\% SiO}_2$); and the spectrum for this pixel has been identified as that of 'pink quartzite' through Spectral Analyst™ and classified accordingly through the MTMF™ processing. The same explanation exists for the pixel where field sample AM1 representing an amphibolite is located. Additionally the pertinent amphibolite dike in the center of the study area has been distinctly mapped on the various ASTER-based spectral lithologic maps (fig. 9.1). Ambiguity exists primarily between carbonates and pelites with high mafic content, and amphibolites. Granite, pegmatite and arkosic quartzite outcrops tend to appear common on spectral maps owing to an overall similarity in chemical composition. Due to relatively higher degree of weathering these rock units have a general spectral match with that of brown sand or loam. Differences in spectral lithology and field lithology are an outcome of a combined influence of spectral mixing (owing

to low spatial resolution and high lithologic heterogeneity), inaccuracies in pixel-to-pixel co-registration within a dataset and between datasets (L1B and L2), and GPS-derived location errors of field samples.

As regards the absolute values of silica weight percent, the incongruence between the results obtained using the K-value technique and the spectral curve-fit modeling is highlighted in Table-9.1. The underlying reasons for this incongruence have been described in section 7.3.4, Chapter 7. However, it can be noted that even as discrepancies in absolute values exist between the two techniques, within individual maps the variation is adequately representative of relative lithologies. It has been generally observed, though, that the absolute values obtained from the K-value technique are closer to the anticipated SiO₂ weight percent values (Table-9.1).

9.2.2 Spectral surface/alteration mineral mapping

As with the spectral lithologic maps, the validation of the surface/alteration mineral maps generated through processing of the ASTER VNIR-SWIR data described in Chapter 8 involves a combined observation of the variously generated spectral maps with the compiled field lithologic map and results of thin-section petrography. Point locations of the field samples and their pixel representation on the classified spectral mineral/alteration maps provide a means of comparison and validation. Superior spatial resolution of ASTER VNIR and SWIR data (15 m and 30 m, respectively) affords a higher approximation confidence and closer comparison with the ground-truth. Since the spectral alteration mineral maps are primarily a representation of the surface composition alone, attempts have been made to explain and correlate the composition identified/inferred through remote sensing with the compiled field lithologic map and petrographic evidences based on the expected alteration mechanism of parent rock and derived materials (minerals). Also as the ground-truth for the area is site-specific (rather 'point-/pixel-specific') due to high degree of lithologic complexity, validation has been done using

the SAM-classified spectral mineral maps with discrete pixel classes as shown in figs. 8.20-8.23 derived following the end-member selection criteria for the four cases as outlined in section 8.4.2 (Chapter 8). Validation has been based on tabulation of site-specific sample/field data, and the pixel composition for the sample-site determined through spectral analysis for the four cases, and the composition of select field samples determined through conventional thin-section petrography. The lithologically diverse and spatially scattered field samples used in validation represent the eight image windows used to build the end-member spectral library for spectral classification (fig. 8.15, Chapter 8). While all of these field samples are in the vicinity of known mineralized pockets, of these three samples fall on or close to the main shear zone.

Table-9.2 shows the samples used in validation, their field characteristics, corresponding pixel compositions obtained using SAM classification for the four individual cases, and mineralogy determined through thin-section petrography. Disposition of these field samples has been marked on the lithologic map of the study area, as shown in fig. 9.2. Figure-9.3 shows the pixel reflectance spectra of the sample sites, with the main absorption features marked as thick vertical lines. For each sample site, the validation has been discussed separately.

Table-9.2 Validation of ASTER VNIR-SWIR spectral mineral mapping results.

Sample ID	Area	Location Coordinates	Rock Type	SAM Pixel Spectral Class				Minerals identified under microscope	
				Case 1	Case 2	Case 3	Case 4	Major	Minor
B1	Akwali	N 27 55 50.1 E 75 45 25.9	Altered amphibolite	Amphibole, Corrensite	Hornblende, tremolite, phlogopite	Corrensite, illite, chlorite	Chlorite, phlogopite, celsian	Hornblende, actinolite, K-feldspar	Biotite and opaques, iron oxide
Ch2	Chandmari	N 28 00 07.7 E 75 46 20.6	Limonitized overburden (amphibole quartzite and andalusite, mica schist)	Ferrihydrite, tremolite, celsian	Hornblende, tremolite, phlogopite	Phlogopite, tremolite, ferrihydrite, corrensite, scapolite	Jarosite, chlorite, phlogopite, celsian	ND	
DH1	Dhauri	N 27 57 55.1 E 75 53 36.6	Hematite-rich altered calc-silicate	Ferrihydrite, tremolite, celsian	Hornblende, tremolite, phlogopite	Scapolite, kaolinite/illite, hematite	Grossular, scapolite (dipyre, cookeite), oligoclase	ND	
Su3	Suredi Ki Dhani	N 27 53 53.7 E 75 46 26.6	Micaceous quartzite (sheared, altered and intruded by pegmatites)	Illite	Desert Varnish, chlorite	Quartz, illite	Muscovite, illite, montmorillonite, cordierite, albite	Quartz, mica	Some clay minerals
T3	Bilaiwali	N 27 53 14.6 E 75 45 28.1	Micaceous quartzite (altered and sheared)	Illite	Muscovite, illite, montmorillonite, oligoclase	Quartz, illite	Muscovite, illite, montmorillonite, cordierite, scapolite, oligoclase, tourmaline	Quartz, malachite, clay minerals	Feldspar, some opaques, muscovite
BDOW	Bandha Ki Dhani	N 27 56 55.3 E 75 46 41.9	Malachite-stained altered quartzite	Amphibole, corrensite	Desert varnish, chlorite	Desert varnish, quartz	Chlorite (prochlorite), garnet	Quartz	Garnet (?), malachite, iron-oxide, some opaques
BUGR1	Bukri Ki Dhani	N 27 55 21.0 E 75 48 28.3	Altered granite	Adularia	Muscovite, illite, montmorillonite,	Chlorite, alunite, quartz	Muscovite, illite, montmorillonite,	Quartz, K-feldspar	Muscovite, biotite,

					oligoclase		cordierite, scapolite, oligoclase, tourmaline		plagioclase, some opaques
B15	Tutiwali	N 27 55 19.9 E 75 46 21.2	Altered amphibole quartzite	Ferrihydrite, tremolite, celsian	Hornblende, tremolite, phlogopite	Hematite, corrensite, chlorite	Hematite, garnet	Hornblende, K-feldspar	Quartz, biotite, some opaques, iron oxide
B3/17	Kalota	N 27 53 29.7 E 75 44 24.3	Altered amphibolite	Adularia	Hornblende, tremolite, phlogopite	Corrensite, alunite	Chlorite, phlogopite, celsian	Quartz, biotite, muscovite, chlorite	Plagioclase, some opaques, iron oxide

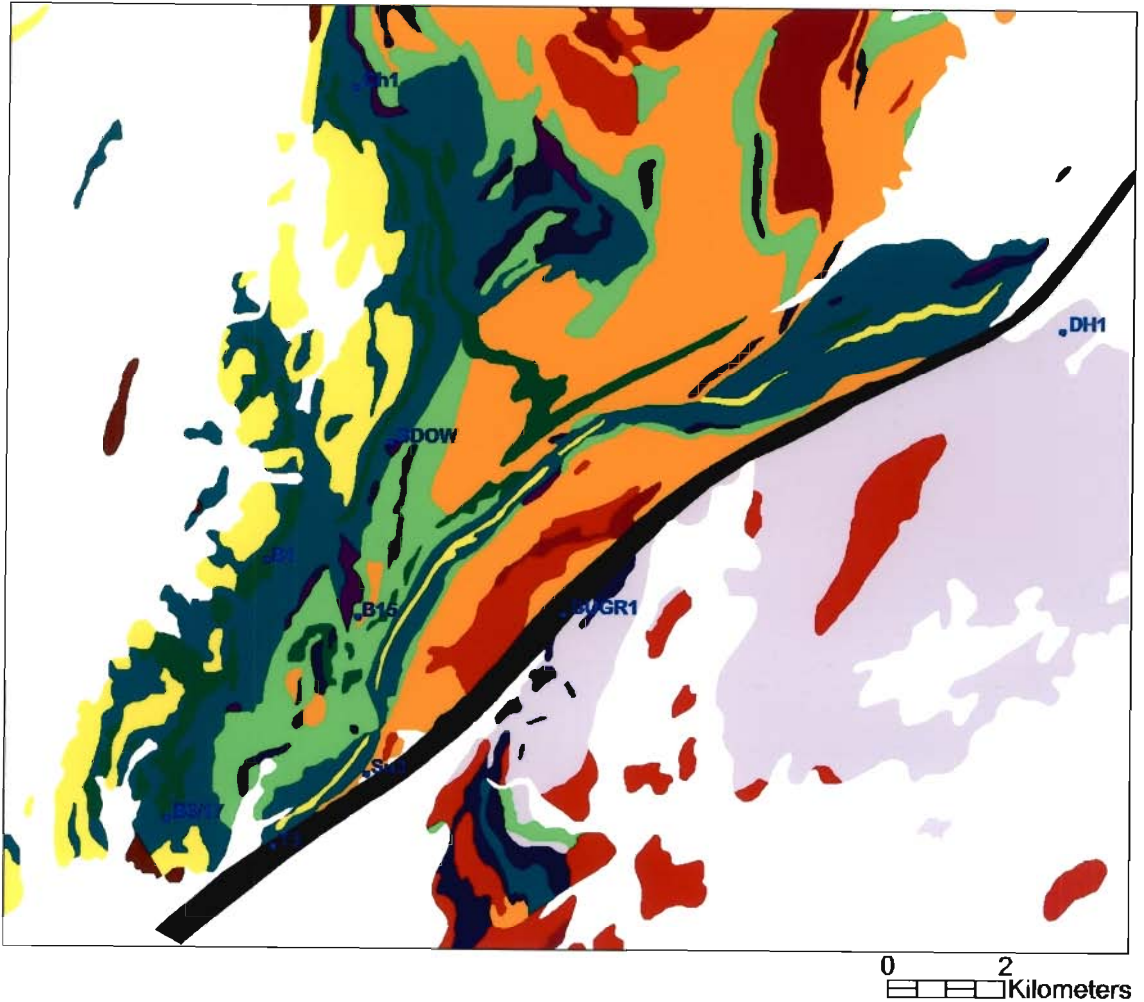
Chemical description and formulae of minerals listed in Table-9.2

Mineral Chemical Formula

Adularia	KAlSi_3O_8
Alunite	$\text{KAl}_3(\text{SO}_4)_2(\text{OH})_6$
Biotite	$\text{K}(\text{Mg},\text{Fe})_3\text{AlSi}_3\text{O}_{10}(\text{F},\text{OH})_2$
Celsian	$\text{BaAl}_2\text{Si}_2\text{O}_8$
Corrensite	$(\text{Mg},\text{Fe})_9(\text{Si},\text{Al})_8\text{O}_{20}(\text{OH})_{10}\cdot n\text{H}_2\text{O}$
Cordierite	$(\text{Mg},\text{Fe})_2\text{Al}_3(\text{Si}_5\text{AlO}_{18})$ to $(\text{Fe},\text{Mg})_2\text{Al}_3(\text{Si}_5\text{AlO}_{18})$
Ferrihydrite	$\text{Fe}_2\text{O}_3\cdot 2\text{FeOOH}\cdot 2.6\text{H}_2\text{O}$
Jarosite	$\text{KFe}_{3+3}(\text{OH})_6(\text{SO}_4)_2$
Grossular	$\text{Ca}_3\text{Al}_2(\text{SiO}_4)_3$
Chlorite	Group of phyllosilicate minerals: Clinochlore: $(\text{Mg}_5\text{Al})(\text{AlSi}_3)\text{O}_{10}(\text{OH})_8$ Chamosite: $(\text{Fe}_5\text{Al})(\text{AlSi}_3)\text{O}_{10}(\text{OH})_8$ Nimite: $(\text{Ni}_5\text{Al})(\text{AlSi}_3)\text{O}_{10}(\text{OH})_8$ Pennantite: $(\text{Mn},\text{Al})_6(\text{Si},\text{Al})_4\text{O}_{10}(\text{OH})_8$ In addition to above, Zn, Li and Ca varieties are also known.
Scapolite	Scapolite, is a group of rock-forming silicate minerals composed of aluminium, calcium and sodium silicate with chlorine, carbonate and sulfate. It is a continuous series between $\text{Ca}_4(\text{Si},\text{Al})_{12}\text{O}_{24}(\text{CO}_3,\text{SO}_4)$ [meionite] and $\text{Na}_4(\text{Al},\text{Si})_{12}\text{O}_{24}\text{Cl}$ [marialite]

Mineral Chemical Formula

Hornblende	$(\text{Ca},\text{Na})_{2-3}(\text{Mg},\text{Fe},\text{Al})_5(\text{Al},\text{Si})_8\text{O}_{22}(\text{OH},\text{F})_2$
Illite	$(\text{K},\text{H}_3\text{O})(\text{Al},\text{Mg},\text{Fe})_2(\text{Si},\text{Al})_4\text{O}_{10}[(\text{OH})_2,(\text{H}_2\text{O})]$
Muscovite	$\text{KAl}_2(\text{AlSi}_3\text{O}_{10})(\text{F},\text{OH})_2$
Oligoclase	$(\text{Na},\text{Ca})[\text{Al}(\text{Si},\text{Al})\text{Si}_2\text{O}_8]$
Phlogopite	$(\text{K},\text{Mg})_3\text{AlSi}_3\text{O}_{10}(\text{F},\text{OH})_2$
Quartz	SiO_2
Tremolite	$\text{Ca}_2\text{Mg}_5\text{Si}_8\text{O}_{22}(\text{OH})_2$
Tourmaline	General formula: $\text{XY}_3\text{Z}_6(\text{T}_6\text{O}_{18})(\text{BO}_3)_3\text{V}_3\text{W}$; where X=Ca, Na, K, vacancy; Y=Li, Mg, Fe, Mn, Zn, Al, Cr, V, Ti; Z=Mg, Al, Fe, Cr, V; T=Si, Al, B; B=B, vacancy; V=OH, O; W=OH, F, O
Desert Varnish	A dark coating found on exposed rock surfaces in arid environments, primarily composed of particles of clay along with iron and manganese oxides. There is also a host of trace elements and almost always some organic matter. The color of the varnish varies from shades of brown to black.
Montmorillonite	$(\text{Na},\text{Ca})_{0.33}(\text{Al},\text{Mg})_2(\text{Si}_4\text{O}_{10})(\text{OH})_2\cdot n\text{H}_2\text{O}$



LEGEND

- | | |
|-------------------------------------------------------------------------------------------------------------------------------------------------------------------------------------------------------------------------------------------------------------------------------------------------------------------------------------------------------------------------------------------------------------------------------------------------------------------------------------------------------------------------------------------------------------------------------------------------------------------------------------------------------------------------------------------------------------------------------------------------------------------------------------------------------------------------------------------------------------------------------------------------------------------------------------------------------------------------------------------------------------------------------------------------------------------------------------------------------------------------------------------------|------------------------------------------------------------------------------------------------------------------------------------------------------------------------------------------------------------------------------------------------------------------------------------------------------------------------------------------------------------------------------------------------------------------------------------------------------------------------------------------------------------------------------------------------------------------------------------------------------------------------------------------------------------------------------------------------------------------------------------------------------------------------------------------------------------------------------------------------------------------------------------------------------------------------------------------------------------------------------------------|
| <ul style="list-style-type: none"> Biot-musc-silli Gneiss Feldspathic Quartzite Amphibole Quartzite Calc-silicate/para-amphibolite Garn-chlo Schist Biot-anda Phyllite Orthoamphibolite/metadolerite Sills/dykes | <ul style="list-style-type: none"> Pure-/ortho-quartzite Impure Marble/Carbonaceous Shale Undifferentiated Rock Sequence Granite/pegmatite/albitite Alluvium Main Cataclastic/shear Zone |
|-------------------------------------------------------------------------------------------------------------------------------------------------------------------------------------------------------------------------------------------------------------------------------------------------------------------------------------------------------------------------------------------------------------------------------------------------------------------------------------------------------------------------------------------------------------------------------------------------------------------------------------------------------------------------------------------------------------------------------------------------------------------------------------------------------------------------------------------------------------------------------------------------------------------------------------------------------------------------------------------------------------------------------------------------------------------------------------------------------------------------------------------------|------------------------------------------------------------------------------------------------------------------------------------------------------------------------------------------------------------------------------------------------------------------------------------------------------------------------------------------------------------------------------------------------------------------------------------------------------------------------------------------------------------------------------------------------------------------------------------------------------------------------------------------------------------------------------------------------------------------------------------------------------------------------------------------------------------------------------------------------------------------------------------------------------------------------------------------------------------------------------------------|



Figure-9.2 Lithologic disposition of field samples used for validation of the spectral classification results of ASTER VNIR-SWIR surface reflectance data.

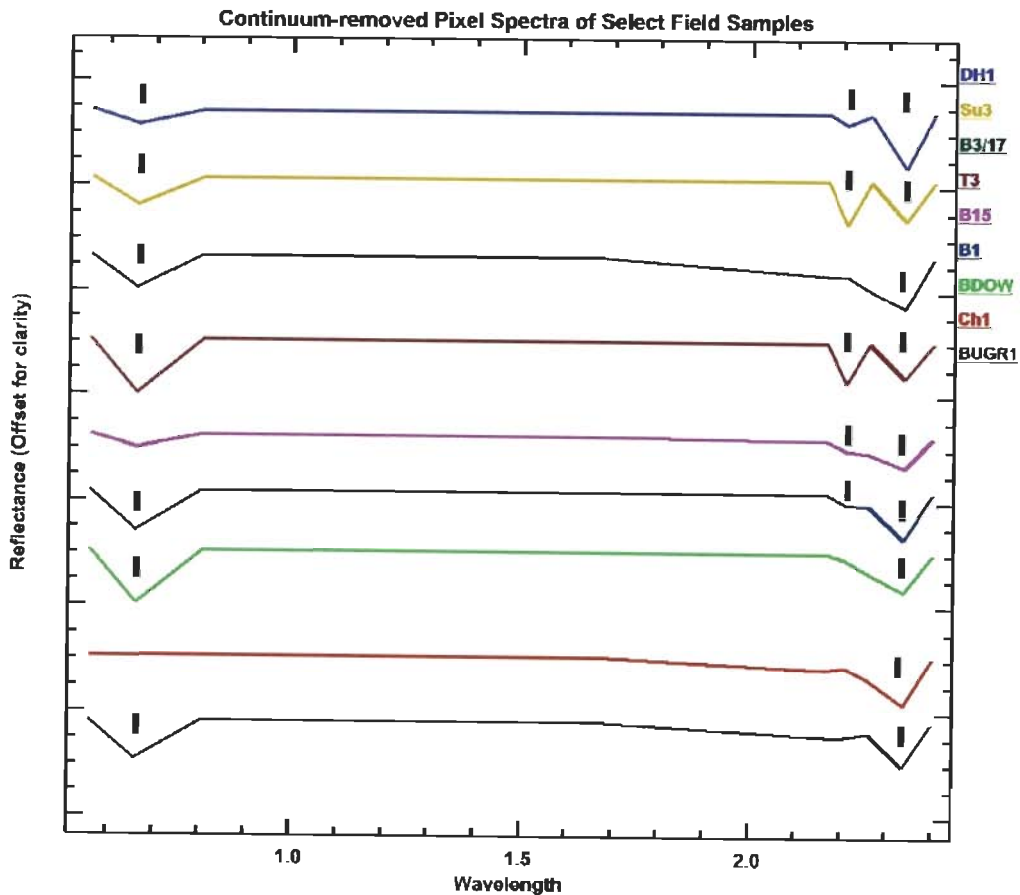


Figure-9.3 Continuum-removed pixel surface reflectance spectra of field samples used in validation of the spectral mineral mapping. The broad vertical lines indicate the positions of the main absorption features.

Discussion: From Table-9.2 it can be readily observed that ASTER data has been successful in spectrally identifying most of the major mineral units actually observed in the field and in thin sections. Ambiguities and differences in mineral identification for different cases investigated arise primarily because of limitations of ASTER's spectral resolution resulting in multiple (and sometimes erroneous) matches of the pixel spectrum with reference spectral library (USGS spectral library) minerals. Also, residual effects of vegetation within an average pixel area of $30 \times 30 \text{ m}^2$ also add to the difficulty in exact identifications. Nevertheless, as explained in the following paragraphs for individual field site, the results show that the ASTER data can provide encouraging and dependable support in identifying and mapping specific minerals which can be linked with the presence of certain mineral deposits.

In the pixel spectrum of sample B1 (fig. 9.3), which represents the altered amphibolite rock overlying the Akwali mines, absorption features centered at bands 2, 6 and 8, respectively due to Fe-O, Al-OH and Mg-OH can be observed. The pixel-class determined for this sample site indicates it to constitute mainly amphibole minerals (hornblende), secondary alteration products of biotite (phlogopite and corrensite), chlorite, which gives rise to the dominant band 8 feature, and some illite, responsible for the band 6 feature. Leached iron oxide on the surface explains the subtle band 2 feature. The thin-section for this sample reveals dominantly hornblende with some actinolite, the feldspar of the rock shows clear indications of weathering and alteration to generate clay minerals, and Fe-O staining along the fractures is also observed (fig. 4.5a, Chapter 4).

Sample Ch2 has been collected from the overburden dump adjacent to the (abandoned) Chandmari open-pit mine towards the northern limit of the study area (fig. 4.3, Chapter 4). The ore lode in this area lies along the contact between the garnet chlorite schist and andalusite-mica phyllites (see fig. 9.2), and is hosted in the banded amphibole quartzites. The overburden is highly weathered, with significant iron oxide leaching and limonitization. The spectral class for this sample site, as determined for various cases, indicates the presence of a variety of closely related minerals, *viz.* ferrihydrite, jarosite, tremolite, celsian, phlogopite, corrensite, andalusite and chlorite. A close observation of the pixel spectrum for this sample site reveals that the dominant absorption feature is in band 8, which is related to Mg-OH; also there is a subtle band 7 feature (low slope between bands 6 and 7), which indicates the presence of jarosite (fig. 9.3). Most of the candidate minerals for the spectrum characteristically have high Mg-OH. Given the presence of sulphides, high degree of limonitization, and the lithologic nature of overburden, the minerals mapped remotely for this site using ASTER data are satisfactorily justified.

For the Dhauli iron ore deposit, a sample DH1 has been collected from the top of the Dhauli hill (fig. 4.3, Chapter 4). The area is a structurally complex calc-silicate country

(banded amphibole-diopside marbles) with hydrothermal hematite/specularite and associated alteration (see Chapter 4 for details). The pixel spectrum for this sample site exhibits well characterized absorption features related to Fe-O (band 2), Al-OH (band 6) and Mg-OH (band 8). The strong band 8 feature is indicative of both chlorite/epidote and calcite. The spectral classes for this pixel for various cases indicate the presence of ferrihydrite, hematite, tremolite, celsian, scapolite and kaolinite/illite. Scapolite is commonly a mineral of metamorphic origin, occurring usually in crystalline marbles and is very common in calc-silicates and usually alters to mica and kaolin. The candidate minerals for this sample site are in every way likely to be present in the area.

Sample Su3 (fig. 4.5b, Chapter 4) is from a minor occurrence proximal to the main cataclastic/shear zone running NE-SW of the study area (fig. 9.3). Due to pegmatite intrusion and shearing, the fabric of the original micaceous quartzite country rock has been severely obliterated and altered. An amphibolite rock lies adjacent to this site (see fig. 9.2). Signs of rich copper mineralization in the form of malachite staining have been observed from this site, as well as clear indications of old working in the form of slag dumps have been seen. Spectrum of this sample site pixel is shown in fig. 9.3. Prominent and strong absorptions in bands 6 and 8 are indicative of the presence of Al-OH and Mg-OH alteration. Spectral matches to this spectrum determined for the four individual cases classify this pixel with those having abundant clay minerals (montmorillonite, kaolinite), muscovite, illite, cordierite, albite, chlorite, and desert varnish, with associated quartz (Table-9.2). Under the microscope, the presence of clay minerals, muscovite and quartz has been confirmed (fig. 4.5b, Chapter 4). The desert varnish is primarily composed of particles of clay along with iron and manganese oxides. There is also a host of trace elements and almost always some organic matter. The presences of dark and hard surfaces in the area are in every way suitable for deposition of desert varnish, and hence justify the spectral mapping results.

Sample T3 (fig. 4.5k, Chapter 4) lies just within the shear zone and represents a zone of significant alteration, brecciation and shearing. Rich malachite staining and almost complete alteration of parent feldspar veins into clay lumps mark the significant features of this site. The spectrum of the sample is similar to that of Su3, since the country rock in both cases is micaceous feldspathic quartzite, as well as the results of spectral classification are also much similar, except that due to absence of any major mafic body in the vicinity, the presence of desert varnish in this area is not indicated on the spectral maps. Spectrum of this pixel also exhibits close matches with the reference spectra of scapolite and tourmaline. The fact that the region is highly sheared and granitic intrusives lie close by; the indicative presence of these minerals leaves little doubt.

The sample BDOW has been collected from an old working along a prominent gossan zone with a regional strike of NE-SW, just towards the foot zone of the Bagor peak quartzite ridge (fig. 9.2). The gossan lies along the contact of garnet-chlorite schist and para-amphibolite and represents the same lithologic setting as that of the Chandmari area, and is hence a promising site of ore deposition. Slag heaps and overburden dumps of small dimensions with malachite stains and carbonaceous coating bear testimony to old workings at the site. In the reflectance spectrum of this sample site, two prominent absorption features centered at ASTER bands 2 and 8 can be readily observed. A subtle feature is also present near band 6. The minerals mapped through SAM processing of the dataset for the four cases indicate that the pixel is abundant in amphiboles, corrensite, chlorite, desert varnish, as well as some garnet with quartz. In thin section of the sample, the presence of abundant iron-oxide alteration and garnet with some malachite and opaques within a matrix of quartz has been confirmed. It is inferred that the signatures of chlorite, corrensite and amphibole indicate chemical associations which could not be distinctly deciphered under the microscope, but which strongly influence the reflectance spectrum.

A gossan zone parallel to the main shear zone has been identified and located in the field. Near Karmari Ki Dhani, along the main Babai-Khetri state highway, just beside the road there is a small old working. This minor occurrence is characterized by the presence of a small body of granite in its neighborhood. A sample (BUGR1) from the intrusive towards the easterly continuation of this minor occurrence near Bukri ki Dhani has been examined under the microscope. Presence of quartz, K-feldspar, plagioclase, muscovite, biotite and some opaques has been confirmed. The feldspar appears cloudy which shows that it is altering to clay minerals. Reflectance spectrum of the corresponding pixel exhibits prominent band 2 and band 8 absorptions, and weak band 6 and band 5 absorptions. A wide variety of closely related minerals have been determined to match the spectrum of this pixel as indicated in Table-9.2, which include muscovite/illite, montmorillonite, cordierite, oligoclase, tourmaline, adularia, alunite, quartz and chlorite. Most of these minerals are characteristic of granites, but the indicated presence of chlorite and alunite within the sampled site and the actual occurrence of sulfide mineralization make it an interesting find.

Sample B15 (fig. 4.5i, Chapter 4) has been collected from the main Tutiwali-Ladniwali-Bhootwali gossan zone (Chapter 2; Gupta, 1974) about 4.25 km NNE of Babai. The lithologic setting in this area is similar to that in Chandmari area. Several small old workings repeatedly testify the presence of buried mineralization in the area. Lithologically the sample site comprises of banded amphibole quartzite in contact with garnet-chlorite schist, and contains thin bands of calc-silicates, and para-amphibolites. Basal arkosic quartzites lie towards the east of the site (fig. 9.2). The sample represents an altered banded amphibole quartzite, with highly limonitized surface. The corresponding pixel spectrum of this sample site has been shown in Figure-9.3, which indicates a strong band 8 absorption and weak band 2 and band 6 absorption features. Spectral analysis of this pixel indicates the presence of ferrihydrite, hornblende, tremolite, hematite, corrensite, garnet and chlorite. Petrographic analysis of the thin section of the field sample has confirmed the presence of hornblende, K-feldspar, biotite,

quartz, and iron oxide. These minerals have been remotely identified to be present in the pixel area and further corroborate the consistency and power of the data and the technique adopted.

Sample B3/17 has been collected from a small zone of altered amphibolite in contact with metapelites towards the north of Kalota village (fig. 9.2). Spectrum of the pixel corresponding to the field location of the sample (fig. 9.3) indicates strong absorption due to Fe-O near band 2, and due to chlorite/epidote/calcite near band 8. In addition to this, weak band 5 absorption is indicative of the presence of alunite and the gentle slope between bands 6 and 7 indicates the presence of jarosite within the pixel area. The remotely identified minerals constituting the pixel include hornblende, tremolite, phlogopite, corrensite, alunite, adularia and celsian. Thin-section petrography of the sample has confirmed the presence of hornblende, plagioclase, quartz, biotite, muscovite, and ubiquitous iron oxide in a highly fractured and weathered rock.

From the foregoing discussion, it can be concluded that in spite of limited spectral resolution, careful processing of ASTER VNIR-SWIR data can yield highly useful and dependable lithologic and mineral maps to aid in a more focused mineral exploration activity as well as in general geologic mapping in areas having poor or inadequate field maps.

9.3 Relating trace-metal anomalies with ASTER spectral maps

An attempt has also been made to check the relationship between the trace-metal concentration and detected alteration in the study area. Towards this end, geochemical trace-metal analysis of about 70 rock and soil samples from the study area for concentrations of copper, cobalt, lead, zinc, molybdenum and arsenic has been carried out (Chapter 4). To investigate the relationship, select samples with marked alteration and metal concentrations above the background values for unaltered equivalents have been used. Except Ch2 and DH1, which were not geochemically analyzed, trace-metal data for the remaining 7 samples used in validation of spectral surface/alteration mineral maps in the previous section and 2 additional samples from the

profile sampled towards the north of Kalota area (B3/19 and B3/20; altered phyllites; fig. 4.5o, Chapter 4) having anomalous trace-metal values have been shown in Table-9.3.

Table-9.3 Trace-metal values of some field samples (for the complete list, see Appendix A).

Sample ID	Rock Type	Unit	Cu	Co	Pb	Zn	Mo	As
B3/17	Altered amphibolite	ppm	51.6	59.1	40.5	123.4	-	27.8
B3/19	Altered phyllite	ppm	1309.7	16.5	16.0	98.3	-	52.6
B3/20	Altered phyllite	ppm	943.5	24.9	53.2	66.2	-	48.2
B/1	Orthoamphibolite	ppm	41.8	33.8	49.1	135.4	2.5	217.5
B/15	Banded Amphibole Quartzite	ppm	39.2	9.6	21.7	70.5	1.5	7.9
T3	Altered micaceous feldspathic Quartzite	ppm	69993.5	1.5	45.9	22.7	4.5	0.6
Su3	Altered micaceous feldspathic quartzite	ppm	35.9	9.7	22.3	197.7	2.7	0.4
BUGR1	Granite	ppm	89.8	4.2	42.6	24.4	2.1	5.1
BDOW	Altered banded amphibole quartzite	ppm	2043.9	1.2	43.1	87.8	2.8	5.2

Figure-9.4 shows the Cu values of the analyzed samples in the form of a color-coded rasterized point distribution map (with a pixel size of 30 m) over a background of ASTER band 3. Sample sites with relatively strong anomalous Cu content, viz. B3/19, B3/20, T3 and BDOW have been shown in zoomed windows along with their positions marked on corresponding SAM-classified spectral mineral/alteration map windows generated for Case 3 (Chapter 8). The legend identifies the pixel-averaged Cu value ranges for analyzed sample points, and the mineral class colors of the spectral mineral map are identified by the legend of Figure-8.22, Chapter 8.

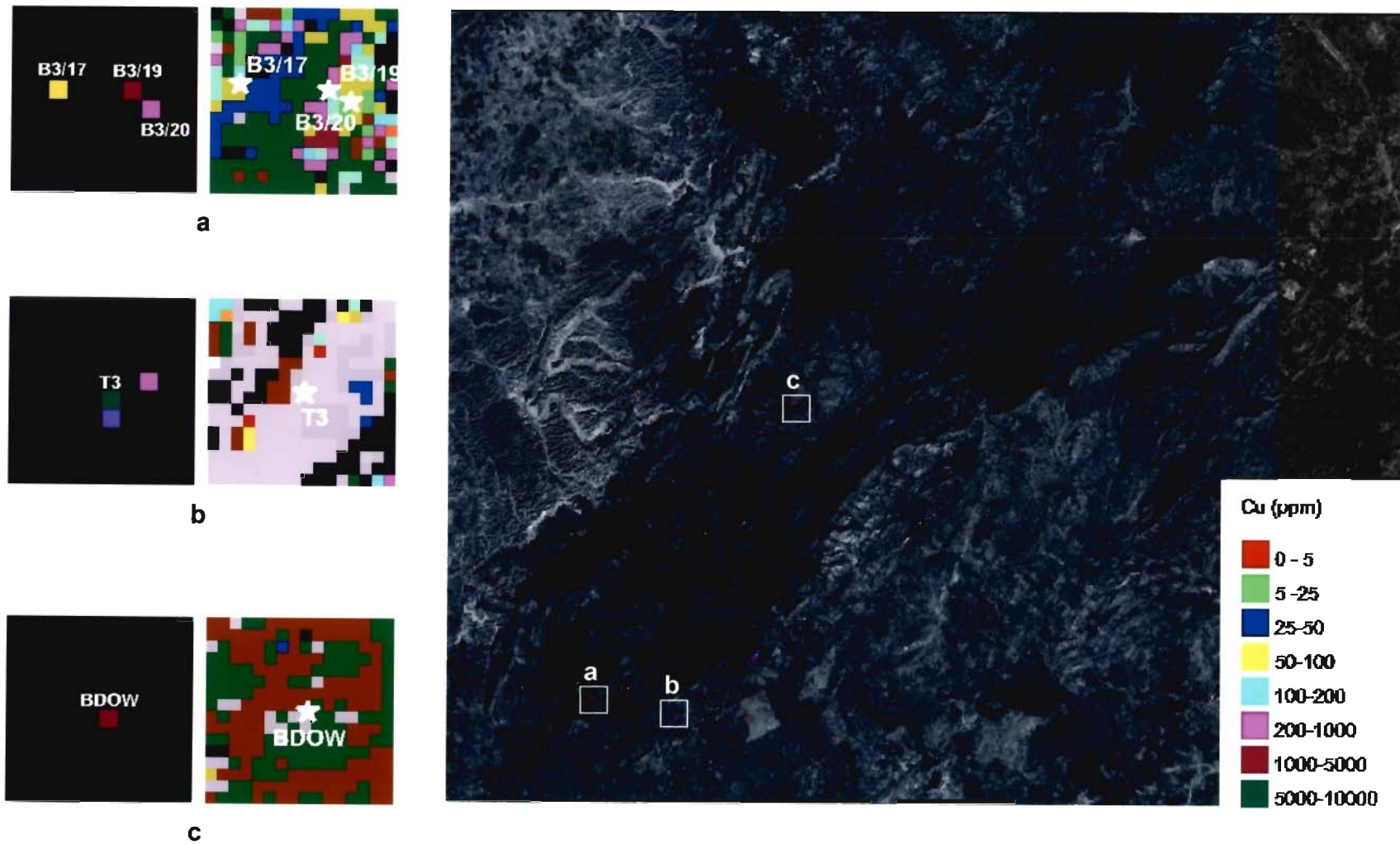


Figure-9.4 Copper trace-metal content map for the samples analyzed from the study area. Three sites with samples containing significantly high copper content have been shown in zoomed windows along with their corresponding SAM-classified mineral/alteration map windows for Case 3.

Discussion: Examination of the nature of trace-metal anomalies and the associated alteration mineralogy for the corresponding pixels determined remotely through ASTER data (Table-9.2) indicate that while there is no direct link between the trace-metal anomalies and the presence or absence of specific minerals or alteration zones, the concentrations of certain trace-metals (*viz.*, Cu, Zn and As) are linked to the relative dominance of alteration minerals typically associated with hydrothermal alteration. For example, sample T3 has unusually high Cu content, it is a part of the main shear zone, and exhibits rich clay alteration as well as rich malachite staining. The remotely mapped minerals for the corresponding pixel are dominantly hydroxyl-bearing, with preponderance of argillic alteration minerals, such as illite and kaolinite and phyllic alteration minerals, such as muscovite (though it is also a constituent mineral of the host micaceous feldspathic quartzite). The same holds true for the two anomalous altered phyllite samples from the profile towards the north of Kalota. Petrographic examination of the thin sections of these samples shows rich presence of opaques and malachite. Interestingly, due to band 5 absorption presence of alunite along with corrensite is also indicated, though microscopic examination of the thin-sections could not confirm this. Phyllite and schist rocks near other mineralized locations are also mapped to contain alunite. Similar explanation exists for the altered quartzite sample BDOW, which is rich in mafic minerals (amphiboles). High Cu values can be directly linked with the presence of malachite stains as well as to the presence of altered biotite, chlorite, phlogopite by analogy with the other mineralized locations, such as that in Akwali and in Chandmari.

Therefore, it can be concluded that though the geochemical anomalies cannot be conclusively linked with the alteration mineralogy detected and mapped using ASTER data, useful leads for such anomalies can be inferred based on the relative distribution of specific alteration minerals.

Summary and Conclusions

Introduction and statement of purpose

Historically, remote sensing has been used by the mineral industry primarily as a tool for preliminary regional structural and geologic reconnaissance mapping, owing to its synoptic field coverage. Availability of reliable geologic/lithologic information and maps of alteration minerals or mineral assemblages are two of the basic prerequisites in every mineral exploration mission, as they alone provide the most direct clue about the existence of an economic mineral deposit. The conventional broad-band spaceborne remote sensors, typically the Landsat TM/ETM+, have been able to fulfill this objective in some part. Hyperspectral remote sensors, such as AVIRIS have proven the real capability of remote sensing in reliable mapping of surface mineralogy; but since they are mostly airborne, their data is of limited geographic coverage; the data acquisition is highly cost-intensive; and the data require specialized processing and expert interpretation. These limitations restrict wide-scale use of such data.

The launch of the ASTER sensor onboard the Terra spacecraft in the year 1999 (with data availability from 2000) has given fresh impetus to the field of geologic remote sensing. This study was undertaken in wake of this development with the aim to investigate the extent to which the ASTER data can be utilized towards the twin objectives of lithologic and surface/alteration mineral mapping, with a case study in a mineralized region of India, the Khetri Copper Belt. The study area has been well documented; and previous TM-based remote sensing studies in the area had indicated some OH⁻ anomaly zones. The work presented in this thesis is an outcome of an exhaustive analysis of the ASTER data, with implementation of some ingenious approaches to extract usable geologic information from the data.

Study area: regional and local geology

The Khetri Copper Belt (KCB) is one of the main copper producing mineral regions in India. KCB forms the northern entity of the Aravalli mountain range in Rajasthan, northwest India, and extends for about 80 km from Singhana in the NE to Raghunathgarh in the SW. The belt is broadly divided into a North Khetri Copper Belt (NKCB) and a South Khetri Copper Belt (SKCB), by the transverse NW-SE Kantli fault.

KCB is covered by rocks of the Delhi Supergroup, which is divided into: (1) an older Alwar Group dominated by psammitic rocks; and (2) a younger Ajabgarh Group dominated by pelitic rocks. The region has been affected by subsequent acidic and basic magmatism, and has undergone metamorphism and deformation with associated base metal (copper, lead, zinc) and iron mineralization.

The study area is located to the north of the Kantli fault in NKCB, and represents a regionally metamorphosed terrain with low to medium grade metasedimentary rocks, such as various kinds of quartzites (banded feldspathic quartzites, micaceous quartzites, amphibole bearing banded quartzites, arkosic and banded arkosic quartzites, and pure quartzites) and metapelites (schists and phyllites), and has witnessed a history of polyphase intrusions of intracratonic felsics (granites, granodiorites and pegmatites) and mafics (amphibolites). A major cataclastic/shear zone, called the Babai-Taonda thrust diagonally passes across the study area. Felsic intrusive activity has been reported along this shear zone, with associated pockets of sulfide mineralization, and widespread hydrothermal wall-rock alterations in the form of silicification, muscovitization-sericitization, limonitization, and sometimes carbonatization and chloritization. Sparse vegetation cover and good rock outcrops with diverse lithologic and alteration characteristics make the area suitable for remote sensing analysis.

Detailed study of the different mineralized areas present in the study area have been carried out in the form of literature review, field studies and laboratory investigations of field samples collected from these zones, which form the ground truth for validation of remote

sensing results. Three major zones of sulfide mineralization and one zone of iron mineralization have been reported from the study area. These are – (i) Akwali zone, (ii) Tutiwali-Ladniwali zone and (iii) Saintali ki Dhani-Karmari ki Dhani zone for copper; and (iv) Dhauli Hill zone for iron. In addition to these zones, many minor and sporadic mineralized sites have been reported from the study area, largely discovered in the form of old-workings. The abandoned open-cast Chandmari mine marks the upper limit of the study area. These mineralized zones contain different forms of surface indicators of mineralization, such as gossanized rocks containing limonite (hematite-goethite-lepidocrocite), specks of malachite, and azurite, and many hypogene gangue minerals such as quartz, muscovite, sericite, chlorite, carbonates; and wall-rock alterations of different degrees and of varying intensities, leading to mineral assemblages of both phyllic and argillic varieties of hypogene origin. Chloritization and silicification is more widespread; accompanying chloritization is biotitization. Other associated wall-rock alterations include carbonitization, muscovitization, sericitization, scapolitization and amphibolization. The alterations vary with the host lithology.

Data and methodology

The study has primarily been based on the processing of an ASTER L1B dataset of the study area. In addition to this dataset, level 2 (L2) standard data products (surface reflectance, AST_09; surface radiance, AST_07; and surface emissivity, AST_05), and a level 3 (L3) standard data product (ASTER stereo DEM; AST14DEM) have also been used. Landsat TM data of a part of the study area has been used in the preliminary phase of the study to identify potential locations for reconnaissance fieldwork. Ancillary geodata include the topographic and geologic base maps of the study area.

The basic GIS processing of the geodata includes georeferencing and coregistration of various ancillary and image data, production of a digital elevation model through raster

interpolation of digitized contour data from the topographic base-map, and compilation of a geologic reference map of the study area by synthesizing various published geologic maps.

In order to fulfill the research objectives, the following methodology has been adopted:

1. A detailed literature review pertaining to the study area, theoretical background of geologic remote sensing, methods of lithologic and alteration mapping using multispectral remote sensing, and use of ASTER in mineral exploration
2. Creation of a GIS database of the image and ancillary geodata of the study area
3. Collection of field samples, their laboratory petrography and trace-metal geochemistry to understand the nature of rock alteration and for verification of remote sensing analyses
4. Precise atmospheric and topographic corrections of the ASTER VNIR-SWIR image data to obtain surface reflectances
5. Assessment of the existing methods to obtain surface emissivities from ASTER TIR radiance data and comparison with the standard L2 TIR surface emissivity data
6. Spectral processing of ASTER TIR data for qualitative and quantitative lithologic mapping including generation of silica weight percent map for the study area using existing as well as novel approaches
7. Spectral processing of the ASTER VNIR-SWIR surface reflectance data to determine alteration and bedrock mineralogy of the exposed surfaces
8. Integration of the results of spectral processing and their validation on the basis of published, field, and laboratory ground-truth

Field and laboratory studies: petrographic and geochemical analyses

As image analysis and ground check are independent operations, the fieldwork and laboratory analyses (petrographic and trace-metal geochemical) have been conducted to develop a ground-truth database of the study area. This data has been used for validation of the results of ASTER image analysis.

The fieldwork has involved collection of location data as well as recording significant field characteristics of the study area, site-by-site. Field samples have been collected to analyze the petrographic/ mineralogic and trace-metal content of the rocks. The primary objective has been the identification of major and accessory minerals, and alteration type and mineralogy, wherever possible. Another objective of petrographic studies has been the identification of the type of alteration: primary (hypogene) or secondary (supergene). In most part, secondary (supergene) alteration in the form of chemical weathering is either the main cause of alteration, or has obliterated the pre-existing primary (hypogene) alteration. Relict traces of primary (hypogene) alteration have been observed in some samples. The results of petrographic analyses in conjunction with the geological literature have been used in selecting the target alteration minerals for the study area, and their corresponding library spectra have been used in spectral classification of the ASTER VNIR-SWIR image data. The alteration mineral assemblage of the study area consists of both hypogene and supergene varieties, and include muscovite/ sericite, chlorite, biotite, clay minerals (kaolinite, montmorillonite, illite (?)), albite, goethite (iron oxide), limonite (ironoxyhydroxide), jarosite (iron sulfate), and scapolite minerals.

Trace-metal concentrations have been used to see whether the metal content has any relationship with the alteration, and hence if alteration can be used as a direct evidence of mineralization. It has been observed that the relationship is in general harmonious, and samples with discernible alteration have significant metal anomalies too, though the individual metal concentrations vary widely depending on the lithology.

Infrared Spectroscopy and Geologic Remote Sensing – Theory, Background and ASTER Application

The primary diagnostic spectral features (absorption bands) of most minerals and rocks are concentrated in the infrared region of the electromagnetic spectrum. A detailed review has been carried out to understand the atomic and molecular processes responsible for these spectral features exhibited by the minerals. Following this, a review of the applications of multispectral and hyperspectral remote sensing in geology, with focus on the remote identification and mapping of lithologic and mineral units has been carried out.

Two main categories of processes that cause absorption of radiation at visible and infrared wavelengths have been explained: 1) electronic processes, which occur at higher energies (or higher frequencies, or shorter wavelengths), and 2) vibrational processes, which occur at lower energies (or lower frequencies, or longer wavelengths). Electronic processes are related to changes in the distribution of electrons within and between atomic orbitals in a crystal field, and can be categorized into four groups – crystal field effects, color centers, conduction bands, and charge transfer between atoms. Most of the features observed in the VNIR spectral region (0.4-1.0 μm) are due to the presence of transition metals, especially of different valence states of iron. Vibrational processes are related to atomic vibrations that cause a change in the charge distribution of a molecule, and typically dominate the spectra in SWIR and TIR regions. In the SWIR region (1.0-2.5 μm), absorptions due to overtones and combination tones occur, and minerals that contain water, hydroxyl, carbonate and sulfate molecules show diagnostic spectral features in this region. Typically, hydrous clays and phyllosilicate minerals such as muscovite exhibit diagnostic absorption features in the SWIR region. The fundamental vibration modes for silicate minerals cause strong absorption features in the 8.0-12.0 μm region, which is known as the Si-O stretching region and also the region of highest emitted radiation of the Earth, making it ideal for terrestrial geologic remote sensing applications. Carbonates and sulfate minerals also have diagnostic spectral emissivity features

in the TIR region. A very useful characteristic of the silicate rock spectra in the TIR region is that there is a systematic shift in the emissivity minima for different rock types, and is linked with their total silica content.

Minerals with diagnostic spectral features in the VNIR and SWIR regions are commonly associated with primary (or hypogene) and secondary (or supergene) alteration related to mineralization. Minerals with diagnostic absorption features in the TIR are the primary rock-forming minerals and offer direct understanding of the lithology. ASTER covers these spectral regions in 14 discrete bands (9 in VNIR-SWIR, 0.5-2.4 μm ; and 5 in TIR, 8.0-11.5 μm) and hence presents a unique advantage in terms of complimentary geologic information in a single data package.

Data preprocessing: Correction of atmospheric and topographic effects

Before the data can be used for detailed spectral analysis, it is vital to compensate for the radiometric, atmospheric and topographic influences on the target radiance reaching the remote sensor. Atmosphere selectively absorbs and scatters the solar radiation in different wavelength regions. The main topographic effects are in the form of differential terrain illumination and terrain adjacency effects.

Sensor calibration is necessary to convert the digital number (DN) values of the image to the units of at-sensor radiances. In the shorter wavelength VNIR region, the atmospheric scattering is the dominant mode of atmospheric influence on the radiances recorded by the remote sensors; this effect is primarily additive in nature. On the other hand, in the SWIR and TIR regions, the main atmospheric effects are in the form of atmospheric absorption, which are characteristically multiplicative in nature. Data preprocessing involves removal of these atmospheric influences such that an estimate of the true target radiance and reflectance (in the solar reflective VNIR-SWIR region), or emissivity (in the TIR region) can be made. A number of methods have been developed over the years to address this objective. These have been

grouped under relative and absolute atmospheric correction methods. Relative methods are generally scene based, with no external inputs and include such methods as Log Residuals (LR), Flat Field (FF, and Modified Flat Field, MFF), Internal Average Relative Reflectance (IARR), *etc.*; whereas, the absolute methods are based on the physical laws of radiative transfer and commonly require external inputs in the form of local atmospheric data, and include various radiative transfer codes (RTCs) such as MODTRAN (Moderate Resolution Atmospheric Radiance and Transmittance) and 6S (Second Simulation of the Satellite Signal in the Solar Spectrum), and the image-based Dark Object Subtraction (DOS) technique.

The radiance in TIR is a function of temperature and emissivity. While emissivity is an intrinsic property of the surfaces, temperature varies with the impending irradiance and meteorological conditions. Planck's function describes the relationship of the two. Retrieval of emissivities from radiance data in the TIR is primarily an underdetermined inversion problem, as the number of unknowns is one more than knowns. In this research, a review of the literature on separation of temperature and emissivity from radiance for the sensors acquiring data in the TIR region has been carried out, including the most recent TES algorithm which is currently being used to generate the ASTER L2 TIR surface emissivity product (AST_05), used in this study.

Preprocessing the ASTER VNIR-SWIR and Landsat TM data (used in the initial stages) has involved application of the known methods of atmospheric correction to select the best correction. The methods of relative atmospheric correction applied include LR, FF, MFF, IARR, and Empirical Line method. The absolute atmospheric correction has been attempted using the FLAASH program (based on the MODTRAN RTC), a modified version of the 6S RTC (used for the TM data correction), the Markham-Barker apparent reflectance model, and the image-based DOS technique. Comparison of the corrections has been done by plotting the pixel spectra of a flat homogeneous surface within the image (the Babai helipad) after application of various atmospheric correction procedures, and examining the plots with

reference to the JHU library spectrum of reddish-brown medium to fine sandy loam, which is the dominant surface composition of the pixel sample used in constructing the plots. Best correction for both data types (ASTER VNIR-SWIR and TM) have been observed in case of the FLAASH-corrected image spectrum. The FLAASH-corrected 9-band ASTER VNIR-SWIR apparent reflectance image data has been subsequently refined by applying the MFF correction to force a match between the image spectra and the library spectra. This approach has been called the hybrid FLAASH+MFF correction.

Atmospheric correction of the recalibrated ASTER TIR at-sensor radiance data has been done using the In-Scene Atmospheric Compensation algorithm. The resulting image has been used with three different temperature and emissivity separation algorithms (*viz.*, the Reference Channel method, the Normalized Emissivity Method or NEM, and the Alpha Residuals method) to retrieve surface emissivities. The results have been compared with the standard L2 AST_08 surface emissivity image data produced after applying the TES algorithm of Gillespie et al. (1998). Spectra of a common pixel on different correction outputs have been plotted along with the JHU library spectrum of the constituent rock type (pink quartzite) to evaluate the success of individual approach. It has been found that the results of the TES algorithm, which combines the NEM and minimum-maximum difference (MMD) methods, are relatively better than the individual approaches, and hence the L2 AST_05 data were retained for further emissivity spectral analysis for lithologic mapping applications.

ASTER TIR data processing for lithologic mapping

A detailed analysis of the ASTER TIR L1B radiance-at-sensor and L2 surface radiance/emissivity data of the study area using the available methods and approaches has been carried out. Beginning with the decorrelation stretch (DCS) processing of TIR L1B data, which has been used to enhance the color contrast of the highly correlated TIR bands to improve qualitative lithologic discrimination, the processing has involved computation of band ratios

and spectral indices to map the quartz-rich, mafic-rich, and carbonate-rich lithologic areas, and finally a full spectral analysis of the surface emissivity data has been performed. Methods based on band ratios and indices have shown that good lithologic discrimination can be achieved even with relatively raw radiance data. Especially widely differencing lithologies, such as felsic and mafic varieties, are clearly distinguished on the TIR index images.

Spectral emissivity data has been used to generate a spectral lithologic map of the area with the spectral classes determined from the image itself using the iterative pixel-purity index (PPI™) method. Determination of the likely lithology of the end-members so determined has been a rather subjective exercise since the numerical spectral fitting approaches like SAM and SFFT™ suffer from bias and inherent inconsistencies. However, these methods have been greatly useful in an approximate identification of the dominant spectral groups. Using a 5-band spectral emissivity dataset, 6 spectral end-members have been determined and Spectral Analyst matches for these end-members have been identified using a reference spectral library consisting of JHU coarse igneous, coarse metamorphic and soil hemispherical reflectance spectra, converted into corresponding emissivity spectra using Kirchhoff's Law. Best matches have been obtained for the reference library spectra of the following rocks/soils: Felsic Granite, Mafic Diabase, Pink Quartzite, Mica Schist, Brown to Dark Brown Sand, and Brown to Dark Brown Sandy Loam. Spectral classification has been achieved using two methods, viz., SAM and MTMF. The results in general have excellent overall agreement with each other.

Two methods of quantitative silica weight percent estimation have been tested. The first method uses spectral modeling of the surface emissivity spectrum for a given sample through a curve-fitting process to estimate the minima of the reststrahlen band, and utilizes the systematic shift observed in this minimum towards longer wavelengths with decreasing silica content in the igneous rocks as an extrapolation to determine the unknown silica weight percent for a known emissivity minimum. Of the various curve-fitting functions investigated, Polynomial 2nd Order function was found to be the most consistent and computationally feasible model. The

second method is based upon the K-value equation of the Metal Mining Agency of Japan (MMAJ). The results from the two techniques have been found to be in excellent overall agreement with the silica content expected for the lithologic classes known for the area, as shown in the geologic map. However, no conclusions about the success of the methods in determining absolute values of the silica content could be drawn since no reference field data was available.

The main conclusions drawn from the analysis of the ASTER TIR data for lithologic mapping in the study area, and the recommendations for further improvements have been summarized as follows:

1. The absence of any spectral channel between 9.0 and 10.5 μm region because of the atmospheric ozone absorption limits the capability of high altitude ASTER's TIR multispectral data. Inclusion of data within this region is necessary to adequately model the main reststrahlen feature in the emissivity spectra of geologic materials.
2. The availability of field spectral information, most desirably *in situ* with the satellite overpass, can greatly improve the mapping results. Field spectra can be used in addition to the image derived end-member spectra to fully realize the spectral diversity contained in the region. They can also be used with the quantitative silica weight percent estimation to improve the absolute values determined using the methods described.
3. Though the TES algorithm used to generate the standard ASTER L2 surface emissivity product is fully validated and has been shown to be robust and reliable for most surface cover-types. However, the validation of the algorithm it has so far been done only for flat areas, such as ponds and playas (Gillespie et al., 1998). Since the study area is a topographically high relief terrain, the results of the temperature and emissivity separation are likely to be erroneous. It has been observed that this inaccurate separation leads to flattening of the spectral signature in shadowed areas. The curve-fitting techniques for silica abundance estimation generate non-representative values for such

spectra. Also, the pixels in the shadows tend to have elevated silica weight percent values due to this phenomenon. Thus, the TES technique works best in flat areas and for images acquired during the noon time. ASTER data is acquired during the early morning hours, therefore, the effects of hill-shadowing limit the overall success of the TES for rugged topographic areas.

4. Small, but important, inaccuracies due to remnant atmospheric contributions affect the overall utility of the spectral data. Atmospheric correction with *in situ* atmospheric radiosonde measurements and a radiative transfer model need to be used to adequately compensate for the local atmospheric conditions.
5. A higher spatial resolution for the TIR data is highly desirable. Spectral mixing has been known for pixel sizes as small as 2 m (SEBASS; Vaughan, 2005), and have immense influence on the uniqueness of surface composition mapping, as well as on the confidence of the results.
6. Though the region represents an arid climate with little vegetation cover, even small spectral mixing with vegetation due to large pixel size (90 m) greatly subdues the diagnostic spectral features and hampers the distinct mapability of surface composition through remote sensing approaches. The same holds true for the surface coatings, especially desert varnish, which is widespread in arid environments, such as the present study area. Higher spectral resolution with better NE Δ T is expected to overcome most of these problems.

ASTER VNIR-SWIR data processing for surface/alteration mineral mapping

One of the primary advantages of ASTER over TM data is the improved resolution of the important SWIR region (2.0-2.5 μm) where the diagnostic signatures of the main alteration minerals are present. In place of just one broad TM band (2.08-2.35 μm); ASTER records data

in 5 strategic bands in the SWIR 2.0-2.5 μm wavelength region. This makes the ASTER data of special utility in mapping of alteration minerals related with most kinds of mineralizing environments.

The second primary objective of this study has been mapping of alteration using ASTER data. Towards this end, the composite 9-band ASTER VNIR-SWIR reflectance data obtained after the hybrid FLAASH+MFF atmospheric correction and C topographic correction has been processed using various image processing techniques to uniquely identify and map the surface/alteration minerals present in the study area. Like the TIR data processing, in this case also, the processing has been designed to exhaustively evaluate the potential of methods from simple to advanced, in extracting usable alteration mineral information from the remote sensing data.

A list of target alteration minerals has been prepared, based on the review of literature (Chapter 2) and the field and laboratory investigations undertaken during the study period (Chapter 4), which includes sericite (or muscovite; belonging to the sericitic or phyllic alteration, with associated quartz), various hydrous clay minerals such as kaolinite, montmorillonite/smectite and illite (belonging to the argillic alteration), alunite (belonging to advanced argillic alteration), biotite (for potassic alteration), calcite/dolomite (for carbonate alteration), chlorite group (belonging to the propylitic alteration), scapolite group of minerals, albite (for the albite alteration), and various minerals belonging to limonite (goethite, jarosite and hematite; associated with weathering of rocks). The spectral characteristics of these minerals have been studied to select appropriate ASTER band combinations for processing.

The processing flow has been designed such that it hierarchically grows from a simple level of processing involving image enhancement and color display of 3-band composites, to image transformation (DCS, PCA and DPCS), band ratioing and spectral indices, logical operator-based band modeling, and finally to advanced spectral processing and image classification methods.

Based on the optimum index factor (OIF) approach, two band combinations have been selected – ASTER bands 6-3-1, for the 9-band VNIR-SWIR combined dataset, having enhanced discrimination of Fe-O and OH⁻ altered areas; and ASTER bands 4-6-8, for the SWIR dataset, displaying the distribution of Al-OH and Mg-OH bearing surfaces, respectively showing clay/muscovite and chlorite/carbonate alterations. Improved color discrimination for the above band composites and the respective mineralogical and alteration information has been obtained using the DCS processing.

A comprehensive list of ASTER band ratios and RBDs reported in the literature has been evaluated. Good discrimination between ferric and ferrous iron, Al-OH, and Mg-OH alteration has been obtained through band ratioing. Ambiguities between the distribution of mafic-rocks having chlorite alteration and carbonate rocks rich in mafic content have been observed. This is because the absorption of both chlorite and calcite occur in ASTER band 8, making them difficult to distinguish on ratios, since the ratios and RBDs utilize only specific parts of the full mineral spectrum, hence ignore the subtle differences in the spectral shapes.

Principal component analysis (PCA) and its variant feature-oriented principal component selection (FPCS) have been used to distinguish and map the distribution of OH⁻ bearing alteration minerals with spectral features in the SWIR region. Alteration maps for alunite, illite, kaolinite+smectite and kaolinite have been prepared through the FPCS procedure. Due to the problem of SWIR filter scratch (Appendix D), sub-vertical banding in the derived maps has made the interpretation difficult in the western parts. However, it has been observed that most of these minerals are concentrated within the main shear zone passing through the study area, as well as in the feldspathic quartzites. Spectral indices based on the five ASTER SWIR bands within the wavelength range 2.0-2.5 μm have been prepared to map the distribution of alunite, kaolinite, montmorillonite and calcite.

An attempt has also been made to combine the individual band ratios for specific mineral species through Boolean logic to map them as categories of argillic and phyllic

alteration. The resulting argillic and phyllic alteration maps indicate that most of the minerals belonging to these alteration types are concentrated along the main shear/cataclastic zone, and appears to coincide with the felsic magmatic activity. Although the host country rocks (micaceous feldspathic quartzite) also contribute to the indicated alterations, the apparent zoning between the two categories (inner argillic and outer phyllic) favors the common hydrothermal alteration model.

Full spectral processing of the VNIR-SWIR reflectance dataset has been carried out to uniquely identify and map the individual surface/alteration minerals based on their spectral shape and absorption features through a hierarchical process involving Minimum Noise Transform (MNF) computation, using the MNF results in the extraction of image end-members (image spectral classes, or unique surface compositions) through PPI™, identification of the image-derived end-member spectra through Spectral Analyst™, and generation of spectral maps through Spectral Angle Mapper (SAM) and Mixture Tuned Matched Filtering (MTMF™) classifiers.

Prior to this processing, an iterative vegetation mask has been prepared through Normalized Difference Vegetation Index (NDVI) computation using bands 3 (NIR) and 2 (red) to exclude vegetated pixels from spectral processing for two reasons: firstly, vegetation significantly alters the native spectral response of the geological materials, as some organic-compound (typically cellulose) absorption features centered near 2.10 μm and 2.30 μm are near the wavelengths of some of the main Al-OH and Fe, Mg-OH absorption features; and secondly because vegetation is of non-interest in this analysis, and inclusion of vegetation would mean loss of a possible geologic image end-member determined through the PPI™ processing.

In order to expand the size of image end-member spectral classes such that the diverse spectral categories present within the area are brought out more representatively, and because no field spectral measurements were available for the area, a novel method has been devised. Eight image windows for areas having different and diverse surface cover types have been

selected, and the image end-members have been determined for each of these image windows. The bands used in the spectral analyses of these areas have been divided into two categories: full 9-band VNIR-SWIR spectral data, and 6-band SWIR spectral data alone. The resulting end-member spectral classes have been selectively grouped to avoid 'crowding' of related spectra and have been used to construct two separate reference end-member spectral class libraries. Thus, four cases have been designed for spectral classification of the ASTER VNIR-SWIR data, namely:

1. *Case 1:* For VNIR+SWIR combined data (9 bands) using the full scene
2. *Case 2:* For SWIR data alone (6 bands)
3. *Case 3:* For VNIR+SWIR combined data individually for 8 spatial windows (see fig. 8.15)
4. *Case 4:* For SWIR data alone individually for 8 spatial windows

Identification of the end-members has been done using ENVI's Spectral Analyst™ module, using the ASTER-convolved USGS mineral library spectra as reference. Two spectral fit techniques (SAM and SFF™) have been used to identify the image end-member spectra based on the fit score for each in relation with the corresponding known reference library spectra. This technique of automated spectral identification suffers from certain limitations and bias. The reasons for this bias have been identified as follows:

1. Owing to the differences in the individual match scores between the two matching techniques used (SAM and SFF), instead of a single best match a range of materials could be predicted with relatively equal or marginally different, overall scores.
2. It has been found that more than one reference spectra representing mineralogically widely different rocks/soils receive the same overall score due to the unequal scores for the two individual techniques. It has been observed that

where the unknown spectrum has well defined diagnostic 'absorption' features, SFF yields results with a better match, and for spectra without any diagnostic feature, SAM match results appear to be superior.

As no single technique could be considered sufficiently accurate, the decision about the candidacy of a particular reference spectrum for its match to the unknown end-member spectrum has been made by interactively examining the individual end-member spectrum in both normal and continuum-removed mode, with a background support of the field knowledge, to assign the reference material spectrum to it. Subsequently, SAM and MTMF™ classified images for the four cases identified above have been obtained.

Synthesis of results and interpretation

In order to assess the usefulness and credibility of the results of spectral lithologic and alteration mapping it is necessary to analyze them in light of existing field and laboratory evidences. The results of ASTER-based spectral lithologic and surface/alteration mineral mapping have been synthesized and interpreted in a geologically meaningful way through a comparative analysis of well-described geology, field locations, and laboratory petrographic and trace-metal data constituting the ground-truth, and their corresponding representation on the respective spectral maps.

The results of ASTER TIR data-based spectral lithologic mapping and quantitative silica abundance estimation have been found to agree with the geologic ground truth in most part. Major lithologic units, *viz.*, pure quartzites, mica schists and phyllites, mafic and felsic intrusives, respectively amphibolites and granites/granodiorites have been uniquely identified and mapped on the spectral lithologic maps. For areas with vegetation-mixed surface cover and good soil development, the TIR image spectra have exhibited close matches with the brown loams and sands. Quantitative silica abundance estimation is in good agreement with the expected values for the rock units observed on geologic maps and in field samples, although

differences in the range of 3-12 % have been observed between the results of the two individual techniques used in the analysis.

Synthesis and interpretation of the results of surface/alteration mapping using the ASTER VNIR-SWIR data have been done by simultaneously examining the compiled reference lithologic map, mineralogical and textural data obtained from microscopic study of the thin-sections of field samples with their GPS-locations, and spectral classification results for eight image windows. Nine field samples have been used to validate the results of spectral alteration/surface mineral mapping. Of the eight image windows used for validation, *viz.*, Akwali, Chandmari, Dhauli, Suredi, Bandha, Bansiyal, Gadrata, and Kalota – first four represent areas with known mineralization and have been used to validate the results of (alteration/surface) mineral mapping, since site-specific field samples from these areas have been analyzed petrographically and geochemically; the last four contain a wider variety of rock types and associated alteration mineral assemblages, and are potential zones of mineralization, as observed on various spectral mineral maps. The field samples used in validation represent areas with known mineralization and have been taken from widely separated parts of the study area. From comparative examination of mineral assemblages indicated in the classification results for four cases used in VNIR-SWIR spectral analysis, it has been observed that ASTER data has been successful in spectrally identifying most of the major mineral units actually observed in the field and in thin-sections. Ambiguities and differences in mineral identification for different cases investigated have arisen primarily because of limitations of ASTER's spectral resolution resulting in multiple (and sometimes erroneous) matches of the pixel spectrum with reference spectral library (USGS spectral library) minerals. Also, residual effects of vegetation within an average pixel area of $30 \times 30 \text{ m}^2$ also add to the difficulty in exact identifications. The results show that the ASTER data can provide fast and dependable support in identifying and mapping specific minerals which can be linked with the presence of economic mineralizations.

An attempt has also been made to check the relationship between the trace-metal concentration and detected alteration in the study area. To investigate the relationship, select samples with marked alteration and metal concentrations above the background values for unaltered equivalents have been individually examined. Their spatial association with the host lithology, and alteration mineralogy identified in thin-sections and on different spectral maps has indicated a possible connection. Three areas with samples having anomalous Cu values have been examined to check this connection. It has been observed that while there is no direct link between the trace-metal anomalies and the presence or absence of specific minerals or alteration zones, the concentrations of certain trace-metals (*viz.*, Cu, Zn and As) are linked to the relative dominance of alteration minerals typically associated with hydrothermal alteration. It has been concluded that though the geochemical anomalies cannot be conclusively linked with the alteration mineralogy, useful leads for such anomalies can be inferred based on the relative distribution of specific alteration minerals, and ASTER data can be effectively utilized for this purpose.

Summary of Conclusions

In connection with the objectives of this research, the results of ASTER data processing and the concomitant observations have led to the following broad conclusions:

1. ASTER data significantly improves the ability of remote detection, identification and mapping of specific minerals related with the processes of hydrothermal alteration hitherto undistinguished using other spaceborne remote sensors, especially the Landsat TM/ETM+. The broad 'OH' alteration class detected using the popular TM7/TM5 ratios can be resolved in terms of specific OH-bearing mineralogy (clays, illite and phyllosilicates) by ASTER's 6 SWIR bands.
2. The capability to remotely map silicate mineralogy using spaceborne thermal remote sensing data was a big gap in geologic remote sensing. This gap has been filled to some

extent by ASTER. It is the only spaceborne remote sensing system providing multispectral data in this geologically important region of the EMR.

3. The success of remote identification and mapping of surface materials is governed by the unique retrieval of their spectral signatures. Credible radiometric, atmospheric and topographic corrections are vital in the reliable application of remote sensing in geology. This study has demonstrated that methods of atmospheric correction utilizing principles of radiative transfer can effectively achieve this objective, but availability of local atmospheric data for the image (constrained by date, time and area) are necessary. Useful improvements can be made by combining image-based approaches with these methods.
4. The credibility of spectral lithologic mapping results is largely influenced by the spatial resolution. The factors of spectral mixing in relatively large areas represented in a single $90 \times 90 \text{ m}^2$ pixel of the ASTER TIR data lead to spectral flattening and loss of absorption features. This is an area with a scope of further improvement. Also, the absence of any spectral channel between $9.0\text{-}10.5 \text{ }\mu\text{m}$ due to atmospheric absorption limits the utility of the data.
5. Results of quantitative silica abundance estimation have shown the capability of ASTER TIR data in reliable lithologic mapping. These results, when combined with the results of spectral analysis, can greatly reduce the inherent subjectivity in a remote sensing based lithologic mapping exercise. There is a good scope for future improvements in the methods investigated, and the results can be improved based on the knowledge and availability of actual silica values from field sites.
6. Alteration mapping based on ASTER VNIR-SWIR data processing has revealed the specific advantages of ASTER over the existing spaceborne multispectral remote sensors. Unique identification and mapping of a variety of surface minerals has been achieved. The results can be improved if supplementary field spectral data are available,

since these can be used to construct a truly representative end-member spectral library for the study area, used in spectral classification.

7. Association of trace-metal anomalies with the alteration mineralogy patterns can provide an indirect, yet crucial clue in mineral exploration. ASTER data can be used in regional mapping of alteration minerals and knowledge of such associations, in conjunction with the lithological and structural analogies, can provide the most direct leads in prospecting for mineral deposits in relatively under-explored or virgin terrains.

References

- Abrams, M. J., Abbott, E. A. and Kahle, A. B., (1991).** Combined use of visible, reflected infrared and thermal infrared images for mapping Hawaiian lava flows. *Journal of Geophysical Research*, 96(B1), pp. 475 – 484.
- Abrams, M. J., Brown, D., Lepley, L. and Sadowski, R., (1983).** Remote sensing for porphyry copper deposits in southern Arizona. *Economic Geology*, 78, pp. 591–604.
- Abrams, M. J., Ashley, R. P., Rowan, L. C., Goetz, A. F. H. and Kahle, A., (1977).** Mapping of hydrothermal alteration in the Cuprite mining district, Nevada, using aircraft scanner images for the spectral region 0.46 to 2.36 μm . *Geology*, 5, pp. 713–718.
- Abrams, M., Hook, S. and Ramachandran, B., (2003).** ASTER User Handbook Version 2, JPL, Caltech, California.
- Adler-Golden, S. M., Matthew, M. W., Bernstein, L. S., Levine, R. Y., Berk, A., Richtsmeier, S. C., Acharya, P. K., Anderson, G. P., Felde, G., Gardner, J., Hike, M., Jeong, L. S., Pukall, B., Mello, J., Ratkowski, A. and Burke, H. -H. (1999).** Atmospheric correction for shortwave spectral imagery based on MODTRAN4. *SPIE Proc. on Imaging Spectrometry*, 3753, pp. 61–69.
- Balasundaram, M. S., (1972),** Applied geochemistry in mineral exploration. Geological Survey of India, *Misc. Publ.*, 21, pp. 5–18.
- Bandfield, J. L., (2002).** Global mineral distributions on Mars. *Journal of Geophysical Research (Planets)*, 107 (E6), pp. 9-1.
- Barducci, A. and Pippi, I., (1996).** Temperature and emissivity retrieval from remotely sensed image using the “grey body emissivity” method. *IEEE Transactions on Geoscience and Remote Sensing*, 34(3), pp. 681–695.
- Barton, I. J., (1985).** Transmission model and ground truth investigation of satellite derived sea surface temperatures. *J. Clim. Appl. Meterol.*, 24, pp. 508–516.
- Bastianelli, L., Bella, G. D. and Tarsi, L., (1993).** Alteration mapping: a case study in mid-south Bolivia. *In: Proceedings of the 9th Thematic Conference on Geologic Remote Sensing*, Vol. II, Environmental Research Institute of Michigan, Ann Arbor, Mich., pp. 1133–1144.
- Basu, S. K., (1986).** Petrology and geochemistry of the Singhana-Muradpur sulphide deposit: a Precambrian syngenetic copper deposit in the Khetri copper belt, Rajasthan, India. *Indian Minerals*, 40(3), pp. 1–16.
- Baugh, W. M., Kruse, F. A. and Atkinson, W. W. (1998).** Quantitative geochemical mapping of ammonium minerals in the southern Cedar Mountains, Nevada, using the air-borne visible/infrared imaging spectrometer (AVIRIS). *Remote Sensing of Environment*, 65, pp. 292–308.
- Becker, F. and Li, Z. L., (1990).** Temperature-independent spectral indices in thermal infrared bands. *Remote Sensing of Environment*, 32, p. 17–33.
- Becker, F., (1987).** The impact of spectral emissivity on the measurement of land surface temperatures from a satellite. *International Journal of Remote Sensing*, 8(10), pp. 1509–1522.

- Beratan, K. K., Peer, B., Dunbar, N. W. and Blom, R. (1997).** A remote sensing approach to alteration mapping AVIRIS data and extension related potassium metasomatism, Socorro, New Mexico. *International Journal of Remote Sensing*, 18(17), pp. 3595–3609.
- Berger, B. R., King, T. V. V., Morath, L. C. and Phillips, J. D. (2003).** Utility of high-altitude infrared spectral data in mineral exploration: application: application to Northern Patagonia mountains, Arizona. *Economic Geology*, 98, pp. 1003–1018.
- Berk, A., Bernstein, L. S. and Robertson, D. C., (1989).** MODTRAN: A Moderate Resolution Model for LOWTRAN 7. *Final Report, AFGL-TR-0122*, Air Force Geophysics Laboratory, Hanscomb AFB, Mass., 42 p.
- Berk, A., Bernstein, L. S., Anderson, G. P., Acharya, P. K., Robertson, D. C., Chetwynd, J. H. and Adler-Golden, S. M., (1998).** MODTRAN cloud and multiple scattering upgrades with application to AVIRIS. *Remote Sensing of Environment*, 65(3), pp. 367–375.
- Boardman, J. W. and Goetz, A. F. H., (1991).** Sedimentary facies analysis using AVIRIS data: a geophysical inverse problem. In: *Proceeding of the 3rd Airborne Visible/Infrared Imaging Spectrometer (AVIRIS) Workshop, JPL Publ. 91-28*, Jet Propulsion Laboratory, California Institute of Technology, Pasadena, California, pp. 4–13.
- Boardman, J. W. and Huntington, J. H., (1996).** Mineral mapping with 1995 AVIRIS data. In: *Summaries of the 6th Annual JPL Airborne Earth Science Workshop, JPL Publ. 96-4*, Vol. 1. AVIRIS Workshop, Jet Propulsion Laboratory, California Institute of Technology, Pasadena, California, pp. 9–11.
- Boardman, J. W. and Kruse, F. A., (1994).** Automated spectral analysis: a geologic example using AVIRIS data, north Grapevine Mountains, Nevada. In: *Proceedings of the 10th Thematic Conference on Geologic Remote Sensing*, Environmental Research Institute of Michigan, Ann Arbor, Michigan, pp. 1-407–1-418.
- Boardman, J. W., Kruse, F. A. and Green, R. O., (1995).** Mapping target signatures via partial unmixing of AVIRIS data. In: *Summaries of the 5th JPL Airborne Geoscience Workshop, JPL Publ. 95-1*, Vol. 1, Jet Propulsion Laboratory, California Institute of Technology, Pasadena, California, pp. 23–26.
- Bowers, T. L. and Rowan, L. C., (1996).** Remote mineralogic and lithologic mapping of the Ice River Alkaline Complex, British Columbia, Canada, using AVIRIS data, *Photogrammetric Engineering and Remote Sensing*, 62, pp. 1379–1385.
- Brooke, J. C., (1864).** The mines of Khetree in Rajpootana. *Journal As. Sec. Beng.*, vol. XXXIII, pp. 519–529.
- Burns, R., (1993).** Mineralogical Applications of Crystal Field Theory, 2nd ed., Cambridge University Press, Cambridge, 551 p.
- Carranza, E. J. M. and Hale, M., (2002).** Mineral imaging with Landsat Thematic Mapper data for hydrothermal alteration mapping in heavily vegetated terrain. *International Journal of Remote Sensing*, 23, pp. 4287–4852.
- Carrere, V. and Abrams, M. J. (1988).** An assessment of AVIRIS data for hydrothermal alteration mapping in the goldfield mining district, Nevada. In: *Proceedings of the Airborne Visible/Infrared Imaging Spectrometer (AVIRIS) Performance Evaluation Workshop, JPL Publ. 88-38*, Jet Propulsion Laboratory, California Institute of Technology, Pasadena, California, pp. 134–154.
- Chahine, M. T., (1983).** Interaction mechanisms within the atmosphere. In: *Manual of Remote Sensing. American Society of Photogrammetry*, Fall Church, VA, pp. 165–230.

- Chakrabarti, B. and Gupta, P., (1992).** Stratigraphy and structure of the North Delhi Basin. *Geological Survey of India Records*, 124, pp.5–9.
- Chandra Chowdhury, Y. M. K., Banerjee, A. K. and Rao, A. M., (1971).** Geology and ore mineralization in the Akwali section, Khetri Copper Belt, Rajasthan. *Misc. Publ.*, 16, Geological Survey of India, pp. 369–378.
- Chandrasekhar, S., (1950).** Radiative Transfer. Oxford University Press.
- Chavez, P. S., Jr. and Howell, J. A., (1984).** Imaging processing techniques for Thematic Mapper data. *American Society of Photogrammetry Special Publication*, 0277-2094, pp. 728–743.
- Chavez, P. S., Jr., (1996).** Image-based atmospheric corrections revisited and improved. *Photogrammetric Engineering and Remote Sensing*, 62, pp. 1025–1036.
- Chavez, P. S., Jr., (1988).** An improved dark object subtraction technique for atmospheric scattering correction of multispectral data. *Remote Sensing of Environment*, 24, pp. 459–479.
- Chavez, P. S., Jr., (1989).** Radiometric calibration of Landsat Thematic Mapper multispectral images. *Photogrammetric Engineering and Remote Sensing*, 55(9), pp. 1285–1294.
- Chavez, P. S., Jr., Berlin, G. L. and Sowers, L. B., (1982).** Statistical method for selecting Landsat MSS ratios. *J App. Photogr. Eng.*, 8 (1), pp. 23–30.
- Civco, D. L., (1989).** Topographic normalization of Landsat Thematic Mapper digital imagery. *Photogrammetric Engineering and Remote Sensing*, 55(9), pp. 1303–1309.
- Clark, R. N., King, T. V. V., Klejwa, M., Swayze, G. and Vergo, N., (1990a).** High spectral resolution reflectance spectroscopy of minerals. *Journal of Geophysical Research*, 95, pp. 12653–12680.
- Clark, B. E., Helfenstein, P., Bell III, J. F., Peterson, C., Veverka, J., Izenberg, N. I., Domingue, D., Wellnitz, D. and McFadden, L. (2002).** Near infrared spectrometer photometry of Asteroid 433 Eros. *Icarus*, 155, pp. 189–204.
- Clark, R. N. and Roush, T. L., (1984).** Reflectance spectroscopy: quantitative analysis techniques for remote sensing applications, *Journal of Geophysical Research*, 89, pp. 6329–6340.
- Clark, R. N., Swayze, G. A. and Gallagher, A., (1993).** Mapping minerals with imaging spectroscopy. In: *Advances Related to United States and International Mineral Resources: Developing Frameworks and Exploration Technologies*, USGS Bull. 2039, U.S. Geological Survey, Washington, D.C., pp. 141–150.
- Clark, R. N., Swayze, G. A., Wise, R., Livo, K. E., Hoefen, T. M., Kokaly, R. F. and Sutley, S. J., (2003).** USGS Digital Spectral Library splib05a, U.S. Geological Survey, *Open File Report 03-395*.
- Clark, R. N., Gallagher, A. J. and Swayze, G. A., (1990b).** Material absorption band depth mapping of imaging spectrometer data using complete band shape least squares fit with library reference spectra. In: *Proceedings of the 2nd Airborne Visible/Infrared Imaging Spectrometer (AVIRIS) Workshop, JPL Publ. 90-54*, Jet Propulsion Laboratory, California Institute of Technology, Pasadena, California, pp. 176–186.
- Clark, R. N., Swayze, G. and Gallagher, A. (1992).** Mapping the mineralogy and lithology of Canyonlands, Utah with imaging spectrometer data and multiple spectral feature mapping algorithm. In: *Summaries of the Third Annual JPL Airborne Geoscience Workshop, JPL Publ. 92-14*, Vol. 1, Jet Propulsion Laboratory, California Institute of Technology, Pasadena, California, pp. 11–13.

- Clark, R. N., (1999).** Spectroscopy of rocks and minerals, and principles of spectroscopy. *In: Rencz AN (ed) Remote Sensing for the Earth Sciences, Manual of Remote Sensing*, 3rd edn, vol 3, American Society of Photogrammetry and Remote Sensing, John Wiley, pp 3–58
- Conel, J. E., Green, R. O., Vane, G., Bruegge, C. J., Alley, R. E. and Curtiss, B. (1987).** Airborne Imaging Spectrometer-2: Radiometric spectral characteristics and comparison of ways to compensate for the atmosphere. *Proc. SPIE*, 834, pp. 140–157.
- Conradsen, K. and Harpoth, O., (1984).** Use of Landsat multispectral scanner data for detection and reconnaissance mapping of iron oxide staining in mineral exploration, Central East Greenland. *Economic Geology*, 79, pp. 1229–1244.
- Crippen, R. E., Blom, R. G. and Heyada, J. R., (1988).** Directed band ratioing for the retention of perceptually-independent topographic expression in chromaticity-enhanced imagery. *International Journal of Remote Sensing*, 9, pp, 749–765.
- Crippen, R.E., (1988).** The dangers of underestimating the importance of data adjustments in band ratioing. *International Journal of Remote Sensing*, 9. pp. 767–776.
- Crist, E. P. and Cicone, R. C., (1984).** A physically based transformation of thematic mapper data — the TM tasseled cap. *IEEE Transactions on Geoscience and Remote Sensing*, GE-22(3), pp. 256–263.
- Crósta, A. P. and Moore, J. M., (1989).** Enhancement of Landsat thematic mapper imagery for residual soil mapping in SW Minas Gerais State, Brazil: a prospecting case history in greenstone belt terrain. *In: Proceedings of the 7th Thematic Conference on Remote Sensing and Exploration Geology*, Vol. II, Environmental Research Institute of Michigan, Ann Arbor, Michigan, pp. 1171–1187.
- Crósta, A. P., Sabine, C. and Taranik, J. V., (1998).** Hydrothermal alteration mapping at Bodie, California using AVIRIS hyperspectral data. *Remote Sensing of Environment*, 65, pp. 309–319.
- Crósta, A. P., De Souza Filho, C. R., Azevedo, F. and Brodie, C., (2003).** Targeting key alteration minerals in epithermal deposits in Patagonia, Argentina, using ASTER imagery and principal components analysis. *International Journal of Remote Sensing*, 24 (21), pp. 4233–4240.
- Crowley, J. K. (1991).** Visible and near-infrared (0.4–2.5 μ m) reflectance spectra of playa evaporate minerals. *Journal of Geophysical Research*, 96(B10), pp. 16,231–16,240.
- Crowley, J. K. and Clark, R. N., (1992).** AVIRIS study of Death Valley evaporite deposits using least-squares band-fitting methods. *NASA (non Center Specific) Publication (Abst.)*, Added to NTRS: 2004–11–03, Accession Number: 94N16676; Document ID: 19940012203.
- Crowley, J. K., Brickey, D. W. and Rowan, L. C., (1989).** Airborne imaging spectrometer data of the Ruby Mountains, Montana: mineral discrimination using relative absorption band-depth images. *Remote Sensing of Environment*, 29, pp.121–134.
- Crowley, J. K. (1993),** Mapping playa evaporite minerals with AVIRIS data: a first report from Death Valley, CA. *Remote Sensing of Environment*, 44, pp. 337–356.
- Cudahy, T. J., Whitbourn, L. B., Conner, P. M., Mason, P. and Phillip, R. N., (1999).** Mapping surface mineralogy and scattering behaviour using backscattered reflectance from a hyperspectral midinfrared airborne CO₂ laser system (MIRACO(2)LAS). *IEEE Transactions on Geoscience and Remote Sensing*, 37, pp. 2019–2034.
- Cuday, T. J., Okada, K., Yamato, Y., Maekawa, M., Hackwell, J. A. and Huntington, J. F., (2000).** Mapping skarn and porphyry alteration mineralogy at Yerington, Nevada,

using airborne hyperspectral TIR SEBASS data. *CSIRO Exploration and Mining Report 734*, CSIRO Exploration and Mining Co., Flore at Park, WA, Australia.

- Das Gupta, S. K., (1992).** Copper mineralization and Ni-Co in sulphides of Khetri, Rajasthan, India, *International Geological Congress, Kyoto, (Abst.)*, pp. 724.
- Das Gupta, S. P., (1962a).** Petrological studies in the Khetri Copper Belt, Jhunjhunu district, Rajasthan. *Indian Minerals*, 16, pp. 167.
- Das Gupta, S. P., (1962b).** Twinning in cummingtonite of Khetri Copper Belt, Jhunjhunu district, Rajasthan. *Indian Minerals*, 16, pp.176.
- Das Gupta, S. P., (1962c).** On the relationship between hornblende and cummingtonite in altered wall rocks, Khetri Copper Belt, Rajasthan. *Indian Minerals*, 16, pp.299.
- Das Gupta, S. P., (1963).** Preliminary notes on the genesis of sulphide deposits of Khetri Copper Belt, Rajasthan. *Indian Minerals*, 17, pp.87.
- Das Gupta, S. P., (1964a),** Petrology of the anthophyllite-cummingtonite bearing rocks of the Khetri Copper belt, Rajasthan. *Spl. vol. 'Researches in Petrology'* Geological Survey of India, pp.91–112.
- Das Gupta, S. P., (1964b).** Genesis of sulphide mineralization in Khetri Copper Belt, Rajasthan, India. *Rep. Int. Geol. Cong., New Delhi*, V. pp.239–257.
- Das Gupta, S. P., (1968).** The structural history of the Khetri copper belt, Jhunjhunu and Sikar districts, Rajasthan. *Memoir Geological Survey of India*, 98, 170p
- Das Gupta, S. P., (1974).** Geological setting and origin of sulphide deposits in the Khetri Copper Belt, Rajasthan. *Golden Jubilee Volume: Geological Mineral and Metallurgical Society of India*, pp. 223–238.
- Das Gupta, S. P., Chakraborty, S., Bhadra, A. and Saha, H., (1963).** Notes on chloritization in Khetri Copper Belt, Rajasthan. *Indian Minerals*, 17, 187p.
- Das Gupta, S. P., Sen Gupta, P. R. and Murthy, M. V. N., (1965).** Nature and significance of wall rock alteration in some hydrothermal ore deposits of India. *Economic Geology*, 60, pp. 1702–1708.
- Das Gupta, S. P., Sen Gupta, P. R. and Murthy, M. V. N., (1971).** On the importance of geological setting in the exploration of base metal mineral deposits. *Misc. Publ.*, 16, pp. 69–78.
- Davidson, D., Bruce, B. and Jones, D., (1993).** Operational remote sensing mineral exploration in a semi-arid environment: the Troodos Massif, Cyprus. *In: Proceedings of the 9th Thematic Conference on Geologic Remote Sensing*, Vol. II, Environmental Research Institute of Michigan, Ann Arbor, Michigan, pp. 845–859.
- Deb, M. and Sarkar, S. C. (1990).** Proterozoic tectonic evolution and metallogenesis in the Aravalli-Delhi Orogenic Complex, northwestern India. *Precambrian Research*, 46, pp. 115–137.
- Deb, M., Thorpe, R. I., Cumming, G. L. and Wagner, P. A. (1989).** Age, source and stratigraphic implications of Pb isotope data for conformable, sediment-hosted, base metal deposits in the Proterozoic Aravalli-Delhi orogenic belt, northwestern India. *Precambrian Research*, 43, pp. 1–22.
- Deb, S., (1948).** Microscopic characters of some metamorphic rocks from the Khetri mine area, Rajputana. *Proc. Indian Science Congress, (Abst.)*, Vol.III, pp.152.

- Ducart, D. F., Crósta, A. P. and Filho, C. R. S., (2006).** Alteration mineralogy at the Cerro La Mina Epithermal Prospect, Patagonia, Argentina: field mapping, short-wave infrared spectroscopy, and ASTER images. *Economic Geology*, 101, pp. 981–996.
- Dunn, J. A., (1965).** Copper. *Bull. Geological Survey of India, Series A, No.23, Economic Geology*, Revised and enlarged by Jhingran, A.G.
- Elachi, C. and van Zyl, J., (2006).** Introduction to the physics and techniques of remote sensing. Second edition, John Wiley & Sons, New York, 724, pp. 547.
- ENVI User's Guide, (2005).** Envi User's Guide, ENVI version 4.2, 2005.
- Farmer, V.C. (ed) (1974).** The infrared spectra of minerals. *Mineralogical Society Publication*, London.
- Farrand, W. H. (1997).** Identification and mapping of ferric oxide and oxyhydroxide minerals in imaging spectrometer data of Summitville, Colorado, USA, and the surrounding San Juan Mountains. *International Journal of Remote Sensing*, 18(7), pp. 1543–1552.
- Feely, K. C. and Christensen, P. R., (1999).** Quantitative compositional analysis using thermal emission spectroscopy: application to igneous and metamorphic rocks, *Journal of Geophysical Research*, 104, pp. 24,195–24,210.
- Fraser, S. J., (1991).** Discrimination and identification of ferric oxides using satellite thematic mapper data: a Newman case study. *International Journal of Remote Sensing*, 12, pp. 635–641.
- Gaffey, S. J., (1987).** Spectral reflectance of carbonate minerals in the visible and near infrared (0.35–2.55 μm): anhydrous carbonate minerals. *Journal of Geophysical Research*, 92, pp. 1429–1440.
- Gaffey, S. J., McFadden, L. A., Nash, D. and Pieters, C. M., (1993).** Ultraviolet, visible, and near-infrared reflectance spectroscopy: laboratory spectra of geologic materials. In: *Remote Geochemical Analysis: Elemental and Mineralogical Composition*, C. M. Pieters, and P. A. J. Englert (eds.), Cambridge University Press, Cambridge, pp. 43–78.
- Galvão, L. S., Filho, R. A. and Vitorello, I., (2005).** Spectral discrimination of hydrothermally altered materials using ASTER short-wave infrared bands: evaluation in a tropical savannah environment. *International Journal of Applied Earth Observation and Geoinformation*, 7, pp. 107–114.
- Gillespie, A. R., (1985).** Lithologic mapping of silicate rocks using TIMS. *The TIMS Data Users' Workshop, June 18-19, 1985, JPL Publication*, 86-38, pp. 29–44.
- Gillespie, A. R., (1992b).** Enhancements of multispectral thermal infrared images: decorrelation contrast stretching. *Remote Sensing of Environment*, 42, pp. 147–156.
- Gillespie, A. R., (1992a).** Spectral mixture analysis of multispectral thermal infrared images. *Remote Sensing of Environment*, 42, pp. 137–145.
- Gillespie, A. R., Kahle, A. B., Walker, R. E., (1986).** Color enhancement of highly correlated images: I – decorrelation and IHS contrast stretches. *Remote Sensing of Environment*, 20, pp. 209–235.
- Gillespie, A. R., Rokugawa, S., Hook, S. J., Matsunaga, T. and Kahle, A. B., (1999).** Temperature/emissivity separation algorithm theoretical basis document, version 2.4, Jet Propulsion Laboratory, Pasadena, California.
- Gillespie, A. R., Rokugawa, S., Matsunaga, T., Steven Cothorn, J., Hook, S. and Kahle, A. B., (1998).** A temperature and emissivity separation algorithm for advanced spaceborne thermal emission and reflection radiometer (ASTER) images. *IEEE Transactions on Geoscience and Remote Sensing*, 36(4), pp. 1113–1126.

- Goetz, A. F. H., Rock, B. N. and Rowan, L. C., (1983).** Remote sensing for exploration: an overview. *Economic Geology*, 78 (4), pp. 573–590.
- Golani, P. R., Gathania, R. C., Grover, A. K. and Bhattacharjee, J., (1992).** Felsic volcanics in south Khetri Copper Belt, Rajasthan, and their metallogenic significance. *Journal of Geological Society of India*, 40(1), pp. 79–87.
- Goyal, R. S., (2001).** Implications of geology, metallogeny, geochemistry, and tectonics over the spatial distribution of Cu, Pb, Zn and associated metals in Bethumbi-Rajpura-Dariba and Jashma-Bhupalsagar Belts, southern Rajasthan. *Unpublished PhD Thesis*, University of Rajasthan, Jaipur.
- Green, A. A. and Craig, M. D., (1985).** Analysis of aircraft spectrometer data with logarithmic residuals. *JPL Proc. of the Airborne Imaging Spectrometer Data Anal. Workshop*, pp. 111–119, (SEE N86-11618 02-43); US.
- Green, A. A., Berman, M., Switzer, P. Graig, M. D., (1988).** A transformation for ordering multis-pectral data in terms of image quality with implications for noise removal. *IEEE Transactions on Geoscience and Remote Sensing*, 26, pp. 65–74.
- Green, R. O., Eastwood, M. L., Sarture, C. M., Chrien, T. G., Aronsson, M., Chippendale, B. J., Faust, J. A., Pavri, B. E., Chovit, C. J., Solis, M., Olah, M. R. and Williams, O., (1998).** Imaging spectroscopy and the airborne visible/infrared imaging spectrometer (AVIRIS). *Remote Sensing of Environment*, 65, pp. 227–248.
- Green, R. O., ed. (1990).** *Proceedings of the Second Airborne Visible/Infrared Imaging Spectrometer (AVIRIS) Workshop*. JPL Publication, pp. 90–54.
- GSI, (1997).** Geological map of North Khetri Copper Belt, Rajasthan, India.
- Gupta, P., Guha, D. B. and Chattopadhyay, B., (1998).** Basement-cover relationship in the Khetri Copper Belt and emplacement mechanism of granite massifs, Rajasthan. *Journal of Geological Society of India*, 52, pp. 417–432.
- Gupta, R. P., (1974).** Studies on structure, petrography and associated iron and copper deposits of Babai and Taonda area, Khetri Copper Belt, Rajasthan. *Unpublished Ph.D. Thesis*, Department of Geology and Geophysics, University of Roorkee, India, pp.342.
- Gupta, R. P., (2003).** Remote sensing geology. Springer-Verlag, Berlin-Heidelberg.
- Gupta, R. P., Ghosh, A. and Haritashya, U. K., (2007).** Empirical relationship between near-IR reflectance of melting seasonal snow and environmental temperature in a Himalayan basin. *Remote Sensing Environ.*, 107, pp. 402–413.
- Hackwell, J. A., Warren, D. W., Bongiovi, R. P., Hansel, S. J., Hayhurst, T. L., Mabry, D. J., Sivjee, M. G. and Skinner, J. W., (1996).** LWIR/MWIR imaging hyperspectral sensor for airborne and ground-based remote sensing. *In: Proceedings of SPIE -- Volume 2819, Imaging Spectrometry II*, Michael, R. D., Jonathan, M. M., (eds.), pp. 102–107.
- Hall, F. G., Strelbel, D. E., Nickeson, J. E. and Goetz, S. J., (1991).** Radiometric rectification: towards a common radiometric response among multirate, multisensor images. *Remote Sensing of Environment*, 35, pp. 11–27.
- Hamilton, V. E. and Christensen, P. R., (2000).** Determining the modal mineralogy of mafic and ultramafic igneous rocks using thermal emission spectroscopy. *Journal of Geophysical Research*, 105(E4), pp. 9609–9621.
- Hamilton, V. E., Christensen, P. R. and McSween Jr., H. Y., (1997).** Determination of Martian meteorite lithologies and mineralogies using vibrational spectroscopy. *Journal of Geophysical Research*, 102, pp. 25593–25603.

- Harris, D. C. and Bertolucci, M.D., (1989).** Symmetry and spectroscopy: an introduction to vibrational and electronic spectroscopy. Dover Publication, Inc., New York.
- Harsanyi, J.C. and Chang, C. I., (1994).** Hyperspectral image classification and dimensionality reduction: an orthogonal subspace projection approach. *IEEE Transactions on Geoscience and Remote Sensing*, 32(4), pp. 779–785.
- Hernandez-Baquero, E. D., (2000).** Characterization of the Earth's surface and atmosphere from multispectral and hyperspectral thermal imagery. *Unpublished PhD Thesis*, 17th July, 2000.
- Heron, A. M., (1923).** Geology of western Jaipur. *Records Geological Survey of India*, LIV, pp. 345–397.
- Heron, A. M., (1925).** Geology of northeastern Rajputana and adjacent districts. *Memoir Geological Survey of India*, XLII, pp. 1-128.
- Heron, A. M., (1935).** Mineral resources of Rajasthan. *Transactions of Mineralogical and Geological Institute of India*, XXIX, pp. 356–362.
- Hook, S. J., Abbott, E. A., Grove, C., Kahle, A. B. and Palluconi, F., (1999).** Use of multispectral thermal infrared data in geological studies. In: *Rencz AN (ed) Remote Sensing for the Earth Sciences, Manual of Remote Sensing*, 3rd edn, vol 3, American Society of Photogrammetry and Remote Sensing, John Wiley, pp 59–110.
- Hook, S. J. and M. Rast, (1990).** Mineralogic mapping using airborne visible/infrared imaging spectrometer (AVIRIS) shortwave infrared (SWIR) data acquired over Cuprite, Nevada. In *Proceedings of the 2nd Airborne Visible/Infrared Imaging Spectrometer (AVIRIS) Workshop*, R.O. Green, ed., JPL Publ. 90-54, Jet Propulsion Laboratory, California Institute of Technology, Pasadena, California, pp. 199–207.
- Hook, S. J., Cudahy, T. J., Kahle, A. B. and Whitbourn, L. B., (1998).** Synergy of active and passive airborne thermal infrared systems for surface compositional mapping. *Journal of Geophysical Research*, 103, pp. 18269–18276.
- Hook, S. J., Dmochowski, J. E., Howard, K. A., Rowan, L. C., Karlstrom, K. E. and Stock, J. M., (2005).** Mapping variations in weight percent silica measured from multispectral thermal infrared imagery — examples from the Hiller mountains, Nevada, USA and Tres Virgenes-La Reforma, Baja California Sur, Mexico. *Remote Sensing of Environment*, 95, pp. 273–289.
- Hook, S. J., Gabell, A. R., Green, A. A. and Kealy, P. S., (1992).** A comparison of techniques for extracting emissivity information from thermal infrared data for geologic studies. *Remote Sensing of Environment*, 42, pp. 123–135.
- Hook, S. J., Karlstrom, K. E., Miller, C. F. and McCaffery, K. J. W., (1994).** Mapping the Piute Mountains, CA with thermal infrared multispectral scanner (TIMS) data. *Journal of Geophysical Research*, 99, pp. 15605–15622.
- Hook, S. J., Myers, J. J., Thome, K. J., Fitzgerald, M. and Kahle, A. B. (2001).** The MODIS/ASTER airborne simulator (MASTER) – a new instrument for earth science studies. *Remote Sensing of Environment*, 76, pp. 93–102.
- Hubbard, B. E., Crowley, J. K. and Zimbelman, D. R. (2003).** Comparative alteration mineral mapping using visible to shortwave infrared (0.4–2.4 μm) Hyperion, ALI and ASTER imagery. *IEEE Transactions on Geoscience and Remote Sensing*, 41(6), pp. 1401–1410.
- Hunt, G. R., (1977).** Spectral signatures of particulate minerals in the visible and near-infrared. *Geophysics*, 42, pp. 501–513.

- Hunt, G. R., (1980).** Electromagnetic radiation: the communication link in remote sensing. *In: Siegal B.S. Gillespie A.R. (eds.) Remote Sensing in geology.* Wiley, New York, pp 5–45.
- Hunt, G. R. and Salisbury, J. W., (1974).** Mid-infrared spectral behavior of sedimentary rocks. *U.S. Air force Cambridge research laboratory technical report, AFCRL-TR-74-0625.*
- Hunt, G. R. and Salisbury, J. W., (1975),** Mid-infrared spectral behavior of igneous rocks. *Air force Cambridge research laboratory technical report, AFCRL-TR-75-0376.,* 142p.
- Hunt, G. R. and Salisbury, J. W., (1976),** Mid-infrared spectral behavior of metamorphic rocks, *Environ. Res. Pap., 543 AFCRL-TR-76-0003,* 67p, Air Force Cambridge Res. Lab., Hanscom AFB, Mass.
- Hutsinpillar, A. and Taranik, J. V., (1988).** Spectral signatures of hydrothermal alteration at Virginia City, Nevada. *In: Bulk minerable precious metal deposits of the western United States, Robert W. Schafer (ed.), Geological Society of Nevada Symposium Proceedings,* pp. 505–530.
- Iwasaki, A. and Oyama, E., (2005).** Correction of stray light and filter scratch blurring for ASTER Imagery. *IEEE Transactions on Geoscience and Remote Sensing,* 43(12), pp. 2763–2768.
- Iwasaki, A. and Tonooka, H., (2005).** Validation of a crosstalk correction algorithm for ASTER/SWIR. *IEEE Transactions on Geoscience and Remote Sensing,* 43(12), pp. 2747–2751.
- Iwasaki, A., Fujisada, H., Akao, H., Shindou, O. and Akagi, S., (2001).** Enhancement of spectral separation performance for ASTER/SWIR. *Proc. SPIE,* 4486, pp. 42–50.
- Jackson, R. D., (1983).** Spectral indices in n-space. *Remote Sensing of Environment,* 13, pp. 409–421.
- Jensen, J. R., (2006).** Remote sensing of the environment: an earth resource perspective, second edition, Prentice Hall International Limited, London, UK (2006).
- Johnson, B.R. and Young, S. J., (1998).** Inscene atmospheric compensation: application to SEBASS data at the ARM Site. *Aerospace Report,* No. ATR-99(8407)-1 Parts I and II.
- Kahle, A. B., (1980).** Surface thermal properties. *In: Siegal, B. S., Gillespie, A. R., (eds.) Remote sensing in geology.* Wiley, New York, pp. 257–273.
- Kahle, A. B., (1987).** Surface emittance, temperature and thermal inertia derived from Thermal Infrared Multispectral Scanner (TIMS) data for Death Valley, California. *Geophysics,* 52, pp. 858–874.
- Kahle, A. B. and Rowan, L. C., (1980).** Evaluation of multispectral middle near infrared aircraft images from lithologic mapping in the east Tintic Mountains, Utah. *Geology,* 8, pp. 234–239.
- Kahle, A. B., Gillespie, A. R., Abbott, E. A., Abrams, M. J., Walker, R. E. and Hoover, G., (1988).** Relative dating of Hawaiian lava flows using multispectral thermal infrared images: A new tool for geologic mapping of young volcanic terrains. *Journal of Geophysical Research,* 93(B12), pp. 15239–15251.
- Kahle, A. B. and Goetz, A. F. H., (1983).** Mineralogic information from a new airborne thermal infra-red multispectral scanner. *Science,* 222, pp. 24–27.
- Kahle, A. B., Madura, D. P. and Soha, J. M., (1980).** Middle infrared multispectral aircraft scanner data analysis for geological applications. *Applied Optics,* 19, pp. 2279–2290.

- Kahle, A. B., Palluconi, F. D., and Christensen, P. R., (1993).** Thermal emission spectroscopy: application to Earth and Mars. Ch 5 in : *Topics in Remote Sensing for Remote Geochemical Analysis: Elemental and Mineralogical Compositions*, Pieters, C. M. and Englert, P. A. J. (eds.), Cambridge University Press.
- Kaufman, Y. J. and Sendra, C., (1988).** Algorithm for automatic atmospheric correction to visible and near-IR imagery. *International Journal of Remote Sensing*, 9, pp. 1357–1381.
- Kaufman, Y. J., Wald, A. E., Remer, L. A., Gao, B. C., Li, R. R. and Flynn, L., (1997).** The MODIS 2.1 μ m — channel correction with visible reflectance for use in remote sensing of aerosol. *IEEE Transactions on Geoscience and Remote Sensing*, 35, pp. 1286–1298.
- Kaufmann, H. J., (1988).** Mineral exploration along the Aqaba-Levant structure by use of TM-data- concepts, processing and results. *International Journal of Remote Sensing*, 9(10-11), pp. 1639–1658.
- Kauth, R. J. and Thomas, G. S., (1976).** The tasseled cap — a graphic description of the spectral-temporal development of agricultural crops as seen by Landsat. In *Proc. the Symposium on Machine Processing of Remotely Sensed Data*, Purdue University, West Lafayette, Indiana, pp. 4B-41– 4B-50.
- Kealy, P. S. and Gabell, A. R., (1990).** Estimation of emissivity and temperature using alpha coefficients. In: *Proc. 2nd TIMS Workshop, JPL Publication*, California Institute of Technology, Pasadena, California, pp. 90–55.
- Kealy, P. S. and Hook, S., (1993).** Separating temperature and emissivity in thermal infrared multispectral scanner data: implication for recovering land surface temperatures. *IEEE Transactions on Geoscience and Remote Sensing*, 31, pp. 1155–1164.
- Kenea, N. H. (1997).** Improved geological mapping using Landsat TM data, southern Red Sea Hills, Sudan: PC and IHS decorrelation stretching. *International Journal of Remote Sensing*, 18(6), pp. 1233–1244.
- Klein, C. and Hurlburt, C. S. (1985).** Manual of mineralogy. 20th edition, John Wiley & Sons.
- Knight, J., Lowe, J., Joy, S., Cameron, J., Merrillees, J., Nag, S., Shah, N., Dua, G. and Jhala, K., (2002).** The Khetri Copper Belt, Rajasthan: iron oxide copper-gold terrane in the Proterozoic of NW India. In: *Porter, T. M. (ed.), Hydrothermal Iron Oxide Copper-Gold & Related Deposits: A Global Perspective*, 2, PGC Publishing, Adelaide, pp. 321–341.
- Kruse, F. A., (1987).** Use of high spectral resolution remote sensing to characterize weathered surfaces of hydrothermally altered rocks. Unpublished Ph. D. thesis, Colorado School of Mines, Golden, 139p.
- Kruse, F. A., (1999).** Visible infrared sensors case studies. In: *Rencz AN (ed) Remote Sensing for the Earth Sciences, Manual of Remote Sensing*, 3rd ed, vol 3, American Society of Photogrammetry and Remote Sensing, pp. 567–611.
- Kruse, F. A., (2004).** Comparison of Atrem, Acorn, and Flaash atmospheric corrections using low-altitude AVIRIS data of Boulder. *Co. proceedings 13th JPL Airborne Geoscience Workshop*.
- Kruse, F. A. and Boardman, J. W., (2000).** Characterization and mapping of kimberlites and related diatremes using hyperspectral remote sensing. In: *Proceedings, 2000, IEEE AeroSpace Conference*.
- Kruse, F. A., Lefkoff, A. B., Boardman, J. B., Heidebrecht, K. B., Shapiro, A. T., Barloon, P. J., and Goetz, A. F. H., (1993).** The Spectral Image Processing System (SIPS) -

- interactive visualization and analysis of imaging spectrometer data. *Remote Sensing of Environment, Special issue on AVIRIS*, May-June 1993, 44, pp. 145–163.
- Kruse, F. A., Boardman, J. W. and Huntington, J. F., (2003).** Comparison of airborne hyperspectral data and EO-1 hyperion for mineral mapping. *IEEE Transactions on Geoscience and Remote Sensing, Special Issue*, 41(6), pp. 1388-1400.
- Lahren, M. M., Schweickert, R. A. and Taranik, J. V., (1988).** Analysis of the northern Sierra accreted terrane, California, with airborne thermal infrared multi spectral scanner data. *Geology*, 16, pp. 525–528.
- Lane, M. D. and Christensen, P. R., (1997).** Thermal infrared emission spectroscopy of anhydrous carbonates. *Journal of Geophysical Research*, 102 (E11), pp. 25581–25592.
- Li, W.-H., Weeks, R. J. and Gillespie, A. R., (1998).** Multiple scattering in the remote sensing of natural surfaces. *International Journal of Remote Sensing*, 19(9), pp. 1725–1740.
- Liang, S., Fallah-Adl, H., Kalluri, S., JaJa, J., Kaufman, Y. and Townshend, J., (1997).** Development of an operational atmospheric correction algorithm for TM imagery. *Journal of Geophysical Research*, 102, pp.17173–17186.
- Lillesand, T. M. and Kiefer, R. W., (2000).** Remote sensing and image interpretation. Fourth edition, Wiley, New York, 724 p.
- Loughlin, W., (1991),** Principal component analysis for alteration mapping. *Photogrammetric Engineering and Remote Sensing*, 57, pp. 1163–1169.
- Lowell, J. D. and Guilbert, J. M., (1970).** Lateral and vertical alteration-mineralization zoning in porphyry ore deposits. *Economic Geology*, 65(4), pp. 373–408.
- Lu, D., Mausel, P., Brondizio, E. and Moran, E., (2002).** Assessment of atmospheric correction methods for Landsat TM data applicable to Amazon basin LBA research. *International Journal of Remote Sensing*, 23(13), pp. 2651–2671.
- Lyon, R. J. P., (1965).** Analysis of rocks by spectral infrared emission (8 to 25 microns). *Economic Geology*, 60, pp. 715–736.
- Markham, B. L. and Barker, J. L., (1986).** Landsat MSS and TM post-calibration dynamic ranges, exoatmospheric reflectances and at-satellite temperatures. *EOSAT technical notes*, 1, pp. 3–8.
- Markham, B. L. and Barker, J. L., (1987).** Thematic Mapper bandpass solar exoatmospheric irradiances. *International Journal of Remote Sensing*, 8(3), pp. 517–523.
- Mars, J. C. and Rowan, L. C., (2006).** Regional mapping of phyllic- and argillic-altered rocks in the Zagros magmatic arc, Iran, using advanced spaceborne thermal emission and reflection radiometer (ASTER) data and logical operator algorithms. *Geosphere*, 2(3), pp.161–186.
- Marsh, S. E. and McKeon, J. B., (1983).** Integrated analysis of high-resolution field and airborne spectroradiometer data for alteration mapping. *Economic Geology*, 78, pp. 618–632.
- Masuda, K., Takashima, T. and Takayama, Y., (1988).** Emissivity of pure and sea waters for the model sea surface in the infrared window region. *Remote Sensing of Environment*, 24, pp. 313–329.
- Mather, P. M., (2004).** Computer processing of remotely-sensed images- an Introduction. Third edition, John Wiley & Sons, Ltd., 318p.

- Matsunaga, T., (1994).** A temperature-emissivity separation method using an empirical relationship between the mean, the maximum, and the minimum of the thermal infrared emissivity spectrum. *Journal of Remote Sensing Society of Japan*, 14(2), pp. 230–241, (in Japanese with English abstract).
- Matthew, M. W., Adler-Golden, S. M., Berk, A., Richtsmeier, S. C., Levine, R. Y., Bernstein, L. S., Acharya, P. K., Anderson, G. P., Felde, G. W., Hoke, M. P., Ratkowski, A., Burke, Hsiao-H., Kaiser, R. D. and Miller, D. P., (2000).** Status of atmospheric correction using a MODTRAN4-based algorithm. *Proc. SPIE, Algorithms for Multispectral, Hyperspectral, and Ultraspectral Imagery VI*, 4049, April 2000.
- Matthew, M. W., Adler-Golden, S. M., Berk, A., Felde, G., Anderson, G. P., Gorodestzky, D., Paswaters, S. and Shippert, M., (2003).** Atmospheric correction of spectral imagery: evaluation of the FLAASH algorithm with AVIRIS Data, *SPIE Proceeding, Algorithms and Technologies for Multispectral, Hyperspectral, and Ultraspectral Imagery IX*.
- Mazer, A. S., Martin, M., Lee, M. and Solomon, J. E., (1988).** Image processing software for imaging spectrometry data analysis. *Remote Sensing of Environment*, 92, pp. 13619–13634.
- McMillan, L. M. and Crosby, D. S., (1984).** Theory and validation of the multiple window sea surface temperature technique. *Journal of Geophysical Research*, 89(C3), pp. 655–3661.
- MMAJ, (2001).** Report on overseas satellite remote sensing survey program: Indochina malay project: Myanmar. 207p. (in Japanese with English appendix)
- Michalski, J. R., Reynolds, S. J., Sharp, T. G. and Christensen, P. R., (2004).** Thermal infrared analysis of weathered granitic rock compositions in the Sacaton Mountains, Arizona : implications for petrologic classification from thermal infrared remote sensing data. *Journal of Geophysical Research*, 109(E03007), doi : 10.1029/2003JE002197.
- Mickus, K. and Johnson, E., (2001).** Mapping sedimentary and volcanic units within and surrounding Petrified Forest National Park, Arizona, using Landsat-5 and SPOT Panchromatic data. *International Journal of Remote Sensing*, 22, pp.1919–1935.
- Miyatake, S., (2002).** Regional lineament analysis and alteration mineral mapping for intrusive-related copper exploration in the Myanmar Central volcanic belt. <http://www.gisdevelopment.net/aars/acrs/2002/pos3/039.pdf>.
- Moghtaderi, A., Moore, F. and Mohammadzadeh, A., (2007).** The application of advanced spaceborne thermal emission and reflection (ASTER) radiometer data in the detection of alteration in Chadormalu paleocrater, Bafq region, Central Iran. *Journal of Asian Earth Sciences*, 30, pp. 238–252.
- Mukherjee, A. D., (1966).** Mineraography of ore-minerals around Khetri Jhunjhunu, Rajasthan. In: *Proceedings of Indian Science Congress, (Abst.)*, 54th session.
- Mukherjee, A. D., (1967a).** Occurrence of mackinawite in the sulphide ores of Madhan-kudan and Kolihan sections of Khetri Copper Belt, Jhunjhunu district, Rajasthan. *Symposium on Genetic Prob. Indian Ore Deposits, (Abst.)*, Jadavpur University, pp.35–36.
- Mukherjee, A. D., (1967b).** Trace element study of sulphide ores from Madhan-Kudan and Kolihan sections, Khetri Copper Belt, Rajasthan. *Genetic Prob. Ind. Ore Deposits, (Abst.)*, Jadavpur University, pp. 39.
- Mukherjee, A. D., (1968).** Study of pyrrothites from Madhan-Kudan sections of Khetri Copper Belt, Jhunjhunu district., Rajasthan. In: *Proceedings of the Indian Science Congress, (Abst.)*, 55th session Pt.III.

- Mukherjee, A. D., (1969).** Genesis of the ore-deposits along Madhan-Kudan and Kolihan sections of Khetri Copper belt, Rajasthan. *In: Proceedings of the Indian Science Congress, (Abst.), 56th session Pt.III.*
- Muktinath, Natrajan, W. K. and Mathur, A. C., (1969).** Gossans derived from pyrite-pyrrothite near Saladipura, Sikar district, Rajasthan. *Misc. Publ., 16, Geological Survey of India, pp. 364–368.*
- Mustard, J. F. and Sunshine, J. M., (1999).** Spectral analysis for earth science: Investigations using remote sensing data. *In: Rencz, A. N. (ed) Remote Sensing for the Earth Sciences, Manual of Remote Sensing, 3rd ed, Vol 3, American Society of Photogrammetry and Remote Sensing, Wiley, New York, pp 251–306.*
- Naha, K., Mukhopadhyay, D. K. and Mohanty, R., (1988).** Structural evolution of the rocks of the Delhi Group around Khetri, northeastern Rajasthan. *In: Roy, A.B., (ed.) Precambrians of the Aravalli Mountains, Rajasthan, India. Geological Society of India Memoir, 7, pp. 207–245.*
- Narsimhan, M., (1989).** Compendium on Khetri Copper Belt, Rajasthan – suggestions for further search of ore. MECL.
- Nassau, K., (2000).** Synthetic moissanite: a new man-made jewel. *Current Science, 79(11), pp. 1572–1577.*
- Nicodemus, F. E., (1965).** Directional reflectance and emissivity of an opaque surface. *Applied Optics, 4, pp. 767–774.*
- Ninomiya, Y., Fu, B. and Cudahy, T.J., (2005).** Detecting lithology with advanced spaceborne thermal emission and reflection radiometer (ASTER) multispectral thermal infrared ‘radiance-at-sensor’ data. *Remote Sensing of Environment, 99, pp. 127–139.*
- Paul, P. C., (1968).** Geophysical surveys in the Khetri Copper Belt with emphasis on electromagnetic studies near Paprona and Singhana, Jhunjhunu district, Rajasthan. *Misc. Publ., 13, Geological Survey of India, pp.275–287.*
- Podwysocki, M. H., Segal, D. B. and Abrams, M. J., (1983).** Use of multispectral scanner images for assessment of hydrothermal alteration in the Marysville, Utah mining area. *Economic Geology, 78, pp. 675–687.*
- Potter, R. M. and Rossman, G. E., (1977).** Desert varnish: the importance of clay minerals. *Science, 196, pp. 1446–1448.*
- Prabhakara, C. and Dalu, G., (1976).** Remote sensing of surface emissivity at 9 μ m over the globe. *Journal of Geophysical Research, 81(21), pp. 3719–3724.*
- Prabhakara, C., Dalu, G. and Kunde, V. G., (1974).** Estimation of sea surface temperature from remote sensing in the 11- to 13- μ m window region. *Journal of Geophysical Research, 79(33), pp. 5039–5044.*
- Price, J. C., (1984).** Land surface temperature measurements from the split window bands of the NOAA 7 advanced very high resolution radiometer. *Journal of Geophysical Research, 89, pp. 7231–7237.*
- Qari, M. Y. H. T., (1989).** Lithological mapping and structural analysis of Proterozoic rocks in part of the southern Arabian Shield using Landsat images. *International Journal of Remote Sensing, 10(3), pp.499–503.*
- Ramsey, M. S. and Christensen, P. R., (1998).** Mineral abundance determination: quantitative deconvolution of thermal emission spectra. *Journal of Geophysical Research– Solid Earth, 103, pp. 577–596.*

- Ramsey, M. S., Christensen, P. R., Lancaster, N. and Howard, D. A., (1999).** Identification of sand sources and transport pathways at the Kelso Dunes, California using thermal infrared remote sensing. *Geological Society of America Bulletin*, 111, pp. 646–662.
- Ranjbar, H., Honarmand, M. and Moezifar, Z., (2004).** Application of Crosta technique for porphyry copper alteration mapping, using ETM+ data in the southern part of the Iranian volcanic sedimentary belt. *Journal of Asian Earth Sciences*, 24, pp. 237–243.
- Rao, N. K. and Rao, G. V. U., (1966).** Ore microscopic study of copper ore from Kolihan prospect, Rajasthan. In: *Proceedings of Indian Science Congress, (Abst.)*, 53rd Session, Pt.III.
- Rao, N. K. and Rao, G. V. U., (1968a).** Study of pyrrohtites in the copper ore from Kolihan, Rajasthan. In: *Proceedings of Indian Science Congress, (Abst.)*, 55rd Session, Pt.III.
- Rao, N. K. and Rao, G. V. U., (1968b).** Ore microscopic study of copper ore from Kolihan, Rajasthan, India. *Economic Geology*, 63(3), pp. 277–287.
- Rao, S. K. L., (1971).** Note on the study of gossan samples collected from the copper deposits at Khetri. *Misc. Publ.*, 16, *Geological Survey of India*, pp. 442–450.
- Ray, S. K., (1974).** Structural history of the Saladipura pyrites-pyrrohtite deposits and associated rocks, Khetri Copper Belt, Northeastern Rajasthan. *Journal of Geological Society of India*, 15, pp. 237–238.
- Realmuto, V. J., (1990).** Separating the effects of temperature and emissivity: emissivity spectrum normalization. In: *Proc. 2nd TIMS Workshop, JPL Publication*, Jet Propulsion Lab., California Institute of Technology, Pasadena, California, pp. 90–55.
- Riano, D., Chuvieco, J. S. and Aguado, I., (2003).** Assessment of different topographic corrections in Landsat-TM data for mapping vegetation types. *IEEE Transactions on Geoscience and Remote Sensing*, 41(5), pp.1056–1061.
- Richter, R., (1996).** A spatially adaptive fast atmospheric correction algorithm. *International Journal of Remote Sensing*, 17, pp. 1201–1214.
- Rivard, B., Petroy, S. B. and Miller, J. R., (1993).** Measured effects of desert varnish on the mid-infrared spectra of weathered rocks as an aid to TIMS imagery interpretation. *IEEE Transactions on Geoscience and Remote Sensing*, 31(1), pp. 284–291.
- Roberts, D. A., Yamaguchi, Y. and Lyon, R. J. P., (1985).** Calibration of airborne imaging spectrometer data to percent reflectance using field spectral measurements. In: *Proceedings of the 19th international symposium on remote sensing of environment*, ERIM, Ann Arbor, Michigan, pp. 295–298.
- Roberts, D. A., Yamaguchi, Y. and Lyon, R. J. P., (1986).** Comparison of various techniques for calibration of AIS data. In *Proceedings of the 2nd AIS workshop, JPL Publication, JPL Publ.*, vol. 86–35, California Institute of Technology, Pasadena, California, pp. 21–30.
- Ross, S. D., (1974).** Sulphates and other oxy-anions of group VI. In: *Farmer, V.C. (ed.), The infrared spectra of minerals. Mineralogical Society Monograph*, vol. 4, Mineralogical Society, London.
- Rowan, L. C. and Mars, J. C., (2003).** Lithologic mapping in the Mountain Pass, California area using advanced spaceborne thermal emission and reflection radiometer (ASTER) data. *Remote Sensing of Environment*, 84, pp. 350–366.
- Rowan, L. C., Hook, S. J., Abrams, M. J. and Mars, J. C., (2003).** Mapping hydrothermally altered rocks at Cuprite, Nevada, the advanced spaceborne thermal emission and

- reflection radiometer (ASTER), a new satellite imaging system. *Economic Geology*, 98(5), pp. 1019–1028.
- Rowan, L. C., Goetz, A. F. H. and Ashley, R. P., (1977).** Discrimination of hydrothermally and unaltered rocks in visible and near-infrared images. *Geophysics*, 42, pp. 522–535.
- Rowan, L. C., Crowley, J. K., Schmidt, R. G., Ager, C. M. and Mars, J. C., (2000).** Mapping hydrothermally altered rocks by analyzing hyperspectral image (AVIRIS) data of forested areas in the Southeastern United States. *Journal of Geochemical Exploration*, 68, pp. 145–166.
- Rowan, L. C., Mars, J. C. and Simpson, C. J., (2005).** Lithologic mapping of the Mordor, NT, Australia ultramafic complex by using the advanced spaceborne thermal emission and reflection radiometer (ASTER). *Remote Sensing of Environment*, 99(1-2), pp. 105–126.
- Rowan, L. C., Schmidt, R. G. and Mars, J. C., (2006).** Distribution of hydrothermally altered rocks in the Reko Diq, Pakistan mineralized area based on spectral analysis of ASTER data. *Remote Sensing of Environment*, 104(1), pp.74–87.
- Rowan, L. C., Wetlaufer, P. H., Goetz, A. F. H., Billingsley, F. C. and Stewart, J. H., (1974).** Discrimination of rock types and detection of hydrothemally alerted areas in south-central Nevada by use of computer-enhanced ERTS images. *USGS Prof. Pap*, 883, 35 p.
- Rowan, L. C., Bowers, T. L., Crowley, J. K., Anton-Pacheco, C., Gumiel, P. and Kingston, M. J. (1995).** Analysis of Airborne Visible-Infrared Imaging Spectrometer (AVIRIS) data of the Iron Hill, CO, carbonatite-alkalic igneous rock complex. *Economic Geology*, pp.1966–1982.
- Roy Chowdhary, M. K. and Das Gupta, S. P., (1965).** Ore localization in Khetri copper belt. *Economic Geology*, 60, pp. 69–88.
- Roy Chowdhury, M. K. and Venkatesh, V., (1971).** The regional controls of base-metal mineralization in India. *Misc. Publ.*, 16, Geological Survey of India, pp. 60–68.
- Roy, B. C., (1962).** General report of the Geological Survey of India for the year 1958. *Records Geological Survey of India*, 93, p.32.
- Ruff, S. W., (1998).** Quantitative thermal infrared emission spectroscopy applied to granitoid petrology. *Unpublished Ph.D. thesis*, 234 p., Ariz. State Univ., Tempe.
- Ruiz-Armenta, J. R. and Prol-Ledesma, R. M., (1998).** Techniques for enhancing the spectral response of hydrothermal alteration minerals in thematic mapper images of central Mexico. *International Journal of Remote Sensing*, 19(10), pp. 1981–2000.
- Sabine, C., (1999).** Remote sensing strategies for mineral exploration. In: *A. Rencz (ed.), Remote Sensing for the Earth Sciences – Manual of Remote Sensing*, 3rd Edition. American Society of Photogrammetry and Remote Sensing, John Wiley and Sons, New York, pp. 375–447.
- Sabine, C., Realmuto, V. J. and Taranik, J. V., (1994).** Quantitative estimation of granitoid composition from thermal infrared multispectral scanner (TIMS) data, Desolation Wilderness, northern Sierra-Nevada, California. *Journal of Geophysical Research*, 99, pp. 4261–4271.
- Sabins, F. F., (1999).** Remote Sensing for Mineral Exploration. *Ore Geology Reviews*, 14, pp. 157–183.
- Sakuma, F., Tonooka, H., Ohgi, N. and Ono, H., (2005).** Prediction of the radiometric calibration coefficients of ASTER/TIR. *Proc. SPIE*, 5978, pp. 277-284.

- Salisbury, J. W., (1993).** Mid-infrared spectroscopy: laboratory data. *In Remote Geochemical Analysis: Elemental and Mineralogical Composition*, Pieters, C. M. and Englert, P. A. J., (eds.), Cambridge University Press, Cambridge, pp. 79–98.
- Salisbury, J. W. and D'Aria, D. M., (1992).** Emissivity of terrestrial materials in the 8-14 μm atmospheric window. *Remote Sensing of Environment*, 42, pp. 83–106.
- Sandmeier, S. and Itten, K. I., (1997).** A physical-based model to correct atmospheric and illumination effects in optical satellite data of rugged terrain. *IEEE Transactions on Geoscience and Remote Sensing*, 35(3), pp. 708–717.
- Sarkar, S. C., Bhattacharya P. K. and Mukherjee A. D., (1980).** Evolution of sulphide ores of Saladipura, Rajasthan, India. *Economic Geology*, 75, pp. 1152–1167.
- Sarkar, S. C. and Das Gupta, S., (1980).** Geological setting, genesis and transformation of sulfide deposits in the northern part of Khetri Copper Belt, Rajasthan, India – an outline. *Mineralium Deposita*, 15, pp. 117–137.
- Schanda, E., (1986).** Physical fundamentals of remote sensing. Springer, Berlin Heidelberg New York Tokyo, 187 p.
- Schott, J. R. (1997).** Remote sensing: the image chain approach. Oxford University Press, New York.
- Shepherd, J. D. and Dymond, J. R., (2003).** Correcting satellite imagery for the variance of reflectance and illumination with topography. *International Journal of Remote Sensing*, 24(17), pp. 3503–3514.
- Siegel, B. S., and Gillespie, A. R., (1980).** Remote Sensing in Geology. John Wiley and Sons, New York.
- Sikka, D. B., Royce, J. and Nehru, C. E., (1966a).** Mineralogy and petrology of anthophyllite-cummingtonite bearing rocks, Madhan-Kudan section, Khetri Copper Belt, Rajasthan. *Seminar on Mafic and Ultramafic rocks*, Osmania University.
- Sikka, D. B., Royce, J. and Nehru, C. E., (1966b).** Chlorite from Madhan-Kudan section, Khetri Copper Belt, Rajasthan. *Seminar on Mafic and Ultramafic rocks*, Osmania University.
- Sinha-Roy, S., (1988).** Proterozoic Wilson cycles in Rajasthan. *In: Roy, A.B., (ed.), Precambrians of the Aravalli Mountains, Rajasthan, India, 7, Geological Society of India Memoir*, pp. 95–108.
- Slater, P. N., (1980).** Remote Sensing — optics and optical systems. Addison-Wesley, reading, MN, 575p.
- Sommer, S., Lorcher, G. and Endres, S. (1993).** Application of MAC Europe AVIRIS data to the analysis of various alteration stages in the landmannalaugar hydrothermal area (South Iceland). *In: Summaries of the Fourth Annual JPL Airborne Geoscience Workshop*, Jet Propulsion Laboratory, California Institute of Technology, Pasadena, California, pp. 165–168.
- Swayze, G., Clark, R. N., Kruse, F. A., Sutley, S. and Gallagher, A., (1992).** Ground truthing AVIRIS mineral mapping at Cuprite, Nevada. *In: Summaries of the 3rd Annual JPL Airborne Geoscience Workshop*, Green, R. O., (ed.), JPL Publ. 92-14, Jet Propulsion Laboratory, California Institute of Technology, Pasadena, California, pp.47–49.
- Tanre, D., Deroo, C., Duhaunt, P., Herman, M., Morcrette, J. J. and Perbos, J., (1990).** Description of a computer code to simulate the satellite signal in the solar spectrum: the 5S code. *International Journal of Remote Sensing*, 11(4), pp. 659–668.

- Taranik, J. V., (1988).** Application of aerospace remote sensing technology to exploration for precious metal deposits in the western United States. *In: Bulk Minerable Precious Metal Deposits of the Western United States*, Geological Society of Nevada, Reno, Nev., pp. 551–576.
- Teillet, P. M. and Fedosejevs, G., (1995).** On the dark target approach to atmospheric correction of remotely sensed data. *Canadian Journal Remote Sensing*, 21, pp. 374–387.
- Teillet, P. M., Guindon, B. and Goodenough, D. G., (1982).** On the slope-aspect correction of multispectral scanner data. *Canadian Journal Remote Sensing*, 8(2), pp. 84–106.
- Thome, K. J., Biggar, S. and Takashima, T., (1999).** Algorithm theoretical basis document for ASTER Level 2 B1 - surface radiance and ASTER Level 2 B5 - surface reflectance, 45p.
- Thome, K., Biggar, S. and Slater, P., (2001).** Effects of assumed solar spectral irradiance on intercomparisons of earth-observing sensors. *Proc. SPIE, Sensors, Systems, and Next-Generation Satellites*, Fujisada, H., Luire, J., and Weber, K., (eds.), 4540, pp. 260-269.
- Thome, K., Markham, B., Barker, J., Slater, P., and Biggar, S., (1997).** Radiometric calibration of Landsat. *Photogrammetric Engineering and Remote Sensing*, 63, pp. 835–858.
- Tomasso, I. D. and Rubinstein, N., (2006).** Hydrothermal alteration mapping using ASTER data in the Infiernillo porphyry deposit, Argentina. *Ore Geology Reviews*, 32(1-2), pp. 275–290.
- Tonooka, H., Sakuma, F., Kudoh, M. and Iwafune, K., (2003).** ASTER/TIR onboard calibration status and user-based recalibration. *Proc. SPIE*, 5234, pp. 191-201.
- Torres-Vera, M. A. and Prol-Ledesma, R. M. (2003).** Spectral enhancement of selected pixels in Thematic Mapper images of the Guanajuato district (Mexico) to identify hydrothermally altered rocks. *International Journal of Remote Sensing*, 24(22), pp. 4357–4373.
- Ustin, S. L., Roberts, D. A., Green, R. O., Zomer, R. J. and Garcia, M. (1999).** Remote sensing methods monitor natural resources. *Photonics Spectra*, 33(N10), pp.108–113.
- Van der Meer, F., Vazquez-Torres, M. and Van Dijk, P. M., (1997).** Spectral characterization of ophiolite lithologies in the Troodos ophiolite complex of Cyprus and its potential in prospecting for massive sulphide deposits. *International Journal of Remote Sensing*, 18, pp. 1245–1257.
- Vane, G., Green, R. O., Cherian, T. G., Enmark, H. T., Hansen, E. G. and Porter, W. M., (1993).** The airborne visible/infrared imaging spectrometer (AVIRIS). *Remote Sensing of Environment*, 44, pp.127–143.
- Varadan, V. K. S., and Narasimhan, M., (1971).** Results of Proving operations in madhan-Kudan section, Khetri Copper Belt, Jhunjhunu district, Rajasthan. *Misc. Publ.*, 16, *Geological Survey of India*, pp. 474–496.
- Varma, O. P. and Krishnanunni, K., (1963).** On the origin of copper deposits of Madhan section of Khetri Copper Belt, Rajasthan. *In: Proceedings of Indian Science Congress, (Abst.)*, 50th session, Pt. III, pp. 270.
- Vaughan, R. G., Calvin, W. M. and Taranik, J. T. (2003).** SEBASS Hyperspectral thermal infrared data: surface emissivity measurements and mineral mapping. *Remote Sensing of Environment*, 85, pp. 48–63.

- Vaughan, R. G., Hook, S. J., Calvin, W. M. and Taranik, J. V., (2005).** Surface mineral mapping at Steamboat Springs, Nevada, USA, using multi-wavelength thermal infrared images. *Remote Sensing of Environment*, 99(1-2), pp. 140–158.
- Vermote, E. F., Tanre, D., Denze, J. L., Herman, M. and Morcrette, J. J., (1997).** Second simulation of the satellite signal in the solar spectrum, 6S: an overview. *IEEE Transactions on Geoscience and Remote Sensing*, 35, pp. 675–686.
- Vermote, E., Tanre, D., Denze, J. L., Herman, M. and Morcrette, J. J., (1994).** Second simulation of the satellite signal in the solar spectrum (6S). User guide version 2.
- Vidal, A., (1991).** Atmospheric and emissivity correction of land surface temperatures measured from satellite using ground measurements or satellite data. *International Journal of Remote Sensing*, 12(12), pp. 2449–2460.
- Wan, Z. and Dozier, J., (1989).** Land-surface temperature measurement from space: physical principles and inverse modeling. *IEEE Transactions in Geoscience and Remote Sensing*, 27(3), pp. 268–278.
- Watson, K., (1992a).** Spectral ratio method for measuring emissivity. *Remote Sensing of Environment*, 42, pp. 113–116.
- Watson, K., (1992b).** Two-temperature method for measuring Emissivity. *Remote Sensing of Environment*, 42, pp. 117–121.
- Watson, K., Kruse, F. A. and Hummer-Miller, S., (1990).** Thermal infrared exploration in the Carlin trend, northern Nevada. *Geophysics*, 55(1), pp. 70–79.
- Watson, K., Rowan, L. C., Bowers, T. L., Anton-Pacheco, C., Gumiel, P. and Miller, S. H., (1996).** Lithologic analysis from multispectral thermal infrared data of the alkalic rock complex at Iron Hill, Colorado. *Geophysics*, 61, pp. 706–721.
- White, W. B., (1974).** The carbonate minerals. In: *The Infrared Spectra of Minerals*, Farmer, V. C. (ed.), Mineralogical Society, London, pp. 227–284.
- Wyatt, M. B., Hamilton, V. E., McSween, H. Y. J., Christensen, P. R. and Taylor, L. A., (2001).** Analysis of terrestrial and Martian volcanic compositions using thermal emission spectroscopy: 1. determination of mineralogy, chemistry, and classification strategies. *Journal of Geophysical Research*, 106(E7), pp. 14,711–14,732.
- Yamaguchi, Y. and Naito, C. (2003).** Spectral indices for lithologic discrimination and mapping by using the ASTER SWIR bands. *International Journal of Remote Sensing*, 24(22), pp. 4311–4323.
- Yamaguchi, Y., Kahle, A. B., Tsu, H., Kawakami, T. and Pniel, M., (1998).** Overview of advanced spaceborne thermal emission and reflection radiometer. *IEEE Transactions on Geoscience and Remote Sensing*, 36(4), pp. 1062–1071.
- Zhang, X., Pazner, M. and Duke, N., (2007).** Lithologic and mineral information extraction for gold exploration using ASTER data in the south Chocolate Mountains (California). *ISPRS Journal of Photogrammetry and Remote Sensing*, 62(4), pp.271–282.

Internet Resources

ASTER Websites: <http://asterweb.jpl.nasa.gov> (USA); <http://ersdac.or.jp/eng> (Japan)

Web reference: www.wikipedia.com

Mineral Formulae: www.mindat.com

APPENDIX A

Geochemical Data of Analyzed Samples (ICP-MS trace-metal concentrations)

SampleID	RockType	UNIT	Cu	RSD	Co	RSD	Pb	RSD	Zn	RSD	Mo	RSD	As	RSD
B3/3	Qtzt	ppm	6.437027		1.317133		17.15743		40.89444		2.281656		3.751969	
B3/3S	Qtzt	ppm	35.32562	0.7	2.880525	0.9	30.00755	0.8	58.31899	0.3	1.748369	1.6	25.93478	3.2
B3/4	Phyl	ppm	66.51186		9.994071		17.12055		57.48419		NA		3.952569	
B3/4S	Phyl	ppm	70.58627	3.6	14.66275	5.7	32.84902	6.2	102.4451	7.8	NA		4.084314	0.1
B3/8	Ambl	ppm	13.72817		30.61579		22.22397		137.1262		2.148054		5.843254	
B3/8S	Ambl	ppm	34.46792	1.4	36.71858	1.3	37.0867	0.5	150.3918	1	2.119792	2.2	159.3794	2.3
B3/9	Phyl	ppm	34.23913		11.89526		20.76087		53.36759		NA		16.69565	
B3/9S	Phyl	ppm	80.82387	0.4	30.67906	1.1	34	1.8	62.36791	0.6	NA		43.97847	1.3
B3/14	Ambl	ppm	16.50225		36.36224		21.9757		176.7018		0.800708		2.493124	
B3/14S	Ambl	ppm	57.52507	0.3	41.43182	0.6	40.40415	0.4	196.6404	0.1	2.551875	0.4	221.4912	1.7
B3/15	Ambl	ppm	68.26084		59.69793		22.60537		136.465		1.156971		1.815476	
B3/15S	Ambl	ppm	131.3349	0.7	40.69047	1.7	39.07371	0.7	131.6304	0.3	2.113791	1.4	198.6201	1.1
B3/17	Phyl	ppm	42.21373		32.97843		23.51373		84.97647		NA		22.78431	
B3/17S	Phyl	ppm	51.59136	3.6	59.15521	5.4	40.47348	3.7	123.4499	6	NA		27.82515	3.6
B3/19	Phyl	ppm	1309.747		16.53137		16.00588		98.32353		NA		52.64314	
B3/19S	Phyl	ppm	1399.893	2.8	22.79297	1.6	25.62891	1.8	134.832	4.8	NA		101.3652	2.5
B3/20	Phyl	ppm	943.5214		24.94942		53.24514		66.22957		NA		48.24903	
B3/20S	Phyl	ppm	585.0455	2.6	26.32277	2.4	72.42178	3.3	117.2	7.3	NA		24.35446	2.8
B3/21	Ambl	ppm	12.77519		4.354372		16.17818		59.91796		2.821936		3.413519	
B3/21S	Ambl	ppm	48.97801	0.3	8.880859	0.9	32.59432	0.4	77.24286	0.2	5.019879	1.3	1.414063	1.8
B3/22	Carb	ppm	3.331524		6.627014		13.70235		79.14979		2.970714		1.774067	
B3/22S	Carb	ppm	7.864804	0.5	18.74307	1	37.5165	1.3	124.1779	1.2	4.204464	2.2	3.733333	2.3
B3/23	Sest	ppm	26.81584		11.89307		55.61584		121.1208		NA		3.714851	
B3/23S	Sest	ppm	27.11591	1.1	20.44401	1.3	75.11591	1.7	150.8723	0.3	NA		5.125737	3.9
B3/24	Sest	ppm	25.99802		11.81225		75.96245		74.08498		NA		5.784585	
B3/24S	Sest	ppm	30.81349	3.6	15.34325	4.4	82.29563	3.3	94.99802	6.3	NA		6.539683	0
B3/25	Sest	ppm	26.59843		8.074803		57.44291		162.376		NA		3.202756	
B3/25S	Sest	ppm	49.29528	6.6	10.47441	6.2	70.1063	5.2	591.5236	7.6	NA		9.354331	3
B3/26	Sest	ppm	10.71912		13.98406		23.69721		81.72709		NA		0.958167	
B3/26S	Sest	ppm	10.71912	28.5	13.98406	4.7	23.69721	7.6	81.72709	35.9	NA		0.958167	3.7

B3/27	AmQz	ppm	91.51947		30.23625		19.10809		47.19201		2.24088		1.33996	
B3/27S	AmQz	ppm	81.94174	1.1	30.67591	1.1	33.79421	0.6	109.4244	1.1	4.2876	1	1.170297	2.6
B3/28	AmQz	ppm	20.72574		3.851914		17.11671		46.39846		1.590652		0.781925	
B3/28S	AmQz	ppm	30.8677	0.2	5.005508	0.7	44.77593	0.4	108.6684	0.4	5.796673	1.4	1.994048	2.5
B/1	Ambl	ppm	24.38361		25.82079		43.71439		144.3323		4.638335		1.094488	
B/1S	Ambl	ppm	41.81837	1.2	33.8478	1.4	49.09868	0.1	135.4441	0.8	2.552343	6.8	217.4931	3.1
B/2	Ambl	ppm	17.50653		32.39708		49.35391		164.8414		3.820596		1.757396	
B/2S	Ambl	ppm	14.32072	0.6	40.23415	0.3	45.07676	0.1	171.3053	0.6	5.101528	3	1.94664	2.8
B/3	Scst	ppm	23.20453		17.3933		45.56996		139.6872		3.70502		4.106509	
B/3S	Scst	ppm	42.86566	0.4	23.40891	0.5	40.16043	2.3	98.31693	0.6	2.506033	2.5	146.6548	0.4
B/4	Scst	ppm	39.55652		20.4134		21.91161		69.29205		2.248897		4.803119	
B/4S	Scst	ppm	123.9398	0.7	30.56586	0.1	32.20031	0.6	91.75784	0.5	2.167808	1	190.8221	2.8
B/5	Scst	ppm	58.33399		13.03929		23.00785		76.08841		NA		5.628684	
B/5S	Scst	ppm	94.33006	2.7	21.52652	2.8	40.65619	2.3	83.53831	4.9	0		222.8782	2.1
B/6	Ambl	ppm	12.75972		23.88268		22.16003		102.0508		2.590947		2.28655	
B/6S	Ambl	ppm	30.12623	0.6	29.15334	1.1	36.65478	0.5	105.4619	0.8	2.050855	4.1	234.1843	0.6
B/7	Ambl	ppm	34.033		46.15066		25.15805		101.515		0.769099		2.455621	
B/7S	Ambl	ppm	48.56607	0.5	48.17361	1.2	33.5093	0.2	115.1772	0.4	2.104413	2.6	209.3051	1.6
B/14	Carb	ppm	26.0159	0.9	17.42346	2.1	22.28628	3.1	45.37773	0.7	1.894632	10.1	7.807157	0.5
B/15	Carb	ppm	39.18452	0.2	9.609127	1.5	21.7123	1.7	70.46825	0.6	1.571429	3	7.914683	1.7
B/16	Carb	ppm	45.52174	1.3	78.09289	0.8	22.00198	0.9	62.53162	2.2	1.618577	1.7	9.347826	1.1
B/17	Carb	ppm	37.37773	0.5	92.96223	1.2	23.26441	0.4	77.55467	0.9	1.596421	1	7.369781	0.6
B/18	AmQz	ppm	24.62624	0.6	17.31014	2.6	22.92644	1.8	68.54274	1.2	4.168986	0.5	8.996024	1.1
B/19	AmQz	ppm	75.75944	1.4	6.652087	0.6	29.37376	1	43.34394	0.6	1.449304	3.2	4.182903	1.9
B/20	AmQz	ppm	229.8915	1.3	13.21499	2	43.30572	3.2	62.58383	1.7	3.619329	2	3.998028	0.8
A1	ArQz (type)	ppm	11.9916		1.426842		22.60447		54.56903		4.471085		1.043564	
A1S	ArQz	ppm	47.54595	1	2.398069	0.8	36.73053	0.4	45.70652	0.1	1.921196	3.2	28.12302	0.4
A2	Carb (type)	ppm	NA		NA		NA		NA		NA		NA	
A2S	Carb	ppm	4.77487	1.2	9.030805	0.7	22.14882	0.5	46.02364	0.2	3.256818	0.7	0.52381	1.9
A4	Qtzt (type)	ppm	40.5552		2.058123		27.23812		86.78059		3.632654		1.94664	
A4S	Qtzt	ppm	63.29615	1.3	2.700224	1.8	36.89011	0.7	48.84176	0.8	2.688993	1.9	38.71513	2.2
A5	Scst (type)	ppm	24.26582		16.083		70.15613		107.8123		NA		3.658103	
A5S	Scst	ppm	47.643	2.9	27.20316	2.5	65.98817	1.4	102.2229	4.5	NA		251.7396	2.3
A6	AmQz (type)	ppm	13.43439		23.16542		26.61416		76.25166		4.985789		1.826772	
A6S	AmQz	ppm	33.09672	0.5	21.29088	1.4	23.36976	1	49.7044	0.4	1.678609	0.9	210.8471	1.8
AM1	Ambl (type)	ppm	64.71992	1	47.42012	1.3	35.4497	0.6	127.5759	1.6	1.879684	1.1	0.343195	1.1
GRANIT	Granite	ppm	54.74704	3.9	0.796443	3.5	22.72925	1.5	31.95059	1.6	3.369565	1.2	4.466403	1.4

PEG	Peg (type)	ppm	37.29563	1.7	0.732143	4.4	37.43056	2	29.56746	0.6	4.652778	2.1	3.65873	0.9
T1	Altered MiQz	ppm	379.5527	0.6	4.11332	4.2	24.5825	1.5	29.86282	2.3	3.326044	1.7	0.461233	2.5
T2	Altered MiQz	ppm	6523.44	1.4	54.91287	2.8	34.7604	2.1	143.8792	0.8	3.138614	1.9	0.550495	2.1
T3	Altered MiQz	ppm	69993.55	0.9	1.562624	0.7	45.96024	1.1	22.75547	2.2	4.487078	2.5	0.614314	1.7
T5	Altered MiQz	ppm	285.9724	6.4	4.73622	2.2	28.56693	1.1	27.62402	1.3	3.031496	0	0.474409	0.7
T6	Altered MiQz	ppm	74.38171	3.1	1.385686	2	20.92445	0.4	14.44732	1	1.248509	5	0.314115	2.5
Su1	Altered MiQz	ppm	2021.837	0.5	78.42043	1.4	28.63654	1.4	47.22004	1.4	4.996071	2.5	2.184676	6.3
Su2	Altered MiQz	ppm	388.7435	0.5	3.795229	3.2	24.97217	1.7	46.09543	2.1	5.491054	2.4	0.298211	1.7
Su3	Altered MiQz	ppm	35.91929	3.9	9.787402	1.6	22.27559	2	197.7559	0.7	2.71063	1	0.403543	1
Su4	Altered MiQz	ppm	174.86	0.9	32.43787	1.7	34.643	1.8	29.32544	1.8	2.913215	1.4	0.589744	2.2
Su5	Altered Peg	ppm	531.2711	0.7	65.02947	0.8	35.18861	0.8	47.02554	0.7	3.212181	4.3	7.072692	2
Su6	Altered MiQz	ppm	157.7008	1.3	5.769685	2.1	42.9626	0.4	46.8878	1.4	1.352362	1.4	0.572835	1.1
Su7	Altered MiQz	ppm	1989.992	1.5	4.207101	0.7	27.12032	1.3	53.67061	1.4	7.404339	0.7	4.019724	0.8
Su8	Altered MiQz	ppm	786.7183	0.9	276.5258	0.7	25.25198	1.1	43.87103	0.5	3.732143	2.9	2.628968	1.4
Su9	Altered Carb	ppm	35.30452	1.9	13.44401	2.5	21.25344	1.9	69.03733	1.5	3.373281	1.6	0.345776	1.3
Su10	Altered MiQz	ppm	514.7854	0.5	39.00591	1.9	42.06102	1.5	43.46457	0.6	2.809055	2.3	0.744094	0.7
Su11	Altered MiQz wC	ppm	191.6102	1.65	37.11024	1.7	32.18504	2.9	41.27953	0.5	11.05709	3.7	0.801181	1.7
Su12	Altered MiQz	ppm	48.91749	1.7	7.227898	1.7	35.01375	0.8	33.25737	1.6	7.801572	1.6	0.304519	0.7
Su13	Altered MiQz	ppm	6543.109	0.4	157.8221	0.8	27.24308	1.6	81.29842	1	8.132411	1.1	14.70158	0.7
Su14	Altered MiQz	ppm	6599.42	0.4	556.2387	1.4	33.34911	2.2	76.3215	2.3	1.783037	6.3	8.224852	1.2
Su15	Altered MiQz wC	ppm	1502.757	0.9	222.9427	1.3	27.03557	2.3	79.96245	0.8	5.644269	1	2.250988	1.5
AMQ	AmQz	ppm	529.1443	0.5	11.26482	2.2	35.90316	1.1	29.43874	2.5	0.788538	6.7	0.284585	0.9
G1	Gossan	ppm	NA		NA		NA		NA		NA		NA	
G2	Gossan	ppm	1333.227	1.7	6.813121	1.9	1363.276	2.4	474.0676	1.2	11.39761	1.6	27.0159	0.3
Tu1	Qtzt	ppm	162.5536	2.4	100.1647	2	40.15278	4.2	156.746	2.4	2.134921	5	7.595238	2.3
BUGR1	Granite	ppm	89.89412	1.2	4.233333	1.7	42.63725	1.2	24.49216	1.1	2.092157	2.3	5.14902	0.9
BANDHA	ArQz	ppm	42.18738	1	2.676529	1.4	22.72978	0.9	27.5286	1.6	2.418146	3.9	3.001972	2.2
Z1	Ambl	ppm	NA		NA		NA		NA		NA		NA	
Z2	AmQz	ppm	NA		NA		NA		NA		NA		NA	
Z3	Carb	ppm	NA		NA		NA		NA		NA		NA	
BDOW	Altered Carb	ppm	2043.968	1.8	1.285149	15.2	43.08119	1.4	87.83366	1.7	2.778218	0.7	5.223762	0.7
BDOW1	Altered Carb	ppm	5470.085	0.8	8.615842	2.7	26.7901	0.7	245.8099	0.8	1.748515	0.8	15.8198	2.2
X2	Soil (Babai Helipad)	ppm	NA		NA		NA		NA		NA		NA	

Qtzt=Quartzite, AmQz=Amphibole Quartzite, ArQz=Arkosic Quartzite, MiQz=Micaceous Quartzite, wC=Graphitic, Ambl=Amphibolite, Carb=Carbonate, Scst=Schist, Phyl=Phyllite, Peg=Pegmatite, NA = Not Analyzed

APPENDIX B

Specifications of Johns Hopkins University (JHU) Spectral Library Data

Two different kinds of spectral data are present in this library. Spectra of minerals were measured in bidirectional (actually biconical) reflectance (see Salisbury et al., 1991). These spectra, recorded from 2.08-25 micrometers, cannot be used to quantitatively predict emissivity because only hemispherical reflectance can be used in this way. This means that the library spectra do not provide a quantitative measure of the infrared radiation scattered in all directions, as do the relatively few directional hemispherical reflectance spectra described in the next section. However, laboratory and field measurements have repeatedly shown that biconical reflectance measurements may be used qualitatively to predict emissivity (Lyon, 1964; Hunt and Vincent, 1968, Bartholomew et al., 1989). That is, the shape of the spectral curves in JHU mineral library can be used to predict the shapes, but not the absolute intensities, of spectral curves in emittance. Thus, these mineral spectra may be used qualitatively in spectral searches of remote sensing data to identify unknown minerals.

All other spectral data (for rocks, vegetation, *etc.*) were measured in directional hemispherical reflectance. Under most conditions, the infrared portion of these data can be used to calculate emissivity using Kirchhoff's Law ($\epsilon = 1-R$), which has been verified by both laboratory and field measurements (Salisbury et al., 1994; Korb et al., 1996).

The apparently seamless reflectance spectra from 0.4 to 14 micrometers of rocks and soils were generated using two different instruments, both equipped with integrating spheres for measurement of directional hemispherical reflectance, with source radiation impinging on the sample from a centerline angle 10 degrees from the vertical.

Unless specified otherwise, all visible/near-infrared (VNIR) spectra were recorded using a Beckman Instruments model UV 5240 dual-beam, grating spectrophotometer at the U.S. Geological Survey, Reston, Virginia, USA. The data were obtained digitally and corrected for both instrument function and the reflectance of the Halon reference using standards traceable to the U. S. National Institute of Science and Technology. Measurements of such standards indicate an absolute reflectance accuracy of ± 3 percent. Wavelength accuracy was checked using a holmium oxide reference filter and is reproducible and accurate to within $\pm 0.004 \mu\text{m}$ (one digitization step). Spectral resolution is variable because the Beckman uses an automatic slit program to keep the energy on the detector constant. The result is a spectral bandwidth typically $< 0.008 \mu\text{m}$ over the 0.4 to 2.5 μm spectral range measured, but slightly larger at the two extremes of the range of the lead sulfide detector (0.8-0.9 μm and 2.4-2.5 μm). This instrument has a grating change at 0.8 μm , which sometimes results in a spectral artifact (either a small, sharp absorption band, or a slight offset of the spectral curve) at that wavelength.

Two similar instruments were used to record reflectance in the infrared range (2.08 to 15 μm). Briefly, both are Nicolet FTIR spectrophotometers and both have a reproducibility and absolute accuracy better than $\pm 1\%$ over most of the spectral range. Early measurements of igneous rocks with an older detector were noisy in the 13.5-14 μm range and do not quite meet this standard. Because FTIR instruments record spectral data in frequency space, both wavelength accuracy and spectral resolution are given in wavenumbers (cm^{-1}). Wavelength accuracy of an interferometer type of instrument is limited by the spectral resolution, which yields a data point every 2 wavenumbers for these measurements. The X-axis was changed from wavenumbers to micrometers for all of these data before the infrared segment was joined to the VNIR data from the Beckman.

Spectra from the Beckman and the FTIR instruments were compared in the overlap range of 2.08-2.5 μm . If the difference was greater than 3%, measurements were repeated.

Typically, however, the agreement was within the 3% limit. In view of the greater accuracy of the FTIR measurements, any small discrepancy between the two spectral segments was resolved by adjusting the Beckman data to fit the reflectance level of the segment measured by the FTIR instruments.

References

- Korb, A. R., Dybwad, P., Wadsworth, W., and Salisbury, J. W., (1996).** Portable FTIR spectrometer for field measurements of radiance and emissivity. *Applied Optics*, 35, pp. 1679-1692.
- Salisbury, J. W., D'Aria, D. M., and Jarosevich, E., (1991a).** Midinfrared (2.5-13.5 micrometers) reflectance spectra of powdered stony meteorites. *Icarus*, 92, pp. 280-297.
- Salisbury, J. W., Wald, A., and D'Aria, D. M., (1994).** Thermal-infrared remote sensing and Kirchhoff's law 1. Laboratory measurements. *Journal of Geophysical Research*, 99, pp. 11,897-11,911.
- Salisbury, J. W., Walter, L. S., Vergo, N., and D'Aria, D. M., (1991b).** Infrared (2.1-25 micrometers) Spectra of Minerals. Johns Hopkins University Press, 294 p.

APPENDIX C

Results of ASTER TIR Spectral Modeling

A. For the full resolution emissivity spectra of quartz monzonite within the wavelength range 8-12 μm , on application of different curve-fitting options the following results were obtained:

General rule: Robust = Bisquare; Algorithm (where applicable) = Levenberg Marquardt

1. Gauss 3-term

General model:

$$f(x) = a \cdot \exp(-((x-b1)/c1)^2/2)$$

where x is normalized by mean 9.538 and std 1.008

Coefficients (with 99% confidence bounds):

$$a = 6.861 \quad (-777.2, 790.9)$$

$$b1 = 104.2 \quad (-5584, 5792)$$

$$c1 = 50.88 \quad (-1340, 1442)$$

Goodness of fit:

SSE: 0.3718

R-square: 0.3727

Adjusted R-square: 0.3663

RMSE: 0.04367

2. Gauss 4-term

General model:

$$f(x) = a \cdot \exp(-((x-b1)/c1)^2/2) + d1$$

where x is normalized by mean 9.538 and std 1.008

Coefficients (with 99% confidence bounds):

$$a = -0.1596 \quad (-0.1671, -0.1521)$$

$$b1 = -0.4217 \quad (-0.4438, -0.3996)$$

$$c1 = 0.9325 \quad (0.8791, 0.986)$$

$$d1 = 0.9451 \quad (0.9372, 0.9529)$$

Goodness of fit:

SSE: 0.01454

R-square: 0.9755

Adjusted R-square: 0.9751

RMSE: 0.008658

3. Poly2

Linear model Poly2:

$$f(x) = p1 \cdot x^2 + p2 \cdot x + p3$$

where x is normalized by mean 9.538 and std 1.008

Coefficients (with 99% confidence bounds):

$$p1 = 0.0212 \quad (0.01777, 0.02464)$$

$$p2 = 0.04237 \quad (0.03916, 0.04559)$$

$$p3 = 0.8134 \quad (0.8088, 0.818)$$

Goodness of fit:

SSE: 0.05437

R-square: 0.9083

Adjusted R-square: 0.9073

RMSE: 0.0167

4. Poly3

Linear model Poly3:

$$f(x) = p1*x^3 + p2*x^2 + p3*x + p4$$

where x is normalized by mean 9.538 and std 1.008

Coefficients (with 99% confidence bounds):

$$p1 = -0.02007 \quad (-0.02233, -0.01782)$$

$$p2 = 0.03865 \quad (0.0364, 0.04091)$$

$$p3 = 0.06781 \quad (0.06345, 0.07217)$$

$$p4 = 0.806 \quad (0.8033, 0.8087)$$

Goodness of fit:

SSE: 0.01815

R-square: 0.9694

Adjusted R-square: 0.9689

RMSE: 0.009672

5. Poly4

Linear model Poly4:

$$f(x) = p1*x^4 + p2*x^3 + p3*x^2 + p4*x + p5$$

where x is normalized by mean 9.538 and std 1.008

Coefficients (with 99% confidence bounds):

$$p1 = 0.008726 \quad (0.005339, 0.01211)$$

$$p2 = -0.03564 \quad (-0.03941, -0.03188)$$

$$p3 = 0.03056 \quad (0.02181, 0.03932)$$

$$p4 = 0.08232 \quad (0.07597, 0.08866)$$

$$p5 = 0.8066 \quad (0.8023, 0.811)$$

Goodness of fit:

SSE: 0.03147

R-square: 0.9469

Adjusted R-square: 0.9458

RMSE: 0.01277

6. Fourier1

General model Fourier1:

$$f(x) = a0 + a1*\cos(x*w) + b1*\sin(x*w)$$

where x is normalized by mean 9.538 and std 1.008

Coefficients (with 99% confidence bounds):

$$a0 = 0.8603 \quad (0.8517, 0.869)$$

$$a1 = -0.05563 \quad (-0.06393, -0.04733)$$

$$b1 = 0.05062 \quad (0.04714, 0.05411)$$

$$w = 1.289 \quad (1.175, 1.402)$$

Goodness of fit:

SSE: 0.04047

R-square: 0.9317

Adjusted R-square: 0.9307

RMSE: 0.01444

7. Fourier2

General model Fourier2:

$$f(x) = a0 + a1*\cos(x*w) + b1*\sin(x*w) + \\ a2*\cos(2*x*w) + b2*\sin(2*x*w)$$

where x is normalized by mean 9.538 and std 1.008

Coefficients (with 99% confidence bounds):

$$\begin{aligned} a_0 &= 0.8537 (0.7517, 0.9557) \\ a_1 &= -0.0377 (-0.1539, 0.07851) \\ b_1 &= 0.05827 (0.01208, 0.1045) \\ a_2 &= -0.01255 (-0.0289, 0.003797) \\ b_2 &= -0.003437 (-0.04012, 0.03325) \\ w &= 1.124 (0.6003, 1.647) \end{aligned}$$

Goodness of fit:

$$\begin{aligned} \text{SSE} &: 0.04974 \\ \text{R-square} &: 0.9161 \\ \text{Adjusted R-square} &: 0.9139 \\ \text{RMSE} &: 0.0161 \end{aligned}$$

B. For the ASTER-resampled 5-band emissivity spectra of quartz monzonite within the wavelength range 8-12 μm , on application of different curve-fitting options the following results were obtained:

General rule: Robust = Bisquare; Algorithm (where applicable) = Levenberg Marquardt

1. Gauss 3-term

General model:

$$f(x) = a \cdot \exp(-((x-b_1)/c_1)^2/2)$$

where x is normalized by mean 9.59 and std 1.297

Coefficients (with 99% confidence bounds):

$$\begin{aligned} a &= 4.122 (-1230, 1238) \\ b_1 &= 45.44 (-8610, 8701) \\ c_1 &= 25.57 (-2419, 2471) \end{aligned}$$

Goodness of fit:

$$\begin{aligned} \text{SSE} &: 0.001709 \\ \text{R-square} &: 0.8909 \\ \text{Adjusted R-square} &: 0.7818 \\ \text{RMSE} &: 0.02923 \end{aligned}$$

2. Gauss 4-term

General model:

$$f(x) = a \cdot \exp(-((x-b_1)/c_1)^2/2) + d_1$$

where x is normalized by mean 9.59 and std 1.297

Coefficients (with 99% confidence bounds):

$$\begin{aligned} a &= -0.1547 (-2.056, 1.746) \\ b_1 &= -0.519 (-7.779, 6.741) \\ c_1 &= 0.8807 (-13.33, 15.09) \\ d_1 &= 0.9516 (-0.995, 2.898) \end{aligned}$$

Goodness of fit:

$$\begin{aligned} \text{SSE} &: 0.0001316 \\ \text{R-square} &: 0.9916 \\ \text{Adjusted R-square} &: 0.9664 \\ \text{RMSE} &: 0.01147 \end{aligned}$$

Important Note: The startpoint selection greatly affected the gaussian 4-term fit. A startpoint of 0.01 for coefficient 'a' generated the best fit output.

3. Poly2

Linear model Poly2:

$$f(x) = p_1 \cdot x^2 + p_2 \cdot x + p_3$$

where x is normalized by mean 9.59 and std 1.297

Coefficients (with 99% confidence bounds):

$$\begin{aligned} p1 &= 0.02969 \quad (-0.1759, 0.2352) \\ p2 &= 0.04905 \quad (-0.07512, 0.1732) \\ p3 &= 0.8266 \quad (0.638, 1.015) \end{aligned}$$

Goodness of fit:

SSE: 0.0008646
R-square: 0.9448
Adjusted R-square: 0.8896
RMSE: 0.02079

4. Poly3

Linear model Poly3:

$$f(x) = p1*x^3 + p2*x^2 + p3*x + p4$$

where x is normalized by mean 9.59 and std 1.297

Coefficients (with 99% confidence bounds):

$$\begin{aligned} p1 &= -0.03256 \quad (-1.134, 1.069) \\ p2 &= 0.04392 \quad (-0.9329, 1.021) \\ p3 &= 0.08226 \quad (-1.15, 1.314) \\ p4 &= 0.8239 \quad (0.0407, 1.607) \end{aligned}$$

Goodness of fit:

SSE: 0.0001788
R-square: 0.9886
Adjusted R-square: 0.9543
RMSE: 0.01337

5. Poly4

R-square: 1.0

The fit uses all available datapoints, and hence marks the upper limit for the 5-band ASTER TIR dataset

6. Fourier1

General model Fourier1:

$$f(x) = a0 + a1*\cos(x*w) + b1*\sin(x*w)$$

where x is normalized by mean 9.59 and std 1.297

Coefficients (with 99% confidence bounds):

$$\begin{aligned} a0 &= 0.8661 \quad (0.3001, 1.432) \\ a1 &= -0.04684 \quad (-0.8497, 0.7561) \\ b1 &= 0.05045 \quad (-0.3471, 0.448) \\ w &= 1.622 \quad (-14.77, 18.01) \end{aligned}$$

Goodness of fit:

SSE: 0.000119
R-square: 0.9924
Adjusted R-square: 0.9696
RMSE: 0.01091

7. Fourier2

Did not converge; as at least 6 datapoints are needed to calculate 6 coefficients.

APPENDIX D

ASTER Data Defects

1. **SWIR crosstalk** (Iwasaki and Tonooka, 2005): In remote sensing, the term ‘crosstalk’ refers to the phenomenon of the leakage of optical or electrical signals from one band to other bands. ASTER data suffers from the problem of crosstalk in the SWIR bands. ASTER SWIR crosstalk was not recognized until the satellite was launched and the acquired images were analyzed. In ASTER SWIR instrument (focal plane of each band is shown in fig. 1), since band 4 exists in 1.6 μm region, it has stronger reflection as well as wider band width than bands 5-9, which makes radiation incident on band 4 about 5 times stronger than that of the other bands. ‘Ghosts’ are generated when the strong incident radiation into band 4 goes through an interference filter, reflects near the border of the detector surface, circuit surface and interference filter, and reaches detectors of other bands after going through multiple reflection on filter or the detector surface. In case of the SWIR detector, areas simultaneously observed by its bands slightly differ one by one and it does not fall on exactly the same point on the ground because of which the ghosts shift in the along-track direction.

A method for the correction of this defect has been suggested (Iwasaki and Tonooka, 2005) and has been implemented in the form of a software tool available from ERSDAC of Japan. The basis of the algorithm lies in assuming that the phenomenon is reduced by subtracting the along-track-shifted blurred image of band 4 from each image of the affected bands. In the actual software, the crosstalk image is calculated by two dimensional Gaussian distribution with amplitude, and x and y standard deviations as parameters. Default values of the parameters are shown in Table-1 (for version 1.0 of the software). Amplitudes of band 5, 6, 7, 8 and 9 are estimated to be 9-15, 3-6, 2-4, 3-6 and 9-15%, respectively.

Table-1 Default Crosstalk parameters (ver 1.0) (Iwasaki and Tonooka, 2005)

Band	Parameter (default)		
	a	σ_x	σ_y
5	0.09	28	20
6	0.03	30	26
7	0.02	34	30
8	0.03	30	26
9	0.09	28	20

a: amplitude of leaked incident radiation of band 4 to other bands (%)

σ_x, y : σ of Gaussian function (cross-track and along-track direction) (pixel)

2. **Filter scratch in SWIR** (Iwasaki and Oyama, 2005): Figure-1 shows the focal plane configuration of the SWIR. Each band is arranged in parallel on the focal plane, and the time for which each band observes the specific ground target is different. Since the cross-track position of the specific detectors is different for each band due to the Earth's rotation, the degenerated area becomes distinct upon band ratioing (see examples of this effect in the decorrelation images, spectral indices, RBD images, and band ratio images of the study area, shown in Chapter 8). The faint scratch on the interference filter (fig. 1), which is attached on the detectors, causes these artifacts. This problem was found before the launch because the gain coefficient is larger at the scratched area, indicating that the scratch on the filter causes back scattering of the incident light, and hence larger gain is needed for compensation. This scratch also causes forward scattering, making the image under the affected area slightly blurred.

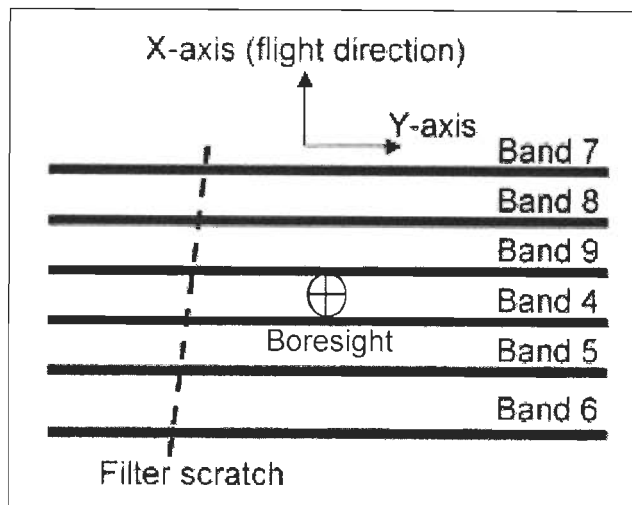


Figure-1 Focal plane array of ASTER SWIR detectors and effects of SWIR crosstalk and filter scratch; discussion in text

3. **Inflight straylight in VNIR and SWIR** (Iwasaki and Oyama, 2005): In addition to the ghost phenomenon (unwanted radiation) due to crosstalk in SWIR, the image of band 4 also suffers from straylight that originates from its focal plane. The straylight components are also observed in VNIR images. The reflection from the dichroic filter used for spectral separation in VNIR is found to be the reason for the straylight. In band 4 (SWIR) the straylight originates from an aluminum film under the detector, which is employed to double the sensitivity of the PtSi-CCD detector. The detectors are arranged in the cross-track direction, and thus the stray light component is larger in the horizontal direction. The radiometric sensitivity is determined during ground calibration using an integrating sphere, but the on-axis (inflight) straylight influences the detected incident light; necessitating its

correction to ensure radiometric accuracy. Iwasaki and Oyama (2005) have suggested a simple method, which is equivalent to the van Cittert method of deconvolution (van Cittert, 1931), for the correction of this effect. The straylight components in their method were estimated using the image obtained during lunar observation, and the improvement in image quality was examined after straylight correction.

4. ***Inflight straylight in TIR*** (Tonooka, 2005): In the thermal infrared (TIR) region, straylight is caused by emission from an outside source or the instrument itself, and is often investigated in laboratory testing. In the case of the five TIR bands of ASTER, straylight testing on the ground was conducted by viewing a heated panel through a hole bored in a water-cooled panel, and the results showed that straylight effects were at most less than 0.4% of the input radiance (JAROS, 1996). However, straylight characterization for TIR sensors is generally less accurate than for reflective sensors, mainly because zero-radiation targets cannot be prepared for laboratory testing unlike the case for reflective sensors, though ray-tracking methods can be used for TIR sensors as well as for reflective sensors. Thus, straylight effects on TIR sensors are not always well-known in comparison with reflective sensors.

The digital number (DN) obtained by each ASTER/TIR band is radiometrically calibrated by a quadratic function with three radiometric calibration coefficients (RCCs) for each of 50 detectors. Since the ASTER/TIR instrument has a single onboard blackbody and cannot view deep space, only the offset coefficient can be adjusted by viewing the blackbody before every Earth observation. The blackbody is set to 270 K for the offset adjustment. The gain coefficient is periodically measured by long-term calibration (LTC) in which the blackbody is observed at 270, 300, 320, and 340 K. Not every LTC result is applied to the level-1 products. Recent studies have demonstrated that the level-1 products contain a calibration error caused by delays in updating the gain coefficients in the level-1 software (Tonooka et al., 2003; Tonooka et al., 2005). A user-based recalibration method has been developed to correct for these delay-induced errors (Tonooka et al., 2003), and implemented to determine the recalibration coefficients for the 5 TIR bands, and can be found from the ERSDAC website (www.ersdac.or.jp) for a specified acquisition date and radiometric database version ID for a particular scene.

5. ***Geolocation error***: Geographic coordinates for each ASTER scene are stored within the image data files. Latitude/longitude values are assigned to certain image pixels, based on knowledge of spacecraft attitude and pointing, instrument pointing, and line of sight

vectors for each detector. Over the last 5 years, several small errors that can affect the accuracy of these coordinates have been detected, *viz.*:

1. An error in the value of the Earth rotation rate caused a geolocation error in the daytime scenes of up to 300 m near the poles, but less than 100 m below 70 degrees latitude.
2. Not compensating for nutation of the earth's rotation axis caused an acquisition-date-dependent longitude error of up to 200 m.
3. Altitude compensation: ASTER coordinates are projected to the WGS-84 ellipsoid, rather than the real earth's surface. In the most extreme case for areas of high relief (Tibet, for example), and maximum off-nadir viewing, the relief displacement in longitude can be 400 m. Compensation requires a digital elevation model.

References

- Iwasaki, A., and Oyama, E., (2005).** Correction of stray light and filter scratch blurring for ASTER Imagery. *IEEE Transactions on Geoscience and Remote Sensing*, 43(12), pp. 2763–2768.
- Iwasaki, A., and Tonooka, H., (2005).** Validation of a crosstalk correction algorithm for ASTER/SWIR. *IEEE Transactions on Geoscience and Remote Sensing*, 43(12), pp. 2747–2751.
- Tonooka, H., and Iwasaki, A., (2003).** Improvement of ASTER/SWIR crosstalk correction. *Proceedings of SPIE*, 5234, pp. 168–179.